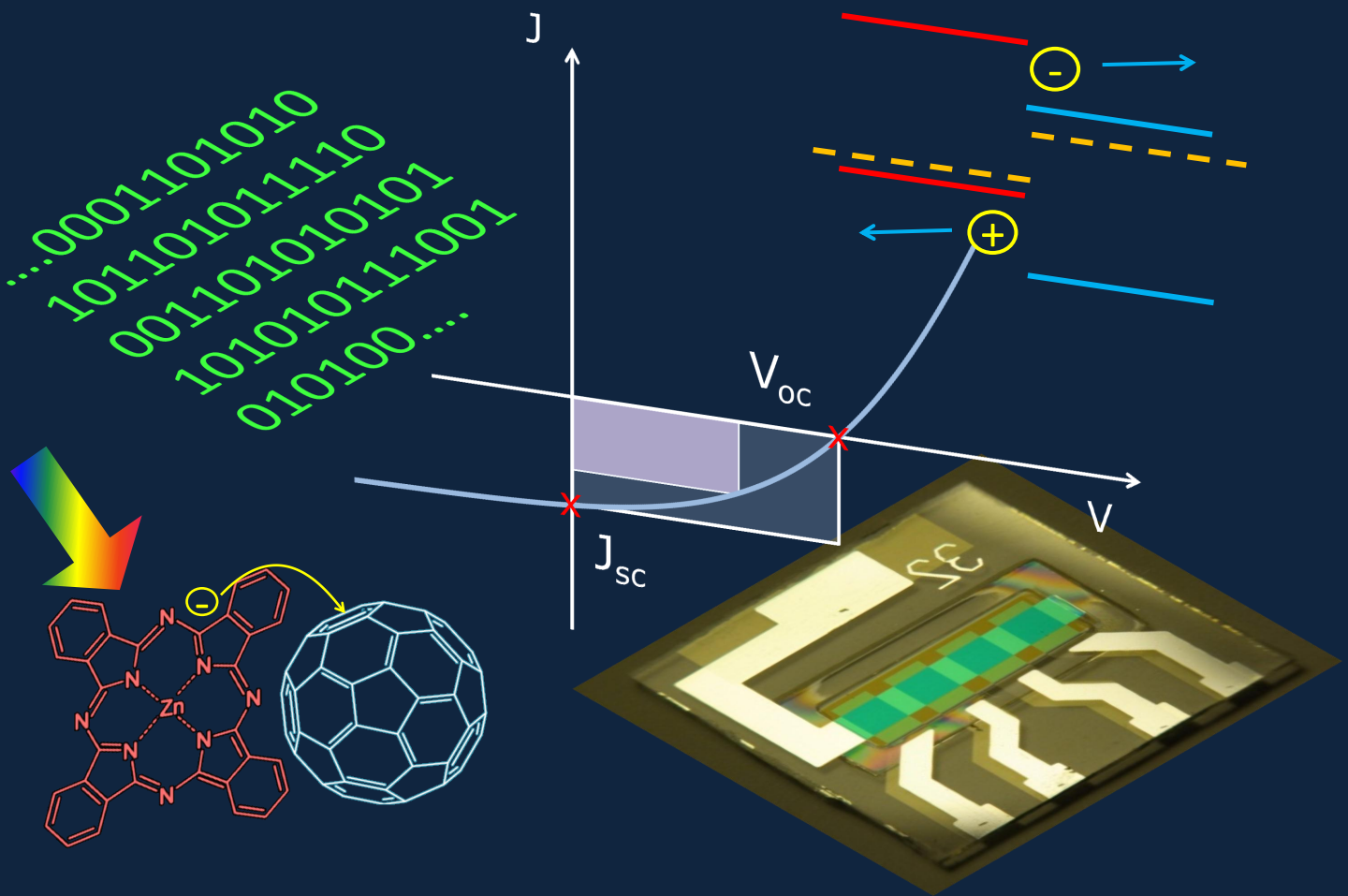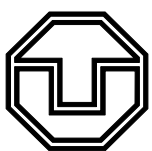# Wolfgang Tress

Device Physics of Organic Solar Cells

Drift-Diffusion Simulation in Comparison with Experimental Data of Solar Cells Based on Small Molecules

TECHNISCHE UNIVERSITÄT DRESDEN

RLS REINER LEMOINE STIFTUNG

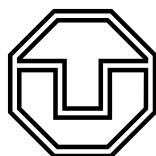A book on the device physics of organic solar cells is planned to be published based on this work.

Institut für Angewandte Photophysik
Fachrichtung für Physik
Fakultät für Mathematik und Naturwissenschaften
der Technischen Universität Dresden

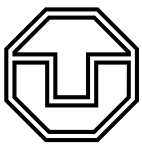# Device Physics of Organic Solar Cells

Drift-Diffusion Simulation in Comparison with Experimental Data of Solar Cells Based on Small Molecules

Dissertation
zur Erlangung des akademischen Grades
Doktor der Naturwissenschaften
(Doctor rerum naturalium)

vorgelegt von
Wolfgang Tress
geboren am 15.08.1981 in Münsingen

REINER LEMOINE
STIFTUNG

Dresden 2011

Gefördert durch

Abstract

This thesis deals with the device physics of organic solar cells. Organic photovoltaics (OPV) is a field of applied research which has been growing rapidly in the last decade leading to a current record value of power-conversion efficiency of 10 percent. One major reason for this boom is a potentially low-cost production of solar modules on flexible (polymer) substrate. Furthermore, new application are expected by flexible or semitransparent organic solar cells. That is why several OPV startup companies were launched in the last decade.

Organic solar cells consist of hydrocarbon compounds, deposited as ultrathin layers (some tens of nm) on a substrate. Absorption of light leads to molecular excited states (excitons) which are strongly bound due to the weak interactions and low dielectric constant in a molecular solid. The excitons have to be split into positive and negative charges, which are subsequently collected at different electrodes. An effective dissociation of excitons is provided by a heterojunction of two molecules with different frontier orbital energies, such that the electron is transfered to the (electron) acceptor and the positive charge (hole) remains on the donor molecule. This junction can be realized by two distinct layers forming a planar heterojunction or by an intermixed film of donor and acceptor, resulting in a bulk heterojunction. Electrodes are attached to the absorber to collect the charges by providing an ohmic contact in the optimum case.

This work focuses on the electrical processes in organic solar cells developing and employing a one-dimensional drift-diffusion model. The electrical model developed here is combined with an optical model and covers the diffusion of excitons, their separation, and the subsequent transport of charges. In contrast to inorganics, charge-carrier mobilities are low in the investigated materials and charge transport is strongly affected by energy barriers at the electrodes.

The current-voltage characteristics (J-V curve) of a solar cell reflect the electrical processes in the device. Therefore, the J-V curve is selected as means of comparison between systematic series of simulation and experimental data. This mainly qualitative approach allows for an identification of dominating processes and provides microscopic explanations.

One crucial issue, as already mentioned, is the contact between absorber layer and electrode. Energy barriers lead to a reduction of the power-conversion efficiency due to a decrease in the open-circuit voltage or the fill factor by S-shaped J-V curve (S-kink), which are often observed for organic solar cells. It is shown by a systematic study that the introduction of deliberate barriers for charge-carrier extraction and injection can cause such S-kinks. It is explained by simulated electrical-field profiles why also injection barriers lead to a reduction of the probability for charge-carrier extraction. A pile-up of charge carriers at an extraction barrier is confirmed by measurements of transient photocurrents. In flat heterojunction solar cells an additional reason for S-kinks is found in an imbalance of electron and hole mobilities. Due to the variety of reasons for S-kinks, methods and criteria for a distinction are proposed. These include J-V measurements at different temperatures and of samples with varied layer thicknesses.

Most of the studies of this this work are based on experimental data of solar cells compris-

ing the donor dye zinc phthalocyanine and the acceptor fullerene C_{60}. It is observed that the open-circuit voltage of these devices depends on the mixing ratio of ZnPc:C_{60}. A comparison of experimental and simulation data indicates that the reason is a changed donor-acceptor energy gap caused by a shift of the ionization potential of ZnPc. A spatial gradient in the mixing ratio of a bulk heterojunction is also investigated as a donor(acceptor)-rich mixture at the hole(electron)-collecting contact is supposed to assist charge extraction. This effect is not observed, but a reduction of charge-carrier losses at the "wrong" electrode which is seen at an increase in the open-circuit voltage.

The most important intrinsic loss mechanism of a solar cell is bulk recombination which is treated at the example of ZnPc:C_{60} devices in the last part of this work. An examination of the dependence of the open-circuit voltage on illumination intensity shows that the dominating recombination mechanism shifts from trap-assisted to direct recombination for higher intensities. A variation of the absorption profile within the blend layer shows that the probability of charge-carrier extraction depends on the locus of charge-carrier generation. This results in a fill factor dependent on the absorption profile. The reason is an imbalance in charge-carrier mobilities which can be influenced by the mixing ratio.

The work is completed by a simulation study of the influence of charge-carrier mobilities and different recombination processes on the *J-V* curve and an identification of a photo-shunt dominating the experimental linear photocurrent-voltage characteristics in reverse bias.

Kurzfassung

Diese Dissertation beschäftigt sich mit der Physik organischer Solarzellen. Die organische Photovoltaik ist ein Forschungsgebiet, dem in den letzten zehn Jahren enorme Aufmerksamkeit zu Teil wurde. Der Grund liegt darin, dass diese neuartigen Solarzellen, deren aktueller Rekordwirkungsgrad bei 10 Prozent liegt, ein Potential für eine kostengünstige Produktion auf flexiblem (Polymer)substrat aufweisen und aufgrund ihrer Vielfältigkeit neue Anwendungsbereiche für die Photovoltaik erschließen.

Organische Solarzellen bestehen aus ultradünnen (einige 10 nm) Schichten aus Kohlenwasserstoffverbindungen. Damit der photovoltaische Effekt genutzt werden kann, müssen die durch Licht angeregten Molekülzustände zu freien Ladungsträgern führen, wobei positive und negative Ladung an unterschiedlichen Kontakten extrahiert werden. Für eine effektive Trennung dieser stark gebundenden lokalisierten angeregten Zustände (Exzitonen) ist eine Grenzfläche zwischen Molekülen mit unterschiedlichen Energieniveaus der Grenzorbitale erforderlich, sodass ein Elektron auf einem Akzeptor- und eine positive Ladung auf einem Donatormolekül entstehen. Diese Grenzschicht kann als planarer Heteroübergang durch zwei getrennte Schichten oder als Volumen-Heteroübergang in einer Mischschicht realisiert werden. Die Absorberschichten werden durch Elektroden kontaktiert, wobei es für effiziente Solarzellen erforderlich ist, dass diese einen ohmschen Kontakt ausbilden, da ansonsten Verluste zu erwarten sind.

Diese Arbeit behandelt im Besonderen die elektrischen Prozesse einer organischen So-

larzelle. Dafür wird ein eindimensionales Drift-Diffusionsmodell entwickelt, das den Transport von Exzitonen, deren Trennung an einer Grenzfläche und die Ladungsträgerdynamik beschreibt. Abgesehen von den Exzitonen gilt als weitere Besonderheit einer organischen Solarzelle, dass sie aus amorphen, intrinsischen und sehr schlecht leitfähigen Absorberschichten besteht.

Elektrische Effekte sind an der Strom-Spannungskennlinie (I-U) sichtbar, die in dieser Arbeit als Hauptvergleichspunkt zwischen experimentellen Solarzellendaten und den Simulationsergebnissen dient. Durch einen weitgehend qualitativen Vergleich können dominierende Prozesse bestimmt und mikroskopische Erklärungen gefunden werden.

Ein wichtiger Punkt ist der schon erwähnte Kontakt zwischen Absorberschicht und Elektrode. Dort auftretende Energiebarrieren führen zu einem Einbruch im Solarzellenwirkungsgrad, der sich durch eine Verringerung der Leerlaufspanung und/oder S-förmigen Kennlinien (S-Knick) bemerkbar macht. Anhand einer systematischen Studie der Grenzfläche Lochleiter/Donator wird gezeigt, dass Energiebarrieren sowohl für die Ladungsträgerextraktion als auch für die -injektion zu S-Knicken führen können. Insbesondere die Tatsache, dass Injektionsbarrieren sich auch negativ auf den Photostrom auswirken, wird anhand von simulierten Ladungsträger- und elektrischen Feldprofilen erklärt. Das Aufstauen von Ladungsträgern an Extraktionsbarrieren wird durch Messungen transienter Photoströme bestätigt. Da S-Knicke in organischen Solarzellen im Allgemeinen häufig beobachtet werden, werden weitere Methoden vorgeschlagen, die die Identifikation der Ursachen ermöglichen. Dazu zählen I-U Messungen in Abhängigkeit von Temperatur und Schichtdicken. Als eine weitere Ursache von S-Knicken werden unausgeglichene Ladungsträgerbeweglichkeiten in einer Solarzelle mit flachem Übergang identifiziert und von den Barrierefällen unterschieden.

Weiterer Forschungsgegenstand dieser Arbeit sind Mischschichtsolarzellen aus dem Donator-Farbstoff Zink-Phthalozyanin ZnPc und dem Akzeptor Fulleren C_{60}. Dort wird beobachtet, dass die Leerlaufspannung vom Mischverhältnis abhängt. Ein Vergleich von Experiment und Simulation zeigt, dass sich das Ionisationspotenzial von ZnPc und dadurch die effektive Energielücke des Mischsystems ändern. Zusätzlich zu homogenen Mischschichten werden Solarzellen untersucht, die einen Gradienten im Mischungsverhältnis aufweisen. Die Vermutung liegt nahe, dass ein hoher Donatorgehalt am Löcherkontakt und ein hoher Akzeptorgehalt nahe des Elektronenkontakts die Ladungsträgerextraktion begünstigen. Dieser Effekt ist in dem hier untersuchten System allerdings vergleichsweise irrelevant gegenüber der Tatsache, dass der Gradient das Abfließen bzw. die Rekombination von Ladungsträgern am "falschen" Kontakt reduziert und somit die Leerlaufspannung erhöht.

Der wichtigste intrinsische Verlustmechanismus einer Solarzelle ist die Rekombination von Ladungsträgern. Diese wird im letzten Teil der Arbeit anhand der ZnPc:C_{60} Solarzelle behandelt. Messungen der Leerlaufspannung in Abhängigkeit von der Beleuchtungsintensität zeigen, dass sich der dominierende Rekombinationsprozess mit zunehmender Intensität von Störstellenrekombination zu direkter Rekombination von freien Ladungsträgern verschiebt. Eine gezielte Variation des Absorptionsprofils in der Absorberschicht zeigt, dass die Ladungsträgerextraktionswahrscheinlichkeit vom Ort der Ladungsträgergeneration abhängt. Dieser Effekt wird hervorgerufen durch unausgeglichene Elektronen- und Löcher-

beweglichkeiten und äußert sich im Füllfaktor.

Weitere Simulationsergebnisse bezüglich des Einflusses von Ladungsträgerbeweglichkeiten und verschiedener Rekombinationsmechanismen auf die *I-U* Kennlinie und die experimentelle Identifikation eines Photoshunts, der den Photostrom in Rückwärtsrichtung unter Beleuchtung dominiert, runden die Arbeit ab.

Publications

The following publications resulted from the work of this thesis:

Journal Papers

M. Riede, T. Mueller, W. Tress, R. Schueppel, and K. Leo. *Small Molecule Solar Cells - Status and Perspectives.* Nanotechnology **19**, 424001 (2008)

S. Olthof, W. Tress, R. Meerheim, B. Lüssem, and K. Leo. *Photoelectron spectroscopy study of systematically varied doping concentrations in an organic semiconductor layer using a molecular p-dopant.* Journal of Applied Physics **106**, 103711 (2009)

J. Meiss, M. Hermenau, W. Tress, C. Schuenemann, F. Selzer, M. Hummert, J. Alex, G. Lackner, K. Leo, and M. Riede. *Tetrapropyl-tetraphenyl-diindenoperylene derivative as new green absorber for high-voltage stable organic solar cells.* Physical Review B **83**, 165305 (2011)

W. Tress, A. Petrich, M. Hummert, M. Hein, K. Leo, and M. Riede. *Imbalanced mobilities causing S-shaped I-V curves in planar heterojunction organic solar cells.* Applied Physics Letters **98**, 063301 (2011)

W. Tress, S. Pfuetzner, K. Leo, and M. Riede. *Open circuit voltage and I-V curve shape of ZnPc:C_{60} solar cells with varied mixing ratio and hole transport layer.* Journal of Photonics for Energy **1**, 011114 (2011)

W. Tress, K. Leo, and M. Riede. *Influence of hole-transport layers and donor materials on open-circuit voltage and shape of I-V curves of organic solar cells.* Advanced Functional Materials **21** (11), 2140 - 2149 (2011)

W. Tress, K. Leo, and M. Riede. *Effect of concentration gradients in ZnPc:C_{60} bulk heterojunction organic solar cells.* Solar Energy Materials and Solar Cells **95** (11), 2981 - 2986 (2011)

W. Tress, K. Leo, and M. Riede. *Optimum mobility, contact properties, and the open-circuit voltage of organic solar cells: A drift-diffusion simulation study.* Physical Review B **85**, 155201 (2012)

M. Tietze, W. Tress, S. Pfuetzner, S. Olthof, M. Riede, and K. Leo. *The correlation of the open-circuit voltage and the ionization potential of ZnPc:C_{60} solar cells with varied mixing ratio*, in preparation

W. Tress, A. Merten, M. Furno, K. Leo, and M. Riede. *Influence of charge carrier generation profile on organic solar cell performance*, in preparation

W. Tress, S. Corvers, K. Leo, and M. Riede. *Dominating recombination processes in ZnPc:C_{60} solar cells*, in preparation

Conference Contributions (first author only)

Wolfgang Tress, Moritz Riede, and Karl Leo. *Electrical modelling of organic solar cells - A first comparison study with experimental data.* DPG Spring Meeting 2009, Dresden, Germany, 22.-27. March 2009, Poster

Wolfgang Tress, Moritz Riede, and Karl Leo. *Electrical modelling of organic solar cells - A first comparison study with experimental data.* European Spring School 2009 on Supramolecular Organized Nanostructured Materials for Optoelectronic Applications, Peñiscola, 19.-25. April 2009, Poster

Wolfgang Tress, Mauro Furno, Karl Leo, and Moritz Riede. *Modelling and simulation of multilayer organic solar cells - Crucial parameters for device performance.* 24th European Photovoltaic Solar Energy Conference and Exhibition, Hamburg, Germany, September 2009, Poster

Wolfgang Tress, Moritz Riede, and Karl Leo. *Influence of injection and extraction barriers on organic solar cell performance.* DPG Spring Meeting 2010, Regensburg, Germany, 21.-26. March 2010, Talk

Wolfgang Tress, Markus Hummert, Annette Petrich, Karl Leo, and Moritz Riede. *Charge transport in organic solar cells - Imbalanced mobilities as reason for S-kinks in flat heterojunction devices.* Gordon Research Conference, South Hadley, MA, USA, July 2010, Poster

Wolfgang Tress, Mauro Furno, Markus Hummert, Annette Petrich, Karl Leo, and Moritz Riede. *Simulation of the current-voltage characteristics of organic solar cells.* 10th International Conference on Numerical Simulation of Optoelectronic Devices (NUSOD), Atlanta, GA, USA, 6.-9. September 2010, Talk

Wolfgang Tress, David Wynands, Karl Leo, and Moritz Riede. *Role of drift and diffusion in organic solar cells measured by transient photocurrents - S-kink devices as extreme cases.* DPG Spring Meeting 2011, Dresden, Germany, 13.-18. March 2011, Talk

Wolfgang Tress, Mauro Furno, André Merten, Karl Leo, and Moritz Riede. *Influence of the exciton generation profile within the active layer on organic solar cell performance.* DPG Spring Meeting 2011, Dresden, Germany, 13.-18. March 2011, Poster

Wolfgang Tress, David Wynands, Toni Mueller, Ronny Timmreck, Martin Hermenau, Moritz Riede, and Karl Leo. *Fundamental Processes and Limits of Small Molecule Organic Solar Cells.* MRS Spring Meeting 2011, San Francisco, CA, USA, 25.-29. April 2011, Invited Talk

Wolfgang Tress, Zhe Li[1], Christopher R. McNeill[1], Karl Leo, and Moritz Riede. *Role of drift and diffusion in organic solar cells measured by transient photocurrents.* E-MRS Spring Meeting 2011, Nice, France, 9.-13. May 2011, Poster

Wolfgang Tress, Jan Meiss, David Wynands, Mauro Furno, Moritz Riede, and Karl Leo. *Small molecule OPV at the Dresden cluster: status and research topics.* 4th International Symposium on Flexible Organic Electronics (ISFOE11), Thessaloniki, Greece, July 2011, Invited Talk

Wolfgang Tress, Mauro Furno, André Merten, Karl Leo, and Moritz Riede. *Influence of the exciton generation profile within the active layer on organic solar cell performance.* 26th European Photovoltaic Solar Energy Conference and Exhibition, Hamburg, Germany, 5.-9. September 2009, Poster

Wolfgang Tress, Steef Corvers, Karl Leo, and Moritz Riede. *Distorted S-Shaped I-V Curves of Organic Solar Cells in Experiment and Simulation: Rules and Methods for Distinction of the Reasons and Ways of Avoidance.* MRS Fall Meeting 2011, Boston, MA, USA, December 2011, Invited Talk

Invited Seminar Talks

Influence of Hole Transport Layers and Donor Materials on Open-Circuit Voltage and (S-)shape of I-V Curves of Organic Solar Cells. Stanford University, Stanford, CA, USA, 6. August 2010

The I-V Curve of Organic Solar Cells – where Simulation meets Experiment. NREL, Golden, CO, USA, 26. August 2010

Device Physics of Organic Solar Cells – a Drift-Diffusion Approach. Helmholtz-Zentrum Berlin, Berlin, Germany, 31. May 2011

Influence of Contacts and the Mixing Ratio of ZnPc:C_{60} Solar Cells on the Open-Circuit Voltage and Fill Factor. University of Linköping, Linköping, Sweden, 10. November 2011

Fill Factor and Open-Circuit Voltage of Organic Solar Cells: Role of Energy Barriers at the Contacts and Recombination. Imperial College, London, UK, 17. November 2011

Organic p-i-n Solar Cells – The Role of Energy Levels in Absorber and Charge Transport Layers. Princeton University, Princeton, NJ, USA, 5. December 2011

---

[1]Department of Physics, Cavendish Laboratory, University of Cambridge, J. J. Thomson Avenue, Cambridge CB3 0HE, United Kingdom.

Contents

III Summary and Outlook   293

12 Main Results   295

13 Further Analyses and Possible Extensions of the Simulation   305

IV Appendix   313

A Lists   315

B Simulation data   321

C Experimental data   333

Bibliography   335

Acknowledgments - Danksagung   361

Chapter 1

Introduction

1.1 Energy supply and climate change

Photovoltaics and in particular organic photovoltaics are fields of applied research whose support by the society is based on the insight that this technology can significantly contribute to worldwide electricity generation by conversion of sun light into electrical energy. Apart from wind, photovoltaics is the most promising among the emerging renewable energy technologies due to its large theoretical potential. This potential is estimated to be 6,000 times larger than the current primary energy demand of $\approx$11,000 million tons of oil equivalent (≈ 14 TW mean power) [Fig. 1.1(a)]. The technical potential of solar energy conversion is also very large and can be illustrated by a rough estimation showing that an area of less than $6\,\%$ of the Sahara[1] would be enough to satisfy the world energy demand with today's technologies. However, this estimation neglects distribution and storage issues. Currently, energy is provided to a large extent ($> 80\,\%$) by fossil fuels [2].

Mainly two issues arise from fossil-powered energy conversion. First, fossil resources are finite and their distribution on the earth surface is very unbalanced. Second, burning fossil fuels is accompanied by carbon dioxide (CO_2) emissions which result in climate change, because CO_2 acts as a greenhouse gas. The greenhouse effect is caused by the atmosphere reflecting (infrared) heat radiation back to the surface of the earth. This effect is essential for the development of life on earth, because the radiation balance between the sun, atmosphere, and the earth surface yields a mean earth-surface temperature of $\approx 14\,°C$ which would be $-15\,°C$ [3] without this effect. The temperature was very stable in the last millennia and the global temperature distribution created climate zones with their characteristic flora and fauna, which are very sensitive to temperature. An increased greenhouse gas concentration in the atmosphere disturbs this equilibrium and leads to a higher global temperature, which has been observed within the past decades [Fig. 1.1(b)]. In recent years it became broad consensus in science and politics that this rise in temperature is anthropogenic and correlates with the amount of CO_2 in the atmosphere which has increased significantly compared to pre-industrial times [Fig. 1.1(b)] [4].

---

[1]assumptions: area $9 \times 10^6\,km^2$, mean irradiation $285\,W/m^2$ [1], power conversion efficiency $10\,\%$.
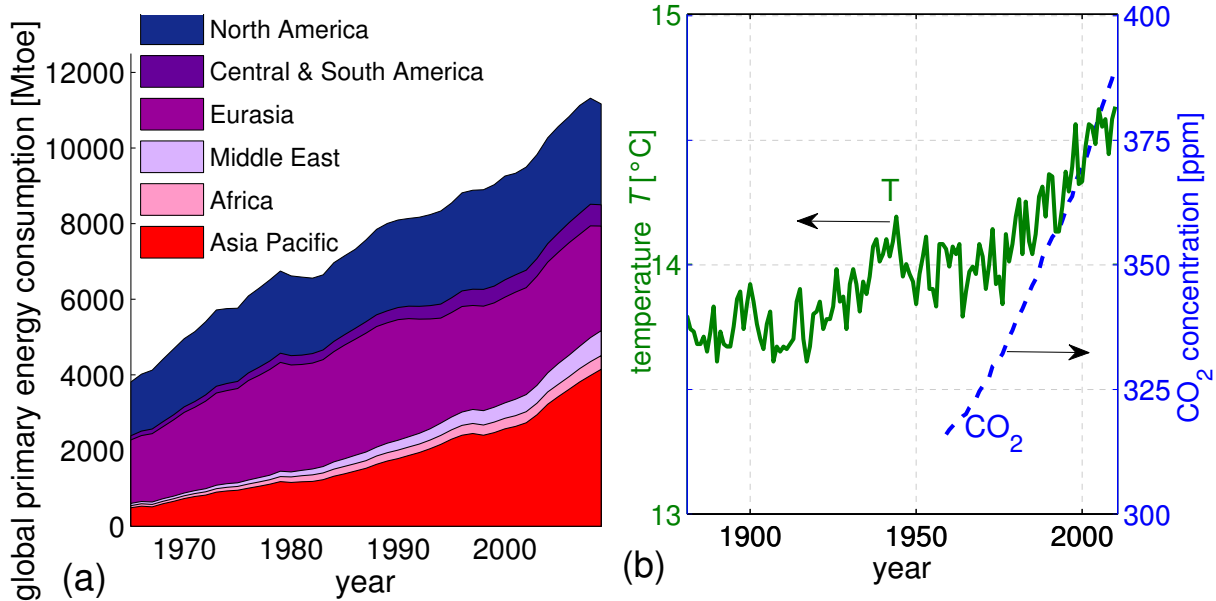
Figure 1.1: (a) Development of the regional distribution of primary energy demand in million tons of oil equivalent (1 Mtoe $\approx$ 42 PJ). Source: BP [5]. (b) Annual mean CO_2 concentration in the atmosphere from measurements at the Mauna Loa Observatory, Hawaii [6]. In pre-industrial times the CO_2 concentration was 280 ppm [4]. The development of the mean global temperature in the last century is also plotted [7]. Both curves describe a significant increase.

The impacts of global warming are very severe and potential consequences are a rise in sea level due to an expansion of the oceans and the melting of on-shore ice shields. Furthermore, desertification and water shortages are becoming more likely and even collapses of whole ecosystems and changes of ocean currents being essential for the global balance of living nature are expected. The last point represents one of the many non-linear effects which are hard to predict, but contain a very high risk of a rapid change. Based on the elaborations of several researchers, summarized in the latest IPCC report [4], these issues are discussed by policy makers on international summits on climate change. In 1992 during the Earth Summit in Rio de Janeiro, the United Nations Framework Convention on Climate Change (UNFCCC) was initiated with the aim of reducing the impacts of global warming. On a succeeding summit the Kyoto Protocol (1997) was adopted which contains reduction targets of CO_2 emissions. However, it is not ratified on a global scale. Also the common 2-degree-target was only recently officially agreed on in Cancun (2010). This target demands for a maximum global mean temperature rise of 2 °C compared to pre-industrial times. This number was chosen because the consequences of a rise of mean earth surface temperature by two degrees are supposed to be in a manageable range. For a higher increase in temperature non-linear effects become more likely.

To fulfill this 2 °C target (which is not very likely given the current trajectory) the energy

sector has to be decarbonized completely within the next three decades. Renewable energies are the most sophisticated and most developed kind of technology which can contribute to a quick decarbonization. The main obstacle are the electricity-generation costs which are until now higher than those of conventional energy technologies. This is, however, to a large extent due to the fact that the external costs of the conventional technologies are not internalized. This means that the long-term damages caused by these technologies have to be burdened by the broad world population.

This cost problem was recognized by the German parliament, having initiated a feed-in tariff in 2000, where all electricity customers support in their electricity bill the introduction of renewable energies for electricity generation. On the one hand, supporting photovoltaics in Germany is a very expensive way of reducing carbon-dioxide emissions and the feed-in tariff has shown the problem of oversubsidizing and the risk of favoring non-economic concepts also on the long run. On the other hand, this concept was very successful in bringing costs down, which significantly reduced the time until photovoltaics will be an economic and CO_2-saving way of electricity generation in southern countries. It lead to installed capacities of 28 GW (wind) [8] and 17 GW (photovoltaics) [9] at a total installed electrical capacity of 160 GW [10] in Germany in 2010. These data are nominal capacities, which represent peak values (W_p) in the case of the renewable technologies. This means that solar and wind energy can already now provide from 0 to 50 % of the instantaneous power[2] dependent on the weather, season, and demand. This shows that grid extensions and/or an increase in the electricity-storage capacity will become very important for a further extension of renewable energy technologies. As these measures introduce additional costs and drops in the overall energy conversion efficiency, they require very cost-effective solar and wind energy harvesting units.

In the first half of 2011, renewable energy technologies had a share of 20 % (3.5 % photovoltaics) in Germany's electricity generation [12]. The costs, especially of photovoltaics, have decreased significantly, following a learning curve due to economy of scale and technological improvements. Today, photovoltaics is already economical in off-grid systems and attractive for self-consumption in southern countries (grid parity) [13].

1.2 Development of (organic) photovoltaics

The first silicon solar cell with an efficiency of around 4 % was invented in the Bell Laboratories in 1953, six years after the discovery of the p-n junction by William B. Shockley, Walther H. Brattain, and John Bardeen (Nobel price for the transistor in 1956). Five years after the invention of the solar cell, the first solar module was used in space. In the 1960s commercial modules were available for terrestrial use and showed cell efficiencies of 14 %. At the end of the seventies an annual production of 500 kW$_p$ was reached. The modules powered remote telecommunication systems (e.g. in the Australian Outback) with an estimated cost of 100 EUR/W$_p$. Prices decreased due to incentives during the oil crisis in

---

[2]In Germany the typical Sunday peak load around noon is approximately 60 GW [11].

the seventies, the German 1000 and 100,000 "Dächer (roofs) Programm" in the 1990s, and the feed-in tariff starting in the year 2000. The prices are still decreasing, e.g., on the German market from $5\,\mathrm{EUR/W_p}$ in 2006 to $2\,\mathrm{EUR/W_p}$ in 2011 (system price for roof top installation). The cumulated, globally installed capacity rose to $39\,\mathrm{GW}$ in 2010 [14].

The working principle of solar cells is based on the (inner) photoelectric ("photovoltaic") effect, first discovered by the physicist Alexandre E. Becquerel (1839) at electrolytic cells [15]. Photoconductivity was shown for selenium by Willoughby Smith in 1873 [16], and the outer photoelectric effect was systematically investigated by Heinrich Hertz and Wilhelm Hallwachs in 1886 [17]. In 1904 the physicist and Nobel Prize laureate Phillip Lenard discovered the role of the frequency of light regarding the energy of the emitted electrons [18]. His results were theoretically explained by Albert Einstein in 1905 [19] who received the Nobel Prize for this work in 1921.

First investigations of the electronic properties of organic materials, which are based on hydrocarbon molecules, were reported for anthracene at the beginning of the 20th century [20–22]. In the 1970s (semi)conducting polymers were discovered [23]. Allan J. Heeger, Alan G. MacDiarmid, and Hideki Shirakawa received the Nobel Prize in chemistry in 2000 for the discovery and development of these conductive polymers. In the 1980s high electroluminescence efficiencies were reached which lead to the development of organic light emitting diodes (OLEDs) as first broad application of organic electronics [24, 25]. Today, OLEDs can be found in flat panel displays [26] and are about to become an alternative light source with a high efficiency and a pleasant irradiation spectrum [27].

The first photocurrent was observed also in anthracene by Kalman and Pope in 1959 [28]. In the following two decades, several organic photovoltaic devices were reported. They consisted of a metal-organic junction which showed efficiencies of less than $0.1\,\%$ (for a contemporary review, see Ref. [29]). The first major breakthrough in the deployment of organic semiconductors in solar cells has been made by Ching Tang who published the donor-acceptor solar cell and reported an efficiency of 1% [30]. Tang's cell comprised a junction of two materials, one electron- and the other hole accepting and transporting (a perylene tetracarboxylic derivative and copper phthalocyanine). The second major step was the invention of the bulk heterojunction which is a mixed layer of donor and acceptor, fabricated by a co-deposition of the two molecules. This approach was firstly reported in Refs. [31, 32]. An overview of the development of organic photovoltaics can be found in Ref. [33].

After these achievements the amount of publications rose nearly exponentially in the last decade. Efficiencies recently reached $10\,\%$ (Fig. 1.2) [34, 35], also pushed by several spin-offs and established companies turning focus on this topic. The reason for this boom can be found in the expected high potential of organic semiconductors, which are either (vacuum or solution processed) small molecules or (cast or printed) polymers.

The main advantages of organic solar cells are:

- Cheap production by high-throughput roll-to-toll printing or other low-temperature deposition techniques;

- High versatility and efficiencies due to the toolbox of organic chemistry;
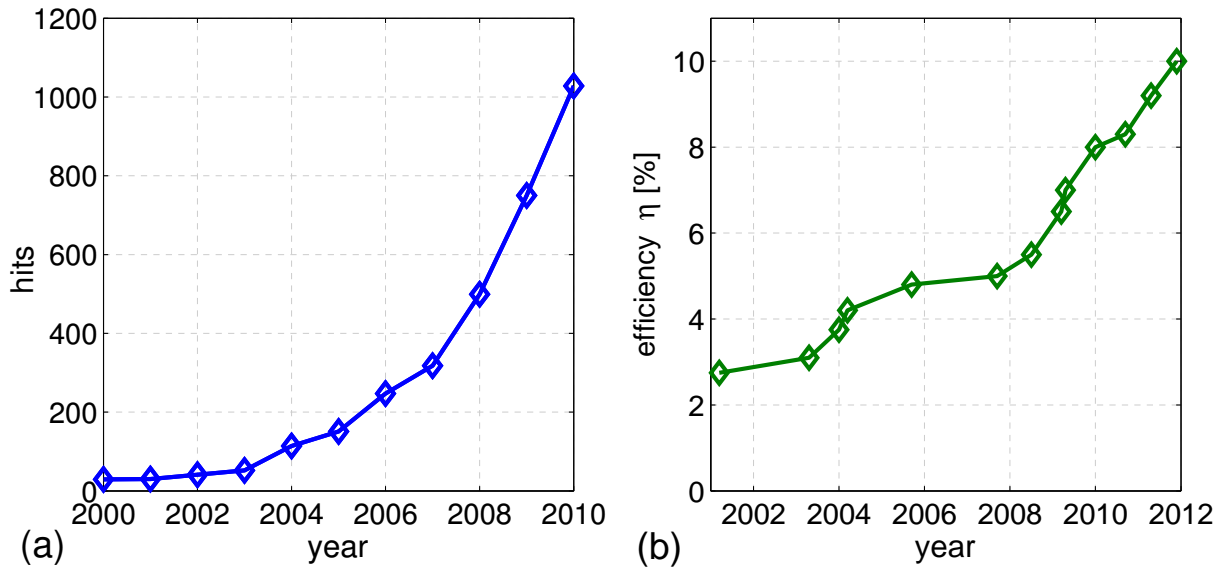
Figure 1.2: (a) Hits of WebOfScience search with Topic=("organic photovoltaic" OR "organic photovoltaics" OR "organic solar cell" OR "organic solar cells" OR "polymer solar cell" OR "polymer solar cells") performed on 14.09.2011. (b) Development of laboratory organic-solar-cell power-conversion efficiencies during the last decade where most of the established technologies did not show significant improvements in efficiencies except multi-junction concentrator cells. Source: NREL [36] and Ref. [34].

- Non-toxicity and low consumption (a few grams per m^2) of abundant absorber materials;

- New products containing and merging with photovoltaics, e.g., in architecture due to a tunability of color and (semi-)transparency;

- Application in mobile devices due to mechanical flexibility and low weight;

- Low energy payback times due to a fabrication process avoiding expensive purification methods or energy-intensive steps;

- High energy yield due to a good low-light performance and a positive temperature coefficient of the efficiency.

The main challenge will be to realize these potential properties within the next few years. Here, the main difficulty is the competition with established technologies. As already mentioned, crystalline silicon photovoltaics showed a tremendous reduction of production costs in the last decade. Furthermore, the developments in inorganic thin-film photovoltaics reveal the potential of these technologies to cover several of the mentioned advantages of

organic photovoltaics as well, e.g., mechanical flexibility. That is why an increase in solar-cell efficiencies (and later in module efficiencies) beyond 10. . . 12 % is essential for a success of organic photovoltaics. Nevertheless, in the long term and for the TW scale, only silicon and organic photovoltaics meet the criteria of material abundance.

Although first modules consisting of organic solar cells are on the market (e.g. as chargers of mobile devices in bags [37]), the physics of these devices is far from being completely understood. However, a further increase in efficiencies, which is required to become competitive, increasingly demands for a detailed understanding of the processes limiting the device efficiency. Whereas in the first years, research was mainly based on trial-and-error experiments and simple material screening, in recent years modeling and simulations became more important (e.g. large-scale computational screening projects [38]). However, often the results obtained by theory are far from experimental results.

This work covers both, simulation and experiment. It employs the results of drift-diffusion simulations to qualitatively explain experimental findings. It shows to what extent this kind of simulation technique can be helpful for reproducing and interpreting experimental data.

1.3 Structure and scope of this thesis

The scope of this thesis is to give the interested reader a comprehensive insight into the device physics of organic solar cells. It is an attempt to bridge the gap between experimentalists and theoreticians or computational physicists. The grouping of the chapters in three main parts (I-III) distinguishes the main scope of the chapters belonging to a respective part.

Part I containing Chapters 2 to 4 gives a broad introduction to the topic of organic solar cells. The main focus is the working principle of devices. It is elaborated starting from general considerations of solar-thermal energy conversion and semiconductor physics in the first chapter. Based on these principles, organic solar cells are discussed in the subsequent chapter. The basics of organic chemistry are reviewed to understand the main semiconductive properties of organic molecules. Ideas from literature are not only reported but also evaluated. The last chapter of this part describes the electronic models and the algorithms implemented in the developed simulation tool.

Part II (Chapters 5 to 11) contains the main results which have been obtained during this work. Each chapter of this part is organized in a way that the reader can follow it without having read all previous chapters. Although elaborated on experimental and simulation data of selected material systems, most of the conclusions of this part are of general nature. Thus, they may be helpful for scientists who are dealing with the interpretation of current-voltage data of organic solar cells in general. The first chapters (5-7) of this part contain discussions on the origin and limiting processes regarding the open-circuit voltage and give explanations for distorted *J-V* curves which follow S-shaped characteristics. The subsequent chapters (8-10) contain detailed investigations on the most common small-molecule solar-cell system based on zinc phthalocyanine (ZnPc) and the

fullerene C_{60}. In particular, the effect of the mixing ratio, a gradient in the active layer, and the role of the absorption profile are discussed. The results provide a detailed picture of the interplay between energy levels, charge carrier mobilities, and recombination mechanisms in ZnPc:C_{60} solar cells. The last chapter (11) of Part II provides a possible explanation for the linear photocurrent-voltage behavior of organic solar cells under reverse bias.

Part III (Chapters 12 and 13) contains a summary of the general results of the chapters of the second part. This summary is arranged in a catalog of guidelines on how to interpret experimental J-V curves from the drift-diffusion point of view. The last chapter gives an outlook including first exemplary studies on the simulation of tandem cells. In conclusion, the limits and the potentials are presented which drift-diffusion simulations provide for the description of further effects in organic solar cells. The list of possible subjects to investigate illustrates that this work has to be seen as the beginning of a detailed investigation of multilayer small-molecule organic solar cells by drift-diffusion simulations.

Part I

Basics

Chapter 2

Photovoltaic Energy Conversion

Since this thesis is dealing with the simulation of organic solar cells, it is very important to review basic principles of solar thermal energy conversion, which lead to fundamental limits of the conversion efficiency. Therefore, this chapter addresses the steps of energy conversion and its thermodynamic limits. Furthermore, basics of semiconductor physics are described which are necessary to understand the working principle of a solar cell and the fundamentals of the simulation. Both the gradient and the splitting of electrochemical potentials are identified as the origin of driving forces for electrical current. This chapter follows mainly the ideas by Würfel [3] and focuses on his ideal solar-cell structure to convert thermal radiation into chemical and subsequently into electrical energy. Later, the p-n junction as mostly employed realization of a solar cell is discussed. Finally, the Shockley-Queisser limit for band-edge absorbers and approaches to go beyond it are reviewed.

2.1 Fundamentals of solar thermal energy conversion

2.1.1 The solar spectrum

The energy potentially harvested by a solar energy converter is the thermal radiation from the sun. The spectral energy flux density (spectral irradiance) $dj_\mathrm{E}/d\hbar\omega$ from the sun at distance earth, the so-called solar spectrum, is plotted in Fig. 2.1 (blue line) as a function of energy expressed by the light frequency $\nu(\omega)$ multiplied by Planck's constant $h(\hbar)$. The maximum of the spectrum is found in the infrared range at 1.4 eV (340 THz, 880 nm).

Spectra are also commonly plotted as a function of the wavelength λ of the light (Fig. 2.2). Such a plot of $dj_\mathrm{E}/d\lambda$ as a funtion of the wavelength $\lambda = {}^c\!/\nu$ with the velocity of light c shows another position of the maximum located in the middle of the visible spectral range at 500 nm (600 THz, 2.5 eV). The reason is that the wavelength interval $d\lambda = -\frac{2\pi c}{\hbar\omega^2}d\hbar\omega = -\frac{\lambda^2}{hc}d\hbar\omega$ does not correspond to a constant energy interval $d\hbar\omega$.

The discussed spectrum with an integral radiant flux of 1353 W/m^2 is measured outside the earth atmosphere and is called air mass (AM) 0. The air mass is defined as $1/\cos(\alpha)$ with the angle of incidence α measured to the vertical. This means AM describes the
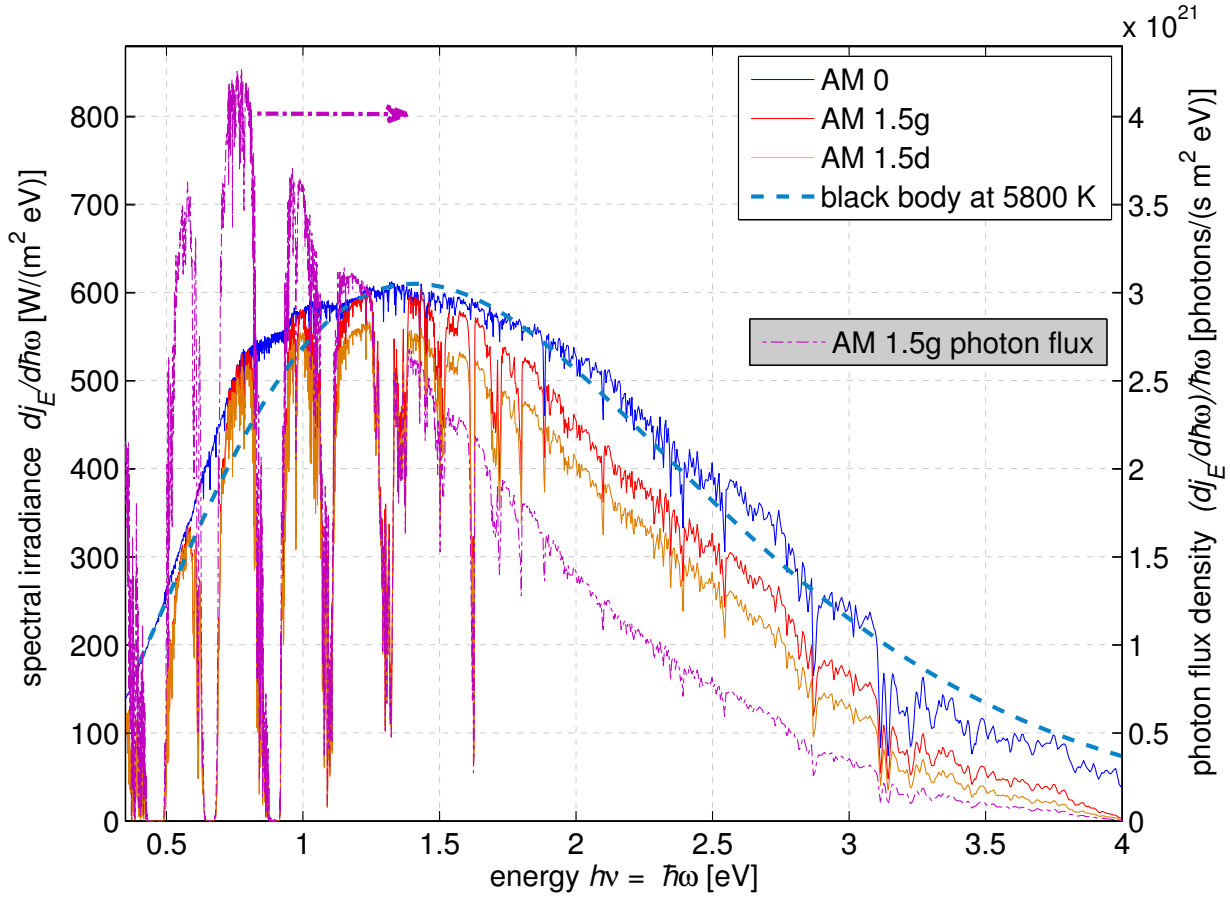
Figure 2.1: Solar spectrum and spectral photon flux density as a function of the light frequency ν multiplied by Planck's constant h. The quantities are displayed per unit energy $h\nu$. Data are from ASTM [39]. The solar spectrum outside the atmosphere (AM 0) approximately follows a black body at 5800 K.

ratio of the actual path of a sunray through the atmosphere to the path of perpendicular incidence. The latter is the radial extension of the atmosphere. Hence, AM 1 defines the spectrum of a sunray under perpendicular incidence on the earth surface after having crossed the atmosphere. The standard spectrum for solar-cell characterization is AM 1.5, characterizing an angle of incidence of 48°. This value is approximately reached, e.g., in Münsingen located in the south of Germany at noon on the 21.03. and the 23.09. The integral over AM 1.5, i.e. the total energy flux, is defined as $1\,\text{kW/m}^2 = 100\,\text{mW/cm}^2$. In Germany an average annual energy flux density of $1000\,\text{kWh/(m}^2\text{a)}$ is observed, which corresponds to an average intensity of $115\,\text{W/m}^2$ and around 1000 to 2000 sunshine hours (intensity $> 120\,\text{W/m}^2$) [40] dependent on the location. These values can be doubled in desert regions closer to the equator [1].

AM 1.5 spectra are shown in Figs. 2.1 and 2.2 as well. Some parts of the AM 0 spectrum, especially in the infrared, are filtered out by absorption of molecules in the atmosphere
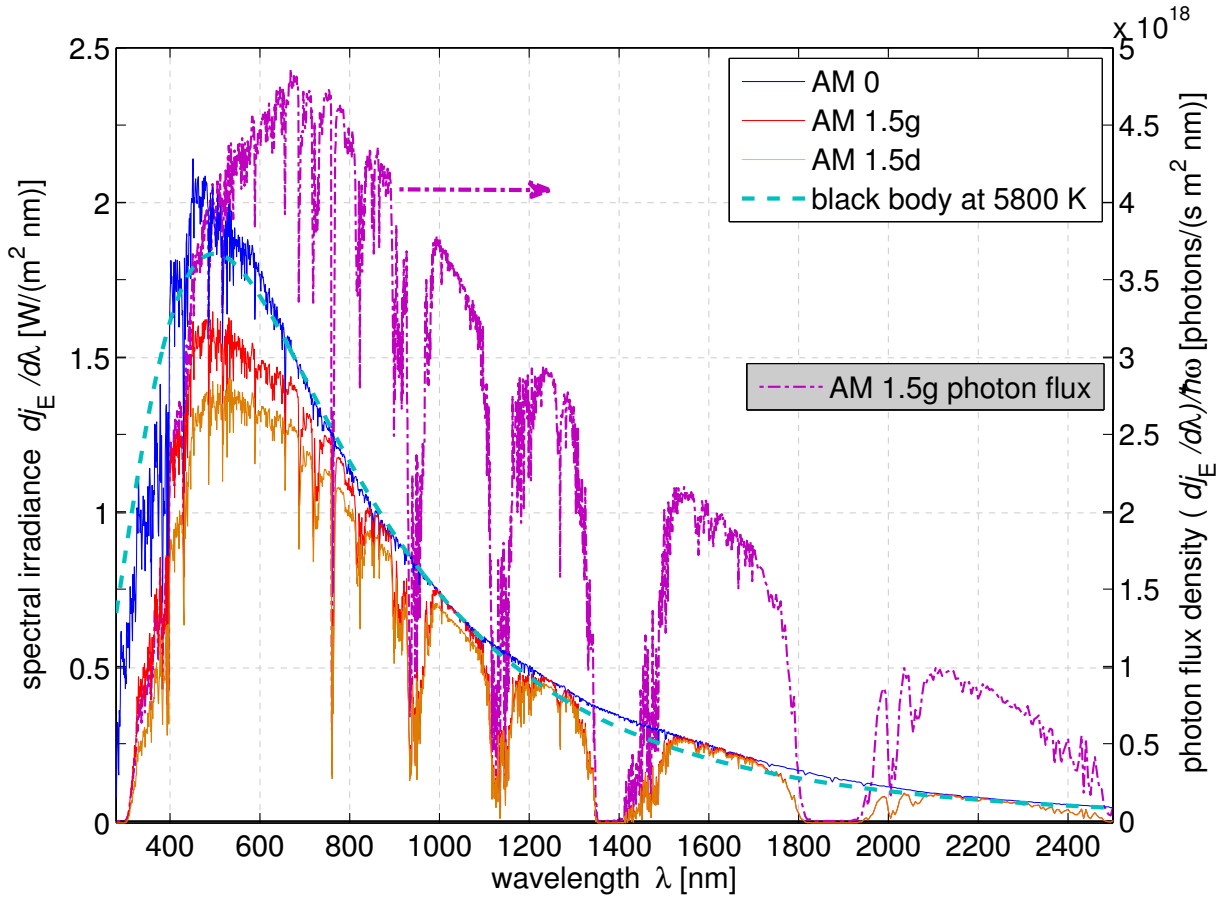
Figure 2.2: Solar spectrum and spectral photon flux density as a function of the wavelength λ. In contrast to Fig. 2.1, the quantities are displayed per unit wavelength. Data are from ASTM [39].

like water vapor, carbon dioxide, and methane. Oxygen and in particular ozone are well known as UV shields, absorbing in the ultraviolet part of the spectrum. AM 1.5 can be further specified in AM 1.5g and AM 1.5d. The first is the global spectrum including direct and diffuse light. The latter only describes the direct beam from the sun including a 2.5° circumsolar component, which is important for solar concentrator devices.

Additionally, the quantity $\frac{dj_E/d\hbar\omega}{\hbar\omega}$ ($\frac{dj_E/d\lambda}{\hbar\omega}$, Fig. 2.2) for the AM 1.5g spectrum is plotted. As we will see subsequently, this number correlates with the maximum photocurrent which can be harvested at a particular wavelength. Apart from the mentioned absorption bands, the AM 1.5 spectrum follows approximately a black-body radiation spectrum with a temperature of 5800 K, which is also plotted in the figures as dashed line.

2.1.2 Black-body irradiation

A black body is defined as an idealized body that completely absorbs incoming light of every wavelength, which means an absorption $a(\hbar\omega) = 1$ for all ω. It can be realized by a black box with a small hole or by a real body, which is sufficiently thick and non-reflecting. According to Kirchoff's law of thermal radiation, a black body is also a perfect emitter. The emission is characterized by the temperature and can be described by Planck's law, which is a consequence of the quantized nature of light. These quantities, the photons, obey the Bose-Einstein statistics and show a density of states limited by the Heisenberg uncertainty principle. The energy per unit volume and per unit energy interval $d\hbar\omega$ in a solid angle interval $d\Omega$ can be written as product of density of states $D_{\gamma,\Omega}$, occupation probability f_γ with Boltzmann constant k_B and absolute temperature T, and photon energy $\hbar\omega$:

$$\frac{de_\gamma(\hbar\omega)}{d\hbar\omega} = D_{\gamma,\Omega} f_\gamma \hbar\omega \, d\Omega = \frac{(\hbar\omega)^2}{4\pi^3\hbar^3 c^3} \frac{1}{e^{\frac{\hbar\omega}{k_B T}} - 1} \hbar\omega \, d\Omega. \tag{2.1}$$

Multiplying this expression with the velocity of light c and exchanging the energy $\hbar\omega$ by the frequency ν leads to the common expression of the spectral radiance $dj_{\gamma,\Omega}(\nu)/d\nu$ ($dj'_{\gamma,\Omega}(\lambda)/d\lambda$), which is the emitted power per unit area, per unit solid angle, and per unit frequency or wavelength (if ν is replaced by λ):

$$\begin{aligned}
\frac{dj_{\gamma,\Omega}(\nu)}{d\nu} &= \frac{2h\nu^3}{c^2} \frac{1}{e^{\frac{h\nu}{k_B T}} - 1} \\
\frac{dj'_{\gamma,\Omega}(\lambda)}{d\lambda} &= \frac{2hc^2}{\lambda^5} \frac{1}{e^{\frac{hc}{\lambda k_B T}} - 1}.
\end{aligned} \tag{2.2}$$

The maximum of j is found at $\hbar\omega_{max} = h\nu_{max} = 2.82 k_B T$ (1.41 eV for $T = 5800$ K) and of j' at $\lambda_{max} = \frac{hc}{5k_B T} \to h\nu = 4.97 k_B T$ (2.48 eV for $T = 5800$ K), respectively. An integration over all photon energies and a half sphere leads to the Stefan-Boltzmann law, which describes the total emitted energy flux density (black-body irradiance) as a function of temperature:

$$j_E = \frac{\pi^2 k_B^4}{60\hbar^3 c^2} T^4 = \sigma T^4 \tag{2.3}$$

Here, the natural constants are combined into the Stefan-Boltzmann constant σ.

Having introduced the concept of photons, we identify the additional curve $\frac{dj_E/d\hbar\omega}{\hbar\omega}$ in Fig. 2.1 ($\frac{dj_E/d\lambda}{\hbar\omega}$, Fig. 2.2) with the spectral distribution of photons emitted from the sun per unit time and area. This photon flux shows a broad maximum shifted to the red/infrared compared to the solar (intensity) spectrum $dj_E/d\hbar\omega$ ($dj_E/d\lambda$). The reason is that a certain intensity for higher λ originates from a larger number of low-energy photons.
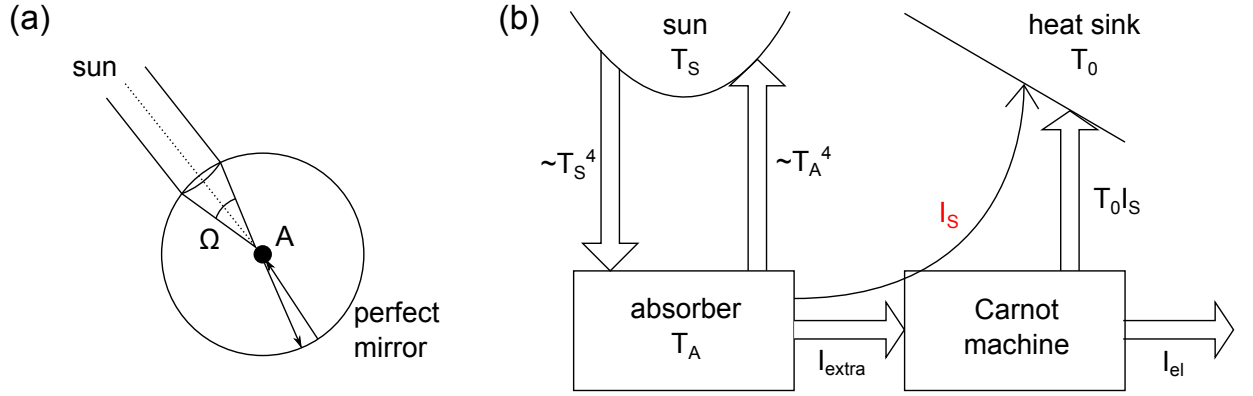
Figure 2.3: (a) Arrangement of absorber with area A within a perfect mirror and a lens to couple in and concentrate solar irradiation. (b) Schematic energy (large arrows) and entropy (I_S) flux diagram of an ideal solar thermal engine.

2.1.3 Maximum power-conversion efficiency

To build an ideal thermal engine, Würfel [3, 41] suggests a black body as absorber, which is arranged in a way that it sees only the solar (black-body) irradiation (from a solid angle Ω) and itself. Such an arrangement can be imagined as an absorber in a cavity with perfect mirrors on the wall and a hole with a lens to couple in the solar irradiation [Fig. 2.3(a)]. This leads to a maximum concentration factor of 46,200 limited by the solid angle (6.8×10^{-5}) of sun light which arrives on the earth surface. As long as power is not extracted, the absorber is in equilibrium with the sun and its temperature T_A reaches the temperature of the sun T_S. When extracting power (I_{extra}) from the absorber with area A, its temperature is decreased. The extracted energy is the difference of the absorbed (I_{abs}) and emitted radiation according to the Stefan-Boltzmann law (Eq. 2.3): $I_{extra} = \frac{\Omega}{\pi}\sigma(T_S^4 - T_A^4)A$. Here, Ω is the solid angle, the sun and the absorber see each other. This results in a power-conversion efficiency of

$$\eta_{extra} = \frac{I_{extra}}{I_{abs}} = 1 - \frac{T_A^4}{T_S^4}. \tag{2.4}$$

The efficiency η_{extra} increases with a decreased absorber temperature. As illustrated in Fig. 2.3(b), the heat energy flux I_{extra} is accompanied by an entropy flux of $I_S = I_{extra}/T_A$. As entropy cannot be destroyed according to the second law of thermodynamics, it has to be at least conserved and then released. The Carnot machine as ideal thermal engine provides an entropy conservation. However, a heat energy flux is connected with the entropy release at T_0. Hence, the entropy-free energy, i.e. electrical energy, is $I_{el} = I_{extra} - T_0 I_S = T_A I_S - T_0 I_S$ and the efficiency becomes

$$\eta_C = \frac{I_{el}}{I_{extra}} = 1 - \frac{T_0}{T_A}. \tag{2.5}$$

15

This is the Carnot efficiency, which increases with temperature difference. As T_0 is the ambient temperature, T_A should be high. This in combination with Eq. 2.4 leads to a tradeoff for the overall efficiency η resulting in a maximum value of

$$\eta_{\mathrm{max}} = \eta_{\mathrm{extra}} \eta_{\mathrm{C}} = 0.85 \qquad (2.6)$$

for $T_A = 2478\,\mathrm{K}$ ($T_S = 5800\,\mathrm{K}$, $T_0 = 300\,\mathrm{K}$).

   In the following sections we review fundamentals of semiconductors. These materials are well suited as absorbers because, in contrast to a black body, they provide states with absorption at low temperatures without the creation of entropy.

2.2 Basics of semiconductor physics

This thesis deals with organic solar cells. Although this class of materials shows significant differences compared to conventional crystalline semiconductors, its physics has to follow the same fundamental principles. Especially a self-consistent (numerical) simulation of organic semiconductor devices has to obey the principle of detailed balance and the laws of statistical and quantum mechanics. That is why a brief introduction to semiconductor physics is given here. Since the style of this section is very compact, the reader is referred, e.g., to Refs. [42–44] for a detailed introduction to semiconductor physics.

2.2.1 Band structure, electrons and holes

Bandgap

Semiconductors are characterized by an energy gap E_{g} in the range of $0.5 \ldots 4\,\mathrm{eV}$. This gap in the electronic energy landscape separates the valence band, which is fully occupied by electrons at $T = 0\,\mathrm{K}$, from the empty conduction band. The existence of an energy gap can be easily explained, imagining a free electron with parabolic dispersion (energy (E)-momentum (p) relation) in a periodic crystal [Fig. 2.4(a)]. Due to the wave-particle duality, the electron constitutes a de Broglie wave, which faces Bragg reflection at the lattice. This causes a region of forbidden energies and hence a bandgap, because the reflection inverts the direction of propagation and leads to standing waves. A superposition of waves propagating to the right and to the left results in two standing waves. Their potential energies are, dependent on the sign of superposition, lower and higher than the middle energy of a free electron as propagating wave.

   Another option for making the existence of bands plausible starts from single atoms whose electrons occupy discrete states [Fig. 2.4(b)]. Bringing them close to each other leads to interactions and electron-wave-function overlap (tight binding approach). The equilibrium interatomic distance a, i.e. lattice constant for primitive lattices, is given by the minimization of the total energy of the crystal. The band structure then results from the coupling of all atoms in a periodic crystal and is mainly a consequence of the Pauli principle, which forbids that more than two electrons as fermions with spin up and down
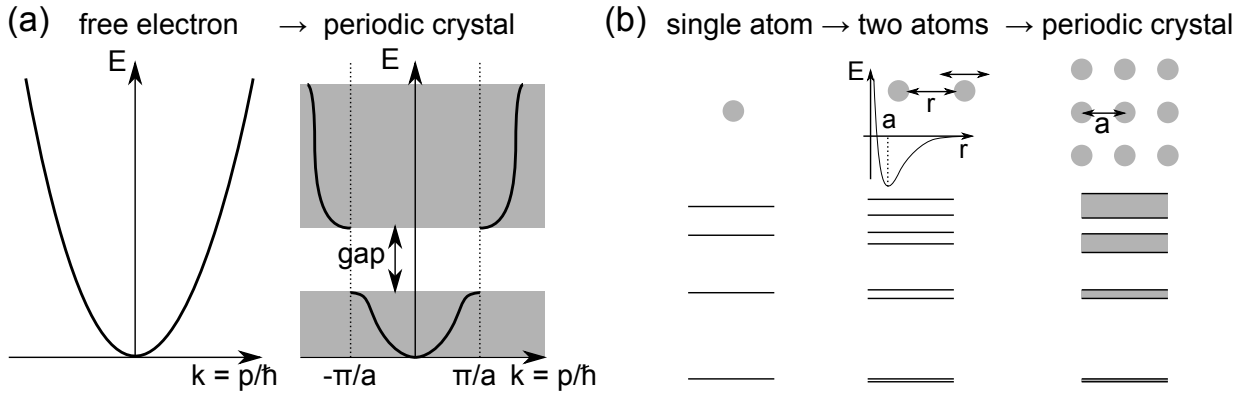
Figure 2.4: Schematic explanations for the existence of bands and bandgaps. Energy band diagrams are commonly drawn using the reciprocal space k, which scales with the crystal momentum p, as abscissa. (a) Free-electron approximation with parabolic dispersion relation of a free electron, which is modified when the electron faces the periodic potential of the crystal atoms. (b) Tight-binding-model: Discrete degenerate atomic levels split, when atoms interact with each other. This leads to a quasi-continuum of states.

occupy one state. Therefore, the discrete (between isolated atoms degenerate) atomic energy levels are shifted and split. These levels form a quasi-continuum of states for the electrons which are delocalized over the complete assembly of atoms. This distribution of states is called a band, with a total density of states equaling two times (spin degeneracy) the number of all atoms. Two bands can be separated by the bandgap, as it is the case for valence and conduction band in a semiconductor. Bands can also be partly occupied like in metals. Furthermore, valence and conduction band can overlap for some values of the momentum p giving the material quasi-metallic properties and the name metalloid.

A quantum mechanical treatment of this multi-particle system "crystal" means solving a Schrödinger equation with wave functions of states containing the coordinates of every particle. The Born-Oppenheimer (also called adiabatic) approximation allows for separate treatments of the atom cores (nuclei with core electrons) and the valence electrons, because their masses differ strongly and hence their energy eigenvalues. An approximated solution of the Schrödinger equation for the whole atoms as quantum mechanical harmonic oscillators leads to the phonons as vibrational states of the lattice. The wave function of a single electron (the many-body problem is reduced to a single-particle problem) in a periodic crystal is a Bloch wave and can be assigned a quasi or crystal momentum and a wave vector $\mathbf{k} = \mathbf{p}/\hbar$. Due to the periodicity, the energy dispersion can be fully described by taking into account the first Brillouin zone only, which is the reciprocal unit cell (Wigner-Seitz cell) of a lattice.

Only incompletely occupied bands contribute to charge transport, because an empty band does not contain an electron which can be moved. In a fully occupied band there is no room to shift electrons or in other words the momentum (and energy respectively) of an
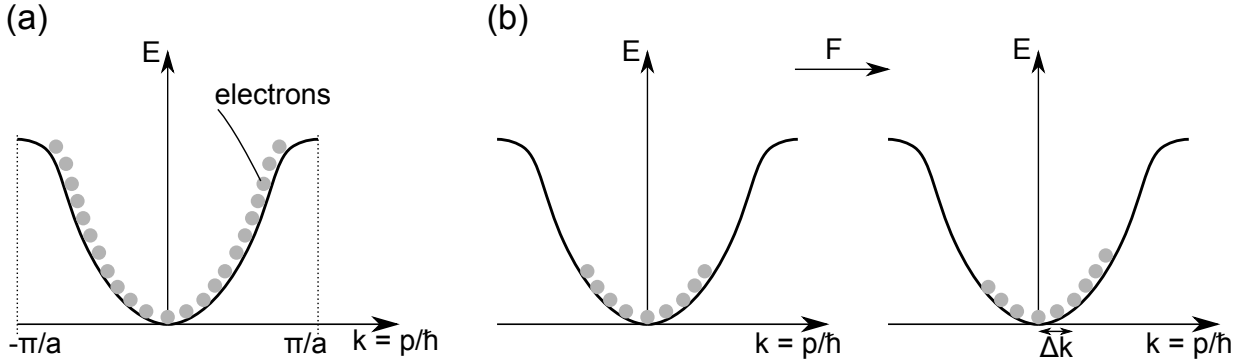
Figure 2.5: Electrical current in k-space. Shown is the energy dispersion of the first Brillouin zone: (a) Fully occupied band. (b) Partly occupied band, which receives in contrast to a fully occupied band a change in crystal momentum Δk under an applied electric field F at the presence of scattering.

electron cannot be changed continuously. This means that the electron cannot receive energy from an applied electrical field F. An explanation in the quantum mechanical picture (Fig. 2.5) starts from the inversion symmetry $E(k) = E(-k)$, which exists for all crystal lattices. In equilibrium it leads to a uniform time averaged occupation probability of states with wave vector k and $-k$. Applying a field in combination with lattice scattering results in a dk. In a not-fully occupied band [Fig. 2.5(b)] this means an asymmetric occupation of the states in respect to $k = 0$. This situation represents an effective force and thus current with group velocity $v = \frac{\partial \omega}{\partial k} = \frac{\hbar dk}{m^*}$, where m^* is the effective mass of the quasi-free electrons. In a fully occupied band, however, shifting electrons by dk out of the first Brillouin zone means shifting them into the zone at the "other side". Effectively, dk and consequently the electron velocity are zero.

Occupation statistics

Analogously to the photon density of a black body (Eq. 2.1), the occupation of the bands in thermal equilibrium is described by the integral in energy over the product of density of states (DOS) $g(E)$ and the probability of occupation $f(E)$:

$$\int_{\text{band}} g(E)f(E)dE. \tag{2.7}$$

The probability of occupation for electrons as half-integer spin particles when neglecting mutual interaction of the particles is given by the Fermi-Dirac statistics (FD function)

$$f(E) = \frac{1}{e^{\frac{E-E_{\text{F}}}{k_{\text{B}}T}} + 1}, \tag{2.8}$$

which can be approximated by a Boltzmann term for $E - E_{\text{F}} > 3k_{\text{B}}T$, as illustrated in Fig. 2.6(a). Here, E_{F} is the Fermi energy which is defined as the energy where the FD

function is ¹/₂. For $T = 0$, E_F describes the energy of the highest occupied electron state in a metal. The transition of the FD function from 1 to 0 at E_F is broadened with higher temperature. The reason is that the probability of occupying energetically higher states increases with T due to the higher thermal energy in the system.

The density of states $g(E)$ can be a complicated function. Assuming parabolic band minima (at E_C) or maxima (at E_V) (like in the energy dispersion of a free electron), this function depends on the square root of the energy in a three dimensional semiconductor and on the effective mass m^*, which is proportional to the reciprocal curvature of the energy dispersion:

$$\frac{1}{m^*} = \frac{1}{\hbar^2} \frac{\partial^2 E}{\partial k^2}. \tag{2.9}$$

The effective mass is an operand, which replaces the free-electron mass (e.g. in the equation of motion) and incorporates the electronic interactions with the lattice.

To give an idea about the shape of $g(E)$, we elaborate a simple derivation of the DOS of a free electron gas in three-dimensional space. We start from the condition $k = 2\pi/L$, which results directly from the solution of the stationary Schrödinger equation of an electron in a box with edge length L in real space. Hence, the volume of one allowed k-value in three dimensions is $(2\pi/L)^3$. Imagining a sphere in k-space, the number of allowed states N is the ratio between the volume of the sphere and the volume of one k-value multiplied by two due to the spin degeneracy:

$$N(k) = 2\frac{4/3\pi k^3}{(2\pi/L)^3} = \frac{V}{3\pi^2}k^3. \tag{2.10}$$

Here, $V = L^3$ is the volume of the crystal in real space. Replacing k by the dispersion relation of an electron $E(k) = \frac{\hbar^2 k^2}{2m^*}$ leads to the number of states per energy interval dE:

$$\frac{dN}{dE} = \frac{d\left(\frac{V}{3\pi^2}\left(\frac{2m^* E}{\hbar^2}\right)^{3/2}\right)}{dE} = \frac{V}{2\pi^2}\left(\frac{2m^*}{\hbar^2}\right)^{3/2} E^{1/2} =: g(E)V \tag{2.11}$$

In this context we can explain the expression used in Eq. 2.1 for the photon density of states: Applying the dispersion of a photon $|p| = \hbar k = \hbar\omega/c$ delivers directly D_γ, which in Eq. 2.1 is normalized to solid angle and hence divided by 4π.

The integral in Eq. 2.7 can be approximately solved under the discussed assumptions. The result is the following expression for the electron density $n = N/V$ in the conduction band:
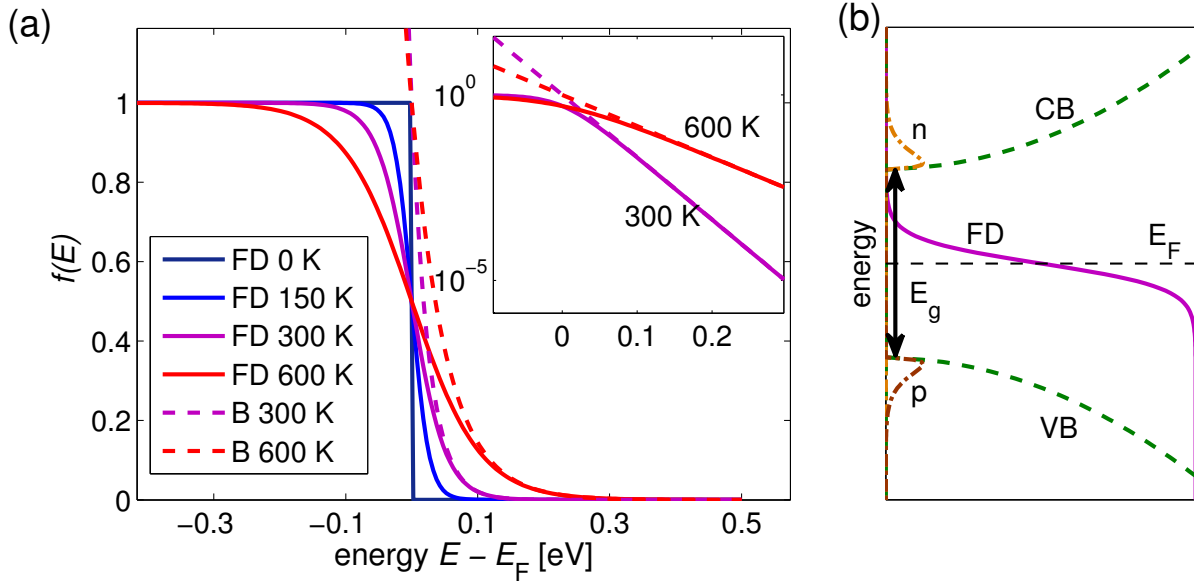
Figure 2.6: (a) Fermi-Dirac (FD) function for different temperatures and Boltzmann approximation (B) in a linear and logarithmic (inset) plot. (b) Fermi-Dirac distribution, density of states (DOS), and electron and hole densities in the parabolic conduction (CB) and valence band (VB), respectively, at $T > 0$.

$$n = \int_{E_C}^{\infty} g(E)f(E)dE = \int_{E_C}^{\infty} 4\pi \left(\frac{2m^*}{h^2}\right)^{3/2} (E - E_C)^{1/2} \frac{1}{e^{\frac{E-E_F}{k_B T}} + 1} dE$$

$$\overset{E-E_F \geq 3k_B T}{=} \int_{E_C}^{\infty} 4\pi \left(\frac{2m^*}{h^2}\right)^{3/2} (E - E_C)^{1/2} e^{-\frac{E-E_F}{k_B T}} dE \tag{2.12}$$

$$= N_C \exp\left(-\frac{E_C - E_F}{k_B T}\right).$$

Here, $N_C = 2\left(\frac{2\pi m^* k_B T}{h^2}\right)^{3/2}$ is the so-called effective density of states, which is a volume density (in cm^{-3}) having the energy dependency of the DOS $g(E)$ already included. One might think of it as a reduced DOS with value N_C located only and directly at the band edge with its occupation described by Boltzmann statistics ($E_C - E_F > 3k_B T$). Figure 2.6(b) visualizes the determination of n via Eqs. 2.7 and 2.12.

Holes as defect electrons

Because it is much easier to follow fewer particles, we describe charge transport in the valence band via hole densities p, which are missing (or defect) electrons and carry the charge $+e$ (elementary charge). The occupation probability for holes is then 1-FD(E), which is equal to the FD function (FD($-E$)) due to its symmetry with respect to E_F. It

follows analogously to Eq. 2.12:

$$p = \int_{-\infty}^{E_\mathrm{V}} g(E)[1 - f(E)]dE = N_\mathrm{V} \exp\left(-\frac{E_\mathrm{F} - E_\mathrm{V}}{k_\mathrm{B}T}\right) \tag{2.13}$$

The product

$$np = n_\mathrm{i}^2 = N_\mathrm{C} N_\mathrm{V} \exp\left(-\frac{E_\mathrm{g}}{k_\mathrm{B}T}\right) \tag{2.14}$$

is independent of the position of E_F. Thus, Eq. 2.14 is valid in equilibrium, even if $n \neq n_\mathrm{i}$. It is a result of the law of mass action. In a pristine, so-called intrinsic semiconductor, electrons in the conduction band can only result from a thermal activation of valence electrons. This process is identical to a creation of holes in the valence band, leading to $n = p = n_\mathrm{i} = p_\mathrm{i}$. Here, the index i means intrinsic. For common and optically interesting values of the bandgap $(1.0 \ldots 3.5\,\mathrm{eV})$, n_i is very low at room temperature. For example, n_i is $1.45 \times 10^{10}\,\mathrm{cm}^{-3}$ for silicon $(E_\mathrm{g} = 1.12\,\mathrm{eV})$ at room temperature, which is very low compared to the density of atoms $(5 \times 10^{22}\,\mathrm{cm}^{-3})$ [42]. As the conductivity scales with the free charge carrier densities (cf. Eq. 2.28), it is very poor for intrinsic semiconductors. However, it is technologically very challenging to reach intrinsic properties due to the required high material purity.

Doping

To manipulate and improve conductivity, doping is applied by replacing some crystal atoms (less than 0.1%) by atoms having one excess valence electron which does not enter a covalent bond. This additional electron can approximately be described by the hydrogen problem, replacing the free electron mass by the effective mass and considering the dielectric constant ε_r of the semiconductor. This leads in a rough estimation to a binding energy in the range of $13.6\,\mathrm{eV} \times \frac{m}{m^*}\frac{1}{\varepsilon_\mathrm{r}^2} \approx 13.6\,\mathrm{eV} \times \frac{1}{10}\frac{1}{10^2} = 13.6\,\mathrm{meV}$. This value is by a factor of 1000 lower than the binding energy of the hydrogen electron. At room temperature this electron is released and increases the number of free electrons n. As this treatment is an approximation not considering the effect of the other electrons of the doping atom, measured values for the binding energy depend on the doping element and are in the range of several 10s of meV. The described electron delivery to the crystal is called n-doping, and the guest atom is a donor. For p-doping, atoms with one missing valence electron are inserted, so-called acceptors. The dominating type of charge carriers is called majorities in contrast to the minorities. According to Eqs. 2.12 and 2.13 the Fermi level shifts towards E_C in the case of n-doping and towards E_V for p-doping. The saturation regime, which is characterized by the ionization of all dopant atoms N_D, is commonly reached at room temperature. In the case of n-doping $n \approx N_\mathrm{D}$ (majorities) and with Eq. 2.14 $p \approx {n_\mathrm{i}^2}/{N_\mathrm{D}}$ (minorities) are good approximations of the charge carrier densities.
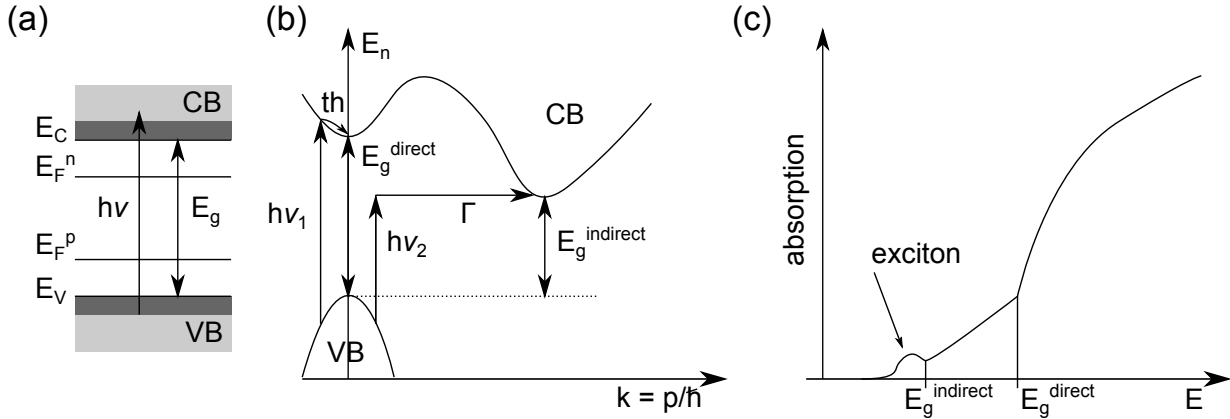
Figure 2.7: (a) Sketch of the absorption of light with an energy $h\nu$ larger than the bandgap E_g. This process increases the electron and hole concentration in conduction and valence band (CB and VB), respectively. Combined with a fast thermalization within the bands, this leads to two separate quasi-Fermi levels for electrons (E_F^n) and holes (E_F^p). (b) Scheme of direct ($\Delta k \approx 0$) and indirect (phonon (Γ)-assisted) absorption processes and thermalization (th). (c) Schematic absorption of an indirect semiconductor as a function of photon energy.

2.2.2 Quasi-Fermi levels and electrochemical potentials

Absorption

As long as the semiconductor is in equilibrium, the occupation of valence and conduction band can be described by a single Fermi distribution. Under illumination, however, electrons from the valence band can be excited into the conduction band. Thus, additional electrons and holes are created. This results in values of n and p larger than n_i. Therefore, the semiconductor is not in equilibrium. A minimization of the energy of the photogenerated charge carriers leads to a fast ($< \mathrm{ps}$) thermalization to the band edge. Consequently, the distribution within the band is also described by an FD function considering the Pauli principle. The thermalized electrons have a certain lifetime ($\mu\mathrm{s}$), before they release their energy ideally via photons when recombining with holes. This difference in timescale between relaxation and recombination results simply from quantum mechanical transition rates according to Fermi's Golden Rule: A variety of states exists within the band and possible interactions of charge carriers with low-energy phonons are very likely as the phonons are capable of absorbing small quantities of energy in several subsequent steps. In contrast, band-band recombination requires an interaction between the electron and a photon with the large energy of the bandgap. This process is less probable.

Therefore, both thermalized n and p follow FD statistics again. However, n and p are much larger than in the dark. As the electrons are thermalized, their temperature is the one of the crystal. Hence, E_F moves towards the conduction band for properly describing the distribution of electrons and towards the valence band for holes. This can only be

fulfilled by two distinct Fermi distributions and two Fermi levels E_F^n and E_F^p, one for each band [see Fig. 2.7(a)]. They are called quasi-Fermi distributions and applying Eqs. 2.12 and 2.13, the following holds:

$$n \times p = N_C \exp\left(-\frac{E_C - E_F^n}{k_B T}\right) \times N_V \exp\left(-\frac{E_F^p - E_V}{k_B T}\right) = n_i^2 \exp\left(\frac{E_F^n - E_F^p}{k_B T}\right). \quad (2.15)$$

The occupation of eventually present intra-gap states between the quasi-Fermi levels is described neither by E_F^n nor by E_F^p, but by the dynamics of occupation and release.

Generation, as already mentioned, can happen via photon absorption, where conservation of energy and momentum has to be fulfilled as visualized in Fig. 2.7(b). Because of the very low impulse of a photon, a direct transition, i.e. a transition at the same momentum or k-vector in k-space, has a much higher probability than an indirect transition. An indirect transition is a multi-particle process, because phonons as particles with low energy, but high momentum, have to deliver the required Δk, when they are created or absorbed. That is the reason why silicon with an indirect bandgap has an orders of magnitude lower absorption coefficient for energies close to the bandgap than, e.g., gallium arsenide. Direct and indirect absorption processes are sketched in Fig. 2.7(b,c), where the absorption shows an additional feature below the bandgap, which is attributed to a so-called excitonic absorption into a Coulombically bound electron-hole pair. Its binding energy is the distance of the absorption peak to the band edge. Such excitonic states will become important when we discuss organic materials in Chapter 3.

Radiative recombination

The reverse process to generation is the annihilation of an electron-hole pair, which is called recombination R. In dark and in equilibrium (index 0) R equals the generation caused by the thermal background radiation G_0:

$$R_0 = \beta n_0 p_0 = G_0 \quad (2.16)$$

Here, R is proportional to the charge carrier densities and the radiative recombination constant β. The generation rate G_0 can be expressed by:

$$G_0 = \int_0^\infty a(\hbar\omega) dj_\gamma^0(\hbar\omega) d\hbar\omega = \frac{\Omega}{4\pi^3 \hbar^3 c^3} \int_0^\infty \frac{a(\hbar\omega)(\hbar\omega)^2}{e^{\frac{\hbar\omega}{k_B T_0}} - 1} d\hbar\omega. \quad (2.17)$$

Here, $a(\hbar\omega)$ is the absorption and $dj_\gamma^0(\hbar\omega)$ is the spectral background radiation (energy flux), which is a black body radiation at the temperature T_0 of the surrounding (Eq. 2.1). The quantity $c = c_0/n$ describes the velocity of light in the medium, i.e. semiconductor with refractive index n, and is reduced compared to the velocity in vacuum c_0 or air. As the energy at an interface air/semiconductor has to be conserved, this implies directly a smaller solid angle Ω in the medium, which is equal to Snell's law, describing refraction towards the vertical. Knowing a and n_i ($n_0 p_0 = n_i^2$), β can be calculated and is independent

of the doping concentration as long as doping does not change a. $R_0 = G_0$ is fulfilled for every $\hbar\omega$ according to the theory of detailed balance, where every single process and hence absorption and emission at each wavelength are in balance. Thus, the emitted photon flux can be expressed by $dj_\gamma^{\text{em}}(\hbar\omega) = \alpha(\hbar\omega)dj_\gamma^0(\hbar\omega)$ for every ω.

In non-equilibrium, the charge carrier densities n_0 and p_0 are changed by absorption of photons or injection and extraction of electrons. The recombination rate is simply modified using the actual charge carrier densities n and p in Eq. 2.16 and 2.15:

$$R = \beta np = \frac{G_0}{n_0 p_0} np = \frac{G_0}{n_i^2} np = G_0 \exp\left(\frac{E_F^n - E_F^p}{k_B T}\right). \tag{2.18}$$

This is allowed, because charge carriers still follow Fermi-Dirac statistics in their respective band and have the lattice temperature so that only the rate of the emitted photons changes, whereas the spectrum contained in G_0 (Eq. 2.17) remains unmodified. This equation shows that an increased quasi-Fermi level splitting leads to higher recombination. Equation 2.18 contains some approximations (e.g. Boltzmann distribution), so that inserting the expression for G_0 (Eq. 2.17) does not lead to the exact result for the emitted photon flux, which is obtained from another derivation [45]:

$$dj_\gamma^{\text{em}}(\hbar\omega) = a(\hbar\omega)\frac{np}{n_i^2}dj_\gamma^0(\hbar\omega) = a(\hbar\omega)\frac{\Omega}{4\pi^3\hbar^3 c^2}\frac{(\hbar\omega)^2}{e^{\frac{\hbar\omega - \left(E_F^n - E_F^p\right)}{k_B T}} - 1}d\hbar\omega. \tag{2.19}$$

Compared to Eq. 2.1 this expression can be called generalized Planck's law, describing thermal and luminescence irradiation.

Radiative recombination requires an electron to meet a hole. Hence, this mechanism can be classified as bimolecular recombination (order 2) with a net recombination rate of $R = \beta(np - n_i^2)$ which we will use later on.

Non-radiative recombination

Radiative recombination is unavoidable because of the thermodynamic radiation equilibrium of bodies at a certain temperature. Apart from radiative recombination other types of recombination can be present and play a significant role. They are sketched in Fig. 2.8. In Auger recombination the energy of a recombining electron-hole pair is transferred to another free electron in the conduction band, which thermalizes afterwards. This is a three-particle mechanism with $R_{\text{Aug}} = Cn^2p$. It is important in indirect semiconductors to conserve the crystal momentum and limits the performance of highly efficient silicon solar cells. Commonly, recombination via intra-bandgap states is dominant in real semiconductors. Such states, called traps, result from crystal defects, which could be dislocations, impurities, or surfaces. Recombination via these trap states can be described by the Shockley-Read-Hall (SRH) model as a two-step process [46]: At first a free electron (i.e. an electron in the conduction band) is captured by an intragap state and becomes immobile. This process can be described by a capture constant, which is a product of thermal
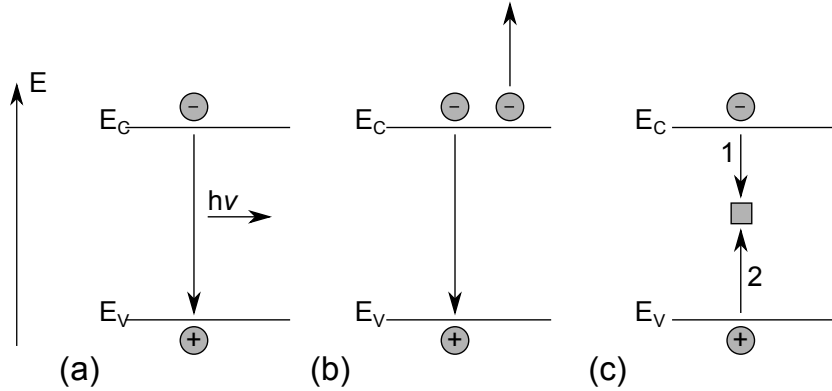
Figure 2.8: Recombination processes between electron and hole: (a) radiative emitting a photon, (b) Auger transferring the energy to another electron in the conduction band, and (c) trap-assisted (indirect) recombination as two-step process.

velocity v and cross section σ of the trap with density N_T. The second step to complete the recombination process is the emission of the electron into the valence band, which is equivalent to a capture of a hole. SRH recombination can be described by the following expression, which is found after longer derivation [46]:

$$R_\mathrm{SRH} = \frac{np - n_\mathrm{i}^2}{\frac{n + N_\mathrm{C}\exp(-(E_\mathrm{C}-E_\mathrm{T})/k_\mathrm{B}T)}{N_\mathrm{T}\sigma_p v_p} + \frac{p + N_\mathrm{V}\exp(-(E_\mathrm{T}-E_\mathrm{V})/k_\mathrm{B}T)}{N_\mathrm{T}\sigma_n v_n}}. \tag{2.20}$$

Examining the denominator of this equation shows that traps with energy E_T close to the middle of the bandgap, so-called midgap traps, are most active as recombination centers. In this case the sum of the denominator is minimized which gives the highest value of R_SRH. This sum is mainly governed by the exponential functions and gets larger, if E_T moves closer to E_C or E_V. Speaking in an intuitive picture, the occupation probability of a midgap trap is comparable for electrons and for holes. However, a charge carrier can easily escape thermally in the case of a shallow trap, which is located close to a band edge. This decreases the recombination probability, e.g., of an electron trapped close to the conduction band edge with a hole. SRH-recombination is also called monomolecular recombination, as a free charge carrier recombines with a localized, trapped charge, and it roughly holds $R \propto n$.

A further source of recombination are surfaces. Surface recombination can be described by a surface recombination velocity s_n, leading to a surface recombination rate

$$R_\mathrm{sf} = s_n(n - n_0). \tag{2.21}$$

The effect of G_0 and R_0 are already included by the subtraction of n_0, i.e. R_sf is the net recombination rate. At a metal contact s_n is very high ($\to \infty$). This implies that the contact is in equilibrium independent of the applied voltage or illumination. Thus, $n = n_0$
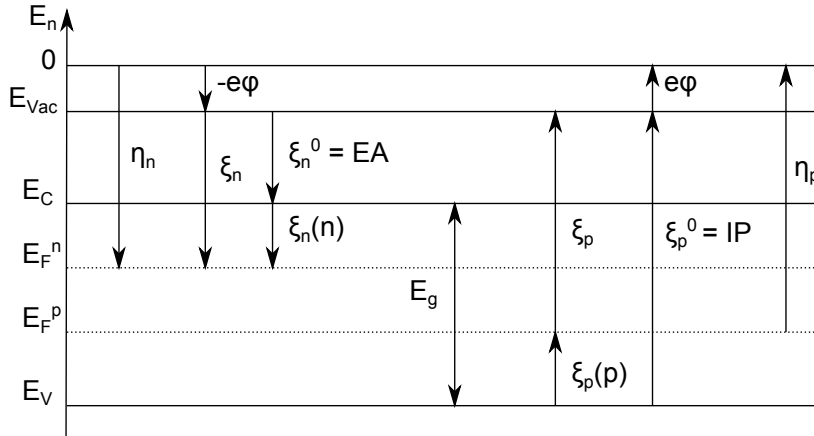
Figure 2.9: Energy diagram for electrons (n) and holes (p). Shown are the relations between electrical potential ϕ, chemical potential ξ, and electrochemical potential η compared to the quasi-Fermi levels E_{F}^{n} and E_{F}^{p}. ξ can be divided into a constant part ξ^{0}, which is a material property (electron affinity EA, ionization potential IP), and into a part, which is dependent on the charge carrier concentration. All energies are given with respect to the vacuum level E_{Vac}, which is shifted by the electrical potential ϕ. (Redrawn after Ref. [3].)

and $np = n_{\mathrm{i}}^{2}$ are valid.

Overall recombination

To every recombination process j a lifetime τ can be assigned, because every recombination term (here shown for electrons) can be written as

$$\Delta R_j = \beta_j \Delta n = \frac{\Delta n}{\tau_j}. \tag{2.22}$$

However, τ is only a (constant) material property (including impurities and defects) for monomolecular recombination processes. Otherwise, τ depends also on the density of the other charge carrier type, here the holes p. In the case of highly doped layers, a minority lifetime can be defined, because the majority concentration is approximately independent of a small perturbation Δp ($p \gg \Delta p \to p \approx$ const.). The overall lifetime is the inverse of the sum of all inverse lifetimes, because all processes are running in parallel ($1/\tau_{\mathrm{tot}} = \sum_j 1/\tau_j$).

Driving forces

Until now we discussed the Fermi energy only related to occupation statistics. Now we extend the discussion to variations in space (x) and examine the forces on electrons and holes, where we will identify gradients in the quasi-Fermi levels as driving forces.

The basic concept is that forces and hence particle currents vanish, as soon as a system is
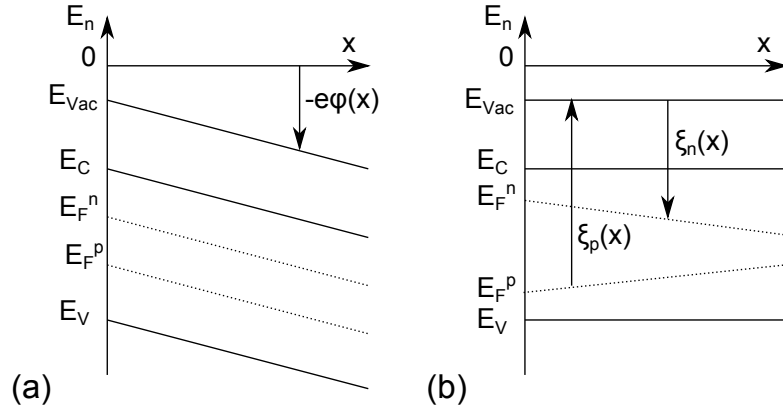
Figure 2.10: Spatial (x) energy diagrams for (a) an electrical potential difference and (b) a concentration gradient. Both result in a tilt of the quasi-Fermi levels E_F^n and E_F^p and consequently in an electron and hole current.

in equilibrium. A system can be in equilibrium with respect to each single intensive variable [3]. Intensive variables are variables, which do not depend on the amount of material, like temperature, pressure, chemical and electrical potential. Each variable reaches a constant value in space if the system is in equilibrium regarding the respective parameter. Dependent on the linking element of two subsystems, which allows exchange of heat but not particles, e.g., the system reaches temperature but not chemical equilibrium.

Concerning semiconductors, we assume a constant temperature, neglect any magnetic or gravitational forces on the electrons, and consider only the electrical (ϕ) and chemical (ξ) potential. Starting from the energy balance of a system and some thermodynamic considerations [3] the Fermi energy is found to be identical to the electrochemical potential η:

$$
\begin{aligned}
\eta_n(x) &= -e\phi_n(x) + \xi_n(x) = E_F^n(x) \\
\eta_p(x) &= e\phi_p(x) + \xi_p(x) = -E_F^p(x)
\end{aligned}
\tag{2.23}
$$

Thus, E_F is constant in a semiconductor in equilibrium. Consequently, a gradient in E_F denotes non-equilibrium and constitutes a force, which generates a particle current, as we will see in the following sections. The splitting of electron and hole quasi-Fermi level at a certain position x_0 represents the free or chemical energy of an electron-hole pair. Figure 2.9 summarizes all quantities in an energy diagram for electrons. Spatial non-equilibrium situations are shown in Fig. 2.10, where in (a) the electrochemical potential is tilted due to an applied field, changing the electrical potential. Subfigure (b) shows a change in the chemical potential due to a higher concentration of electrons and holes on the left.

2.3 Transformation of thermal radiation into chemical energy

As gedankenexperiment Würfel [3] divided photon absorption into two steps: In a first step electrons and holes are generated by absorption of light with an energy $h\nu > E_{\mathrm{g}}$. Excluding scattering at the lattice, the charge carriers reach sun temperature T_{S} under maximum concentration. The energy of an electron-hole pair is then $E_{\mathrm{g}} + 3k_{\mathrm{B}}T_{\mathrm{S}}$. As the semiconductor is in thermal equilibrium with the sun, the Fermi energy for electrons and holes is the same, and it holds according to Eqs. 2.12 and 2.13:

$$E_{\mathrm{C}} - E_{\mathrm{F}} = k_{\mathrm{B}}T_{\mathrm{S}} \ln(N_{\mathrm{C}}/n); \ E_{\mathrm{F}} - E_{\mathrm{V}} = k_{\mathrm{B}}T_{\mathrm{S}} \ln(N_{\mathrm{V}}/p) \tag{2.24}$$

After allowing scattering at the lattice in the second step, the electrons cool down to the lattice temperature T_0. This thermalization is accompanied by the creation of entropy in form of phonons. The remaining energy per electron-hole pair can be calculated using the same expression as Eq. 2.24 replacing T_{S} by T_0 and E_{F} by the respective quasi-Fermi level (Eq. 2.15): $E_{\mathrm{C}} - E_{\mathrm{F}}^{n} = k_{\mathrm{B}}T_0 \ln(N_{\mathrm{C}}/n); \ E_{\mathrm{F}}^{p} - E_{\mathrm{V}} = k_{\mathrm{B}}T_0 \ln(N_{\mathrm{V}}/p)$. This potential energy is the chemical energy ξ, which is represented by the quasi-Fermi level splitting. It can be summarized replacing the logarithms by the expressions of Eq. 2.24:

$$\xi_n + \xi_p = E_{\mathrm{F}}^{n} - E_{\mathrm{F}}^{p} = E_{\mathrm{g}}(1 - T_0/T_{\mathrm{S}}) \tag{2.25}$$

This equation allows an estimation of the maximum efficiency of the transformation of heat radiation into chemical energy. If we assume that we do not extract any charge carrier and there is no thermalization (i.e. monochromatic illumination with $h\nu = E_{\mathrm{g}}$), the incoming photon energy is E_{g} and hence $\eta_{\mathrm{max}} = 1 - T_0/T_{\mathrm{S}}$, which is the Carnot efficiency. Note that this expression derived from Eq. 2.25 includes also the condition of maximum concentration. In the recombination process the chemical energy is transferred to a photon, which is emitted at $T = T_0$ and has a chemical potential $\xi \neq 0$. This type of radiation is called luminescence, in contrast to the heat radiation of the sun at $T = T_{\mathrm{S}}$ and $\xi = 0$.

In the situation discussed, the whole energy is reirradiated to the sun. If we want to extract an electron-hole current j_{E}, a difference between absorbed and emitted photon flux has to exist:

$$j_{\mathrm{E}} = j_{\gamma}^{\mathrm{abs}} - j_{\gamma}^{\mathrm{em}} = j_{\gamma}^{\mathrm{abs}} - j_{\gamma}^{0} n p / n_{\mathrm{i}}^{2} = j_{\gamma}^{\mathrm{abs}} - j_{\gamma}^{0} \exp\left(\frac{\xi_n + \xi_p}{k_{\mathrm{B}}T}\right) \tag{2.26}$$

This expression is obtained by inserting Eq. 2.18 and 2.23 to replace j_{γ}^{em}. A sketch of this function in Fig. 2.11 shows a maximum of extractable power as product of particle current j_{E} and energy $\xi_n + \xi_p$. The reason is a tradeoff between number and energy of the collected electron-hole pairs. For low chemical energies, very few photons are emitted and almost all electron-hole pairs can be collected, however, at this low energy. With increasing energy,
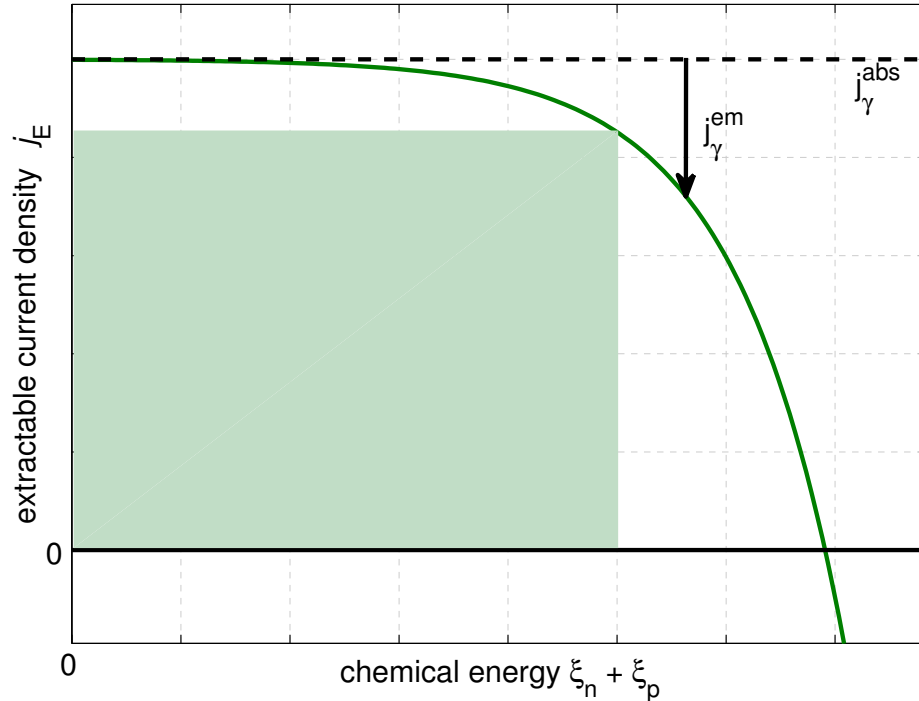
Figure 2.11: Extractable current density j_E of electron-hole pairs as a function of their chemical energy $\xi_n + \xi_p$. The rectangle marks the maximum power which can be delivered as product of energy and current.

j_E decreases due to higher radiative recombination. The remaining question of how to extract these electrons and holes to get an electrical current is addressed in the following section.

2.4 From chemical energy to electrical energy

To extract the chemical energy of an electron-hole pair in form of an electrical current, electron and hole have to be collected at two different positions in the absorber, e.g., by metal contacts. This requires in the optimum case selective contacts and driving forces for holes towards the one and for electrons towards the other contact. These forces are discussed in an intuitive way here. A detailed derivation is found in Chapter 4, because these equations are of fundamental importance for the simulation. Again, we exclude gravitation, magnetism, and temperature gradients as driving forces acting on the charged particles electrons and holes, and focus on the electric field and the concentration gradient.

Drift current

The force Z acting on an electron due to the electric field F is given by $Z = -eF$. Inserting this expression as driving force into the equation of motion (Newton's second law) and assuming friction due to scattering with the average scattering time τ_r leads to the expression $-eF = Z = m^*(dv/dt + v/\tau_\mathrm{r})$. In steady state ($dv/dt = 0$) the drift velocity v of the electron is:

$$v = -\frac{e\tau_\mathrm{r}}{m^*}F = -\mu F \tag{2.27}$$

with the definition of the mobility μ as measure of an achievable charge carrier velocity for a particular electric field. The electric current density j is the product of particle density, the particles' average velocity, and the charge a particle carries. This holds for holes as well and leads to the microscopic Ohmic law:

$$j_\mathrm{drift} = (-env_n + epv_p) = e(n\mu_n F + p\mu_p F) = \sigma F \tag{2.28}$$

Here, the conductivity σ is defined as proportionality constant relating the current to the electrical field. The semi-classical picture of band theory supports this approach, first postulated by Drude, because Newton's dynamics is valid for the description of electrons in a solid. In a crystal, where k represents the crystal momentum, $d(\hbar k)/dt = eF$ and the parabolic energy dispersion of a free electron are replaced by the one of the crystal $E(k)$. As already mentioned, $E(k)$ is symmetric and periodic with any inverse lattice vector. This means that accelerating an electron by an electric field without scattering leads to a fast acceleration of the electron out of a band minimum, which is followed by a retardation due to a reversed curvature of the dispersion relation (negative effective mass, cf. Fig. 2.5). This leads to oscillations between the minimum and maximum energy of a band and hence to an average dk and subsequently a v of zero. In such a situation current does not flow in real space. The electrons perform so-called Bloch oscillations [47], which have been observed in semiconductor superlattices [48]. Thus, scattering is essential for an electric current in a periodic crystal, because it provides an equilibrium dk. This change in the momentum of the crystal electrons upon the application of an electric field is $\hbar dk = \tau(-eF)$ with the average relaxation time τ. For an electron located in a parabolic band minimum with a constant effective mass, we can write $d(\hbar k) = m^* dv = -e\tau F$, which is identical to Eq. 2.27.

Diffusion current

A non-constant particle density leads to an additional (electrical) current, according to Fick's law:

$$j_\mathrm{diff}^n = -(-e)D\nabla n; \quad j_\mathrm{diff}^p = -(+e)D\nabla p. \tag{2.29}$$

This law says that the chemical equilibrium is reached in the absence of other forces if the concentration gradient vanishes. It assumes a current which is proportional to the negative gradient of the particle density. To bring this equation into a form comparable to Eq. 2.28, one uses a mathematical trick and replaces ∇n by $n\frac{\nabla n}{n} = n\nabla(\ln n - \ln N_\mathrm{C}) =$

$n\nabla\ln\left(\frac{n}{N_C}\right) = n\frac{\nabla\xi}{k_BT}$. Thereby, Eqs. 2.23 and 2.12 are applied, introducing the chemical potential ξ. Using the Einstein relation $\frac{D}{\mu} = \frac{k_BT}{e}$, the diffusion coefficient can be replaced by an expression containing only the mobility as material parameter. This results in the following equation for the total diffusion current:

$$j_{\text{diff}} = n\mu_n\nabla\xi_n - p\mu_p\nabla\xi_p \tag{2.30}$$

The origin and applicability of the Einstein relation is discussed in Chapter 4 in detail, because it is not a priori given for each type of semiconductor.

Total current

The total current is the sum of diffusion and drift current. Combining Eq. 2.30 with Eq. 2.28 and expressing the electric field as gradient of the electrical potential ϕ ($F = -\nabla\phi$), we get:

$$\begin{aligned} j_n &= j_{\text{drift}}^n + j_{\text{diff}}^n = -n\mu_n e\nabla\phi + n\mu_n\nabla\xi_n &= n\mu_n\nabla E_{\text{F}}^n \\ j_p &= j_{\text{drift}}^p + j_{\text{diff}}^p = -p\mu_p e\nabla\phi - p\mu_p\nabla\xi_p &= p\mu_p\nabla E_{\text{F}}^p \end{aligned} \tag{2.31}$$

Here, we merged drift and diffusion current in one expression, resulting in the gradient of the electrochemical potential or of the quasi-Fermi levels (Eq. 2.23) as driving force. We illustrate the benefit of examining quasi-Fermi levels at the example of a metal-insulator-metal (MIM) device with length L. The metals shall have different work functions (i.e. Fermi energies). The electrochemical potential and consequently E_{F} are constant in equilibrium. This results in a built-in field, which can be seen at the tilt of the bands in Fig. 2.12(a). This field is directly accompanied by a diffusion gradient, resulting from the spatially varying distance between Fermi level and the band edges (compare Eq. 2.12 and 2.13). In steady state, field and diffusion current cancel each other. More precisely, the net force as superposition of the forces of the diffusion gradient and the field on the ensemble of electrons and holes is zero. So, physically there is not a current flowing in the one direction, which is compensated by another current in the reversed direction. This is intuitively clear because an electrical current implies energy dissipation due to the resistivity of the material caused by charge carrier scattering. The result would be a continuous generation of heat, which is not allowed in thermodynamic equilibrium due to the conservation of energy.

If we take the MIM-device of Fig. 2.12(a) and assume that the (intrinsic) semiconductor absorbs light, we might get a quasi-Fermi level splitting at open circuit, which looks like the one depicted in Fig. 2.12(b). The voltage seen and measurable from outside is the difference of the respective electrochemical potential at electron and hole contact. The sketched gradients in the electrochemical potentials show that the electrical energy eV_{oc} is lower than the chemical energy found in the maximum splitting located in the middle of the device. These gradients are due to significant surface recombination at the electrodes and cause an internal current flow at open circuit. However, open circuit is defined as the situation where no net-current flows. This postulates a (this time physically real) compensation of electron
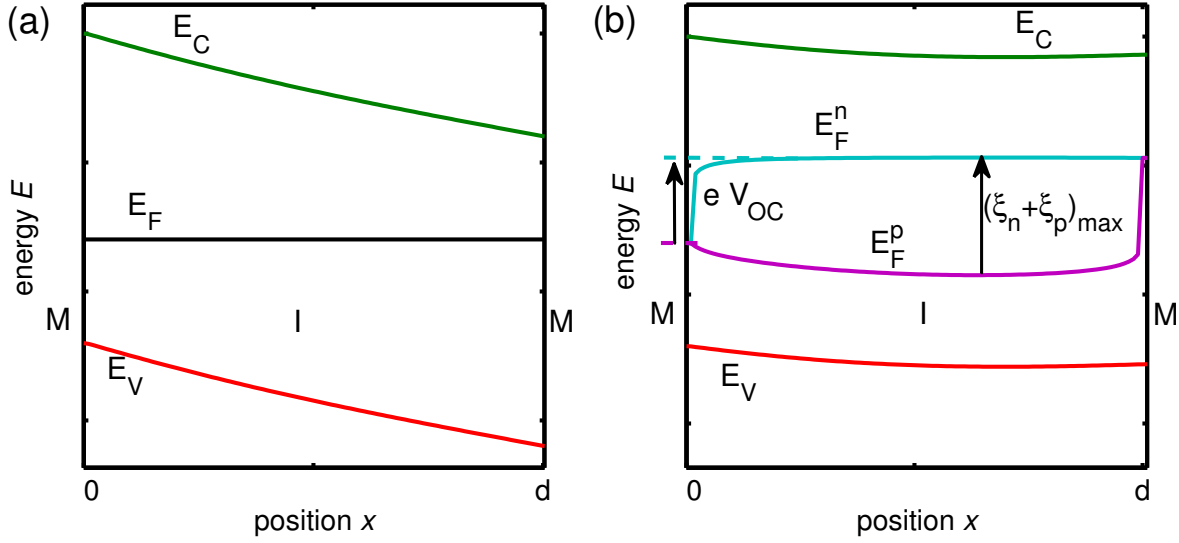
Figure 2.12: (a) Equilibrium band diagram of a MIM device with hole contact at $x = 0$ and electron contact at $x = d$. The band tilt represents a built-in field caused by a lower work-function contact on the right compared to the one on the left. (b) The device under illumination with split quasi-Fermi levels and a V_{oc} lower than the maximum chemical potential of an electron-hole pair due to surface recombination.

and hole current by identical particle currents in the same direction. Such compensating currents are represented according to Eq. 2.31 in an inverse curvature of E_{F}^p and E_{F}^n at each position x. This equation also explains the different amount of the bending of E_{F}^n and E_{F}^p dependent on charge carrier density and mobility. In Fig. 2.12(b) ∇E_{F}^n is larger close to the left contact due to the much lower electron density there. Additionally, the overall bending of E_{F}^p is more strongly pronounced compared to E_{F}^n due to the assumption of a lower hole mobility in this device.

This simple example already demonstrates, how an ideal solar-cell structure should look like: Additional sources of recombination (to the processes present in the absorber anyway, determining the chemical energy) should be avoided and especially contacts should be selective. If this is fulfilled, the maximum chemical energy will be completely transferred via flat quasi-Fermi levels to electrical energy at open circuit: $\xi_n^{\max} + \xi_p^{\max} = eV_{\text{oc}}$. However, this condition is not sufficient for highly efficient solar cells. As already discussed for the chemical potential (cf. Fig. 2.11), power extraction is not possible at open circuit, but requires a current flow. This involves a gradient in the electrochemical potential and leads to ohmic losses in the case of low-conductivity absorber materials or transport layers. In other words, the electrodes have to be capable of receiving the maximum quasi-Fermi level splitting for every applied voltage. Under this condition the chemical energy is converted completely into electrical energy. The subject of the next section will be technological

realizations targeting the ideal solar-cell structure.

2.5 Possible solar-cell realizations

2.5.1 The p-n junction

The p-n junction is the best-known realization of a photovoltaic device, because it is applied in the most common type of solar cells, which consists of crystalline silicon. In Chapter 4 this structure will be used as a test structure for the developed simulation tool, because, in the ideal case, its current-voltage characteristics can be calculated analytically.

A derivation of the characteristic equations is presented in the following, where we start with the behavior of the junction in dark. A p-n junction consists of a p-doped and an adjacent n-doped region. The doping concentrations are N_A and N_D. We assume that all dopants are active, which gives for the equilibrium hole (electron) densities in the p-(n-)region $p_p^0 = N_A$ ($n_n^0 = N_D$). The position of the Fermi levels is according to Eq. 2.13 and 2.12 close to the valence band edge for p-doping and close to the conduction band edge for n-doping. Bringing both regions into contact, the electrochemical potential must be constant in equilibrium and hence E_F aligned. The resulting band diagram is shown at the bottom of Fig. 2.13(a). It goes along with a redistribution of free charge carriers. The chemical gradient between p and n region causes a diffusion of electrons to the p-doped and holes to the n-doped semiconductor, where they recombine. Since the semiconductor was neutral, immobile ionized doping atoms remain [top of Fig. 2.13(a)]. They build up a space charge (ρ) region, which creates a field according to Poisson's equation. This field opposes the diffusion current and stops it in equilibrium, which is represented by a constant E_F. The potential difference is called the built-in potential V_{bi} and is the difference between the Fermi energies in the neutral (doped) regions, which can be expressed by the equilibrium charge carrier concentrations n_n^0 and p_p^0 according to Eq. 2.13 and 2.12:

$$
\begin{aligned}
eV_{bi} = E_F^n - E_F^p &= E_g - k_B T \ln\left(\frac{N_C}{n_n^0}\right) - k_B T \ln\left(\frac{N_V}{p_p^0}\right) \\
&= k_B T \ln\left(\frac{N_C N_V}{n_i^2}\right) - k_B T \ln\left(\frac{N_C N_V}{n_n^0 p_p^0}\right) \approx k_B T \ln\left(\frac{N_A N_D}{n_i^2}\right)
\end{aligned}
\tag{2.32}
$$

Assuming the Schottky approximation, i.e. an abrupt end of the space charge region [cf. Fig. 2.13(a)], the peak electric field F_m is simply given according to Poisson's equation by

$$
F_m = \int_{-x_p}^0 \rho_n dx = \frac{eN_A}{\epsilon_0 \epsilon_r} x_p = -\int_0^{x_n} \rho_p dx = \frac{eN_D}{\epsilon_0 \epsilon_r} x_n.
\tag{2.33}
$$

Integrating the linear electric field distributions from $-x_p$ to x_n gives the potential, which is equal to V_{bi}:

$$
V_{bi} = \frac{eN_A}{\epsilon_0 \epsilon_r}\frac{x_p^2}{2} + \frac{eN_D}{\epsilon_0 \epsilon_r}\frac{x_n^2}{2} = \frac{1}{2}F_m x_n + \frac{1}{2}F_m x_p = \frac{1}{2}F_m w.
\tag{2.34}
$$
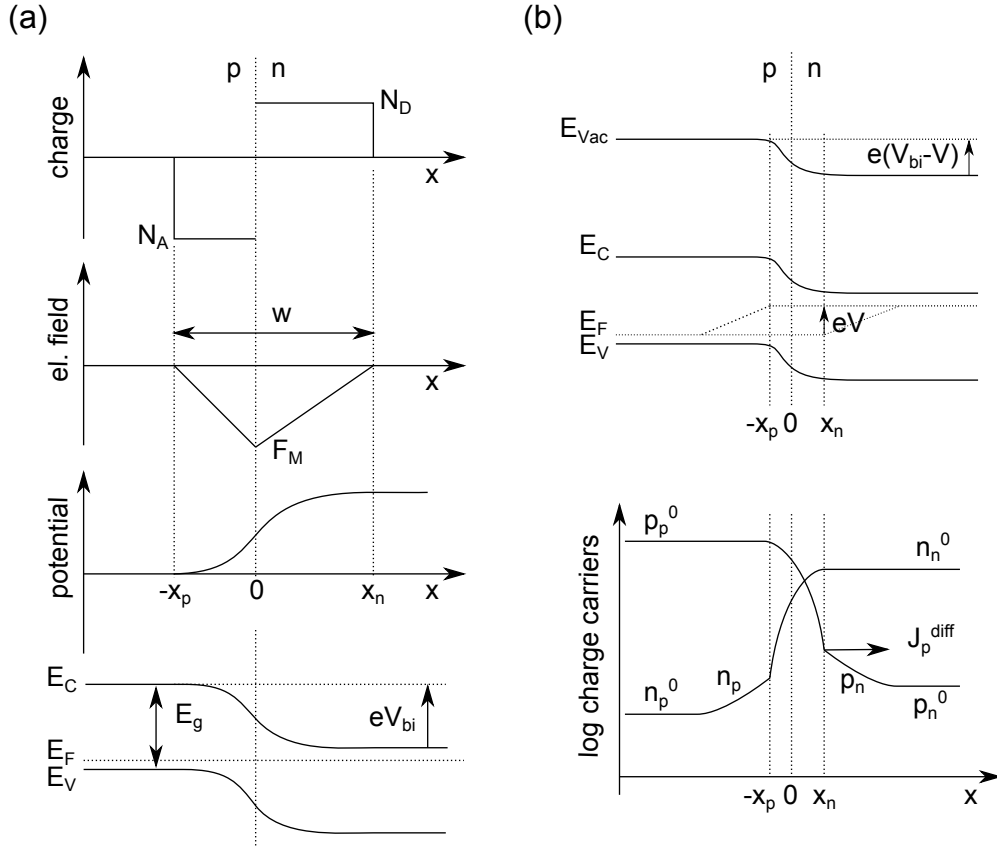
Figure 2.13: (a) Space charge, electric field, potential, and band diagram of a p-n junction in equilibrium. The width of the space charge layer is $w = x_n + x_p$. (b) Band diagram and free charge carrier densities under an applied forward bias voltage V.

We used Eq. 2.33 and defined w as the length of the space charge region. Applying both equations, w can be expressed as a function of doping concentrations, dielectric constant, and V_{bi}:

$$w = \sqrt{\frac{2\epsilon_0 \epsilon_r}{e} \frac{N_A + N_D}{N_A N_D} V_{bi}} \tag{2.35}$$

Here, V_{bi} can be replaced using Eq. 2.32. Thus, w depends apart from material parameters only on the temperature. The reason for the increase of w with T can be easily understood, considering the mentioned drift-diffusion equilibrium: The diffusion current increases with T due to the dependence of D in Eq. 2.29 on T. Therefore, it has to be compensated by a higher drift current, which demands for a higher field and hence a larger space charge provided by an increased w.

A p-n junction under applied bias voltage shows rectifying behavior, because biasing the device in reverse [(+) at n-side and (-) at p-side] attracts the charge carriers towards the electrodes and increases the space charge region, where no mobile carriers are located.

Therefore, a current does not flow under reverse bias. In forward bias [Fig.2.13(b)], this region is flooded by charge carriers and after reaching a certain threshold, a significant current flows.

Neglecting generation and recombination in the space charge region, the current-voltage characteristics can easily be calculated resulting in the Shockley equation. Additional preconditions are Boltzmann statistics (as in the whole chapter), an abrupt end of the depletion region with extensions x_n and x_p, and operation in the low-injection regime. This means that injected minority concentrations are much smaller than the amount of majorities resulting from doping. In steady state electron and hole current in the space charge region must be constant due to the exclusion of recombination. Hence, we can select the most simple position to calculate the current. This is the boundary of the space charge region to the n-doped layer x_n for the hole current and x_p for the electron current, respectively. As the region $x \geq x_n$ is field free, only diffusion of the holes, being minorities, p_n into the n-doped region has to be considered (Eq. 2.29):

$$J_p(x) = -eD_p\frac{dp_n(x)}{dx} \tag{2.36}$$

A constant hole current for $x < x_n$ postulates an almost constant E_F in the space charge region. A significant gradient would result in a current (cf. Eq. 2.31), which is not constant due to the strong variation of p within the space charge region, as shown in the bottom graph of Fig. 2.13(b). That means, an applied voltage changes directly the distance between E_F^p and E_V at x_n, resulting in the following correlation of p_n under bias and the equilibrium hole density p_n^0:

$$p_n(x_n) = p_n^0 \exp\left(\frac{eV}{k_BT}\right). \tag{2.37}$$

As the additional holes $p_n - p_n^0$ are subject to minority diffusion into the n-region accompanied by recombination with electrons, the following continuity equation must be solved, where Eqs. 2.36 and 2.22 are applied:

$$\frac{dp}{dt} = -\frac{1}{e}\frac{dJ_p}{dx} - R = D\frac{d^2(p_n(x) - p_n^0)}{dx^2} - \frac{p_n(x) - p_n^0}{\tau} = 0 \tag{2.38}$$

The solution of this differential equation gives an exponential decay of the hole density with the minority diffusion length $L_p = \sqrt{D_p\tau_p}$:

$$p_n(x) - p^0(x) = \left(p_n(x_n) - p_n^0\right)e^{-(x-x_n)/L_p} = p_n^0(e^{eV/k_BT} - 1)e^{-(x-x_n)/L_p} \tag{2.39}$$

Using this expression for the excess charge carriers in Eq. 2.36 and evaluating it at $x = x_n$ leads to

$$J_p(x_n) = \frac{eD_pp_n^0}{L_p}(e^{eV/k_BT} - 1). \tag{2.40}$$

Finally, this term in sum with the analog result for electron diffusion into the p-side

delivers the Shockley equation:

$$J = J_p + J_n = \left(\frac{eD_p p_n^0}{L_p} + \frac{eD_n n_p^0}{L_n} \right) (e^{eV/k_{\mathrm{B}}T} - 1) = J_{\mathrm{S}}(e^{eV/k_{\mathrm{B}}T} - 1). \tag{2.41}$$

Here, J_{S} is the saturation current, which is proportional to $n_{\mathrm{i}}^2/N_{D/A}$, if one uses Eq. 2.14 to replace the minority charge carrier density p_n^0 or n_p^0. This leads to an exponential temperature dependence of $J_{\mathrm{S}} \propto e^{-E_{\mathrm{g}}/k_{\mathrm{B}}T}$.

Under illumination electrons and holes are created and are extracted by a drift current, as soon as they enter the depletion region. Assuming this current J_{photo} to be independent of the field, which means that every charge carrier in this region is always extracted, allows its subtraction from the diode dark current of Eq. 2.41:

$$J = J_{\mathrm{S}}(e^{eV/k_{\mathrm{B}}T} - 1) - J_{\mathrm{photo}}. \tag{2.42}$$

The open-circuit voltage V_{oc} can be calculated by setting J to zero:

$$V_{\mathrm{oc}} \approx \frac{k_{\mathrm{B}}T}{e} \ln \left(\frac{J_{\mathrm{photo}}}{J_{\mathrm{S}}} \right) \overset{J_{\mathrm{S}}=J_{\mathrm{S0}}e^{-\frac{E_{\mathrm{g}}}{k_{\mathrm{B}}T}}}{=\!=\!=} \frac{E_{\mathrm{g}}}{e} - \frac{k_{\mathrm{B}}T}{e} \ln \left(\frac{J_{\mathrm{S0}}}{J_{\mathrm{photo}}} \right). \tag{2.43}$$

Here, we used the condition $J_{\mathrm{S}} \ll J_{\mathrm{photo}}$. Assuming not too high illumination intensities, the photocurrent scales linearly with light intensity. Thus, according to Eq. 2.43 V_{oc} increases logarithmically with intensity. Furthermore, due to the temperature activated J_{S} and $J_{\mathrm{S0}} \gg J_{\mathrm{photo}}$, V_{oc} decreases linearly with T. It is evident that a high J_{S} decreases V_{oc}. Equation 2.43 is formally identical to Eq. 2.18, which contains the maximum $V_{\mathrm{oc}}^{\mathrm{max}}$ in the chemical energy or quasi-Fermi level splitting, when optical generation and (radiative) recombination are equal:

$$V_{\mathrm{oc}}^{\mathrm{max}} = \frac{k_{\mathrm{B}}T}{e} \ln \left(\frac{j_\gamma^{\mathrm{abs}}}{j_\gamma^0} \right). \tag{2.44}$$

Coming back to the ideal solar-cell structure, the p-n junction shows some drawbacks [49]: Minorities have to reach the space-charge region via diffusion. If their diffusion length is too low, they recombine. Additionally, the contacts are not selective and constitute recombination centers for minorities, which reach the contact instead of the space charge region. Technological solutions like doping profiles, generating a so-called back-surface field [50], and surface passivation can reduce these negative effects. As we will see in the following, more sophisticated concepts exist, which include the requirements for an ideal solar cell already as built-in property.

2.5.2 Heterojunction and dye solar cells

Heterojunction solar cells are becoming more important. Reasons are that materials used in some thin-film solar cells can only be doped either by acceptors or donors, so that two different materials have to be employed to realize a p-n junction. The (organic) solar
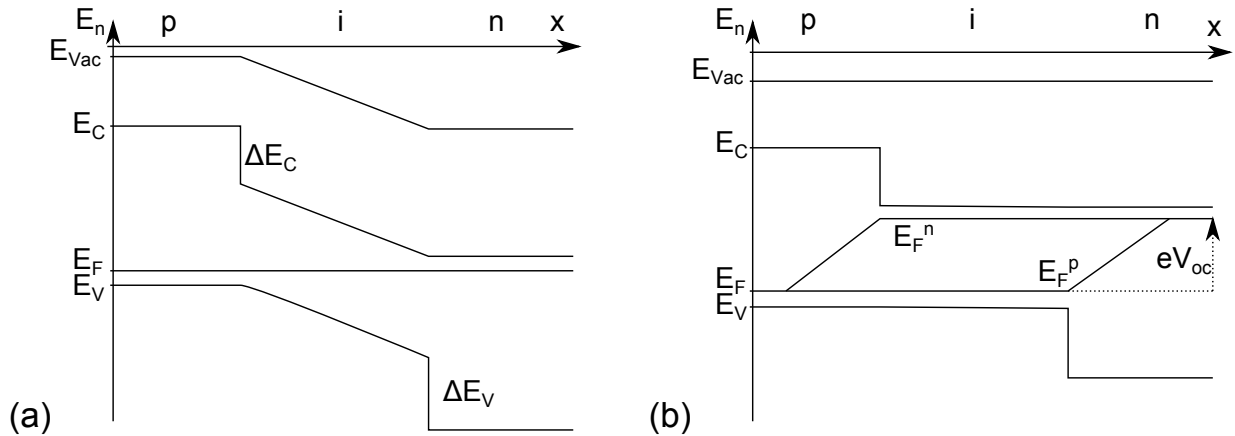
Figure 2.14: (a) Sketch of the band diagram of a p-i-n device with wide-gap transport layers in equilibrium. (b) The p-i-n device as ideal solar-cell structure in open circuit with constant quasi-Fermi levels within the intrinsic absorber delivering the maximum open-circuit voltage V_{oc}.

cells investigated in this work are exclusively of this type. A p-n heterojunction works comparably to a homojunction and has the same drawbacks. However, if the built-in potential introduced by doping is low or there is no doping applied, the band offsets at the heterojunction assist a directive extraction of charge carriers, as an electron, created or having once reached the n-side faces the energy barrier and cannot flow (back) to the p-side. This will be discussed in detail in Chapter 6 for so-called flat heterojunction organic solar cells, where charge carriers are directly generated at the junction and therefore located separately on their respective side of the junction. Another comparable realization is the dye (sensitized) solar cell (DSSC), where the absorber consists of a monolayer of dye molecules, which are located between an electron and hole conducting material [51, 52]. After excitation of the dye, the electron is transferred to a porous titanium dioxide (TiO_2) film, whereas the hole is transported by ions in a (polymeric or liquid) electrolyte. If recombination between the electrons on TiO_2 and the charge of the ions can be suppressed, this structure provides a built-in selectivity.

2.5.3 The p-i-n concept with wide-gap transport layers

An energy diagram of a p-i-n structure, consisting of three layers, is sketched in Fig. 2.14 in equilibrium (a) and under illumination in the open-circuit situation (b). Band offsets (ΔE_C, ΔE_V) cause high energy barriers for the electrons (holes) at the p-contact (n-contact). They guarantee the selectivity of the contacts and avoid recombination of charge carriers at the "wrong" electrode. The highly doped transport layers are responsible for an excellent collection of the Fermi-levels and avoid losses due to voltage drops in the case of current flow. This concept can be seen as ideal solar-cell architecture [3], which provides a high freedom of choice and arrangement of the absorber. It is realized in many
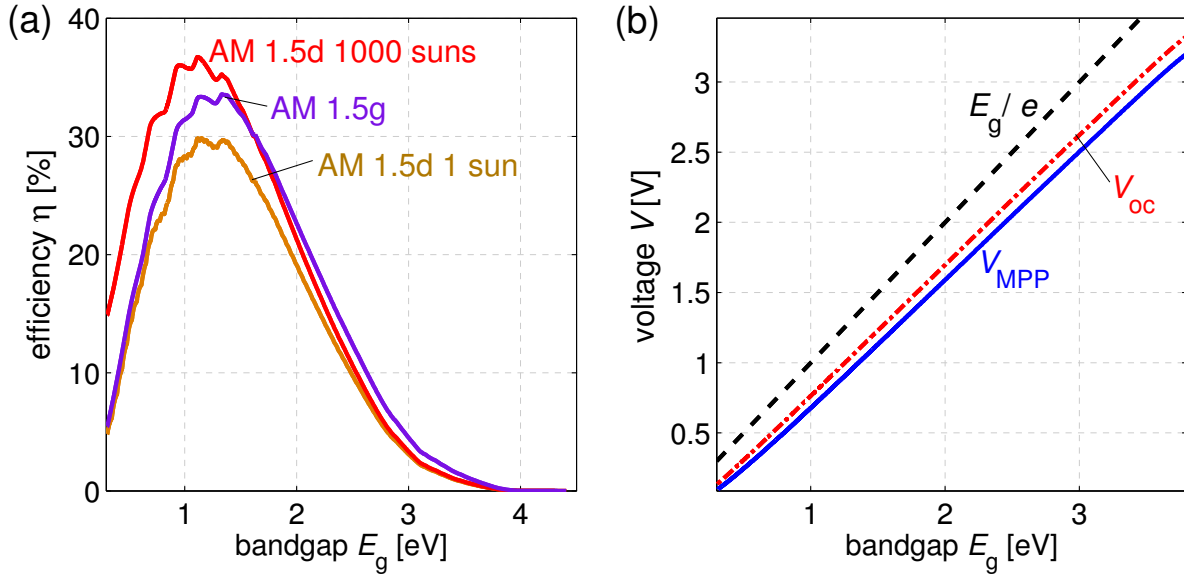
Figure 2.15: (a) Maximum efficiency of a single-gap absorber as a function of the bandgap E_g for different illumination spectra (AM 1.5 direct and global) and intensities. (b) V_{oc} and V_{MPP} as a function of the bandgap. They are lower than E_g/e due to radiative recombination. All data are shown for $T = 300\,\mathrm{K}$.

of the organic solar cells discussed in this work [53]. A built-in field exists in the p-i-n device due to the doped transport layers comparable to the p-n junction. However, this is not necessarily required for the conditions shown in Fig. 2.14(b). The same situation for the electrochemical potentials, which means an entropy-free charge carrier collection, can be realized by imagining a constant E_{Vac} in (a) with a continuous change in the electron affinity and ionization potential of the intrinsic material [3]. E_{Vac} in (b) would then rise from the p to the n region, representing a field due to the photogenerated charges.

2.6 Maximum efficiency – Shockley-Queisser limit

To find the ultimate efficiency limit, we assume an ideal single-gap solar cell, which does not exhibit extrinsic losses caused by series resistances or by reflection and transmission of light due to detrimental properties of the surface or too thin absorbers. We only consider physical ("intrinsic") losses, which are unavoidable.

At the beginning of this chapter we found the thermodynamic limit of solar thermal energy conversion to be 85 %. A terrestrial solar cell based on semiconductors cannot reach this limit, because it is not working under maximum concentration of the sun light. Additionally, thermalization losses are unavoidable. Furthermore, photons below the bandgap are not absorbed. Shockley and Queisser [54] calculated the maximum efficiency for a single bandgap semiconductor as a function of the bandgap approximating the sun as a
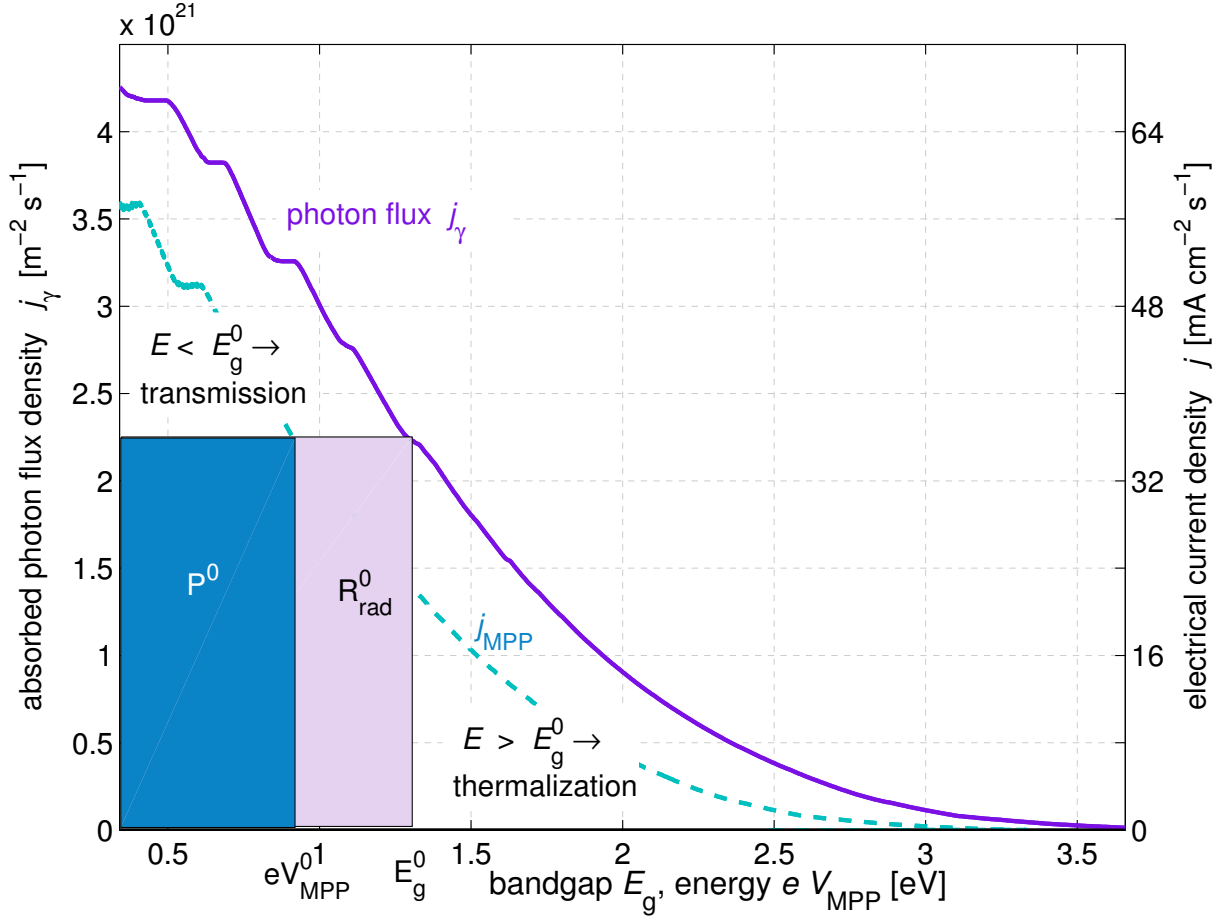
Figure 2.16: Solar photon flux density j_γ that can be harvested as a function of the bandgap E_g of an absorber and the corresponding electrical current density. The area below the curve describes the total energy of the photon flux. The maximum power which can be harvested by a single-bandgap absorber is the product of j_γ and the energy $eV_{MPP}^0 < E_g^0$ of the extractable electron-hole pairs. This is represented by the area of the rectangle marked by P^0.

black body. Henry refined the data using the AM1.5 spectrum [55]. Figure 2.15(a) shows the ideal efficiency η as a function of the bandgap. The maximum efficiency at 1 sun is around 30 % and increases to 36 % for a concentration factor of 1000 (AM 1.5d). AM 1.5g gives a value of 33 %. The ideal bandgap is between 1.1 and 1.6 eV. Lower bandgaps lead to a decrease in η due to high thermalization losses resulting in a low V_{oc}. Higher bandgap semiconductors do not absorb photons with energies lower than the bandgap. This tradeoff and additionally unavoidable radiative recombination (cf. Eq. 2.19), which limits V_{oc} below E_g, result in the curve.

Figure 2.16 gives a graphical illustration of the losses. Plotted is the photon flux density j_γ, which can be absorbed by a one-band-edge absorber with a band edge at a particular

E_{g}, which is the abscissa. The absorber is assumed to be sufficiently thick to absorb every photon larger than E_{g} ($a(\hbar\omega) = 1 \; \forall \; \hbar\omega > E_{\mathrm{g}}$). So, every value of j_{γ} at E_{g} is the result of an integration over the spectral photon distribution shown in Fig. 2.1 from E_{g} to infinity:

$$j_{\gamma}(E_{\mathrm{g}}) = \int_{E_{\mathrm{g}}}^{\infty} \frac{dj_{\mathrm{E}}^{\mathrm{AM\,1.5g}}/d\hbar\omega}{\hbar\omega} d\hbar\omega \tag{2.45}$$

Consequently, $j_{\gamma}(E_{\mathrm{g}} = 0)$ is the total photon flux from the sun. This kind of plot visualizes losses of not absorbed photons for an increasing E_{g}. The area under this curve represents the total intensity emitted from the sun. The largest rectangle with area $E_{\mathrm{g}}^0 \times j_{\gamma}(E_{\mathrm{g}}^0)$ would be the maximum usable intensity of a single bandgap absorber with E_{g}^0 ignoring any recombination. The area on its right to higher energy is lost due to thermalization, because these photons are collected at energy E_{g}^0 instead of using their total energy. The area above the rectangle represents losses due to the transmission of photons with too low energy.

We have already discussed the thermodynamics of a band-edge absorber and the unavoidable radiative recombination. This recombination limits the electrical energy of an extracted electron-hole pair to a value below E_{g}. The radiative losses R_0 can be calculated according to Eq. 2.17:

$$R_0(E_{\mathrm{g}}) = \frac{2\pi}{\hbar^3 c^3} \int_{E_{\mathrm{g}}}^{\infty} \frac{(\hbar\omega)^2}{e^{\frac{\hbar\omega}{k_{\mathrm{B}}T_0}} - 1} d\hbar\omega \tag{2.46}$$

With Eq. 2.18 we can calculate the ideal current-voltage characteristics as difference between absorbed and re-emitted photon flux, which is equivalent to the curve in Fig. 2.11:

$$J(V, E_{\mathrm{g}}) = e\left(j_{\gamma}(E_{\mathrm{g}}) - R_0(E_{\mathrm{g}})e^{\frac{eV}{k_{\mathrm{B}}T}}\right) \tag{2.47}$$

The maximum power can then be calculated by finding the maximum of the electrical power $J \times V$. The current at this maximum power point (MPP) is plotted as a function of the voltage at the MPP in Fig. 2.16 as well (dashed line). Figure 2.15(b) illustrates that the difference between both curves in Fig 2.16 is due to a decreased voltage at the MPP and also at open circuit (obtained by setting $J(V, E_{\mathrm{g}}) = 0$ in Eq. 2.47). Consequently, the maximum power-conversion efficiency is represented by the area marked by P^0 which is 33 % of the whole area under the curve and shows roughly 30% (13% absolute) loss due to radiative recombination. A higher concentration of the sunlight would shift the J_{MPP}-curve closer to J_{γ}. For an ideal absorber at the bandgap of silicon $E_{\mathrm{g}} = 1.12\,\mathrm{eV}$, the following values are obtained: $V_{\mathrm{oc}} = 0.87\,\mathrm{V}$, $J_{\mathrm{sc}} = 44\,\mathrm{mA/cm^2}$, and $\eta = 33.3\%$. More detailed calculations of the recombination losses, including device geometry and the equilibrium between absorption, emission, and re-absorption can be found in Refs. [54, 55]. Experimentally realized efficiencies with silicon solar cells are in the range of 20 % (commercial module) to 25 % (record cell) [56].

2.7 Novel concepts and classification of solar cells

Several ideas for overcoming the Shockley-Queisser limit have been proposed [57–59]. The most simple approach is the stacking of solar cells with different bandgaps creating a multi-junction device. In this approach, the low-bandgap cell is positioned at the back contact and absorbs light which is transmitted through the front cell(s). The thermalization losses are reduced, because high-energy photons are harvested by the high-bandgap cell(s) which deliver a higher V_{oc}. A tandem cell would mean drawing two rectangles in Fig. 2.16, covering a larger area than a single rectangle. The maximum efficiency is 42% ($E_g^1 = 1.0$ eV; $E_g^2 = 1.9$ eV) [60] rising to 50 % at 1000 suns [55]. Henry also calculated the maximum efficiency of a 36-gap cell to 72 % at 1000 suns [55]. Technically, multi-junction cells are usually realized monolithically. This results in a series connection of the single subcells, which increases V_{oc}, but requires current matching. The most recently reported record efficiency for an GaInP/GaAs/GaInNAs triple cell measured at 418 suns is 43.5 % [56].

All other concepts like the extraction of hot carriers or the insertion of intra-gap states, which are not active as recombination centers, but allow a two-step absorption, are theoretically interesting. However, they have not yet been successfully realized. Neither multiple electron-hole pair generating absorbers nor up- and down conversion materials lead to highly efficient solar cells. These ideas belong to the third generation of photovoltaics [57]. According to this classification the first generation consists of the conventional single or poly-crystalline (mostly Si) solar cell, which is energy intensive and expensive in production. The second generation is said to consist of cheap thin-film technologies employing less crystalline absorbers and providing moderate efficiencies.

Another classification describes the third generation of solar cells as cheap and efficient. Organic photovoltaics showing the potential of low-cost production technologies are sometimes included in this field. According to actual knowledge no significantly stricter theoretical limits are to be expected compared to those discussed in this chapter, although the energy conversion requires additional steps. The development in the last years has shown an increase in organic-solar-cell efficiencies of around 1 %/yr recently reaching 10 % [34, 35]. Consequently, 12 to 15 % should be within reach in the next years. These results are promising and show that it is worth to discuss the principles of organic photovoltaics in more detail in the subsequent chapter.

Chapter 3

Organic Solar Cells

This chapter starts with the characteristic electronic structure and charge transport properties of organic semiconductors. This topic is followed by a detailed discussion of the working principle of organic solar cells, where we apply the general knowledge from Chapter 2 to organic solar-energy converters. Starting from the description of the steps involved in energy conversion, which limit the quantum efficiency and the maximum extractable energy, the chapter shifts focus towards real structures and materials. It concludes with more experimental aspects concerning fabrication and characterization. Whereas the first sections review very basic chemistry knowledge, the solar cell section gives a detailed evaluation of currently used models and ideas to explain the current-voltage characteristics of organic solar cells.

3.1 Energetics of organic molecules

The main difference of organic semiconductors compared to atomic semiconductors is the presence of molecules, which maintain most of their characteristics also in the solid. This has consequences for the optical properties like absorption and luminescence and the electrical properties like transport gaps, charge carrier localization, separation, and transport. The latter are connected to the fact that organic thin films are mostly amorphous or nanocrystalline. Before coming to the properties of the solid, we briefly discuss its sub-units, which are the molecules. As we do not explicitly consider single molecules in the simulation, they are covered very briefly and on an intuitive basis.

3.1.1 From atoms to molecules

We have seen in the previous chapter that a basic requirement for electrical conductivity is the presence of delocalized electrons capable of receiving energy from an applied field. This delocalization is much less pronounced in an organic solid compared to a crystalline semiconductor forming energy bands. However, the delocalization is given by the π-system of the molecules as subunits of an organic solid. In the following, we derive the formation of molecular orbitals by assembling the molecules from single atoms. As we are dealing
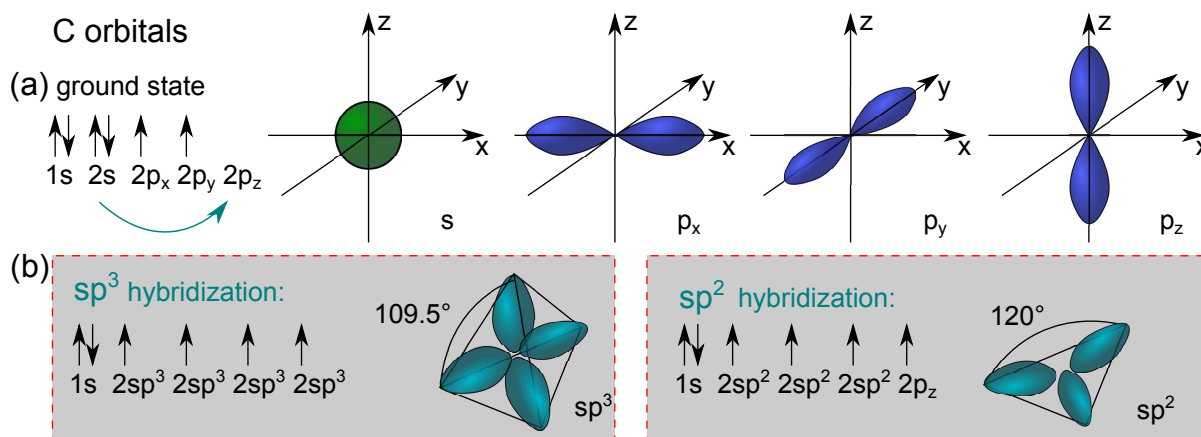
Figure 3.1: (a) Electron configuration and molecular orbitals of a single carbon (C) atom. (b) Hybridization, where the three (two) 2p orbitals and the 2s orbital form four sp^3 (three sp^2) hybrid orbitals.

with organic chemistry, the main component is the element carbon (C) having six electrons including four valence electrons. From atomic physics it is known that the electrons are organized in shells around the core. Each shell consists of orbitals describing the spatial region, within which an electron is located with a certain probability (mostly 90 %). Each orbital can host two electrons with different spins. Carbon is described by the electronic configuration $1s^2 2s^2 2p^2$, which means that the s-orbitals of the first and second shell are fully occupied by two electrons. The two remaining electrons are found in two of the three degenerate p-orbitals which can host up to six electrons, and are each filled by one electron first according to Hundt's rule. The mentioned orbitals are known from the solution of the Schrödinger equation for the hydrogen problem and correspond to particular quantum numbers. The principle quantum number describes the shell ($N = 1, 2, \ldots$), and the angular momentum quantum number is represented by the letters s, p, d,.... Figure 3.1(a) shows the shape and orientation of the symmetric s- and the three dumbbell-shaped p-orbitals. For chemical bonds only valence electrons play a role, which are the electrons of the outer shell (for C $N = 2$). To make a stable bond with another atom, the atom tries to reach a noble gas configuration. This configuration is characterized by eight valence electrons and results from an energy minimization (octet rule). If the electrons are shared between both atoms, this bond is called covalent, in case of a complete electron transfer it is called ionic (e.g. sodium chloride, Na^+Cl^-).

We start our study of covalent bonding with a simple hydrocarbon, the methane CH_4: The central carbon atom with four valence electrons shares one with each hydrogen, also delivering one electron for the bond, which is represented by a line in the Lewis structure of Fig. 3.2(a). This results for both, H and C in a noble gas configuration (He and Ar). The four bonds represent overlapping orbitals and the equilibrium angle between the bonds is 109.5°, such that a symmetric tetrahedron is formed. This configuration allows for the maximum distance between the (repulsive) electron orbitals according to valence shell
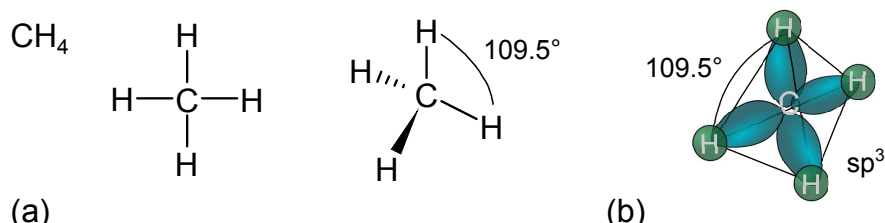
Figure 3.2: Methane (CH_4) molecule: (a) Compact Lewis structure and (b) visualization of the bonding orbitals and the bonding angle.

electron pair repulsion (VSEPR) theory [61]. These four orbitals cannot result from a simple overlap of the three orthogonal p-orbitals and the single symmetric s-orbital of the binding partners. They constitute four new orbitals, called sp^3 (Fig. 3.1(b)), because they result from an overlap of one electron in the s- and one electron in each p-orbital. This effect is called hybridization and implies that one C valence electron, which was originally in an s-orbital, has entered a p-orbital. This energy cost is compensated by the formation of a so-called σ (sigma) bond, consisting of two electrons in the overlapping sp^3(C)-s(H) orbital shared between C and H [Fig. 3.2(b)]. In the quantum mechanical picture, these bonds are approximately formed by linear combinations of the single-atom orbitals (LCAO method [62]), leading to a splitting of the energy eigenvalues. Dependent on the sign (or the phase) of the two overlapping wave functions ϕ, bonding and antibonding (high energy) states Ψ are formed, as illustrated in Fig. 3.3(d). Bonding orbitals are characterized by a lower energy than antibonding orbitals and a high probability of finding an electron between the atoms. Due to symmetry reasons only these two combinations are allowed. If one imagines a bond between two identical atoms, this is directly plausible, because the probability distribution $\Psi\Psi^*$ remains symmetric only in these two cases. In a relaxed state, only the bonding orbital is expected to be occupied.

Proceeding with a more complex molecule, ethene C_2H_4, we find a double bond between the two C atoms, so that every C atom has only three neighbors [Fig. 3.3(a)]. This means one electron is provided by the s- and two by the p-orbitals so that three new sp^2 hybridized orbitals [Fig. 3.1(b)] are created. The molecule is planar, because the optimum occupation of space leads to a configuration with 120° angles between the bonds, which lay within one plane. The perpendicular p-orbital of each C atom remains unchanged. Both overlap in a region out of the plane and form a so-called π (pi) bond, which is again dependent on the sign of the combination, bonding (π) or antibonding (π^*). Thus, a double bond, indicated by two lines in the Lewis structure, consists of a σ [line in Fig. 3.3(b)] and a π bond, i.e. two overlapping sp^2 and two overlapping π-orbitals. A triple bond would have two π bonds. The location of the π-orbital is shown in the figure as well and can be easily made plausible considering electrostatic forces on the π electron gas: Attraction from the positive carbon cores and repulsion from the C-C and C-H σ bonds favor a location out of the plane of the σ bonds, however close to the cores.

The discussed chemistry of covalent bonding is also present in inorganic semiconductors, e.g., diamond or silicon with exactly the sp^3 tetragonal binding angles. Such a
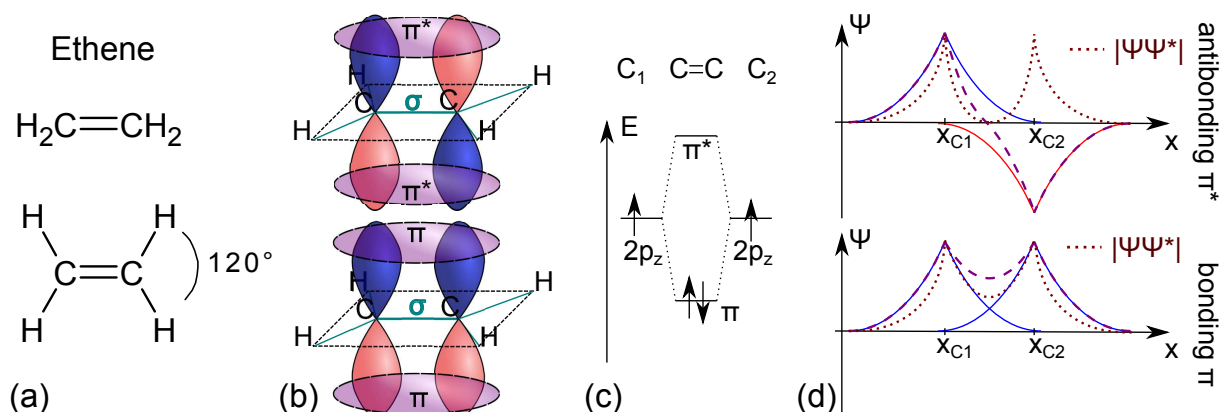
Figure 3.3: (a-c) Ethene (C_2H_4) molecule: (a) Compact Lewis structures, (b) visualization of bonding and antibonding π-orbitals and (c) their energies. Colors of the orbitals denote the phase of the wave function as sketched in (d). An anti-bonding orbital lies higher in energy than the occupied bonding orbital. (d) Linear combination of atomic orbitals (solid lines) with the cores located at x_{C1} and x_{C2} defining the molecular electron wave function (dashed) and probability distribution (dotted).

three-dimensional configuration leads to stable intrinsic materials, showing semiconductive properties due to their band structure and due to a high delocalization of additionally inserted electrons. Organic semiconductors, however, consist of (covalently bound) hydrocarbon molecules as their basic units, which develop only weak bonds between each other. Among these molecules, aromatic compounds are very interesting, because they show extended π-systems, which are capable of electron transport due to a high delocalization. Aromatics are planar ring molecules, which consist of atoms, each having one p-orbital perpendicular to the plane. The number of these π electrons has to fulfill $4n + 2$ with $n \in \mathbb{N}$ according to Hückels rule [63].

The most simple aromatic compound is benzene, consisting of six C atoms in a ring, each entering a bond with one H and a double and single bond with the neighboring C [64]. Two possible realizations, so-called resonant (mesomeric) structures, can be imagined and are shown in Fig. 3.4(a), where neither configuration is preferred due to symmetry reasons. In reality, energy minimization leads to the same length of each bond ($\approx 140\,\mathrm{pm}$) [65], which is found between the length of a single ($146\ldots148\,\mathrm{pm}$) and a double bond ($130\ldots135\,\mathrm{pm}$) [66]. One might draw a circle in the Lewis structure, which has the disadvantage that electrons cannot be counted. Double bonds with one single bond in between are called conjugated and are the condition for a delocalization. In the molecular orbital picture, every C atom forms three sp^2-orbitals (σ bonds) and one perpendicular p-orbital [Fig. 3.4(b)]. The overlap results in six π-orbitals, with different energies depending again on the phase overlap, which means on the number of "nodes" as shown in Fig. 3.4(c). The six electrons occupy the 3 bonding (π)-orbitals, whereas the 3 anti-bonding (π^*-) orbitals are unoccupied. The difference between the highest occupied molecular orbital (HOMO, π) and the
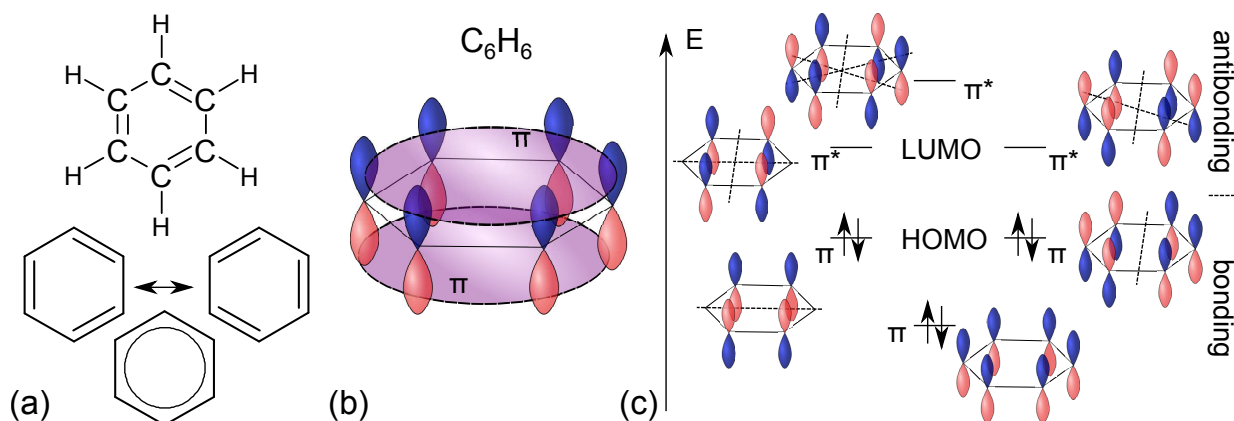
Figure 3.4: Benzene: (a) Kekulé structure, consisting of two resonance (mesomerism) structures. (b) Visualization of the location of the lowest bonding π-orbital. (c) The position of the six energy levels resulting from the overlap of the six p_z orbitals. The more nodes are found in the wave function, the higher is the energy.

lowest unoccupied molecular orbital (LUMO, π^*) of benzene is in the range of 6 eV, which corresponds to a UV photon wavelength of 250 nm [67]. An extension of the π-system by, e.g., adding more rings, leads to a further splitting of the energy levels and delocalization, which decreases the HOMO-LUMO distance. For example, the HOMO-LUMO gap of pentacene (5 rings) is 2.2 eV (560 nm) [67]. This trend in the HOMO-LUMO gap can be illustrated considering an electron in the π-system as particle in a box [68] with the dimensions of the system. A solution of the Schrödinger equation of this system directly results in a decreased distance between the energy eigenvalues for a larger box size. The adjustability of the gap provides tunable optical transitions in the visible spectral range. This property together with an extended π-system makes aromatic compounds very interesting for optoelectronic applications.

In a typical absorption spectrum of a single molecule (measured in a molecular ensemble in gas phase), $\pi - \pi^*$ transitions can be seen as sharp lines, accompanied by the superposition of vibrational states. The vibrational manifolds show a characteristic spacing of around 100 meV, each superimposed by rotational and translational sublevels of energies in the range of 10 meV. The energy levels of excited states and possible transitions are summarized in Fig. 3.5, which shows an extended Jablonski diagram of valence electrons of a molecule.

The excited states can be categorized by their multiplicity, $2s + 1$, where s is the spin, which is a kind of angular momentum of an electron. Its direction (up $s = \frac{1}{2}$ or down $s = -\frac{1}{2}$) can be seen as an additional degree of freedom, allowing according to the Pauli principle two electrons occupying the same energetic state. The ground state of a molecule usually shows multiplicity of 1, called singlet, because all orbitals up to the HOMO are occupied by paired electrons. They have inverted spins, leading to an overall spin s of zero.

The ground state with energy 0 is called S_0. Excited states are called S_1, S_2... Two
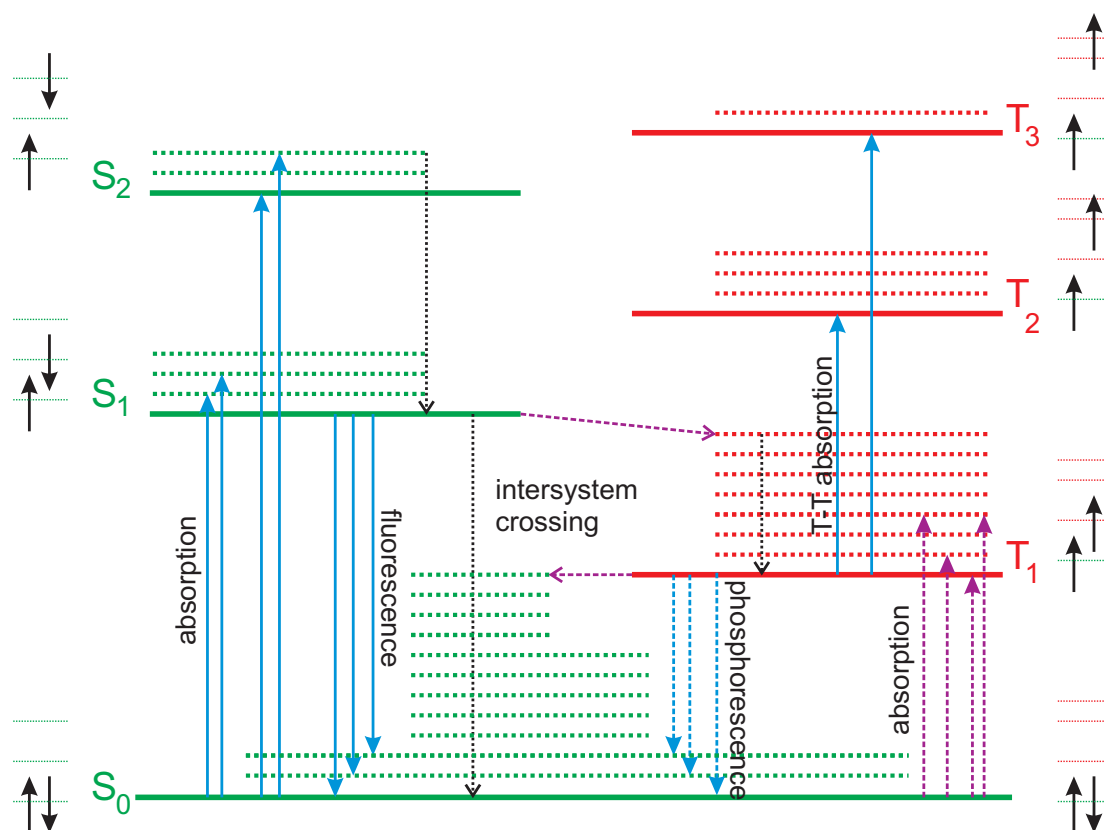
Figure 3.5: Jablonski scheme with singlet (S) and triplet (T) states and their vibrational manifolds (dotted). Solid lines denote optical transitions, dashed lines spin-forbidden transitions (intersystem crossing), and dotted lines non-radiative internal conversion paths. (Redrawn after Refs. [67, 69].)

electrons with unpaired (i.e. parallel) spins ($\pm 1/2$ each) have a multiplicity of three and are called triplets T_1, T_2... Triplet energies are commonly found to be lower than singlet energies. The reason is the Pauli exclusion principle, allowing a larger wave-function overlap (some overlap is needed for a transition) of electrons with antiparallel spins in two different orbitals. Hence, on average electrons with antiparallel spins (singlets) are found closer together, which causes a larger Coulombic repulsive energy. So, singlets have a higher energy than triplets [69]. Singlet-triplet transitions are spin-forbidden, however can occur due to spin-orbit coupling, which allows for intersystem crossing. Hence, a T_1 state, which has to decay to S_0, has a much higher lifetime (commonly msec) than an S_1 state (typically μs-ns) [67, 69]. Higher excited states ($S_{2,3}$... $T_{2,3}$...) show very low lifetimes and relax to the first excited state by internal conversion within picoseconds. Internal conversion is a non-radiative process, whereas transitions (according to Kasha's rule mainly from S_1 and T_1) to the ground state are often radiative [70]. This luminescence radiation from singlets is called fluorescence and from the longer living triplets phosphorescence. The photoluminescence signal is commonly shifted to higher wavelengths compared to the absorption
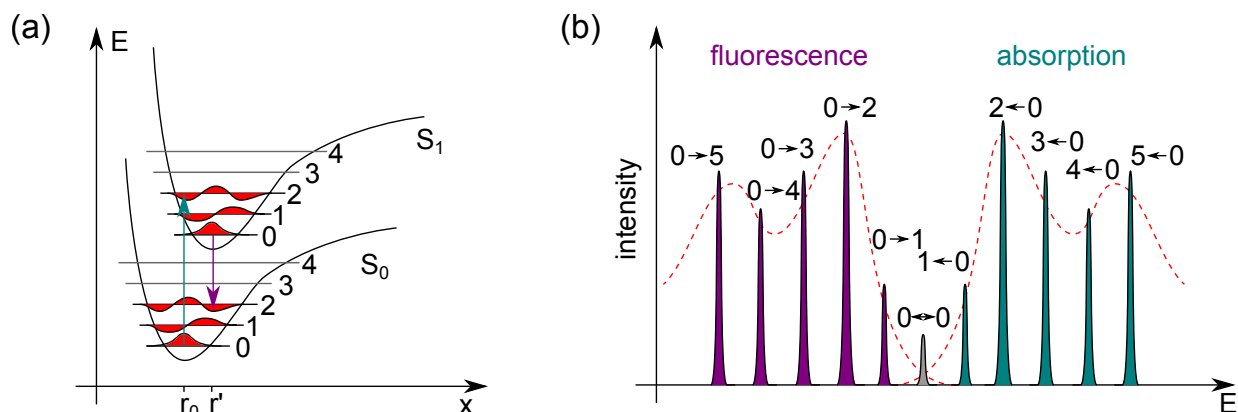
Figure 3.6: Franck-Condon shift due to vibronic transitions: (a) Sketch for a two-atomic molecule where the interatomic distance differs between excited (r') and ground state (r_0). (b) Absorption and shifted emission from the vibrational ground states into vibrational manifolds. The $2 \leftrightarrow 0$ peak is largest due to the favored vertical vibronic transition shown in (a). In solution or solid phase the peaks of the gas phase are broadened (dashed line). (Redrawn after Refs. [67, 69].)

spectrum (Stokes shift) due to lattice relaxations, minimizing the electronic energy of the excited state.

The Franck-Condon principle explains the probability of so-called vibronic transitions, which are characterized by a simultaneous change of electronic and vibrational states. This principle says that an optical transition is most probable for a vertical transition, where no motion of the much slower nuclei is required. Such a transition usually does not occur between two vibrationally relaxed states, because they exhibit, as already mentioned for the Stokes shift, different equilibrium positions of the nuclei. Quantum mechanically spoken, the most probable (vibronic) transition is the one with the highest wave-function overlap, as sketched in Fig. 3.6 for a two-atomic system.

According to Koopmans' theorem [71], the HOMO level is approximately equal to the energy needed to ionize the molecule, which is called ionization potential (IP). As a result of the ionization, the molecule is positively charged and forms a cation, whose electronic structure and hence excited states differ from the ones of the neutral molecule. The energy gained when adding an additional electron to a neutral molecule, then forming an anion, is the electron affinity (EA). An unpaired electron of a radical occupies the single occupied molecular orbital (SOMO), which is a half-filled HOMO (and thus also identical to the LUMO) of the radical. Due to the negative (positive) net-charge, one might assume that the value of the EA (IP) of the anion (cation) is decreased (increased). This implies an energetic position of the SOMO of an anion (cation) slightly higher (lower) than the LUMO (HOMO) of the neutral molecule. However, a reorganization due to a structural relaxation of the ion leads to an opposite shift of the frontier orbitals into the HOMO-LUMO gap of the neutral molecule [72, 73]. The reorganization energy results in an optical gap of radical ions which is decreased in comparison to the ground state absorption of the neutral
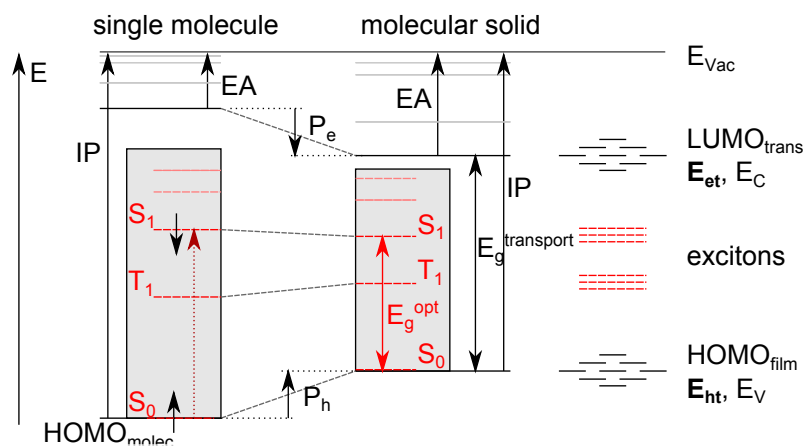
Figure 3.7: The evolution of the energy levels of a molecular solid from single-molecule levels. Gaps are decreased due to a polarization effect of the surrounding. Also excited states are plotted on a separate scale, where the ground state S_0 is placed at the position of the HOMO. Disorder leads to a broadening of the levels.

molecule (see e.g. in Refs. [74, 75]).

3.1.2 From single molecules to a molecular solid

The main difference of a molecular solid to a covalently bound solid (characterized by a high melting point, brittleness, and low intrinsic conductivity) is found in the weak so-called van der Waals bonds between molecules, promoted by fluctuating charges. These fluctuations induce temporary dipoles, resulting in an attractive force. Commonly, no other type of intermolecular bond can be formed due to a closed shell of each molecule. The weak van der Waals bonds are the reason for the low stability of organic solids, classified as soft matter. The main spectroscopic properties of the solid coincide to a large extent with those of the single molecule. Absorption edges are usually shifted to lower energies due to intermolecular interactions. For a highly ordered molecular crystal, the energies of excited states split due to wave function overlap and form (comparable to inorganics) narrow excitonic bands. Since the films of materials commonly applied in organic solar cells do not form single crystals, but are rather amorphous, we do not discuss the properties of molecular crystals any further. The interested reader is referred to Ref. [67]. Amorphous layers do not show a long-range order and the concept of delocalized crystal waves and energy bands is not suitable. The absorption spectrum of an amorphous solid is comparable to a solution spectrum, where the molecular absorption peaks are shifted (solvent shift) and strongly broadened due to a distribution of intermolecular distances.

Disorder has a strong impact on charge transport properties and energy levels. So far we only discussed excited states of neutral molecules, which we also call excitons from now on.

Charge transport, however, requires free electrons or holes. Their energies are commonly depicted in showing the potential for an electron, which is a single-particle picture, like the band diagrams in Chapter 2. This description is not directly compatible with the excitonic picture, shown in the Jablonski diagram of Fig. 3.5 [76]. Nevertheless, Fig. 3.7 is an attempt to visualize all energy levels within one picture, where the ground state S_0 of the molecule is positioned at the HOMO which is referred to the vacuum level, whereas the excited state energies refer to the ground state. Phenomenologically spoken, the charge transport levels of a solid are for a positive charge (hole) the ionization potential (IP) and for a quasi-free electron the electron affinity (EA), as defined in the previous section. In the orbital picture, a mobile electron is in first approximation located in the LUMO, whereas a hole is transported in the HOMO. This is not completely true, and more precisely in case of a strong localization of the charge the electron (hole) is located in the SOMO of the anion (cation), which is expected to be close to the LUMO (HOMO) of the neutral molecule.

Figure 3.7 shows that HOMO and LUMO levels shift, when a solid is formed out of several single molecules. Responsible are polarization effects, resulting from an electrostatic screening, as the charges of neighboring molecules are redistributed in the presence of an ion. Additionally, lattice relaxations contribute to polarization. Consequently, the transport gap of a solid is significantly lower than the one expected from a single molecule. The polarization energy P_h can be determined by (ultraviolet) photoelectron spectroscopy (UPS, cf. Ch. 4.9), comparing the IPs of a single molecule and a solid. In a first approximation, the polarization can be assumed to be independent of the sign of the charge. This implies that P_e equals P_h. The hole (electron) in combination with this polarization is commonly called a positive (negative) polaron. For convenience we will also use the term electron and hole, keeping in mind that polaronic effects are already included in these terms. To avoid confusion we call the energy levels of the charge carriers when discussing charge transport simulations **transport energies E_{et} and E_{ht}** with $E_{et} \approx \text{LUMO}_{film}$ and $E_{ht} \approx \text{HOMO}_{film}$. Excitons and polarons can interact, which usually results in exciton quenching (non-radiative relaxation).

In the case of a highly ordered crystal, E_{et} and E_{ht} of Fig. 3.7 are not sharp lines. The degenerate levels split and form bands as discussed for classical semiconductors in Chapter 2. Here, however, bands are narrow (several 100s of meV) due to the low wave-function overlap [67]. Thin films employed in solar cells are, as already mentioned, mostly amorphous. Consequently, bands are not formed. Though, the energy levels are not sharply defined and are commonly assumed to follow a Gaussian distribution due to disorder-induced changes in polarization energy. Typical values of the width σ of the distribution are in the range of 50...150 meV. Additionally, trap states within the transport gap can emerge from regions with significantly higher polarization energies due to impurities or regions with a higher crystallinity. Models for the transport mechanisms of excitons and polarons are discussed in the next section.
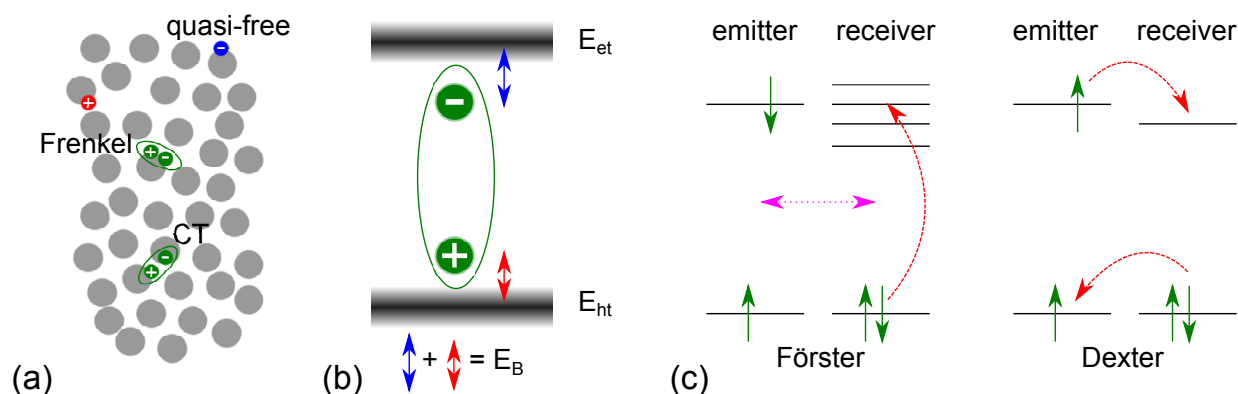
Figure 3.8: (a) Visualization of quasi-free charge carriers, Frenkel and charge-transfer (CT) exciton in a molecular solid. (b) Visualization of an exciton as excited state with exciton binding energy E_B in a one-electron potential diagram. (c) Exciton transport: Resonant Förster (only singlet transport) and hopping Dexter transfer (also triplet).

3.2 Energy and charge transport in organic semiconductors

Energy (exciton) and charge (polaron) transport in a highly ordered molecular crystal and at low temperatures are comparable to the processes in conventional semiconductors described in the previous chapter. These quasi-particles are coherently transported in energy bands with a crystal momentum k. The coherence time is then the time until scattering at a defect occurs. If the distance covered by the particle during this time is reduced to the range of the lattice constant or intermolecular distance, coherence is completely lost and the transport can be described by hopping from site to site. This kind of transport is dominant in organic thin films employed in solar cells, because they are commonly nanocrystalline or amorphous.

3.2.1 Exciton transport

An excited state can be transfered to a neighboring molecule. The excited state is then called an exciton, which provides an energy transport by migration. Such an exciton can be delocalized in case of strong intermolecular interactions as present in a highly crystalline solid. It is then called a Wannier exciton. This is not the case in the studied disordered materials, where the exciton is mainly located on one molecule and can be treated as a neutral quasi-particle with polaronic nature, called Frenkel exciton [Fig. 3.8(a)]. Such a Frenkel exciton can be seen as a tightly bound electron-hole pair with the exciton binding energy as difference between its energy and the energy of a completely separated electron-hole pair. The binding energy is in the range of several 100 meV [67], because the dielectric constant of common organic materials is relatively low (3...6) compared to typical inor-

ganic semiconductors (13...16 [42]). Visualizing this energy in an energy-level diagram with transport levels, which is a potential diagram for electrons, leads to the already mentioned difficulty of representing excited states in such a diagram. In this work, an exciton is symbolized by an ellipsoid around an electron and hole located in the energy gap, as shown in Fig. 3.8(b). If the two charges are located on separate neighboring molecules, the exciton is called a charge transfer (CT) exciton, which can be found especially between different molecular species, as we will see later.

The transport of a Frenkel exciton as neutral quasi-particle is most easily described by a diffusive motion from one molecule (emitter) to a molecule in the surrounding (receiver). The probability is given by a matrix element with a perturbation Hamiltonian, including electrostatic and electron-exchange interaction potentials. The first one is responsible for so-called Förster and the second one for Dexter energy transfer. They are visualized in Fig. 3.8(c). Förster transfer is based on a dipole-dipole interaction, characterized by the spectral overlap of emission and absorption spectrum of emitter and receiver. It can be of long range (several nm) and decays with distance R^{-6}. This resonant transfer conserves each spin of emitter and receiver. Therefore, it allows only for singlet transfer.

Dexter transfer does not require allowed transitions between emitter and receiver. Electrons can be exchanged by a wave function overlap only between nearest neighbors with a rate exponentially decreasing with distance (e^{-R}). One might think of a simultaneous transfer of electron and hole between neighboring molecules, which is comparable to hopping charge transport. All transitions which conserve the total spin of the involved molecules are allowed, including triplet-triplet transitions. Organic solar cell materials show energy migration occurring in the range of 5-40 nm [77, 78], which is much larger than the range of Dexter transfer. Thus, exciton transport can be described by a multi-step diffusion process.

Energy migration can be experimentally observed by sensitized fluorescence in a guest-host system, where most of the light is absorbed by the host, constituting, e.g., more than 99 % of the film [67]. However, emission is predominantly observed from the guest with a lower S_1 energy, which favors energy transfer. The large signal of the emission of the guest can only be explained by an exciton diffusion in the host. Other methods to prove exciton migration use a quencher at a location far away from the locus of absorption or excitonic processes like exciton annihilation, when two excitons meet after diffusion (cf. Ch. 4.9).

3.2.2 Charge transport - Gaussian disorder model

Although electrons are delocalized on an intramolecular scale in π-electron systems, they are localized on an intermolecular scale in amorphous organic solids. Thus, each molecule or more precisely π-system constitutes a hopping site with a transition probability to a neighboring π-system, which is in first approximation proportional to the overlap of the two adjacent π-orbitals (HOMOs) for hole transport or two π^*-orbitals (LUMOs) for electron transport. More precisely, the polarization effect of the hole (electron) should be considered, and depending on the screening capability of the surroundings, the transport is better described as hop from the SOMO of the ion to the HOMO (LUMO) of a neutral molecule.
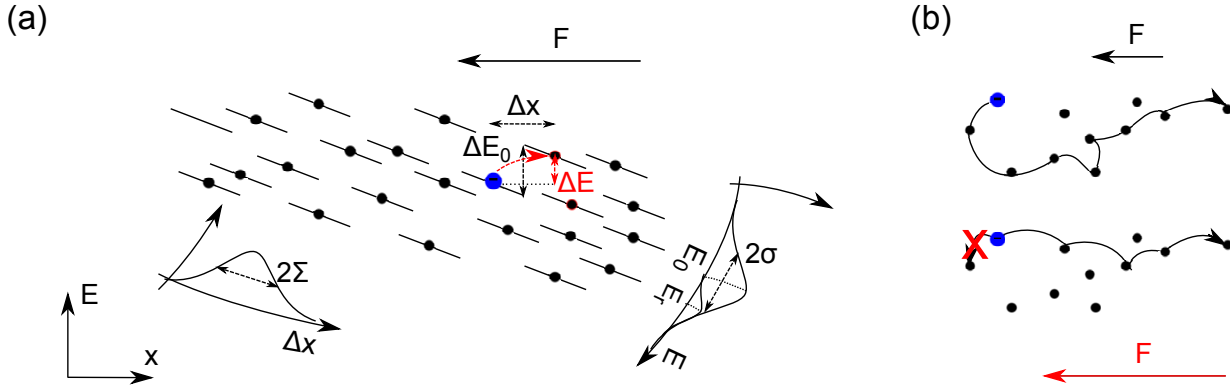
Figure 3.9: Sketch of hopping transport from site to site (dots): (a) Illustration of diagonal (σ) and off-diagonal Σ disorder and the effect of an electric field F (visualized by the tilted lines) on the effective barrier ΔE. (b) Negative field effect for large spatial disorder: The most probable electron path is suppressed by a higher field. This reduces the mobility.

The low overlap in less densely packed amorphous films results in charge carrier mobilities which are several orders of magnitude lower compared to crystalline semiconductors. Furthermore, they show a "reverse" temperature dependence around room temperature: In organic semiconductors the mobility increases with temperature due to thermally activated hopping, whereas in case of band transport it decreases due to increased phonon scattering. Additionally, disorder leads to a dispersive transport, making an experimental determination of the mobility difficult and the applicability of the (theoretic) material parameter mobility questionable.

The most common model for a theoretic description of hopping is the Bässler model [79], also called Gaussian disorder model (GDM), which will be introduced in the following and is illustrated in Fig. 3.9(a):

Although the energy levels of charge transport are not directly measurable by optical spectroscopy due to the discussed favored excitonic transitions, one might transfer the Gaussian shape of absorption and fluorescence to the charge transport levels as well. Thus, we can write for the density of states (DOS):

$$g(E) = \frac{N_{\text{sites}}}{\sqrt{2\pi}\sigma} \exp\left(-\frac{(E-E_0)^2}{2\sigma^2}\right). \tag{3.1}$$

Here, E_0 is the center of the DOS and the energies of all discrete hopping sites with density N_{sites} follow a Gaussian distribution with width σ. The reason are the already discussed changes in polarization energy due to disordered surroundings. This approach assumes that the energies of adjacent sites are uncorrelated, which is not necessarily true.

The jump rate ν from site i to j is assumed to be of Miller-Abrahams type [80]:

$$\nu_{ij} = \nu_0 \exp\left(-2\gamma\Delta R_{ij}\right) \begin{cases} \exp\left(-\frac{E_j - E_i}{k_{\mathrm{B}}T}\right) & ; E_j > E_i \\ 1 & ; E_j < E_i \end{cases} \tag{3.2}$$

The first exponential term of this equation describes the wave-function overlap and represents a tunneling probability, dependent on the site distance ΔR_{ij} and the wave-function decay parameter γ. Energetic upward jumps follow a Boltzmann factor with an effective energy offset $E_j - E_i$, which can be lowered by a macroscopic electrical field F pointing from $\mathbf{r}_j$ to $\mathbf{r}_i$. This field is assumed to be constant between $\mathbf{r}_i$ and $\mathbf{r}_j$ and gives $E_j - E_i = E_j^0 - E_i^0 - eF\left|\mathbf{r}_j - \mathbf{r}_i\right|$. Downward jumps are assumed to be not influenced by the field. In addition to the distribution of E, the hopping distance ΔR_{ij} and hence the overlap factor is also affected by the disorder and assumed to follow a Gaussian distribution with width Σ (off-diagonal disorder). The Miller-Abrahams equation, which neglects polaronic effects, is a simplified expression of the Marcus rate, used in chemistry to describe electron transfer [81]:

$$\nu_{ij} = \frac{I_{ij}^2}{\hbar}\sqrt{\frac{\pi}{\lambda k_{\mathrm{B}}T}} \exp\left(-\frac{(\Delta G + \lambda)^2}{4\lambda k_{\mathrm{B}}T}\right) \tag{3.3}$$

Here, ΔG is the free energy, containing the potential energy difference $E_j - E_i$. I_{ij} is the overlap integral between molecular wave functions and λ is the reorganization energy, e.g., due to polarization effects upon charging/discharging a molecule.

The probability of a jump from site i to j is finally given by the jump rate divided by the total jump probability including all potential destination sites j' in the neighborhood of site i:

$$p_{ij} = \frac{\nu_{ij}}{\sum_{j',j'\neq i} \nu_{ij'}} \tag{3.4}$$

To extract some information from this model, Bässler performed Monte Carlo simulations, placing one particle at an arbitrary energy for a random walk in a three dimensional solid with the dimensions of 70 x 70 x 70 sites. The first result is a relaxation of the excess charge carrier to a Gaussian equilibrium distribution with a maximum E_0^{relax}, which lies below E_0:

$$E_0^{\mathrm{relax}} = E_0 - \sigma^2/k_{\mathrm{B}}T. \tag{3.5}$$

This is a considerable value, if we assume, e.g., $\sigma = 50\,\mathrm{meV}$, E_0^{relax} would be $100\,\mathrm{meV}$ below the center of the DOS at room temperature. Such a relaxation is difficult to determine experimentally. Note that Fermi-Dirac statistics are not important in this model, because only one charge carrier travels in an otherwise empty DOS.

Whereas E_0^{relax} can be calculated analytically, the following expression for the mobility μ is not a theoretically derived formula, but results from fits of selected analytical equations
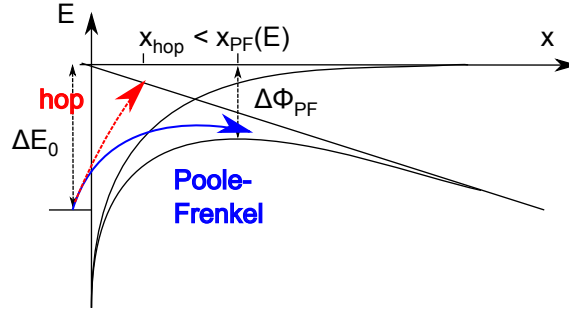
Figure 3.10: Comparison between Poole-Frenkel effect with a field dependent barrier lowering ($\Delta\Phi_{\mathrm{PF}}(F)$) at a long-range distance x_{PF} and hopping with a short fixed distance x_{hop}. The barrier is lowered by the superposition of the Coulomb and the macroscopic potential.

to numerical Monte Carlo simulation results:

$$\mu(\sigma, \Sigma, F, T) = \mu_0 \exp\left(-\left(\frac{2\sigma}{3k_\mathrm{B}T}\right)^2\right) \begin{cases} \exp\left(C\left(\left(\frac{\sigma}{k_\mathrm{B}T}\right)^2 - \Sigma^2\right)\sqrt{F}\right) & ; \Sigma \geq 1.5 \\ \exp\left(C\left(\left(\frac{\sigma}{k_\mathrm{B}T}\right)^2 - 2.25\right)\sqrt{F}\right) & ; \Sigma < 1.5 \end{cases} \qquad (3.6)$$

This equation with the empiric constant $C = 2.9 \times 10^{-4}\sqrt{\mathrm{cm/V}}$ summarizes the field and temperature dependence of μ considering both disorder parameters (σ and Σ). A strong temperature dependence of μ is expected, because hopping is a thermally activated process. Equation 3.6 describes an $\exp(-1/T^2)$-dependence instead of the commonly known thermal activation following $\exp(-1/T)$. The $\exp\sqrt{F}$ behavior coincides with phenomenological equations previously found to describe $\mu(F)$ in organic solids. It is formally identical to the Poole-Frenkel effect [82], used to describe charge transport via shallow traps:

$$\mu \propto \exp\sqrt{\gamma F}; \quad \gamma = \gamma_{\mathrm{PF}} = e^3/\pi\epsilon_\mathrm{r}\epsilon_0. \qquad (3.7)$$

This coincidence is anticipated, because a macroscopic field increases the electron jump or escape probability in both models. However, the Poole-Frenkel effect considers an electron in the Coulomb potential of a positively charged (trap) state (Fig. 3.10). When applying a constant field, the effective barrier for leaving this potential is reduced and can be calculated as the maximum of the superposition of the two potentials: $V = -e^2/(4\pi\epsilon_\mathrm{r}\epsilon_0 x) - eFx$, resulting in:

$$\Delta\phi(x = \sqrt{e/4\pi\epsilon_\mathrm{r}\epsilon_0 F}) = e\sqrt{eF/\pi\epsilon_\mathrm{r}\epsilon_0}. \qquad (3.8)$$

However, the distance x for reasonably strong fields $F = 10^5 \ldots 10^6\,\mathrm{V/cm}$ is in the range of several nm and thus significantly larger than the distance covered by a jump ($0.5 \ldots 1\,\mathrm{nm}$). Consequently, the expression of Eq. 3.6 is favored compared to γ_{PF}. In the case of a phenomenological description of hopping transport, γ is mostly used as a fit parameter.

Interestingly, Eq. 3.6 proposes also regions with a negative field dependence caused by a

high Σ. Figure 3.9(b) illustrates the reason for this effect in an intuitive picture: The high off-diagonal disorder increases the probability of a non-straight electron traveling path (i.e. non-parallel to the field direction) being the favored one. This implies some jumps that do not occur in the direction of the applied field. These jumps are suppressed by the field and the otherwise positive effect of the field on the direct path is overcompensated by the elimination of the favored indirect path. In particular, such an effect could be important for layers consisting of a mix of different materials [83].

In contrast to the physically justified Gaussian distribution of the energetic disorder, the description of the geometrical (off-diagonal) disorder with a Gaussian distribution is not well-justified and other models are proposed (see Ref. [84]). It was found that a spatially correlated energetic disorder is better suited to describe the $\sqrt{F}$ behavior over the entire field range. The reason for correlations could be long-range interactions of charges with randomly distributed permanent electric dipole moments, e.g., from polar molecules, that change the potential energy and hence the site energy considerably. This leads to a correlation of energies E_i and E_j of neighboring sites.

A very compact extension of the GDM model was given by Pasveer *et al.*, who also included the dependence of the mobility on charge carrier density [85]. The main result is an increase of μ with higher charge carrier density. The larger the charge carrier density, the more higher-lying sites of the Gaussian DOS are filled. Electrons located on these sites require lower activation energies for hopping and are thus more mobile than electrons occupying deep (trapped) states.

Now, we leave these very detailed microscopic transport models, which are capable of describing several mechanisms in organic solar cells, and move on to the complete sequence of photovoltaic energy conversion based on organic semiconductors.

3.3 Working principle of donor-acceptor heterojunction solar cells

Here, an overview is given of the general working principle of an organic solar cell, discussing the main parameters and mentioning common theories. In the first section we follow the particles and define quantum efficiencies of the single processes. In the second part we will examine the energy balance and finally present some analytical models for the current-voltage characteristics. As the working principle of organic solar cells is the main content of this work, some of the presented models will be evaluated in comparison with simulation data in Part II in detail.

3.3.1 Particle losses, quantum efficiency, and photocurrent

Photocurrent is generated by the absorption of a photon, which is finally extracted as an electron-hole pair, whereby the electron has to be collected at another position of the solar cell than the hole (see Ch. 2.4). Compared to inorganics, organic solar cells show

one important peculiarity: Light absorption does not lead to instantaneously free charge carriers, but, as discussed in Ch. 3.2.1, to localized excited states or highly bound excitons ($E_B > 0.3\,\text{eV}$). These excitons have to be separated in a subsequent step. However, efficiencies for a spontaneous separation and free charge carrier generation via (temperature activated) autoionization are commonly below several per cent [67]. Therefore, the so far most successful approach consists of the application of a donor-acceptor (D-A) heterojunction [30]. Such a junction comprises an arrangement of two different molecules with an electronic structure that favors charge transfer instead of, e.g., energy transfer (Fig. 3.11). Consequently, one molecule is of electron-donating type and the other one shows strong electron-accepting properties. This means in the molecular orbital picture [Fig. 3.11(b) and 3.12] a difference in LUMO and HOMO values, so that it is favorable for the electron of an excited donor state (S_1, π^* orbital) to jump onto the acceptor into an orbital located close to the LUMO of the neutral acceptor, which becomes an anion. Taking the energy levels for charge transport in a molecular solid [Fig. 3.11(b)], a D-A heterojunction is characterized by sufficiently large steps in ionization potential (absorption on acceptor) ΔIP/HOMO and electron affinity (absorption on donor) ΔEA/LUMO. The "intrinsic" offsets resulting from the assumption of vacuum level alignment can be influenced and modified by eventually occurring dipoles at the heterojunction.

The whole energy conversion chain can be divided into the following steps [86], each with a quantum conversion efficiency η_i as illustrated in Fig. 3.11:

- Photon absorption with efficiency $\eta_{PA}(\lambda)$. It depends on the absorption coefficient $\alpha(\hbar\omega)$ of the absorber molecule, which shows (usually narrow) peaks. Additionally to transmitted photons, reflected ones are lost. Since the thickness of the layers of organic solar cells is in the range of the coherence length of the sun light, not only the thickness of the absorber determines $\eta_{PA}(\hbar\omega)$ but its position within the optical field distribution created by interference. Hence, an optimization of η_{PA} means finding molecules with high absorption in the desired spectral range and an optimization of the stack regarding optics.

- Exciton diffusion with efficiency $\eta_{ED}(T)$. The exciton has to reach a D-A interface to be split. During this process, diffusion and relaxation are competing. A high diffusivity D and lifetime τ lead to a large exciton diffusion length $L_D = \sqrt{D\tau}$. Thus, η_{ED} is mainly determined by the ratio of L_D to the absorber layer thickness. Common values of L_D of amorphous organic films are in the range of $10\,\text{nm}$ [86]. A device optimization leads to a tradeoff with η_{PA}, requiring layers with thicknesses of $50\ldots100\,\text{nm}$ (for $\alpha \approx 10^5\text{cm}^{-1}$). To overcome this problem, the planar arrangement shown in Fig. 3.11(a:i) is changed to a volume structure by mixing (or blending) donor and acceptor to form a bulk heterojunction (ii) [31, 32]. Parasitic absorption in regions which are not electrically active decreases the exciton harvesting efficiency as well and can either be assigned to exciton losses (η_{ED}) or to absorption losses (η_{PA}), as absorption does not take place in the designated material.

- Charge transfer with efficiency η_{CT}. This process is known to be very efficient and
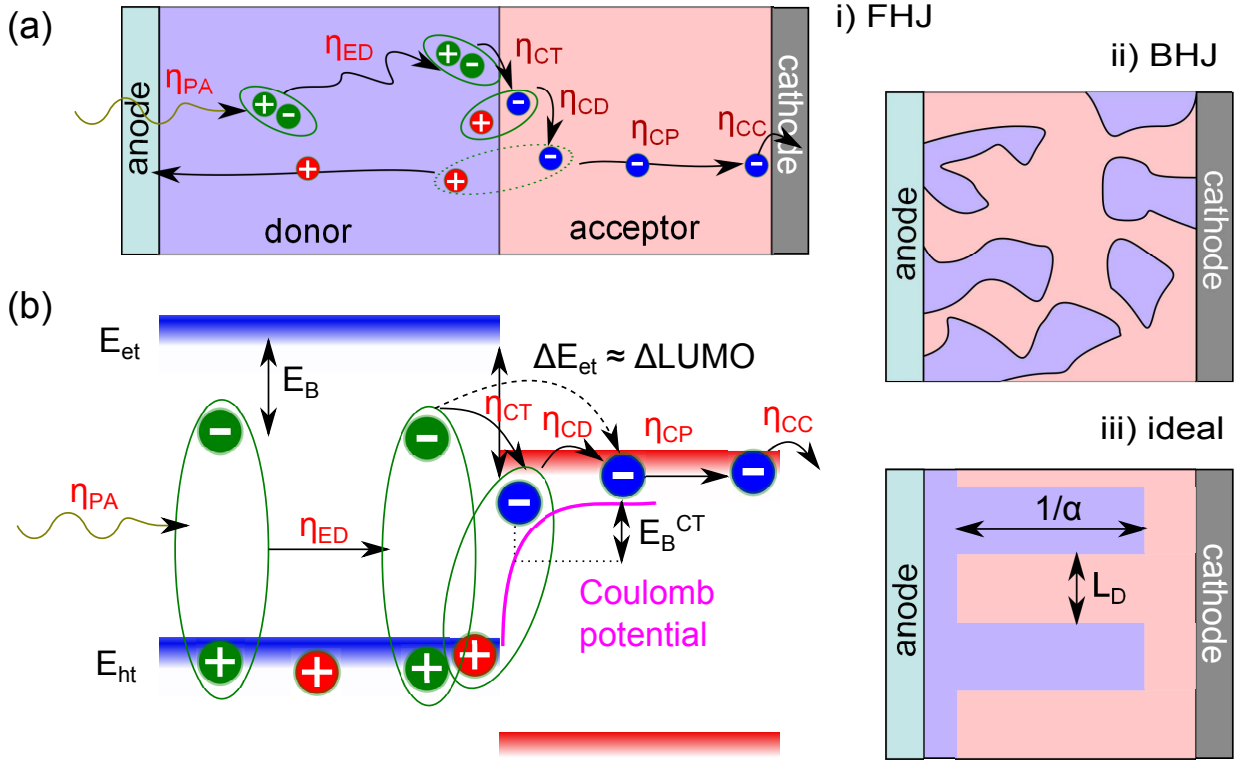
Figure 3.11: Donor-acceptor concept: (a) Possible realizations: flat/planar heterojunction (FHJ, bilayer), bulk heterojunction (BHJ, blend), comb-like structure. (b) Steps of energy conversion with associated quantum efficiencies η_i in the one-electron picture where ΔLUMO is the driving force to overcome the exciton binding energy E_B. The Coulomb attraction of an electron in the acceptor due to a positive charge located on the donor at the heterojunction is also shown.

fast (45 to several hundreds of femtoseconds) for several donor-acceptor combinations [87–91]. As mentioned, an efficient charge transfer requires an offset in the electron affinities (ionization potentials) for electron (hole) transfer between donor and acceptor, which is larger than the exciton binding energy.

- Dissociation of the electron-hole pair with efficiency $\eta_{CD}(F, T)$. This step is seen as the essential process in an organic solar cell. It is not yet completely understood and matter of controversial discussions (for a review, see Ref. [92]). The main question is whether the dissociation happens via an intermediate state, a so-called charge-transfer (CT) exciton which is the first excited state of a charge-transfer complex at the heterojunction. The other proposal is that the energy gained from the energy level offset is used to directly generate free charge carriers via hot excitons.

In the first approach, the CT exciton can be described as a bound electron-hole pair,
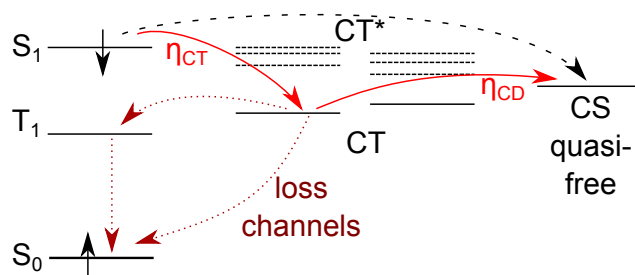
Figure 3.12: Donor-acceptor concept in an excited-state diagram. Solid arrows show the dissociation of a singlet exciton S_1 via charge-transfer (CT) states. The dashed line represents an alternative path via hot CT states to charge separated (CS) states. Dotted lines show loss channels via relaxation of CT states or energy back transfer to a triplet state T_1 on the donor.

or an electron in the Coulomb potential of a localized positive charge, as depicted in the free-electron potential diagram of Fig. 3.11(b) [93]. A complete dissociation of this pair into free charge carriers is then temperature-activated and field-dependent. Furthermore, it is in competition with the relaxation of the CT state (geminate recombination). The photocurrent yield is then commonly described by the Onsager-Braun theory [94, 95] (details in Ch. 4.4.2). Some calculations showed good agreement with the high $\eta_{CD}(F, T)$ measured [96–98], although mostly either the lifetimes of the CT states are strongly overestimated or the binding energies underestimated when compared to spectroscopic measurements. In other cases this theory could not describe the field dependence of the photocurrent [99]. In Ref. [100] it is proposed by Monte Carlo simulations that the high dissociation yield is due to a high delocalization of charges on polymer chains. According to Ref. [101] the Onsager-Braun theory requires some modification.

A description of the CT state may be preferred and even more accurate using an excited-state diagram (cf. Fig. 3.5) shown in Fig. 3.12 instead of regarding the CT state as Coulombically bound electron-hole pair. If allowed, radiative transitions between ground state and CT state should be observable. In recent years they have been reported for several donor-acceptor combinations in absorption [102], external quantum efficiency [103], photoluminescence [104], and electroluminescence [105, 106] measurements. Sensitive measurement techniques are required due to a very low cross section [107]. An observed reduction of $\eta_{CD}(F, T)$ for a heterojunction exhibiting a low difference between CT and S_1 [108] gives evidence for the importance of the CT state. Also the importance of the donor triplet energy T_1 compared to the CT energy is a clear hint for the participation of the CT state at photocurrent generation [109]. In that work Veldman *et al.* showed that well working solar cells posses a T_1 above the CT state energy. Otherwise, η_{CD} suffers significantly because, assuming a large intersystem-crossing probability of the CT state, a T_1 lower than the CT state favors back transfer of the energy to the donor with a subsequent relaxation

of the triplet state (Fig. 3.12). The irrelevance of the excess energy resulting from ΔLUMO was also shown in Ref. [110]. There, the temperature dependence of the photocurrent for excitations above the optical gap and below the gap (direct CT excitation) were similar. The authors concluded that in both cases, free charge carrier generation happens via CT states. Their implicit assumption is that the temperature dependence of the CT-state dissociation (η_{CD}) limits the total η.

Although the existence of the CT state is undoubted, the dissociation mechanism of this state with binding energies between 0.2 and 0.5 eV is still unclear. This supports the second idea of an instantaneous separation and complete dissociation of excitons reaching the interface. In this process the excess energy from the energy offsets is directly used for overcoming the Coulomb attraction via hot CT excitons CT* [dashed path in Fig. 3.11(b) and 3.12]. Thus, a relaxation into a CT ground state, which has to be reactivated for a later dissociation, is omitted. Evidence for the excess energy being important is reported by Ohkita *et al.* who find that η_{CD} scales with the difference between the S_1 state and the energy difference between the IP of the donor and the EA of the acceptor [111]. Time-resolved two-photon photoemission spectroscopy at pentacene surfaces gives evidence for the existence of hot CT excitons with low Coulomb binding energy [112, 113]. This leads to the suggestion of a strong coupling between S_1 and CT* at a D-A interface. The coupling can be described by nonadiabatic theory and results in a separation rate which competes with the thermalization of CT* states [114].

In conclusion, as long as no quantitative results are reported, the question remains whether CT excitons are the exclusive path of exciton dissociation. Furthermore, significant differences between different donor-acceptor combinations regarding CT excitons seem to exist. In principle, sufficiently long lifetimes of CT states can yield high dissociation probabilities despite binding energies which are much larger than $k_B T$.

- Charge transport with efficiency $\eta_{CP}(F, T)$. Once separated, charges have to be transported through the organic materials to the electrodes. The only possible loss mechanism is recombination between electrons and holes. In a planar heterojunction, the recombination probability of once separated charges should be low, because electrons are located on the acceptor and holes on the spatially separated donor. In a bulk heterojunction, however, electrons and holes can meet each other during extraction and recombine non-geminately. A common measure for η_{CP} is the mobility-lifetime ($\mu\tau$) product, which expresses the average distance a charge carrier travels at a fixed electric field before it recombines. However, as already discussed in Chap. 2.2.2, assigning a τ to a charge carrier in an ambipolar device is difficult. In general, η_{CP} depends on the present field and the diffusion gradient (cf. Chapter 2), which will be the topic of subsequent sections and Chapters 5 and 6. The increased recombination probability going along with the bulk heterojunction concept is unfavorable for a high η_{CT}. Hence, the optimum donor-acceptor solar cell structure would be comb-

shaped with lateral dimensions of L_{D} and vertical dimensions of $1/\alpha$, as depicted in Fig. 3.11(a:iii).

- Charge collection at the electrodes with efficiency $\eta_{\mathrm{CC}}(F)$. This is only a direct loss path if contacts are not selective and a charge carrier reaches the "wrong" contact, where it recombines (cf. Fig. 2.12 in Ch. 2.4, p. 32). Selective contacts themselves cannot lead to a direct particle loss. Though, as charge collection is also in competition with recombination within the device, a very low charge carrier collection rate could lead to a pile-up of charge carriers at the electrode, which then effectively reduces η_{CP} or η_{CD}. This will be elaborated in Chapter 6.

The overall efficiency (so-called external quantum efficiency, EQE or incident-photon-to-electron conversion efficiency, IPCE) as function of wavelength λ, applied voltage V (influencing the electric field F), and temperature T is the product of the single efficiencies:

$$\begin{aligned}
\mathrm{EQE}(\lambda, V, T) &= \eta_{\mathrm{PA}}(\lambda)\mathrm{IQE}(\lambda, V, T) \\
&= \eta_{\mathrm{PA}}(\lambda)\eta_{\mathrm{ED}}(T)\eta_{\mathrm{CT}}(T)\eta_{\mathrm{CD}}(F, T)\eta_{\mathrm{CP}}(F, T)\eta_{\mathrm{CC}}(F, T).
\end{aligned} \tag{3.9}$$

The EQE divided by η_{PA} is called the internal quantum efficiency (IQE) and contains only the electric processes within the device. Whether parasitic absorption is already considered as loss in η_{PA} remains undefined. A reasonable definition of the IQE depends on the object of study. If the IQE is used to evaluate the processes after absorption in the active layer, which is the usual case, η_{PA} should already be corrected for parasitic absorption. The parasitic absorption has to be determined by optical simulation. The IQE might then be called effective $\mathrm{IQE}^{\mathrm{active}}$ [115].

3.3.2 Energy losses, potential energy, and photovoltage

In the previous section, we examined the quantum efficiency describing the conversion of photons to electrons in the causal direction. Now, we investigate the maximum energy that can be extracted per electron-hole (e-h) pair, directly starting at the point of charge collection. As discussed in Ch. 2.3 in detail, the maximum free energy of an e-h pair as part of a charge carrier ensemble is found when it is not extracted, i.e. at open circuit. This energy is represented in the quasi-Fermi level splitting or chemical potential $\xi_n + \xi_p$, which is in the ideal case present at the contacts in form of the measurable open-circuit voltage V_{oc}. According to Eq. 2.44

$$eV_{\mathrm{oc}} = E_{\mathrm{F}}^n - E_{\mathrm{F}}^p = \xi_n + \xi_p = k_{\mathrm{B}}T\ln\left(\frac{j_\gamma^{abs}}{j_\gamma^0}\right) \tag{3.10}$$

holds. Here, V_{oc} is defined by the equilibrium between absorbed photon flux j_γ^{abs} and recombination flux j_γ^0. As free charge carrier generation and recombination happens at the donor-acceptor heterojunction, one can assume that the processes limiting V_{oc} take place at this junction. An energy diagram neglecting recombination losses in the layers is depicted
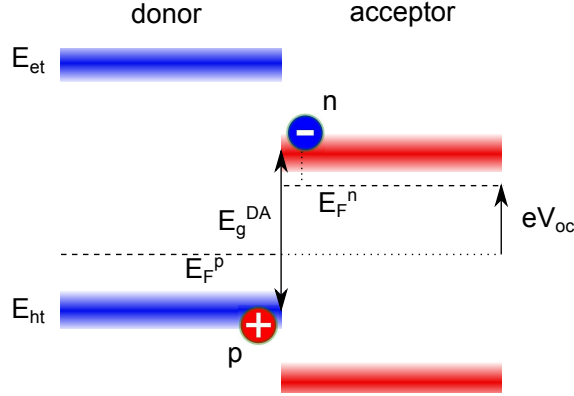
Figure 3.13: Visualization of the quasi-Fermi level splitting at an illuminated donor-acceptor heterojunction and definition of the effective donor-acceptor gap E_g^{DA}.

in Fig. 3.13. In this case, the following equation resulting from Eq. 2.15 is equivalent to Eq. 3.10:

$$eV_{\mathrm{oc}} = E_{\mathrm{F}}^n - E_{\mathrm{F}}^p = E_g^{\mathrm{DA}} - k_{\mathrm{B}}T \ln \frac{N_{\mathrm{C}} N_{\mathrm{V}}}{np} \qquad (3.11)$$

Here, the quasi-Fermi level splitting is expressed by the charge carrier densities np at the heterojunction and the effective donor-acceptor gap E_g^{DA}, which is defined as difference between the electron transport level ($E_{\mathrm{et}} \cong$ -EA $\approx$ LUMO) of the acceptor and the hole transport level ($E_{\mathrm{ht}} \cong$ -IP $\approx$ HOMO) of the donor. V_{oc} does not reach E_g^{DA} completely for $T > 0$.

Equation 3.11 is valid under the assumption of Boltzmann statistics with parabolic band minima characterized by effective densities of states N_{C} and N_{V} (see Eq. 2.12). A rough estimation of typical charge carrier densities at 1 sun illumination ($10^{16} \dots 10^{17}\,\mathrm{cm}^{-3}$ [116]) and $T = 300\,\mathrm{K}$ gives the commonly observed value of $\approx 0.3\,\mathrm{V}$ [117] for the last term in Eq. 3.11. A comparable relationship with $eV_{\mathrm{oc}} < E_g^{\mathrm{DA}}$ and as a function of T also holds for Fermi-Dirac statistics and other shapes of the DOS, because V_{oc} is defined by the distribution and the density of charge carriers n and p. The latter is limited by thermodynamic considerations as discussed in Chs. 2.2.2 and 2.6. They are responsible for radiative recombination losses, decreasing the charge carrier densities n and p. Garcia-Belmonte [118] found for a Gaussian DOS the following expression, where N_{C} and N_{V} represent the total amount of states/hopping sites of the DOS:

$$eV_{\mathrm{oc}} = E_g^{\mathrm{DA}} - \frac{\sigma_n^2 + \sigma_p^2}{2k_{\mathrm{B}}T} - k_{\mathrm{B}}T \ln \frac{N_{\mathrm{C}} N_{\mathrm{V}}}{np} \qquad (3.12)$$

In comparison to Eq. 3.11, E_g^{DA} is replaced by the difference between the transport levels (cf. Eq. 3.5). Whereas Eq. 3.11 predicts a linear dependence of V_{oc} with $-T$ and a $V_{\mathrm{oc}}(T = 0) = E_g^{\mathrm{DA}}/e$, Eq. 3.12 describes a decreased (non-constant) temperature coefficient of V_{oc}

with T.

Possible reasons for the "loss" resulting from the difference between E_g^{DA} and eV_{oc} were highly debated, although it is a direct consequence of the fact that V_{oc} is not formed by one e-h pair but by an ensemble of charge carriers, following Fermi-Dirac statistics if charge carriers are relaxed in their DOS. This can be verified for every solar cell by the observation of V_{oc} depending on light intensity.

Equation 3.11 predicts a lower quasi-Fermi level splitting and hence higher "loss" for an increased density of states. This dependence holds qualitatively for an arbitrary DOS and resolves the apparent conflict of the presented theory with the wide-spread idea of "band-bending" at the contacts as loss mechanism [109, 119]. In Ch. 5.2.6 we will show in detail that the decrease in V_{oc} for higher $N_{C/V}$ is due to a decreased quasi-Fermi level splitting and decoupled from the charge carrier density and energy level bending at the contacts, which can be an accompanying phenomenon.

The role of the built-in potential V_{bi}, which is defined as the difference of the contact work functions, was briefly mentioned in Ch. 2.4. For a planar heterojunction device, it was proven by analytical calculations by Cheyns $et\ al.$ [120] that V_{bi} and the spatial profile (bending) of the transport levels do not influence V_{oc}. The equation they obtained considering drift and diffusion currents is formally identical to Eq. 3.11, where they replaced the charge carrier densities n and p by generation (αP_0) and recombination (κ) terms, assuming $n \propto p$:

$$eV_{\mathrm{oc}} = |\mathrm{HOMO_D}| - |\mathrm{LUMO_A}| - n_\kappa k_{\mathrm{B}} T \ln \frac{N_{\mathrm{C}} N_{\mathrm{V}}}{\kappa \alpha P_0} \qquad (3.13)$$

In the original equation of the paper, V_{oc} contains some losses due to barrier lowering during thermionic injection. We do not show these expressions because they are not physically correct. They result from an inconsistent treatment of the barrier height and equilibrium charge carrier densities at the contacts in Ref. [120], as will be discussed in Ch. 4.5.

The variable κ contains expressions for bimolecular and SRH recombination. The pre-factor n_κ is 1 for solely bimolecular recombination and 2 for solely SRH recombination. Thus, it allows for a discrimination of recombination processes when examining the slope of the logarithmic intensity dependence of V_{oc}, as applied, e.g., in [121]. We will derive and employ the dependence of V_{oc} on light intensity to identify recombination processes in Ch. 10.3.2.

Another similar equation was presented by Nelson $et\ al.$[122], who started from a completely different point of view by balancing jump and relaxation rates at a donor-acceptor heterojunction as two level system:

$$eV_{\mathrm{oc}} = E_{\mathrm{g}} - k_{\mathrm{B}} T \ln \left(\frac{K_{\mathrm{g}}}{G_{\mathrm{s}} + G_0} + 1 \right) \qquad (3.14)$$

Here, K_g is a recombination and the G_i are generation terms.

Ignoring the described statistical effects, other attempts have been made in literature to explain the difference between E_g^{DA} and eV_{oc}.

Cravino [72] postulates that taking the single occupied molecular orbital (SOMO) instead of the HOMO level to calculate the effective gap, the difference between E_g^{DA} and V_{oc} (at 1 sun and at 300 K!) decreases to very low values. The reason is that the SOMO as polaronic level is supposed to lie higher than the HOMO, because it includes the polarization energy of a positively charged molecule (cf. Ch. 3.1.1). Although not improving the understanding of V_{oc}, this paper is a good example for the ambiguity, which energy value to assume as hole transport level: the HOMO, the SOMO, or the ionization potential (IP)? In this work, as already mentioned, the IP of molecules in an organic thin film is supposed to be the transport energy level for holes E_{ht}. The IP, as measured by photoelectron spectroscopy, includes polarization effects of the film and is the best approximation for the energy level a hole is transported on. For electrons, the electron affinity (EA) in a thin film is chosen for E_{et}, which, unfortunately, is hard to determine experimentally.

The most interesting question is whether V_{oc} is influenced or limited by the CT state like η_{CP} in the previous section; or more precisely, whether the CT-state energy correlates with V_{oc} as proposed by Vandewal *et al.* [103, 106], who among others found a correlation of V_{oc} with the CT energy [109]. In the picture presented here, at first glance, a direct correlation is not expected, because the CT-state energy is the internal energy of an excited state which has to be separated to form free charge carriers. The charge carriers occupy the transport levels when they are collected at the electrodes. Therefore, one could assume that the CT-binding energy is not relevant. It had to be overcome to result in the free charge carriers which cause the quasi-Fermi level splitting defining V_{oc}. The CT state itself would act as a modified recombination channel which has indirect influence on V_{oc}. This recombination probability is then ruled by rate equations describing the transitions between the states rather than by the energy of the CT state.

However, the energy of the CT state is connected to the equilibrium between dissociation and charge carrier recombination into this state, as will be discussed in Ch. 5.2.3. Assuming the CT-state recombination running at the radiative limit and applying detailed balance theory on the CT state, eV_{oc} is limited to a value below the CT state energy. This is comparable to the radiative limit of a quasi-free electron-hole pair in inorganic semiconductors. By applying detailed balance theory, Kirchartz *et al.* showed that in case of a discrete CT-state, V_{oc} is completely determined by the CT state properties independent of the recombination dynamics of free charge carriers [123].

Recently, Vandewal *et al.*[124] derived an analytical equation relating the energy of the CT state E_{CT} to eV_{oc}. They start from the basic detailed balance equation (Eq. 2.47), which is formally identical to the Shockley equation (Eqs. 2.42 and 2.43). In contrast to Eq. 2.47, where a complete absorption of photons with energies larger than the bandgap is presumed, Vandewal *et al.* take an EQE derived from Marcus theory [125]. Furthermore, they include also non-radiative recombination and replace J_S in Eq. 2.43 by an expression derived by Rau [126], who considered the reciprocity between electroluminescence and absorption efficiency. The result is the following equation:

$$eV_{oc} = E_{CT} + k_B T \ln\left(\frac{J_{sc}h^3c^2}{fe2\pi(E_{CT} - \lambda)}\right) + k_B T \ln(EQE_{EL}) \qquad (3.15)$$

Its structure is comparable to Eq. 3.11, which means a V_{oc} depending logarithmically on light intensity (via J_{sc}) and linearly on $-T$. The main difference is that $V_{oc}(T = 0\,\mathrm{K})$ is given by the energy of the CT state E_{CT}. The second summand in Eq. 3.15 is the radiative recombination derived from Marcus theory, where f is a measure of the electronic coupling between donor and acceptor and λ the reorganization energy. The last summand describes non-radiative recombination losses, as soon as the electroluminescence efficiency is lower than 1. Although good agreement with experiment is found, some questions arise, e.g., due to the voltage dependence of the photovoltaic and electroluminescence EQE. In Ch. 5.2.3 we will derive a similar, however more simple and intuitive, equation connecting V_{oc} and E_{CT}.

A recent study by Maurano *et al.* [127] where the charge carrier density and recombination parameters have been measured, showed that V_{oc} of several different organic solar cells follows exactly the dependence on charge carrier density presented in Eq. 3.11. In their study the authors were able to explain the slight deviations of the linear scaling of V_{oc} of several donor-acceptor heterojunctions with E_g^{DA} by changed recombination probabilities of free charge carriers, which means changes of the last term of Eq. 3.11.

In summary, both, the energetics of the CT state and the dynamics of free charge carriers have been shown to describe the origin of V_{oc} of several material combinations. In Chapters 5, 6, and 10 it will be discussed to what extent the results of the presented drift-diffusion model can contribute to the explanation of the mentioned effects, which are the influence of energy level bending, contact (recombination) properties and V_{bi}, a Gaussian density of states, and the presence of a CT-state.

3.3.3 Maximum power-conversion efficiency

The absolute EQE(λ, $0\,\mathrm{V}$) multiplied by the number of incident photons at λ (cf. dash-dotted line in Fig. 2.2) integrated over the whole spectrum gives the short-circuit current density J_{sc} of a solar cell. In short circuit, as well as at V_{oc}, power cannot be extracted (cf. Ch. 2.3). The optimum operation point is the so-called maximum power point (V_{MPP}, J_{MPP}), where the product of current and voltage is maximized, as illustrated in Fig. 3.14.

The power-conversion efficiency (η) as product of V_{MPP} and J_{MPP} divided by the illumination intensity P_γ can be rewritten as a function of J_{sc} and V_{oc} with the *FF* as new proportionality constant, describing the ratio between $V_{MPP} \times J_{MPP}$ and $V_{oc} \times J_{sc}$. Thus, the *FF* is a measure of the squareness of the *J-V* curve.

$$\eta = \frac{V_{MPP} J_{MPP}}{P_\gamma} = \frac{V_{oc} J_{sc} FF}{P_\gamma} \tag{3.16}$$

In Ch. 2.6 we have derived that the maximum power-conversion efficiency of a single band edge absorber is given by the Shockley-Queisser limit with radiative recombination as the only loss mechanism. In principle, this upper limit holds also for organic solar cells. Theoretically, it should be achievable if the energy offset between the LUMOs in case of absorption only in the donor is adjusted to cover exactly the exciton binding energy.
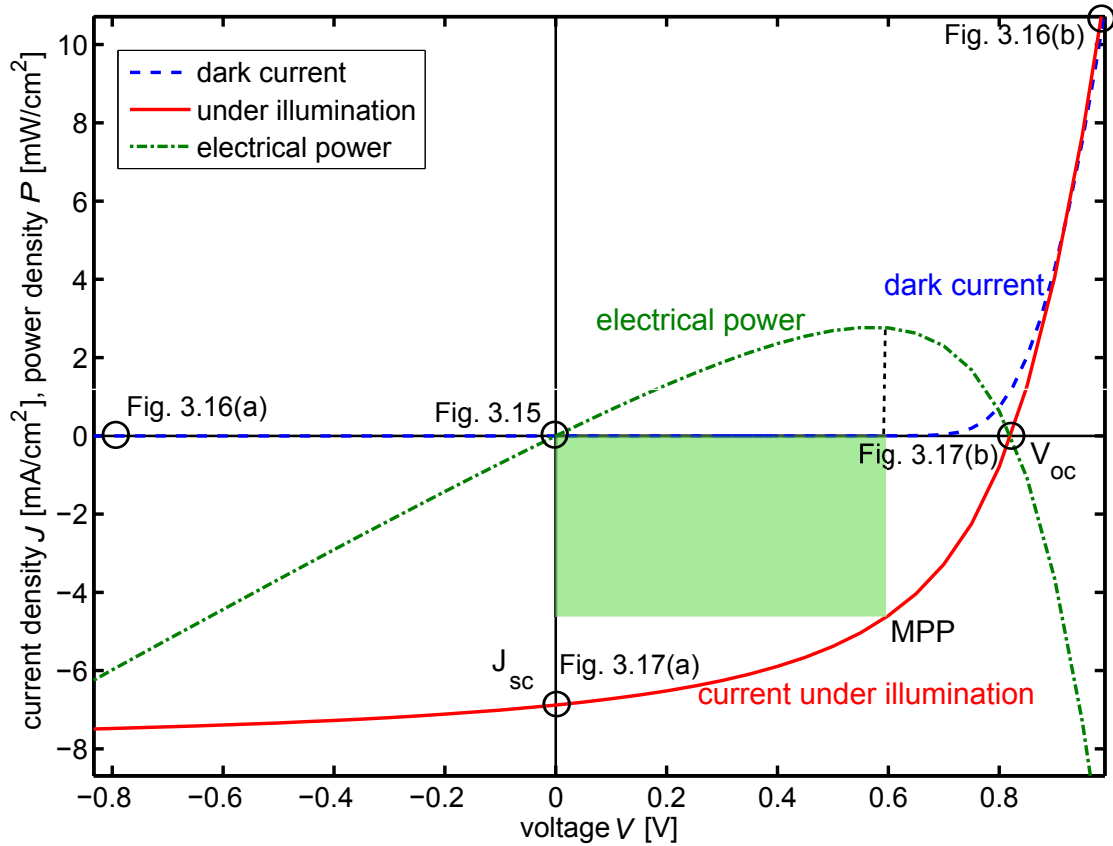
Figure 3.14: Current-voltage characteristics of a solar cell in dark and under illumination. In the fourth quadrant, electrical power is provided with a maximum at the maximum power point (MPP).

This means that the values of optical and electrical (effective) gap are identical and the maximum efficiency is given by the radiative lifetime of the exciton. The differentiation between optical and electrical gap contains an additional complexity when applying the Shockley-Queisser limit to organic solar cells. In the inorganic solar cell, only generation and (radiative) recombination of free electron-hole pairs has to be considered, whereas in organic semiconductors radiative transitions are excitonic and charge transport is polaronic. Additionally, two materials are involved, the donor and the acceptor. If the CT state is participating in exciton separation and charge carrier recombination, the ultimate efficiency will be limited by the energy and radiative recombination of this state [123, 124]. Furthermore, disorder introduces intragap tails which decrease the maximum efficiency [128]. In state-of-the-art devices, too narrow absorption bands, non-radiative exciton loss paths at the heterojunction, and low mobilities in combination with bimolecular recombination limit the device efficiency to below 10 % [129].
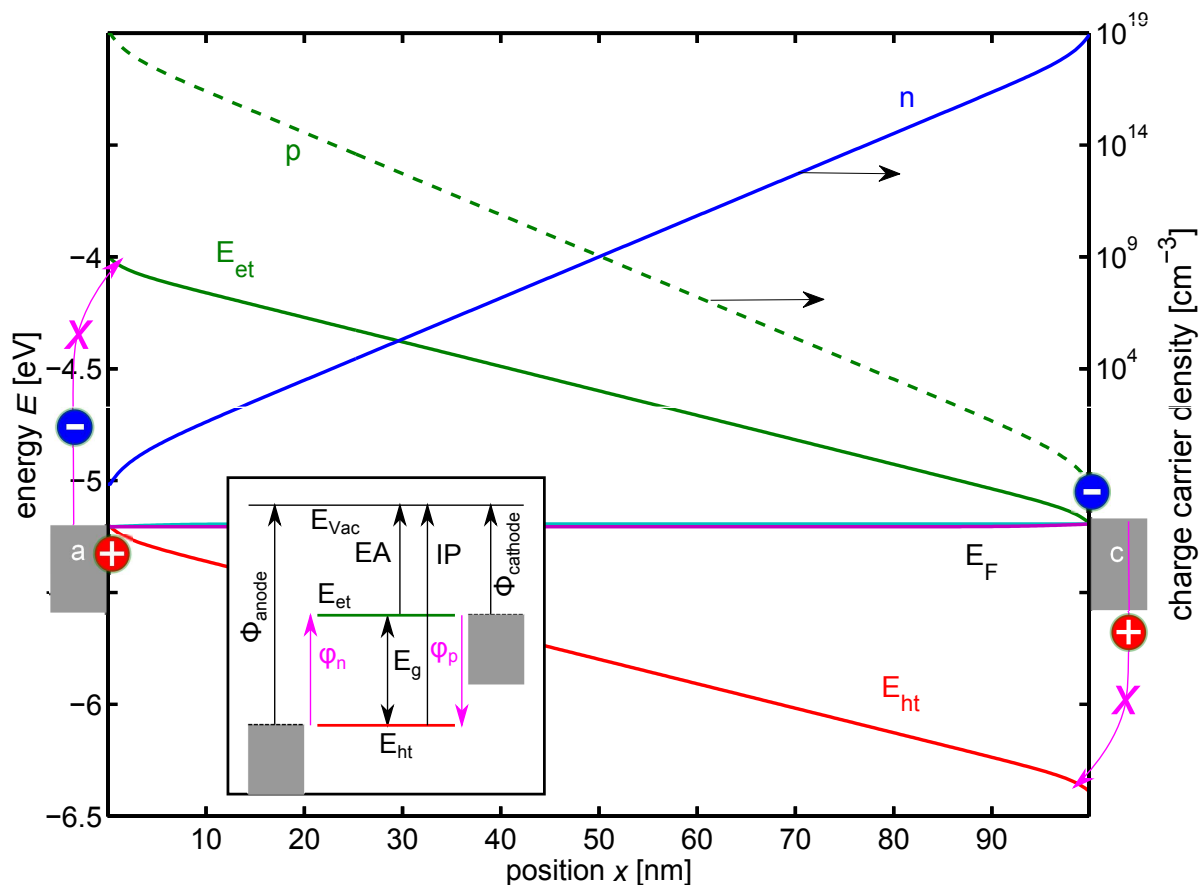
Figure 3.15: Energy level diagram and charge carrier densities (n and p) of a metal-insulator-metal (MIM) device at electrochemical equilibrium (dark, 0 V). The work function of the contacts match the respective charge transport level. Electron (hole) injection at the anode (cathode) is suppressed by a high energy barrier. The inset shows the energy levels before contact.

3.3.4 Understanding the *J-V* curve in the MIM picture

The already briefly described metal-insulator-metal (MIM) picture (cf. Ch. 2.4, Fig. 2.12, p. 32) is applied to understand the rectifying behavior of an organic solar cell. This property is the origin of a photovoltaic behavior, which has to be distinguished from a solely photoconductive effect. The following qualitative discussions hold as well for a p-i-n structure with highly (p and n) doped transport layers and the intrinsic layer consisting of a bulk heterojunction absorber. Whether the solar cell is experimentally realized as MIM or p-i-n device depends on the technology used. In general, a p-i-n architecture provides higher flexibility (see Ch. 3.5.1).

Figure 3.15 shows the energy diagram of a MIM device in thermodynamic equilibrium, which means in dark and at 0 V applied bias. The work functions of the metals are chosen to

match the IP and EA, respectively. This configuration has two main properties: First, only holes can be injected at the anode and only electrons at the cathode due to high injection barriers for the "other" charge carrier. This directly leads to a rectifying behavior, because dependent on the sign of the applied voltage, electrons and/or holes reverse their direction of flow, and hence change the contact where they are injected. Figure 3.16(a) shows a strong depletion of charge carriers under negative bias, as the bias pulls holes (electrons) towards the anode (cathode).

Second, this structure has a built-in potential V_{bi} like the p-n junction discussed in Ch. 2.5.1. Here, V_{bi} is simply the difference between the work functions of the two contacts and equals the effective energy gap in this case of matched contact work functions. The resulting electric force on charge carriers has to be compensated in equilibrium (0 V applied bias in the dark), such that an electric current does not flow. This is provided by the concentration gradient of free charge carriers. From Eq. 2.12 and 2.13 we know that the distance of the Fermi energy to the conduction band and to the valence band is a measure for the electron and hole concentrations, which increase exponentially with decreasing distance. Thus, in the MIM device the hole (electron) concentration at the anode (cathode) is very high and at the cathode (anode) very low, causing a diffusion force opposing the electric field, as shown in Fig. 3.15.

For low applied forward bias, the current flows against the built-in field and is therefore very small. This forward current for voltages below the built-in voltage is a diffusion current, as the applied bias decreases the field and the diffusion gradient stays mainly the same assuming the contacts in equilibrium. Thus, in first approximation this current can be described like the one in a p-n junction by a general exponential function $\exp(^{eV}/_{n_D k_B T})$ with a factor n_D discussed later. The threshold where the MIM diode turns on depends then mainly on V_{bi} and the charge carrier concentrations at the contacts defined by the density of states. Figure 3.16(b) shows energy levels and highly increased charge carrier densities in forward direction.

If we consider the device under illumination (Fig. 3.17), charge carriers are generated in the intrinsic layer, which is either a bulk heterojunction (as in the figure) or a bilayer of donor and acceptor (flat heterojunction). These additional charge carriers are then driven by the field and constitute a current in reverse direction comparable to the photocurrent generated in the space charge region of a p-n junction (Ch. 2.5.1). The current-voltage characteristics under illumination are then a superposition of both contributions leading to a J-V curve showing a J_{sc} and a V_{oc}. This is the characteristic difference to a photoconductor, which only shows a decreased resistivity upon illumination, but no electric power generating regime. The main difference between a MIM device and the conventional p-n junction is that the assumption of a constant photocurrent is not valid. Therefore, other models have been proposed which are discussed briefly in the next section. Although V_{bi} is essential in the discussed MIM device, we know from Ch. 2.4 that a built-in field is not necessarily required for solar cell behavior. We will demonstrate this in Chapter 6 by some devices (flat heterojunction solar cells or devices with selective contacts), exhibiting a built-in diffusion gradient. Such devices, however, show poor performance due to low fill factors.
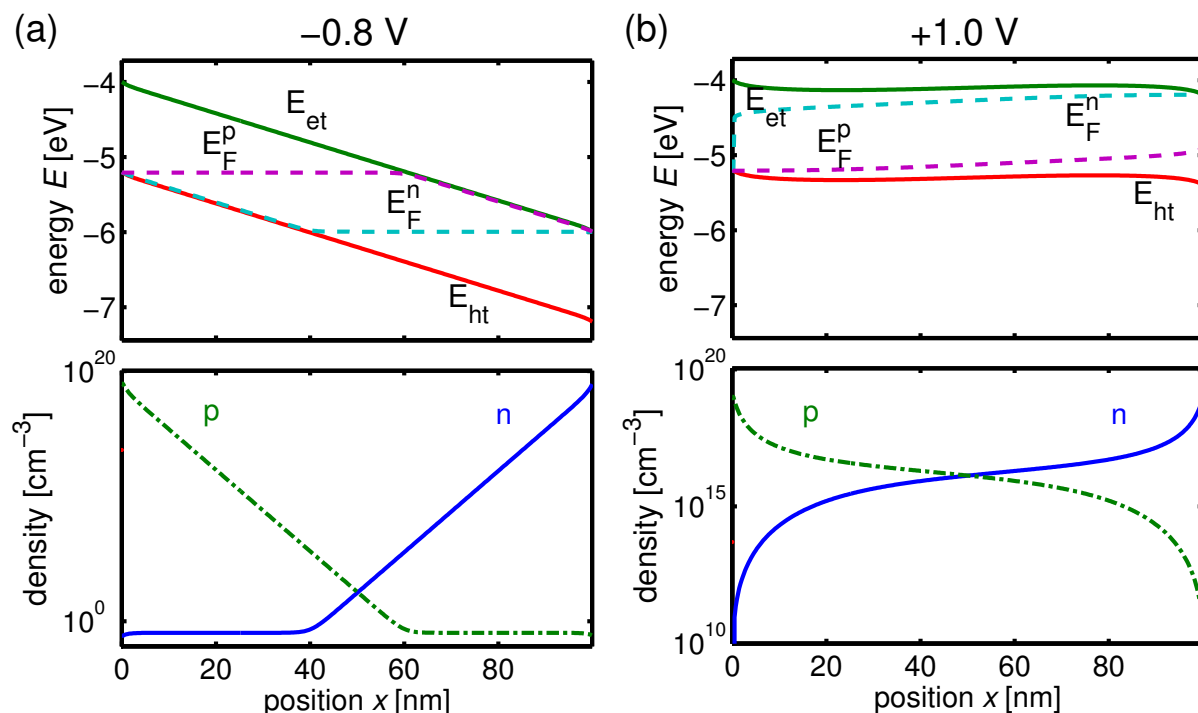
Figure 3.16: Energy level diagram and charge carrier densities of a MIM device (a) in reverse (-0.8 V), where electrons and holes are pulled out of the device and no significant current flows (apart from thermally generated charge carriers) and (b) in forward (1 V), where electrons flow from right to left and holes from left to right. The applied bias is found in the difference between the Fermi levels at the contacts.

3.3.5 Introduction to analytical models describing the photocurrent

Analytical models describing the whole J-V curve or voltage dependence of the photocurrent are very useful for a fast interpretation of measured data. However, such models include several assumptions, which are not necessarily fulfilled in an organic solar cell. For example, space charge effects are mostly neglected, which play a crucial role in low-conductive organic materials. More complicated J-V curve shapes including inclination points cannot be described by simple analytical equations. Nevertheless, we want to briefly introduce a few approaches applied in literature, which are equivalent-circuit models, the concept of the $\mu\tau$-product, and the description of the photocurrent by an equation derived by Sokel and Hughes [130].

Equivalent circuit

The equivalent-circuit model is characterized by a very high level of abstraction, because physics is represented by ideal electrical components like resistors, diodes, and current sources. They result from the interplay of several physical processes. The basic assumption
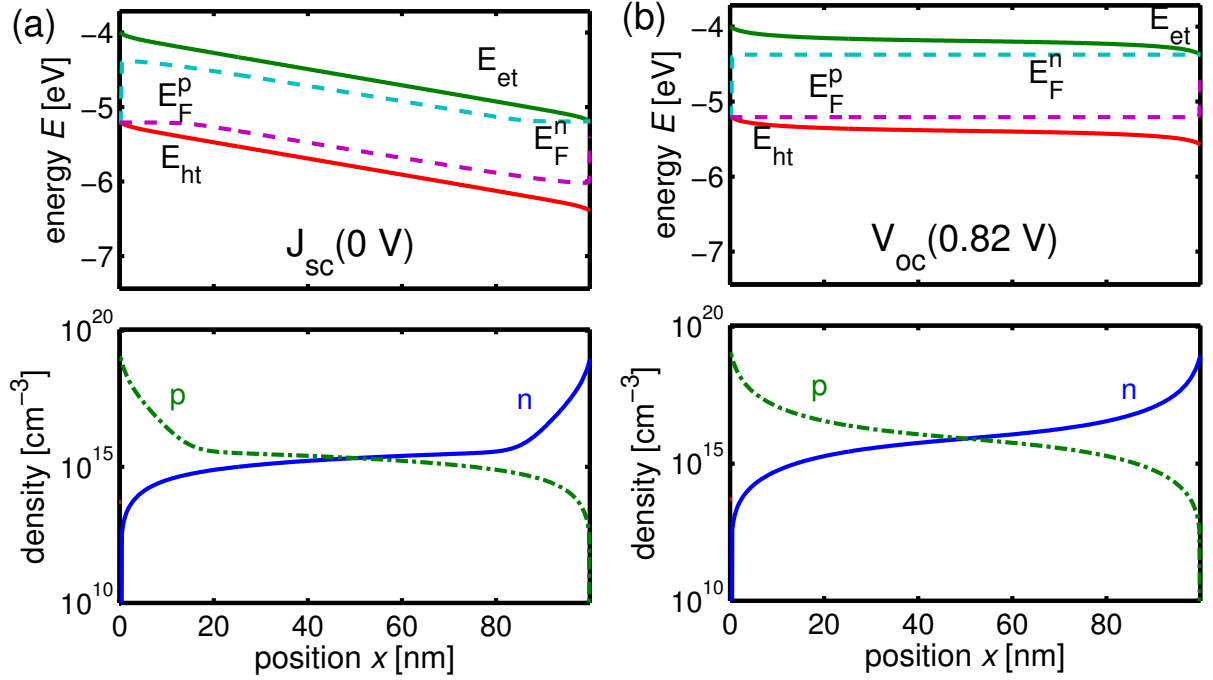
Figure 3.17: Energy level diagram with split quasi-Fermi levels and charge carrier densities of a MIM device under illumination (a) at short circuit and (b) at open circuit (0.82 V). The voltage measurable from outside is the difference between the Fermi levels at the contacts.

of an equivalent-circuit model with a diode and (photo)current source as main components [Fig. 3.18(a)] is the applicability of the Shockley equation (Eq. 2.41), derived for an ideal p-n junction. This approach might be legitimate in a first approximation, if one assumes that an organic solar cell can be described in the previously depicted MIM picture with a built-in potential and a diffusion-driven forward current. Hence, Eq. 2.41 can be applied. This equation is modified by the introduction of a diode ideality factor n_D which represents recombination in the space charge layer of the p-n junction. As the space charge layer of a p-n junction corresponds to the intrinsic bulk heterojunction absorber layer of an organic solar cell, recombination is expected or, if contacts are selective, even necessary for driving a forward current. Thus, the ideality factor, which modifies the slope of the exponential diode current, is capable of giving some information about the dominant recombination mechanism in an organic solar cell (cf. Ch. 10.3.1). The current density in the circuit of Fig. 3.18(a) is described by:

$$J = J_S(e^{e(V-JAR_S)/n_D k_B T} - 1) + \frac{V - JAR_S}{R_P} - J_{photo}(V). \qquad (3.17)$$

This equation takes into account losses due to a macroscopic series resistance R_S lowering the effective voltage at the junction by $R_S JA$ (area A), and a parallel/shunt resistance R_P,
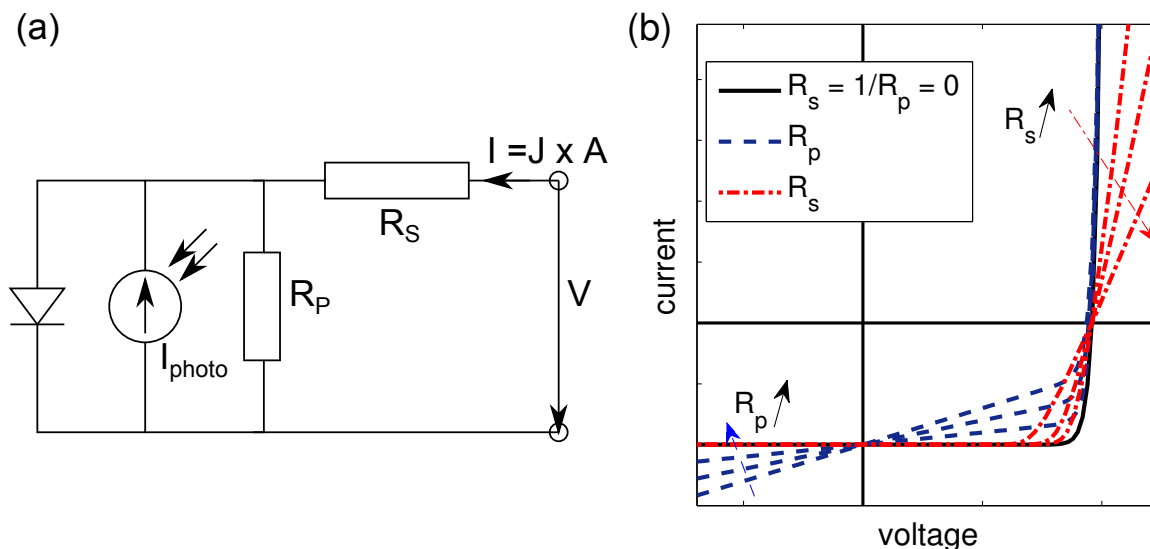
Figure 3.18: (a) Simple equivalent circuit of a real solar cell. It contains a diode, a photocurrent source and parallel and series resistances. (b) Influence of series resistance R_S and parallel resistance R_P, mainly changing the fill factor.

comprising a leakage current path. The characteristic influence of these resistivities is shown in Fig. 3.18(b).

Equation 3.17 describes real diodes quite well. It has also been used in several publications [131–135] to fit the dark current of organic solar cells. However, it is very challenging to correctly identify the saturation behavior and determine the saturation current. Another unresolved issue are too high values of n_D, which are difficult to explain physically. To describe more complicated solar cell structures or to include additional recombination mechanisms, the model can be arbitrarily extended, adding more diodes and resistors [136]. Although adequate fits to measured dark curves have been obtained, the benefit of such models for a deeper physical understanding of organic solar cells remains questionable.

Photocurrent $\mu\tau$

We assumed the photocurrent J_{photo} to be constant when discussing the p-n junction (Chap. 2.5.1). Experiments clearly show that this assumption cannot be maintained for organic solar cells, where a strong dependence of the photocurrent on voltage is observed. A clear hint for this behavior is a commonly seen crossing of the dark J-V curve and the one under illumination at a voltage slightly higher than V_{oc}. A simple approach to describe the voltage dependence is the $\mu\tau$ product, where it is assumed that a charge carrier within the blend has a certain lifetime before it vanishes, which means recombines. Thus, the expression $\mu F\tau = v\tau = l$ describes the maximum distance l (drift length) that the charge carrier travels at a certain electric field F (Fig. 3.19). If this distance is smaller or
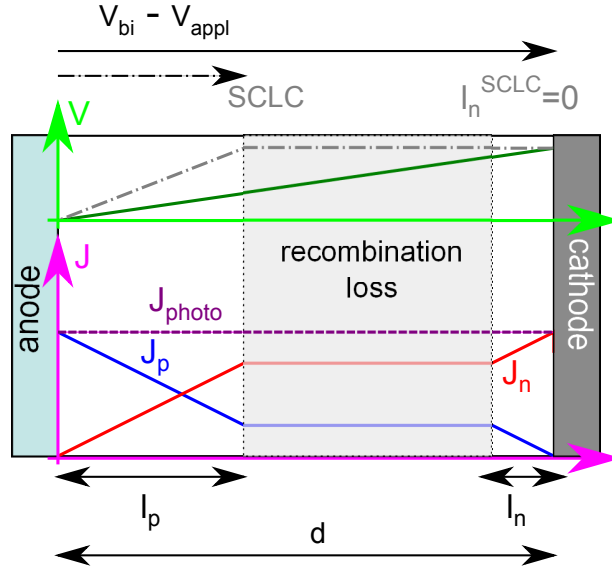
Figure 3.19: Electron and hole current (J_n and J_p) collection as assumed by the $\mu\tau$ approach: Only the regions (white) within the drift lengths l_n and l_p close to the contacts contribute to the photocurrent. In case of $\mu_p\tau_p \ll \mu_n\tau_n$, a space charge builds up and the voltage completely drops over l_p (dash-dotted). The photocurrent can then be described by a space-charge-limited current (SCLC).

in the range of the device thickness d, a voltage dependence of J_{photo} will be seen. Under the assumption of a spatially constant generation rate of electron-hole pairs $G =$ absorbed photon flux density$/d$ and a constant field $F = (V_{\text{bi}} - V_{\text{bias}})/d$ in the device with thickness d, $J_{\text{photo}} = J_{\text{illu}} - J_{\text{dark}}$ under an applied bias V_{bias} can be expressed by [137, 138]:

$$J_{\text{photo}}(V) = \begin{cases} eG\mu\tau(V_{\text{bi}} - V_{\text{bias}})/d & ; l \leq d \\ eGd & ; l > d \end{cases} \tag{3.18}$$

As shown in Fig. 3.19, a photo-active region exists at each electrode, limited by the $\mu\tau$ product of holes at the anode and electrons at the cathode.

If τ is known, the charge carrier density can be calculated as $G\tau$ and the conductivity of the layer as $G\tau\mu$. One can directly see that this approach is based on averaging. A space charge is not considered, because the field is assumed to be constant and the generation rate is assumed to be constant. The lifetime τ is assumed to be a material property, which is only valid for minority carriers or for non-direct/bimolecular recombination. Otherwise, as discussed in Ch. 2.2.2, τ depends on the concentration of the other charge carrier type. We will see in Part II of this thesis (e.g. Chapter 10) that often these assumptions are not valid for real devices.

Extension to space charge limit

In case of imbalanced transport ($\mu_p\tau_p \ll \mu_n\tau_n$), a space charge region builds up in the device, because charge carriers of the slower type pile up (here holes) and the region at the other contact (here cathode) remains field-free (dash-dotted in Fig. 3.19). In a first approximation the photocurrent is only generated in the space charge region, as in the field-free region photogenerated electrons and holes recombine. Furthermore, the total electric potential drops over this region, which means that the device thickness d in Eq. 3.18 has to be exchanged by the length of the space charge region. Thus, it holds $l = \mu_p\tau_p(V_{\mathrm{bi}} - V_{\mathrm{bias}})/l$ and

$$J_{\mathrm{photo}}(V) = eGl = eG(\mu_p\tau_p)^{1/2}\left(V_{\mathrm{bi}} - V_{\mathrm{bias}}\right)^{1/2}. \tag{3.19}$$

Goodman and Rose [139] discussed this case and found that in the electrostatic limit J_{photo} equals the space charge limited current $J_{SCLC} = 9/8\varepsilon_0\varepsilon_{\mathrm{r}}\mu_p V^2/L^3$. Equating this expression with Eq. 3.19 gives for the current:

$$J_{\mathrm{photo}}(V) = e\left(\frac{9\varepsilon_0\varepsilon_{\mathrm{r}}\mu_p}{8e}\right)^{1/4} G^{3/4}\left(V_{\mathrm{bi}} - V_{\mathrm{bias}}\right)^{1/2} \tag{3.20}$$

This result is very interesting, because it predicts a $G^{3/4}$-dependence of J_{photo}, which was indeed shown by Mihailetchi *et al.* [140]. However, this extended analysis also assumes non-injecting contacts and considers only drift currents.

The Hecht equation

Commonly, the photocurrent is not linear with voltage as predicted by Eq. 3.18. Therefore, Street *et al.* [141] applied the Hecht equation [142] to describe the dependence of photocurrent on voltage:

$$J_{\mathrm{photo}}(V) = \frac{eG\mu\tau(V_{\mathrm{bi}} - V_{\mathrm{bias}})}{dl'}\left(1 - \exp\left(\frac{dl'}{\mu\tau(V_{\mathrm{bi}} - V_{\mathrm{bias}})}\right)\right) \tag{3.21}$$

Here, d is again the device thickness and l' describes the collection length of charge carriers. This equation is used in Ref. [141] to describe a photocurrent that is limited by recombination via trap states.

Photocurrent after Sokel and Hughes

The simple $\mu\tau$ ansatz completely ignores diffusion-driven currents. A more complicated approach which is sometimes used to evaluate the photocurrent [96, 98, 134, 135, 143, 144], is presented in a paper by Sokel and Hughes [130]. On the one hand, they present a numerical analysis of the photoconductivity of insulators. On the other hand, they derive an analytical equation for the photocurrent under the following assumptions: first, a constant generation rate; second a constant electric field as in the approaches discussed previously; third, diffusion is allowed and very important. However, recombination of

charge carriers in the bulk material is neglected. The continuity equation for holes is then simply:

$$\frac{\partial p}{\partial t} = -\frac{1}{e}\frac{\partial J_p}{\partial x} + G \tag{3.22}$$

This equation expresses that a change in p with time is either due to a generation G of holes or due to a gradient in the current, causing some redistribution of holes. Replacing J_p by the drift-diffusion equation ($J_p = e\mu_p p F - \mu_p k_\mathrm{B} T \frac{\partial p}{\partial x}$, Eq. 2.31) and the electric field F by the applied bias $V = F/d$ yields a differential equation containing only p as variable which is dependent on x. The solution is in steady state ($\frac{\partial p}{\partial t} = 0$) and under the condition of vanishing charge carrier densities at the contacts ($p(0) = p(d) = 0$):

$$p(x) = \frac{Gd^2}{\mu_p V}\left(\frac{x}{d} - \frac{e^{\frac{eV}{k_\mathrm{B}T}\frac{x}{d}} - 1}{e^{\frac{eV}{k_\mathrm{B}T}} - 1}\right); \ V > 0 \tag{3.23}$$

The hole density derived from this equation is plotted in Fig. 3.20(a). Inserting Eq. 3.23 and its derivation into the drift-diffusion equation (Eq. 2.31) gives the hole current, which is plotted in Fig. 3.20(b). The same can be done for the electrons. The final result for the total current, which is independent of x in steady state, is

$$J = eGd\left(\frac{e^{\frac{eV}{k_\mathrm{B}T}} + 1}{e^{\frac{eV}{k_\mathrm{B}T}} - 1} - \frac{2k_\mathrm{B}T}{eV}\right); \ V > 0. \tag{3.24}$$

For high voltages V, the last expression of Eq. 3.24 approaches zero and the first one 1, giving a current $J = eGd$, which means that all generated charge carrier pairs are extracted. In the case of an organic solar cell, where a built in field V_bi is present (cf. Chap. 3.3.4), V is again replaced by $V_\mathrm{bi} - V_\mathrm{bias}$. Here and in this whole section, V_bi is implicitly assumed as the point where the photocurrent becomes zero (see discussion about V_0 in Ch. 5.3).

Mihailetchi *et al.* [96] extended this model, introducing a field dependent generation rate of free charge carriers:

$$G = G_0 P(F, T) \tag{3.25}$$

The introduction of the probability $P(F, T)$ is motivated by a strong dependence of photocurrent on high applied negative voltages. It is justified by the proposed presence and the geminate recombination of a CT-state. The temperature and field dependence of the dissociation of the Coulombically bound electron-hole pair is described by Onsager-Braun theory [94, 95] (for details, see Ch. 4.4.2). This approach of representing most of the dependence of the photocurrent on voltage by η_CD(cf. Ch. 3.3.1) gives acceptable results in some cases. In other cases it seems to be not adequate to describe the *J-V* curve [99].

Apart from the discussion of the presence and relevance of a CT state and the correct modeling of its dissociation probability [101], this approach shows two main drawbacks. First, recombination between charge carriers is not included ($\eta_\mathrm{CP} = 1$). The original approach by Sokel and Hughes assumes that every photogenerated charge carrier leaves the device at every applied voltage. Losses are then only caused by a diffusion to the
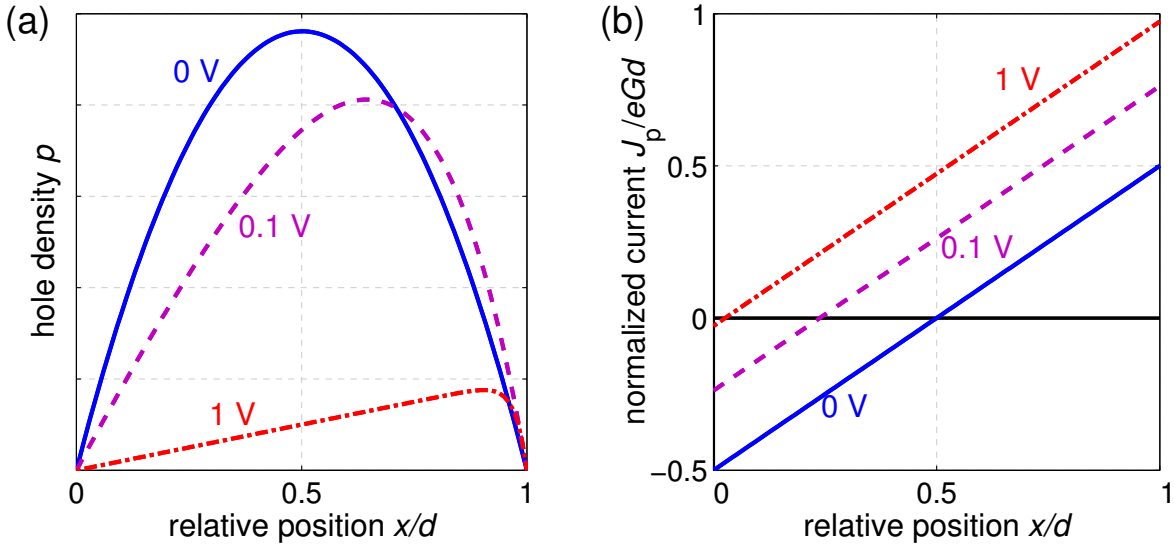
Figure 3.20: Model for the photocurrent according to Sokel and Hughes: (a) Hole density calculated by Eq. 3.23 dependent on the applied voltage. Charge carrier extraction upon an applied voltage reduces the charge carrier density. (b) Hole current, which is in case of 0 V only a diffusion current to both electrodes (zero net current) and in case of a positive applied voltage directed towards the right contact. The electron current (not shown) is equivalent to the hole current, mirrored at $x/d = 0.5$.

"wrong" contact ($\eta_{CC} < 0$). Well-working organic solar cells, however, employ selective contacts [cf. Figs. 2.14(a) and 3.24(b)]. The second assumption is that only photogenerated charge carriers are in the device and charge carrier concentrations at the contacts are zero. However, especially in the low-voltage regime, when diffusion is dominant, the diffusion gradient will be altered by the presence of the dark carriers, starting to deliver forward current.

Both methods, the one according to Goodman and Rose and the other after Sokel and Hughes, have originally been developed for the description of photoconductivity in insulators with non-injecting contacts. We will show in Ch. 5.3 by comparison to numerical solutions of the MIM device that subtracting the dark current and correcting the applied bias for V_{bi} do not convert the photovoltaic device into a simple photocarrier-extracting device in general. Thus, the applicability of the presented analytical equations to solar cells, which show high forward currents, is limited. They could be best employed to solar cells without transport layers at the contacts and with high injection barriers. In this case contacts are not selective, which means that electrons and holes can flow to both contacts. Furthermore, the conditions $n(0/d) \approx 0$ and $p(0/d) \approx 0$ are valid.
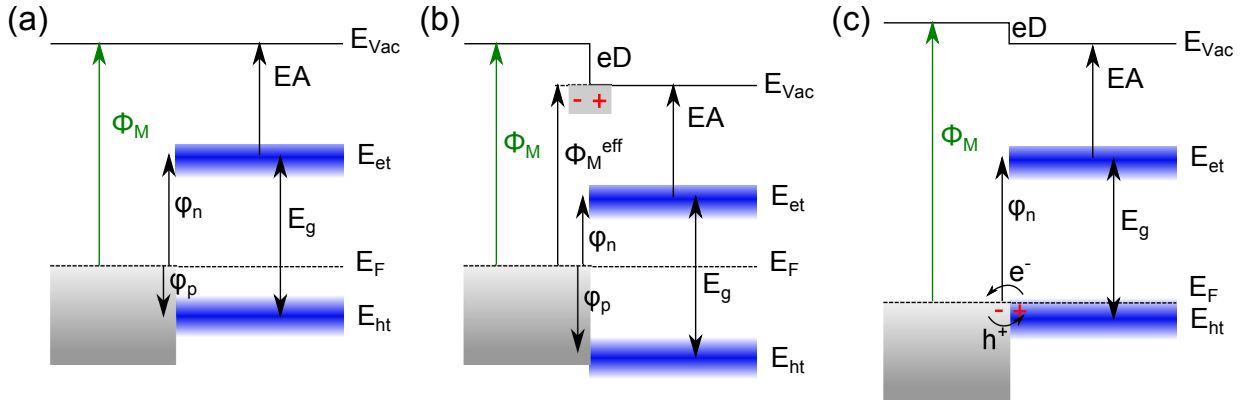
Figure 3.21: Metal-organic interfaces with intrinsic semiconductor considering (a) vacuum level alignment, (b) an interface dipole D, and (c) Fermi-level pinning at E_{ht}, which occurs if the work function of the metal Φ_{M} is larger than the sum of electron affinity (EA) and gap E_{g} of the semiconductor. In this case charge transfer is favorable.

3.4 Metal-organic interfaces

To collect the photogenerated charge carriers in a solar cell, metal electrodes or metal-like (degenerate) highly doped transparent conductive oxides are attached to the organic layers. These interfaces determine the collection efficiency η_{CC} defined in Ch. 3.3.1. Therefore, a brief overview of metal-organic interfaces is given. We start with conventional metal-semiconductor interfaces.

3.4.1 Conventional metal-semiconductor interfaces: Barriers and Schottky contacts

In case of an intrinsic semiconductor, the work function within the semiconductor close to the interface is defined by the metal, as shown in Fig. 3.21(a). As electrons in the metal occupy states up to the Fermi edge, the distance between E_{F} and the hole (electron) transport level describes the injection barrier for holes ϕ_p (electrons, ϕ_n) under the assumption of vacuum level alignment (Schottky-Mott theory). This injection barrier can be changed by interface dipoles (D), which can be seen as modifiers of the effective surface work function Φ^{eff} of the metal [Fig. 3.21(b)]. The field between the two dipole charges is mainly located between them and manifests in the potential by an offset in the vacuum level and a following shift of all energy levels. Such dipoles can occur undesiredly or are introduced intentionally, e.g., by monolayers of polar molecules. If the work function of the metal is higher (lower) than the IP (EA) of the semiconductor, an interface dipole is commonly formed, resulting in a pinning of E_{F} to E_{et} or E_{ht}, as shown in Fig. 3.21(c). The reason is that E_{F} would be within the band without this pinning, constituting a degenerate semiconductor with very high electron or hole concentrations. This is usually a non-equilibrium
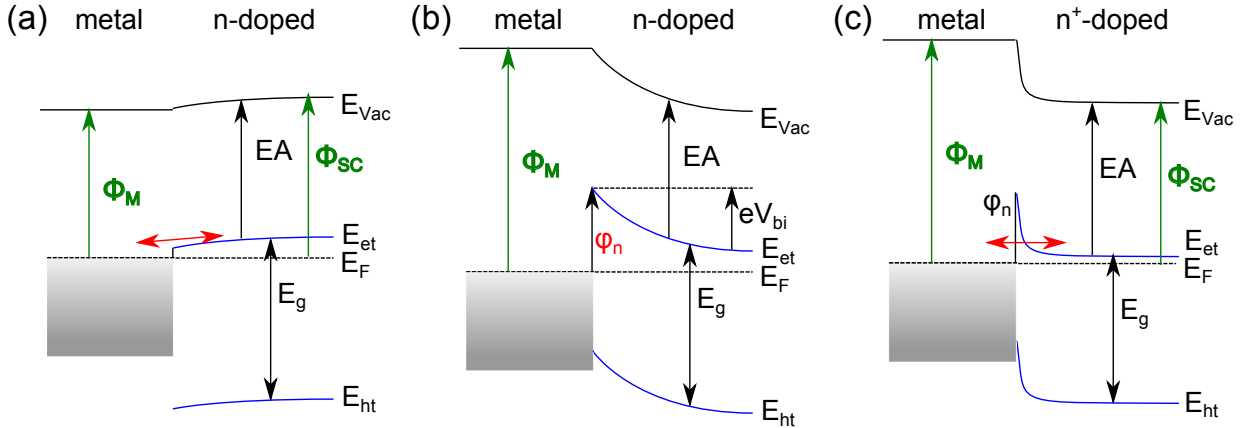
Figure 3.22: Metal-organic interfaces with n-doped semiconductor: (a) $\Phi_M < \Phi_{SC}$ forms an ohmic contact and (b) $\Phi_M > \Phi_{SC}$ forms a Schottky contact with electron injection barrier φ_n. (c) A high doping concentration allows for a tunneling current through the barrier.

situation which drives free-charge transfer from the metal into the semiconductor. The redistributed charge at the interface constitutes the dipole leading to the pinning.

Relevant conventional metal-semiconductor interfaces are produced by using doped layers. They contain free and localized charges, which can bring the semiconductor to its own equilibrium at a particular distance to the interface. This equilibrium is characterized by a certain position of E_F determined by the active doping concentration (Eq. 2.12). Dependent on the work function offsets and the type of doping, so-called ohmic or Schottky contacts are formed. Figure 3.22 gives an overview. Considering an n-type semiconductor, a lower metal work function leads to an ohmic contact (a), whereas a higher metal work function results in a Schottky contact (b). Such a contact is characterized by the already defined electron injection barrier and a built-in potential V_{bi} due to the work function difference, which causes a bending of E_{et} comparable to a p-n junction. For a p-doped semiconductor the situation is the other way round. A Schottky contact shows rectifying behavior, because electrons (holes in the p-doped case) cannot be injected from the metal. A significant forward current flows after the positive applied voltage has reached a certain value. This is comparable to the diffusion current in a p-n junction. The common approach of making a Schottky contact ohmic, i.e. not rectifying, consists of using a very high doping concentration at the contacts, which reduces the width of the space charge region and allows for a high tunneling probability for electrons in both directions [Fig. 3.22(c)]. This approach is also applied in the organic p-i-n type solar cells described in Ch. 3.5.1.

Figure 3.23(a) shows a sketch of the barrier height ϕ_B dependent on the metal work function Φ_M. The linear regime within the bandgap (solid line) is described by the Schottky-Mott [145, 146] law:

$$\phi_n = \Phi_M - EA_{SC} \tag{3.26}$$

The slope $d\phi_n / d\Phi_M$ is unity for Φ_M within the band gap. However, in experiment lower
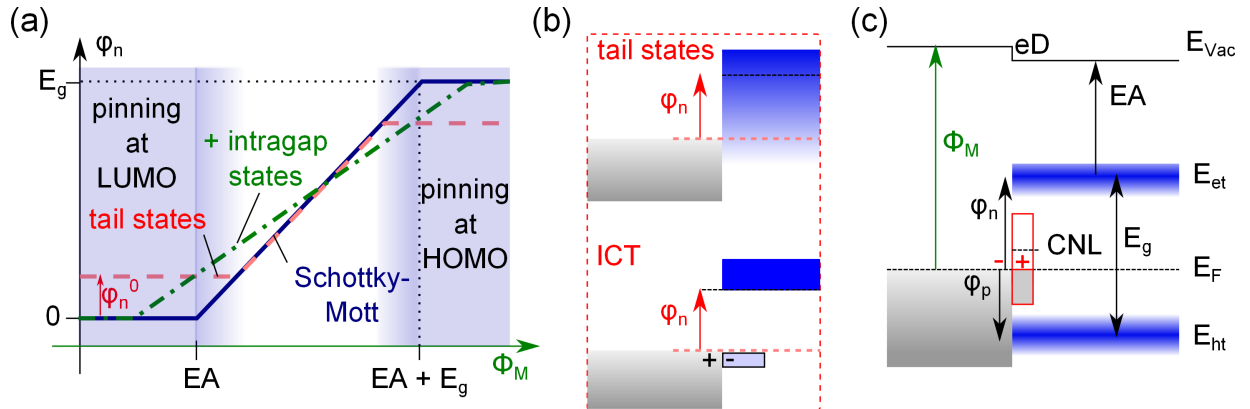
Figure 3.23: Metal-organic interfaces: (a) Electron injection barrier height φ_n as a function of the metal work function Φ_M. Without tail states the barrier depends on Φ_M as long as $\mathrm{EA} < \Phi_M < \mathrm{EA} + E_g$ and does not exceed E_g. (b) Illustration of Fermi-level pinning at tail states or at a polaronic level. (c) Surface states not filled up to the charge neutrality level (CNL) cause an interface dipole.

slopes have been reported [147], which can be explained by interface states as proposed by Bardeen [148]. In the simplest case one might assume a continuum of interface states [149] within the bandgap, where a characteristic energy, called the charge neutrality level (CNL), defines the polarity of the interface [Fig. 3.23(c)]. An E_F equal to the CNL represents a net surface charge of zero. If there is a difference, the amount of surface charge is proportional to this difference. The reverse charge is then located on the metal and a dipole layer is formed. This leads to a modification of Eq. 3.26, decreasing the slope $d\phi_n/d\Phi_M$ due to the additional dipole, which lowers ϕ_n. A very high density of intragap states would lead to a pinning of E_F to the CNL and thus a ϕ_n independent of Φ_M as already discussed for the pinning at the band edges. Several microscopic models exist like the metal-induced gap state model, where the states are formed by the decaying complex wave functions of metal electrons [150], which penetrate the semiconductor. However, there are several other more simple mechanisms, which contribute to intragap states, like surface states of the finite semiconductor crystal (for an overview, see [151]).

3.4.2 Metal-organic interfaces: Disorder and ICT

In principle, the previously described effects hold for organic semiconductors as well. For example, the CNL approach is applied to describe metal-organic interfaces [152]. However, organics introduce additional complexities, as described in the reviews by Ishii *et al.* and Hwang *et al.* [153, 154]. The main differences to conventional semiconductors are found in a low screening within organic materials and in the presence of significant disorder. The former changes the position of E_{et} and E_{ht} close to the interface [155]. The gap close to the metal becomes smaller due to the much higher screening capability of the metal, which increases the polarization energy (cf. Fig. 3.7).

The latter implies a high occupation of intragap/tail states, which cause a pinning of E_F to values within the energy gap away from the charge transport level. A treatment of this effect is comparable to the defect model in inorganic semiconductors, describing intragap interface states [Fig. 3.23(b)]. Fermi level pinning within the electrical gap is commonly observed experimentally in photoelectron spectroscopy studies. Here, typical values between the ionization potential and E_F are in the range of 0.3 - 0.5 eV [156]. A second theory to explain this pinning is the integer charge transfer (ICT) model [157–160], which assumes polaronic or bipolaronic states at the metal-organic interface [Fig. 3.23(b)]. These states are further relaxed states due to the screening of the metal electrons. Therefore, they lie within the energy gap. As soon as the work function of the metal reaches this polaronic level, a charge transfer to the electrode is favorable and, consequently, an interface dipole is created.

The described effects should rather result in an interface dipole than in a bending of the energy levels, because a bending can only result from spatially localized charges like ionized dopant molecules. Free charge carriers face the field and will pile up directly at the interface. A spatial extension of the free charge carriers could only be possible in the case of a very low density of states, which hinders the relocation of all charge carriers to an interfacial monolayer. Blakesley and Greenham [161] tried to distinguish between the impacts of ICT and tail states on the bending of energy levels, comparing simulation and photoelectron spectroscopy measurements. They found that both theories can fit the experimental data.

Furthermore, chemical effects exist which change the interface properties. Some organic molecules react with the metal and form metal-organic complexes, as it was observed, e.g., in Refs. [162, 163]. If these complexes are electrically active, they constitute interface states ruling the energy level alignment. Metal evaporated onto organic material can diffuse into the organic film and create gap states [164]. Energy level alignment is also affected by the push-back effect: Commonly, the electron wave function extends out of a metal surface into vacuum. When depositing an organic film on the surface, these electrons are pushed back by the repulsive force of occupied electron orbitals of the deposited material. Therefore, molecules deposited on a metal surface change the surface work function of the metal.

A verification of these theories and the identification of the dominating process is complicated, because the additional levels (polaronic, CN, or tail states) are hard to determine experimentally. This field is topic of intense research, which combines experimental techniques like sophisticated photoelectron spectroscopy and scanning tunneling microscopy with quantum-mechanical calculations to describe the electronic structure and dynamics at metal-organic interfaces [165–167].

3.5 Experimental realization of small-molecule solar cells

Organic solar cells can be divided by material class into polymer based and small-molecule organic solar cells, where small molecules cover oligomers or molecules with a molar weight $\lesssim 1000\,\mathrm{g/mol}$. Whereas polymers are exclusively solution processed, small molecules can

also be deposited via sublimation in a vacuum system.

Solution processing requires a molecule soluble in a specific solvent. The solvent has to evaporate after deposition of the layer. In laboratory setups the solution is usually spin-coated onto the substrate. For large-scale production inkjet printing, screen printing [168, 169], slot-die coating [170], gravure coating, and other coating technologies are under investigation [171, 172]. These technologies employed in a roll-to-roll facility to coat flexible substrates provide the potential for a fast and cost-efficient device fabrication. However, solution processing of multilayer stacks requires orthogonal solvents not to dissolve the underlying layer.

Vacuum processing is supposed to be more cost-intensive considering initial investments, although these costs should not be the main issue for a high-throughput technology, where the main costs are given by the operation costs of the tools and the prices of the required raw materials. At the moment they are dominated by the price of the transparent electrode ITO [173]. The main advantages of vacuum sublimation are a higher purity of the deposited films not containing any remaining solvent and a controllable deposition of multi-layer stacks by a consecutive evaporation of the separate layers. All solar cells fabricated in the context of this work are processed by vacuum sublimation.

3.5.1 Stacks

The solar cell stacks in this thesis represent state-of-the-art small-molecule devices, employing doped charge transport layers [174, 175]. This approach results in a p-i-n architecture [53, 176], which has already been sketched in Ch. 2.5.3 (Fig. 2.14, p. 37) when having discussed possible realizations of the ideal solar cell structure. It is stressed that in contrast to some publications of organic solar cells, where p and n refer only to the type of conductivity (hole or electron), here, p and n mean electrically p- and n-doped semiconductor layers as discussed in Ch. 2.2.1. A stack with typical layer thicknesses is depicted in Fig. 3.24(a). The absorber which contains a donor-acceptor heterojunction is found in the middle of the stack and can be realized either by a bilayer (flat heterojunction, FHJ) or by a co-evaporated mixture (bulk heterojunction, BHJ). A combination of both leads to a hybrid heterojunction, comprising a BHJ sandwiched between intrinsic donor and acceptor layers [177, 178]. Attached are the doped transport layers, hole transport layer (HTL) and electron transport layer (ETL), optionally with some intrinsic HTL or ETL between absorber and doped transport layer. The scope of this intrinsic layer is to keep dopants away from the absorber, because they are supposed to quench excitons [179]. Additionally, solar cells with improved long-term stability have been realized by this structure. The doped layers are supposed to fulfill the following functions, visualized in Fig. 3.24(b):

- Selective contacts: A high LUMO (HOMO) offset between active material(s) and the HTL (ETL) blocks electrons (holes). Thus, these charge carriers are hindered in penetrating the HTL (ETL). Therefore, recombination or diffusion to the "wrong" contact is avoided. In terms of Ch. 3.3.1 this guarantees an $\eta_{CC} = 1$.

- Optical spacer and exciton reflector: HTL and ETL are transparent due to the large
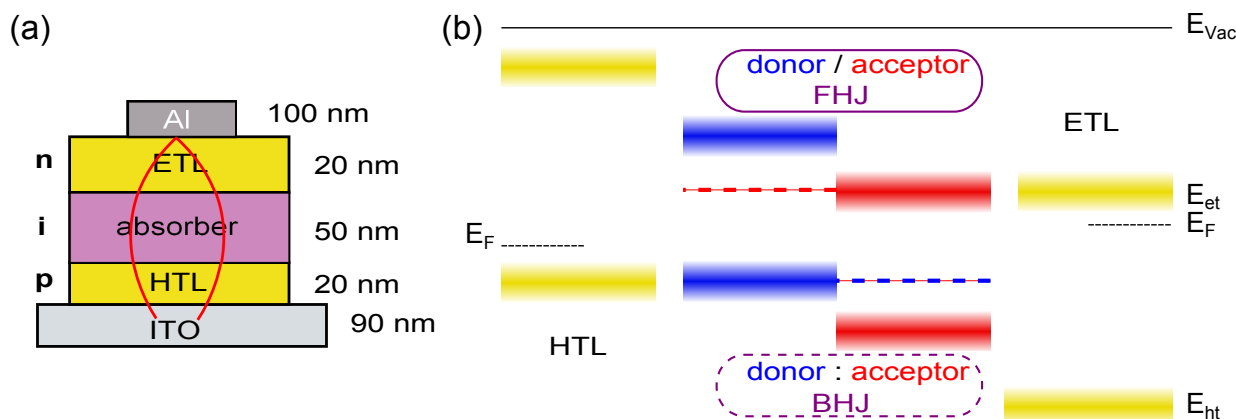
Figure 3.24: p-i-n concept: (a) Solar cell stack with common layer thicknesses and a sketch of a standing wave, reflected by the Al contact. (b) Energy levels with respect to the vacuum level, i.e. without contact of the materials. The position of the Fermi level E_F is close to the electron-transport level E_{et} in the n-doped electron-transport layer (ETL) and close to the hole-transport level (E_{ht}) in the p-doped hole-transport layer (HTL).

optical gap of the employed materials. Therefore, they are sometimes called window layers, which are required because commonly the thickness of the absorber layer is limited due to transport constraints. Thus, the absorber should be positioned in the optical field maximum to optimize η_{PA}. The transparency of the layers implies that the excited states S_1 and T_1 of HTL and ETL are higher in energy than those in the absorber. Thus, energy transfer to the HTL/ETL is unlikely and excitons are hindered from passing through and being quenched at the metal contact. This provides a high η_{ED}.

- Ohmic contact to electrodes: The doped layers are highly conductive and a tunneling contact to the electrode is achieved as described in Ch. 3.4.1, independent of the work function of the electrode.

- Connection of tandem cells: A highly doped p-n junction can be used for a tandem cell as recombination contact, converting electron into hole current without losing energy.

In the classical p-i-n stack the HTL is deposited on a transparent glass substrate, covered by tin-doped indium oxide (ITO). Aluminum (Al) is used as electrode and reflecting back contact. The n-doped layer can be exchanged by an intrinsic organic buffer layer in combination with Al, resulting in the same performance of the solar cell, which is then called a p-i-metal device. The mentioned properties of the transport layers imply that inverted structures can be realized without difficulty by exchanging HTL and ETL. The stack is then of n-i-p type.
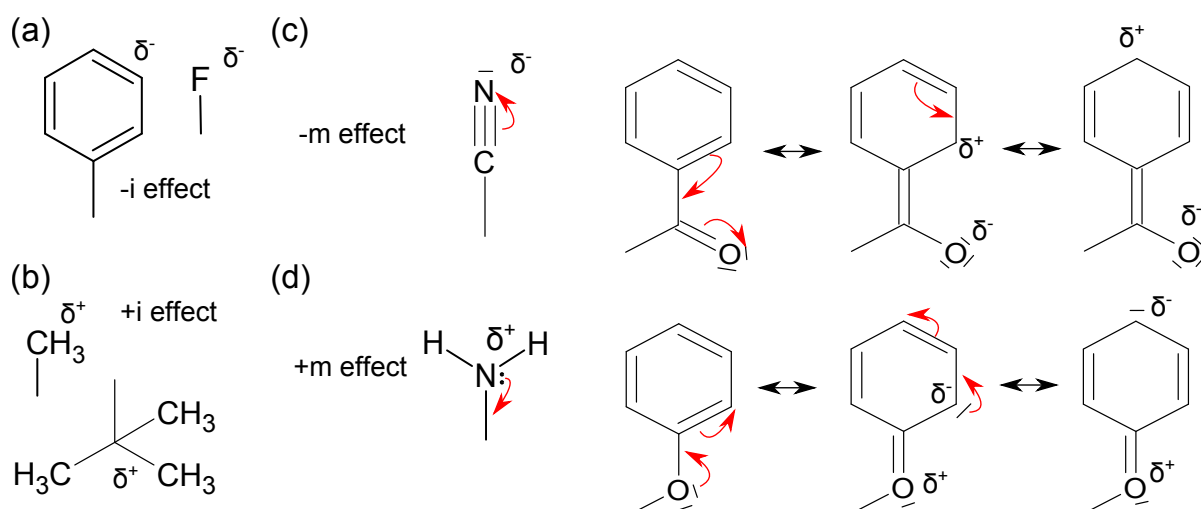
Figure 3.25: Examples for typical functional electron withdrawing and electron releasing groups: (a+b) Phenyl, fluorine, methyl, and tert-butyl groups with inductive effect. (c+d) Amine and nitrile (cyano) group showing a mesomeric effect. Visualization of the mesomeric effect by resonance structures of a π-system containing oxygen.

3.5.2 Materials

In this section the materials are introduced which are employed to realize the until now discussed various functions in an organic solar cell (donor, acceptor, HTL, ETL). Based on the basics of Ch. 3.1.1 and on intuitive rules of chemistry, we discuss the properties of these molecules. The desired properties of a solar cell material differ, depending on its function in the solar cell stack. Charge transport layers should be transparent in the visible spectral range, HTLs should have a HOMO in the range of the HOMO of the absorber materials and ETLs a LUMO in the range of the LUMO of the absorber to guarantee efficient hole and electron transfer between absorber and HTL/ETL. Absorber layers are desired to grow (micro-)crystalline, resulting in a high exciton diffusion length and charge carrier mobility [180, 181], because grain boundaries are the main factor limiting transport [182]. Transport layers, however, are preferred to grow amorphous to provide smooth layers. The conductivity of these amorphous layers is still sufficient due to the employment of a high doping concentration.

Basically two main approaches are focused on to manipulate these energetic and morphological properties: First, a variation of the size and arrangement of aromatic systems, contributing to the π-system. The size mainly influences the HOMO-LUMO gap as discussed in Ch. 3.1.1. The three-dimensional structure of the molecule changes the morphology of the film. For example, side groups that are free to rotate with temperature reduce the tendency of the molecular film to crystallize.

The second approach is the application of functional groups which are electronically

active as electron donating or withdrawing groups. They define the absolute location of the orbitals and therefore the type of a molecule, or more precisely of its π-system, being a stronger donor or acceptor. Two major effects can be distinguished that functional groups can take advantage of: The inductive effect, which is present between a σ bond of two different atoms with different electronegativity. The higher the electronegativity of an atom or functional group [183], the higher are its electron-withdrawing properties and the higher is the positive partial charge remaining on the core of the molecule (-i effect). As depicted in Fig. 3.25(a), fluorine (F) and phenyl (C_6H_5) show the -i effect, whereas methyl (CH_3) displayed in Fig. 3.25(b) is electron releasing (+i effect). The second is the so-called mesomeric effect which acts on conjugated π bonds. Figure 3.25(c) shows an example for oxygen, where in one mesomeric resonant structure, four non-bonding valence electrons are located on the oxygen. Flipping bonds leads to other mesomeric resonant stuctures, revealing a partial negative charge (-m effect) or in the case of 3.25(d) positive charge (+m effect) on the oxygen. Other groups show this effect as well. A nitrile (cyano) group (CN), e.g., introduces a strong -m effect, whereas an amine group (NH_2) shows a +m effect. A quantification of the electronic effects of substituents can be done using the Hammett constant, which is determined by a comparison of the dissociation constant of substituted (X-C_6H_4-COOH) and unsubstituted benzoic acid (C_6H_5-COOH) in water [184]. The higher the electron-withdrawing properties of the substituent the closer the chemical equilibrium at the ionized form of the acid X-$C_6H_4COO^- + H^+$ which can be measured by the pKa value.

Absorber materials

Figure 3.26 shows the absorber molecules used in this work. Zinc phthalocyanine (ZnPc) (a), which is a relatively planar molecule with an extended aromatic system, is the most common absorber in small-molecule solar cells [185, 186]. Its absorption coefficient is plotted in Fig. 3.27. The Zn as central metal atom can be exchanged by other elements. This can lead to a change in the energetic [187] and absorption properties of the phthalocyanine molecule due to a large interaction of the metal atom with the π-system. For example, Sn [188], Pb, and Cl-Al [189] shift the absorption towards lower energies (infrared). Additionally, larger metal atoms (Sn, Pb) decrease the planarity of the molecule [190]. This leads to changes in the spatial structure and hence influences the stacking of molecules. ZnPc (and comparably CuPc) crystallizes in herringbone structure in different phases dependent on substrate and deposition conditions [191]. The HOMO of ZnPc in solution is around -5.4 eV, determined by an electrochemical measurement (cyclic voltammetry, CV). UPS measurements of a thin film deliver a value of -5.07 eV (UPS onset), which can be shifted downwards by the amount of fluorination (-i effect) of the naphthyl groups at the corner of the molecule (F_4ZnPc -5.46 eV (IP, UPS) [192], F_{16}ZnPc -6.1 eV (CV) [193]). The same effect is observed for CuPc with an IP of 5.2 eV and for F_{16}CuPc of 6.3 eV [194]. Furthermore, the IP can also depend on the molecular orientation, which is according to Ref. [195] 5.15 eV (5.65 eV) for lying CuPc (F_{16}CuPc) molecules and 4.75 eV (6.5 eV) for molecules standing upright on a graphite substrate.
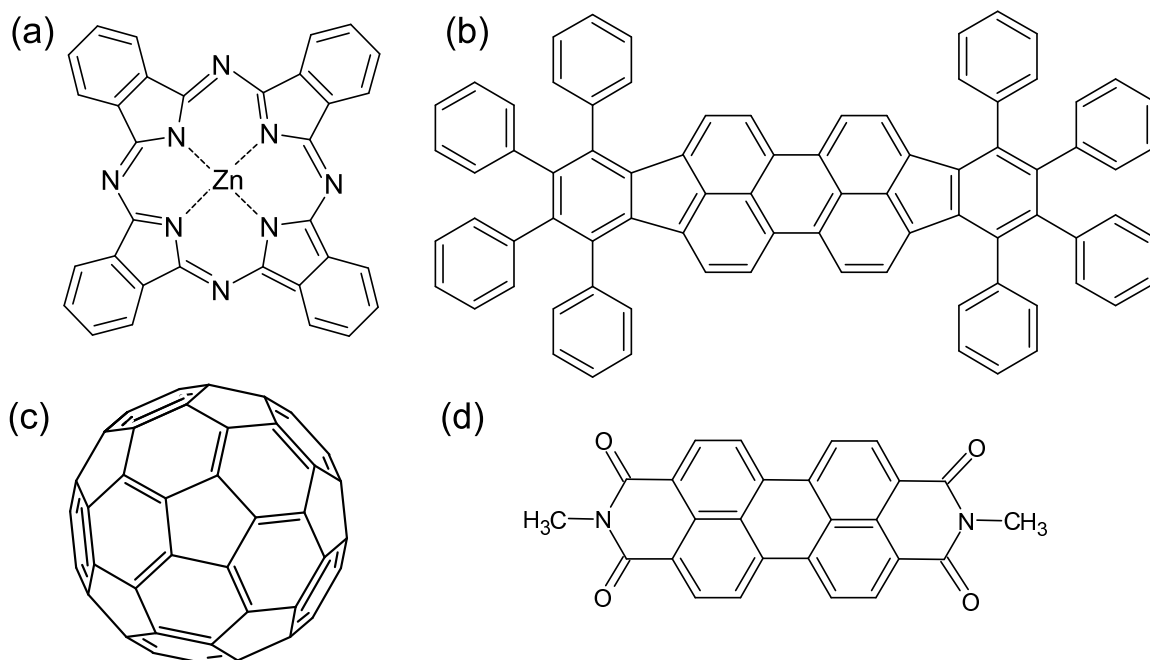
Figure 3.26: Absorbers used in this work: the donors (a) ZnPc and (b) Ph4-Ph4-DIP and the acceptors (c) C_{60} and (d) Me-PTCDI.

Another class of absorbers shown in Fig. 3.26(b+d) are perylenes. The Ph4-Ph4-DIP, a di-indeno-perylene (DIP) with eight phenyl groups as substituents, exhibits the π-system located on the core [196]. Whereas unsubstituted DIP is completely planar and grows crystalline [197, 198], the phenyl groups rotate out of the plane and prevent a crystalline growth. The crystallinity of the pure DIP is supposed to give a large exciton diffusion lengths in the range of several 10s of nm (100 nm reported by Ref. [182]). Ph4-Ph4-DIP absorbs between 500 and 600 nm (see Fig. 7.4, p. 214), whereas the also depicted Me-PTCDI shows an absorption maximum in the blue [199] due to the smaller π-system. Ph4-Ph4-DIP consisting only of hydrocarbons is ambipolar, whereas Me-PTCDI is an n-typ molecule with lower lying molecular orbitals due to the electron withdrawing oxygens, making the π-system more acceptor-like. The prevailing type (donor or acceptor) can also be estimated from the average oxidation state of the carbon, which is negative in the Ph4-Ph4-DIP due to the positive hydrogens, whereas it is expected to be close to zero for the Me-PTCDI, because the effect of the hydrogens (oxidation number +I) is approximately compensated by the oxygen (-II).

The oxidation state of zero also allows to understand the strong acceptor properties of the fullerene C_{60} consisting of 12 pentagons and 20 hexagons with a carbon atom in each corner [200–202]. They constitute a spherical molecule, also called buckyball, with a nucleus diameter of 0.7 nm (average C-C bond lengths of 1.4 Å [203]), a van der Waals diameter of 1 nm, and a crystal lattice constant in a cubic system of 1.4 nm [204]. Its absorption is also plotted in Fig. 3.27, showing complementary parts to ZnPc. The ZnPc
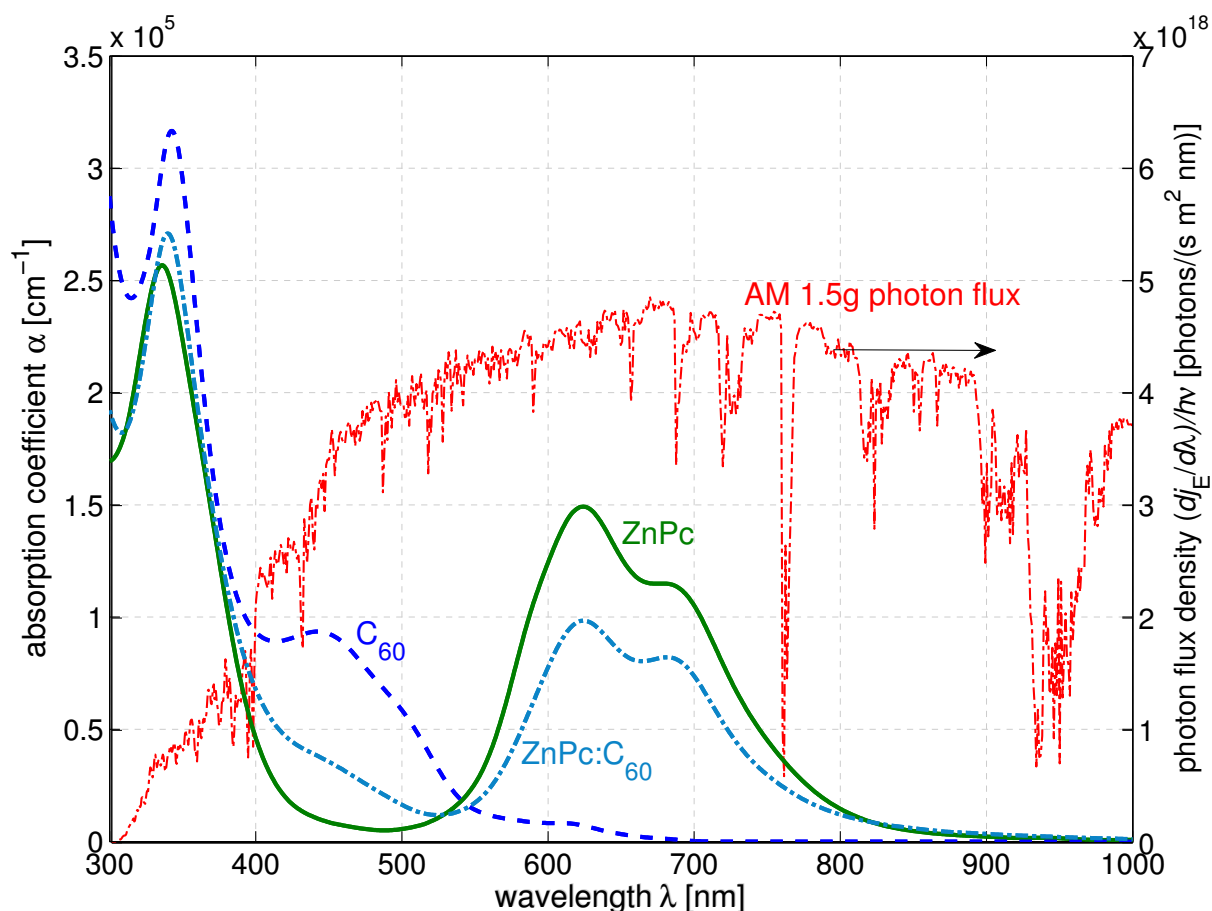
Figure 3.27: Absorption coefficient $\alpha = {}^{4\pi k}/\lambda$ of ZnPc, C_{60}, and a 1:1 blend with k determined by reflectance and transmission measurements of samples with several layer thicknesses[1]. The absorption of ZnPc shows a characteristic double peak between 600 and 700 nm. C_{60} shows a peak at 450 nm. The absorption of the blend contains the fingerprints of both compounds. The AM 1.5g photon flux is plotted for comparison.

absorption between 550 and 800 nm is called the Q-band, where the low energy peak at 680 nm is attributed to an exciton and the other peak at 625 nm to the first $\pi - \pi^*$ transition [205]. The dimer absorption is seen in a broadening of the high-energy region of the absorption spectrum [206] and increases with larger crystallinity. The probability of dimer absorption is decreased when blending ZnPc with C_{60}. This may explain the slightly different spectral shape of the absorption of ZnPc in the blend, where the shoulder at 580 nm is not visible and the peak at high energy is decreased more strongly than the low energy peak. In general, the absorption spectra of molecules in a film depend on the morphology of the film, which is influenced, e.g., by the substrate material, the deposition temperature [205], and post-annealing [207], although the main spectral shape is commonly

preserved.

The absorption coefficient of organic molecules depends strongly on the orientation of the polarization of the light with respect to the extension of the π-system, which is mostly planar, i.e. two-dimensional. The probability of a photon-electron interaction is much higher when the electric field oscillates within the plane of the π-system. A very illustrative explanation for the increased transition dipole moment in plane is the picture of the electric field of the electro-magnetic (light) wave shaking an electron to lift it to an excited state. This is more probable within an iso-energetic region, which means within the lateral extension of the π-system. Thus, for thin film-solar cell applications it is favorable if ZnPc or DIP molecules lie on the substrate. This arrangement means an orientation of their π-system parallel to the surface of the substrate and perpendicular to the direction of incidence of the light. Also the transport properties perpendicular to the substrate are supposed to be improved by the higher π orbital overlap of lying molecules. That is why much research focuses on getting molecules lying flat [208, 209].

The absorption coefficient of ZnPc (Fig. 3.27) and other organic dyes is much larger than the one of inorganic band edge semiconductors close to the band edge, which can be explained by Fermi's golden rule, describing the transition probability T between two states i and j:

$$T_{i \to j} = \frac{2\pi}{\hbar} |\langle j|H'|i\rangle|^2 \rho(E_j).\qquad(3.27)$$

Here, $T_{i \to j}$ is proportional to $\langle j|H'|i\rangle$, which is the matrix element of the perturbation H' between the two states. This perturbation represents the interaction of the field of the electromagnetic wave with the transition dipole moment of the substance. Furthermore, T is proportional to the density of states ρ. Due to the large interaction between atoms within a crystal, energy levels split strongly and form wide bands with a relatively low density of states (increasing with $\sqrt{E}$) close to the band edge. For example, silicon with an absolute density of states = atom density = 5×10^{22} cm^{-3} has an effective density of states $N_C = 3 \times 10^{19}$ cm^{-3}. Molecular solids show very narrow absorption bands, resulting in a much higher density of states and consequently in a high absorption coefficient in this narrow region.

Transport layers

Several hole transport materials are displayed in Fig. 3.28. Characteristic are the nitrogen atoms with three single bonds, which lie roughly in one plane (C-N-C angle $\approx 120°$). The π-system is disturbed by these single bonds between the ring systems, hindering planarity and allowing rotations. Non-planarity is energetically more favorable for the π-electron cloud, which results in an equilibrium torsional angle for an unsubstituted biphenyl $(C_6H_5)_2$ of $44.4°$. Angles in the range of $40 \ldots 50°$ are expected between the plane of N and its bonds with the plane of the attached rings. When depositing such a material, not every molecule is found in its equilibrium structure and hence an amorphous layer (supercooled melt) is

---

[1]Measurements performed by André Merten, IAPP

formed. The difference in the HOMO$^{\text{UPS}}$ of MeO-TPD (-5.1 eV) and α-NPD (-5.5 eV) can again be attributed to the impact of functional groups. The methoxy group as electron donating group (+m effect) shifts the orbitals upwards. The justification of employing exactly the depicted complicated molecular structures is found in the restrictions and procedures of organic chemistry, providing a set of common precursors and allowing only particular substitution reactions.

Charge transport layers are electrically doped to increase their conductivity. HTLs can be p-doped by dopant molecules, which are very strong acceptors with a LUMO in the range of the HOMO of the matrix. As example, F$_4$-TCNQ is shown, which has a very high electron affinity due to the cyano group and fluorine substituents. The doping process is comparable to inorganics (Ch. 2.2.1) and results from an electron transfer, leaving a hole in the HTL material and a localized negative charge on the ionized dopant molecule (anion). It is not entirely known whether the hole is completely free or still bound in a charge-transfer state. The detailed mechanisms and the efficiency of the doping process are still under research [156, 210].

For technical reasons (chamber contamination by F$_4$TCNQ) the proprietary dopants NDP2, NDP9, and NDN1 (Novaled AG, Dresden) are mostly applied in this work. We will focus on HTLs when examining variations of the charge transport layers. On the n-side, commonly a thin (< 10 nm) layer of BPhen is employed, whose structure is also shown in Fig. 3.28. Its function is mostly a buffer protecting the absorber layers during metal evaporation.

Degradation

Most of the discussed molecules are subject to degradation. They are in particular sensitive to water and oxygen. The higher the HOMO, the higher is the probability of an electron transfer to an oxygen molecule by forming a covalent bond. Such oxidations affect mainly electrical properties like conductivity and interface energetics, which commonly result in a decrease of solar cell performance [211]. Molecular oxygen is also known to p-dope ZnPc [179], which is a less harmful and to some extent reversible process. Ultraviolet light is another source of degradation [212]. It causes photochemical reactions, because the UV energy is sufficiently high to break up the molecules with bond dissociation energies of a carbon single bond of around 3.5 eV and for a double bond of around 6.2 eV. If other reaction partners are available, the broken bonds can be replaced by other substances.

3.5.3 Fabrication details

As simulation requires reproducible data series, all devices are fabricated in a tool allowing the fabrication of several solar cells with systematic variations in one evaporation run. This implies the same material batches and exactly the same substrate treatment and evaporation conditions. This is very important, as quality and purity of materials from different suppliers or batches vary in a certain range. Although a common purity of, e.g., $\gtrsim 99\%$ is high in terms of chemical properties, the remaining impurities can be crucial for electri-
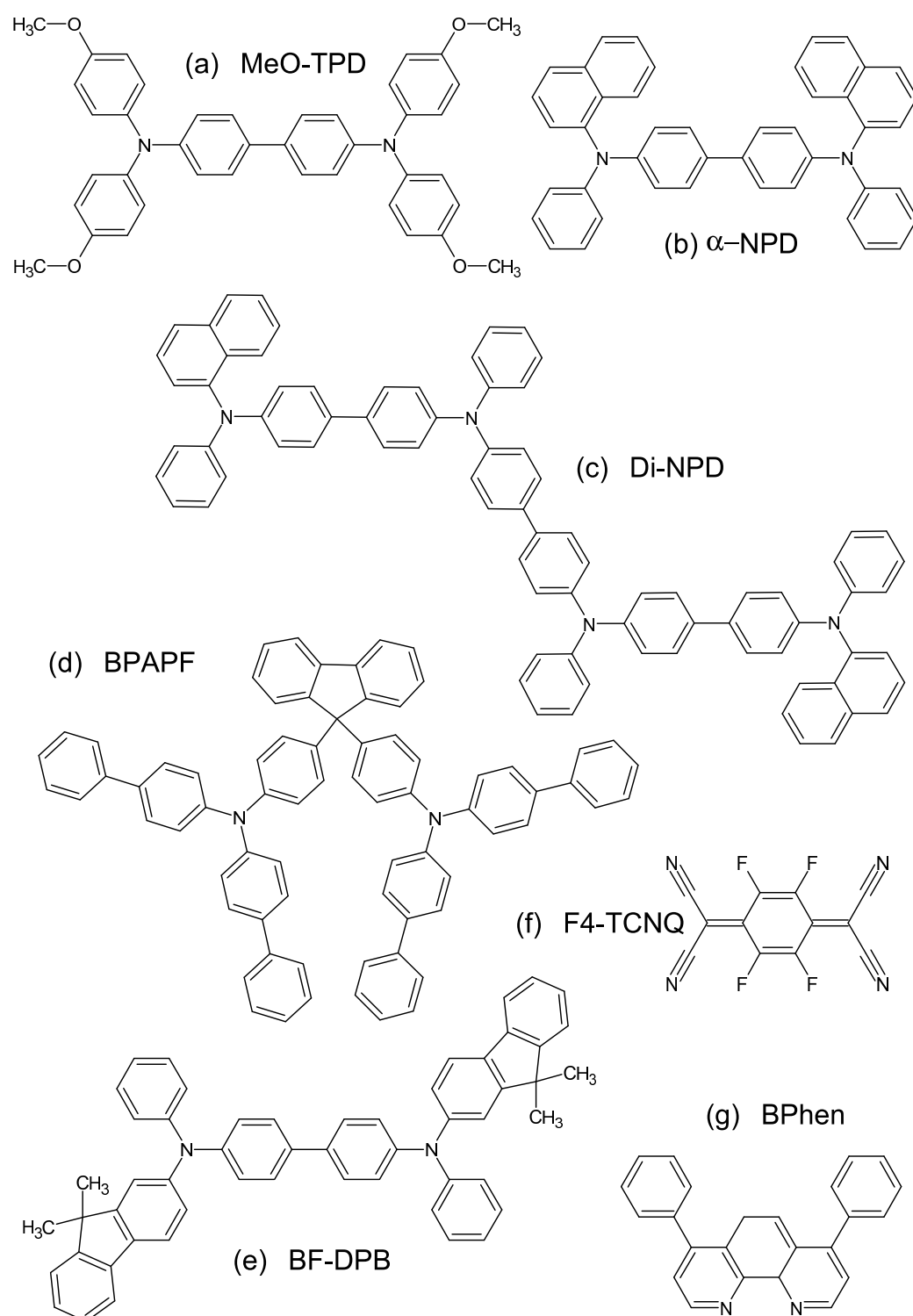
Figure 3.28: Molecules employed in the transport layers used in this work: (a-e) Hole transporting materials (a) MeO-TPD, (b) α-NPD, (c) Di-NPD, (d) BPAPF, and (e) BF-DBP. (f) p-dopant F4-TCNQ (g) electron-transporting material BPhen.
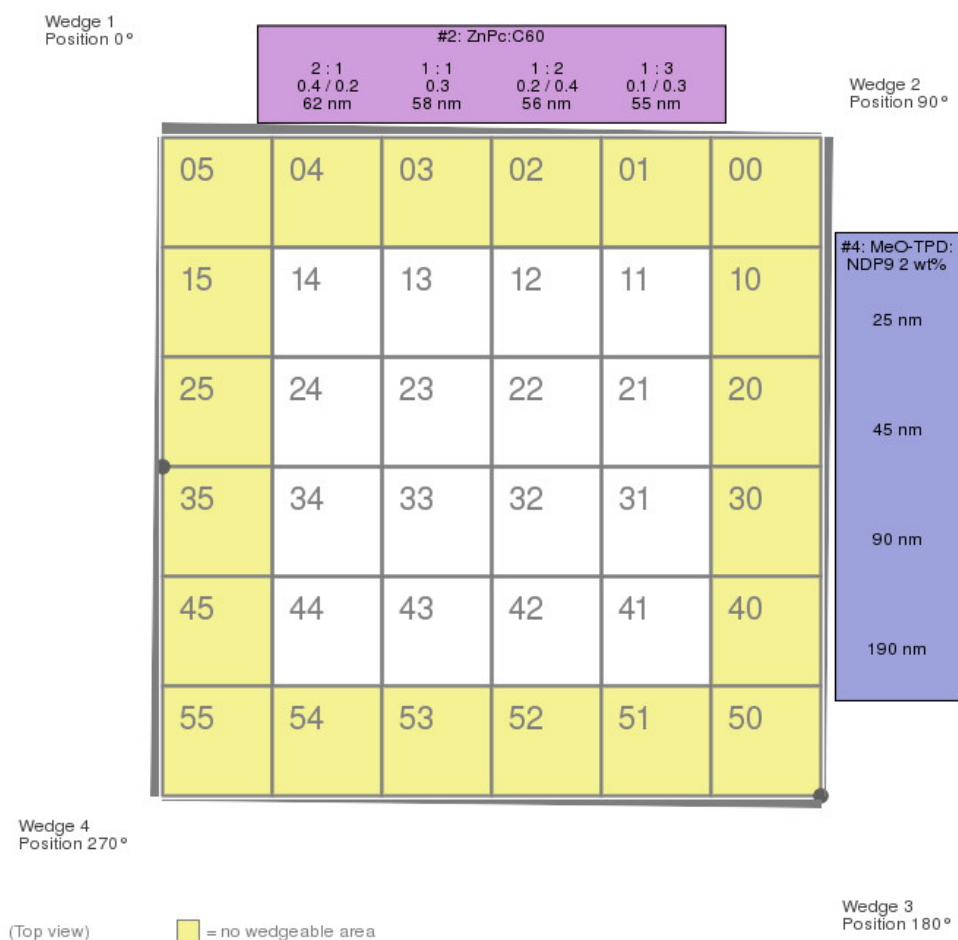
Figure 3.29: Example of a wafer layout: The 15 x 15 cm^2 wafer consists of 36 samples. Single columns (and rows) are addressable by wedges shading the remaining parts of the wafer during the deposition process.

cal effects like doping and traps. The evaporation tool consists of a custom-made single vacuum chamber from K. J. Lesker company, equipped with 11 organic and three/four metal sources[2]. Hence, it allows to fabricate complicated structures without breaking the vacuum. It handles glass wafers with 15 x 15 cm^2, consisting of 36 substrates (25 x 25 mm^2) arranged in six rows and columns (Fig. 3.29). Due to technical reasons mostly only the inner four are available, resulting in 16 devices per wafer. During evaporation, single columns are addressed by wedges, which can be positioned to shadow designated columns. By rotating the wafer by 90° relative to the wedge, also single rows can be addressed. This geometry allows, e.g., layer thickness variations or all combinations of two layers, each consisting of different materials or layer thicknesses. This variation scheme is often reflected

---

[2]The two tools available, Lesker A and B, are operated by the IAPP operator team.
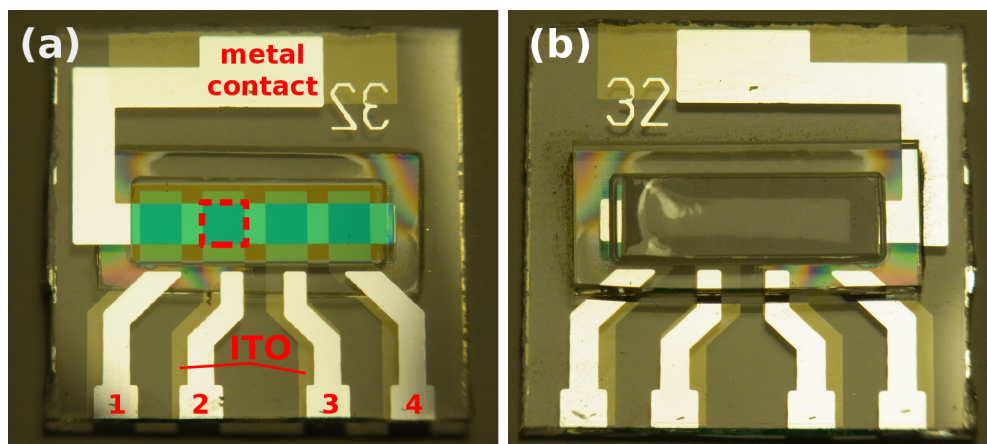
Figure 3.30: Photograph of a sample containing four solar cell pixels (blue, one is marked by a dashed rectangle). Their area is defined by the overlap of the ITO (yellow) and the metal electrode (shiny). The four ITO fingers are reinforced by metal. (b) Top view, showing getter and encapsulation glass with interference fringes due to thickness variations in the glue which have been caused by mechanical stress. Usually this indicates a failure of the encapsulation.

in the presented experimental data consisting of a 4 x 4 matrix.

Each substrate contains four single solar cells, called pixels, with a nominal area of $2.54 \times 2.54 \, \text{mm}^2 = 6.44 \, \text{mm}^2$. This area is defined as geometrical overlap between the pre-structured ITO contact and the top metal contact which is a common contact for all four pixels, as shown in Fig. 3.30. The deposition areas are defined by separate shadow masks for organic and metal layers. The purpose of the metal stripes covering the ITO is a reinforcement of the ITO fingers to decrease the parasitic series resistance of the device, which is then found in the range of $30 \ldots 50 \, \Omega$.

The definition of the active area via a geometrical overlap of electrodes is difficult, because the active regions extend slightly over the edges and contribute to the overall photocurrent by lateral currents from the surrounding which is illuminated as well. This effect depends strongly on the lateral conductivity of the layers. Assuming additional electrically active areas extending the edges by less than $1 \, \mu\text{m}$, this effect is expected to be less significant than the effect of slightly misaligned shadow masks during evaporation. Using an aperture to define the exact illuminated area during a measurement increases the accuracy on the one hand, but includes the effect of a dark solar cell in parallel on the other hand. Thus, the aperture should be taken as area calibration by measuring the short-circuit-current density only. This value is then used to scale the I-V curve, which is measured without aperture, to the correct J-V curve. As this work does not focus on measuring exact solar-cell efficiencies, all I-V measurements are done without aperture. The current density J is obtained by dividing the measured current by the nominal device area of $6.44 \, \text{mm}^2$.

The sample preparation procedure is as follows: The ITO-coated and pre-structured glass substrate is cleaned with acetone and afterwards kept in a N-Methyl-2-pyrrolidon (NMP) bath for 20 min. These processes are followed by a rinse under deionized (DI) water, and ultra sonic baths in DI water and acetone (10 min each). Finally, the substrate is treated by oxygen plasma (10 min). Organic materials are commonly purified by vacuum gradient sublimation [213, 214], where the material is placed in a tube with a temperature gradient. After the cleaning, the material can be collected at a certain position in the tube, being separated from impurities which exhibit different sublimation temperatures. This treatment is repeated up to three times. The purified material is filled into crucibles, surrounded by resistive heating wires, constituting the evaporation source. All layers are evaporated subsequently at a base pressure of $\lesssim 10^{-7}$ mbar and with typical rates of $0.1\ldots0.5$ Å/sec. Although it is possible to heat the substrate during evaporation to assist the rearrangement of arriving molecules on the surface, all samples discussed in this work are fabricated at room temperature. The wafer is rotating during evaporation with a speed of 10 rpm to increase homogeneity.

Bulk heterojunctions or doped layers are processed by co-evaporation of both materials. Layer thicknesses are measured via independent quartz crystal monitors, which detect the mass of the evaporated material. As these monitors cannot directly be located at the substrate position, a tooling factor has to be determined, describing the proportionality factor between expected material at the substrate and actually measured material at the position of the monitor. The densities of the materials have to be known for thickness calculations. Density values of 1.34 g/cm^3 for ZnPc and 1.54 g/cm^3 for C$_{60}$ are used, although recent X-ray diffraction measurements result in slightly different values. Stating errors in layer thickness is very difficult due to errors in the material density, a dependence of the tooling factor on the filling of the crucibles, and the mostly unknown density of mixed films. Relative variations are expected to be less than 10 %, including an inhomogeneity of $\approx 2\%$ on one single wafer [215][3]. After processing, every 2.5 x 2.5 cm^2 substrate is encapsulated with a cover glass, fixed by UV hardened epoxy glue. Additionally, a moisture getter (Dynic Ltd., China) is placed between cover glass and solar cell. Organic electronic devices degrade rapidly under exposure to air (especially oxygen and water vapor). That is why a good encapsulation is essential for a reliable characterization of the solar cells described in the next section.

3.6 Basic characterization methods

3.6.1 Current-voltage characteristics

The most important characterization method is the measurement of the current-voltage characteristics (*I-V* curve), delivering the power-conversion efficiency η (Eq. 3.16). Ideally, this measurement should be performed under real solar illumination and at a well-defined temperature. Standard reporting conditions for solar cell characterization are the AM 1.5g

---

[3]regarding the central sixteen samples at Lesker B.

spectrum (cf. Fig. 2.1) and $T = 25\,°\mathrm{C}$. For practicability reasons, laboratory setups are used employing a solar simulator. It consists of a light source, mostly a Xenon lamp with a specific gas mixture, which emulates the real solar spectrum. All I-V curves shown in this work are measured under the sun simulator 16S-150 V.3 by Solar Light Co., USA, whose spectrum is shown in Fig. 3.31. Illumination of the sample is provided via fiber optics with a spot of several millimeters in diameter. The light intensity is measured by a calibrated silicon reference photodiode. It can be varied by adjusting the power supply of the lamp, employing neutral density filters (fine metal grids), or varying the distance between fiber and sample. To record the I-V data, a voltage sweep is applied and the current is measured by a source measuring unit (Keithley 2400).

The main source of errors is the deviation of the solar simulator spectrum from AM 1.5g, as visualized in Fig. 3.31. Considering this spectral mismatch is very important for a correct determination of η, especially for (organic) solar cells with spectrally narrow absorption bands. The intensity monitored by the silicon reference diode is the overall intensity, integrated over all wavelengths (smaller than the wavelength corresponding to the silicon band-gap energy). It averages the positive and negative deviations of the simulator spectrum compared to the AM 1.5g spectrum. If, e.g., the positive deviations are located in the spectral region, where the test (organic) solar cell mainly absorbs, the efficiency will be overestimated. Therefore, the spectral mismatch factor has to be taken into account, describing the ratio between the intensity seen by the organic solar cell and the one measured by the reference cell. The spectral response of the solar cell has to be known to carry out the mismatch correction.

3.6.2 Spectrally resolved measurements

External quantum efficiency

The spectral photocurrent response describes the current density per unit wavelength and incoming intensity in the unit mA/(mW nm). Converting the incoming intensity into the number of photons (division by $h\nu$) and the current into the number of electrons (division by elementary charge), the external quantum or incident photon to collected electron efficiency (EQE / IPCE) can be obtained. The spectral mismatch (MM) for an illumination with spectrum SoSim(λ) given as spectral photon flux density ($^\gamma$) can then be calculated as:

$$\mathrm{MM(V)} = \frac{\int \mathrm{EQE}(\lambda, \mathrm{V})\mathrm{SoSim}^\gamma(\lambda)\mathrm{d}\lambda/\int \mathrm{SoSim}^{\gamma/\mathrm{P}}(\lambda)\mathrm{d}\lambda}{\int \mathrm{EQE}(\lambda)\mathrm{AM1.5g}^\gamma(\lambda)\mathrm{d}\lambda/\int \mathrm{AM1.5g}^{\gamma/\mathrm{P}}(\lambda)\mathrm{d}\lambda}. \tag{3.28}$$

It is a measure of the sensitivity of the solar cell with respect to the illumination spectrum, i.e. the dependence of the EQE on λ in spectral regions, where the spectra show differences. Thus, it is in particular important for organic solar cells with distinct features in the EQE. The normalization in Eq. 3.28 can be done with respect to the photon number ($^\gamma$) or more commonly to the incident intensity (^{P}).
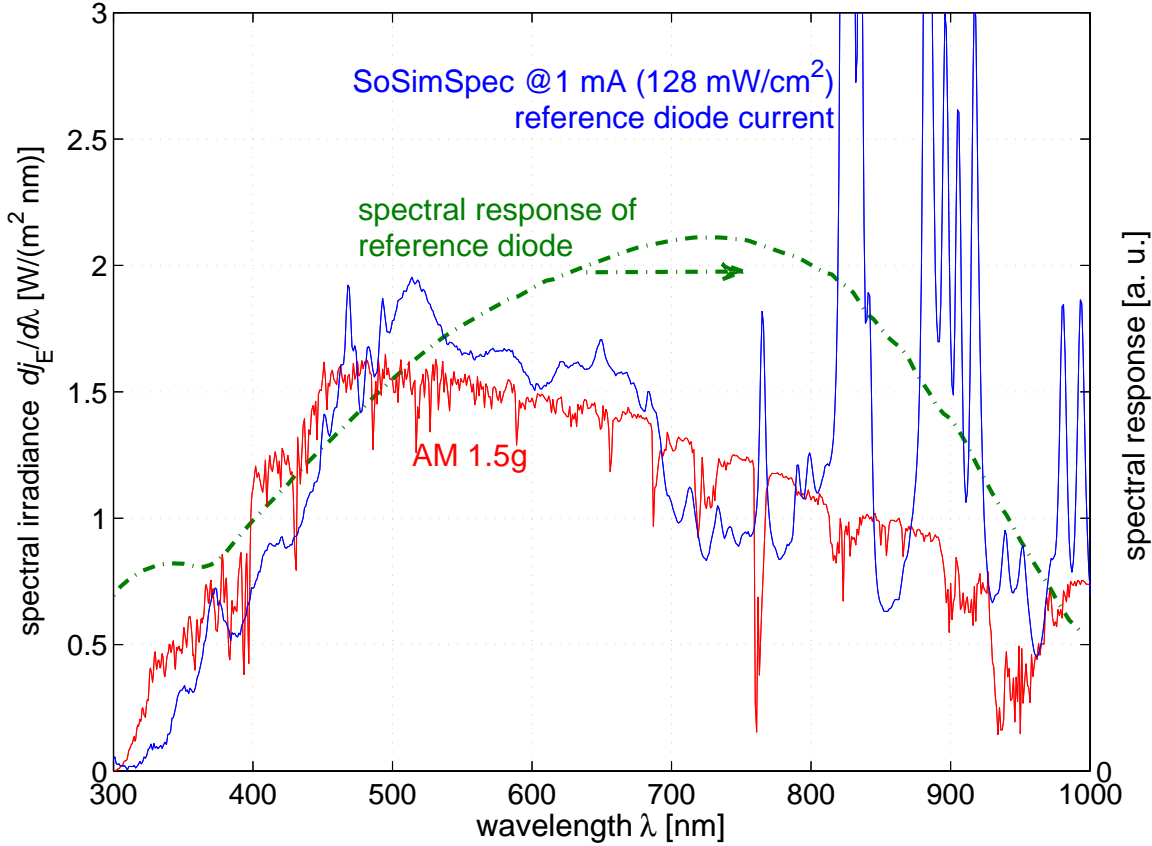
Figure 3.31: Spectrum of the solar simulator in comparison to AM 1.5g. The peaks for wavelengths larger than 800 nm result in a mismatch factor for ZnPc:C$_{60}$ solar cells smaller than 1 ($\approx 0.7\ldots0.8$). The reason is that ZnPc:C$_{60}$ solar cells mainly absorb below 800 nm (cf. Fig. 3.27), whereas the spectral response of the silicon reference diode extends to ≈ 1100 nm.

In general, the MM depends on the applied voltage due to the dependence of the EQE on the applied voltage. However, this dependence is expected to be weak. Therefore, the MM is commonly calculated at $V = 0$. As the photocurrent of a reference diode is used to adjust the intensity of the sun simulator, the overall correction factor m is needed. It describes the ratio between the current to use $J_{\text{sel}}^{\text{ref}}$ and the current J_0^{ref}, which is known from the calibration of the reference diode to correspond to a defined intensity, e.g., one sun under AM1.5g illumination. Hence, instead of normalizing to the overall intensity (Eq. 3.28), the EQE of the reference cell has to be considered as well:

$$m = \frac{J_0^{\text{ref}}}{J_{\text{sel}}^{\text{ref}}} = \frac{\int \text{EQE}^{\text{ref}}(\lambda)\text{AM1.5g}^{\gamma}(\lambda)\text{d}\lambda}{\int \text{EQE}^{\text{ref}}(\lambda)\text{SoSim}^{\gamma}(\lambda)\text{d}\lambda} \frac{\int \text{EQE}(\lambda,\text{V})\text{SoSim}^{\gamma}(\lambda)\text{d}\lambda}{\int \text{EQE}(\lambda)\text{AM1.5g}^{\gamma}(\lambda)\text{d}\lambda}. \tag{3.29}$$

It is equivalent to replace the EQE by the spectral response of the solar cell and use the irradiance spectra $(^P)$ instead of photon fluxes.

The EQE itself is recorded under monochromatic light generated by a Xenon arc-lamp (Oriel Apex Illuminator, Newport, USA) in combination with a monochromator (Cornerstone 260 1/4m, Newport, USA). The light is chopped and the current response of the sample is detected by a lock-in amplifier (7265 DSP Signal Recovery, UK). The lock-in technique increases the signal to noise ratio, as the lock-in amplifier only measures the signal at the chopping frequency. Consequently, parasitic signals and noise having another frequency (distribution) are filtered out. The calibration of the setup is done by measuring a silicon reference diode with known spectral response. The photocurrent data of the reference cell are used to calculate the spectral intensity distribution which reaches the sample. The EQE can also be measured under a bias illumination or bias voltage applied to the sample.

Absorption

As already discussed in Ch. 3.3.1, the internal quantum efficiency of a solar cell is an interesting physical quantity, which can be calculated as ratio between EQE and spectral absorptance. The absorptance is measured in reflectance mode employing a combined Deuterium and Halogen light source (Avalight-DH-S-BAL, Avantes, The Netherlands) and a spectrometer (OMT-ct60, OMT, Germany). The Al contact of the sample is used as reference and transmission is assumed to be zero.

3.6.3 Transient measurements

In Ch. 11.3.1 transient photocurrents recorded in the Cavendish Laboratories (Cambridge)[4] are shown. These measurements are performed using a pulse generator (Hewlett Packard 8116A) driving a high intensity light-emitting diode (Nichia NSPB300A, peak emission wavelength of 465 nm, 35 nm full width at half maximum) with pulse durations of several $100\,\mu$s. The light intensity is varied using a neutral density filter wheel and monitored by a Hamamatsu S8746-01 calibrated silicon photodiode. The photocurrent of the device is measured by an Agilent DSO6052A digitizing oscilloscope with input impedance of $50\,\Omega$. As low-noise voltage source, a battery with a resistive voltage divider (potentiometer) is used to apply the voltage bias, measured by a multimeter.

A similar setup is used for the transient data shown in Chs. 6.5.4, 7.2.2, and 10.3.3[5]. In this setup the pulse generator is an HP 8114A (100V/2A) and the oscilloscope an HP infinium (500MHz/1Gs). White Lumitronix Luxeon high power LEDs are used as light source. Charge carrier lifetimes are determined by a transient photovoltage measurement [217]. Here, the device is kept at open circuit by a bias illumination. The decay of the

---

[4]Measurements done together with Zhe Li and Dr. Chris McNeill. Funding for traveling to Cambridge was provided by the European Science Foundation (ESF) within the framework of OrganiSolar.

[5]The setup was built up by Steef Corvers who did his master project under the supervision of the author of this thesis. For further details regarding the setup, see Ref. [216].

voltage induced by a small-signal illumination pulse is measured by the oscilloscope set to high-impedance input ($1\,\mathrm{M\Omega}$). A variation of the illumination intensity is done by changing the current which drives the LEDs.

Chapter 4

Modeling

After having discussed general principles of solar energy conversion and the elementary processes in organic solar cells, we will focus on the simulation in this chapter. The first part deals with the conditions regarding the applicability of drift-diffusion simulations and the Einstein relation. In the second part, the physical processes implemented into the simulation are reviewed, which range from mobility and recombination models to the description of CT states, traps, interface barriers, and a Gaussian-shaped density of states. In a third, more technical part, the algorithm, the numerics, and the special treatment of interfaces are elaborated, concluding with a validation of the simulation based on analytical solutions of simple test structures. Therefore, this last part is mainly technical and only interesting for computational physicists, although its content is essential for a physical and self-consistent simulation.

4.1 Overview

Modeling and in particular numerical simulations can fulfill several tasks which range from theoretical discussions of physical mechanisms to the assistance in the interpretation of experiments. The latter implies parameter extraction by fitting of (quantitative) experimental data or a (qualitative) explanation of dominating processes in the experiment. As state-of-the-art simulations of organic semiconductor devices are not yet predictive, this work focuses mainly on the last point.

Simulation of semiconductors and organic solar cells in particular can be performed on different scales of abstraction (Fig. 4.1). In the previous chapter, models with a very high level of abstraction have already been discussed, like the equivalent-circuit model. Such models are characterized by effective parameters rather than by physical processes, whose characteristic variables can be measured independently with other techniques than a current-voltage measurement. On the other hand, when reviewing the Bässler model, we discussed results of a Monte Carlo simulation, which is a more microscopic modeling approach. It is commonly applied in charge carrier transport simulation in disordered and blended materials [79, 144, 218–221] and for geminate-pair dissociation [100, 222,
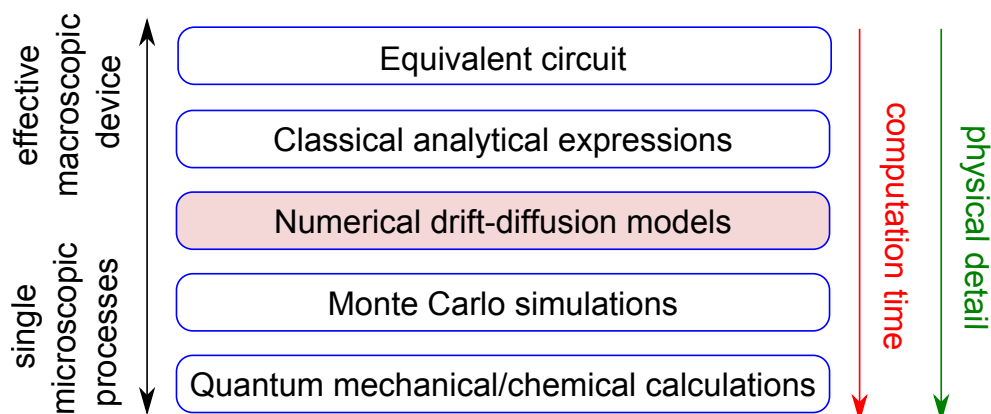
Figure 4.1: Overview of approaches for organic semiconductor (device) modeling. In this thesis, only numerical drift-diffusion simulations are performed, which are categorized between microscopic and macroscopic models.

223]. Within this technique, charge carrier interaction and transport are described by rate equations. The way of a charge carrier through a three dimensional solid is calculated via the evaluation of the probabilities for particular hops, considering the disorder within the stochastic calculations. The final result is obtained as an average of a sufficiently large number of simulation runs. The main advantage of this method is the description of charge carrier transport and mobilities within a semiconductor, correlating these properties to disorder parameters and the electric field. However, when extending this method to a large solid, which means many hopping sites, or to several charge carriers, it requires much computational time. Thus, it has not often been used to simulate a whole set of *I-V* curves. Another reason is that the *I-V* curve and especially V_{oc} are, as discussed previously, a function of charge carrier densities and diffusion gradients within the device, which can hardly be modeled by single-carrier hops.

Although being microscopic, Monte Carlo simulation requires several input parameters, which cannot be derived directly from chemical or physical structure data obtained by measurements or from the knowledge of single-molecule properties. Therefore, models which are even more microscopic are necessary. First approaches exist, which include a complete simulation chain to describe organic solar cells (almost) ab initio (Fig. 4.2) [219]. This chain involves multiscale models, considering different time and length scales. The energy levels and wave functions of the molecules can be calculated by quantum chemistry electronic structure methods like the Hartree Fock approximation or (time dependent) density functional theory. These methods deliver an approximated numerical solution of the electronic Schrödinger equation of a molecule. A further step are atomistic molecular dynamics simulations, calculating atomic and molecular movements due to interatomic(-molecular) interactions. They deliver as result an arrangement of molecules ("molecular packing") in a film, which can be called morphology. This structure is the starting point for quantum chemical techniques to calculate the parameters of the charge transfer rate
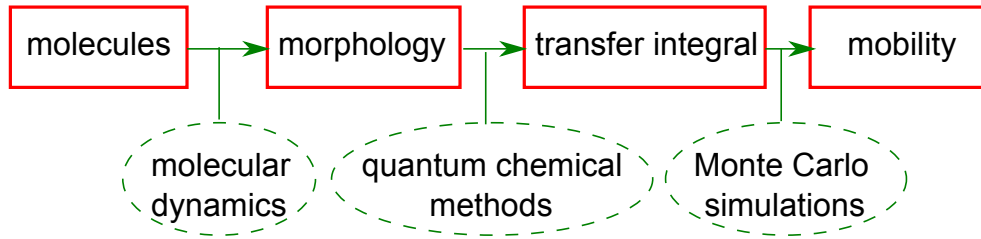
Figure 4.2: Steps and methods for microscopic charge-transport simulations in organic semiconductors covering the whole chain from properties of single molecules to the mobility of a solid.

equation (Eq. 3.3) according to non-adiabatic Marcus theory. These parameters include site energies, reorganization energies, and electronic transfer integrals resulting from molecular orbital overlap. These are used as input for kinetic Monte Carlo simulations of hopping transport, finally resulting in some mobility values of the molecular film or current-voltage characteristics of a device.

Apart from these very time-consuming simulations, drift-diffusion models are commonly applied in semiconductor device simulation and in particular, in the simulation of organic light emitting diodes [224, 225] and solar cells [154, 226–231]. In Fig. 4.1 they are classified into the microscopic and the macroscopic approaches and are a tradeoff between physical depth on the one hand and computational cost on the other hand. They provide *I-V* simulations of multilayer devices consisting of complicated structures. Both effective parameters for the description of not yet well known processes and the implementation of explicitly known processes, can be combined into the framework of drift and diffusion currents. The main condition is the existence of quasi-free particles (electrons and holes) without mutual interactions, carrying charge, and obeying a continuity equation. It is discussed in the following section whether it is legitimate to use such a continuum approach also in organic semiconductors.

4.2 The drift-diffusion model in general

4.2.1 Derivation and conditions

Drift and diffusion currents have already been dealt with when we discussed the transformation of chemical energy into electrical energy in the first chapter (Ch. 2.4) of Part I. We have also applied continuity equations when describing recombination and diffusion of minorities in the p-n junction (Ch. 2.5.1). Within this chapter, a microscopic derivation of these equations and the accompanied conditions shall be briefly discussed to give an idea where the drift-diffusion approach theoretically originates from. For a rigorous derivation the reader is referred to textbooks, e.g., Ref. [44].

Continuity and drift-diffusion equation are contained in the Boltzmann equation, whose
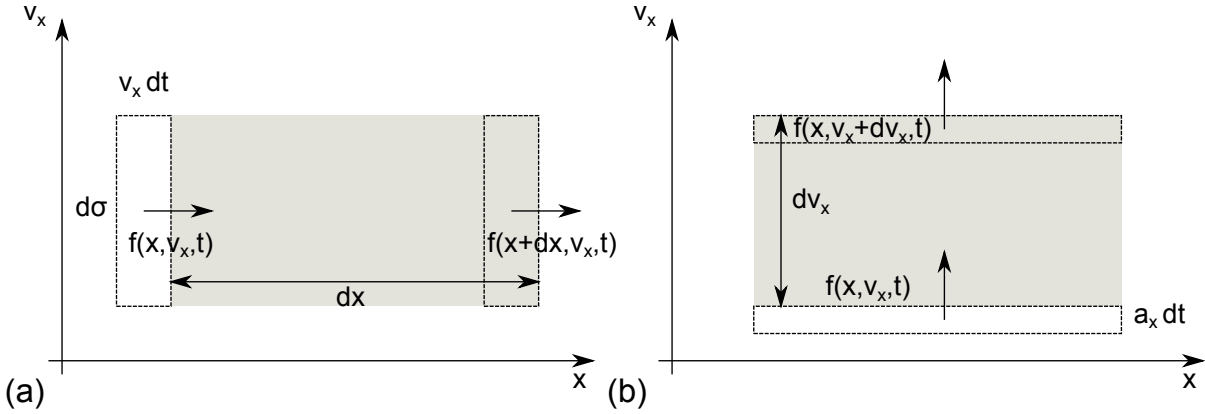
Figure 4.3: An area in $x - v_x$ space, where horizontal lines represent constant velocities v_x and vertical lines constant locations x. f is the distribution function defining the state of particles. The visualizations of (a) a change of location dx and (b) a change of velocity dv are used for the derivation of the Boltzmann equation.

derivation according to Ref. [44] is sketched in the following: The basic idea is a so-called distribution function $f(\boldsymbol{r}, \boldsymbol{v}, t)$, which completely describes the state of a (semi-)classical particle ensemble. The expression $f(\boldsymbol{r}, \boldsymbol{v}, t)d\boldsymbol{r}d\boldsymbol{v}$ denotes the number of particles around position $\boldsymbol{r}$ and with velocity around $\boldsymbol{v}$ at time t. Thus, an integration over $\boldsymbol{r}$ and $\boldsymbol{v}$ gives the total number of particles N. An integration over only $\boldsymbol{v}$ at a certain position $\boldsymbol{r}$ results in the charge carrier density $n(\boldsymbol{r}, t)$ at $\boldsymbol{r}$.

To investigate the variation of f with time, we discuss the one dimensional case: Assume a parallelepiped in $x - v_x$ space as shown in Fig. 4.3(a), where x denotes the position in space and v_x the velocity in x-direction and $d\sigma$ the extension of the parallelepiped in direction of v. The number of particles entering (or leaving) the sketched infinitesimal area from the left is $f(x, v_x)v_x dt d\sigma$. The number of particles leaving (or entering) the depicted area at position dx is $f(x + dx, v_x)v_x dt d\sigma$. Consequently, the change of particles in x-direction is given by the difference between both:

$$(\partial N)_x = (\partial f(x, v_x)d\sigma dx)_x = -\frac{f(x + dx, v_x) - f(x, v_x)}{dx}dx v_x dt d\sigma. \qquad (4.1)$$

Here, we expanded the right expression by dx/dx. It directly follows that the rate of change of f due to particles moving in x-direction is:

$$\left.\frac{\partial f}{\partial t}\right|_x = -\frac{\partial f}{\partial x}v_x. \qquad (4.2)$$

The same can be done for particles crossing the horizontal lines of the parallelepiped in Fig. 4.3(b). This case represents a change in the velocity. Comparable to the fact that velocity changes the position of the particles (Eq. 4.2), an acceleration is the reason for a

change in the velocity of particles:

$$\frac{\partial f}{\partial t}\bigg|_{v_x} = -\frac{\partial f}{\partial v_x}a_x. \tag{4.3}$$

The overall change of the distribution function with time is the sum of both contributions including all three space coordinates:

$$\frac{\partial f}{\partial t} + \boldsymbol{v}\nabla_r f + \boldsymbol{a}\nabla_v f = 0 \tag{4.4}$$

This expression is called Boltzmann equation, which is a very general equation in physics. For charge transport within a crystal, $\boldsymbol{v}$ might be replaced by an expression containing the crystal momentum $\boldsymbol{k}$.

If there are perturbations due to collisions, these additional processes changing v have to be added to Eq. 4.4 by replacing the right hand side by $\partial f/\partial t\big|_{coll}$.

To derive the continuity and drift-diffusion equation from Eq. 4.4, the momentum method is used, where the Boltzmann equation is multiplied by powers α of the velocity (or momentum) with a subsequent integration over the velocity:

$$\int \boldsymbol{v}^\alpha \left(\frac{\partial f}{\partial t} + \boldsymbol{v}\nabla_r f + \boldsymbol{a}\nabla_v f\right)d\boldsymbol{v} = \int \boldsymbol{v}^\alpha \frac{\partial f}{\partial t}\bigg|_{coll} d\boldsymbol{v}. \tag{4.5}$$

Setting α to zero results in the following four expressions (three addends on the left side and one on the right side) to evaluate: The first one as integration over all velocities of the derivative in time of the distribution function results simply in the change of the particle density $n(\boldsymbol{r})$ with time:

$$\int \frac{\partial f(\boldsymbol{r},\boldsymbol{v},t)}{\partial t}d\boldsymbol{v} = \frac{\partial}{\partial t}n(\boldsymbol{r}). \tag{4.6}$$

The second one can be rewritten, knowing that $\boldsymbol{v}$ and $\boldsymbol{r}$ are independent:

$$\int \boldsymbol{v}\nabla_r f(\boldsymbol{r},\boldsymbol{v},t)d\boldsymbol{v} = \int \nabla_r \left(f(\boldsymbol{r},\boldsymbol{v},t)\boldsymbol{v}\right)d\boldsymbol{v} = \nabla_r \int \boldsymbol{v}f(\boldsymbol{r},\boldsymbol{v},t)d\boldsymbol{v} \tag{4.7}$$

With the definition of the mean value of a quantity, here $\boldsymbol{v}$, $\langle\boldsymbol{v}(\boldsymbol{r})\rangle = \frac{\int \boldsymbol{v}fd\boldsymbol{v}}{\int fd\boldsymbol{v}} = \frac{\int \boldsymbol{v}fd\boldsymbol{v}}{n(r)}$, Eq. 4.7 becomes:

$$\nabla_r \int \boldsymbol{v}f(\boldsymbol{r},\boldsymbol{v},t)d\boldsymbol{v} = \nabla_r(n(r)\langle\boldsymbol{v}(\boldsymbol{r})\rangle) = \nabla_r\boldsymbol{j}(\boldsymbol{r}) \tag{4.8}$$

Here, $\boldsymbol{j}(\boldsymbol{r})$ is the particle current density. The third term under an applied field $\boldsymbol{F}$ is proportional to

$$\int_{-\infty}^{\infty} \boldsymbol{F}\nabla_v fd\boldsymbol{v}. \tag{4.9}$$

This integral is zero, because f is evaluated at infinity, where it has to be zero. The collision integral is also zero because it consists of an integration over all scattering-in

and scattering-out events for each velocity. As a scattering-in at a certain velocity means a scattering-out at another velocity, an integration over all velocities gives a zero net-scattering term. Thus, the first two expressions of Eq. 4.5 are remaining and result in the following equation:

$$\frac{\partial}{\partial t}n(\boldsymbol{r}) + \nabla_{\boldsymbol{r}}\boldsymbol{j}(\boldsymbol{r}) = 0, \tag{4.10}$$

which is known as the continuity equation.

An evaluation of the first-order momentum ($\alpha = 1$ in Eq. 4.5) results after a longer derivation [44] in the drift-diffusion equation:

$$n\mu\boldsymbol{F} - D\nabla_{\boldsymbol{r}}n = \boldsymbol{J} \tag{4.11}$$

with the charge carrier mobility $\mu = {}^{e\tau}/m$, where τ is the scattering time (average time between scattering events) and m the mass of the particle.

We briefly summarize the conditions used in the presented derivation to estimate whether these equations are applicable to organic semiconductors:

- Low particle densities and no mutual interactions;

- Collisions which are described by scattering at the lattice with an average time of a scattering event smaller than the time between scattering events;

- A small $d\boldsymbol{r}$ on a macroscopic scale, but large on a microscopic scale, so that it can contain sufficient particles;

- The existence of $f(\boldsymbol{r}, \boldsymbol{v}, t)d\boldsymbol{r}d\boldsymbol{v}$ completely describing the macroscopic situation of the system.

When we consider electrons located on single molecules and hopping from site to site, the jump time is expected to be much smaller than the time the charge is localized on the molecule. Additionally, very thin layers consisting only of some 10s of molecules complicate a definition of $f(\boldsymbol{r}, \boldsymbol{v}, t)$. This makes the applicability of such a continuum approach and the definition of the mobility via lattice scattering questionable.

However, electrons and holes are located on molecules and consist a charge carrier density n and p, averaged over a larger space. The device dimensions are much larger than the hopping distance and the lifetime of charge carriers is in a range that they can perform several hops before recombining. Thus, charge transport occurs via a multistep hopping process of charge carriers. This current can be described by the laws of drift and diffusion despite the localization of charges. Especially in steady-state, it is assumed that these densities averaged over several hopping sites can be described by a DOS and Fermi-Dirac statistics as discussed in Ch. 2.2.1.

As consequence, one has to be aware of the fact that the drift-diffusion approach is a rather macroscopic model for organic semiconductors. This implies that the parameters (μ and D) in Eq. 4.11 have to be handled as effective parameters, which cannot be rigorously connected to physical processes known from conventional semiconductor physics. Either

they have to be found from experiment, or they can be related to novel theories describing the microscopic processes within organic semiconductors (cf. Bässler model [79], Eq. 3.6, p. 56). Despite this peculiarity, it is shown in Part II of this work that drift-diffusion simulations are very powerful means of describing the current-voltage characteristics of organic solar cells.

4.2.2 The Einstein Relation

The diffusion coefficient D can be related to the charge carrier mobility μ. This correlation is called the Einstein relation. It can be derived by an intuitive approach sketched in the following: Considering a semiconductor layer in equilibrium, drift and diffusion forces must cancel each other. Thus, an electric field, if present, leads to a redistribution of charges. Similarly, a diffusion gradient causes an initial diffusion current, which stops after a compensating field has been built up. This was discussed for the p-n junction and the MIM device in the previous chapters. Equilibrium implies the following condition for each space coordinate (here x) according to Eq. 4.11:

$$n\mu F = D\frac{\partial n}{\partial x} \tag{4.12}$$

Using Eq. 2.23 for the electrochemical potential η, one obtains the generalized Einstein relation:

$$\frac{D}{\mu} = \frac{nF}{\frac{\partial n}{\partial x}} = \frac{nF}{\frac{\partial n}{\partial \eta}\frac{\partial \eta}{\partial x}} = \frac{n}{e\frac{\partial n}{\partial \eta}} \tag{4.13}$$

We were able to eliminate the electric field by the explicit x-dependence of the electrical potential $\phi = eFx$, which is included in η (Eq. 2.31). In other words, the motion of an electron by dx causes a change in the electrochemical potential (quasi-Fermi level) which is proportional to $eF\,dx$. Assuming Boltzmann statistics, Eq. 4.13 can be further simplified because $n \propto e^{\eta/k_\mathrm{B}T}$:

$$\frac{D}{\mu} = \frac{k_\mathrm{B}T}{e}. \tag{4.14}$$

This equation is known as the classical Einstein relation, which is commonly used in semiconductor device simulations.

If the Boltzmann approximation is not valid, one has to apply the generalized form, which has to be fulfilled independent of statistics and shape of the DOS. Otherwise, zero current in equilibrium is not guaranteed and self-consistency of the model is lost. Several studies exist on the applicability of the Einstein relation in disordered semiconductors [232–236]. Roichman and Tessler [232] computed D/μ as a function of charge carrier density or the position of the electrochemical potential assuming a quasi-equilibrium situation (chemical potential defined and Fermi-Dirac statistics applicable) for charge carriers within a Gaussian density of states (DOS). They found that the classical Einstein relation is valid for a realistic width of the DOS ($< 100\,\mathrm{meV}$) and charge carrier densities four orders of magnitude lower than the total density of states. This situation corresponds to a chemical

potential with a distance of $0.5\,\text{eV}$ ($T = 300\,\text{K}$) away from the center of the Gaussian DOS. The mentioned conditions are commonly fulfilled in organic solar cells as we will see in Part II. Neumann *et al.* [235] showed that the classical Einstein relation is valid even for the whole experimentally relevant charge carrier density range under the assumption of a mobility edge [237] located at the center of the Gaussian DOS. This means that charge carriers in the DOS below this energy are trapped and do not contribute to charge transport at all. Consequently, the mobility is defined as an average value of the mobility of charges above the mobility edge. Such a definition naturally decreases the effect of a broad DOS. Li *et al.* [236] proposed a more realistic assumption for the mobility edge, declaring charge carriers between the Fermi level and a so-called transport energy as free charge carriers. Their result is that the generalized Einstein relation has to be considered for charge carrier densities as present in field-effect transistors or highly doped layers. In summary, the debate reflects the general discussion about the disputable definition of the charge carrier mobility in disordered organic semiconductors.

In the simulation either the classical or the generalized Einstein relation is applied, dependent on the used statistics (Boltzmann or Fermi-Dirac).

4.2.3 Poisson's equation

We have already seen that space-charge effects are very important when discussing the p-n junction. This holds in particular for low-mobility semiconductors, where apart from localized ionized dopants also the "free" charge carriers can pile up and create a space charge ρ. Such a space charge causes a spatial change (i.e. gradient ∇) in the electric field F according to Maxwell's first equation (Gauss's law):

$$\nabla F = \frac{\rho}{\varepsilon_0 \varepsilon_\mathrm{r}}. \tag{4.15}$$

This field in turn causes a modification of the electrical potential, which can be expressed by Poisson's equation of electrostatics:

$$\Delta \phi = -\frac{\rho}{\varepsilon_0 \varepsilon_\mathrm{r}}. \tag{4.16}$$

4.2.4 Differential equation system

The following system of (coupled) differential equations has to be solved for a one-dimensional drift-diffusion simulation including space-charge effects:

$$\frac{\partial n}{\partial t} = G - R - \frac{1}{-e}\frac{\partial J_n}{\partial x} \tag{4.17}$$

$$\frac{\partial p}{\partial t} = G - R - \frac{1}{e}\frac{\partial J_p}{\partial x} \tag{4.18}$$

$$J_n = en\mu_n F - (-e)D\frac{\partial n}{\partial x} \tag{4.19}$$

$$J_p = en\mu_p F - eD\frac{\partial p}{\partial x} \tag{4.20}$$

$$\frac{\partial^2 \phi}{\partial x^2} = -\frac{e}{\epsilon_0 \epsilon_r}(p - n + N_D^+ - N_A^- + \dots) \tag{4.21}$$

$$\frac{\partial s}{\partial t} = G_{\text{opt}} - \frac{s}{\tau} - R_{\text{Sep,Quench}} + \frac{L_D^2}{\tau}\frac{\partial^2 s}{\partial x^2}. \tag{4.22}$$

Here, x denotes the variable of space, which is perpendicular to the surface of the sample. This one-dimensional treatment is justified as the lateral device dimensions are about 10^5 times larger than the device thickness.

Equations 4.17 and 4.18 are the continuity equations for electrons (n) and holes (p), including generation (G) and recombination terms (R). Both equations can be interconnected, e.g., by a direct recombination term. The current densities J_n (Eq. 4.19) and J_p (Eq. 4.20) are expressed by drift and diffusion currents with the charge carrier mobility μ, electric field F and the diffusion constant D. D is replaced using the Einstein relation (Eq. 4.14) which yields $D = \mu k_B T/e$ in the case of Boltzmann statistics. Equation 4.21 is Poisson's equation (Eq. 4.16), where the space charge is given by the free charge carrier densities and localized ionized dopant densities N_D^+ and N_A^-. Other charges like trapped charge carriers can be added as well.

The last equation (4.22) is the continuity equation for excitons s. This equation is decoupled from the others, as long as exciton-electron interactions are neglected. However, such interactions like exciton quenching at free charge carriers are reported. This leads to a coupling and requires a simultaneous solution of Eq. 4.22 with the overall equation system. We do not further consider such interactions because experimental data is not available and these interactions are supposed to be negligible for illuminations smaller than a few suns.

According to Eq. 4.22, changes in exciton density occur via an optical generation term G_{opt}, via a relaxation of the excited state with lifetime τ, and via some exciton separation or quenching terms R. Furthermore, a gradient in the diffusion current changes s, where the (one dimensional) exciton diffusion length $L_D = \sqrt{D\tau}$ is introduced. The separation (quenching) rate is assumed to be zero at all x apart from exciton splitting (quenching) interfaces like a donor-acceptor (D-A) interface. The generation term is obtained by optical

simulations according to a transfer matrix algorithm, including interference effects[1]. Calculating the gradient in the Poynting vector from the simulated optical field distribution within the solar-cell stack yields directly the absorption profile. This profile is identical to the exciton generation profile under the assumption that each absorbed photon creates one exciton. The transfer matrix algorithm is described elsewhere [238, 239] in detail. The idea of this thin-film model is to treat the layers coherently and describe the properties of interfaces and of the bulk layers by matrices for forward and backward running waves. A multiplication of all matrices gives the overall reflection, transmission, and absorption. The matrices contain the complex refractive indices of the materials. Therefore, this method requires apart from layer thicknesses the optical constants (complex refractive index $n+ik$) of each material/layer as input. The simulation gives reasonable results as long as layer thicknesses are not too small (different $n\&k$ comparable to thick layers), the device stack is not too thick (coherence), and interfaces are smooth (scattering negligible). Although they are not valid for every employed organic material (combination), these assumptions are mostly given for the devices discussed in this thesis [78, 191].

Considering the one-dimensional continuity equation for excitons (Eq. 4.22) makes only sense in the case of a flat heterojunction device, where R_{sep} at the D-A interface enters the charge carrier generation term G in Eqs. 4.17 and 4.18. In case of a homogeneous blend, the exciton diffusion is skipped and G is set to cG_{opt}, where c accounts for a mean exciton loss within the domains. Reported values of IQEs close to unity [115] indicate that c is close to unity as well in weakly phase-separated blends. Considering charge transport, the blend itself is treated as one effective medium.

4.3 Implementation of the algorithm

Equations 4.17-4.22 constitute a system of coupled quasilinear partial differential equations, where Eq. 4.21 is of elliptic type and Eq. 4.17 with 4.19 (4.18 with 4.20) is of parabolic type. They can only be solved numerically as sketched in this section. Non-linearities are introduced by the expressions for recombination and mobility, which are in general non-linear functions of n, p, and F.

During this work a self-made solver is implemented due to several reasons: Apart from technical advantages, allowing customized parameter variations and automations more easily than commonly available free semiconductor simulation tools, the knowledge and control over the physics is rated very important. Until now, validated solvers which have implemented all the peculiarities of organic materials do not exist. Additionally, many processes are still under discussion. Thus, a simple self-made solver is developed, which provides detailed insight during development and delivers traceable outputs.

---

[1]Here, the software OSOLemio is used, programmed by Mauro Furno, IAPP, 2010
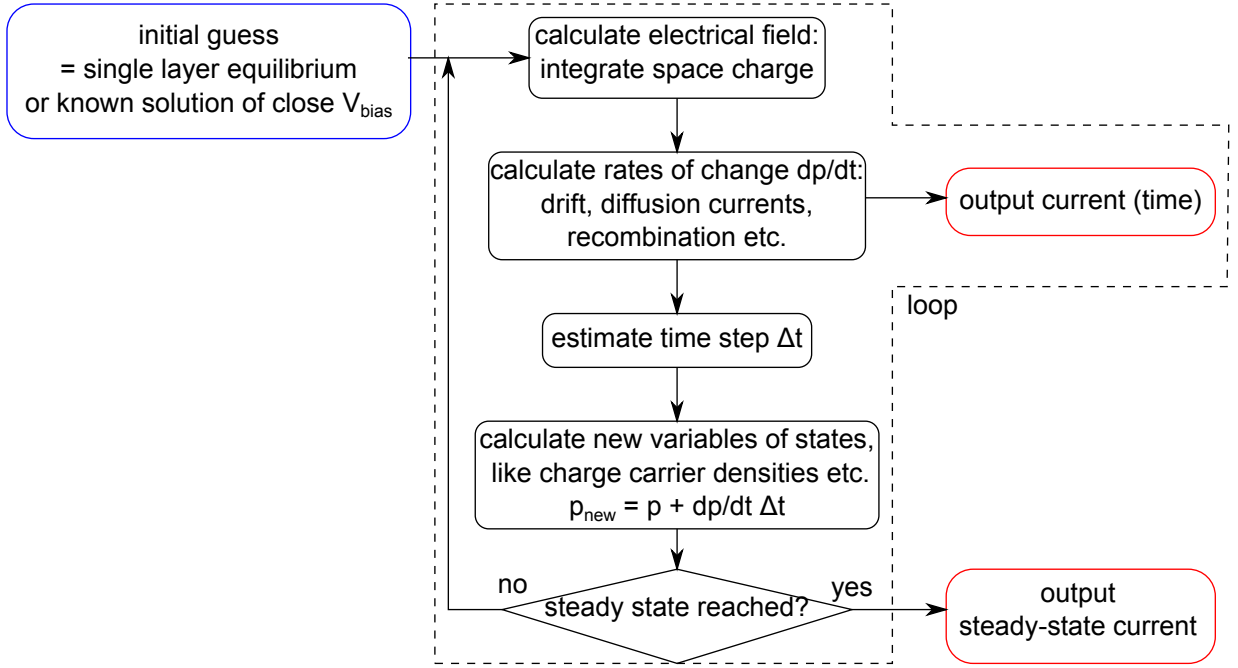
Figure 4.4: Flowchart of the iterative algorithm for solving the drift-diffusion problem. The loop terminates after steady state is reached. An output of the current during the iteration allows for a description of transient currents.

4.3.1 Basics of the algorithm and discretization

Although we are mainly interested in the steady-state solution of the differential equation system represented by Eqs. 4.17-4.22, a transient algorithm is implemented. On the one hand, it additionally provides transient simulations (see Ch. 4.3.5) and on the other hand, it allows for a simple description of processes via time-dependent rate equations. The basic solution procedure is oriented at the work by Staudigel *et al.* [224], who presented a numerical model for organic light emitting diode simulation. Although the model of this work includes several improvements and additional processes, the algorithm of finding the steady-state solution is the same. It is sketched in Fig. 4.4 giving an overview on how to find the solutions for the variables of state n, p, and F. Starting from initial values, these variables are modified within an iterative loop which contains the calculation of the electric field according to Poisson's equation, the calculation of rates of change, the determination of a maximum time step, and subsequently the calculation of the new charge carrier concentrations:

$$F(x_i) \propto \int (-n + p + ...)dx; \quad n(x_i)^{t+\Delta t} = n(x_i)^t + \frac{\partial n}{\partial t}(n, p, F, \dots)\Delta t \qquad (4.23)$$

As these calculations cannot be done analytically, they are performed numerically at discrete values of x. We choose an adjustable, however constant discretization interval
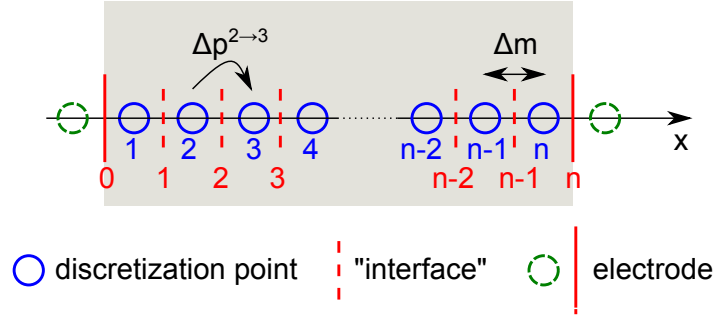
Figure 4.5: Sketch of the discretization scheme with the distance Δm between adjacent grid points.

Δm, which can be set to an arbitrary value before the iterative algorithm starts (Fig. 4.5). It is then fixed over the whole x-range and kept constant during the whole calculation. Although Staudigel *et al.* identified this interval with the spacing of molecules and set it to $1\,\mathrm{nm}$, in this work, a reliable solution is characterized by its independence of the discretization interval. This seems more reliable than using a fixed spacing in combination with a continuum approach. Furthermore, charges localized on a molecule occupy molecular orbitals with extensions even larger than the hopping distance. Figure 4.5 clarifies the numbering of grid points and the "interfaces" in between.

Mathematically spoken, the subsequently elaborated solution procedure is a finite difference method with discretization in space and time. The solution is found by an explicit Euler solver, which is a non-optimized, however very intuitive and stable method. Its single steps within each iteration shall be content of the next sections.

4.3.2 Calculation of the electric field

The electric field is obtained employing Poisson's equation (Eq. 4.16). Discretization results in the following equation for the electric field F_{if}^i between two grid points i and $i+1$:

$$F_{\mathrm{if}}^i = \frac{\Delta m}{2\epsilon_0}\left(\sum_{j=1}^{i}\frac{\rho^i}{\epsilon_{\mathrm{r}}^i} - \sum_{j=i+1}^{N}\frac{\rho^i}{\epsilon_{\mathrm{r}}^i}\right) + \frac{\rho^{\mathrm{anode}}}{\epsilon_0\epsilon_{\mathrm{r}}^i}. \tag{4.24}$$

Here, ϵ_{r} is the dielectric constant and ρ^i the local space charge, consisting of the sum of all charged species at position i:

$$\rho^i = p^i - n^i + N_{\mathrm{D}}^{+i} - N_{\mathrm{A}}^{-i} + p_{\mathrm{t}}^i - n_{\mathrm{t}}^i + \ldots \tag{4.25}$$

The electric field F^i at a grid point i is in the most simple case calculated by a linear interpolation:

$$F^i = \frac{F_{\mathrm{if}}^{i-1} + F_{\mathrm{if}}^i}{2}. \tag{4.26}$$

An integration, which means a summation in discretized space, over the electric field results in the potential difference between anode and cathode. This potential difference is defined by the superposition of the applied bias V and the built-in voltage V_{bi} caused by metals with different work functions. Thus, the following equation has to be fulfilled:

$$\sum_{i=1}^{N} F^i \Delta m = V - V_{\mathrm{bi}}. \tag{4.27}$$

This boundary condition determines the anode surface charge ρ^{anode} in Eq. 4.24. The anode is selected arbitrarily and ρ^{anode} is identical to an inverse cathode charge.

4.3.3 Calculation of rates of change

To update charge carrier densities, their rates of change $\partial/\partial t \approx \Delta/\Delta t$ have to be calculated. The respective procedure is exemplary shown for holes. The transition rate of the hole density $\Delta p^{i \to i+1}/\Delta t$ from position i to position $i+1$ is proportional to the charge carrier density itself and to the velocity divided by the distance the charge carrier travels. In other words, the amount of holes $\Delta p^{i \to i+1}$ traveling from position i to $i+1$ within the time Δt is given by their velocity v multiplied by Δt and divided by the distance between i and $i+1$:

$$\frac{\Delta p^{i \to i+1}}{\Delta t} \approx \frac{\partial p^{i \to i+1}}{\partial t} = \frac{v^i}{\Delta m} p^i \tag{4.28}$$

Inserting the drift velocity for v gives:

$$\frac{\partial p_{\mathrm{drift}}^{i \to i+1}}{\partial t} = \begin{cases} \frac{\mu_p^i F^i}{\Delta m} p^i, & F^i > 0 \\ 0, & F^i \leq 0 \end{cases} \tag{4.29}$$

The case differentiation ensures a drift current of holes only in the direction of the electric field.

Using the diffusion velocity

$$v_{\mathrm{diff}} = \frac{D_p}{\Delta m} = \frac{\mu_p k_{\mathrm{B}} T}{e \Delta m} \tag{4.30}$$

including the classical Einstein relation (Eq. 4.14), yields an equation for the hole transition rate due to diffusion:

$$\frac{\partial p_{\mathrm{diff}}^{i \to i+1}}{\partial t} = \frac{\mu_p k_{\mathrm{B}} T}{e d \Delta m^2} p_i. \tag{4.31}$$

When necessary, the general Einstein relation is used, which means a modification of v_{diff} according to Eq. 4.13. Due to the undirected nature of diffusion, it holds:

$$\frac{\partial p_{\mathrm{diff}}^{i \to i+1}}{\partial t} = \frac{\partial p_{\mathrm{diff}}^{i \to i-1}}{\partial t}. \tag{4.32}$$

The question arises whether a field-dependent mobility, as found, e.g., by Bässler (Eq. 3.6), has any structural influence on the equations mentioned. Intuitively, the rates of change

of charge carrier densities in the direction of the electric field should be increased by the field-dependent term describing a field-assisted hopping. A modification of the drift current (Eq. 4.29) can easily be done replacing μ_p by $\mu_p(F)$, as drift occurs only in the direction of the field. However, the diffusion current described in Eq. 4.31 occurs in both directions, parallel and anti-parallel to the electric field. Due to the Einstein relation, it contains the mobility as well. Staudigel *et al.*[224] decided to use $\mu(F)$ for diffusion in the direction of the electric field and $\mu(F = 0)$ against the field. In this work, it is preferred to use $\mu(F)$ for both diffusion directions. Using the field dependence only in one direction would result in a quasi-Fermi level splitting and hence a net driving force at zero applied bias in a device with a built-in field. This means that the Einstein relation is violated and the resulting current at zero applied bias is an unphysical situation.

The approach presented in Eq. 4.26 is based on a linear interpolation of the electric field between two "interface" grid points to calculate the electric field used in Eq. 4.29. Scharfetter and Gummel [240, 241] proposed a local solution of the drift-diffusion problem under the assumption of a constant electric field between mesh points:

$$\frac{\partial p_{\text{drift+diff}}^{i \to i+1}}{\partial t} = \frac{1}{\Delta m} \frac{F_{\text{if}}^i \mu_p}{1 - \exp(-eF_{\text{if}}^i \Delta m / k_{\text{B}} T)} p_i. \tag{4.33}$$

This expression allows the selection of a larger discretization distance Δm compared to the linear approximation to yield converging results. Note that the values for field and mobility are chosen at the interface instead of taking an averaged value of the field at the discretization point according to Eq. 4.26.

The continuity equation 4.18 states that Δp^i can be additionally changed by trapping, recombination or generation. Thus, the overall change at position i is:

$$\begin{aligned}
\Delta p^i = &-\Delta p_{\text{drift}}^{i \to i+1} - \Delta p_{\text{drift}}^{i \to i-1} - \Delta p_{\text{diff}}^{i \to i+1} - \Delta p_{\text{diff}}^{i \to i-1} \\
&+ \Delta p_{\text{drift}}^{i-1 \to i} + \Delta p_{\text{drift}}^{i+1 \to i} + \Delta p_{\text{diff}}^{i-1 \to i} + \Delta p_{\text{diff}}^{i+1 \to i} \\
&- \Delta p_{\text{rec}}^i + \Delta p_{\text{gen}}^i - \Delta p_{\text{trap}}^i + \Delta p_{\text{detrap}}^i.
\end{aligned} \tag{4.34}$$

Here, the additional rates depend on the used models and are described in the next sections. Electrons follow an analog expression. The overall electrical (particle) current density J can be simply calculated by

$$J^i = J_n^i + J_p^i = e \left(\frac{\partial p^{i \to i+1}}{\partial t^i} - \frac{\partial p^{i+1 \to i}}{\partial t^i} - \frac{\partial n^{i \to i+1}}{\partial t^i} + \frac{\partial n^{i+1 \to i}}{\partial t^i} \right) \Delta m. \tag{4.35}$$

Considering discretization, the continuity equation of excitons (Eq. 4.22) is similarly treated as the one of the charge carriers. The same expression as Eq. 4.31 is found for the diffusion, where the exciton diffusion constant D_s is replaced by the one dimensional exciton diffusion length L_{D} and the exciton lifetime τ:

$$\frac{\partial s_{\text{diff}}^{i \to i+1}}{\partial t} = \frac{v_s}{\Delta m} s^i = \frac{D_s}{\Delta m^2} s^i = \frac{L_{\text{D}}^2}{\tau \Delta m^2} s^i. \tag{4.36}$$

A drain for excitons is the relaxation simply described by a rate which is the inverse of τ. Exciton interactions like annihilation or quenching at impurities or free charge carriers can be added if interaction rates and reaction cross sections are available. The overall change of exciton densities including optical generation $\Delta s^i_{\text{gen}_{\text{opt}}}$ reads:

$$\Delta s^i = -\Delta s^{i\to i+1}_{\text{diff}} - \Delta s^{i\to i-1}_{\text{diff}} + \Delta s^{i-1\to i}_{\text{diff}} + \Delta s^{i+1\to i}_{\text{diff}} - \frac{1}{\tau}s_i + \Delta s^i_{\text{gen}_{\text{opt}}} - \Delta s^i_{\text{quench}}. \quad (4.37)$$

4.3.4 Calculation of the time step

To calculate the new values of the variables of state, the time step Δt has to be known. It is chosen according to the Courant-Friedrichs-Lewy condition (CFL condition) $\frac{v\Delta t}{\Delta x} \leq C$ to guarantee a stable iteration. The term $v/\Delta x$ with velocity v is a rate of change and C a constant which in general depends on the differential equations and is chosen to unity here. An optimization of the time step is important, because too large time steps lead to instabilities and too small time steps increase the number of iteration steps and thus computing time. Hence, Δt is continuously adjusted by a recalculation within each pass of the iterative loop by choosing the inverse of the maximum relative rate of change. This conservative criterion can be written as:

$$\Delta t = \min_{\text{i}} \left(\frac{1}{\sum \frac{\partial p^i_{\text{drift,diff}}}{\partial t}/p^i}, \frac{1}{\frac{\partial p^i_{\text{rec}}}{\partial t}/p^i}, \frac{1}{\frac{\partial p^i_{\text{gen}}}{\partial t}/p^i}, \frac{1}{\frac{\partial p^i_{\text{(de)trap}}}{\partial t}/p^i}, \cdots \right). \quad (4.38)$$

Here, the minimum over all positions i is taken. Equation 4.38 displays only the rates of change for the hole density (p). Naturally, the minimum is taken over all rates of change considering all variables of state, which additionally include electrons, traps, and excitons.

Once having fixed Δt, the new values of the variables of states can be calculated by

$$p^{i,t_{j+1}} = p^{i,t_j} + \frac{\partial p^{i,t_j}}{\partial t}\Delta t^{t_j}, \quad (4.39)$$

where analog equations hold for n and s. The resulting densities $p/n/s^{i,t_{j+1}}$ are the starting values of the subsequent iteration step, beginning again with the calculation of the electric field.

4.3.5 Detection of steady state and transient currents

The iteration loop shall terminate as soon as steady state has been reached. One can detect steady state by several criteria:

1. All relative rates of change of the variables of state are below a certain threshold value C_{max}: $\max_i \left(\frac{\partial n/p/s^i}{\partial t} \frac{1}{n/p/s^i} \right) < C_{\text{max}}$.

2. The charge-carrier current J as sum of hole and electron current is spatially constant: $1 - C < \left| \frac{J_i}{J_{i0}} \right| < 1 + C$, $\forall i$ and with an arbitrary reference current $J_{i_0}, i_0 \in (0, n)$ and a relative threshold C.

3. The displacement current vanishes. This is identical to condition 2.

In this work, mostly criterion 2 is applied for the charge carriers in combination with criterion 1 for the excitons.

Displaying the current over time is possible by using a time variable t and storing time/current pairs during the iteration. An introduction of perturbations in the generation rate (representing, e.g., light pulses) allows for a simulation of a transient photocurrent experiment. Changing V_{bias} sinusoidally and monitoring the current gives a value for the impedance of the device dependent on frequency. Such transient situations imply that steady state is not reached. Consequently, the particle current within the device is not constant and the electric field shows a variation with time. This variation $\partial F / \partial t$ causes a displacement current which has to be added to the electrical particle current to obtain the total current J_{total} measurable from outside:

$$J_{\text{total}} = J_n^i + J_p^i + J_{\text{displ}}^i = J_n^i + J_p^i + \epsilon_0 \epsilon_{\text{r}} \frac{\partial F^i}{\partial t} \approx J_n^i + J_p^i + \epsilon_0 \epsilon_{\text{r}} \frac{F^{t_{j+1}} - F^{t_j}}{\Delta t}. \qquad (4.40)$$

According to Maxwell's fourth equation the overall current at an arbitrary time has to be constant within the device, which is the case in the simulation. The integral formulation of this Maxwell equation is Ampère's circuital law:

$$\oint_c H dS = \iint_S J_{\text{total}} dA \qquad (4.41)$$

with the magnetic field H. It says that the path integral of H over a closed curve is equal to the overall current flowing through an area A enclosed by S. Imagining S being a fixed circle around the device and in plane with the device, the position x, where A crosses the device can be arbitrarily chosen (Fig. 4.6). As current is only flowing through the part of A, where A is crossing the device ($A_1^{\text{active}} = A_2^{\text{active}}$ which are $\gg \Delta x^2$), it holds for the homogeneous current density $J_1 = J_2 = J$.

Delivering current transients is the main advantage of a transient solver, extending its capability for simulating also time-dependent experiments. Another advantage of the chosen implementation is its vicinity to real physical processes. That is why the common scaling [242] of the equations is abandoned. The main drawback of a transient solver is a long computation time if processes of different timescales are involved. The maximum time step according to Eq. 4.38 is limited by the fastest process. However, steady state is reached after the slowest process has converged. This combination requires many iterations. An improvement could be achieved by separately updating selected processes dependent on their timescale [243]. This method allows for a separate treatment of fast processes. Computation time is saved by selectively updating the variables of states at
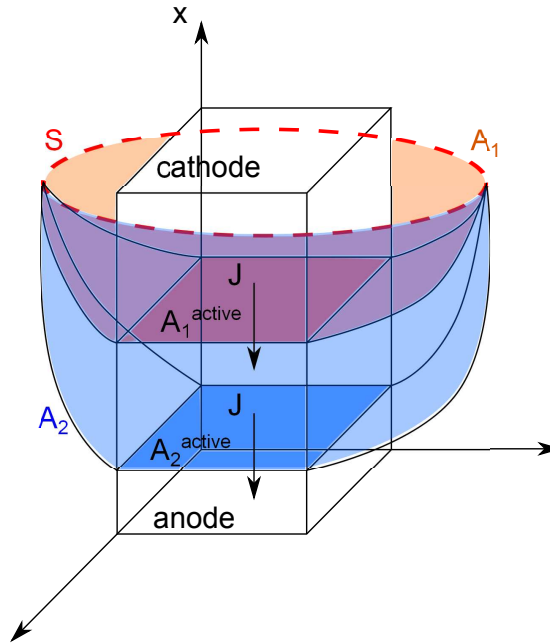
Figure 4.6: Visualization of the application of Ampère's circuital law to a device which is inhomogeneous only in x-direction. A_1 and A_2 are two arbitrary areas with the same active/effective area at different positions x in the device. Both areas have the same border curve S. This means that the current J including the displacement current is independent of x for all times.

positions where fast changes occur. Slower processes are updated less frequently. Bringing all processes together is a sophisticated task because an elaborate synchronization is required. As the focus of this work is on physics, simply Eq. 4.38 is applied. Optionally, the exciton continuity equation is solved separately, before handling the free charge carriers. As long as interactions between charge carriers and excitons are not considered, Eq. 4.22 is independent of n and p and this approach does not result in any restrictions.

4.4 Implemented models

In the previous chapters several charge transport and recombination mechanisms have been mentioned. Here, we present the equations used in the simulation to describe these processes. Many models are alternative or facultative, which means that a choice or selective (de)activation of several submodules are possible and necessary when running the simulation.

4.4.1 Charge carrier mobility

The charge carrier mobility is the fundamental parameter describing the property of charge carriers to move, either by drift due to an electric field or by diffusion according to the (generalized) Einstein relation. The mobility can theoretically be derived for crystalline semiconductors "going back" to the effective mass and scattering time of a quasi-free particle in a periodic crystal (cf. Ch. 2.4). The assumptions are not fulfilled for amorphous organic semiconductors. However, using the mobility as phenomenological parameter is still very convenient, where the simple definition of μ as proportionality factor, relating the electric field to the average charge-carrier velocity (Eq. 2.28) is applied. Experimentally found [188, 244–246] and theoretically motivated (hopping transport, etc. [79, 247, 248]) non-linearities between electric field and current lead to a modification of μ, which itself becomes dependent on the electric field. Most common is the Poole-Frenkel behavior (Ch. 3.2.2, [82]), which is implemented in the simulation with γ as additional parameter:

$$\mu(F) = \mu_0 \exp\left(\gamma\sqrt{|F|}\right). \tag{4.42}$$

Typical values for γ are found in the range of $10^{-2} \ldots 10^{-4} \, (\text{cm/V})^{1/2}$ [188, 246].

The temperature dependence of the mobility of organic semiconductors can be described by the following simple equation assuming a thermal activation of the transport properties:

$$\mu(T) = \mu_\infty \exp\left(-\frac{\Theta}{k_\text{B}T}\right). \tag{4.43}$$

Here, μ_∞ denotes the mobility for $T \to \infty$ and Θ represents the activation energy.

In case of a field and temperature dependence, we apply the following equation which allowed to fit experimental data of single carrier devices reasonably well [249]:

$$\mu(T, F) = \mu_\infty \exp\left(\frac{-\Theta + \gamma\sqrt{|F|}}{k_\text{B}T}\right). \tag{4.44}$$

Alternatively, the temperature dependence is reported to follow

$$\mu(T) = \mu_\infty \exp\left(-\left(\frac{2\sigma}{3k_\text{B}T}\right)^2\right), \tag{4.45}$$

which contains the width σ of the Gaussian DOS as parameter and is consistent with a $1/T^2$ dependence expected from the Bässler model (Eq. 3.6). This equation is used to describe the temperature dependent J-V curves of samples, where ZnPc is evaporated on a gold grid [250].

The simulation is easily capable of dealing with other mobility models. The more variables of states (F, p, n) are involved and the more complex the interrelation is, the more computing time is required.

For example, the Gaussian disorder model with a parameterization as proposed by Pasveer *et al.* [85] is tested as well. It additionally includes a dependence of μ on the charge carrier density, which has been motivated in Ch. 3.2.2 by a filling of the DOS starting with the deep low-mobility states. This unified model for the field, temperature, and charge-carrier density dependence of μ can be described by solely three material parameters, namely the width σ of the DOS, the average hopping distance, and an intrinsic hopping rate. For the complicated analytical equations, the reader is referred to the original paper [85]. It is noted that these equations have been obtained by fitting selected analytical expressions to Monte-Carlo simulations. Thus, they are only valid in a certain parameter space with a certain error. By performing simulations of a single-carrier device at a constant temperature, it is found that a reasonable fit of *J-V* curves is achievable using either a field dependence according to Eq. 4.42 or the charge carrier dependence of the Pasveer model. In the simulations presented in Part II, mainly a constant mobility or Eq. 4.42 are applied, which are found sufficient as long as there is no clear experimental evidence for a more complex behavior of μ.

4.4.2 Recombination

As the dominating recombination mechanism in organic solar cells is currently under debate and seems to depend on the specific organic material and the morphology in the case of a mixed film, several proposed models are implemented:

Direct/bimolecular recombination

The most simple mechanism is direct or bimolecular recombination of a mobile electron with a hole. The recombination probability is expected to be proportional to both charge carrier densities (that is why it is called bimolecular). The recombination constant β is commonly described by Langevin theory (β_{L}), although usually deviations are observed in experiment [251–253].

$$R = \beta(np - n_{\mathrm{i}}^2); \quad \beta_{\mathrm{L}} = \frac{e(\mu_n + \mu_p)}{\epsilon_0 \epsilon_{\mathrm{r}}}. \tag{4.46}$$

Langevin theory [254] describes recombination of electrons with holes in low-mobility materials. Here, β is simply proportional to the sum of the charge carrier mobilities and to the inverse permittivity representing the screening capability of the material. Thus, the factor limiting recombination is the diffusion of charge carriers to each other and not the actual recombination process itself.

The advantage of Langevin theory from the simulations' point of view is the reduction of material parameters, as β is expressed by mobilities and the dielectric constant (Eq. 4.46). This is essential because the charge carrier collection efficiency (cf. Ch. 3.3.1) and hence the shape of the *J-V* curve are dominated by the interplay between charge carrier extraction and recombination. As there is no other straight-forward description of β available, Langevin theory is broadly applied in reported simulations [224, 226], although using such a theory of a transport limited recombination rate in a (one-dimensional) simulation, where

recombination only occurs when charge carriers have already moved to each other, is not very intuitive.

Several efforts are made to motivate experimentally determined modifications of this theory: Koster *et al.*[255] came up with the idea of replacing the sum in Eq. 4.46 by the minimum of μ in bulk heterojunction layers, because recombination is only possible if both, electron and hole, being present in the different material phases, meet each other at an interface. This means the mobility of the slower charge carrier is dominating, because figuratively spoken the faster charge carrier has to wait for the slower one to reach a heterointerface. Others introduced a pre-factor β_0 ($\beta = \beta_0\beta_L$) which is also attributed to the nanomorphology of the blend [251] or simply motivated by a wrong data analysis of the charge extraction measurement data as pointed out in Ref. [256]. Also sophisticated modeling approaches exist which consider the fluctuations of the potential landscape of HOMO and LUMO as reason for a separation of electrons and holes and hence reduced recombination rate [223, 257]. The most simple explanation for the deviations from Langevin theory observed in experiment is that the prevailing recombination process cannot be described by direct (Langevin) recombination between free charge carriers. Reasons are that other recombination mechanisms like, e.g., multiple trapping [122, 223] dominate. In the present simulation, the standard Langevin theory, the modification by Koster, a freely selectable pre-factor, and an arbitrary mobility-independent value of β are implemented and evaluated in Ch. 5.2.

Indirect/trap-assisted recombination

Recently, the importance of traps in organic semiconductor devices became a research topic and it was proposed that trap-assisted recombination as described in Ch. 2.2.2 plays an important role [121, 128, 141, 258]. The following equation is derived from Eq. 2.20, assuming capture rates $C_{n/p}$ for electrons and holes:

$$R = C_n C_p N_t \frac{np - n_i^2}{C_n(n + n_1) + C_p(p + p_1)}.$$ (4.47)

Here, n_1 and p_1 contain the energetic position of the trap state, which is defined here as fraction u of the energy gap E_g:

$$p_1 = N_V \exp\left(\frac{-uE_g}{k_B T}\right); \ n_1 = N_C \exp\left(\frac{-(1-u)E_g}{k_B T}\right); \ u \in (0 \dots 1).$$ (4.48)

Assuming midgap traps and the same capture coefficients for electrons and holes, the four parameters in Eq. 4.47 reduce to one, which is the product of trap density N_T and C. This is sufficient for a qualitative comparison of trap-assisted and direct recombination. If demanded by experimental data, all parameters can be chosen independently to consider, e.g., different charge carrier lifetimes by different capture cross sections.

Geminate recombination and recombination via CT states

Geminate recombination, i.e. the recombination of an electron with a hole resulting from one photoexcitation, is discussed as a potentially important loss mechanism in organic solar cells (cf. Ch. 3.3.1). This process is equivalent to a relaxation of a charge transfer state (CT) at a donor-acceptor heterojunction. As depicted in Fig. 4.7, the relaxation (k_{relax}) is in competition with dissociation k_{diss}, resulting in a free charge carrier generation probability of:

$$p = \frac{k_{\text{diss}}}{k_{\text{diss}} + k_{\text{relax}}}. \tag{4.49}$$

So far, predominantly the Onsager-Braun-Model is used to describe the field dependent and temperature dependent dissociation rate of a CT state. Onsager [94] developed his theory for the recombination of ions under the boundary condition that recombination occurs as soon as the distance between both ions is zero. Braun [95] refined the model under the assumption of a finite lifetime of a CT state, which allows a dissociation before a complete recombination/relaxation. This reversible property of forming a CT state, from which recombining charges can make several attempts to be released, is expressed by the dissociation probability in Eq. 4.49.

Although good agreement with experiment has been demonstrated in some studies [96], the theory is under lively debate and modifications are proposed [101]. Especially for bulk heterojunctions, the description of a field enhanced dissociation is very questionable because the donor-acceptor interface is randomly orientated and not perpendicular to the electric field of the one-dimensional simulation, which points simply from anode to cathode. Nevertheless, the Onsager-Braun model is implemented in the simulation to qualitatively show the influence of a geminate recombination process on the *J-V* characteristics. The equation for the dissociation rate reads:

$$k_{\text{diss}} = \frac{3\beta}{4\pi a^3} e^{-E_{\text{B}}/k_{\text{B}}T} \frac{J_1\left(2\sqrt{-2b}\right)}{\sqrt{-2b}}, \tag{4.50}$$

with the bimolecular recombination constant β, the Bessel function of first order $J_1 = 1 + b + \frac{b^2}{3} + \frac{b^3}{18} + \frac{b^4}{180} + \ldots$, $b = e^3 F/(8\pi\epsilon_0\epsilon_{\text{r}}k_{\text{B}}^2T^2)$, and the Coulomb binding energy $E_{\text{B}} = \frac{e^2}{4\pi\epsilon_0\epsilon_{\text{r}}a}$ (a denotes the initial distance between positive and negative charge). The proportionality of k_{diss} to β directly results from the detailed balance condition $k_{\text{diss}}X_0 = \beta n_{\text{i}}^2$ with the equilibrium densities for CT-states X_0 and free charge carriers n_{i}, which are defined by the relaxation/recombination dynamics of the single species at a certain temperature.

The rate of free charge carrier generation within a bulk heterojunction (G in Eq. 4.17) is modified by Eq. 4.49 and the recombination R by $1-p$, as recombination is assumed to form CT states, which reduce the effective recombination rate due to their certain probability of re-dissociation [226]:

$$G = G_0 p; \quad R = R_0(1 - p). \tag{4.51}$$

Here, G_0 is the generation rate of CT states and R_0 the recombination rate according to Eq. 4.46.
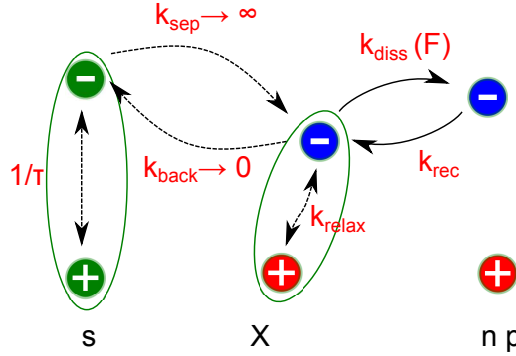
Figure 4.7: Sketch of interaction rates between excitons (s), CT states (X), and free charge carriers (n, p) at a donor-acceptor interface. Geminate recombination is described by k_{relax}. The dissociation of X can depend on the electrical field (F).

Motivated by disorder the initial distance and hence p might follow a distribution $f(a, x)$ around the nominal distance a, giving an overall dissociation probability of

$$P(a, T, F) = \int_0^\infty p(x, T, F) f(a, x) dx, \tag{4.52}$$

where Mihailetchi *et al.*[96] applied the distribution $f(a, x) = \frac{4}{\sqrt{\pi} a^3} x^2 e^{-x^2/a^2}$.

The application of p means an effective treatment of the CT state, changing G and R in the continuity equation for charge carriers (Eq. 4.17) in an effective medium blend according to Eq. 4.51. The CT state is not explicitly included in the simulation. In case of a planar heterojunction, where the donor-acceptor interface is located between two mesh points (see Sec. 4.6), a continuity equation for CT excitons X can be applied, with the rates visualized in Fig. 4.7:

$$\frac{dX}{dt} = R_{\mathrm{sep}} - k_{\mathrm{relax}} X - k_{\mathrm{diss}} X + R. \tag{4.53}$$

This equation contains the separation of excitons $R_{\mathrm{sep}} \propto k_{\mathrm{sep}}$ and the recombination of free charge carriers $R \propto k_{\mathrm{rec}}$ as a source of CT states and relaxation and dissociation as drain terms. No gradient in the current has to be considered as CT states are supposed to be located at the interface and hence immobile in x-direction. Equation 4.53 can be evaluated simply by replacing dX/dt by $\Delta X/\Delta t$. The CT states are assumed to constitute a bipolar space charge located at the discretization point left and right to the donor-acceptor interface. The situation at the interface can be extended by further states like triplets on one material, being generated by energy transfer from the CT state. That would result in an additional drain term in Eq. 4.53.
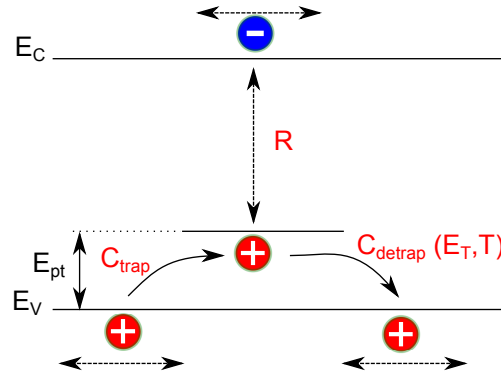
Figure 4.8: Sketch of trapping C_{trap}, detrapping C_{detrap}, and recombination R rates of a hole trap at energy E_{pt}. Detrapping is assumed to depend on the temperature T. A trapped hole can recombine with a free electron.

4.4.3 Traps

Apart from constituting a recombination mechanism, filled traps, which are immobile states within the energy gap of a semiconductor, could yield a considerable amount of space charge. Thus, a description of the occupation of traps is required, where basically two approaches exist.

In the first approach, the occupation statistics are obtained similar to the one within the conduction states by using a Fermi-distribution with the Fermi level calculated from the free charge carrier density: Multiplying this distribution with the density of trap states and integrating the product over energy yields the trapped charge carrier density. This approach is only applicable in an equilibrium situation where one Fermi level is defined. In case of two quasi-Fermi levels for electrons and holes, the occupation of the electron (hole) traps might be described using E_F^n (E_F^p).

In non-equilibrium, the second approach can be selected. Here, the occupation is described by trapping and detrapping rates (visualized in Fig. 4.8) according to the following equations for a single trap state under the assumption of Boltzmann statistics:

$$\left.\frac{\partial p_{\mathrm{t}}}{\partial t}\right|_{\mathrm{trap}} = C_{\mathrm{trap}} p (N_{\mathrm{pt}} - p_{\mathrm{t}}); \ \left.\frac{\partial p_{\mathrm{t}}}{\partial t}\right|_{\mathrm{detrap}} = C_{\mathrm{detrap}} p_{\mathrm{t}} (N_{\mathrm{V}} - p). \tag{4.54}$$

As the two species free holes p and trapped holes p_t are involved, trapping is proportional to the amount of present holes and free trap states (N_{pt} is trap density) with C as proportional constant. The detrapping rate scales with the amount of trapped holes and free valence states. Assuming a thermal detrapping mechanism, expressing C_{trap} by a cross section σ_t and a free hole velocity v_p, and including the trap energy E_{pt}, Eq. 4.54 results in

$$\frac{\partial p_{\mathrm{t}}}{\partial t} = v_p \sigma_{\mathrm{t}} \left(p (N_{\mathrm{pt}} - p_{\mathrm{t}}) - p_{\mathrm{t}} (N_{\mathrm{V}} - p) \exp \left(-\frac{E_{\mathrm{pt}}}{k_{\mathrm{B}} T} \right) \right). \tag{4.55}$$

In comparison to Eq. 4.54, C_{detrap} is related to C_{trap} by the steady-state condition, where trapping and detrapping rate have to be equal (detailed balance). A thermal activation for detrapping yields under the assumption of Boltzmann statistics with $1-\exp\left(\frac{E_V+E_{\text{pt}}-E_F}{k_B T}\right) \approx 1$:

$$C_{\text{detrap}} = C_{\text{trap}} \exp\left(-\frac{E_{\text{pt}}}{k_B T}\right). \tag{4.56}$$

Staudigel *et al.* set v_p to the sum of drift and diffusion velocity $\mu\left(|F| + \frac{k_B T}{e \Delta m}\right)$, although usually the thermal velocity $\sqrt{3 k_B T / m^*}$ [42] is used. Introducing a trapping constant $c_{\text{t}} = v_{\text{t}} \sigma_{\text{t}}$ as distinct parameter might be a pragmatic choice in the case of hopping transport. A variation of this parameter allows already a traceable description of the competition between free charge carrier recombination, transport, and trapping. The described trapping and release rates guarantee an equilibrium trap occupation which is compatible with the first approach.

Within the rate equation approach, we can easily add a further term, describing the recombination probability of a trapped charge with a free charge carrier of opposite sign:

$$\frac{\partial R}{\partial t} = \beta(p_{\text{t}} n - p_{\text{t}0} n_0) = \frac{e \mu_n}{\epsilon_0 \epsilon_{\text{r}}}(p_{\text{t}} n - p_{\text{t}0} n_0). \tag{4.57}$$

This equation with the last expression resulting from the application of Langevin theory with $\mu_{\text{pt}} = 0$ adds as a drain term to the continuity equation for both n and p_{t}. By subtracting the product of equilibrium trap and charge carrier densities, detailed balance is ensured.

In the present simulation, the second approach is implemented as described for a single trap state which can be extended by adding further trap energies or replacing the discrete energy level by a distribution. As the trapped charge carrier concentrations n_{t} and p_{t} are variables of state like n and p and their dynamics are described by the depicted rate equations, they have to be considered in the calculation of the time step as well.

To decrease computation time, the first approach is implemented as well and can in particular be used in steady-state simulations of unipolar devices. Apart from a single-level trap-state, a Gaussian and an exponential distribution are implemented, where the first and latter show an analytical solution for p_{t}:

$$p_{t0} = \int t(E)f(E)dE = \begin{cases} \frac{N_{\text{t}}}{1+\frac{N_V}{p}e^{-E_{\text{t}}/k_B T}}; & \text{discrete level} \\[2mm] N_{\text{t}}\left(\frac{N_V}{p}\right)^{-\frac{k_B T}{E_{\text{t}}}}; & \text{exponential} \\[2mm] N_{\text{t}}\int \frac{1}{\sqrt{2\pi}\sigma}e^{\frac{(E-E_{\text{t}})^2}{2\sigma^2}}\frac{1}{e^{\frac{E-E_F}{k_B T}}+1}dE; & \text{Gaussian} \end{cases} \tag{4.58}$$

4.4.4 Gaussian density of states

The influence of disorder on charge transport is represented in the discussed expressions of the charge carrier mobility (Ch. 4.4.1). The impact of disorder on the energy of charge

carriers is implemented using a Gaussian density of states and Fermi-Dirac statistics to calculate the Fermi level from present charge carrier densities or vice versa. This approach is required when examining the effect of a Gaussian DOS on the open-circuit voltage (see Ch. 5.4). As this calculation cannot be done analytically, it requires a numerical integration at each mesh point and time step, which is very time-consuming. That is why tabulated data are used with an exponential (logarithmic) interpolation to find n from E_F (E_F from n). In this case of non-Boltzmann statistics, the diffusion constant is obtained from the generalized Einstein relation (Eq. 4.13). As convention the parameters HOMO/E_{ht} and LUMO/E_{et} describe the maximum of the DOS with width σ. It will be shown that in many situations the Gaussian shape of the DOS is not necessarily required to describe experimental data. In these cases, Boltzmann statistics and the approximation of an effective density of states at E_{ht} and E_{et}, which are supposed to be located close to the HOMO and LUMO onset, is used.

4.5 Contacts as boundary conditions

A solar-cell device is sandwiched between metal contacts. These contacts represent the starting and the end point of the spatial discretization grid of the simulation and require a special treatment to describe the physical charge injection and extraction mechanism and to guarantee a self-consistent model. In the mathematical nomenclature of differential equation systems, the contacts determine the so-called boundary conditions. Self consistent boundary conditions are very crucial, because the contacts as source of the built-in potential and the diffusion gradient significantly influence the current-voltage characteristics and guarantee that the simulated current through the device in equilibrium (dark and $0\,\mathrm{V}$) is zero. The differential equation system (Eq. 4.17-4.21) demands for six boundary conditions. The first two are included within the potential drop (Eq. 4.27) which is already applied in the calculation of the electric field. As only potential differences are physically defined, the potential at the anode is arbitrarily set to zero in the potential diagrams shown in this work. Thus, the negative potential (in the electron picture) at the cathode is the applied bias voltage V_{bias} minus the built-in potential V_{bi}, calculated by the work function difference of the contacts:

$$V(0) = 0; \ V(d) = V_{bias} - V_{bi}. \tag{4.59}$$

The four additional boundary conditions can be of Dirichlet or Neumann type, the first setting the charge carrier densities at the contacts and the second setting their derivatives in time, which means the currents.

A very basic and phenomenological physical equation for the description of the charge carrier transfer to the electrode was given by Eq. 2.21:

$$J_{sf}^n = e s_n \left(n - n_0 \right). \tag{4.60}$$

This is a condition for a charge carrier extraction/injection current, characterized by a surface recombination velocity s_n and the equilibrium charge carrier density n_0 (here elec-

trons), which guarantees self-consistency. An actual charge carrier density n exceeding n_0 results in charge carrier extraction and a lower n in charge carrier injection. Equation 4.60 implies that the metal-organic interface is not in equilibrium. This means that there is no common E_F between metal and semiconductor and requires the mentioned two parameters s_n and n_0. However, their experimental determination is difficult. For a normal metal contact, s_n is expected to be very large and the assumption of a current which is limited by s_n is only reasonable if there is experimental evidence of some thin insulating interlayer between metal and organics. Setting s_n to infinity leads to $n = n_0$, which characterizes a contact in equilibrium. Such a contact can be described by the commonly applied thermic injection as Dirichlet boundary condition, where n_0 is calculated by a simple Boltzmann factor with the injection barrier ϕ_injec defined as the difference between $E_\mathrm{ht}/E_\mathrm{et}$ and the metal work function Φ_M, which constitutes the Fermi level within the first monolayer of the semiconductor as well:

$$n_0(0/d) = N_\mathrm{C} e^{-\frac{\phi^0_{\mathrm{injec}}(0/d)}{k_\mathrm{B}T}} = N_\mathrm{C} e^{-\frac{E_\mathrm{et}(0/d) - \Phi_\mathrm{M}(0/d)}{k_\mathrm{B}T}}. \tag{4.61}$$

Whereas this expression assumes Boltzmann statistics and is only expected to be valid for $\phi_\mathrm{injec} > 3k_\mathrm{B}T$, the charge carrier density is set according to the more general equation in the case of a Gaussian density of states:

$$\begin{aligned} n_0(0/d) &= \int DOS(E) f(E, E_\mathrm{F} = \Phi_\mathrm{M}) dE \\ &= \int \frac{N_\mathrm{C}}{\sqrt{2\pi}\sigma} e^{\frac{(E - E_\mathrm{et})^2}{2\sigma^2}} \frac{1}{e^{\frac{E - \Phi_\mathrm{M}}{k_\mathrm{B}T}} + 1} dE. \end{aligned} \tag{4.62}$$

Analog expressions hold for holes as well.

Assuming a positive image charge in the metal and a field (F) in the semiconductor, the superposition of the Coulomb potential and the external field (with a sign favoring injection) results in a lowering of the injection barrier similarly to the already discussed Poole-Frenkel effect. The only difference is a pre-factor of $^1/_2$, as the distance between electron (at position x) and image charge in the metal is $2x$ due to the nature of the image charge, located at $-x$, whereas the distance between electron and localized positive core is simply x. Inserting $2x$ in the Coulomb potential of the derivation in Ch.3.2.2, Eq.3.8, p.56 yields:

$$\Delta\phi_\mathrm{injec} = e\sqrt{\frac{eF}{4\pi\epsilon_0\epsilon_\mathrm{r}}}. \tag{4.63}$$

This Richardson-Shockley [42] equation (Eq. 4.61 with $\phi_\mathrm{injec} = \phi^0_\mathrm{injec} - \Delta\phi_\mathrm{injec}$) describes thermionic emission under Boltzmann approximation and implies a barrier lowering which occurs several nm away from the electrode due to a low ϵ_r. This distance makes the applicability of the thermionic injection model in organic devices very questionable due to two reasons: First, in case of low injection barriers, the field close to the contact is not constant over this distance, which is a condition for the derivation of Eq. 4.63. The reason

is a large space charge. Second, the hopping distance is much smaller than the position of the minimized barrier, which means an overestimation of the barrier lowering effect. From the simulation point of view, issues arise as well: Barrier lowering can undermine self-consistency because it increases the charge carrier density of one species without changing the one of the other at a contact at the presence of a built-in field. This means that the equilibrium condition $np = n_i^2$ does not hold any more. In practice this is not crucial when simulating, e.g., realistic MIM devices, because the barrier lowering significantly affects charges in forward direction. Another problem is found in the fact that the boundary condition sets $n(0)$, although physically the injected charge is found at the position of the maximum of the superimposed potentials. This means rigorous self-consistency is lost, because the equilibrium between n and the potential is disturbed. Not taking this into account leads to non-physical expressions in analytical models for V_{oc}, which is, e.g., wrongly supposed to depend on the field dependent lowering term in Ref. [120]. A solution could be to set the majority carrier at the position of the potential maximum, the minority carrier self consistently and assume no space charge in the region between contact and the position of where the charge carriers are set.

Scott and Malliaras [259] proposed a modification of the thermionic model by adding a recombination current, resulting in:

$$J = \frac{16\pi\epsilon_0\epsilon_r(k_BT)^2\mu N_C}{e^2}\exp(-\phi_B/k_BT)\exp(f^{1/2}) - n_ceS(F) \tag{4.64}$$

with a field dependent surface recombination velocity $S(F) = S(0)(1/\psi^2 - f))/4$ ($S(0) = 16\pi\epsilon_0\epsilon_r(kT)^2\mu/e^3$), the reduced electric field $f = eFr_c/k_BT$ (r_c Coulomb radius), and $\psi(f) = f^{-1} + f^{-1/2} - f^{-1}(1 + 2f^{1/2})^{1/2}$. The recombination current velocity is set in a way that it is zero when there is no field applied. This condition, however, is not completely self-consistent in the case of a built-in field, because it creates an effective injection current. However, this effect may be negligible in case of photocurrent modeling.

As the focus of this work is on the simulation of p-i-n solar cells, where highly doped layers are attached to the metal contacts, the discussed injection processes are not directly applicable, because tunneling currents and the build-up of an interface dipole are expected. Although a theoretical description of this situation is difficult, doped layers make the simulation easier, because it is known from experiment that such a contact is not current-limiting. Additionally, energy level bending at the doped semiconductor-metal interface is restricted to several nm ($<5\,$nm) which means that the bulk equilibrium situation of the doped layer with thicknesses larger than $20\,$nm is present in almost the whole layer [260, 261]. Thus, the boundary charge carrier density can be set to the effective doping concentration and V_{bi} can be set as difference between the Fermi levels of the p- and n-doped layer. We will see later that it is even not necessary to know the exact doping concentration, because in the ideal case the J-V curve is independent of the doping concentration as long as this is sufficiently high.

4.6 Organic-organic interfaces

In the previous sections, the mechanisms like charge transport and recombination within bulk layers and the metal contacts as boundary conditions have been discussed. This is sufficient for a simulation of a single-layer device. Organic-organic interfaces, which are found in multilayer organic solar cells like flat heterojunction or p-i-n devices, require a separate treatment. The approach chosen in this work is a solution of Eq. 4.17-4.22 for the whole device and applying modifications of the bulk rates at interfaces. This is comparable to Staudigel *et al.*[224]. Alternatively, multilayers could be treated as multiple boundary value problems, where each layer is dealt with separately and the boundary conditions of two adjacent layers are described by interface conditions and are matched during an iterative algorithm.

4.6.1 Charge transport

There are two factors influencing charge transport at an organic-organic heterointerface: First, different mobilities and second, changes in the DOS, which mean changes in the parameters $N_{C/V}$, σ, and the absolute values of E_{ht} and E_{et}. The latter results in energy barriers ϕ at the interface.

The first one is simple, however requires some modification of the charge carrier transfer rates (which are missing in Staudigel *et al.* [224]), because if Eq. 4.29 and 4.31 are applied for a charge carrier hop from left to right and from right to left, in the first case the mobility of the first layer and in the second case the mobility of the second layer is used. This leads to a built-in selectivity of this interface, which means that this asymmetry is compensated by a higher charge carrier density in the material with the lower mobility. According to Eq. 2.23 this means a jump of the electrochemical potential at the interface in equilibrium, which is physically not allowed. To eliminate the selectivity, the same mobility has to be used for both jumps, where either the mobility of the right or left material can be selected or the average can be used, as long as no data of jump rates (transfer integrals) between the two involved molecules, are known. The influence of taking the average or selecting one or the other mobility is negligible (for $\phi = 0$) as long as the number of discretization points within the layers is much larger than 1. This approach is quite intuitive because it is not the mobility in the material which determines the probability of a jump rate, but the transfer integral between two sites. This leads also to the question whether in case of a field dependent mobility, the field between two grid points shall be taken instead of the field at the position of the grid point, where the charge carrier hop starts. This is more rigorous and fits into the picture of self consistency although discrepancies are expected to be low in the case of a sufficient discretization.

Energy barriers represent a potential offset and result for holes from HOMO(E_{ht}) and for electrons from LUMO(E_{et}) offsets superimposed by the effect of interface dipoles. This means that the charge carrier gains potential energy equal to the barrier if it crosses this barrier. The probability of such an upward jump is described by a Boltzmann factor as
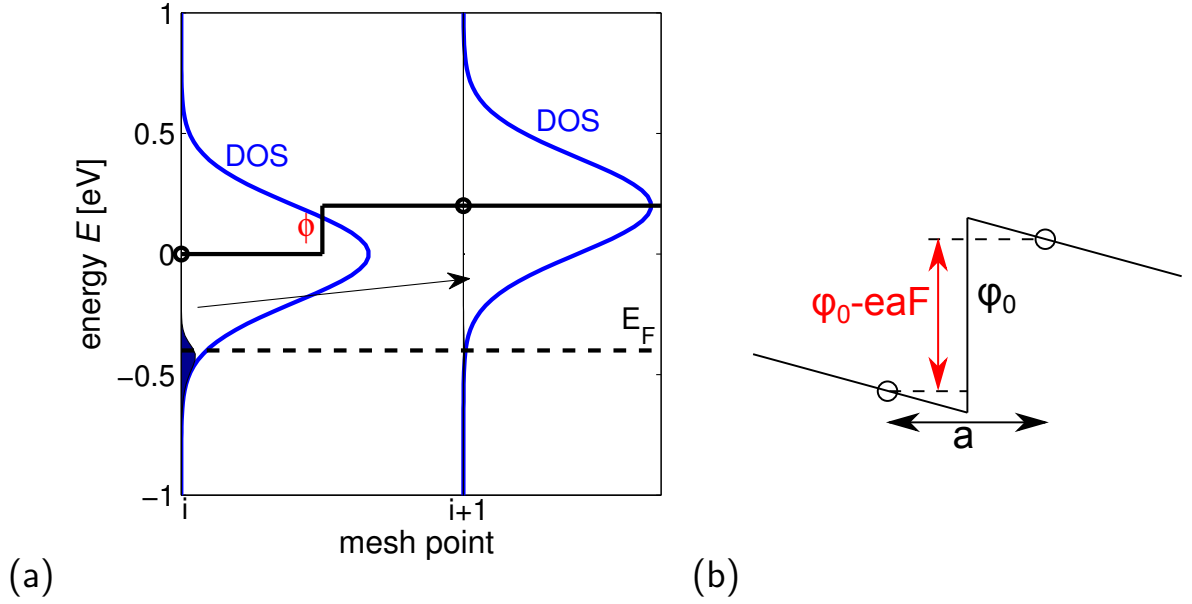
Figure 4.9: (a) Sketch of the energy distribution at an organic-organic interface with barrier ϕ in the case of a Gaussian DOS, which influences the probability of an electron to cross the barrier. (b) An electric field F can lead to a hopping probability which is assisted by tunneling. The reason is a lowering of the effective barrier for a jump covering the distance a.

already discussed in Ch. 3.2.2 (Eq. 3.2) for hopping. Thus, the charge carrier transition rate is modified according to the following equation:

$$\Delta n^{i\to i+1} = \Delta n_0^{i\to i+1} \exp\left(\frac{-\Delta E_{et}}{k_B T}\right). \tag{4.65}$$

Treating barriers in the case of a distribution of states (e.g. a Gaussian DOS), is more complicated (Fig. 4.9a). Staudigel *et al.* [224] calculate a rate of change by an integration over origin and destination density of states, accounting for all possible hopping energy steps. They assume charge carriers equally distributed in the DOS, i.e. a distribution function, which is simply constant in energy with a value n/N_C. This assumption is motivated by the facts that relaxation according to the Bässler model (cf. Eq. 3.5) happens after a large number of hops and that charge carriers are supposed to be injected homogeneously into the DOS at the electrodes. The result is a much higher probability of barrier crossing compared to a Boltzmann factor with the distances between the maxima of E_{et}/E_{ht} of the two adjacent materials. However, this approach is not self-consistent in the case of a drift-diffusion simulation, where the difference between the Fermi levels at the contacts is the applied bias voltage, because an increased barrier crossing probability based on non-equilibrium conditions gives offsets in the electrochemical potential. This can
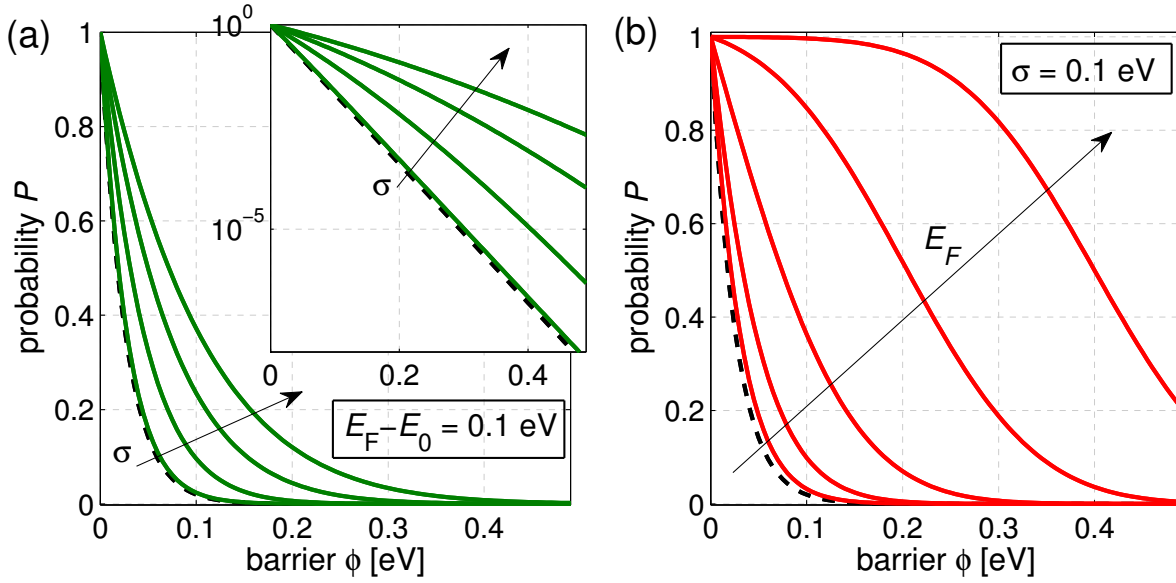
Figure 4.10: Probability P of a jump over a barrier ϕ as a function of the barrier height at (a) varied width of the DOS σ (0.1, 0.15, 0.2, 0.25 eV) and (b) varied relative position of E_{F} to the center of the DOS (-0.4, -0.2, 0, 0.2, 0.4 eV) in the originating layer, which is correlated to the charge carrier density. Dashed lines denote the probabilities in case of a discrete energy step.

possibly be tolerated when describing a device far from equilibrium at several Volt applied bias. However, it is not allowed for solar cell modeling, where every offset in the Fermi levels is directly found in changes of the open-circuit voltage. Here, we assume relaxed states, which can be described by Fermi-Dirac statistics. In case of a Gaussian DOS, the probability of interface crossing is calculated under the condition of a constant Fermi level at the interface. This means that the crossing rate is chosen in a way that the charge carrier density tends to fulfill this equilibrium condition:

$$E_{\mathrm{F}}^{i+1} = E_{\mathrm{F}}^{i} \tag{4.66}$$

which means for an upward-jump from left to right in the case of $\sigma \to 0$:

$$n^{i+1} = n^{i} \exp\left(-\frac{|\Delta E_{\mathrm{et}}|}{k_{\mathrm{B}}T}\right). \tag{4.67}$$

Otherwise, ΔE_{et}, σ^{i}, σ^{i+1}, n, and the Fermi-Dirac distribution define the crossing probability. This probability tends to 1 for a large σ, because ΔE_{et} gets insignificant compared to the distribution of states. Figure 4.10 shows the influence of σ and n (via E_{F}) on the barrier crossing probability depicted over the energy barrier. It can be seen in Fig. 4.10(a) that the probability increases significantly with a higher σ, although not as strongly as

proposed by Staudigel *et al.* (Fig. 3 in [224]). In case of different values of σ between origin and destination, probabilities larger than 1 can occur for a larger σ in the destination layer and a small barrier. Such a situation is treated by a probability smaller than one for the jump in reverse direction. This jump is effectively an upward jump due to the difference in σ overcompensating for the nominal barrier between the maxima of the DOS.

A change of $N_{V/C}$ is treated in the same way, which results simply in the condition

$$\frac{\Delta p^{i \to i+1}}{\Delta p^{i+1 \to i}} = \frac{\Delta p_0^{i \to i+1}}{\Delta p_0^{i+1 \to i}} \frac{N_V^{i+1}}{N_V^i} \tag{4.68}$$

at the interface. In case of non-equilibrium, Eq. 4.66 does not hold and steps in E_F can occur, e.g., due to interface recombination processes.

Additionally, a field dependent barrier lowering effect might be considered, if one assumes the charge carrier covering some distance a when crossing the interface [Fig. 4.9(b)]. This distance can be identified with the hopping distance in Eq. 3.2 and ϕ is modified accordingly:

$$\phi = \phi_0 - eaF. \tag{4.69}$$

Note that the principle of detailed balance might be violated by this equation, if a is larger than the discretization distance and interface crossing of charges is only calculated between the adjacent discretization points.

4.6.2 Generation and recombination

In a blend layer represented by an effective medium, the charge carrier generation (and recombination) rate is a bulk property. In case of a planar/flat heterojunction, generation and recombination occur at a spatially localized interface, which is found between two adjacent mesh points in the simulation. In this case, several rates have to be adjusted at the discretization points left and right to the interface. In the simulation a donor-acceptor type heterojunction is simply identified by analyzing the offsets in E_{ht}/E_{et} and comparing them with the transport gap and the exciton binding energy of the adjacent materials. If the offset in E_{ht} (E_{et}) is larger than the exciton binding energy, excitons from the acceptor (donor) are separated. Of course, the simulation also allows to manually set the interface properties.

Exciton separation means either using the additional relaxation term R_{sep} in Eq. 4.22 with a certain exciton separation rate or, in case of an infinite rate, all excitons diffusing from the adjacent mesh point towards the interface at position i are quenched and form a CT state or directly free charge carriers. The latter one is less sensitive to the choice of the discretization interval. If the quenched excitons form CT states, the charge of these states is assumed to be located at point i and the reverse one at $i + 1$. Their dissociation and relaxation is described like in the bulk via the Onsager-Braun theory. When free charge carriers are generated, they are set to point $i - 1$ and $i + 2$, which means a discrete G in Eq. 4.17 and 4.18. As the creation of charge carriers from neutral excitons at an interface results in the occurrence of positive and negative charge at different location (right and
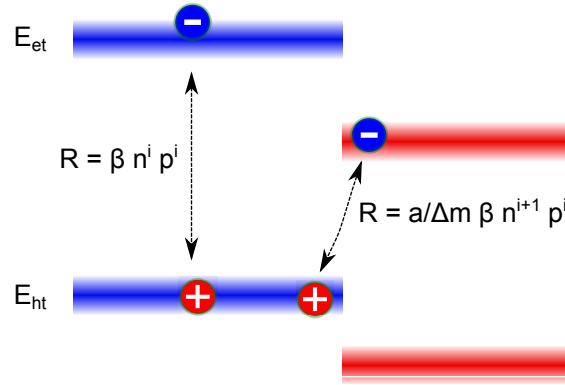
Figure 4.11: Sketch of the difference between bulk ($R = \beta np$) and interface recombination. The latter requires a definition of the average distance a recombining charges travel and causes an electrical current over the interface.

left of the D/A interface), this generation mechanism constitutes an electric current and is added to Eq. 4.35.

Recombination requires a separate treatment as well. On the one hand, it is essential to allow recombination between electrons and holes located on the right and left side of an interface, because it consists a physically important current path in the case of energy barriers. Simply spoken, electrons that face a barrier in their DOS at an interface do not have to cross it to recombine with holes located on the other side of the interface. On the other hand, such a process includes another complication, as recombining charge carriers travel a distance. In conventional semiconductor simulations, commonly surface recombination rates are set, which act in addition to bulk recombination processes.

In Staudigel *et al.* [224], the common bimolecular recombination is chosen with the recombining species located on the two sides of the interface: $R = \beta n^i p^{i+1} + \beta p^i n^{i+1}$. As long as discretization is not changed, this approach works, although there is a significant difference to bulk recombination (illustrated in Fig. 4.11), which is considered to occur only between charge carriers at the same mesh point in the simulation. In the bulk, treating electron-hole recombination only at the same position is not a severe restriction, because drift and diffusion can deliver the charges required for a recombination at the same position. However, it is not sufficient in the case of an interface with an energy barrier. Recombination of charge carriers at the same position (which would by the way be identical to an exciton) does not constitute a current, whereas recombination of charges located on the two different sides of an interface constitutes a current and implies the definition of an average recombination distance to guarantee that this current is independent of the discretization distance. This is explained in the following: Current is according to Eq. 4.35 the product of rate of change, the traveling distance, and the elementary charge:

$$J_{\text{interface}} = eR\Delta m = ec\beta n^i p^{i+1}\Delta m. \tag{4.70}$$

Without adjusting c, the current scales with the discretization distance. Thus, c has to contain $1/\Delta m$. To maintain the unit of R as a rate of charge carrier density changes $(\text{cm}^{-3}\text{s}^{-1})$, c has to contain a value of a length, which is the average recombination distance a. From the energetic point of view, the Coulomb radius might be used to define the average distance recombining charges travel. However, this value is in the range of $10\,\text{nm}$, which is too large for a direct recombination process because it exceeds the average hopping distance. It is most reasonable to take the average hopping distance (e.g. $1\,\text{nm}$) as average recombination distance.

As we are using net-recombination rates (cf. Eq. 4.46) describing recombination only of excess charge carriers, we consider the intrinsic charge carrier densities at the interface as well to guarantee self-consistency:

$$R_{np} = \frac{a}{\Delta m}\beta(n^i p^{i+1} - n_{\text{i}}^{j\,2} e^{-\phi_p/k_{\text{B}}T}); \;\; R_{pn} = \frac{a}{\Delta m}\beta(p^i n^{i+1} - n_{\text{i}}^{j\,2} e^{-\phi_n/k_{\text{B}}T}). \tag{4.71}$$

The exponential terms are valid for Boltzmann statistics and are replaced by the probability of crossing the barrier in the case of a Gaussian DOS.

When CT states are considered, recombination at a D/A interface leads to CT states (cf. Fig. 4.7). Otherwise, recombined charge carriers are assumed to be gone. Analogously, a Shockley-Read-Hall recombination at the interface can be defined and is implemented in the simulation.

4.7 The simulation tool

The discussed models are implemented in a simulation software programmed in C/C++. This software is capable of reading device configurations from ascii input files which allow the setting of the material and interface parameters of each layer and the enabling and disabling of several sub-models. Apart from the iterative algorithm, further algorithms are included to calculate *J-V* curves by voltage sweeps or to do a recursive input parameter variation to show the effect of single parameters or a combination of parameters that is varied. The output of the calculations is written in structured text files, containing *J-V* data and fingerprints. Additionally, transient and steady state data of the variables of state and further parameters are stored in several separate output files. Due to the large number of less defined parameters and models, sophisticated data fitting is not done in this work. Details about the basic input and output of the software can be found in the appendix.

4.8 Verification with analytical solutions

To increase the confidence into the data of a numerical simulation tool, it is advisable to verify it under conditions where analytical solutions are known. This has been done within this work. Here, exemplary two devices are studied: a single layer with ohmic, space-charge

limited, and injection limited current regimes and a simple bilayer device containing a p-n junction. Apart from demonstrating the reliability of the simulation, the results are useful for the visualization and explanation of different cases of *J-V* behavior dependent on the prevailing conditions.

4.8.1 Single-carrier devices

First, a single-carrier device is simulated, where a sufficient charge carrier injection is assumed. The simulation data are compared to simple analytic data of Ohmic conductivity and space-charge-limited current (SCLC) according to the Mott-Gurney Law [262], which predicts a quadratic current-voltage dependence:

$$J = \frac{9}{8}\epsilon_0\epsilon_r\mu\frac{V^2}{d^3}. \tag{4.72}$$

Since this equation contains only the charge carrier mobility, permittivity, and layer thickness d, an SCLC experiment is commonly used to experimentally determine the mobility without knowing the charge carrier density. For high charge carrier densities within the device and low currents, Ohmic conductivity is expected which follows Eq. 2.28.

Figure 4.12 shows simulated *J-V* curves together with graphs of analytic solutions in a log-log plot. The simulation reproduces the analytic results dependent on the voltage range. For high voltages the space-charge region can be seen (slope 2), whereas for low voltages, or more precisely low currents, ohmic behavior is obtained due to a certain amount of charge carriers in the device. The additional curves shown in Fig. 4.12 are obtained assuming a doping density of $2 \times 10^{17}\,\mathrm{cm}^{-3}$ and $10^{18}\,\mathrm{cm}^{-3}$. The charge carriers introduced by doping increase the absolute current for lower voltages and the extension of the linear region of the *J-V* curves. For larger voltages and currents, the charge carrier density is not sufficient and current has to be driven by an injected space charge. An ohmic region is also seen in the simulation of the nominally undoped sample. The reason is a background charge carrier density provided by the electrodes, whose work functions are close to E_{ht}.

Introducing exponentially distributed traps ($E_{\mathrm{t}} = 0.1\,\mathrm{eV}$) in the simulation gives an additional region in the *J-V* curve with a steep slope, as shown by the green dash-dotted line in Fig. 4.12. Theory predicts a value of $E_{\mathrm{t}}/k_{\mathrm{B}}T + 1 \approx 4.9$ for the slope in the ideal case of trap charge limited current [67]. As the simulation describes a superposition of all effects, a lower value of 3.6 is found for the slope around 10 V.

A higher slope compared to the SCLC case can also be caused by an injection limit, which is present in the region from 10 to 200 V of the plot in Fig. 4.13, where a barrier of 0.9 eV is assumed. The inset shows a logarithmic plot of the current as a function of the square root of the applied bias with a linear region. This is expected from the thermionic injection model (Eq. 4.63 in Eq. 4.61) if the field in the device is constant and simply V/d as demonstrated in the following.

Figure 4.14 shows the electric field (F) within the device for four situations at 10 V applied bias. In case of sufficient injection, F is constant for ohmic conductivity [solid
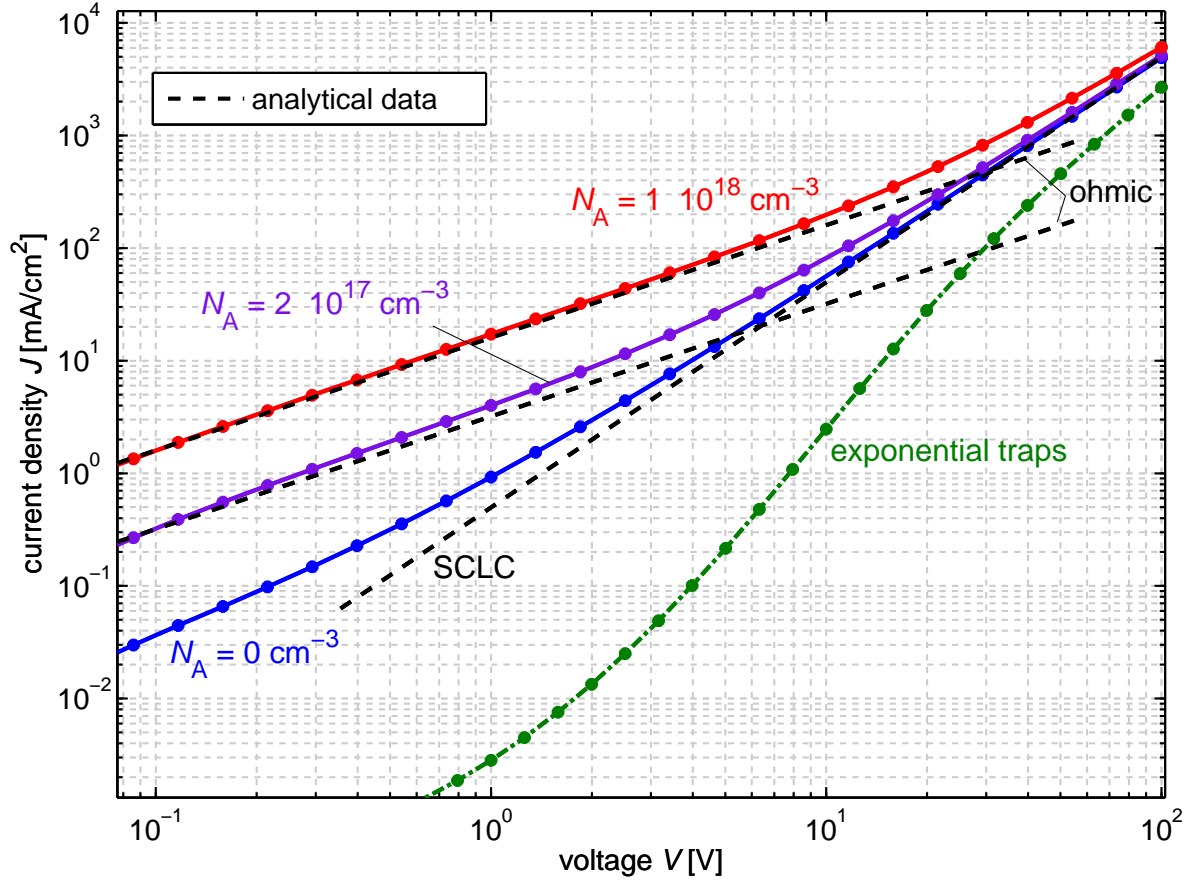
Figure 4.12: Simulated *J-V* curves of a 100 nm thick hole-only device ($\mu_p = 10^{-6}\,\text{cm}^2/\text{Vs}$) with different doping concentrations. Analytic solutions for ohmic (slope 1) and space-charge conductivity (SCLC) (slope 2) are shown as dashed lines. The simulation data visualize the transition from the ohmic to the SCLC regime for higher currents which cannot be provided by the equilibrium charge carriers in the device. Trap-limited currents lead to higher slopes before reaching the SCLC case for higher voltages. Details on the simulation parameters can be found in Appendix B, p. 321.
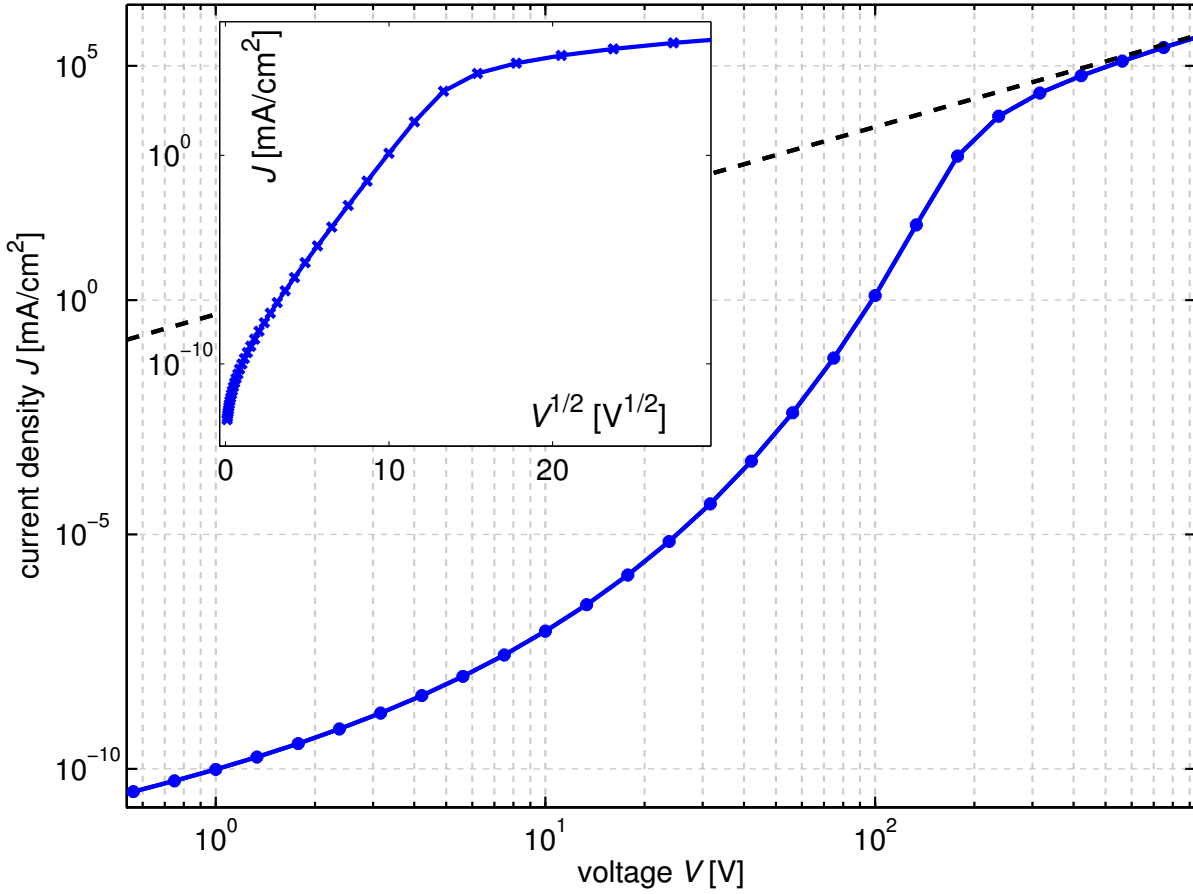
Figure 4.13: Simulated *J*-*V* curve in the case of injection-limited current ($\phi_{\mathrm{injec}} = 0.9\,\mathrm{eV}$). The inset shows a linear behavior of $\exp(J \times \mathrm{mA}^{-1}\mathrm{cm}^2)$ plotted as a function of $\sqrt{V}$ in the injection limited region. This is expected from the thermionic injection model (Eq. 4.63). The *J*-*V* curve reaches the SCLC limit (dashed line) for higher voltages where the injection barrier does not limit the current any more.

line in Fig. 4.14(a)] and grows in a square root dependence for the SCLC case as expected [67, 262] (dashed line). The overshoots close to the contacts are due to the large space charge introduced by the contacts. If the current is injection limited ($\phi_{\mathrm{injec}} = 0.9\,\mathrm{eV}$), *F* is either constant again [dashed line in Fig. 4.14(b)], because the intrinsic device behaves mainly like a capacitor, or most of the potential drops in the space-charge region close to the contact in the case of a doped semiconductor (solid line) forming a Schottky contact (cf. Fig. 3.22).

These data demonstrate the reliability of the simulation, which is in comparison to the analytical solutions also capable of describing transition regions of the *J*-*V* curve. Apart from that, results of simulations of ambipolar MIM devices with a built-in potential have
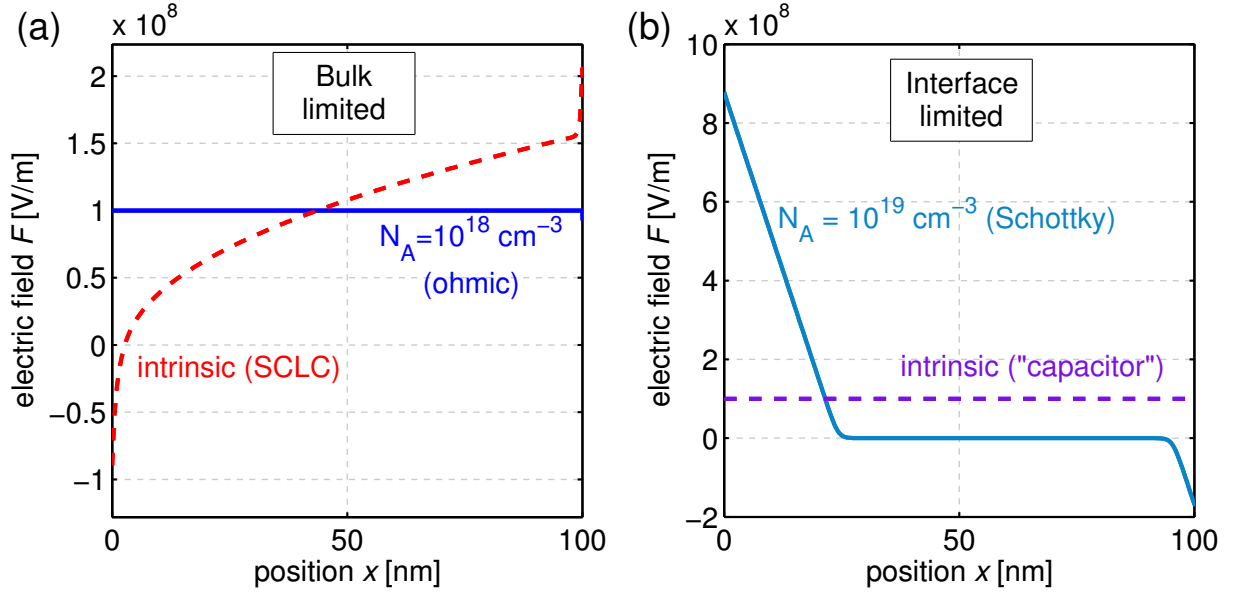
Figure 4.14: Spatial profiles of the electrical field F of a single-carrier device for four different cases at $10\,\mathrm{V}$ ($\mu = 1\,\mathrm{cm^2/Vs}$, $\epsilon_{\mathrm{r}} = 5$): (a) Bulk limit: ohmic with a constant F due to a high doping concentration (solid) and SCLC of an intrinsic semiconductor (dashed). (b) Injection limit ($\phi_{\mathrm{injec}} = 0.9\,\mathrm{eV}$): doped, forming a Schottky contact with space-charge region (solid) and intrinsic semiconductor, behaving like a plane capacitor (dashed).

already been used to visualize the working principle of a bulk heterojunction organic solar cell in Chapter 3.3.4 (see Fig. 3.15), where they qualitatively showed the expected results.

4.8.2 The p-n junction

In Chapter 2.5.1 we discussed the classical p-n junction due to its relevance in conventional solar cells. Here, we apply the analytic equations from that chapter to verify the simulation of a $4\,\mu\mathrm{m}$ thick p-n junction as an example of a simple bilayer device. We use the material parameters of silicon (Si, Appendix B, p. 323) and a doping concentration of $N_{\mathrm{A}} = 10^{16}\,\mathrm{cm^{-3}}$ at the p side and $N_{\mathrm{D}} = 2 \times 10^{16}\,\mathrm{cm^{-3}}$ at the n side. The simulated space-charge density, electric field and band diagram are shown in Fig. 4.15. The results obtained by using Eq. 2.33 and 2.35 are plotted as dashed lines. Simulated and analytic equations coincide in the way expected. The deviations are mainly due to approximations applied for the analytical solution. Especially, the abrupt end of the space-charge region is a quite severe approximation.

The simulated J-V curves under illumination and in the dark are plotted in Fig. 4.16, together with the photocurrent J_{photo} as difference between both. J_{photo} is found to be largely independent of the applied bias as expected from Eq. 2.42. As we know from the
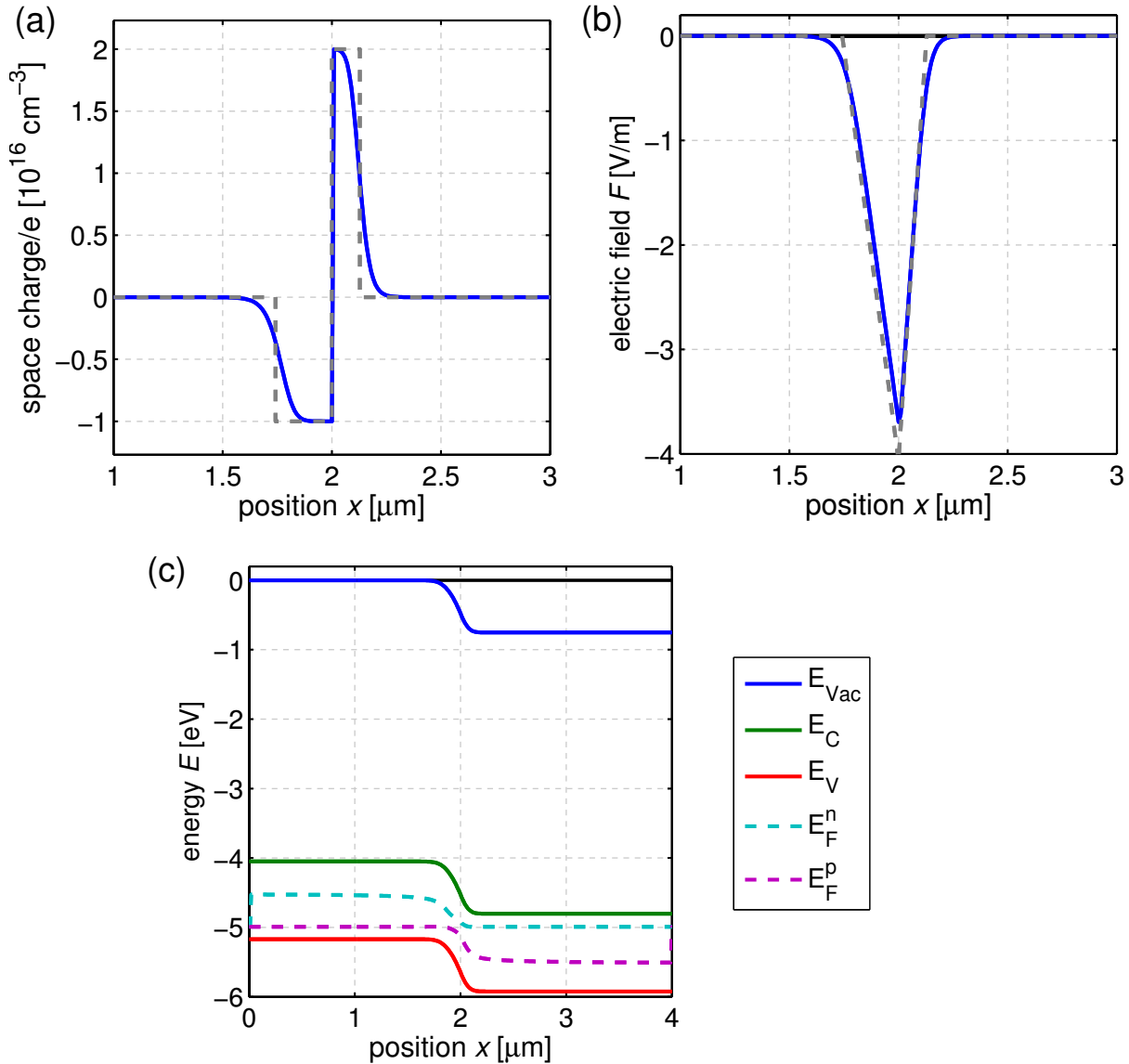
Figure 4.15: Simulated data of an illuminated p-n junction at 0 V: (a) Space charge (analytical solution dashed), (b) electric field F (analytical solution dashed), and (c) band diagram.

discussion of the drawbacks of the p-n junction (Ch. 2.5.1), this demands for a very large minority diffusion length. In the simulation a large diffusion length is given by the high mobility and the fact that Auger or trap assisted recombination are not considered. Additionally, contacts are set selective so that they are not a source of (surface) recombination and minorities are reflected at the respective contact. The semilogarithmic plot shown in the inset visualizes that the ideal slope of $e/k_B T \approx 1/26 \mathrm{mV}$ ($T = 300 \, \mathrm{K}$) according to the
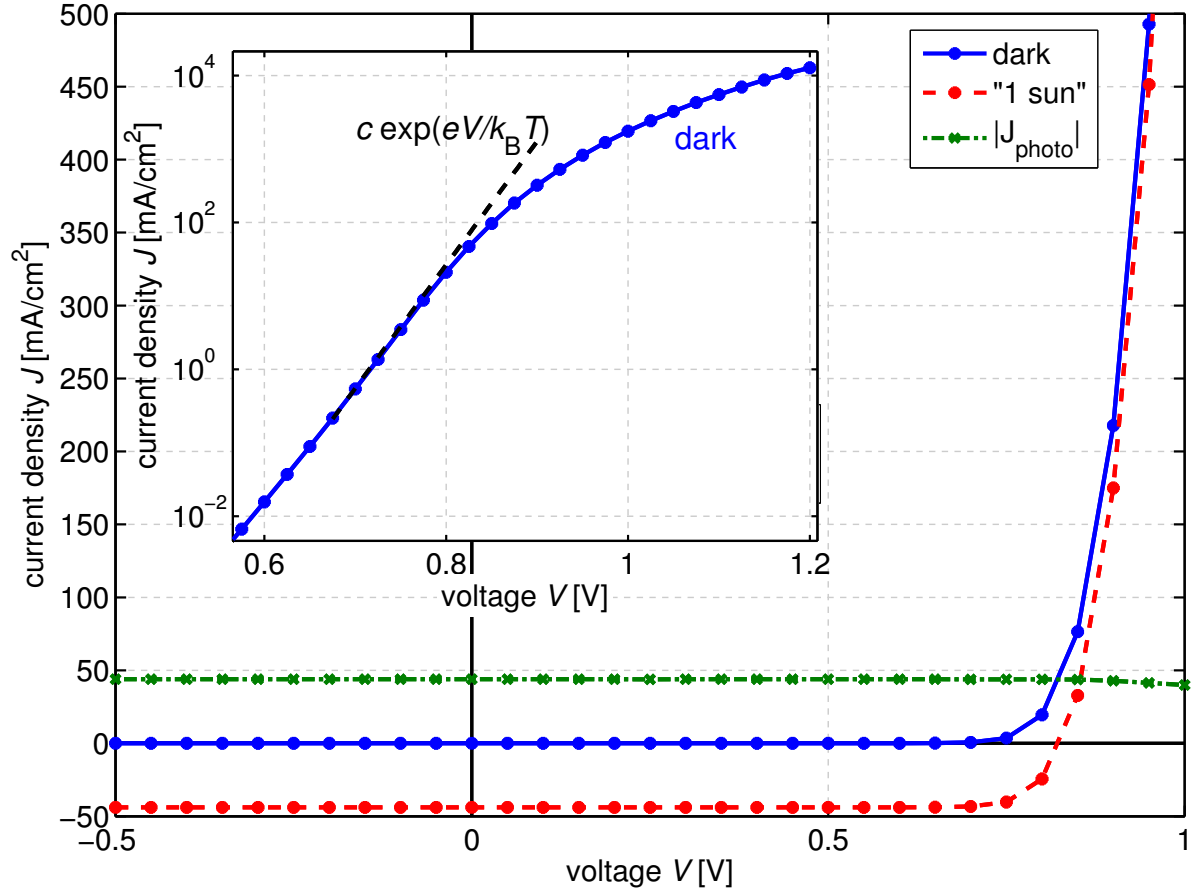
Figure 4.16: Simulated *J-V* curves of a p-n junction in dark and under illumination. The photocurrent J_{photo} as difference between the current under illumination and in the dark is mainly independent of the applied voltage. The inset shows a logarithmic plot of the dark curve, visualizing the slope expected from the Shockley equation before entering the regime limited by the series resistance. All input parameters are found in Appendix B, p. 323.

Shockley equation (Eq. 2.41) is reproduced by the simulation.

To check whether the shape of the *J-V* curve under illumination and especially the calculated value for V_{oc} are reasonable, the fingerprints of the simulated curve are compared to the data of the detailed balance limit (Ch. 2.6, p. 38). However, only a rough comparison shall be done without considering the optics (absorption and re-absorption) in detail. Instead, we simply assume that every photon larger than the band gap is absorbed in the $4\,\mu\mathrm{m}$ thick device and contributes to a homogeneous generation rate. This condition implies an assumed absorption coefficient which is around 100 times larger than the one of Si. As consequence, the radiative recombination constant of Si $\beta_{\mathrm{r}}^{\mathrm{Si}} = 3 \times 10^{-15}\,\mathrm{cm}^3/\mathrm{Vs}$ [3] has to be 100 times larger as well according to the detailed balance limit (Eq. 2.17).

Plugging $100\beta_\mathrm{r}^\mathrm{Si}$ and a generation rate of $6.9 \times 10^{20}\mathrm{cm}^{-3}\mathrm{s}^{-1}$ into the simulation, results in a J_sc of $44\,\mathrm{mA}\,\mathrm{cm}^{-2}$, a V_oc of $0.82\,\mathrm{V}$, and a FF of 0.84, giving an η of 30%. These values are close to the theoretical maximum derived in Ch. 2.6 ($J_\mathrm{sc} = 44\,\mathrm{mA}\,\mathrm{cm}^{-2}$. $V_\mathrm{oc} = 0.87\,\mathrm{V}$, $FF = 0.87$, and $\eta = 33.3\%$). The deviations are supposed to result mainly from the rough approximations for α and β. In conclusion, the data demonstrate that the simulation is well capable of also treating non-equilibrium and generation/recombination situations in accordance with the principle of detailed balance.

4.9 Experimental determination of material properties

Several material properties were discussed during the last chapters. They are required to properly describe charge transport, generation, recombination, charge carrier injection, etc. Some of these input parameters of the simulation can be chosen as fitting parameters. However, most of the parameters should be known. This section gives a very brief summary on experimental techniques to measure several material properties.

Layer thickness d

Layer thicknesses can indirectly be determined during solar-cell processing via quartz crystal monitors (QCM) which detect the amount of evaporated material. Since these devices measure the mass, the material density has to be known to calculate the thickness. Additional inaccuracies result from the fact that the monitor is not located directly at the position of the substrate, which is corrected by tooling, and from a possibly different sticking coefficient between substrate and QCM. Profilometer measurements, where a tip touches the surface of a sample which is laterally moved during a measurement, give information on the topology. For this measurement the organic layer should be covered by metal to achieve acceptable results. The layer thickness is then measured at an edge of the film. However, the results are influenced, e.g., by the pressure applied to the tip during measuring.

More indirect methods can be applied which require a specific model for thickness extraction of a material stack. These are for example ellipsometry, X-ray diffraction, or other spectroscopic methods [263].

Optical constants n **and** k

The optical constants can be determined by measuring reflection and transmission of a series of samples with different layer thicknesses. These data can be used to calculate n and k under the assumption of a model [264]. Ellipsometry data is even suited to reveal information on anisotropic n and k.

Optical gap E_g^{opt}

The optical gap E_g^{opt} can be determined by the onset of absorption deduced from spectrally resolved reflectance and transmittance measurements of an organic film.

Exciton diffusion length L_D

The standard method of investigating exciton diffusion lengths is measuring photoluminescence quenching [77] of layers with different layer thicknesses (or absorption profiles) and a quencher at a defined position in the sample. Alternatively, the quencher can be realized by a heterojunction and the photocurrent can be detected as a function of layer thicknesses [78] or illumination wavelength [238]. In both cases the diffusion equation is applied to extract L_D.

Energy levels E_{ht}, E_{et}, **transport gap** E_g^{DA}, **and dipoles**

Measuring molecular energy levels is very difficult due to two reasons: On the one hand they change with the surrounding of the molecule (polarization) and on the other hand they are a distributions (DOS) rather than discrete values. Cyclic voltammetry gives values for oxidation and reduction potentials of a molecule in solution measured with reference to a known potential (e.g. silver electrode) [265]. We call these values HOMO$_{CV}$ and LUMO$_{CV}$. Since the signal shows broad peaks, it is urgently required to state whether the peak or the (somehow determined) onset of the signal is taken.

In this work, as already mentioned, data from UV photoelectron spectroscopy (UPS)[153, 266] is used. This measurement is performed at a thin film in vacuum and the determined energy levels already include polarization effects. The idea of this method is the utilization of the outer photelectric effect, where electrons are ejected by UV light. Detecting the velocity distribution of the emitted electrons yields the value for the ionization potential (IP), which is HOMO$_{UPS}$. The error of such a measurement is in the range of 0.05 to 0.1 eV [156]. The much more complicated inverse photoemission spectroscopy experiment gives the electron affinity (EA) or LUMO$_{IPES}$ [267, 268]. For these measurements it has to be clarified as well, whether the HOMO/LUMO values refer to the onset or the maximum of the DOS. If not mentioned otherwise, we use the onset because most of the charge carriers are found at the onset of the DOS close to the band edge. We also call these values transport levels E_{ht} and E_{et}. Their difference is the transport gap E_g^{trans}. The exciton binding energy can then be estimated as $E_g^{trans} - E_g^{opt}$. The UPS signal is also capable of revealing information on the relative shape of the DOS.

Another method of monitoring surface potentials is Kelvin Probe Force microscopy (KPFM) [269–272]. During this measurement a metal tip mounted on a cantilever scans over the specimen surface. The work function difference of specimen surface and tip creates an electrostatic potential and charge transfer. This potential is compensated by an applied and monitored voltage. An alternating current signal introducing oscillations of the tip provides a higher sensitivity and allows for a separate monitoring of the topology.

Doping concentrations N_A^-, N_D^+ and Fermi energy E_F

Although the amount of doping molecules co-evaporated with the matrix is roughly known, not all molecules are active. This means that only a fraction of molecules contributes to the doping effect by delivering one free charge carrier.

UPS can determine the position of E_F relative to the HOMO and, thus, give an idea of the doping efficiency. Thickness resolved UPS measurements are capable of monitoring the region of energy level bending starting at an interface [156]. Several subsequent measurements between breaks in the evaporation process are necessary because UPS is only surface sensitive. The result is a width of the space-charge layer which is used to calculate an effective doping concentration. Seebeck measurements are another method for determining the distance between transport and Fermi level [174]. Impedance measurements (see following paragraph) are capable of indirectly giving doping concentrations by measuring the capacity of space-charge (i.e. depletion) layers.

Dielectric constant ϵ

The dielectric constant can be determined by measuring the geometric (plate capacitor) capacitance of a series of MIM devices with different thicknesses by means of impedance spectroscopy [273]. This method applies a small sinusoidal voltage signal and measures the current. A variation of the frequency gives the complex resistance (impedance) as a function of frequency and, additionally, allows for the identification of processes at different time scales.

Traps and charge carrier lifetimes

Trap distributions and response times can be measured by impedance spectroscopy as well. However, equivalent circuit models are mostly applied to fit measurement data. Another method would be thermally stimulated current (TSC) spectroscopy where trap states are filled by optical excitations or electrical injection at low temperatures [274, 275]. When increasing the temperature, trapped charges are thermally released and contribute to a current signal, which is detected. The temperatures at which current peaks occur correspond to the energetic positions of traps within the gap.

Mobility μ

Measuring the conductivity of a film delivers the product of charge carrier density and mobility. In inorganics, Hall measurements are usually applied to separately measure the mobility. This technique is not applicable to organic materials due to their low mobility.

Time of flight (TOF) measurements provide estimations for μ [276]. In this measurement charge carriers are generated close to the surface of a a sample and the transient current response is measured under an applied field. From these data the transit time can be extracted and μ can be calculated by Eq. 2.27 with the knowledge of the layer thickness and the assumption of a constant electrical field. Drawbacks of this method are the required

thicknesses ($> 1\,\mu$m) of samples and the difficulty of defining μ in case of dispersive charge transport.

Another method consists of measuring space-charge limited currents (cf. Ch. 4.8.1). A fit of Eq. 4.72 to the measured J-V curve directly provides μ. A thickness series increases the reliability of this method, which requires ohmic contacts and high current flows. An experimental realization of these conditions is not easy.

Impedance spectroscopy is also capable of delivering values for mobilities [277, 278].

The built-in potential V_{bi}

The built-in potential V_{bi} is a device property. In theory, it is defined as the difference between the work functions of the two contacts, either metal or doped charge transport layers. However, unpredictable interface dipoles change the vacuum level alignment and thus V_{bi}. Consequently, a direct measurement of V_{bi} is desirable. Electro-absorption is an applicable method where the Stark effect is exploited. Here, the change of absorption is measured under an applied small AC-signal under a constant, however adjustable background DC bias voltage [279]. The signal vanishes as soon as the DC bias compensates for V_{bi}.

Another method could be electron holography where the phase shift between electrons passing through a thin specimen cross section and through vacuum gives information about the potential within the specimen [280]. This method, however, requires the knowledge of the inner potential of the investigated material itself. Furthermore, it demands for a complicated preparation of cross sections of samples via the focused ion beam milling of a lamella [281]. The measurement itself is performed in a transmission electron microscope (TEM). The advantage of this method lies in its capability of resolving the potential distribution within a (working) device.

CT-state energy E_{CT} and lifetime $1/k_{\mathrm{relax}}$

A characterization of the CT state is difficult due to its low absorption cross section. Only highly sensitive methods give information about it. Most common is a Fourier transform spectroscopy method [107], showing the EQE caused by absorption of CT states. Time resolved spectroscopy reveals lifetimes.

Properties of blends

Since mixed layers are treated as a new effective material in the simulation, it is most straight-forward to perform the mentioned measurements on blend layers as well and determine the parameters of a specific blend deposited at a specified temperature and mixing ratio. Deriving properties of blends from the single components is difficult. Only some values like energy levels come close to the ones of the single materials, whereas mobilities are totally different and depend on the morphology of the blend.

4.10 Summary and main input parameters

In summary, the implemented device simulation covers the processes discussed in Ch. 3.3.1 in the following way:

- Light absorption and exciton generation are modeled by a transfer matrix algorithm treating the solar cell stack coherently, where the software OSOLemio[2] is employed.

- Exciton diffusion is treated by a diffusion equation according to Fick's law. It is skipped for blend layers, where photogenerated excitons directly lead to free charge carriers.

- The exciton dissociation mechanism at a D/A interface is, as mentioned, highly debated. Without doubt it constitutes a drain for excitons and a source of electron/hole pairs at the heterointerface. When considered, charge transfer (CT) state dissociation is modeled with Onsager-Braun theory.

- Charge carrier transport and extraction/injection at the electrodes are described by a drift-diffusion model, containing all relevant electrical processes like electron and hole transport and recombination. This is the most important part determining the current-voltage characteristics and is, thus, the focus of this work.

Both, the optical and electrical model are one-dimensional. Hence, the main conditions are flat layers with small plane roughness to exclude scattering and allow a definition of a precise layer thickness. The simulation assumes homogeneity within the surface plane and has to be fed by the following main input parameters, where in the case of blend layers effective parameters are taken:

- layer thicknesses,

- optical constants n&k and illumination spectrum for the optical simulation,

- energy levels: E_{ht}, E_{et} (E_{g}), relative positions and offsets and in some cases σ,

- density of charge transport states/sites N_{C} and N_{V},

- doping concentrations of charge transport layers and/or work functions of metal electrodes,

- charge carrier mobilities μ_n, μ_p,

- recombination models and constants: direct/bimolecular recombination coefficient β, CT state parameters (a, k_{relax}), SRH-constant,

- temperature T.

---

[2]programmed by Mauro Furno, IAPP, 2010

Part II

Results and Discussion

Chapter 5

Simulation Study on Single-Layer Bulk-Heterojunction Solar Cells

This chapter contains simulation studies on the influence of crucial parameters like charge carrier mobilities, recombination mechanisms, and a Gaussian-shaped DOS on the modeled solar-cell performance. The approach combines simulation results of parameter variations with simple explanations based on analytical equations. The reported discussions are very basic and a helpful introduction to reading and understanding the graphs of simulation results shown in the following chapters.

In the first section, we investigate the role charge carrier mobility plays for loss mechanisms in organic bulk heterojunction solar cells. It is shown that in case of selective contacts, higher mobilities increase device efficiency, independent of injection barrier heights, energy level bending at the contacts, and the amount of background dark carriers in the device. Non-selective contacts provide a source of photogenerated charge carrier loss at the "wrong" electrode. This is evident from a decrease of the open-circuit voltage (V_{oc}) with an increased role of charge carrier diffusion which originates from a higher mobility or from interface barriers reducing the built-in potential. In this case, V_{oc} furthermore depends on the device thickness. Considering the effect of different recombination models, a too high mobility of one charge carrier decreases V_{oc} significantly for Langevin recombination. That is why balanced mobilities are desirable for high efficiency in this case. In presence of recombination via CT states, V_{oc} is mainly governed by the dynamics of the charge-transfer state. Based on these differentiations it is shown that the existence of an optimum mobility strongly depends on the assumptions made for contact and recombination properties and obtain a comprehensive picture, how charge carrier mobility influences the performance of organic solar cells.

In the second part of the chapter, possible origins of the crossing point between dark and J-V curve under illumination are discussed. It is found that such a point can even exist in the case of selective contacts. In the last part it is shown that disorder which is represented by a Gaussian density of states decreases the open-circuit voltage. Furthermore, disorder

leads to a non-linearity between the open-circuit voltage and temperature.[1]

5.1 Investigated device structure and definitions

To keep the study as simple as possible, we investigate a device which consists of a bulk heterojunction (BHJ) sandwiched between two metal contacts, as depicted in Fig. 5.1. In Ch. 3.3.1 it was discussed that such a BHJ "layer" consists of a blend of two materials, donor and acceptor. Light absorption takes place on one or ideally on both components by creating a molecular excited state. This exciton migrates diffusively and is separated into a free charge carrier pair at a heterojunction. The content of this chapter is dealing with the processes starting at this point. They include electron-hole pair dissociation and the extraction of the electron from acceptor domains and the hole from the donor material.

As stated in Ch. 4.2.4, in a one-dimensional simulation such a BHJ is modeled as a single layer between metal contacts, which define the boundary conditions. This single layer consists of an effective material. The energy levels charges are transported on are defined by the pristine material films, as long as screening effects do not significantly change upon blending. Otherwise, they have to be separately measured for the blend itself. The effect of changes in the energy levels upon blending is content of Chapter 8. The ionization potential (IP), defining the hole transport level E_{ht} of the film, is determined by the donor, and the electron affinity (EA) as electron transport level E_{et} by the acceptor. The energy gap is then an effective gap $E_{\mathrm{g}}^{\mathrm{DA}}$ between these two levels.

During the following discussions the terms "majority" and "minority charge carriers" are used. Commonly, these terms are known from doped layers (cf. Ch. 2.2.1). Here, they refer to the concentrations in an intrinsic BHJ close to the contacts. Therefore, electrons are majorities at the cathode and holes at the anode as long as $\phi_{n,p} < E_{\mathrm{g}}^{\mathrm{DA}}/2$ (cf. Fig. 5.1).

At the contacts a simple temperature-activated injection model (cf. Ch. 4.5) is assumed with the injection barriers ϕ as difference between the charge transport levels and the metal work function (cf. Fig. 5.1). As one aspect of the study is a differentiation between selective and non-selective contacts, we use Eq. 4.60 for the surface current (here for electrons):

$$(n - n_0)\, s_n = \left(n - N_{\mathrm{C}} \exp\left(-\frac{\phi_n}{k_{\mathrm{B}} T} \right) \right) s_n. \tag{5.1}$$

We consider a sufficient extraction of majority charge carriers which is given for a metal/organic contact of working solar cells. This means $s \to \infty$ and thus $n(d) = n_0(d)$ and $p(0) = p_0(0)$. The case of a reduced majority carrier extraction velocity or probability which might result from some insulating layer between metal and active material is not discussed in this chapter. Experimental and simulation results can be found in Ref. [282]. Furthermore, a reduced majority extraction due to barriers is the topic of Chapter 6.

---

[1]The content of section 5.2 of this chapter is published in W. Tress, K. Leo, and M. Riede, *Optimum mobility, contact properties, and the open-circuit voltage of organic solar cells: A drift-diffusion simulation study.* Physical Review B **85**, 155201 (2012)
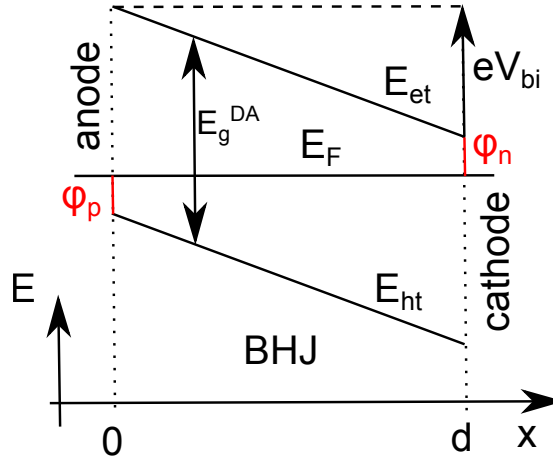
Figure 5.1: A bulk heterojunction (BHJ) as effective medium with thickness d between two metal contacts, determining the built-in potential V_{bi}. Offsets between charge-carrier transport levels and the metal work function (including potentially present dipoles) represent injection barriers ϕ. The effective gap $E_{\mathrm{g}}^{\mathrm{DA}}$ is the difference between the hole transport level of the donor (E_{ht}) and the electron transport level of the acceptor (E_{et}) in the blend.

The selectivity of the contact is defined by the extraction velocity of (minority) charge carriers, reaching the "wrong" contact (electrons the anode and holes the cathode). For non-selective contacts, we set $s \rightarrow \infty$ and thus $p(d) = p_0(d), n(0) = n_0(0)$. Selective contacts mean a perfect blocking of the minorities holes at the cathode ($s_p(d) = 0$) and the minorities electrons at the anode ($s_n(0) = 0$). Usually, metal contacts are non-selective, because both types of charge carriers are extracted. In real devices selective contacts are achieved by introducing passivation or blocking layers between metal and active material.

The built-in potential V_{bi} defined by the difference of the contact work functions can equivalently be expressed by $E_{\mathrm{g}}^{\mathrm{DA}}$ and the injection barriers:

$$V_{\mathrm{bi}} = E_{\mathrm{g}}^{\mathrm{DA}} - \phi_n^{\mathrm{cathode}} - \phi_p^{\mathrm{anode}}. \tag{5.2}$$

The standard input parameters for the simulations are given in Table 5.1. The qualitative conclusions of the following investigations are not sensitive to the fixed parameters. Mainly absolute values will shift, e.g., photocurrents linearly with G and d, and the open-circuit voltage V_{oc} with $E_{\mathrm{g}}^{\mathrm{DA}}$ and $N_{\mathrm{C/V}}$. A change of ± 2 in ϵ has minor effects. Larger values of d require a higher μ to reach the same solar cell performance. However, as all plots show μ in a logarithmic scale, also this influence does not significantly change the presented results.

In the following we will focus on different properties of organic solar cells, like the interplay between generation and recombination, dark current and photocurrent, and between a Gaussian DOS and the temperature.

parameter	name	value
E_g^DA	donor-acceptor transport gap	1.2 eV
$N_\mathrm{C} = N_\mathrm{V}$	effective density of states	$10^{21}\,\mathrm{cm}^{-3}$
ϵ_r	dielectric constant	5
d	device thickness	$50\,\mathrm{nm}$
G	optical generation rate	$1.5 \times 10^{22}\,\mathrm{cm}^{-3}\mathrm{s}^{-1}$
$\phi_n = \phi_p$	injection barriers	$0.1\ /\ 0.3\,\mathrm{eV}$
T	temperature	$300\,\mathrm{K}$

Table 5.1: Standard input parameters for the simulations shown. The values are supposed to fit experimental data of ZnPc:C_{60} bulk heterojunction solar cells.

5.2 On the optimum mobility, contact properties, and the open-circuit voltage

5.2.1 Overview

One major material property with significant influence on device efficiency is the charge carrier mobility μ in an organic bulk heterojunction (BHJ) solar cell. The electron (hole) mobility is a function of the hopping rates between acceptor (donor) molecules and depends strongly on the morphology of the intermixed layer. In the effective medium approach of a one-dimensional simulation, all these effects are included in the effective parameter μ.

Several modeling studies on the impact of μ on device performance have been reported in literature [123, 253, 283–285], mostly claiming the existence of an optimum (finite) value of μ. The specific motivation for such μ-dependent studies in organic materials is the correlation of mobility and recombination in Langevin theory as described in Ch. 4.4.2. In this theory, both, the field-dependent charge carrier extraction probability and the diffusion-limited recombination increase with μ. The studies in literature focus on different points and found different reasons for the fact that too high mobilities might be detrimental for the device performance, seen in a decrease in V_oc. Wang *et al.*[284] and Shieh *et al.*[285] claim recombination with dark charge carriers injected from the contacts to be responsible for a decrease in V_oc, because their density increases with μ. Mandoc *et al.*[283] and Deibel *et al.*[253] state that a high mobility accompanied by too fast charge carrier extraction reduces V_oc.

In the following sections, it is demonstrated that the existence of an optimum mobility is strongly determined by the conditions assumed for the simulations. Therefore, calculations are performed for several recombination models and properties of the contacts. The results are consistently explained starting from the fundamental equilibrium conditions introduced in Chapter 2. It is estimated how realistic the existence of a (not yet experimentally confirmed) optimum mobility is and outlined how to find limiting mechanisms by experiment. Several points are clarified which were not fully elaborated in existing studies.

5.2.2 Investigated mobility and recombination models

In organic materials where hopping transport is dominant, the mobility has to be seen as a relatively macroscopic, effective parameter, relating the effective drift velocity v to the electrical field F via $v = \mu F$. Thus, a constant μ implies a linear relation between v and F. More realistic models include a field, temperature, and charge carrier density dependence (cf. Ch. 4.4.1), which we omit here for reasons of clarity and comprehensibility. According to the mentioned definition, one could conclude that the mobility of the active material is not important for solar cell performance, because it solely determines the velocity of charge carriers at a certain field. This should be reflected in the response time of the device which is irrelevant for solar cells working in steady state. Therefore, the mobility-dominated charge extraction has always to be seen in relation to the competing mechanism of recombination. The equilibrium between both defines the dependence of the photocurrent on voltage which is mainly seen in the fill factor (*FF*) and for very low values of the *FF* in the short-circuit current density (J_{sc}) as well. A higher μ increasing charge-carrier extraction should always be beneficial for the *FF*, and consequently for the efficiency η, as long as μ does not influence recombination rates.

Two possibilities exist in a BHJ, where μ can change recombination properties and thus introduce losses: μ can influence either surface recombination of a charge carrier at the "wrong" electrode (hole at cathode, electron at anode) or recombination at a donor-acceptor interface in the material itself, which we call bulk recombination. The latter can be described by the models presented in Ch. 4.4.2 in detail. For the sake of comprehensibility they are briefly rewritten:

- Direct (bimolecular) recombination, where a free electron recombines with a free hole (Eq. 4.46):

$$R_0 = \beta(np - n_{\mathrm{i}}^2). \tag{5.3}$$

  The recombination constant β can be assumed to be mobility-independent or following Langevin theory according to Eq. 4.46:

$$\beta_L = \frac{e(\mu_n + \mu_p)}{\epsilon_0 \epsilon_{\mathrm{r}}}. \tag{5.4}$$

  Furthermore, a modification of β_L according to Koster *et al.* can be applied, replacing the sum of the mobilties in Eq. 5.4 by the minimum of the two mobilities.

- Recombination via CT states including geminate recombination. Here, on the one hand, a photogenerated bound electron-hole pair recombines before the charges have been separated completely. On the other hand, a free electron-hole pair does not instantaneously vanish after recombination, as electron and hole first form ("recombine" into) a CT state. This state either dissociates again or relaxes with the rates k_{diss} and k_{relax}. According to Eqs. 4.49 and 4.50 this process can be summarized in modified free charge-carrier generation G and recombination R rates by a certain
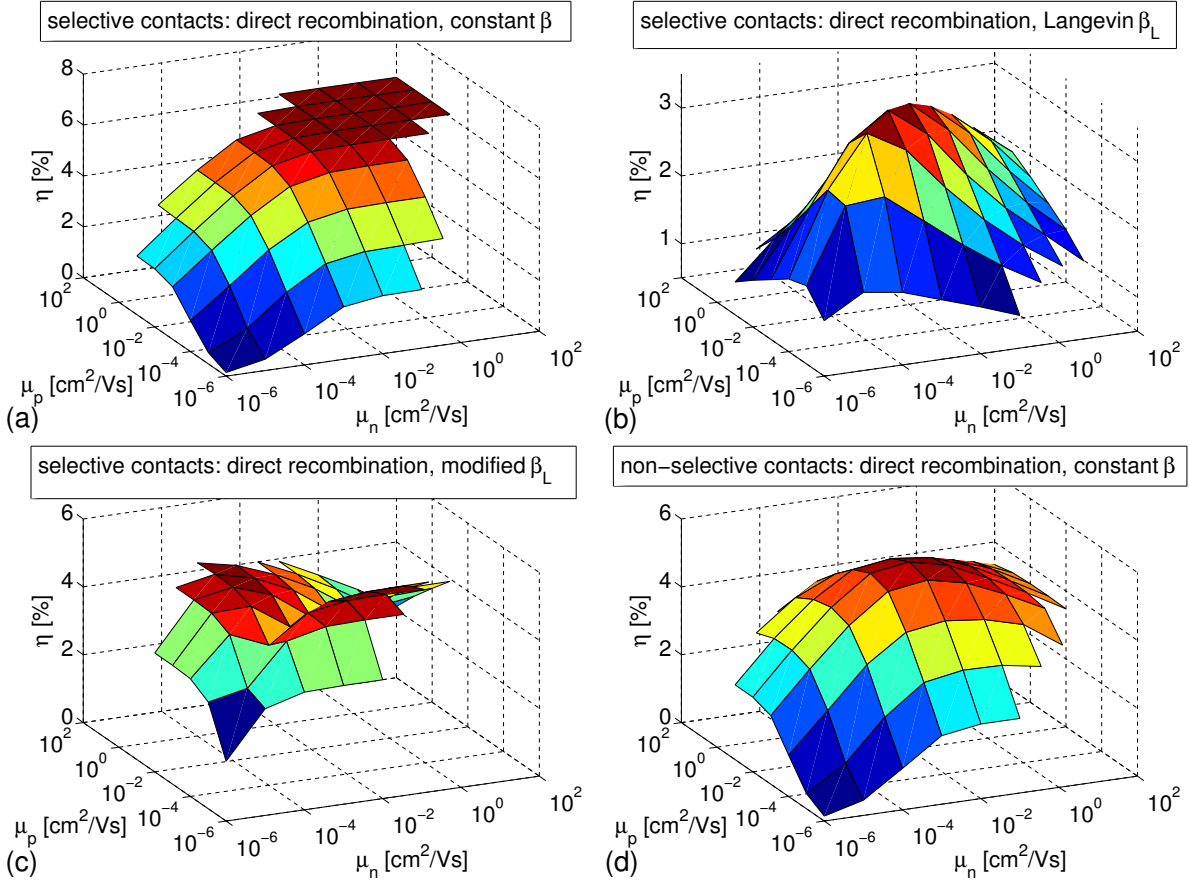
Figure 5.2: Efficiency η as a function of electron and hole mobility μ_n and μ_p for different recombination models and contact properties: (a)-(c) Selective contacts with (a) constant β (qualitatively similar to Langevin recombination via a distinct CT state); (b) direct Langevin recombination (qualitatively similar to Langevin recombination and a distribution of CT states); (c) same as case (b), but with a modified $\beta \propto \min(\mu_n, \mu_p)$. (d) Same as case (a), but for non-selective contacts.

probability P:

$$G = G_0 P; \quad R = R_0(1 - P); \quad P = \frac{k_{\text{diss}}}{k_{\text{diss}} + k_{\text{relax}}} \tag{5.5}$$

with

$$k_{\text{diss}} = \beta e^{-\frac{E_{\text{B}}}{k_{\text{B}}T}} f(E, E_{\text{B}}). \tag{5.6}$$

- Trap-assisted recombination, where a simple SRH expression (Eq. 4.47) is used:

$$R_{\text{SRH}} = c_{\text{t}} N_{\text{t}} \frac{np - n_{\text{i}}^2}{n + p + n_1 + p_1}. \tag{5.7}$$

To investigate the interplay between mobility and recombination, we discuss mobility

variations for several recombination models and contact conditions which can be present in real devices.

5.2.3 Recombination only in the BHJ (selective contacts)

We start with the case of selective contacts, where a loss via surface recombination is excluded. Figure 5.2 shows the efficiency η as a function of electron and hole mobility for the different recombination models. In case of direct recombination with a constant recombination coefficient β [Fig. 5.2(a)], the efficiency increases with mobility of each charge carrier type independently of the mobility of the other one. This is due to an increased charge-carrier collection reaching a saturation at $\mu \approx 10^{-2} \text{cm}^2/\text{Vs}$. The absolute value of η depends on the choice of β (here $7.23 \times 10^{-11} \text{cm}^3 \text{s}^{-1}$). In case of Langevin recombination [Fig. 5.2(b)], balanced mobilities are found to be beneficial, as proposed, e.g., in a recent modeling study[286]. The reason is that the recombination constant is dominated by the faster charge carrier (Eq. 5.4), whereas a sufficient charge carrier extraction always relies on the extraction of both charge carriers. Thus, it is limited by the slower one. The faster charge carrier can compensate for the slower one to some extent by creating a space charge [140] which increases the field close to the electrode where the slower charge carrier is extracted. Therefore, the extraction of the slower charge carrier is enhanced. However, the *FF* is reduced by the imbalance in mobilities compared to the case of balanced high mobilities. Interestingly, an optimum value exists for balanced mobilities ($\mu_n = \mu_p = 10^{-3} \text{cm}^2/\text{Vs}$), above which the efficiency drops. This effect will be discussed subsequently.

Figure 5.2(c) shows η as a function of mobilities under the assumption of a modified β according to Koster *et al.*[255]. It can be seen that an exact balance in μ is detrimental, because the recombination is dominated by the slower charge carrier, whereas extraction can be enhanced by increasing μ of the faster one. However, also in this case, η drops for too high values of μ_n and μ_p.

The effect of μ on V_{oc} for direct recombination

To understand the difference in the observed trends in η we want to investigate the characteristic solar cell parameters entering η. We focus on V_{oc} and the *FF* in the case of $\mu_n = \mu_p$. The short-circuit current density does not give any additional information, because for a constant G_0 it reflects the trend of the *FF*.

Figure 5.3 shows V_{oc} and the *FF* for different recombination models. Comparing the case of a constant β (black crosses) with β_{L} (red diamonds) shows a different trend in V_{oc}. In the case of Langevin recombination V_{oc} decreases with μ. This decay results in a drop in η as soon as the increased charge extraction properties seen in the *FF* cannot over-compensate the V_{oc} loss. This is in contrast to the case of a constant β, where V_{oc} is independent of μ and the monotonous gain with μ in efficiency is due to an increase in *FF* only. This effect was also reported by Wagenpfahl *et al.* when they introduced a mobility [287] where they capped Langevin recombination. The two curves for a constant β and β_{L} according to Langevin theory cross at $\mu_n = \mu_p = 10^{-4} \text{cm}^2/\text{Vs}$ because the constant β was

chosen to be equal to the Langevin recombination at this mobility. Another constant value of β would simply result in a horizontal shift of the black V_{oc} line. To explain the decline in V_{oc} in the Langevin case, we shortly review the origin of V_{oc}.

A photovoltage results from excess free charge carriers being present and spatially separated. Under the assumption of relaxed charge carriers and selective contacts, V_{oc} is defined as the quasi-Fermi level splitting the solar cell can reach under illumination without load (Eq. 3.11):

$$eV_{\mathrm{oc}} = E_{\mathrm{g}}^{\mathrm{DA}} - k_{\mathrm{B}}T \ln \frac{N_{\mathrm{C}}N_{\mathrm{V}}}{np}. \tag{5.8}$$

Although this equation is only valid for Boltzmann approximation with effective densities of states (N_{C} and N_{V}), a comparable equation with possibly modified $E_{\mathrm{g}}^{\mathrm{DA}}$ and $N_{\mathrm{C/V}}$ describes a similar V_{oc} dependence on np for other distributions of the density of states (DOS) and Fermi-Dirac statistics as well. This was elaborated for a Gaussian DOS in Ref.[118]. The central information in Eq. 5.8 is that V_{oc} increases logarithmically with the product of electron and hole density. Therefore, Mandoc *et al.*[283] concluded that a high μ reduced V_{oc} by the reduction of the charge carrier density within the device due to a more efficient extraction. It is correct that a higher μ results in a lower np as long as (drift) current is flowing ($J = en\mu E$), however not at V_{oc}, because there is by definition no current flowing. Hence, no net-charge extraction occurs. The data of a mobility independent β (black crosses in Fig. 5.3) directly contradicts the idea of an enhanced extraction reducing V_{oc}, as V_{oc} does not decrease although charge extraction is strongly increased.

Equation 5.8 shows that the key expression to understand the dependence of V_{oc} on recombination is given by np, which is calculated self-consistently in the numerical simulation. However, the trends in np can be explained in an intuitive way by analytical equations. That is done with the aid of the continuity equation containing the condition that charge carrier densities can only be changed by generation, recombination, and/or a spatial gradient in particle current. The continuity equation reads in steady state (cf. Eqs. 4.17 and 4.18):

$$\frac{\partial p, n}{\partial t} = G_{p,n} - R_{p,n} - \frac{1}{\pm e}\frac{\partial J_{p,n}}{\partial x} = 0 \tag{5.9}$$

Here, G is the free charge carrier generation rate due to exciton dissociation and J the current density. An integration over the total device thickness d gives under the assumption of a constant generation rate:

$$
\begin{aligned}
Gd &= \int_0^d \beta n(x)p(x)dx - (J_p(d) - J_p(0))/e, \\
Gd &= \int_0^d \beta n(x)p(x)dx + (J_n(d) - J_n(0))/e.
\end{aligned}
\tag{5.10}
$$

Here, R is assumed to be of bimolecular type according to Eq. 5.3, where the intrinsic charge carrier density is neglected as it is much smaller than the photogenerated one.

In case of V_{oc}, the overall current density $J = J_n + J_p$ has to be zero at each x, thus $J_p(x) = -J_n(x)$. Regarding Eq. 5.9 this means that if a charge carrier flows in one direction,
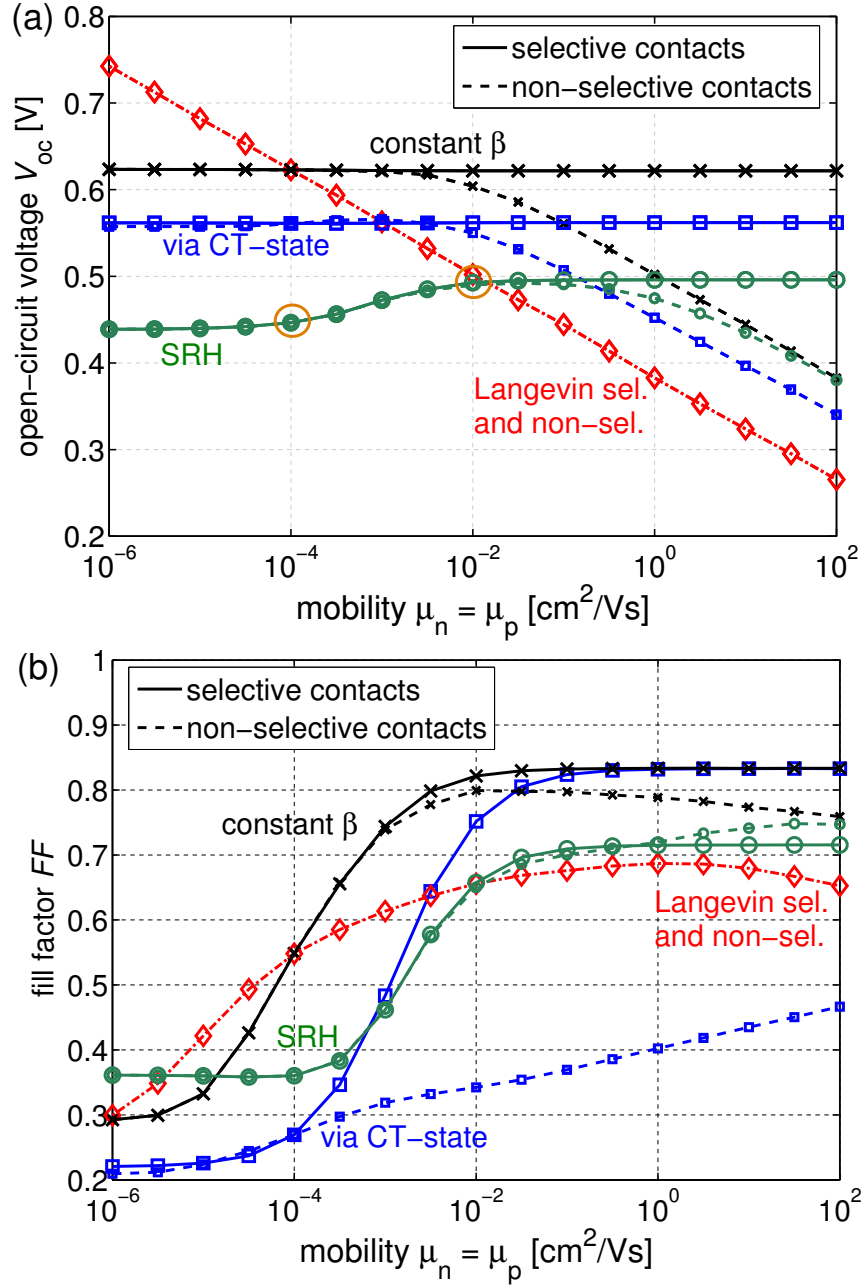
Figure 5.3: (a) V_{oc} and (b) FF as a function of the mobility $\mu_n = \mu_p$ for different recombination models (symbols) and selective (solid lines) and non-selective contacts (dashed lines). In the case of a constant β, it is chosen to $7.23 \times 10^{-11} \text{cm}^3\text{s}^{-1}$, which corresponds to $\beta_L(\mu = 10^{-4} \text{cm}^2/\text{Vs})$. V_{oc} is strongly dependent on μ for direct Langevin recombination without CT states or in the case of non-selective contacts, where diffusion losses to the contacts increase with μ. In the case of Langevin recombination, V_{oc} is limited by bulk recombination for all μ seen at the independence of V_{oc} and FF of the selectivity of the contacts.

also the inversely charged one flows in the same direction and in sum they recombine with each other. In case of selective contacts $J_n(0)(J_p(d))$ is zero, thus $J_p(0)(J_n(d))$ is zero as well. This means that all generated charge carriers recombine within the device at V_{oc}. In this situation, there is no reason for large gradients in the hole or electron current. Thus, $dJ_{p,n}/dx \approx 0$ and $G \approx \beta np$ hold for each x. Consequently, replacing np in Eq. 5.8 yields:

$$eV_{oc} = E_g^{DA} - k_B T \ln \frac{N_C N_V}{G/\beta}. \tag{5.11}$$

According to this equation V_{oc} is influenced by β and decreases with larger values of β. In other words, as G is constant, an increase of β with μ implies a lower np ($G = \beta np$) and thus a lower V_{oc}. This explains that μ, which is not contained in Eq. 5.11 in the case of a constant β, does not influence V_{oc} [black crosses in Fig. 5.3(a)].

However, in the case of Langevin recombination, it holds $\beta = \beta_L(\mu)$. This consideration also explains the logarithmic behavior of V_{oc} with μ [red diamonds in Fig. 5.3(a)], because V_{oc} depends logarithmically on $1/np$, which in turn depends linearly on β and thus on $\mu_n + \mu_p$.

Wang *et al.*.[284] attribute the decrease of V_{oc} with μ to dark carrier recombination as a higher μ increases the spreading of dark charge carriers injected from the contacts. These are supposed to recombine with photogenerated charge carriers. We cannot find any evidence for this effect: The data of Fig. 5.3 clearly visualizes that it is the increase of β that decreases V_{oc}, whereas, an increase of μ in combination with a constant β does not change V_{oc}. Furthermore, recombination profiles (cf. Fig. 5.6) within the device at V_{oc} are homogeneous.

The effect of recombination via CT states on V_{oc}

In the case of recombination via a CT state (blue squares in Fig. 5.3), V_{oc} shows a similar behavior with μ as in the case of a constant β, although Eq. 5.4 is applied for β. The *FF* requires higher mobilities to increase because charge extraction competes with geminate recombination. Choosing $E_B = 350\,\text{meV}$ and $k_{relax} = 10^6 \text{s}^{-1}$ these values result in a V_{oc} of around 0.57 V, which is independent of β and thus of μ also for Langevin recombination.

This independence of V_{oc} on μ was already elaborated by Kirchartz *et al.*[123] within a theoretical detailed balance approach. Here, it is derived as follows. We assume $dJ_{p,n}/dx \approx 0$ in Eq. 5.9 as previously. Applying Eqs. 5.5 and 5.6 gives:

$$G = G_0 P = R = R_0(1 - P)$$
$$\Rightarrow G_0 = R_0 \frac{1 - P}{P} = R_0 \frac{k_{relax}}{k_{diss}} = R_0 \frac{k_{relax}}{\beta e^{-\frac{E_B}{k_B T}} f(F, E_B)}. \tag{5.12}$$

The free charge carrier recombination R_0 is given according to Eq. 5.3. Inserting this

equation into Eq. 5.12 results in

$$G_0 = np \frac{k_{\text{relax}}}{e^{-\frac{E_{\text{B}}}{k_{\text{B}}T}} f(F, E_{\text{B}})}. \tag{5.13}$$

This equation shows that the generation-recombination equilibrium becomes independent of β. It is dominated by the fraction in Eq. 5.13, where close to V_{oc} the field dependence gets small. V_{oc} is then governed by the lifetime $1/k_{\text{relax}}$ and the energy of the CT state. The radiative lifetime of the CT state determines the maximum efficiency and replaces the radiative lifetime of direct recombination as ultimate limit [54].

Replacing np in Eq. 5.8 by Eq. 5.13 yields:

$$\begin{aligned}
eV_{\text{oc}} &= E_{\text{g}}^{\text{DA}} - k_{\text{B}}T \ln \left(\frac{N_{\text{C}} N_{\text{V}}}{G_0} \frac{k_{\text{relax}}}{e^{-\frac{E_{\text{B}}}{k_{\text{B}}T}} f(F, E_{\text{B}})} \right) \\
&= E_{\text{g}}^{\text{DA}} - E_{\text{B}} - k_{\text{B}}T \ln \left(\frac{N_{\text{C}} N_{\text{V}} k_{\text{relax}}}{G_0 f(F, E_{\text{B}})} \right).
\end{aligned} \tag{5.14}$$

Comparing this equation with Eq. 5.11 reveals a significant difference in the temperature dependence of V_{oc}. Equation 5.11 predicts a maximum value for V_{oc} at $T = 0\,\text{K}$ of $E_{\text{g}}^{\text{DA}}/e$. Assuming a temperature independent β, a linear extrapolation of V_{oc} results in this maximum value. The slope of $V_{\text{oc}}(T)$ is determined by β and G, which scales with illumination intensity. This is illustrated in Fig. 5.4 by two curves for different values of β (marker x). In the case of recombination via a CT state (Eq. 5.14) $V_{\text{oc}}(T = 0)$ is reduced to $E_{\text{g}}^{\text{DA}} - E_{\text{B}}$, which is the energy of the CT state. This approach connects V_{oc}, defined by free charge carriers, with the energy of the CT state without any additional assumptions. Thus, it connects two on first glance completely separate approaches on V_{oc} which are recently reported and highly debated in literature: The one expressing V_{oc} by free charge carrier concentrations and lifetimes which are related to β[127] and the one correlating the CT-state energy with V_{oc} in theory and experiment[124]. Therefore, it is not astonishing that both approaches are capable of delivering correct values for V_{oc}.

The slope of $V_{\text{oc}}(T)$ is according to Eq. 5.14 determined by the CT-state parameters (circles in Fig. 5.4). In the case of a distribution of CT states the independence of V_{oc} of β does not hold any more, which is theoretically elaborated for a two-level system in Ref. [123].

The effect of μ on V_{oc} for trap-assisted recombination

If one assumes that the capture coefficient c_{p} in Eq. 5.7 depends positively on μ like in Langevin theory, a qualitatively identical behavior with μ is expected as for the case of Langevin recombination without CT state or with a CT-state distribution (not explicitly shown): V_{oc} decreases with μ. Setting c_{p} independent of μ ($N_{\text{t}} c_{\text{p}} = 10^8 \text{s}^{-1}$) also results in a small dependence of V_{oc} on μ, however, in this case with a slight increase of V_{oc} with μ (green circles in Fig. 5.3). This effect is due to high background majority dark
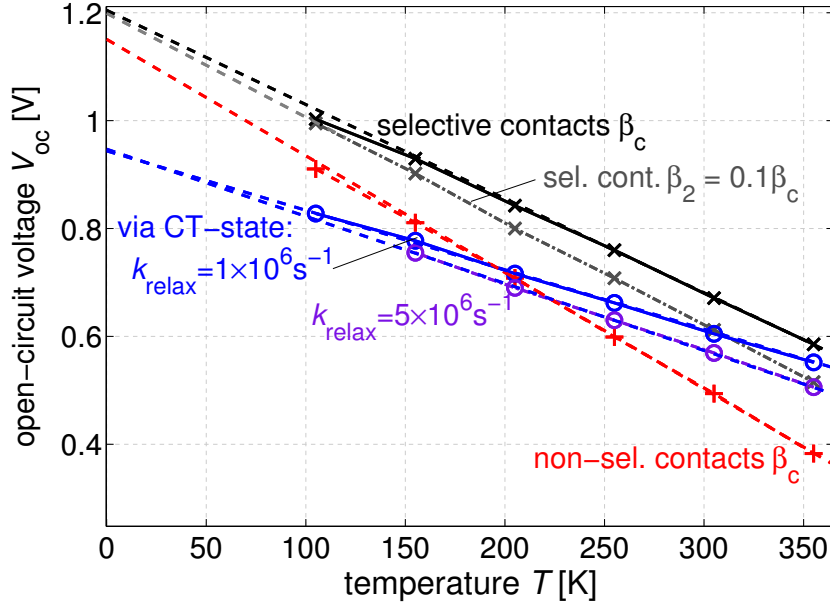
Figure 5.4: Temperature dependence of V_{oc} for different recombination constants β (x) ($\beta_c = 7.23 \times 10^{-11} \mathrm{cm^3 s^{-1}}$), CT state lifetimes $1/k_{relax}$ (o) ($E_B = 290\,\mathrm{meV}$), and non-selective contacts (+) ($\mu = 1\,\mathrm{cm^2/Vs}$). The slope is determined by β for direct recombination without CT state and by k_{relax} for recombination via CT states. Dashed lines are linear extrapolations of the $250\ldots350\,\mathrm{K}$ region, reaching E_g^{DA} for direct recombination and the CT state energy for a recombination via CT states. Surface recombination due to non-selective contacts modifies $V_{oc}(T)$.

charge carrier concentrations close to the contacts. According to Eq. 5.1 these charge carrier concentrations result from the low injection barrier at the contacts. Charge carrier density and recombination profiles at V_{oc} are shown in Fig. 5.5, where two values of μ ($10^{-2}\,\mathrm{cm^2/Vs}$, $10^{-4}\,\mathrm{cm^2/Vs}$) are compared. In case of a high mobility (solid lines), the minority charge carriers tend to move towards the middle of the device to reach their low dark (equilibrium) densities closer to the contact. Thus, the recombination maximum is found in the center of the device. For very low mobilities, charge carrier transport is slower than the recombination process and charge carriers recombine mainly where they are created. This leads to an increased minority density close to the contacts and an increased recombination there, as the dark carrier majority concentration is large at the contacts. The condition for such a redistribution to change V_{oc} is that R is not proportional to np. According to Eq. 5.7 recombination close to the contacts is approximately proportional to the minority charge carrier density. Another indication for the dark carriers being responsible for the change in V_{oc} is that this effect becomes less pronounced for a higher illumination intensity and a lower dark carrier concentration, as shown later on.
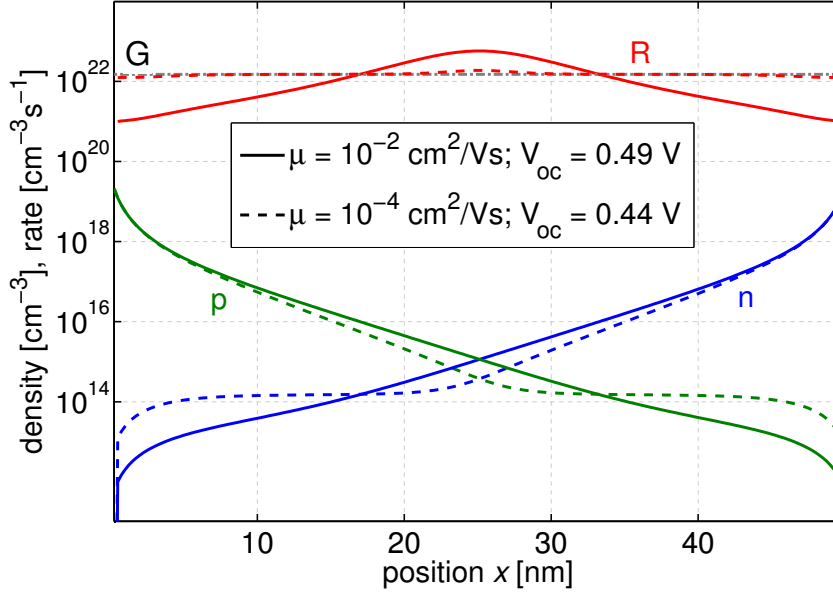
Figure 5.5: Electron (n) and hole (p) density and the recombination rate (R) within a device, where trap-assisted (SRH) recombination is dominating, at V_{oc} of the points marked in Fig. 5.3 (0.49 V for $\mu = 10^{-4}$cm^2/Vs, 0.44 V for $\mu = 10^{-2}$cm^2/Vs). An increased recombination close to the contacts is found for a lower value of μ, which is the reason for a lower V_{oc} in this case.

5.2.4 Recombination (also) at electrodes (non-selective contacts)

We now study the case of non-selective contacts, or in other words a surface recombination velocity of infinity also for minorities. Although not always explicitly mentioned, this is the standard case of most of the simulations in literature [226, 284, 285]. An exception are Refs. [123, 287], where the influence of the selectivity of contacts was already discussed. We complete the picture by showing ways of a simple experimental determination of this surface-recombination limited case, which is usually expected for a metal-organic interface if selective charge carrier blocking layers are not employed.

Figure 5.2(d) shows η as a function of μ_n and μ_p under the assumption of a constant β and non-selective contacts. Compared to the case of selective contacts [Fig. 5.2(a)], η does not reach a plateau but decays again with higher values of μ. Plots of η for the other recombination models and non-selective contacts are not explicitly shown because they exhibit a similar behavior, which means that the shape of η as a function of μ undergoes a decline for high mobilities. Examining V_{oc} and FF shown in Fig. 5.3 as dashed lines reveals that the reason for a decrease in η is, again, a decay of V_{oc} with μ. This drop at around 10^{-2}cm^2/Vs is independent of the recombination model. Only for Langevin recombination there is no difference in V_{oc} between selective and non-selective contacts, because bulk recombination is dominating over surface recombination for all μ.
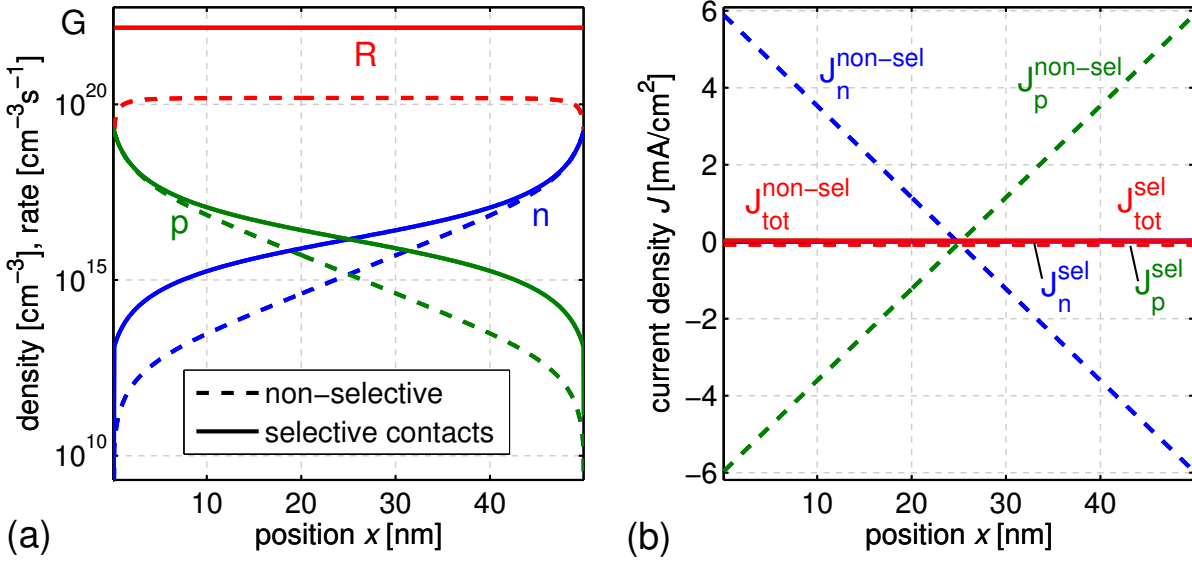
Figure 5.6: (a) Charge carrier density and (b) current profiles at V_{oc} for selective (solid lines, $V_{oc} = 0.62 \, \text{V}$) and non-selective contacts (dashed lines, $V_{oc} = 0.50 \, \text{V}$). Here, $\beta = 7.23 \times 10^{-11} \text{cm}^3\text{s}^{-1}$ and $\mu = 1 \, \text{cm}^2/\text{Vs}$. In case of selective contacts, generation equals recombination, whereas in case of non-selective contacts charge carriers are lost due to a diffusion to both contacts.

Applying Eq. 5.10, the reason for the decrease in V_{oc} is found in a negative contribution of $J_{n,p}$, which leads to a decrease of βnp (G constant). This results for a constant β in a decrease of np and consequently with Eq. 5.8 in a decline of V_{oc}. The recombination and current profiles displayed in Fig. 5.6 illustrate this effect. $G = R$, independent of x, which holds for selective contacts (solid lines), is not valid in the case of non-selective contacts and a high μ (dashed lines). R and especially the minority charge carrier densities are lower in the vicinity to the contacts, where recombination is decreased. Although both recombination profiles describe the situation at V_{oc}, where current is zero, the mean recombination rate R is orders of magnitudes lower than the generation rate G in the case of non-selective contacts and a high μ.

Examining the current profiles [Fig. 5.6(b)] one can directly see that this missing recombination is due to equal particle currents of electrons and holes ($J_{tot} = 0$ at every x in steady state V_{oc}) towards the electrodes. This current of electrons and holes in the same direction is diffusion-driven by a sink at the contacts. Due to the (conventional and generalized [232]) Einstein relation, diffusion and drift current increase linearly with μ. If there is a sink present also at the "wrong" electrode, a higher μ causes more (minority) charge carriers to diffuse to this "wrong" electrode, where they do not contribute to V_{oc}, but are lost.

If bulk recombination is negligible, the solar cell works in a completely diffusion limited mode which means that all charge carrier losses are due to diffusion to the "wrong" contact.
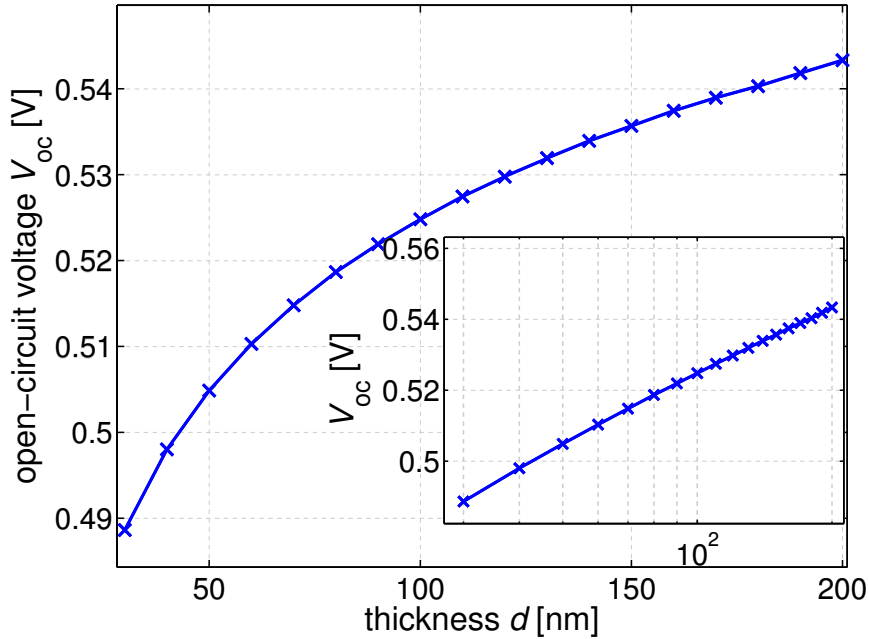
Figure 5.7: Dependence of V_{oc} on device thickness d in case of non-selective contacts, constant G, $\mu = 1\,\mathrm{cm^2/Vs}$, and bimolecular recombination with $\beta = \beta_L(\mu = 10^{-4}\,\mathrm{cm^2/Vs}) = 7.23 \times 10^{-11}\mathrm{cm^3 s^{-1}}$. This behavior can be used to identify the selectivity of the contacts, because V_{oc} is independent of the device thickness for selective contacts.

Only in such a situation is the analytical equation of Sokel and Hughes [130] (Eq. 3.24) applicable, which is often used to describe experimental photocurrents [96, 98]. Evidence for this case being present in experiment is given if the photocurrent as difference between dark current and current under illumination is extracted in forward direction as well. This requires a crossing of the *J-V* curve under illumination and the dark *J-V* curve. In the previously discussed case of selective contacts this equation of Sokel and Hughes is not applicable because all generated charges recombine at V_{oc}.

As diffusion is temperature activated, this effect is expected to be more pronounced for higher T. The red dashed line $(+)$ in Fig. 5.4 shows indeed a stronger decrease in V_{oc} with T compared to the reference with selective contacts (solid black line, x). Therefore, if surface recombination is significant, an extrapolation of $V_{\mathrm{oc}}(T)$ to $T = 0\,\mathrm{K}$ does not result in $E_{\mathrm{g}}^{\mathrm{DA}}$, but in a lower value.

Another indication for the diffusion loss can be found in an examination of V_{oc} dependent on the layer thickness. Figure 5.7 shows the dependence of V_{oc} on the BHJ thickness d for non-selective contacts, whereas for selective contacts V_{oc} is according to Eq. 5.8 independent of d. The inset shows that V_{oc} increases logarithmically with d, which can be explained by the fact that the field in the device decreases approximately linearly with device thickness $(F \approx V/d)$. This means that the drift current $(J \propto F)$, which is at V_{oc} balanced by a diffusion current, decreases linearly with d. Or in other words, as the diffusion current is

proportional to the diffusion gradient, the overall diffusion gradient decreases linearly with d. A decreased diffusion gradient corresponds to a decreased gradient in the quasi-Fermi levels, which are logarithmically related to charge carrier densities. Thus, a diffusion current creates a voltage which scales logarithmically with the current, as, e.g. known from the ideal diode equation [42]. Therefore, this diffusion voltage which is reverse to V_{oc} decreases logarithmically with d and leads to the observed increase in V_{oc}.

This behavior can be taken as a simple experimental proof to estimate losses due to surface recombination. It is important to adjust the light intensity to get a constant averaged generation rate G, which can be seen in a constant ratio between photocurrent and d. Observed deviations in V_{oc} for different thicknesses are then due to charge carrier losses at the "wrong" contact.

A similar explanation holds for the logarithmic decay of V_{oc} with μ seen at the dashed lines of Fig. 5.3(a) in the surface recombination limited case. As the total diffusion gradient is fixed by the charge carrier densities at the contacts according to Eq. 5.1, the diffusion losses are proportional to μ and, therefore, cause a voltage loss which depends logarithmically on μ.

It is concluded that also in the case of non-selective contacts, the increase of the transport parameter μ itself does not decrease V_{oc}. It is the indirect effect of μ being an enhancement factor of surface recombination. In experiments, the qualitative effect of selective and non-selective contacts is well known and seen in, e.g., an enhancement of V_{oc} of BHJs by the addition of a (selective) interlayer between metal and the BHJ [53, 288]. This explains that very high values of V_{oc} of a ZnPc:C_{60} BHJ are reported for devices where the blend is sandwiched between wide-gap transport layers (cf. Chapter. 8) in a p-i-n architecture [53]. In this structure minority charge carriers cannot penetrate the charge transport layers. However, a large amount of molecular dopant adjacent to the BHJ could be a source of minority charge carrier recombination, decreasing the selectivity property of the contact. A planar heterojunction contains this selectivity already as a built-in property. This will be discussed in Chapter 6.

5.2.5 Injection barriers

As the influence of the metal work function in experiment, corresponding to the injection barrier height in simulation, is still under discussion, the same mobility dependent study is performed for an increased injection barrier at the metal contacts ($\phi = 0.3\,\text{eV}$). A higher barrier results in two effects: First, according to Eq. 5.1 the majority charge carrier densities at the contacts are reduced. Second, according to Eq. 5.2 the built-in potential is reduced. The following discussion focuses on the effect of these changes dependent on the selectivity of the contacts.

Selective contacts

In the case of selective contacts and direct recombination, the barrier and, thus, in the thermionic injection model the dark carrier concentrations, are not relevant for V_{oc} because
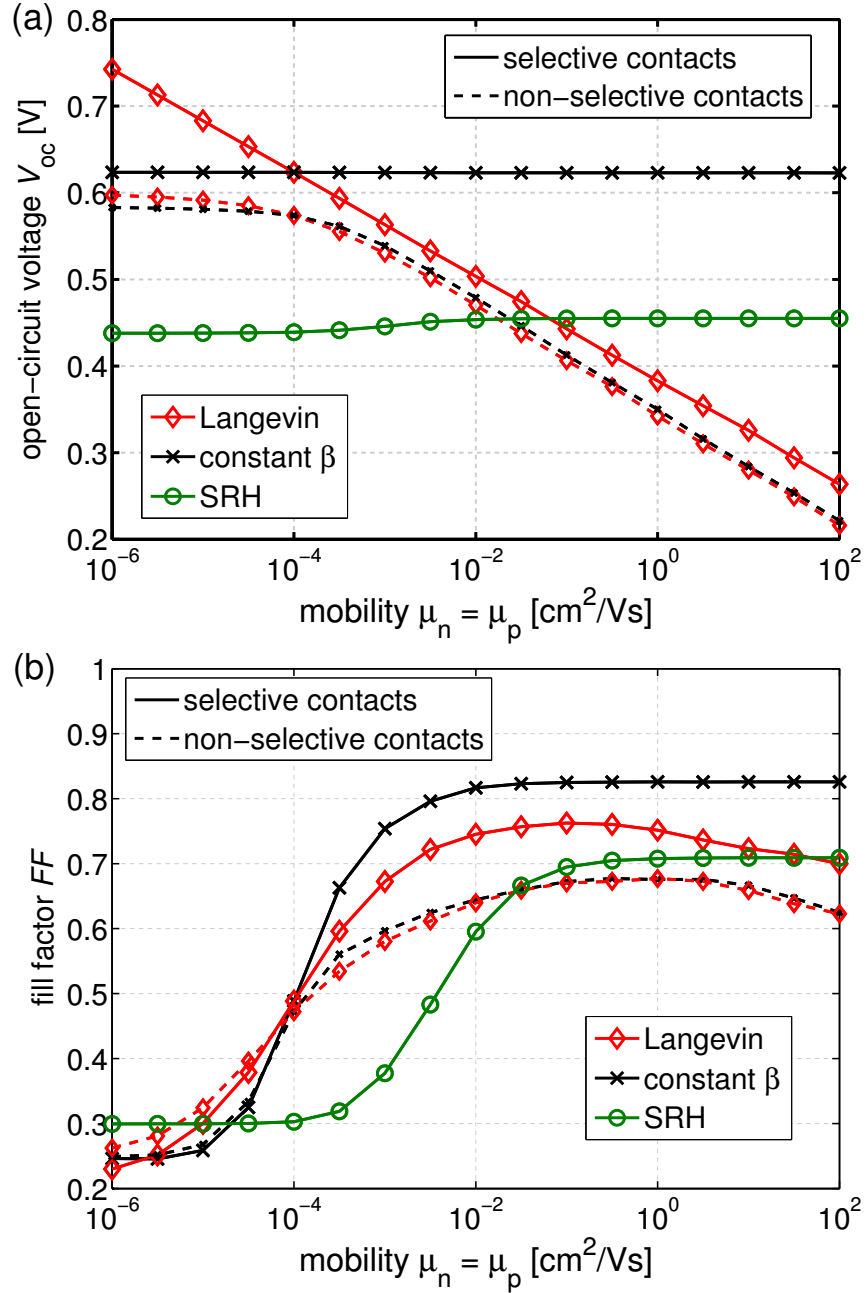
Figure 5.8: (a) V_{oc} and (b) FF as a function of the mobility $\mu_n = \mu_p$ in the cases of an **injection barrier of 0.3 eV**. V_{oc} remains unchanged compared to Fig. 5.3 in the case of selective contacts (solid lines), whereas non-selective contacts (dashed lines) reduce V_{oc} and FF. Compared to the data without significant injection barrier (Fig. 5.3), V_{oc} is more strongly affected in the case of non-selective contacts.

they do not introduce an additional source of recombination (solid lines in Fig. 5.8). V_{oc} can even exceed V_{bi} (0.6 V) if the contacts are selective. Therefore, the statements made above for $\phi = 0.1$ eV still hold.

Although the trend of the *FF* is the same with and without significant barrier, the inset of Fig. 5.9 shows a remarkable change of the *FF* in the case of Langevin recombination. For low mobilities the *FF* is reduced by a higher ϕ due to a stronger dependence of the charge carrier collection on the applied bias caused by a decreased built-in field [Fig. 8.3 (a)]. This results in a higher recombination in the center of the device (dashed in Fig. 5.10(b)) and in an S-kinked *J-V* curve because the current is mainly diffusion driven as will be discussed in Ch. 6.3.1 in detail.

For high mobilities, the *FF* is higher for a larger ϕ. The reason is that the drift current providing charge carrier extraction is sufficient also for the lower built-in field. At the same time the recombination within the device is higher for a lower ϕ. This is shown in Fig. 5.10(c+d), visualizing the high majority charge carrier densities close to the contacts, which result from a lower ϕ. This background dark carrier density increases the recombination probability of photogenerated minorities close to the contacts. Once more, this change in recombination does not influence V_{oc} as it is only present as long as there is charge carrier extraction by a current.

In Fig. 5.8 $V_{\mathrm{oc}}(\mu)$ is also plotted for SRH-recombination. The plot shows that V_{oc} is less dependent on μ compared to the case of a lower ϕ (Fig. 5.3). The reason is a reduced dark carrier concentration close to the contacts due to the increased injection barriers.

Non-selective contacts

In the case of non-selective contacts, η is generally lower with a higher ϕ. The reason is a decrease in V_{oc} compared to devices with a lower ϕ (dashed lines in Fig. 5.8). The diffusion to the "wrong" electrode becomes relevant at lower positive bias voltages because of the lower built-in field. Consequently, one can distinguish two limiting regimes in $V_{\mathrm{oc}}(\mu)$ in such a high-barrier case:

On the one hand, the contact work function can directly limit V_{oc}, which happens if eV_{bi} is lower than the maximum possible quasi-Fermi level splitting in the material. This is the case for low mobilities (up to 10^{-4}cm^2/Vs) in Fig. 5.8 and results in a dependence of V_{oc} on μ, which is insignificant, despite Langevin recombination. Such a behavior was observed in the simulation results of Refs.[284, 285], however it has not been identified as such.

On the other hand, for higher μ ($> 10^{-4}$cm^2/Vs) the diffusion or in the case of Langevin recombination possibly bulk recombination is limiting, which lead to a decrease of V_{oc} with μ. The coincidence of $V_{\mathrm{oc}}(\mu)$ for Langevin theory and a constant β ($\mu > 10^{-4}$cm^2/Vs in Fig. 5.8) below the Langevin curve for selective contacts indicates that the recombination losses at the surface dominate in this case.
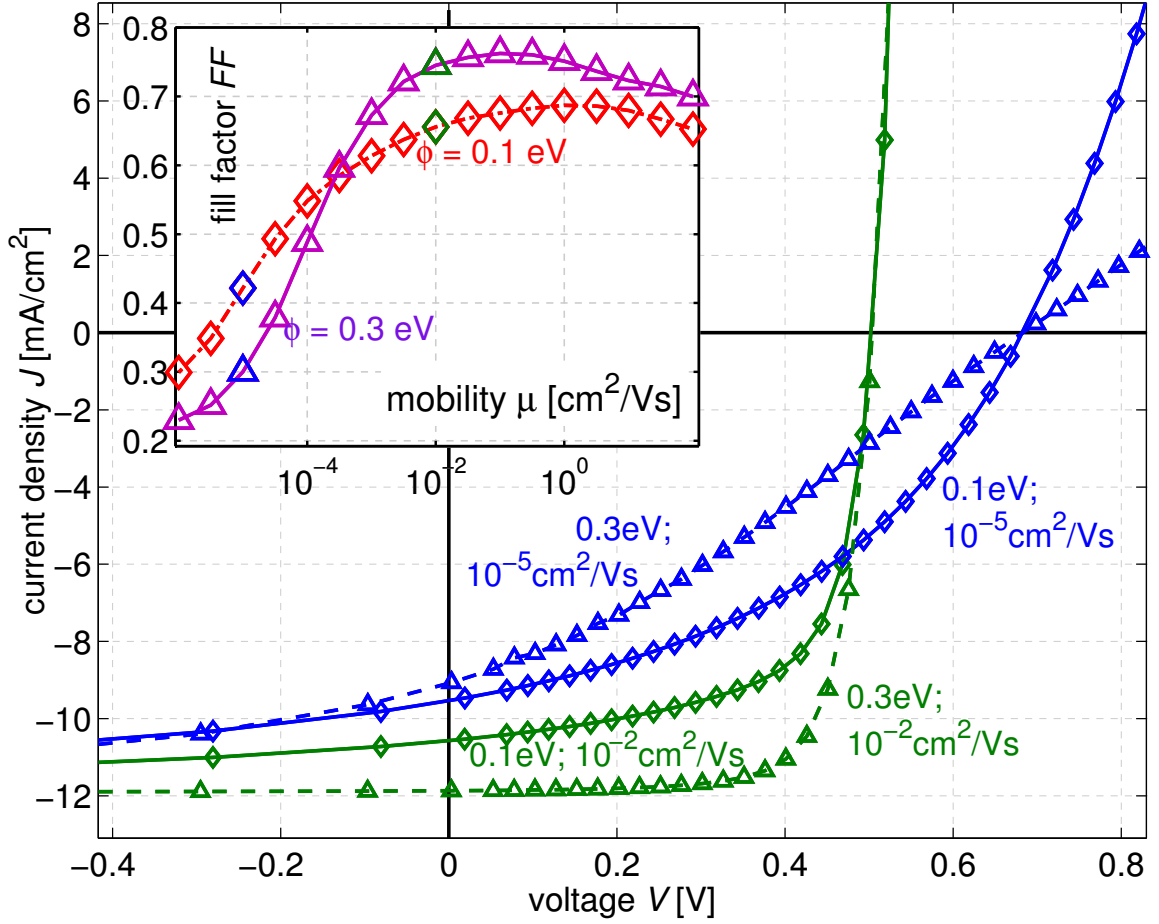
Figure 5.9: *J-V* curves for devices with two different mobilities (10^{-2} and $10^{-5}\mathrm{cm^2/Vs}$), Langevin recombination, and selective contacts. The injection barriers are $0.1\,\mathrm{eV}$ (solid lines, diamonds) and $0.3\,\mathrm{eV}$ (dashed, triangles). The inset compares the dependence of the *FF* on μ for the two barrier heights. Interestingly, the *FF* is higher for the device with a higher barrier in case of high mobilities. This is explained in the next figure.

5.2.6 Effect of energy-level bending on the open-circuit voltage

To complete the elaborations on V_{oc}, charge-transport-level bending ($\Delta\varepsilon_{\mathrm{B}}$) close to the contacts is discussed (inset of Fig. 5.11). In literature this bending is suggested [289] and several times ascribed [109] as loss mechanism for V_{oc}, because it reduces the field in the device to a value $(V_{\mathrm{bi}} - \Delta\varepsilon_{\mathrm{B}}/e)/d$. The reason for the bending is the space charge at the electrodes due to the high majority charge carrier density there (cf. Eq. 5.1). This density approaches its maximum in the case of Ohmic contacts where the Fermi level reaches the charge transport level ($\phi = 0$).

The space charge at the electrodes and hence the bending can directly be influenced by
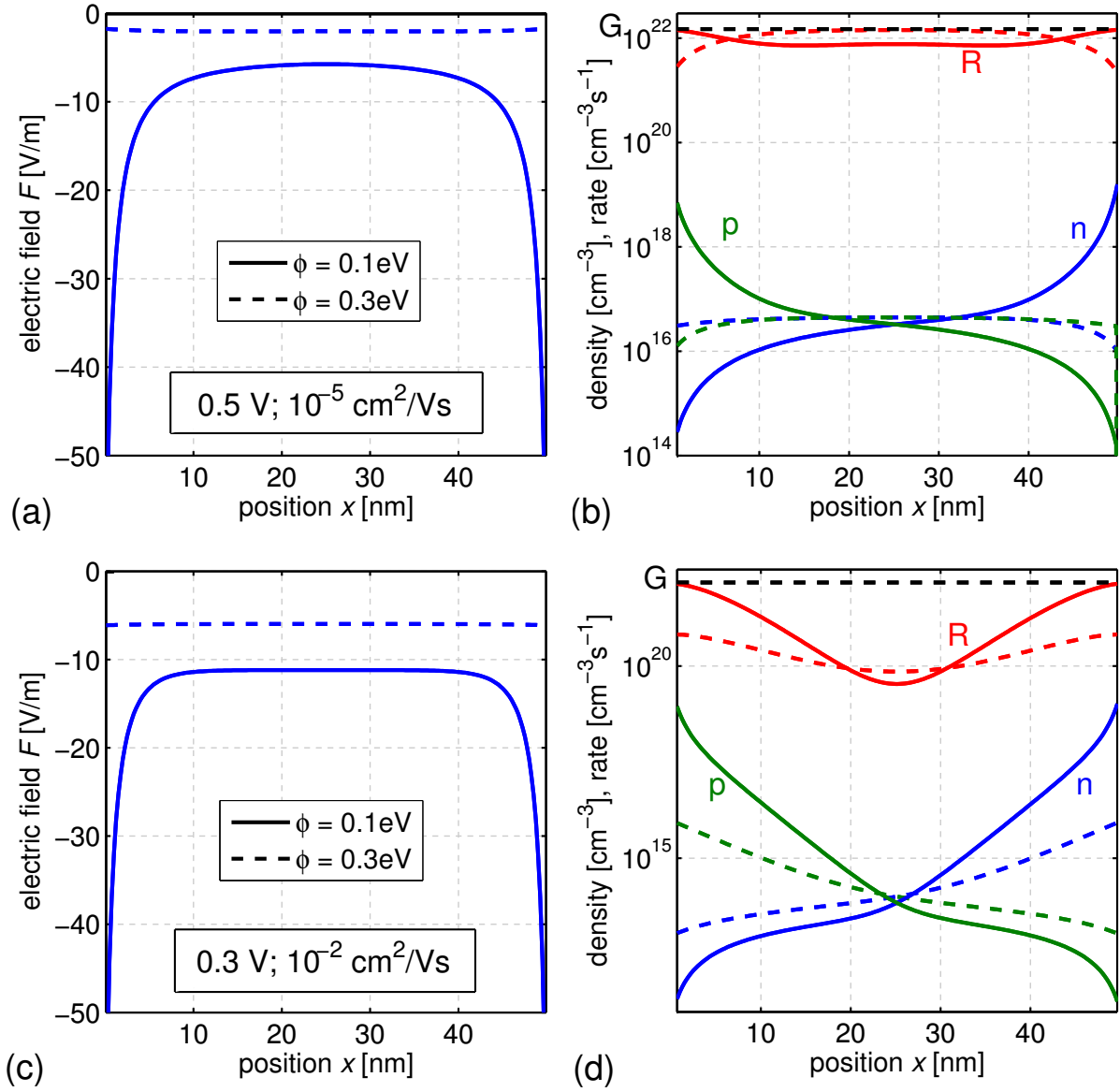
Figure 5.10: Electric field and charge carrier density profiles under the conditions marked in Fig. 5.9 (Langevin recombination, selective contacts and a varied ϕ): (a+b) $V = 0.5\,\mathrm{V}$ and $\mu = 10^{-5}\,\mathrm{cm^2/Vs}$, (c+d) $V = 0.3\,\mathrm{V}$ and $\mu = 10^{-2}\,\mathrm{cm^2/Vs}$. In case of a low μ and a high barrier, the overall recombination is high [dashed in (b)], whereas for a high μ (d) recombination dominates close to the contacts. For a lower ϕ, the majority charge carrier densities at the contacts are increased and that is why the FF is lower for low barriers and a high μ.

changing $N_{C,V}$ (cf. Eq. 5.1) without changing V_{bi}. The increase of $\Delta\varepsilon_B$ with increased $N_{C,V}$ is shown in Fig. 5.11 together with V_{oc}. Although both show the same trend, the change
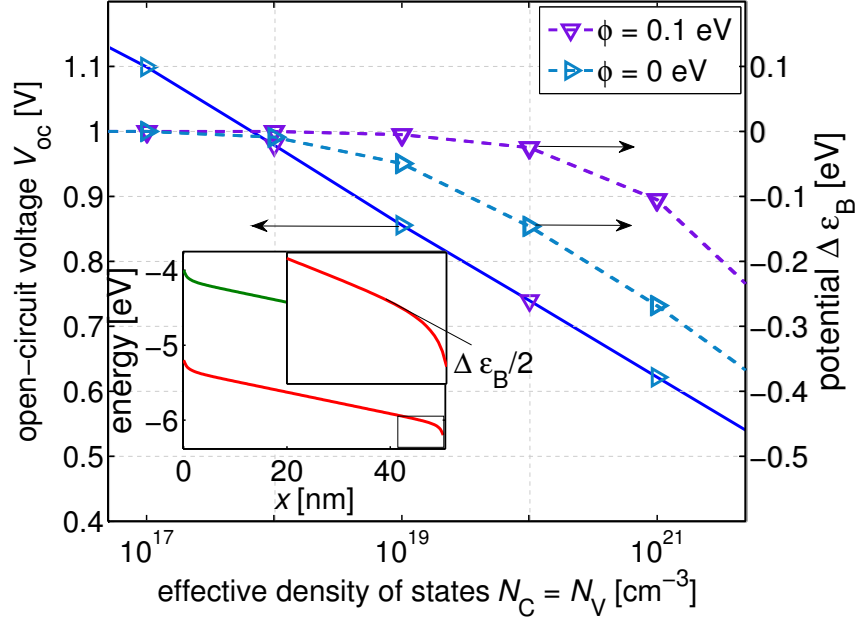
Figure 5.11: The open-circuit voltage as a function of the effective densities of states $N_C = N_V$ and the potential drop $\Delta\varepsilon_B$ for two different injection barrier heights. $\Delta\varepsilon_B$ is due to bending of the energy levels at the contacts as depicted in the inset. V_{oc} is only a function of $N_{C/V}$, is independent of ϕ, and does not directly correlate with $\Delta\varepsilon_B$. The contacts are assumed to be selective and $\beta = 7.23 \times 10^{-11} \text{cm}^3\text{s}^{-1}$.

of V_{oc} is independent of ϕ. However, $\Delta\varepsilon_B$ increases with a lower ϕ. Thus, V_{oc} does not correlate directly with $\Delta\varepsilon_B$. The effect of $N_{C,V}$ on V_{oc} can be seen directly in Eq. 5.8, where an increased $N_{C,V}$ reduces V_{oc} at a constant np because there are more low-energy states to be filled first. Thus, this is the origin of the change in V_{oc} with $N_{C,V}$. The bending itself is only a concomitant phenomenon, which can be seen at very high $N_{C,V}$, although V_{oc} scales for all $N_{C,V}$. This leads to the conclusion that an ohmic contact does not reduce V_{oc}. An ohmic and selective contact is perfect for any type of solar cell [3].

It is worth to mention that a higher layer thickness requires higher mobilities to reach the same charge carrier collection efficiency. Thus, a low mobility is one main factor limiting the *FF* and consequently the maximum layer thickness.

5.3 Photocurrent and characteristic points in simulated *J-V* curves

In Ch. 3.3.5 we discussed analytical models for the photocurrent J_{photo}. In literature it is a common approach to evaluate J_{photo} only to explain the working principle of organic

solar cells. $J_{\text{photo}}(V)$ is obtained by subtracting the dark J-V curve from the one under illumination. The motivation for this is to subtract effects resulting from (dark) charge carrier injection. This procedure allows the definition of several characteristic points in the J-V curve which are of physical interest. In the following it is shown to which extent drift-diffusion simulation can contribute in describing the physical origin of these points which are:

- The open-circuit voltage V_{oc} as point where the overall current under illumination gets zero;

- The compensation voltage V_0 as the point where dark and J-V curve under illumination cross, i.e. $J_{\text{photo}} = 0$;

- The built-in potential V_{bi} as point where the mean field within the device becomes zero;

- A point of optimal symmetry V_{POS} recently introduced as point where most of the bulk gets field free and to which J_{photo} is symmetrical [98, 290].

V_{oc} was already discussed in the previous section where it became clear that the processes dominating at V_{oc} depend on the properties of the contacts. If the contacts are selective, V_{oc} is the point where all charge carriers recombine within the device. In case of non-selective contacts, bulk recombination competes with the diffusion and subsequent extraction/recombination of charge carriers at the "wrong" electrode. Thus, in the extreme case, there is no bulk recombination of charges and Eq. 3.24 might be applied. In the first case, V_{oc} is independent of V_{bi} whereas in the latter case V_{oc} scales with V_{bi} as long as V_{bi} limits V_{oc}. The following discussion distinguishes between the dominating locus of charge carrier recombination, which is either the bulk or the surface, i.e. "wrong" electrode.

5.3.1 Negligible bulk recombination

For an investigation of V_0 we first study the case of recombination mainly at the contacts, which can be realized by a high $\mu = 1\,\text{cm}^2/\text{Vs}$ and a low $\beta = 7.23 \times 10^{-11}\,\text{cm}^3/\text{s}$ under the assumption of non-selective contacts (cf. Fig. 5.6).

Figure 5.12 shows simulated J-V curves dependent on illumination intensity for a device with low dark charge carrier concentrations due to high injection barriers (0.3 eV) at the contacts. All J-V curves cross at $V_0 = 0.6\,\text{V}$ which equals V_{bi}. This can be seen at the photocurrents, all becoming zero at 0.6 V. The reason is that the homogeneous field within the device changes its sign at V_{bi}. Because of the non-selectivity of the contacts, the photocurrent is only field-driven and extracted in both directions symmetrically to V_0. Plotting the normalized photocurrent shows that all curves coincide and can be described by Eq. 3.24 as diffusion-limited case of Ch. 5.2.4. This result means that charge carrier extraction is completely independent of μ. This results in an increase in FF with intensity from 62 % at 0.01 suns to 67 % at 1 and 10 suns in the case of $V_0 = 0.6\,\text{V}$. The reason is that
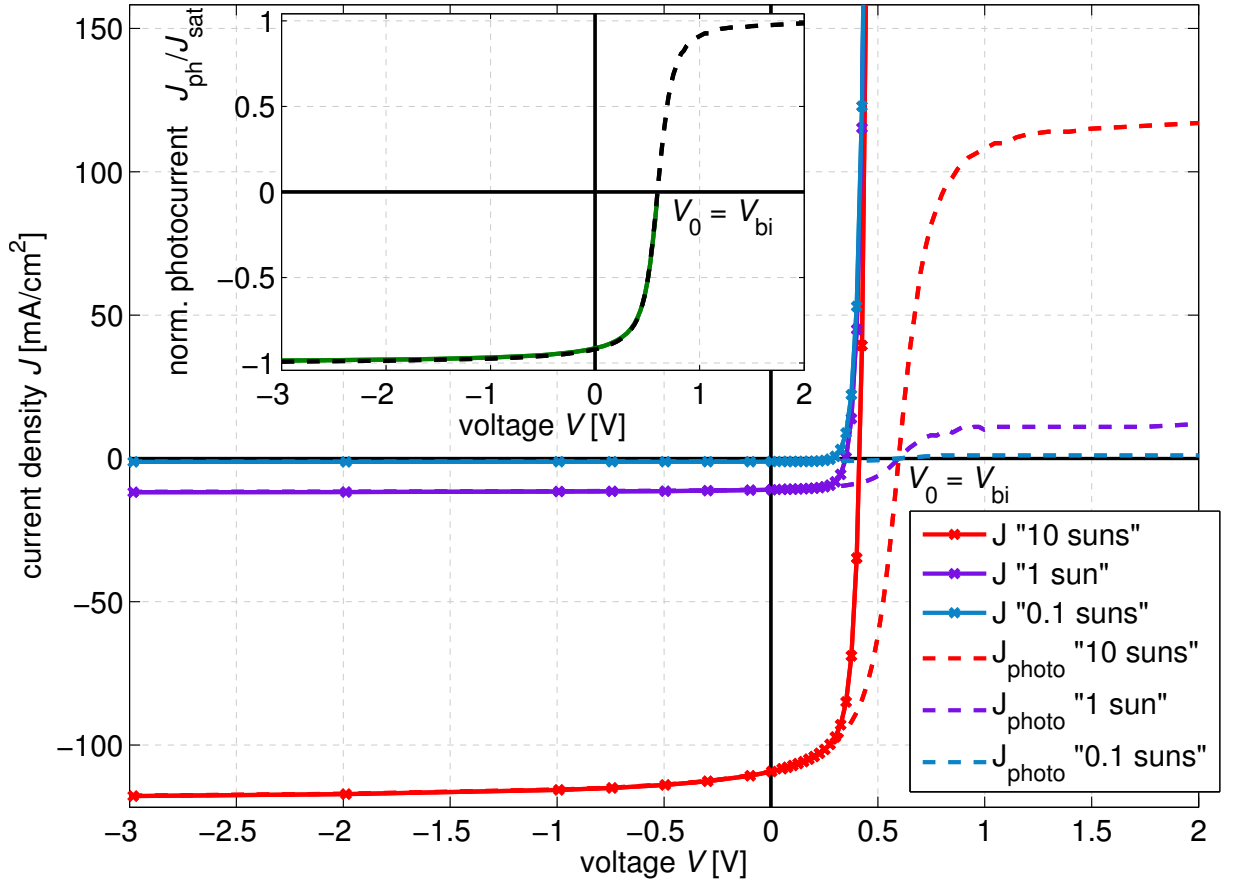
Figure 5.12: Diffusion limit ($\phi_{\text{injec}} = 0.3\,\text{eV}$): *J-V* curves and photocurrent $J_{\text{photo}} = J_{\text{illu}} - J_{\text{dark}}$ as a function of voltage for different illumination intensities. All *J-V* cross at V_0. The inset shows that J_{photo} normalized to the saturation current is independent of light intensity and follows the analytic expression of Eq. 3.24.

the relative photocurrent extracted at each voltage is independent of intensity. However, the *FF* is evaluated at the *J-V* curve under illumination and not at J_{photo} only. Thus, the relative effect of the injected dark forward current, which also decreases V_{oc} with decreased intensity, becomes more important for low illumination intensities. That is why the *FF* decreases for lower illumination intensities, which is in contradiction to most experimental data. The *FF* of common BHJ is mostly lower than 67 %. If Eq. 3.24 is applied to such experimental data, additional losses have to be caused by geminate recombination. In that case, the effective generation rate usually is modified according to Onsager-Braun theory (cf. Ch. 3.3.5 and 4.4.2) [96, 98].

However, this situation is not very realistic for solar cells with an optimized V_{oc} and high forward currents. Such cells comprise selective contacts (cf. p-i-n concept). Simulations of a device with selective contacts are shown in Fig. 5.13(a). The dashed line shows J_{photo}
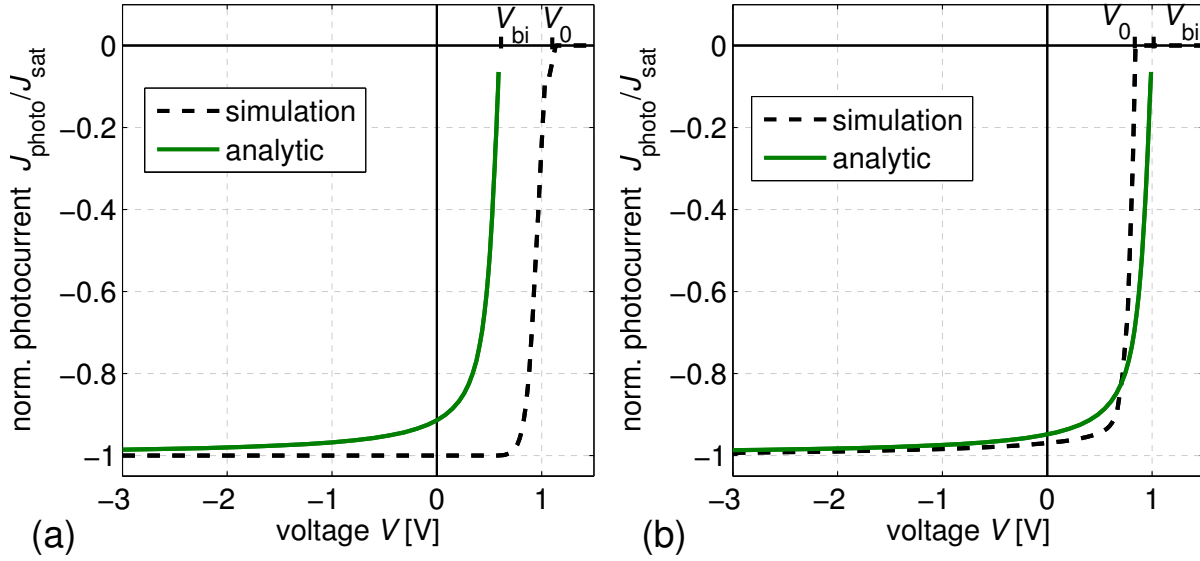
Figure 5.13: (a) J_{photo} under the same conditions (injection barrier $\phi_{\mathrm{injec}} = 0.3\,\mathrm{eV}$) as in Fig. 5.12 only for selective contacts. (b) J_{photo} for $\phi_{\mathrm{injec}} = 0.1\,\mathrm{eV}$. In both cases $V_0 \neq V_{\mathrm{bi}}$ and the analytical equation is not applicable. In (a) the selectivity increases V_0 and in (b) higher charge carrier densities due to a lower ϕ_{injec} increase bulk recombination and decrease V_0.

normalized to its saturation value, as J_{photo} and V_0 are found to be independent of light intensity. Photocurrent cannot be observed in forward direction due to the selectivity of the contacts. However, V_0 is larger than V_{bi}. Eq. 3.24 does not describe the shape of the negative photocurrent. The reason is that the selectivity of the contacts introduces a diffusion force which increases the values of V_{oc}, V_0, and the value of J_{photo} at a certain voltage compared to the results of Eq. 3.24.

Efficient solar cells employ ohmic contacts which imply low values of ϕ and thus high charge carrier densities at the contacts. As discussed previously (Ch. 5.2.6), this is accompanied by energy level bending $\Delta\epsilon_{\mathrm{B}}$ at the contacts with a reduced field in the central region of the device. In this case, it was proposed that the photocurrent gets symmetric to a new point, $V_{\mathrm{POS}} = V_{\mathrm{bi}} - \Delta\epsilon_{\mathrm{B}}$ [98]. At this point, the photocurrent is supposed to be negative. However, the simulation data shown in Fig. 5.13(b) do not provide evidence for a symmetry or the applicability of Eq. 3.24. The shape of $J_{\mathrm{photo}}(V)$ is influenced by dark carrier concentrations which are, especially close to the contacts, in the range or even larger than the photogenerated charge densities (cf. profiles in Fig. 5.10). From Fig. 5.13(b) V_0 might be close to $V_{\mathrm{bi}} - \Delta\epsilon_{\mathrm{B}}$. However, J_{photo} is suppressed in forward direction, although non-selective contacts are assumed. The strong energy level bending close to the contacts (cf. Fig. 5.11) means a large field, which increases the selectivity of the contacts. This is comparable to the back-surface field applied in silicon solar cells, which was mentioned in Ch. 2.5.1.
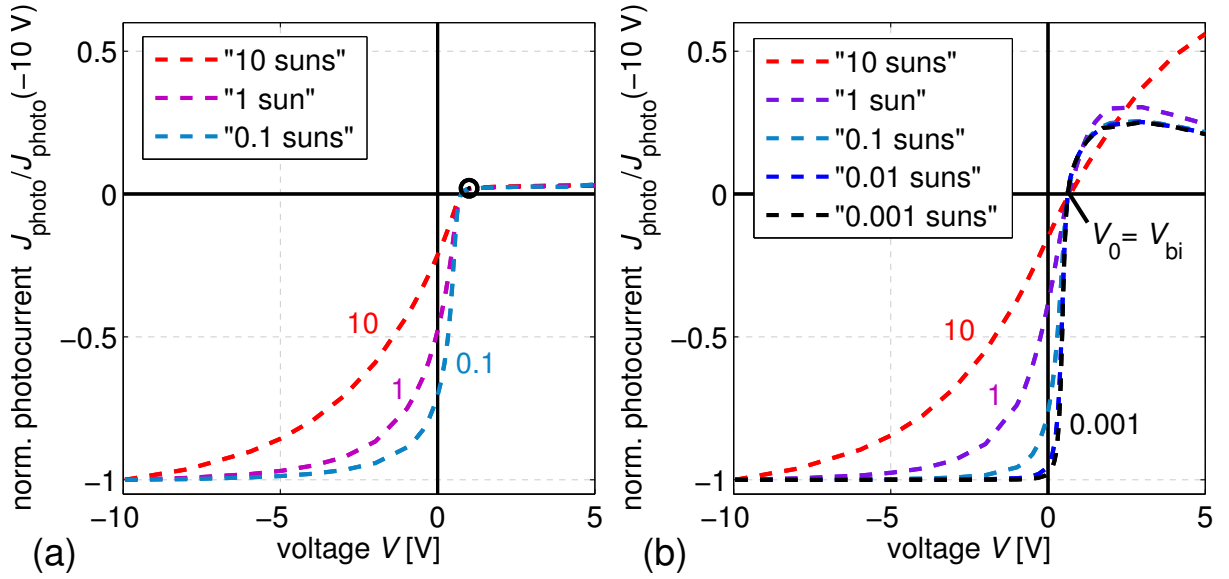
Figure 5.14: Normalized photocurrent $J_{\text{photo}}/J_{\text{photo}}(-10\,\text{V})$ for different intensities and selective contacts for (a) no significant barrier ($\phi_{\text{injec}} = 0.1\,\text{eV}$) and for (b) $\phi_{\text{injec}} = 0.3\,\text{eV}$. Positive values of J_{photo} are due to an enhanced dark injection current. This effect is examined in Fig. 5.15 at the point $(1\,\text{V})$ marked in (a).

Thus, we are not able to confirm the idea of a $V_{\text{POS}} \neq V_0$ in the simulations. The V_{POS}-theory [98] claims that the photocurrent from the region which is free of energy level bending is collected only dependent on the field there. This means that this current changes its sign as soon as the field in this region changes its sign, although the strong field at the contacts is still present. The charge carriers have to pass through the region where the bending is present in both directions in an equally efficient way. This would mean that they are not influenced by the field close to the contacts. This assumption could not be reproduced by the simulations presented here. As visualized in Fig. 5.13(b) the photocurrent does not follow Eq. 3.24 due to the high field at the contacts decreasing the probability of photogenerated charge carriers to recombine at the "wrong" contact.

5.3.2 Bulk-recombination-limited photocurrent

To study the effect of recombination within the device, we select a relatively low mobility ($\mu = 10^{-5}\,\text{cm}^2/\text{Vs}$), selective contacts, and direct recombination ($\beta = 7.23 \times 10^{-11}\,\text{cm}^3/\text{s}$) as dominating recombination mechanism.

Figure 5.14 shows that the shape of the curve is significantly influenced by the illumination intensity. This effect is independent of barrier height. The recombination probability is increased for higher intensities which can be seen by the higher voltage dependence of J_{photo} which corresponds to a lower *FF* of the *J-V* curve. This is usually observed in
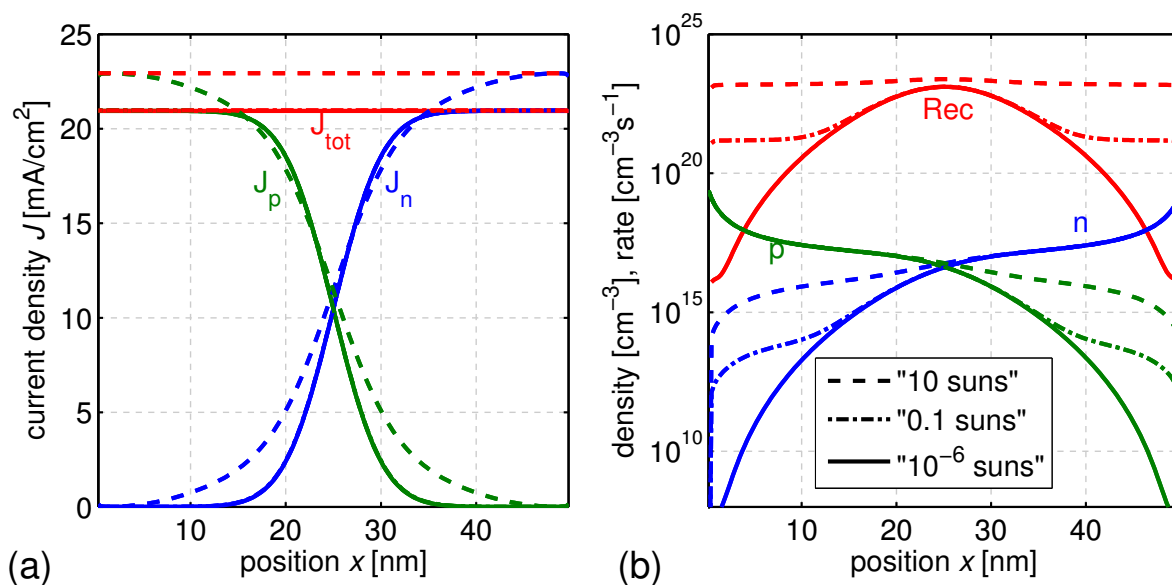
Figure 5.15: Profiles for the device of Fig. 5.14(a) at 1 V: (a) Currents. (b) Charge carrier densities and recombination. The charge carriers additionally present by photogeneration increase the recombination probability also further away from the middle of the device. This leads to a higher overall forward current under illumination.

experiment as well (cf. Fig. 10.16, p. 271). In such a situation Eq. 3.24, which does not contain any dependence on intensity, is not applicable at all. The most interesting feature is a positive photocurrent although the selective contacts do not allow an extraction of photocurrent in forward direction. Thus, the current has to be an enhanced dark-carrier forward current. The reason for this effect can be explained by examining current and charge carrier density profiles shown in Fig. 5.15. For higher illumination, charge carrier densities are increased within the device, especially minority densities (holes at cathode, electrons at anode). This leads to a higher recombination probability and a higher recombination current closer to the contacts which increases the overall forward current. In case of high injection barriers, even a significant change of the electric field can be observed (not plotted), increasing charge carrier injection probability. Consequently, a crossing point of dark and J-V curve under illumination can be observed despite selective contacts.

There is an additional reason for a crossing between dark and J-V curve under illumination. It is photoconductivity, in particular of adjacent layers, e.g. electron or hole transport layers. This means that illumination simply reduces the series resistance of the solar cell. This effect can be seen in experiment if the difference between dark and forward current significantly exceeds the photocurrent. Mostly, the shape in forward is close to linear.

Although results are influenced by layer thicknesses and prevailing values of μ, β, and grade of contact selectivity, this little model study shows that subtracting the dark curve

from the one under illumination does not in all cases simply result in the photocurrent, i.e. the amount of extracted photogenerated electron-hole pairs. The presence of photo-generated carriers influences the forward current driven by injected charge carriers. The presence of dark carriers modifies the photocurrent in reverse. Thus, a careful analysis of the dominating mechanisms is essential before applying approximated solutions.

5.4 The effect of disorder on the open-circuit voltage

Until now we assumed discrete charge transport levels described by an effective density of states. Disorder can lead to a broadened DOS which can be considered in the simulation as well. The effect of (energetic) disorder can be represented by an appropriate mobility model [85]. A charge carrier mobility depending on the electrical field and the charge carrier density increases the probability of charge carrier extraction dependent on the applied voltage. However, the influence of this effect for a solar cell at its working point is expected to be relatively weak. Charge carrier densities do not change over orders of magnitude between J_{sc} and V_{oc}, neither does the field reach values where the strong effect of a field dependent μ might be critical. Thus, for describing J-V curves at 1 sun and 300 K it is mostly sufficient to consider a constant effective μ. When examining temperature or intensity variations, a mobility as a function of T and the charge carrier density should be considered (e.g. Eq. 4.45).

We have concluded in the previous chapters that μ itself does not change V_{oc} and influences mainly the *FF*. However, the energetic disorder may have consequences on V_{oc}. This disorder can directly be represented by explicitly considering a Gaussian DOS. This approach describes the impact of the DOS on the average potential energy of charge carriers and is briefly discussed here.

The strategy of the simulation is to transfer the energetic disorder resulting from an energetic distribution of discrete hopping sites according to the Bässler model into a (narrow) Gaussian density of state (DOS), present at each grid point. This derivation of the DOS is physically different to the one of Ch. 2.2.1 which resulted from the interaction of all atoms. In contrast, in the hopping model one position (site) corresponds to one discrete energy and the Gaussian DOS is given by the distribution of these sites. In the simulation, however, the Gaussian DOS is present at every position and charge carriers are assumed to fill up the DOS according to Fermi-Dirac statistics. The reason is simply that in the simulation charge carrier densities are discussed, which have to be seen as average values over several hopping sites. This is reasonable due to the extension of the device in y and z direction, so that the average charge carrier density in a plane with $x =$ constant can be described by one charge carrier density in a Gaussian DOS.

The temperature is one important parameter defining the occupation of an extended DOS. That is why we investigate the dependence of V_{oc} on T and the width σ of the DOS.

Figure 5.16 shows V_{oc} as a function of σ for several temperatures and a constant energy gap between the maxima of HOMO and LUMO ($E_g^{DA} = 1.2$ eV). V_{oc} decreases with a broader DOS because photogenerated charge carriers occupy the low energy sites first.
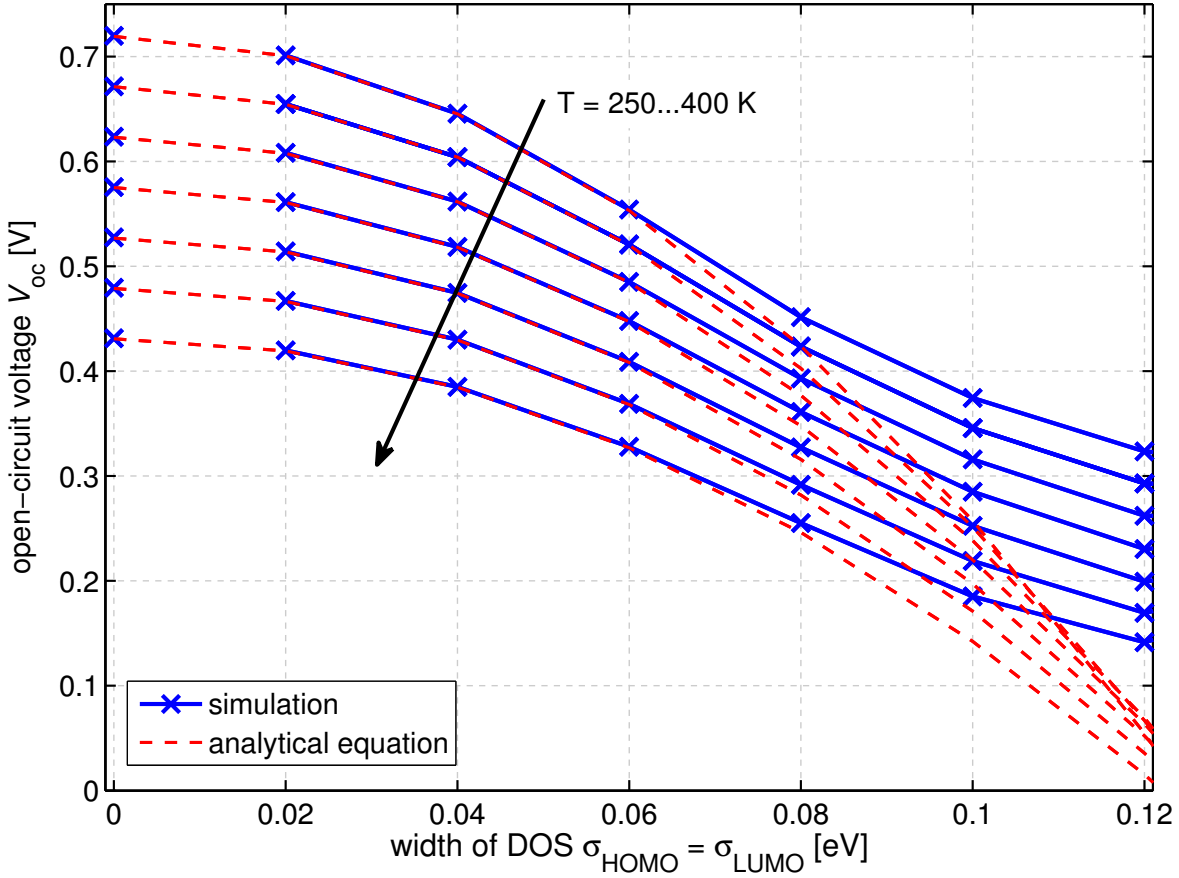
Figure 5.16: The open-circuit voltage V_{oc} as a function of the width of a Gaussian DOS σ for different temperatures $T = 250, 275, 300, 325, 350, 375, 400\,\mathrm{K}$. The red dashed data is obtained by employing Eq. 3.12 where the logarithmic expression is set to 22.3 to fit V_{oc} for $\sigma = 0$. The numerical simulations with Fermi-Dirac statistics deviate from the analytical equation for higher σ.

This reduces the quasi-Fermi level splitting. As long as the distance between quasi-Fermi level and potential energy of the majority of the charge carriers is larger than several kT, one might use Boltzmann statistics and a discrete effective energy gap $E_{\mathrm{g}}^{\mathrm{DA}*}$ which is lower than the peak to peak distance. This energy gap depends on σ and is assumed to follow Eq. 3.12 [118]:

$$E_{\mathrm{g}}^{\mathrm{DA}*} = E_{\mathrm{g}}^{\mathrm{DA}} - \frac{\sigma_n^2 + \sigma_p^2}{2k_{\mathrm{B}}T}. \tag{5.15}$$

The red dashed lines in the figure show that this approximation is capable of representing the effect of a broad DOS by a discrete energy gap for low values of σ. From the temperature dependent series, one might deduce that this approximation is allowed as long as $\sigma < 2\ldots 3k_{\mathrm{B}}T$. For higher values of σ, Eq. 5.15 and thus Eq. 3.12 do not hold anymore. This equation even results in negative values of V_{oc} for $\sigma > 0.12\,\mathrm{eV}$.
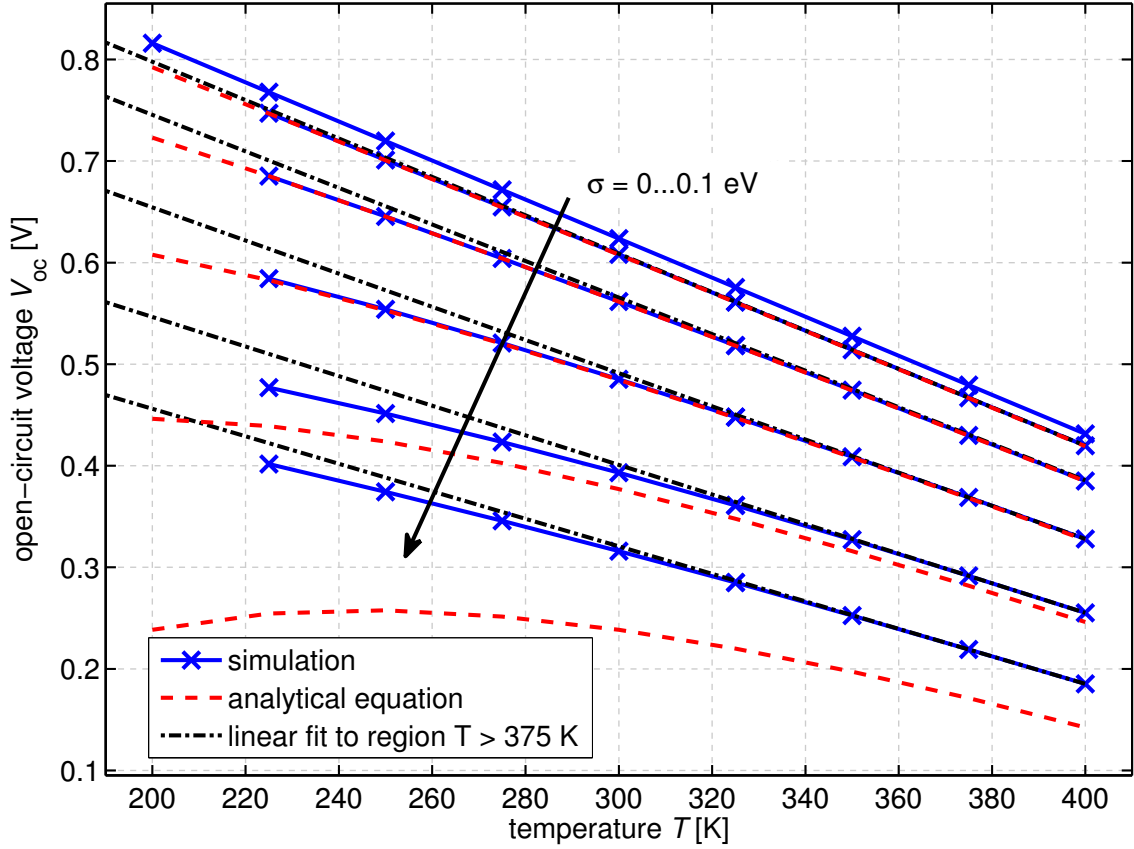
Figure 5.17: The same data as in the previous figure, but plotted as a function of T with $\sigma = 0$, 0.02, 0.04, 0.06, 0.08, $0.1\,\mathrm{eV}$ as parameter. An increased σ can be the reason for non-linearities in $V_{\mathrm{oc}}(T)$.

The temperature dependence of $E_{\mathrm{g}}^{\mathrm{DA}*}$ implies that V_{oc} depends sublinearly on $-T$ (Eq. 3.12). Figure 5.17 illustrates that this sublinearity is present and significantly pronounced for higher values of σ. Again the deviations of the data from Eq. 3.12 to the numerical simulation data becomes visible at low T and high σ.

In conclusion, it was demonstrated that considering the energetic disorder also in the energy levels via a Gaussian DOS and F-D statistics is important when discussing the dependence of V_{oc} on T. Otherwise, it is sufficient to use a modified effective energy gap. In the following chapters, we will explicitly consider the Gaussian DOS only, if the object of study requires this description. The results for V_{oc} follow the predictions from Eq. 3.12 for $\sigma < 3k_{\mathrm{B}}T$. Furthermore these results provide a possible explanation for the saturation tendency of V_{oc} with lower T which is commonly observed in experimental data [291].

5.5 Summary

The simulation studies presented in the first section demonstrated that the results of simple drift-diffusion simulations and especially the existence of an optimum mobility depend strongly on the assumptions made for bulk and surface recombination. It was clarified that selective ohmic contacts are the optimum choice, also for organic solar cells. Then, V_{oc} is limited by recombination in the device and depends only on μ in the case of recombination processes, where the recombination constants are a function of μ (Langevin recombination), or if $R \propto np$ is not given like in SRH-recombination. If free charge carrier generation and recombination happens through a CT state, V_{oc} is governed by the dynamics of this state rather than by free charge carrier recombination coefficients. Furthermore, barriers at the electrode and dark-carrier concentrations in combination with varied mobilities do not alter V_{oc} in the case of bimolecular recombination.

Only if the contacts are non-selective, an additional loss path arises by the extraction of charge carriers at the "wrong" electrode. Then, V_{oc} is decreased by injection barriers or by a very high mobility itself, as both, the first one by a lower built-in field and the second one by a higher diffusivity, increase this diffusion loss. The case of this surface recombination limit is expected to be seen in experiment by a V_{oc} which depends on layer thickness.

It was shown in the second part that a crossing point between dark and *J-V* curve under illumination can have several reasons. This crossing point equals V_{bi} only in the case of a BHJ with negligible dark-carrier concentrations and non-selective contacts. Only in this case, the approximations discussed in Ch. 3.3.5 are applicable. Otherwise, the photocurrent reflects a superposition of dark and photogenerated charge carriers. This superposition can even result in an effective photocurrent in forward despite selective contacts.

Finally, it was demonstrated that a sublinearity of V_{oc} with negative temperature can result from a Gaussian DOS. Thus, this distribution should be considered when performing studies dependent on temperature. Otherwise, an adjusted effective donor-acceptor gap should be sufficient.

Chapter 6

Influence of Injection and Extraction Barriers on Open-Circuit Voltage and *J-V* Curve Shape studied at a Variation of Hole Transport Layer and Donor Materials

The effect of injection barriers at the contacts has already been briefly addressed in the previous chapter, where we have seen that the selectivity of contacts plays an important role. This chapter goes into detail by taking into account experimental data of flat (FHJ) and bulk heterojunction (BHJ) solar cells with injection and extraction barriers at the contacts. The barriers are realized by a combination of p-type materials with HOMOs varying between -5.0 and -5.6 eV as hole transport layer (HTL) and as donor in multilayer p-i-n solar cells. The HTL/donor interface can be seen as a model for the influence of contacts in organic solar cells in general. The experimental J-V curves are compared to simulation data of the device stack and can be qualitatively reproduced and explained by the calculations.

It is shown that in a FHJ, the open-circuit voltage (V_{oc}) is determined by the donor-acceptor combination and is independent of the HTL. In a BHJ, however, V_{oc} decreases if injection barriers are present. This different behavior is caused by a blocking of charge carriers at a spatially localized donor-acceptor heterojunction, which is only present in the FHJ. The forward current is dominated by the choice of the HTL. An energy mismatch in the HOMOs leads to kinks in the J-V curves in the cases, where V_{oc} is independent of the HTL.

Further investigations include measurements dependent on temperature and a variation of HTL and donor thickness. All observed trends in the characteristics of the S-kink are confirmed by respective simulations. Transient photocurrent data show clear evidence for a pile-up of charge carriers at extraction barriers and a redistribution of the electrical field

in the case of injection barriers.[1]

6.1 Methodological approach

In literature, the influence of electrode work functions on V_{oc} is a matter of discussion. On the one hand it was found that V_{oc} depends on the choice of the cathode [119], on the other hand V_{oc} was observed to be independent of metal contacts [120, 292]. It was shown in the previous chapter that the selectivity of the contacts is important if barriers are present. In recent years more and more results have confirmed, that the energy gap between the highest occupied molecular orbital (HOMO) of the donor and the lowest unoccupied molecular orbital (LUMO) of the acceptor (effective gap) is the upper limit of eV_{oc} (e elementary charge). This limit may not be reachable due to the presence of a charge-transfer state with a lower energy [124] (cf. discussion in Ch. 3.3.2, p. 62). As discussed in Chapter 2, the splitting between the hole and electron quasi-Fermi levels at the donor-acceptor (D/A) interface equals eV_{oc} in an ideal solar cell. We have also seen that a finite distance between the quasi-Fermi level splitting and the effective gap exists, defined by the charge carrier density which results from the equilibrium between generation and recombination. It is typically around $0.3 \ldots 0.6\,\mathrm{eV}$ at standard operating conditions and explains the differences between effective gap and V_{oc} [117]. Controversially debated is the correlation between V_{oc} and the built-in potential (V_{bi}, Eq. 5.2), which is defined as difference of the work functions of the metal contacts or doped charge transport layers if present (including interface dipoles). We have already seen in the previous chapter that a high V_{bi}, which means low injection barriers, is beneficial for a well-working solar cell, but not necessarily correlated with V_{oc}.

In this chapter we clarify the interplay between the energy levels of contact – in our case doped charge transport – layers and the energy levels of the active materials. A series of flat heterojunction (FHJ) and bulk heterojunction (BHJ) solar cells is prepared with varied donor and hole transport layer (HTL) to intentionally create a misalignment of the HOMO of the HTL with the HOMO of the donor. By several combinations of HTL and donor, injection as well as extraction barriers (ϕ_h) for holes at the HTL/donor interface, dependent on the sign of the HOMO offset, are realized. For both cases schematic energy diagrams are depicted in Fig. 6.1(b). An injection barrier is formed, when the HOMO of the HTL lies higher than the HOMO of the donor, because holes being injected from the ITO over the HTL into the donor face an energy barrier. An injection barrier is commonly observed at a metal/insulator contact, if the work function of the metal is in the energy gap of the insulator (cf. Ch. 3.4.1). An extraction barrier means an energetic barrier for (photogenerated) holes in the donor to escape the device. This kind of barrier is found at an organic/organic interface, if the HOMO of the destination layer (here the HTL) lies deeper than the HOMO of the originating layer (here the donor).

---

[1]The content of sections 6.1-6.3.3 of this chapter is published in W. Tress, K. Leo, and M. Riede, *Influence of hole-transport layers and donor materials on open-circuit voltage and shape of I-V curves of organic solar cells.* Advanced Functional Materials **21** (Issue 11), 2140-2149 (2011) .
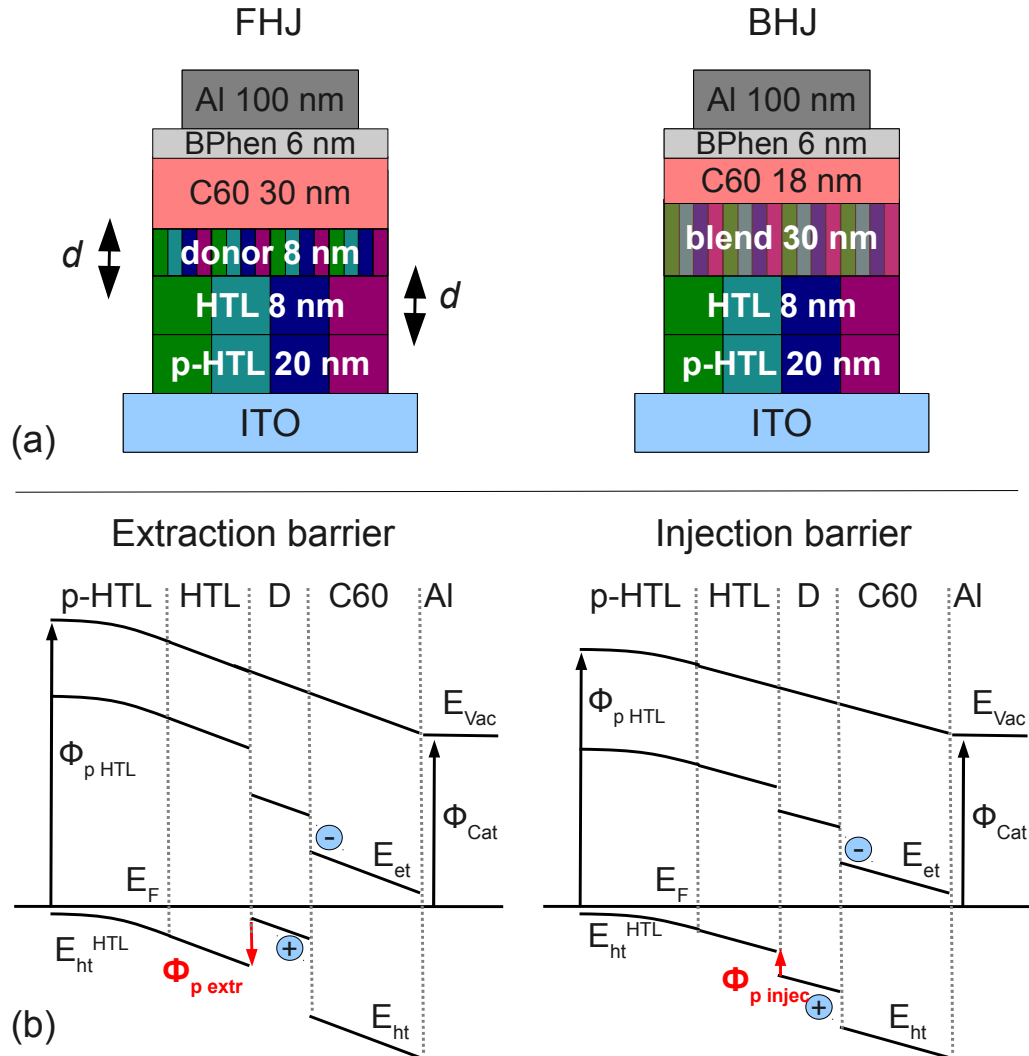
Figure 6.1: (a) Layer stack with p-doped hole transport layer (HTL) for ohmic contact to the ITO, intrinsic HTL, the active material stack, and BPhen-Al contact. The active material stack consists in the case of a FHJ of donor/C_{60} or in the case of a BHJ of a blend layer of donor:C_{60} with a mixing ratio of 1:1, followed by 18 nm C_{60}. (b) Schematic energy-level diagrams of a FHJ with ϕ_p as hole extraction (left) or injection (right) barrier. The type of ϕ (injection or extraction) depends on the hole transport levels $E_{ht} \approx$ HOMO of the HTL and donor materials combined.

The energy levels shown in Fig. 6.1(b) are the charge transport levels (E_{et} and E_{ht}) in thin films. E_{ht} is the ionization potential measured by ultraviolet photoelectron spectroscopy (UPS onset) and according to the convention of this work (cf. Ch. 4.9, p. 137) also regarded

as HOMO$_{\text{UPS}}$. The height of the barrier is the difference between the HOMO values of HTL and donor under the assumption of vacuum level alignment at the HTL/donor interface. Commonly, vacuum level alignment is observed by UPS measurements between these kinds of intrinsic materials [261]. This unique approach of combining different organic materials has several advantages compared to a variation of electrode materials. The properties of metal-organic interfaces depend strongly on an (unintentional) pretreatment of the metal surface and can change by deposition sequence (organic material deposited on metal or metal evaporated on an organic layer). A priori unknown dipoles, the presence of oxide layers, the push-back effect, and polaron states influence the energy level alignment [153, 154] (cf. Ch. 3.4.2). Consequently, the height of injection barriers is difficult to predict. Furthermore, due to Fermi level pinning at the band edge or in the tail of the HOMO (see Ch. 3.4.2), extraction barriers are hard to realize with metal contacts.

Shifting the barrier into the device also has advantages for modeling because the strong influence of less defined boundary conditions at the metal contact is avoided. The effective doping concentration ($5 \times 10^{18} \text{cm}^{-3}$) is chosen as boundary condition representing an ohmic contact. This is justified by J-V measurements with variable layer thickness indicating that a good (tunneling) contact to the metal is guaranteed and the conductivity of the doped layers is high compared to the other layers in a device. UPS measurements show that energy level bending at the interface metal/ highly doped HTL is indeed restricted to 2...5 nm, after which the equilibrium charge carrier density adjusted by doping is reached [156, 260]. Hence, the device characteristics are ruled by the properties of the bulk layers themselves and the organic/organic interfaces for both, simulation and experiment.

Whereas it is sufficient to assume a constant charge carrier mobility in the layers of our devices, disorder has to be taken into account at the interfaces. As first approximation we assume a Gaussian density of states (DOS) with a width σ for HOMO and LUMO and Fermi-Dirac statistics to describe its occupation. As described in the modeling section (Ch. 4.6.1), charge transport rates at the interface are modified by a probability ensuring a constant Fermi level in equilibrium. The width of the Gaussian DOS σ is set to 0.1 eV and the hopping distance a is set to 1 nm. These are reasonable values for organic materials and reported in literature [85]. However, these parameters only change the quantity of the observed features, not the quality, and exact values are therefore not significant for the main conclusions of this section. In subsequent sections, one material combination will be investigated in more detail.

The layout of the investigated devices is depicted in Fig. 6.1(a). It constitutes a p-i-metal geometry with the layer sequence ITO/ p-HTL (20 nm)/ HTL (8 nm)/ active layer stack (48 nm)/ BPhen (6 nm)/ Al. In the FHJ devices the active layer stack consists of a bilayer donor (8 nm)/ C$_{60}$ (40 nm) and in the BHJ devices it consists of a blend donor:C$_{60}$ (30 nm, 1:1) followed by C$_{60}$ (18 nm). The materials used as HTL and donor are ZnPc (HOMO -5.0 eV), MeO-TPD (-5.1 eV), α-NPD (-5.5 eV), and BPAPF (-5.6 eV). Their structures can be found in Figs. 3.26 (p. 85) and 3.28 (p. 89). All molecules are commonly applied as hole transporting materials, showing reasonable mobilities. Although these materials except ZnPc are transparent in the visible spectral range, they can be applied as donors (in the sense of hole acceptors) in a solar cell with a photocurrent resulting from the

absorption in the acceptor C_{60}. As discussed in Ch. 3.5.1 doping of the hole transport layer (HTL) adjacent to the indium tin oxide (ITO) guarantees hole injection/extraction and hence solar cell performance independent of the work function of the ITO anode and HOMO of the HTL [53] by shifting the Fermi level in the doped HTL close to the HOMO [156, 260, 293]. An effect of the dopant molecule itself on the charge transport over the HTL/donor interface is excluded by the 8 nm thick intrinsic HTL contacting the donor. All combinations of these four materials as donor and HTL result in 16 FHJ and 16 BHJ solar cells with nominal barrier heights ranging from 0 eV to injection or extraction barriers of 0.6 eV.

In the second part of this chapter the influence of the thickness (10...50 nm) of the HTL and donor layers will be examined, where we focus on the material combination MeO-TPD/BPAPF. *J-V* curves of these devices are also measured as a function of temperature in a cryostat setup [249]. Furthermore, transient current data of these devices is presented.

6.2 Current-voltage data

6.2.1 Fingerprints

Table 6.1 shows a summary of the main results of the solar cells prepared. The dependence of V_{oc} on the HOMO levels of donor and HTL is visualized in Fig. 6.2, showing a significant difference for FHJ and BHJ solar cells. In the FHJ [Fig. 6.2(a)] V_{oc} is mostly independent of the choice of the HTL and fixed by the donor. It increases with a lower lying HOMO of the donor and scales almost linearly with the effective gap as expected and commonly observed, e.g., in Ref. [117]. However, assuming a LUMO of -4.0 eV for the acceptor C_{60} [294], there is a difference of around 0.6 eV between eV_{oc} and the effective gap. This large difference can be due to a comparably high recombination at the D/A interface (cf. Ch. 5.2.3) or due to the fact that holes (electrons) are located in tail states of the HOMO (LUMO) (cf. Ch. 5.4). Both effects decrease the quasi-Fermi level splitting and hence V_{oc} as demonstrated in the previous chapter. Only ZnPc as HTL reduces V_{oc} of the FHJ devices with α-NPD and BPAPF as donors. The reason could be that ZnPc as the only material growing crystalline with a certain roughness is not completely covered by a donor with a thickness of 8 nm. In contrast to V_{oc}, the *FF* changes with the HOMO of the HTL. This can be gathered from the low values of the *FF* in the entries besides the principle diagonal of Tab. 6.1, where the *FF* decreases with the strength of the HOMO level mismatch, i.e., the dominance of barriers. Another measure for the significance of barriers apart from the *FF* is the slope at V_{oc}. It is also given in the table and decreases for higher injection and extraction barriers.

For the BHJ [Fig. 6.2(b)] V_{oc} is strongly influenced by the HOMO of the HTL. When it is lying higher than the HOMO of the donor (injection barrier), the HOMO of the HTL limits V_{oc}. This leads in the case of ZnPc as HTL to a V_{oc} of around 0.55 V, which is almost independent of the donor. The *FF* and the slope at V_{oc} are affected and therefore decreased by extraction barriers.

Table 6.1 also shows values for the short-circuit current density J_{sc} and calculated power-

HTL	donor	ZnPc FHJ	ZnPc BHJ	MeO-TPD FHJ	MeO-TPD BHJ	α-NPD FHJ	α-NPD BHJ	BPAPF FHJ	BPAPF BHJ
ZnPc -5.0 eV*	V_{oc} [V]	0.38	0.49	0.56	0.55	0.68	0.54	0.82	0.56
	FF [%]	**55**	50	**37**	48	**37**	44	**29**	49
	J_{sc} [mA/cm^2]	4.7	6.9	2.0	2.0	2.3	2.2	2.0	2.8
	η [%]	0.98	1.7	0.41	0.52	0.58	0.52	0.48	0.77
	$\frac{dJ}{dV}\big|_{V_{oc}}$ [mA/V]	60	70	20	20	10	30	2	40
MeO-TPD -5.1 eV*	V_{oc} [V]	0.42	0.57	0.56	0.58	0.85	0.64	1.0	0.69
	FF [%]	**51**	42	**44**	23	**35**	22	**28**	23
	J_{sc} [mA/cm^2]	5.0	8.0	2.4	0.72	2.3	1.2	2.0	1.5
	η [%]	1.1	1.9	0.52	0.10	0.71	0.17	0.56	0.24
	$\frac{dJ}{dV}\big|_{V_{oc}}$ [mA/V]	50	40	30	2	8	3	0.2	10
α-NPD -5.5 eV*	V_{oc} [V]	0.41	0.55	0.56	0.58	0.83	0.83	0.95	0.93
	FF [%]	**9**	22	**38**	32	**51**	31	**45**	28
	J_{sc} [mA/cm^2]	1.55	6.8	2.3	1.0	2.6	1.3	2.2	1.9
	η [%]	0.057	0.81	0.49	0.19	1.1	0.43	0.96	0.50
	$\frac{dJ}{dV}\big|_{V_{oc}}$ [mA/V]	0.4	3	10	5	30	3	20	9
BPAPF -5.6 eV*	V_{oc} [V]	0.39	0.55	0.54	0.58	0.84	0.84	0.95	1.0
	FF [%]	**10**	7.7	**10**	21	**46**	33	**49**	25
	J_{sc} [mA/cm^2]	0.05	1.6	1.1	0.67	2.7	1.5	2.3	1.8
	η [%]	$2 \cdot 10^{-3}$	0.07	0.06	0.08	1.0	0.42	1.0	0.45
*HOMO	$\frac{dJ}{dV}\big|_{V_{oc}}$ [mA/V]	0.02	0.1	0.2	0.6	10	4	20	2

Table 6.1: V_{oc}, FF, short-circuit current density J_{sc}, and power-conversion efficiency η for all combinations of the investigated p-type materials as hole transport layer (rows) and as donor (columns) in FHJ and BHJ solar cells. The values are an average of data of four solar cells of an area of $6.4\,\mathrm{mm}^2$. V_{oc} and FF are with a statistical error of $< 2\,\%$. Here, η is only shown for comparison between the investigated devices. It is calculated from the J-V curve and not corrected for the spectral mismatch of each solar cell. An overall mismatch factor of 0.65 with the used sun simulator spectrum is assumed for all devices.

conversion efficiency η. J_{sc} is used to explain from which layers and materials photocurrent originates. A comparison of J_{sc} to discuss the origin of photocurrent works only for devices without a strong S-kink (see Figs. 6.3 and 6.4). However, also the J-V curves of S-kink devices approach each other for higher negative bias.

First, the J_{sc} data of FHJ devices are discussed: J_{sc} is between 2.0 and $2.7\,\mathrm{mA/cm}^2$ independent of donor and HTL for the transparent donor materials (MeO-TPD, α-NPD, BPAPF) except for the combination BPAPF/MeO-TPD, where a strong extraction barrier and hence S-kink is present. This photocurrent results from absorption in C_{60}. The
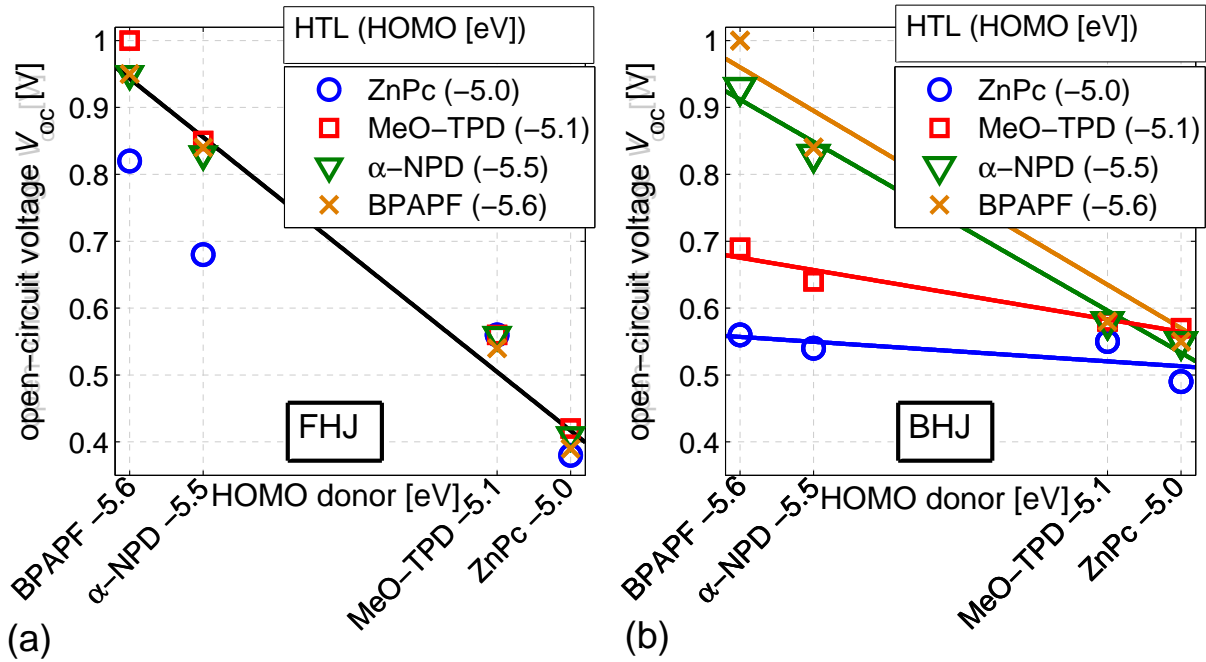
Figure 6.2: The open-circuit voltage V_{oc} as a function of the HOMO of the donor material in devices with different HTLs. Shown are data of (a) flat heterojunction (FHJ) and (b) bulk heterojunction (BHJ) solar cells. V_{oc} is limited by the HTL only in case of a BHJ.

small variations are probably due to a slightly changed morphology and exciton diffusion length in C_{60} depending on the material it is evaporated on. The short-circuit current is increased for the donor ZnPc (4.7 to $5\,\mathrm{mA/cm^2}$), because ZnPc shows absorption in the visible spectral range in contrast to the other donors (cf. Fig. 3.27). Any contribution from the HTL can be excluded, as the photocurrent with ZnPc as HTL does not increase compared to a transparent HTL. Thus, exciton separation at the HTL/donor interface can be excluded, as well as energy transfer from ZnPc as HTL to the transparent donor accompanied by a diffusion of excitons to the D/A interface. J_{sc} even decreases slightly in the case of ZnPc and MeO-TPD as donor in combination with ZnPc as HTL. The reason is (parasitic) absorption in the HTL ZnPc which reduces absorption in donor and acceptor. Optical modeling with exciton diffusion leads to values of J_{sc} in the measured range, when assuming an exciton diffusion length for C_{60} in the range of $10\ldots 15\,\mathrm{nm}$ and for ZnPc in the range of $8\,\mathrm{nm}$. Also the effect of parasitic absorption of the HTL ZnPc can be seen in the optical simulation.

In the BHJ for non-ZnPc devices, the current is low and between 0.7 and $1.9\,\mathrm{mA/cm^2}$, which is presumably due to a poor morphology of these non-optimized blends. In case of ZnPc as donor, J_{sc} approaches $8.0\,\mathrm{mA/cm^2}$ and is reduced to $6.8\,\mathrm{mA/cm^2}$, when ZnPc is also applied as HTL (parasitic absorption). In the case of the other donors, ZnPc as
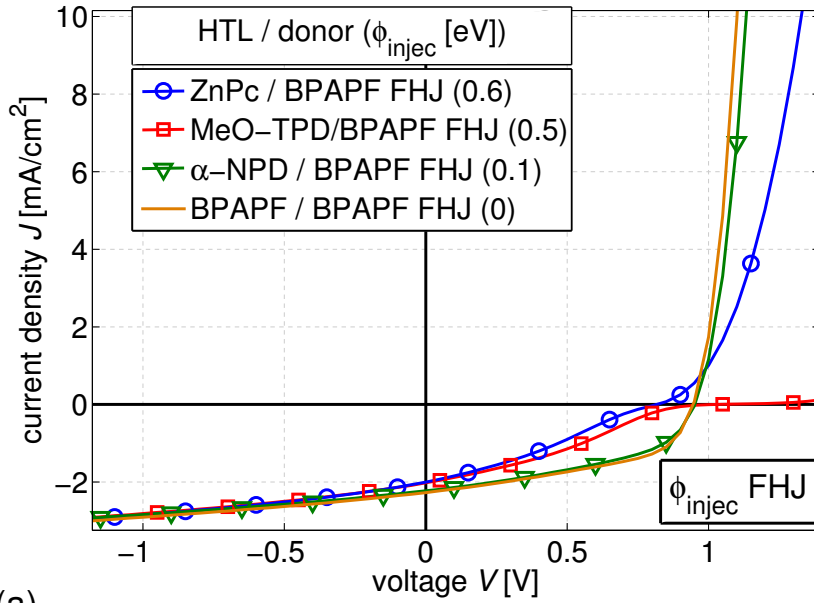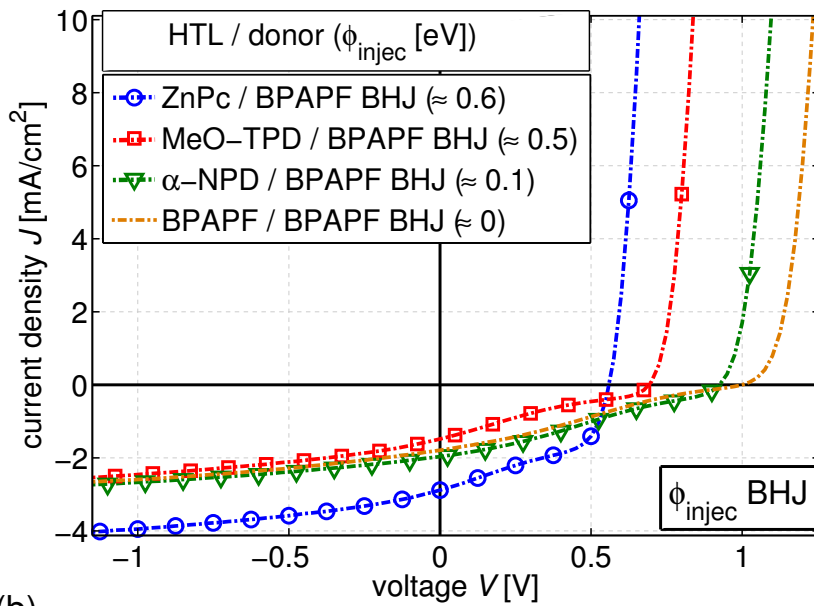
Figure 6.3: **Experimental** *J-V* curves: Injection barriers (ϕ_{injec}) for the fixed donor BPAPF and varied HTL for (a) FHJ and (b) BHJ. V_{oc} is only affected by ϕ_{injec} in case of BHJ, whereas an S-kink occurs in case of FHJ.

HTL increases the current due to absorption in ZnPc close to the blend, which generates additional excitons. They diffuse to the blend, where they are dissociated and contribute

to photocurrent. This makes ZnPc as HTL in the case of a BHJ to a special case, because photocurrent originates from two sources, the donor:C_{60} blend and the ZnPc/C_{60}(:donor) heterojunction. Additionally to the effect of the injection barrier, which is present and also observed at devices with transparent HTLs [Fig. 6.2(b)], a decrease of V_{oc} is expected.

6.2.2 Current-voltage characteristics under illumination

The effect of barriers on the J-V curve of FHJ and BHJ devices is illustrated by selected data shown in Figs. 6.3 and 6.4. The difference between FHJ and BHJ in the injection barrier case is demonstrated in Fig. 6.3 by devices with BPAPF as donor. The forward current of the FHJ is affected by a low hole injection rate caused by the barrier. The *FF* decreases due to a kink in the curve. In the BHJ [Fig. 6.3(b)], an injection limit cannot be observed. However, as already visualized in Fig. 6.2, V_{oc} decreases with increasing injection barrier for a fixed donor.

In the case of extraction barriers in FHJs [Fig. 6.4(a)], where the donor (ZnPc) is fixed and the HTL is varied, V_{oc} remains independent of the HTL. However, with increased barrier height an S-kink emerges in the fourth quadrant explaining the low *FF* seen in Tab. 6.1. The onset of forward current is shifted to higher bias voltages and defined by the HTL. The latter can be seen at the J-V curves where the HTL (BPAPF) is fixed and the donor varied [Fig. 6.4(b)]. The qualitative behavior for a BHJ (exemplary BPAPF/ZnPc shown as dash-dotted lines in Fig. 6.4(a) is the same as for a FHJ.

The observed S-kinks agree with data reported in literature, where charge transport problems at the contact (layer) are found to be the reason for the S-kink [228, 282, 295–298].

6.3 Detailed microscopic explanations

The results shall now be discussed using the simulated J-V curves shown in Fig. 6.5. All relevant input parameters for the calculation of these J-V curves can be found in Appendix B. The characteristic shape of the measured J-V curves (Figs. 6.3 and 6.4) over the whole voltage region is reproduced very well by the simulations. The absolute value of V_{oc} is difficult to predict, because it depends on several parameters including, e.g., the choice of recombination model, which is still under debate (see previous chapter and Ch. 10.3.2) [252, 255]. However, having once fixed these parameters, the position and eventual shift of V_{oc} results only from the combination of HTL and donor. Also the strength of the S-shape as a function of the most important parameter ϕ is reproduced very well, though with a slight overestimation in case of extraction barriers [Fig. 6.5(b)]. Here, allowing for disorder represented in σ, is very important and not negligible to reach a realistic extraction probability. By varying σ and mobilities a fine-tuning of the S-shape can be done. However, this is not the scope of this work. Furthermore, the sensitivity of the barrier crossing probability on ϕ, σ, and d is larger than the ranges which can be given for these parameters from independent experiments. An exemplary characterization of
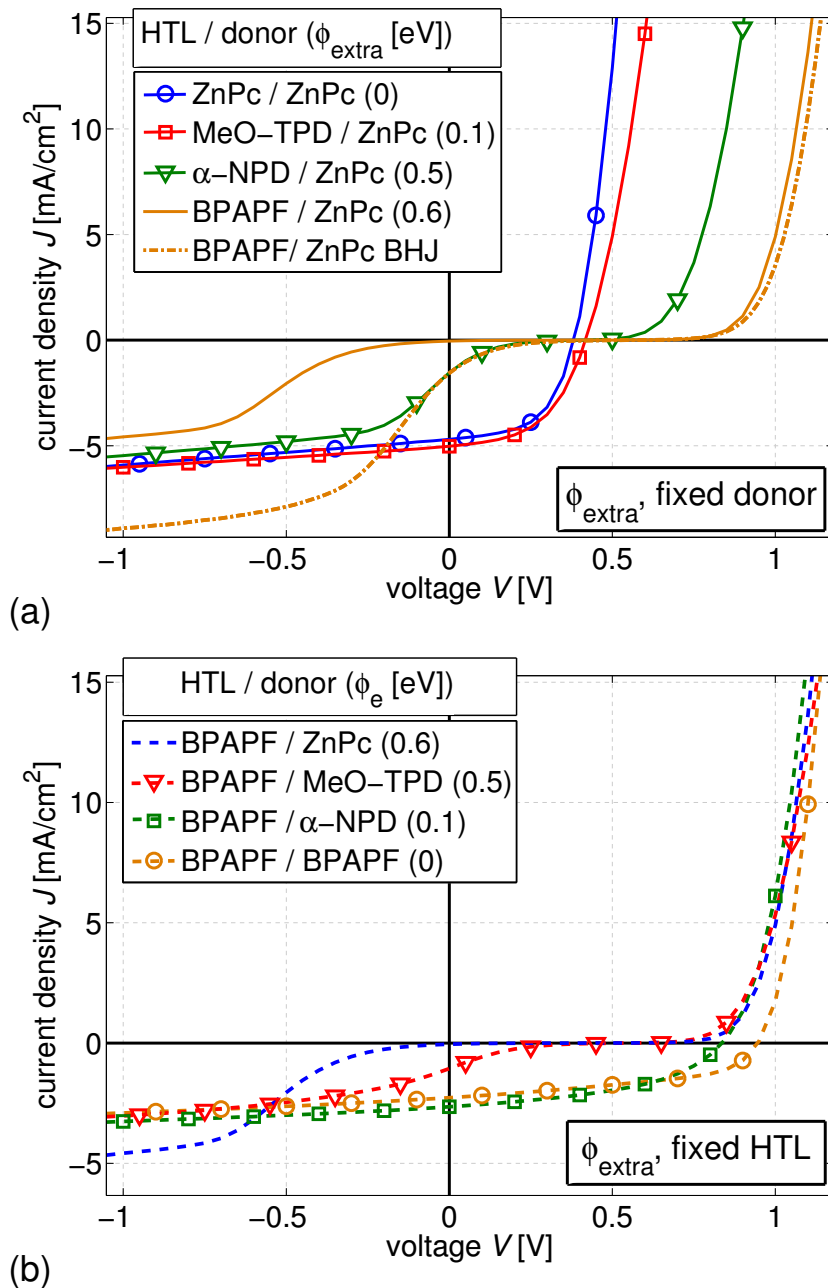
Figure 6.4: **Experimental** *J-V* curves: Extraction barriers (ϕ_{extra}) for FHJs with (a) vary-
ing HTL and fixed donor ZnPc and (b) varying donor and fixed HTL BPAPF.
In (a) data of one BHJ (dash-dotted) is also shown. The open-circuit voltage
is determined by the donor (-acceptor combination) and the onset in forward
by the HTL. Extraction barriers lead to S-kinks for FHJ and BHJ solar cells.
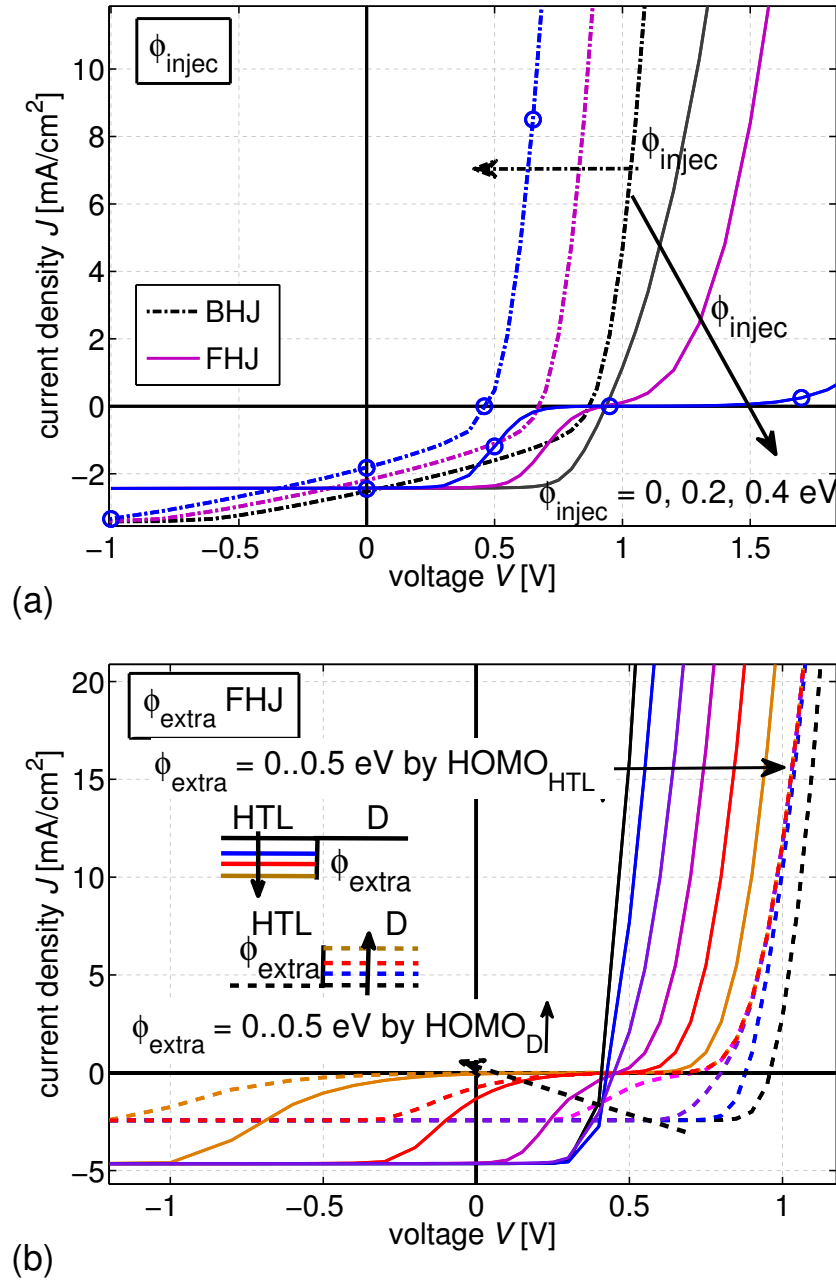
Figure 6.5: **Simulated** *J-V* curves: (a) Injection barriers (0, 0.2, 0.4 eV) at HOMO$_{\text{donor}}$ = -5.6 eV for FHJ (solid lines) and BHJ (dash-dotted). (b) Extraction barriers for FHJs with varying HOMO$_{\text{HTL}}$ and fixed HOMO$_{\text{donor}}$ at -5.1 eV (solid lines), varying donor and fixed HOMO$_{\text{HTL}}$ at -5.6 eV (dashed). The curves show good qualitative agreement with the experimental data of Figs. 6.3 and 6.4. The circles in (a) denote the points which are examined in more detail in Fig. 6.6. For details on the simulation, see Appendix B, p. 323.

the interface MeO-TPD/BPAPF is done in Ch. 6.5.1. Deviations between simulation and experimental data in the saturation regime of the photocurrent ($V_{bias} < 0\,\mathrm{V}$) result from the presence of a strong photoshunt, which is not considered in the simulation, because it is not relevant for the discussions here. Its origin will be briefly addressed in the last chapter of this thesis (Chapter 11).

The good qualitative fit of simulation to experimental data allows the results of the model to be used for an explanation of the *J-V* curves. In the following, we focus on V_{oc} as a function of the barrier type (injection or extraction) and the difference between FHJ and BHJ.

6.3.1 Injection barriers

There is a qualitative difference between FHJ and BHJ in case of injection barriers. This is illustrated by the *J-V* curves in Fig. 6.3 and 6.5(a). In the FHJ the barrier affects the shape of the *J-V* curve and hence the *FF*, whereas it affects V_{oc} in the BHJ. This leads to an S-kink with low forward currents in the case of a FHJ. For a BHJ, the *J-V* curve is basically shifted in voltage. Probably due to poor charge transport properties in the BPAPF:C_{60} blend, there are two inflection points in the fourth quadrant, which cause a slight kink independent of the HTL [Fig. 6.3(b)]. This kink is not affected by the injection barrier and it is qualitatively different to the one discussed here, where one inflection point is located at V_{oc}. The difference between FHJ and BHJ has already been observed for another material system by Uhrich *et al.* [299]. Here, this effect is explained by spatial profiles of simulated charge carrier densities and the distribution of the electric field in the device shown in Fig. 6.6.

For the FHJ, V_{oc} is independent of the choice of HTL, although the built-in field is lowered (or the charge carrier density in the HTL strongly increased) in case of injection barriers. This was shown analytically by Cheyns *et al.* [120] and is reproduced by the simulations shown. Figure 6.6(a) illustrates the reason: In the S-kink region (starting at $0.5\,\mathrm{V}$), the electric field in the donor becomes positive, although the current is still negative. This means, that current is flowing against the field. The photogenerated charge carriers are driven by diffusion, as can be seen in the charge carrier density profiles, exhibiting a diffusion gradient away from the D/A interface for voltages larger than $0.5\,\mathrm{V}$. The higher the injection barrier, the lower V_{bi} and the lower the charge carrier concentration in the donor close to the HTL/donor interface, which leads to a larger diffusion gradient away from the D/A interface. Essential for the establishment of the diffusion gradient towards the electrodes is the fact, that generation of free charge carriers from excitons happens at a spatially localized D/A interface. After exciton dissociation the generated holes are located on the donor and the electrons on the acceptor. Due to the high HOMO (LUMO) offsets at the D/A interface, holes (electrons) cannot penetrate the acceptor (donor) and flow to the Al cathode (ITO-anode). The importance of the diffusion force in excitonic FHJ solar cells has already been described by Gregg and Hanna [300].

Another useful means of illustration is the energy diagram at V_{oc}, shown in Fig. 6.7(a). The positive field in the donor and acceptor close to the D/A interface can be seen in a tilt
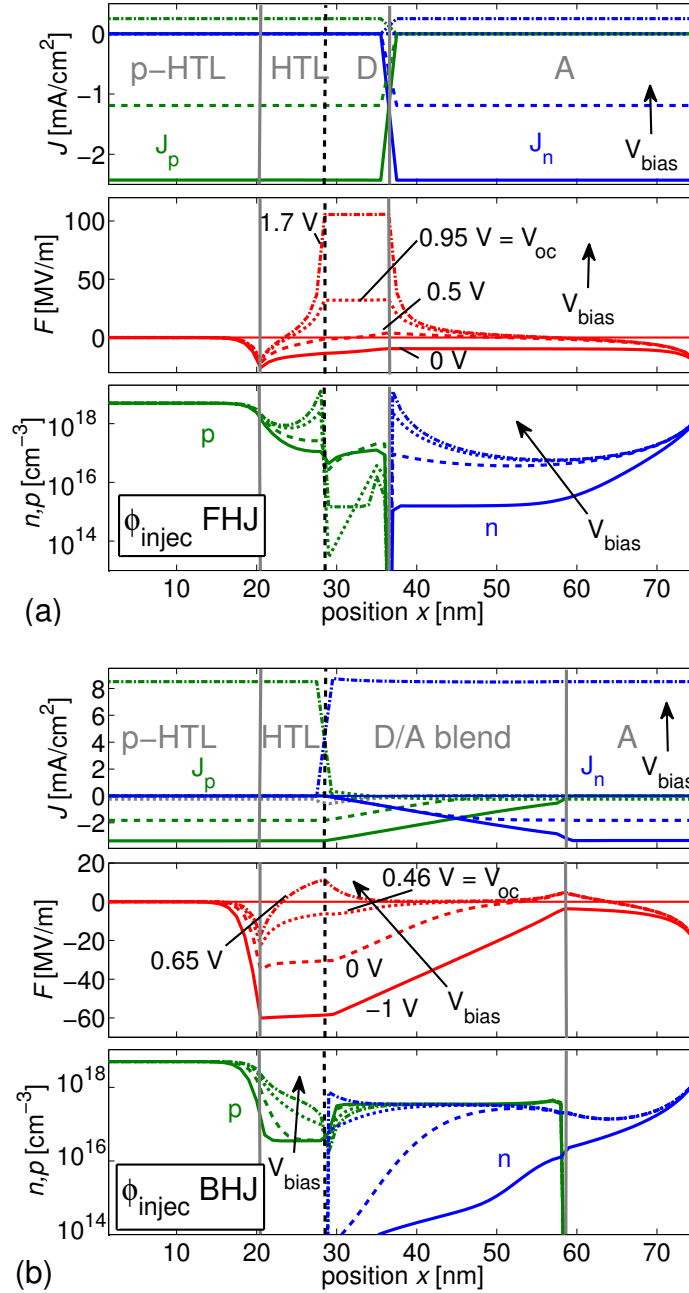
Figure 6.6: For an ***injection barrier of 0.4 eV***: Profiles of current density (J), electric field (F) and charge carrier densities (n, p) with applied bias (V_{bias}) as parameter. x denotes distance from anode, green lines (high values on p-side) show hole currents and densities, respectively, blue lines (high values in acceptor (A)) values for electrons. Field and charge carrier density profiles indicate the applied boundary conditions: constant doping concentration on p-side, thermal injection on n-side with a work function of the cathode of 4.2 eV. (a) FHJ ($V_{bias} = 0, 0.5, 0.95, 1.7$ V); (b) BHJ ($V_{bias} = -1, 0, 0.46, 0.65$ V). These values correspond to the points marked in the *J-V* curves of Fig. 6.5.
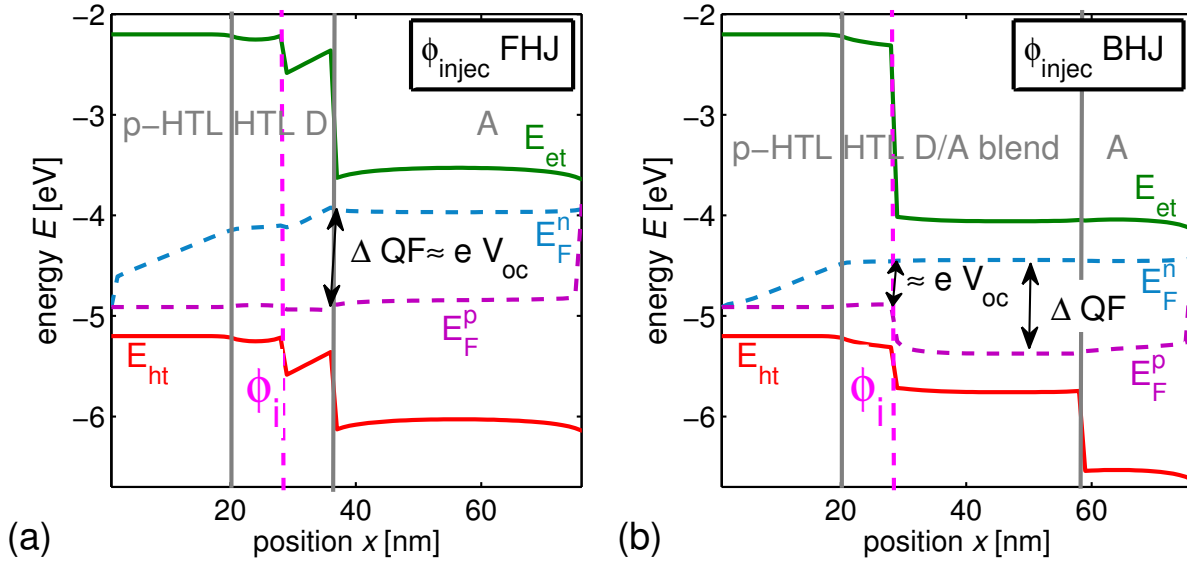
Figure 6.7: For an ***injection barrier of 0.4 eV***: Energy-level diagrams close to V_{oc} for FHJ (a, $V_{bias} = 0.95\,$V) and BHJ (b, $V_{bias} = 0.46\,$V). Shown are the charge transport levels HOMO/E_{ht}, LUMO/E_{et} (lines), and the quasi-Fermi levels (dashed) for electrons and holes. In the case of a BHJ, V_{oc} does not reach the maximum quasi-Fermi level splitting (ΔQF) due to recombination of photo-generated electrons at the HTL/blend interface.

of the energy levels which indicates an electric force on holes in the donor and on electrons in the acceptor towards the D/A interface. The quasi-Fermi levels of the majority carriers are almost constant, so that the splitting at the D/A interface equals the difference at the electrodes and hence eV_{oc}. The reason is that the D/A interface is the only position where (injected) holes and electrons are able to recombine. In forward bias [1.7 V in Fig. 6.6(a)] the current is strongly limited, because holes have to pass the barrier, where they pile up, and travel through the donor to the D/A-interface to recombine with injected electrons accumulating at the D/A interface.

The situation in a BHJ is completely different, because electrons and holes are not spatially separated in the active materials as it is the case in a FHJ, so that there is no diffusion gradient for photogenerated holes to the anode and electrons to the cathode. Figure 6.6(b) demonstrates that the photocurrent is collected over the whole blend layer at -1 V and 0 V. As soon as the field gets positive (0.65 V), a large current of charges injected from the electrodes is flowing in forward direction. The current profile shows that hole injection over the barrier is not necessary, because the current through the blend is driven by electrons, which recombine with holes at the HTL/blend interface. Due to the lower built-in field, the extraction force for photogenerated charge carriers is lower compared to a device without barrier and the same HOMO of the donor. This leads to a lower V_{oc}

and an onset of forward current at lower applied bias. The HOMO level of the donor gets unimportant and the J-V curve follows mainly the curve of an HTL/acceptor solar cell. This is in contrast to the FHJ, where the diffusion gradient compensates for the low V_{bi} and counteracts the field close to V_{oc}. The situation for a BHJ at V_{oc} is depicted in the energy diagram in Fig. 6.7(b). The quasi-Fermi level splitting in the blend is reduced towards the HTL/blend interface, because the recombination probability of electrons with holes at the HTL/blend interface is high due to the presence of holes delivered by the anode. This effect is comparable to a high surface recombination (Fig. 2.12, p. 32) discussed in Ch. 2.4. Thus, eV_{oc} as difference between the hole quasi-Fermi level at the cathode and the electron quasi-Fermi level at the anode does not reach the maximum quasi-Fermi level splitting in the absorber.

The discussed difference between FHJ and BHJ is not caused by the active layer itself. This means, it is not a property of the blend in comparison with a planar heterojunction. The main issue is the device structure. As long as it allows contact of electrons and holes only at the D/A interface, the J-V curve of a BHJ will show the same qualitative characteristics as the one of a FHJ. Avoiding contact of electrons and holes at the electrodes could be achieved by choosing selective contacts, which allow only one species of charge carriers to pass. This was demonstrated theoretically in the previous chapter. There, V_{oc} of a BHJ with selective contacts was independent of ϕ and showed an S-kink (cf. Fig. 5.9, p. 161). A selectivity can easily be realized by a combination of FHJ and BHJ, where the BHJ is sandwiched between neat layers of donor and acceptor [177, 178]. This structure avoids direct contact of the acceptor with a misaligned HTL or metal electrode and profits from the higher photocurrent of a BHJ. If the energy levels (HOMO of HTL to donor, LUMO of electron transport layer to acceptor) are well aligned, the p-i-n structure with wide-gap transport layers guarantees this property of selective contacts. This was already discussed in the theory chapter (Ch. 2.5.3) and the experimental section (Ch. 3.5.1).

6.3.2 Extraction barriers

In the case of extraction barriers, there is no qualitative difference between BHJ and FHJ. As an extraction barrier does not provide an additional path of recombination as it is the case for the injection barrier in a BHJ, V_{oc} is independent of the HTL. It is defined by the quasi-Fermi level splitting at the D/A interface, independent of the presence as blend or bilayer. The strong kink in the curves of Figs. 6.4 and 6.5(b) is due to the hindered extraction of photogenerated holes at the HTL/donor interface. The holes pile up in front of the barrier and require a high reverse voltage to be extracted.

The dependence of the onset of forward current on the HOMO of the HTL can be explained as follows: When discussing the MIM picture in Ch. 3.3.4, we found that forward current flows as soon as the applied bias reaches a value, where the diffusion current exceeds the negative drift current resulting from V_{bi}. The bias at which this point is reached depends only on the charge carrier concentrations in the layers adjacent to the electrodes and V_{bi}. When shifting the HOMO of the HTL downwards, either V_{bi} increases, if the doping concentration (and hence the distance between the Fermi level and the HOMO) stays the

same, or the charge carrier density decreases, if the work function remains constant. Both effects lead to the same shift of the onset of forward current to higher voltages. Thus, only the position of the HOMO of the HTL defines the current onset independent of the actual position of E_F. This allows reliable calculations without knowing the exact amount of active dopants in the HTL.

6.3.3 Comparison between flat and bulk heterojunction

It is often stated that V_{oc} of a blend is lower than V_{oc} of a flat heterojunction comprising the same materials [301]. As can be seen from Tab. 6.1, this is not necessarily the case. It holds for injection barriers, which indicates that often injection barriers are present. Our data even shows that V_{oc} in blend layers can be higher. In combination with the strength of the S-shape, there is evidence that the HOMO level in the blend can shift downwards, especially for ZnPc. A possible reason could be a lower polarization energy due to C_{60} present in the neighborhood of the ZnPc molecules in the blend. An example is shown in Fig. 6.4(a), where the current in the S-kink region of the BHJ with BPAPF (HOMO -5.6 eV) as HTL follows the curve of the FHJ with α-NPD (HOMO -5.5 eV) as HTL, implying a comparable extraction barrier. Consequently, the HOMO of ZnPc in the BHJ is supposed to be shifted 0.1 eV downwards compared to its value in ZnPc as neat layer, which fits to a V_{oc} of the BHJ which is 150 mV higher. Certainly, other parameters influencing V_{oc} change in the blend as well, like recombination probabilities (in Langevin theory e.g. by modified mobilities). Therefore, detailed investigations of this effect will be a major part of Chapter 8, where the effect of the mixing ratio of the blend ZnPc:C_{60} is examined.

The low FF in BHJs compared to FHJs can be attributed to two effects: first, to a lower mobility in the blend due to an unfavorable morphology; second, to the fact that even if the HTL consists of the same material as the donor in the blend, their HOMO levels may not be completely adjusted. This relativates the statement of the previous section that a BHJ sandwiched in between neat donor and acceptor layers is a priori the optimum structure. From Tab. 6.1 and other experiments with high performance solar cells and from simulations, a small extraction barrier of around 0.1 eV seems to be the optimum case. Under this condition extraction works still well and recombination between holes on the HTL and electrons on the acceptor is hindered and V_{bi} high.

6.4 Current-voltage curves in a logarithmic plot

To further discuss the effect of barriers on the J-V curve, logarithmic plots are shown in Fig. 6.8 which visualize the effect of barriers also on dark J-V curves. BHJs [Fig. 6.8(b)] with injection barriers show similar (exponential) slopes in forward and confirm the idea of simply shifted J-V curves due to the higher lying HOMO of the HTL. This slope is governed by the recombination processes within the blend (discussed in Chapter 10) and is not influenced by the HTL. Injection barriers in combination with FHJ [Fig. 6.8(a)] reveal that the slope in the exponential region in forward is strongly affected by the barrier. Con-
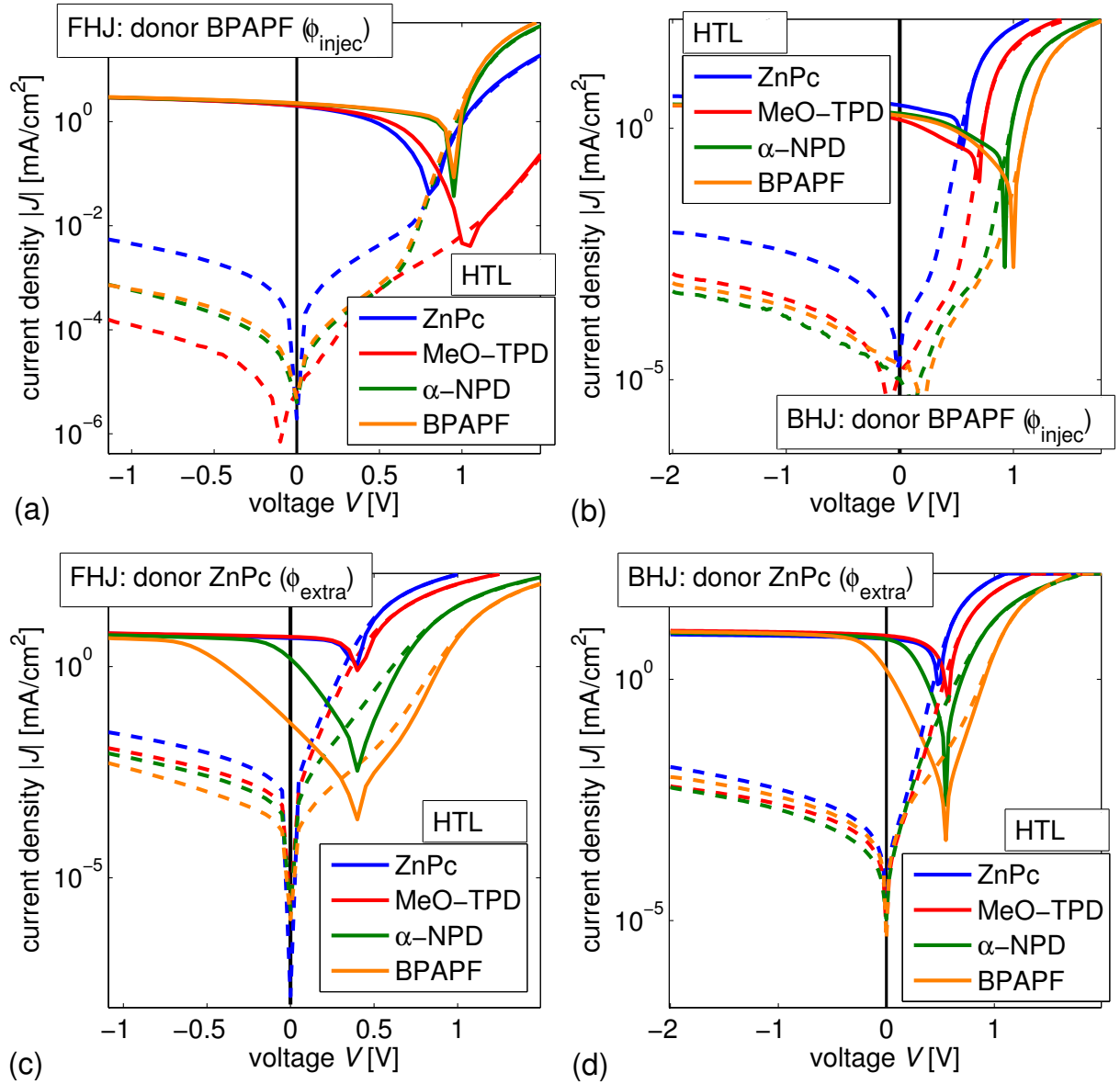
Figure 6.8: **Experimental** *J-V* curves in a logarithmic current scale. Dark curves are dashed. (a + b) ***Injection barrier*** (ϕ_{injec}) devices with fixed donor BPAPF and varied HTL for (a) FHJ and (b) BHJ. (c + d) ***Extraction barrier*** (ϕ_{extra}) devices with varying HTL and fixed donor ZnPc in (c) FHJ and (d) BHJ. In some cases the dark current at $0\,\mathrm{V}$ is not 0 due to measurement inaccuracies for current densities lower than $\approx 10^{-5}\,\mathrm{mA/cm^2}$. Both injection and extraction barriers change forward and reverse currents and make the application of a diode ideality factor difficult.

sequently, the ideality factor n_D is affected if the curves are fitted by the Shockley equation (Eq. 2.41). This means that n_D does not reveal any information about recombination at the D/A interface. Its value is governed by the barrier and can exceed the physical range between 1 and 2 given by the type of recombination (cf. Ch. 3.3.5, Eq. 3.17, p. 71).

For extraction barriers [Fig. 6.8(c+d)] the slope in the exponential region and hence n_D are modified by barriers as well. Consequently, stating ideality factors for organic solar cells is very questionable as barriers at the electrodes can hardly be excluded. This might be an explanation for reported values of n_D larger than 2. In several curves there are additional features visible between 0 and 0.5 V, which are partly due to a parallel resistance if they show a comparable current at the same reverse voltage. Others probably show the overlap of several effects due to barrier crossing and the usual diffusion current effect. The photocurrent in reverse in the case of extraction barriers shows a voltage dependence which is close to exponential [straight lines in Fig. 6.8(c+d)] due to the thermally activated barrier crossing of photogenerated charge carriers.

6.5 Detailed analysis of the material combination MeO-TPD and BPAPF as donor and hole transport layer

For further investigations, we restrict ourselves to one donor/HTL combination. Devices comprising the hole-transporting molecules MeO-TPD and BPAPF are chosen because they show a significant HOMO offset and form amorphous, closed thin layers. Data of this material combination only is shown for reasons of clarity, although other material combinations have been examined in more detail as well during this work. They indicate that the conclusions of this section are of general validity for the description of barrier effects. Furthermore, we discuss FHJ only. BHJ show an additional degree of freedom which is the mixing ratio. This affects also the energy levels and is separately investigated in Chapter 8.

6.5.1 The interfaces BPAPF/MeO-TPD and MeO-TPD/BPAPF measured by photoelectron spectroscopy

For a detailed analysis of organic-organic interfaces the rough estimation of vacuum level alignment may not be sufficient and the (within an experimental error of ± 0.05 eV) exact barrier heights are required. Therefore, ultraviolet photoelectron spectroscopy (UPS) is applied[2]. The investigated samples consist of stacks which are as close as possible to the ones employed in the solar cell. The reason is that ϕ can be modified by interface dipoles, pinning effects, the choice of substrate, and the sequence of layer deposition. The selected stacks are supposed to be the optimum regarding comparability to the real device

---

[2]Measurements performed by Max Tietze, IAPP
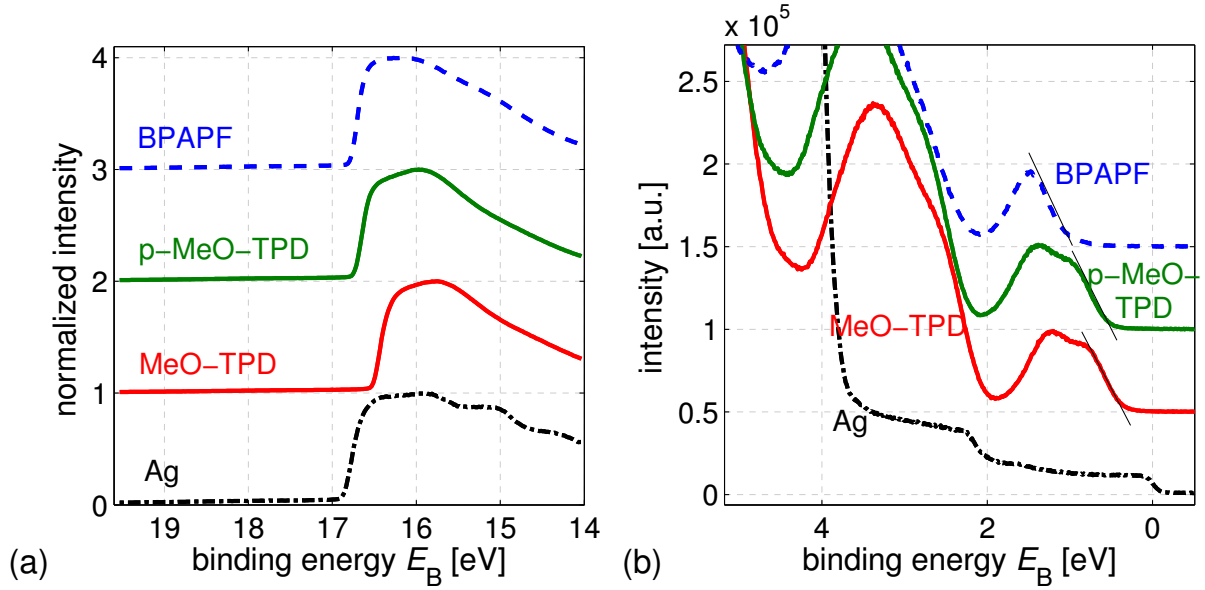
Figure 6.9: Subsequently measured UPS spectra of the sample Ag/p-MeO-TPD(7)/MeO-TPD(5)/BPAPF(3 nm) (a) High-binding-energy cutoff, defining the vacuum level and (b) low binding energy region giving the HOMO. The lines at the HOMO onset visualize the determination of the IP as intersection of these lines with the base line. The reference energy ($E_{\mathrm{B}} = 0$) is the Fermi energy of the silver substrate. The data of this figure is used to draw the energy-level diagram in the next figure.

and measurement restrictions to layer thicknesses due to charging effects during the UPS measurements.

Samples comprising both layer sequences, MeO-TPD/BPAPF (injection barrier) and BPAPF/MeO-TPD (extraction barrier) are prepared. The injection barrier sample consists of Ag/p-MeO-TPD(7)/MeO-TPD(5)/BPAPF(3). Figure 6.9 shows four UPS spectra. They are measured subsequently during breaks in the evaporation procedure of the stack. As UPS is a surface sensitive method, it probes the density of occupied valence states of the topmost layer. MeO-TPD and BPAPF show several molecular orbital peaks [Fig. 6.9(b)], where the one with lowest binding energy (E_{B}) is the HOMO. This graph is also shown to demonstrate the extraction of the IP or E_{ht} from UPS data. In this work, the IP is defined as onset of the HOMO which is determined by attaching a tangent to the turning point of the spectrum and taking its crossing point with the zero line. A shift in the high energy cut-off [Fig. 6.9(a)] represents a shift of the vacuum level E_{Vac}.

Knowing E_{Vac} and the IP allows us to draw the energy diagram shown in Fig. 6.10(a). It has to be noted that this energy diagram with the spatial coordinate as abscissa does not represent the distribution of the potential within the whole layer(s). It is the potential at the surface when the layer (stack) was x nm thick. The Fermi level is close to the HOMO in

the p-doped MeO-TPD layer due to the high doping concentration. The values of the IPs of MeO-TPD and BPAPF reproduce the known values of 5.1 eV and 5.6 eV. The injection barrier is 0.5 eV as expected.

The same investigation is done for an extraction barrier sample with the structure Ag/p-
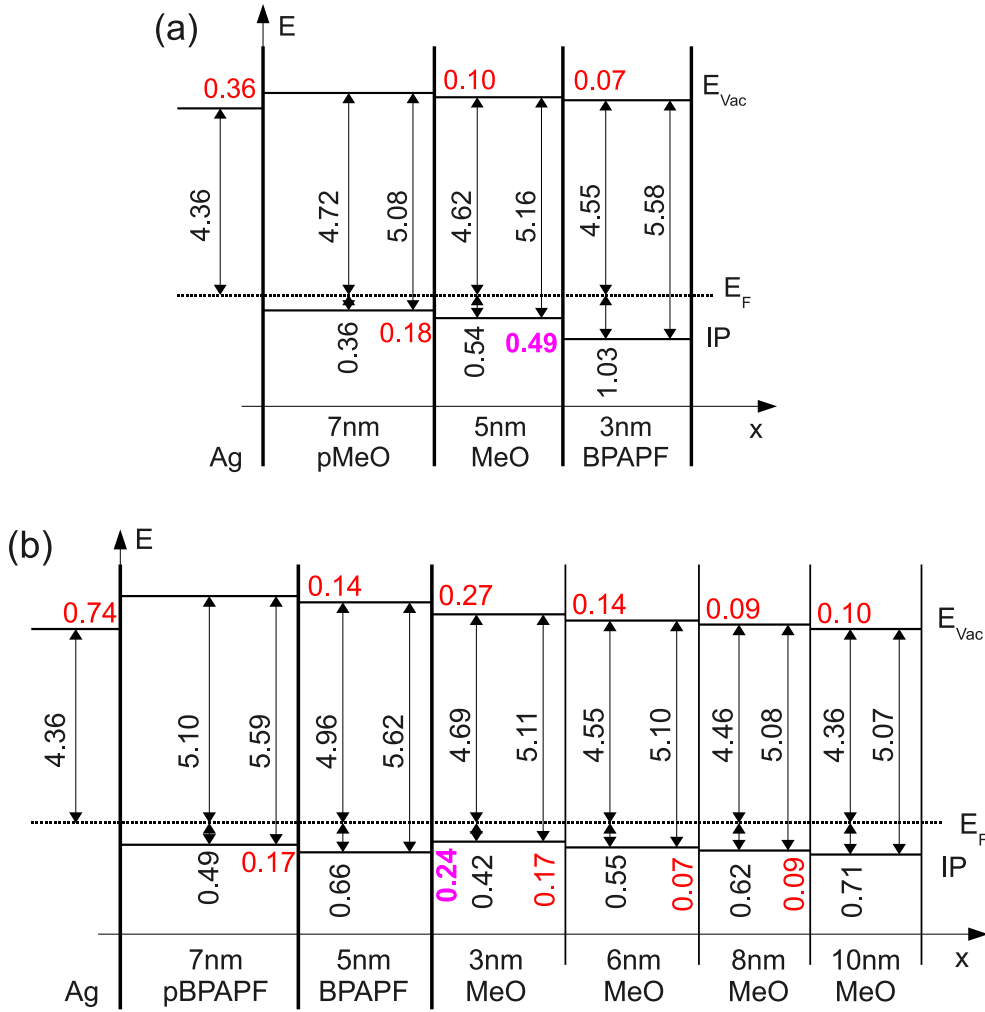
Figure 6.10: Energy level alignment extracted from UPS data. (a) ***Injection barrier*** sample with $\phi_{\mathrm{injec}} \approx 0.5\,\mathrm{eV}$. (b) ***Extraction barrier*** sample with $\phi_{\mathrm{extra}} \approx 0.3\,\mathrm{eV}$. This value is estimated since the distance between IP and E_{F} increases for an increased MeO-TPD thickness and tends towards its value for intrinsic MeO-TPD. The lower value of ϕ_{extra} is due to the interface dipole (0.27 eV) seen in the shift of the vacuum level. Depositing only 1 nm might give a more precise value of ϕ_{extra}, but is experimentally difficult. Data analysis and sketch, M. Tietze, IAPP.
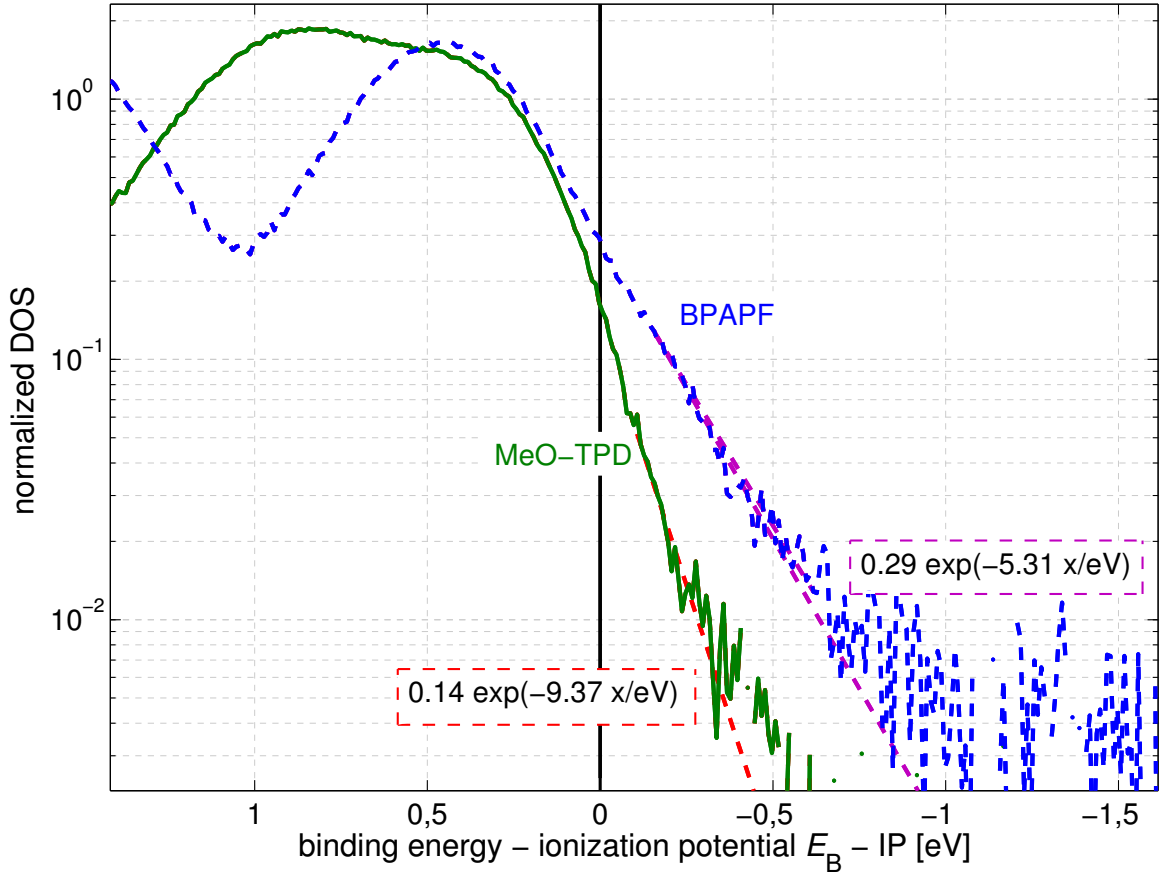
Figure 6.11: UPS measurement data of the normalized HOMO density of states (DOS) with the IP of the respective material as reference (binding energy $E_{\mathrm{B}} = 0$). Exponential tails (red dashed lines) are visualized by fits to the measurement data below the energy gap. The broader tail states for BPAPF might explain the larger distance between Fermi energy and HOMO seen at the doped layers in the previous figure.

BPAPF(7)/BPAPF(5)/MeO-TPD. The energy level alignment is shown in Fig. 6.10(b). The estimated value of $0.3\,\mathrm{eV}$ for the extraction barrier is significantly lower than expected. It is accompanied by a dipole at the BPAPF/MeO-TPD interface. Interestingly, the distance between Fermi level and IP changes with layer thickness. This produces an uncertainty in the value of the extraction barrier, as the first measurement is performed at a MeO-TPD thickness of $3\,\mathrm{nm}$. Using thinner layers is experimentally difficult, because the measured spectrum would consist of an overlap between the HOMO of MeO-TPD and BPAPF. Therefore, the determination of the extraction barrier becomes very difficult. However, it is known that the Fermi-level of MeO-TPD cannot come closer to the IP than $0.35\,\mathrm{eV}$ [156], which limits ϕ_{extra} to $0.31\,\mathrm{eV}$. Such a pinning of E_{F} at a certain distance

from the HOMO is commonly observed at metal/organic contacts and is attributed either to tail states or to polaronic levels as discussed in Ch. 3.4.2. The data of Fig. 6.10(b) and of doped MeO-TPD [156] indicate that the latter can be excluded because the pinning occurs at an intrinsic organic-organic interface. Screening is not expected to be altered as the dielectric constants of two organic materials are in the same range in contrast to the dielectric constants of metal and organic. Chemical reactions at the interface can be excluded as well because the reversed stack sequence [Fig. 6.10(a)] does not show a significant dipole at the MeO-TPD/BPAPF interface. In conclusion, the pinning is most likely due to a significant amount of (trapped) states within the energy gap. These traps can also explain the increased distance between IP and E_F for an increased MeO-TPD thickness. If the layer was totally intrinsic, no energy level shift is expected. A shift, i.e., energy level bending, can only be caused by space charge, which could be provided by trapped holes in this case.

The logarithmic plots of the DOS in Fig. 6.11 visualize these tail states at energies above the IP. The reference energy (abscissa 0) is the value of the IP obtained for MeO-TPD and BPAPF from the onset in the linear plot [Fig. 6.9(b)]. The DOS is normalized by fitting a Gaussian to the BPAPF peak and setting the area of this Gaussian to 1. If one assumes that this area is equal to the density of molecules, this area represents a total amount of states in the order of $10^{21}\,\mathrm{cm}^{-3}$. The tails show that there can be a significant amount of charge carriers located at energies between 0 and 0.5 eV above the hole transport level. The signal at larger energies is limited by the resolution of UPS. One can fit the tails by an exponential function. According to these fits there are states in the order of $10^{17}\,\mathrm{cm}^{-3}$ at an energy of 1 eV above the HOMO onset. These tail states are broader for the BPAPF and could be the reason for the larger distance between the IP and E_F for the p-doped BPAPF compared to the p-doped MeO-TPD (Fig. 6.10).

Instead of using a Gaussian DOS, one might directly apply the UPS DOS in the simulation. However, one major problem arises: These tail states are very unlikely to describe the energetic position of free charge carriers for two reasons: First, the large number of these tail states for low energies would lead to a very low V_{oc} in a solar cell under the assumption of realistic recombination constants and charge carrier densities within the device. Second, the charges in the tail are less mobile than the ones close to the IP. This means that a mobility model is required which describes the dependence of the mobility on charge carrier densities in an exponential DOS comparably to the Pasveer model [85] for a Gaussian DOS. Another option would be the definition of a mobility edge. A recent publication by Kirchartz *at al.* [128] supports that these tail states are rather immobile and a source of trap-assisted recombination.

Due to these reasons we maintain the approach of the simulation taking the IP as transport level for free charges which is broadened by a Gaussian with a small σ representing the effect of disorder on charge transport.
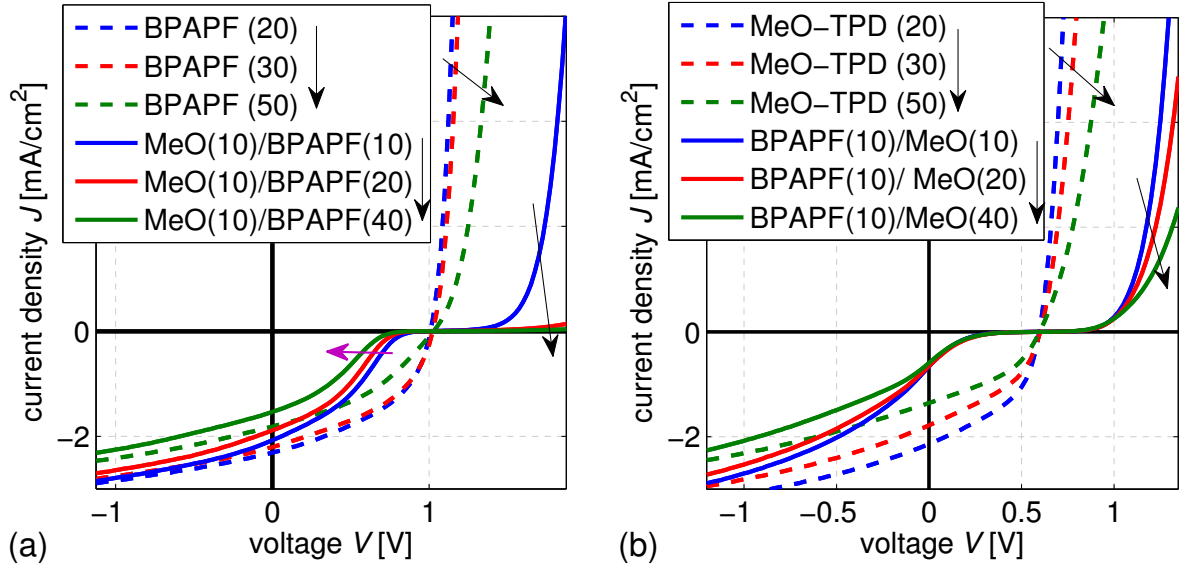
Figure 6.12: **Experimental data**: Thickness (given in nm by the numbers in brackets in the legend) variation of the donor of a device with p-HTL (20 nm)/i-HTL (10 nm)/donor (x nm)/C$_{60}$ (40 nm)/BPhen/Al. Dashed lines show the case where HTL = donor and solid lines the barrier case: (a) **_Injection barrier_** samples with HTL MeO-TPD and donor BPAPF. (b) **_Extraction barrier_** samples with HTL BPAPF and donor MeO-TPD. The S-kink is only affected in case of injection barriers.

6.5.2 Dependence of the *J-V* curve shape on layer thicknesses

The dependence of the S-kink on HTL or donor layer thickness gives information about the role of the electric field or the state of relaxation of photogenerated charge carriers when crossing the interface barrier. Furthermore, it allows a discrimination between injection and extraction barriers.

Donor thickness

At first, a thickness variation of the donor is studied. *J-V* data of devices with the donor BPAPF are shown in Fig. 6.12(a) and MeO-TPD in Fig. 6.12(b).

An increased donor layer thickness should predominantly influence two processes: First, charge transport in the donor: A higher thickness results in a higher series resistance effect due to a low hole mobility. This effect is present independent of the barrier. It can be seen for both materials at the dashed *J-V* curves, where the HTL is equal to the donor. In this case the *FF* and the forward current decrease with donor layer thickness.

Second, a higher thickness of an intrinsic layer reduces the field within the device at a given value of the applied voltage. Therefore, it gives information on the field-dependence of barrier crossing. In the case of injection barriers [Fig. 6.12(a)], a scaling of the strength
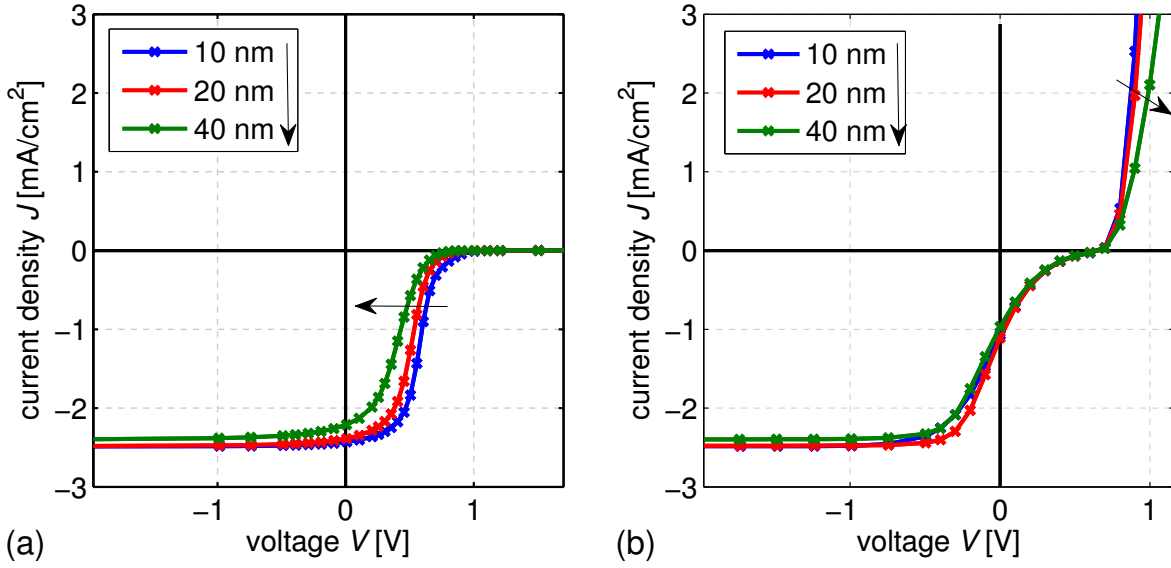
Figure 6.13: **Simulation data**: Variation of the donor layer thickness for (a) an **_injection barrier_** of $0.5\,\mathrm{eV}$ and (b) an **_extraction barrier_** of $0.3\,\mathrm{eV}$. As in experiment, the S-kink is only affected in case of injection barriers. All input parameters for the simulation can be found in Appendix B, p. 325.

of the S-kink with donor thickness is observed. This is also reproduced by simulation data in Fig. 6.13(a). The reason is an increased recombination at the D/A interface due to a lower field and lower diffusion gradient there caused by a thicker intrinsic donor layer. Additionally, forward current, which requires an injection of charges over the barrier, is strongly affected by thicker donor layers.

However, the strength of the S-kink is independent of donor thickness in the case of an extraction barrier. This holds for experiment [Fig. 6.12(b)] and simulation [Fig. 6.13(b)] and can be explained as follows. We stated and will further discuss in Ch. 8.3 that photogenerated holes pile up in front of an extraction barrier. This means that the potential mainly drops over the intrinsic HTL because the piled-up charges screen the field in the donor. Thus, the field at the interface HTL/donor, which determines the extraction current, is mainly independent of donor layer thickness. The independence of the extraction-barrier S-kink of donor layer thickness reveals another important finding: The possibly existent excess energy of photogenerated holes does not play a role. One might have assumed that the free charge carriers generated at the D/A interface are injected into their (Gaussian) DOS at elevated energies and relax according to the Bässler model after several hops until they reach their transport energy. Bässler [79] showed that the relaxation time for a charge carrier in a Gaussian DOS with σ in the range of several $k_\mathrm{B}T$ is in the order of 10 to 1000 times the dwell time of a charge carrier on a site. Therefore, a complete relaxation of charge carriers requires many hops. This would mean that photogenerated holes possess a relatively large energy when they reach the extraction barrier in the case of thin donors.
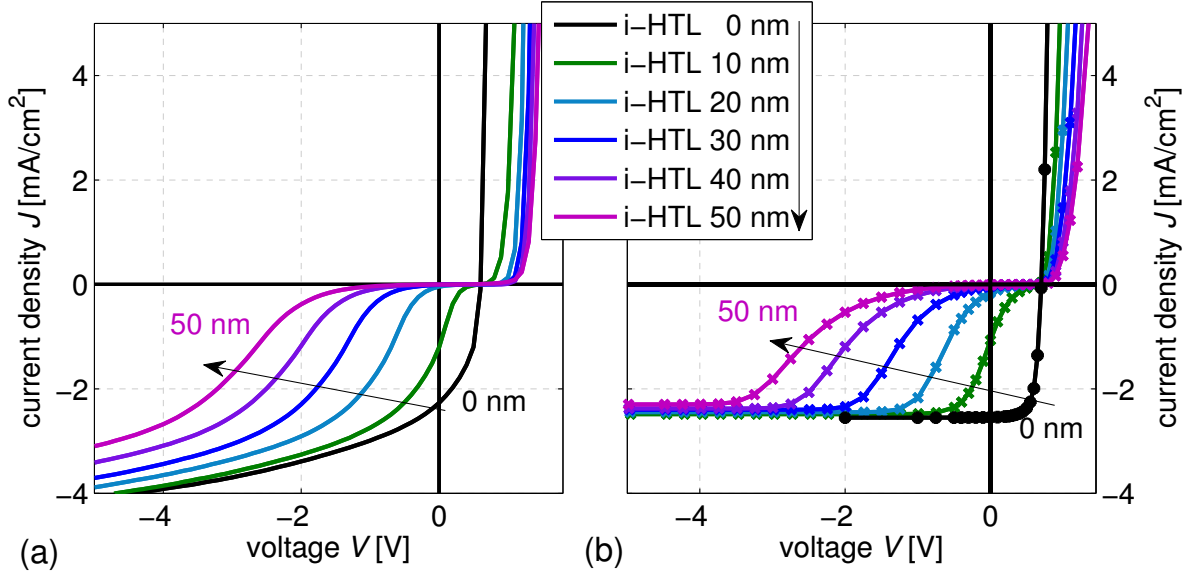
Figure 6.14: Thickness variation of the HTL of an ***extraction barrier*** device with p-BPAPF $(20\,\text{nm})$/BPAPF $(x\,\text{nm})$/MeO-TPD $(10\,\text{nm})$/C_{60} $(40\,\text{nm})$/BPhen/Al. (a) **Experimental data** and (b) **simulation data** with a discrete ϕ_{extra} of $0.3\,\text{eV}$ and hopping distance $d = 1\,\text{nm}$. Both show a significant influence of the HTL thickness on the S-kink. The remaining input parameters for the simulation can be found in Appendix B, p. 325.

This should result in an increased barrier-crossing probability and thus a reduction of the S-kink for lower thicknesses. As this is not observed, one could come to several conclusions: Either σ is negligibly small, or the relaxation time is much faster, or the charge carriers are already generated at the lowest energy possible, because they result from split CT states. Although this question cannot be completely answered here, we can be sure that the modeling assumption of a relaxed distribution at the HTL/donor interface is valid.

Intrinsic HTL thickness

We discussed that the field at the donor/HTL interface is not significantly influenced by the thickness of the donor in the S-kink voltage range in the case of extraction barriers. However, a variation of the thickness of the intrinsic HTL is expected to influence the field. *J-V* data of such a variation are shown in Fig. 6.14(a), which demonstrates that the strength of the S-kink increases significantly with the layer thickness of the intrinsic HTL. This is compatible with the fact that the forward current in the injection barrier case scales with the donor layer thicknesses. It is always the layer behind the barrier, where the voltage mostly drops because charge carriers pile-up in front of a barrier forming a space charge and are missing in the layers after the barrier. The simulation data in Fig. 6.14(b) show excellent agreement with experiment. It is not necessary to assume a broadening of the DOS. Only a hopping distance of $1\,\text{nm}$ is selected. However, a σ in the range of
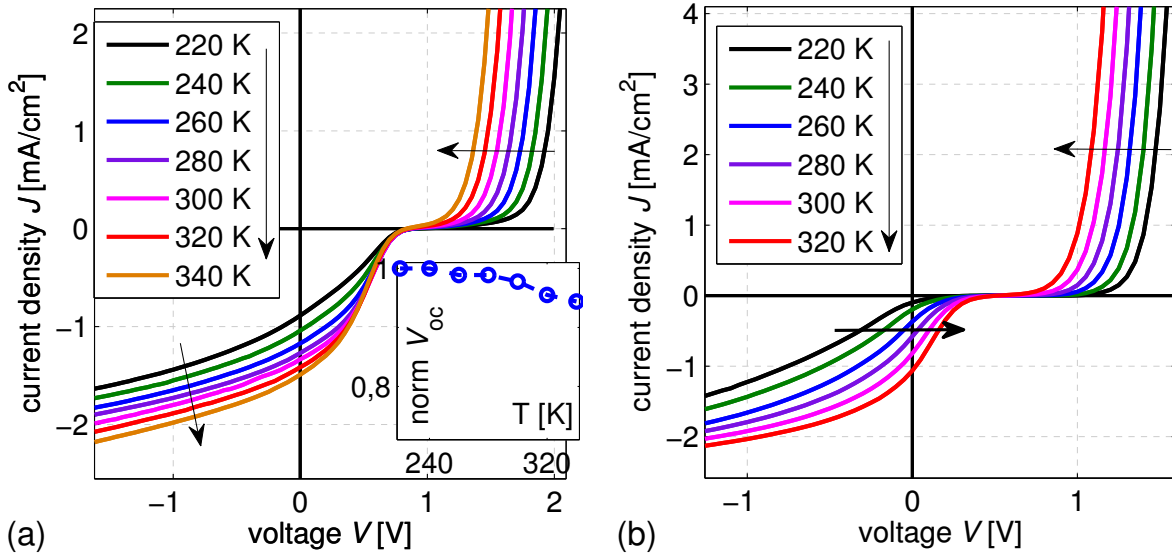
Figure 6.15: **Experimental data**: Temperature dependence of the *J-V* curve for (a) an injection (.../MeO-TPD(10)/BPAPF(10)/...) and (b) an extraction barrier (.../BPAPF(10)/MeO-TPD(10)/...) device. In case (a) the S-kink is relatively independent of temperature whereas it is shifted in case (b).

some $10\,\mathrm{meV}$ leads to comparable results. Consequently, charges are located at a relatively discrete transport level if the value of $0.3\,\mathrm{eV}$ for ϕ_{extra} is correct. Whether d or σ is more important for the barrier crossing probability could not be clarified despite the thickness dependent series. A clarification would require further investigations in comparison with temperature-dependent data which allow a discrimination between processes which are based on tunneling or thermally activated jumps. Further knowledge of the interactions and transfer integrals between the two molecules would be essential for a detailed quantitative discussion.

6.5.3 Dependence of the S-kink on temperature

According to Eq. 4.65 barrier crossing is temperature activated. Consequently, a temperature study is performed to further prove the correct description of the barrier crossing by the model. Therefore, temperature dependent *J-V* data of an injection and extraction barrier device are recorded in the range of 225 to $340\,\mathrm{K}$[3]. Figure 6.15 shows the results. The main difference between an injection (a) and extraction (b) barrier is that the injection barrier S-kink is not affected by the temperature T whereas the S-kink of the extraction barrier becomes more pronounced with lower T. The inset shows that V_{oc} increases sublinearly with decreased temperature, which might be caused by a broad DOS (cf. Fig. 5.17, p. 171). The photocurrent decreases with lower temperatures independent of applied bias

---

[3]Measurements done by Johannes Widmer, IAPP, at a cryostat setup described in Ref. [249].
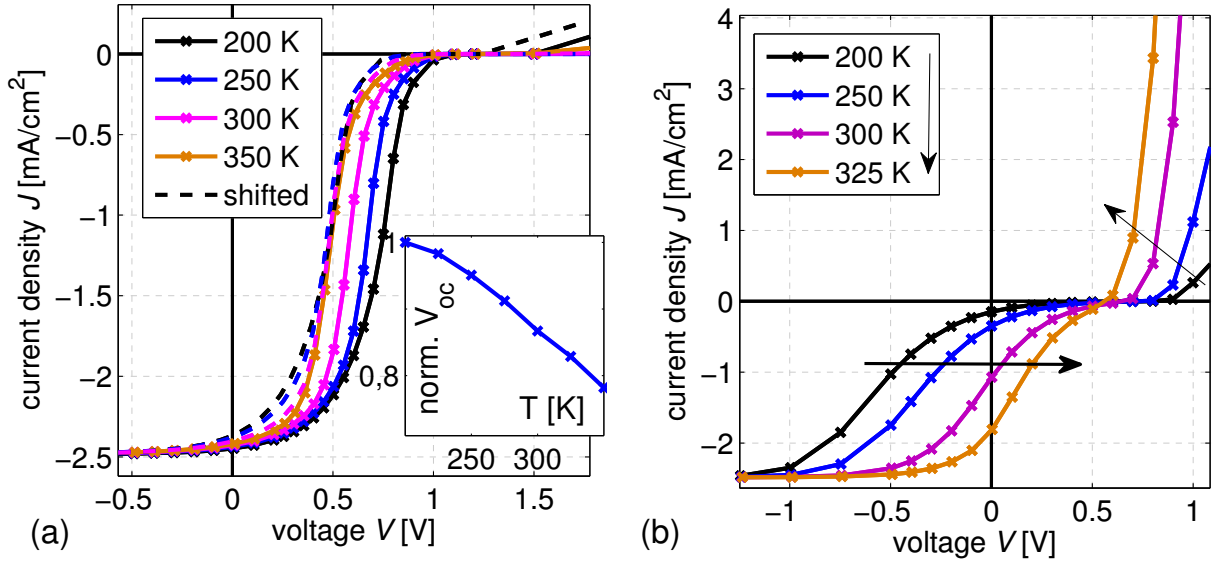
Figure 6.16: **Simulation data**: (a) ***Injection barrier***: The S-kink is shifted to lower voltages for higher temperatures due to a decrease of V_{oc} with T (inset). Dashed lines show the *J-V* curves, where the voltage is corrected for the difference in V_{oc} compared to V_{oc} at $350\,K$. These curves coincide like in experiment, where V_{oc} barely changes with T. (b) ***Extraction barrier***: The S-kink is less pronounced for higher T as observed in experiment.

voltage (curves are parallel in the third quadrant). This is an indication for an exciton diffusion length L_D which depends on temperature. If L_D increases with temperature, the saturated photocurrent scales with T. Changes in charge carrier mobilities do not seem to dominate for these devices in the measured temperature range.

The experimental curves are compared to simulation data where T is varied. The results are shown in Fig. 6.16. First, the injection barrier case is discussed [Fig. 6.16(a)]. It is observed that the S-kink does not significantly change its shape and is shifted to higher voltages with decreased T. At first glance, this contradicts the experimental data. The reason for this discrepancy is the strong increase in V_{oc} with decreased T in the simulation according to Eq. 5.8. However, V_{oc} is only slightly changed in the experimental data of Fig. 6.15. This weak temperature dependence of V_{oc} of a FHJ is not yet well-understood. It implies that Eq. 5.8 requires some modifications due to the fact that electrons and holes are located on different sides of an interface. However, Eq. 5.8 shows validity for BHJs [249], which is a clear indication that the assumption of a BHJ as new effective medium describes the physics even better than the idea of a BHJ as a folded FHJ. This means that in a BHJ other processes are dominating. As this work does not focus on the temperature dependence and on the detailed processes at a FHJ, we do not discuss this effect further.

To still visually compare the effect of T on the strength of the S-kink, we change the point of reference regarding the voltage. The correct point of reference to evaluate the strength

of an S-kink is V_{oc}. Therefore, the simulated J-V curves are shifted by the V_{oc} offset caused by the temperature. The dashed lines in Fig. 6.16(a) show shifted J-V curves with respect to V_{oc} of the J-V curve with $T = 300$ K. The S-kinks coincide, which is in agreement with the experimental data, where a correction for the V_{oc} offset is not necessarily due to the weak dependence of V_{oc} on T. The reason for the independence of the S-kink strength on temperature is found in the role of diffusion. A higher T increases diffusivity and therefore the diffusion current which is dominant in the S-kink region. However, a higher T also increases charge carrier injection over the injection barrier and thus the hole concentration in the donor at the HTL/donor interface. This higher concentration means a decreased concentration gradient from the D/A interface to the HTL/donor interface and thus a decreased diffusion force. In total the effects cancel each other so that the diffusion force remains unmodified.

In case of an extraction barrier [Fig. 6.16(b)] the simulation shows an increase in the strength of the S-kink with decreased T. This is comparable to the experimental data. The reason is that the barrier crossing probability and in turn the charge carrier extraction probability are enhanced by the higher temperature.

To get some deeper insights, temperature dependent measurements of samples without barrier and containing the same materials could be considered in further studies. Additionally, samples with other barrier heights could be investigated. However, the interpretation of temperature dependent data is difficult as temperature changes several processes in organic semiconductors at the same time. The identification of all these processes is beyond the scope of this thesis.

6.5.4 Transient measurements

It was proposed that barriers lead to a redistribution of charge carriers within the device. To probe this effect experimentally, transient photocurrent measurements are carried out, where the current response on square pulses of light is monitored[4]. This method described in Ch. 3.6.3 has been used in literature to determine mobilities [302] and to describe trapping of charge carriers [303]. Here, these measurements are performed under an applied bias voltage to monitor the photocurrent response of the solar cell along the S-kink. This approach in comparison to simulation data allows the identification of different working regimes of an S-kink device. Again, data of MeO-TPD/BPAPF samples is shown only. We start with a .../MeO-TPD(8)/MeO-TPD(8)/... sample, followed by the extraction barrier sample .../BPAPF(10)/MeO-TPD(20)/..., and finish with the injection barrier sample .../MeO-TPD(8)/BPAPF(8)/....

Solar cell without barriers

Figure 6.17 shows transient current curves for the device ITO/p-MeO-TPD(20)/MeO-TPD(16)/C$_{60}$(40)/BPhen(6)/Al which does not contain any barrier. The current signal follows the illumination pulse and reaches steady state within several μs. This is a commonly

---

[4]Measurements performed by Steef Corvers, IAPP, during his Master's project [216].
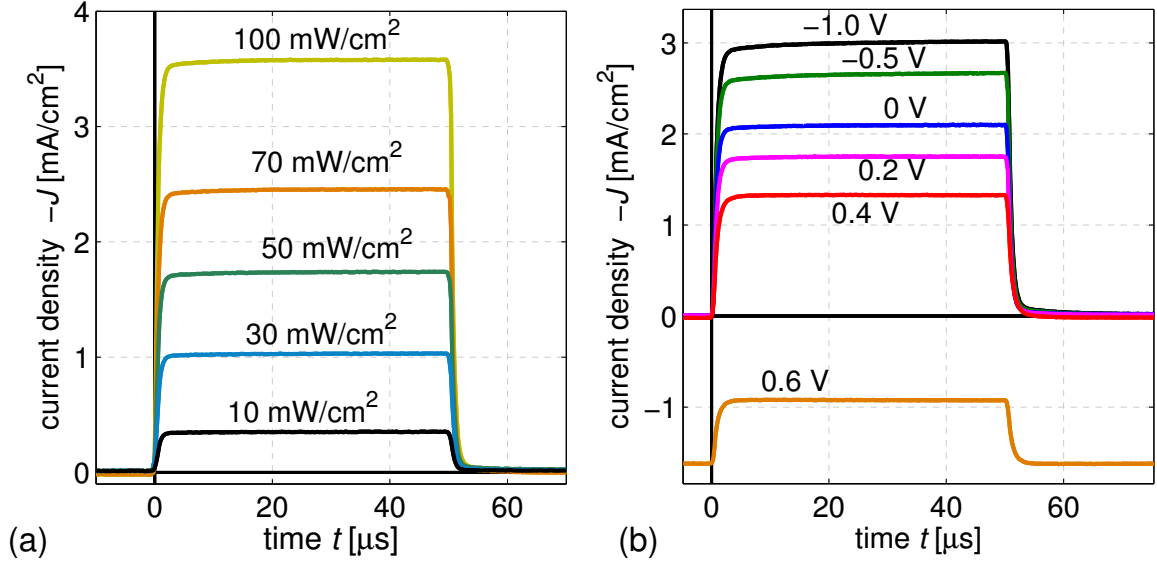
Figure 6.17: **Experimental data**: Transient current response of a sample with HTL = donor = MeO-TPD(8 nm) on a $50\,\mu$s illumination pulse. The sample represents the qualitative response of a well-working solar cell. As convention, positive values mean extracted photocurrent. Thus, the current axis is inverted compared to J-V plots. (a) Intensity dependence; (b) Dependence on the applied bias. At $0.6\,$V there is already a dark forward current visible.

observed feature [303]. The delay time is attributed to low charge transport properties of the intrinsic organic layers, which could result from some shallow trapping mechanism [303]. Decay dynamics with time constants in the range of $1\,\mu$s and lower can already be limited by the macroscopic series resistance and capacitance rather than by charge transport processes in the device itself. This series resistance results from the lateral current through ITO $(30\dots 40\,\Omega)$ and the measurement resistor $(50\,\Omega)$. The assumption of the intrinsic layers with a total thickness of $56\,$nm behaving as one planar capacitor gives a capacity C of

$$C = \epsilon_\mathrm{r}\epsilon_0 \frac{\text{area}}{\text{thickness}} = 5\epsilon_0 * 6.4\,\text{mm}^2/56\,\text{nm} \approx 5\,\text{nF}. \tag{6.1}$$

This results in a time constant $\tau = RC$ of $\approx 0.5\,\mu$s. Thus, it does not dominate the overall shape of the current response to the illumination pulses with widths in the rang of $100\,\mu$s which are applied here. Therefore, the RC time is not significant here as long as we do not extract quantitative data from the decay time.

The photocurrent in Fig. 6.17(a) increases with light intensity, whereas the shape of the response does not change. This indicates that in this intensity regime there is no significant contribution from an intensity dependence of the hole mobility due to filling of deeper states in the HOMO.

Figure 6.17(b) shows the current responses for a voltage sweep. The steady-state cur-
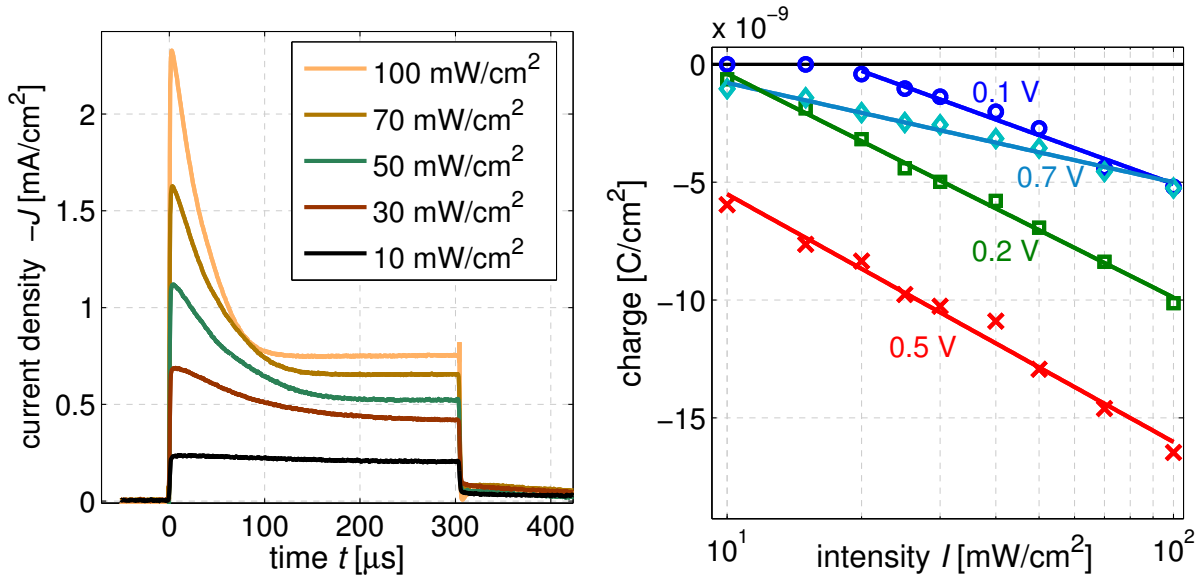
Figure 6.18: (a) Experimental transient photocurrent of ***extraction barrier*** device
.../BPAPF(10)/MeO-TPD(20)/... for different intensities of the illumination
pulse. (b) Piled-up charge obtained by an integration of the area below the
negative overshoot-peak (cf. Fig. 6.19) for several applied bias voltages.

rents in the dark and under illumination follow the respective *J-V* curves, whereas the
characteristic shape of the response remains unchanged.

Extraction-barrier device

In Fig. 6.18(a) light-intensity dependent transient currents at $0\,\mathrm{V}$ for the device ITO/p-
BPAPF(20)/BPAPF(10)/MeO-TPD(20)/C_{60}(40)/BPhen(6 nm)/Al with an extraction bar-
rier of $\approx 0.3\,\mathrm{eV}$ are plotted. The steady-state photocurrent density is smaller than $1\,\mathrm{mA/cm^2}$
as expected from the short-circuit current of the *J-V* curve (cf. Fig. 6.12). However, in-
tensity dependent overshoots exist in the transient curves. Overshoots when switching on
the light have already been observed and attributed to traps in the active layer [303]. In
the case of traps, governing the transient current curve, an overshoot is not expected when
switching off the light. The current decay is then qualitatively comparable to the data
shown in Fig. 6.17, however showing a larger decay time. This larger decay time means a
slower response and is due to the contribution from trapped charges which are extracted
after some detrapping time.

The extraction barrier device, however, shows current in reverse direction upon switching
off the light. This effect occurs at a certain applied voltage as can be seen in Fig. 6.19(a)
which shows the photocurrent responses of a voltage sweep. This means that instead of
the remaining photogenerated charge carriers slowly leaving the device, charge carriers are
entering the device. This characteristic shape is observed for several extraction barrier
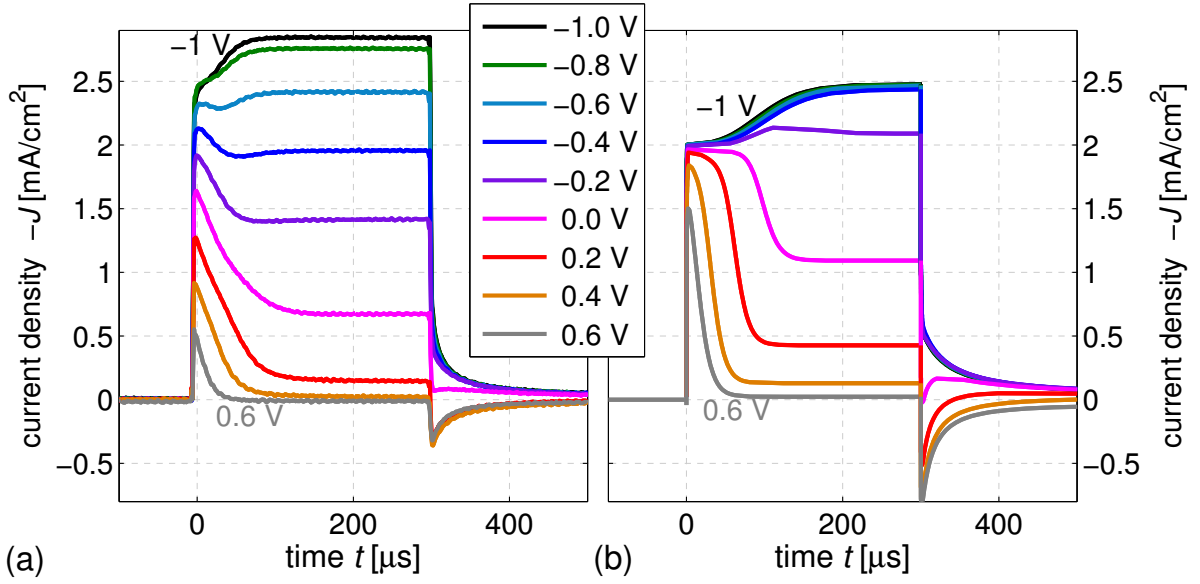
Figure 6.19: Transient photocurrent of the **_extraction barrier_** device . . . /BPAPF(10)/MeO-TPD(20)/. . . for different applied bias voltages: (a) **experiment** and (b) **simulation**.

devices. Thus, it is concluded that this kind of double-overshoot curve is a fingerprint of an extraction barrier.

The data of Fig. 6.19(a) map the whole S-kink region. It can be seen that under increased reverse bias, steady-state current gets larger, which is in accordance to the *J-V* curve (cf. Fig. 6.12). When leaving the S-kink region the positive and negative overshoots vanish, because the blocking effect of the barrier is overcompensated by a field-driven current over the barrier. The simulation data of Fig. 6.19(b) shows this transition as well. Therefore, it is employed to explain the overshoots by investigating time evolutions of charge carrier density distributions within the device.

The overshoot when switching on the light is attributed to photogenerated charge carriers moving away from the D/A interface. The fast electrons in the acceptor exit the device quickly. This leads to a high displacement current over the intrinsic HTL due to the fact that there are no free charge carriers. Photogenerated holes drift and diffuse away from the D/A interface to the donor/HTL interface, where they pile up at the extraction barrier. This current causes the observed overshoot and stops as soon as the device is in steady state, where most of the potential drops over the intrinsic HTL.

Figure 6.20 shows simulated current profiles to illustrate what happens when switching off the illumination. These current profiles are plotted for several time intervals after the light was switched off. The particle current $J_n + J_p$ is constant and negative at $t = 0$ (a). It represents the steady-state photocurrent, provided by the holes (J_p) in the donor and HTL and by the electrons (J_n) in the acceptor. The current $J_n + J_p$ is not constant any more during the transient. The measurable current is the sum of particle and displacement
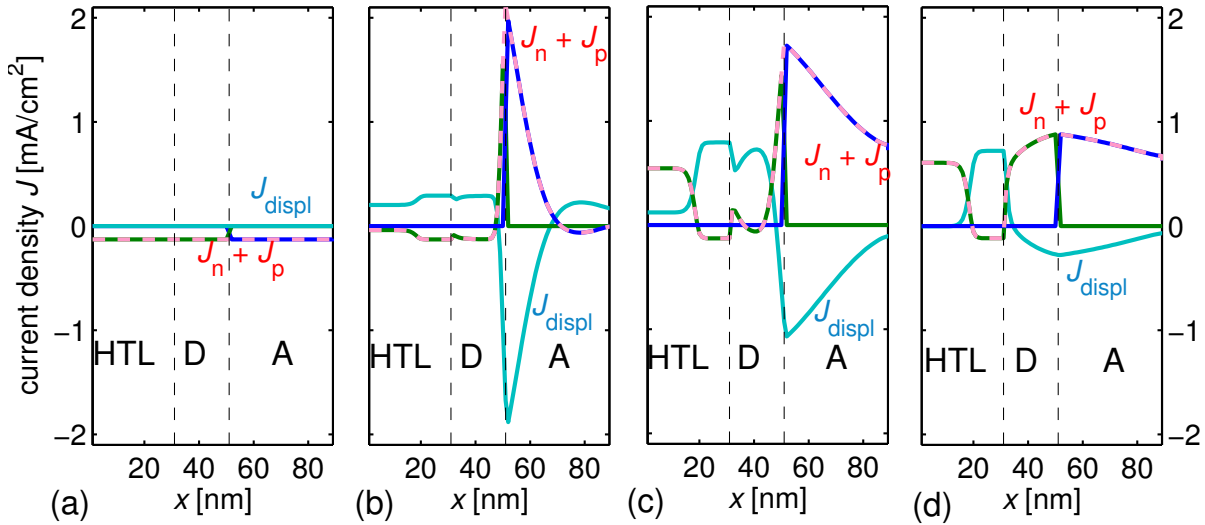
Figure 6.20: Evolution of the current distribution with time at $0.4\,\text{V}$ after switching off the illumination of a device with ***extraction barrier***: (a) $0\,\text{s}$, (b) $30\,\text{ns}$, (c) $0.2\,\mu\text{s}$, (d) $5\,\mu\text{s}$. Positive current means current towards the D/A interface and negative current means extraction current. Shown are electron current (in acceptor A) J_n, hole current J_p, total charge current $J_n + J_p$, and the displacement current J_{displ}. After switching off the light, electrons flow to the D/A interface (b+c), followed by the slower holes, which have been piled-up at the HTL/donor interface. The intrinsic HTL mostly shows displacement current.

current (cf. Ch. 4.3.5). Directly after switching off the light, the electron-hole source at the donor/acceptor interface vanishes, which leads to a strong diffusion gradient for electron and holes towards the D/A interface. The faster electrons respond first and the electron current J_n changes its sign (b). This means that electrons are flowing towards the D/A interface. In (c) they are entering the device at the acceptor/cathode contact (on the right). Together with the injected hole current in the doped HTL on the left side (which is equivalent to an extracted negative current), negative charge is transferred over the external contacts from the left to the right. Finally (d), the piled-up holes in the donor respond. They diffuse from the HTL/donor interface back to the D/A interface, where they recombine with electrons. This process leads to an effective injection current when switching off the light. Such a current as response on switching off the light exists if the holes are stored away from the locus of generation. This proves the predictions of simulation that holes are stored close to the extraction barrier and shows the importance of diffusion. The height of the simulated overshoots is strongly dependent on electron and hole mobilities of acceptor and donor, respectively, and can be significantly suppressed by a high series resistance.

Another approach of explaining these overshoots is an analysis of the device in an

equivalent-circuit model. The intrinsic HTL is then represented by a capacitance which results approximately from a planar capacitor. This capacitor consists of the 10 nm intrinsic HTL as dielectrics and the doped HTL and the interface HTL/donor as electrodes. The overshoot in the current response when switching on the light is a current which charges this capacitor. The charging procedure takes some time, which is represented by the decay and limited by hole transport in the donor and the external resistance. If we consider the short-circuit case of the device, the D/A interface should be capable of delivering the short-circuit current of the device without extraction barrier. However the photocurrent of the extraction barrier device is reduced compared to the short-circuit current of the device without S-kink (cf. *J-V* curves in Fig. 6.12). This means that the D/A heterojunction is not operating at short-circuit, but providing a photovoltage. This voltage drops over the charged capacitance. When switching off the light, the charging current source and hence the voltage at the capacitor vanish and the capacitor is discharged with a current in reversed direction.

The extraction of physical parameters from rise and decay of the curves in Fig. 6.19 is difficult, because charge transport and recombination mechanisms are supposed to happen at sub-microsecond time scales. Therefore, the response is either limited by trapping processes or by the *RC*-time of the setup itself. A reduction of the *RC*-constant would mean another solar cell layout with smaller areas to reduce the capacitance. However, at the same time the reduced area decreases the photocurrent signal. The same holds for a lower measurement resistor, which reduces the series resistance and decreases the quantity to measure, which is the photocurrent as voltage drop over the input resistance of the oscilloscope.

Nevertheless, a time integration of the overshoot current upon switching off the illumination gives an estimate of the amount of charges stored in the device. This gives an idea of the expected charge carrier density close to the barrier. As most of the stored holes cannot overcome the barrier, there is no other way out of the device for them than flowing back to the D/A interface, where they recombine with electrons. Thus, in contrast to a charge extraction measurement of a blend [127], where charge collection after switching off the light is in competition with recombination, this is not the case here, because the recombining charge carriers are measured. The charge (injected electrons) as a function of light intensity is shown in Fig. 6.18(b) for several voltage points and is highest at 0.5 V. The accumulated charge decreases with higher applied bias, because the field in the device, which pushes the charges away from the D/A interface, becomes lower. The current is then mainly diffusion driven, so that there is not much charge driven away and stored at the donor/HTL interface. Under decreased applied bias, the charge decreases as well, because the extraction-barrier-crossing probability increases. The accumulated charge shows a logarithmic dependence on light intensity for all voltages. This is expected, as the stored charge on a capacitor is proportional to the voltage applied to the capacitor. This voltage results from the illumination and scales with the photovoltage of the device, which is known to depend logarithmically on light intensity. The logarithmic dependence of the stored charges indicates that the probability of a charge carrier to overcome the barrier is not increased by a higher charge carrier density. This means that there is no evidence for
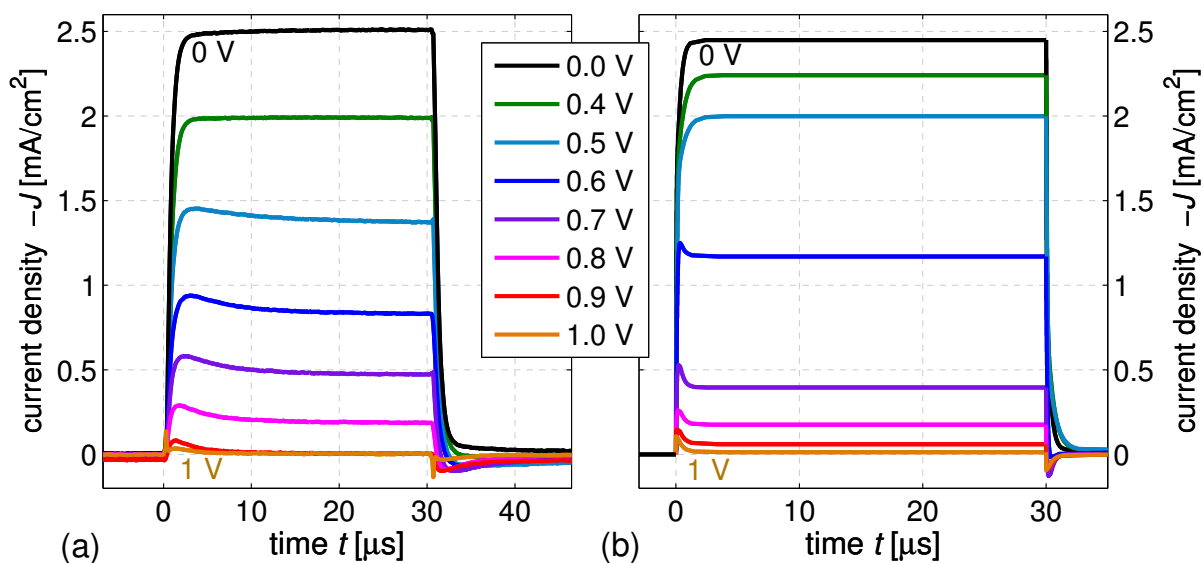
Figure 6.21: Transient photocurrent of the ***injection barrier*** device .../MeO-TPD(8)/BPAPF(8)/... for different applied bias voltages: (a) experiment and (b) simulation.

a filling-up of a possibly existent broad DOS in the examined intensity range.

Injection barrier device

Voltage dependent transient current data for the injection barrier device ITO/p-MeO-TPD(20)/MeO-TPD(8)/BPAPF(8)/C_{60}(40)/BPhen(6 nm)/Al are plotted in Fig. 6.21(a). The curves show mainly a shape which is comparable to the device without barrier, because charge extraction works well. However, there is a difference for voltages (> 0.4 V), where the S-kink is present. There, a small positive overshoot after switching on the illumination and negative overshoot after switching off can be seen. A simulation of injection barrier devices shown in Fig. 6.21(b) reproduces this effect.

Analogously to the extraction barrier we explain the negative overshoot by a time evolution of current distributions within the device starting from the situation of a steady state photocurrent [Fig. 6.22(a)]. We discussed in Ch. 6.3.1 that this current is mainly diffusion-driven. When switching off the light, the source of electron-hole pairs rapidly vanishes and diffusion current stops. However, there are many charge carriers in the donor, which constituted the diffusion gradient. They face the reversed field [cf. Fig. 6.6(a)] and flow back to the D/A interface instead of being extracted. This leads to a short reversed current, which is seen in an overall positive current in Fig. 6.22(c) which gives the negative overshoot in the transient photocurrent. This overshoot is much less pronounced than the one of the extraction barrier and does not show a distinct narrow peak. Therefore, the shape of the overshoot allows for a differentiation between the two types of barriers.
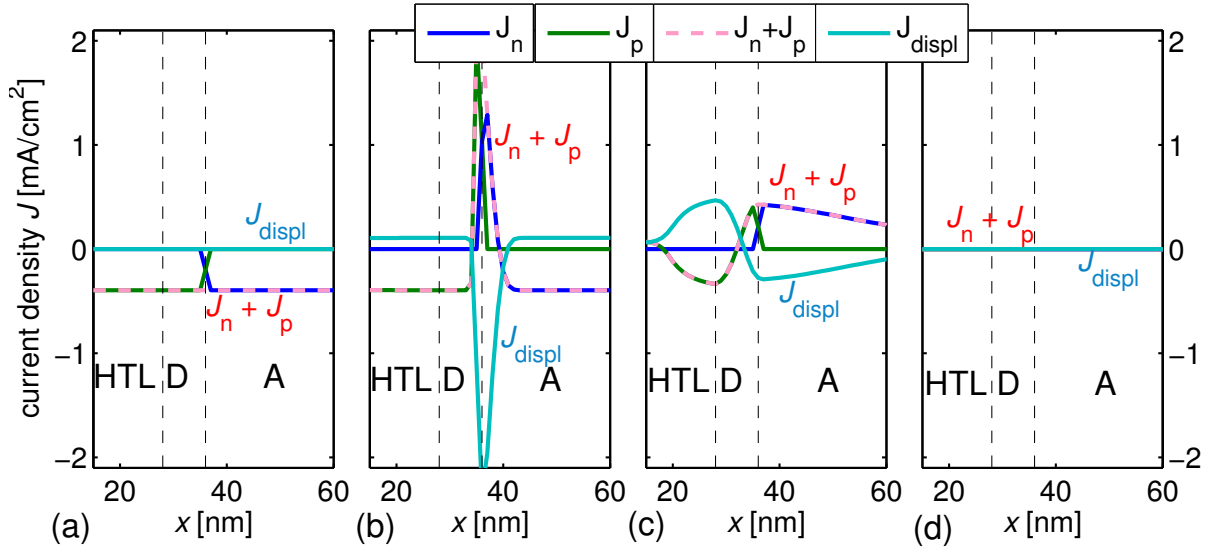
Figure 6.22: **_Injection barrier_** at 0.7 V: Evolution of the current distribution with time after switching off the illumination: (a) 0 s, (b) 1.3 ns, (c) 0.19 μs, (d) steady state. Shown are electron current (in acceptor A) J_n, hole current J_p, total charge current $J_n + J_p$, and the displacement current J_{displ}. A recombination current occurs at the D/A interface (positive) due to the reversed field [cf. Figs. 6.6(a) and 6.7(a)].

Whereas all investigated extraction barrier samples show overshoots, this feature is not observed for every injection barrier sample. For a more detailed picture of barriers and photocurrent transients, more detailed investigations are required including the variation of layer thicknesses and the examination of BHJ [216].

6.6 Summary and final remarks

This chapter contained a study of the influence of the energy levels of donor and HTL on V_{oc} and the shape of the _J-V_ curve. Thereby, it was possible to experimentally prove several predictions of the previous chapter considering the effect of contact properties. It was found that V_{oc} is decreased by injection barriers in the case of BHJs, because contacts are not selective and electrons can directly recombine with holes at the HTL/blend interface. However, V_{oc} is independent of the HTL and scales with the effective gap in the case of FHJs. The reason is the built-in selectivity of a FHJ due to the localized donor/acceptor interface which keeps electrons away from the HTL. Considering extraction barriers, it was found that they do not significantly change V_{oc}.

However, injection and extraction barriers can lead to S-kinks in the _J-V_ curve. In case of an extraction barrier, charge extraction requires higher negative applied voltages. That is why an S-kink is seen. Injection barriers give only S-kinks in case of selective contacts, here realized by FHJs. The reason is that photocurrent is diffusion-driven against the field,

because V_{oc} exceeds V_{bi}.

In an exemplary study for the selected material system BPAPF/MeO-TPD, ideas were demonstrated on how to identify the type of barrier. The S-shapes caused by injection and extraction barriers show a qualitatively different behavior with temperature. Furthermore, the strength of the S-kink is affected by the thickness of the donor in case of injection barriers and by the thickness of the HTL in case of extraction barriers. The reason is that the thickness of the layer "behind" the barrier determines the electrical field and therefore the current at the interface with the barrier. Transient photocurrent measurements were applied to visualize a pile-up of charge carriers at an extraction barrier seen at characteristic overshoots. Injection barriers may also show small overshoots due to the drift current opposing the diffusion current.

All the experimental findings were explained by the aid of simulations which were capable of reproducing the trends qualitatively and in the correct quantitative range. A more quantitative analysis, if desired, remains for further studies. However, also the question remains whether drift-diffusion simulations are capable of providing a quantitative and predictive description of organic-organic interfaces. The transition probability is governed apart from the barrier also by molecular orbital overlap and thus orientation of the two different molecules forming the interface. This effect would have to be known and considered by an additional factor in the description of interface barriers.

Chapter 7

Imbalanced Mobilities causing S-shaped *J-V* Curves in Planar Heterojunction Solar Cells

In the previous chapter barriers have been discussed as reason for S-kinks in the J-V curve of organic solar cells. In this chapter another source of S-kinks is presented: In flat hetero-junction devices, a strong imbalance of charge carrier mobilities (hole mobility in donor, electron mobility in acceptor) can lead to distorted J-V curves. This effect is predicted by simulations for a mobility mismatch of a factor larger than 100 and experimentally verified by solar cells comprising the low-mobility donor material Ph4-Ph4-DIP. This material is combined with the two acceptors C_{60} and Me-PTCDI, which show highly different electron mobilities. This study is the first clearly demonstrating the correlation of imbalanced mo-bilities and S-kinks. Thus, not only interface effects but also the photoactive material itself can cause S-kinks.[1]

7.1 Imbalanced mobilities in simulation

Before discussing the experimental data, simulation data for an exemplary model device are analyzed. It consists of a bilayer with thermionic contacts with low injection barriers ($\leq 0.1\,\mathrm{eV}$). This value shows a negligible effect on the *J-V* curve (cf. Chapter 5) and may results in realistic charge carrier densities at the contacts. Donor and acceptor thicknesses are both chosen as 30 nm, which is a common value for small-molecule organic solar cells. The other parameters are found in Tab. 7.1. Figure 7.1 shows the calculated *J-V* curves for a variation of hole mobility in the donor (μ_p^{D}) and electron mobility in the acceptor (μ_n^{A}). For better comparability of the curves, the recombination constant for bimolecular recombination is set independent of mobility to a value of 5×10^{-10} cm^3/s, which is ex-pected for Langevin theory at a mobility of 10^{-3} cm^2/Vs. Using the Langevin expression

---

[1]Most of the content of this chapter is published in W. Tress, A. Petrich, M. Hummert, M. Hein, K. Leo, and M. Riede, *Imbalanced mobilities causing S-shaped IV curves in planar heterojunction organic solar cells.* Applied Physics Letters **98**, 063301 (2011)
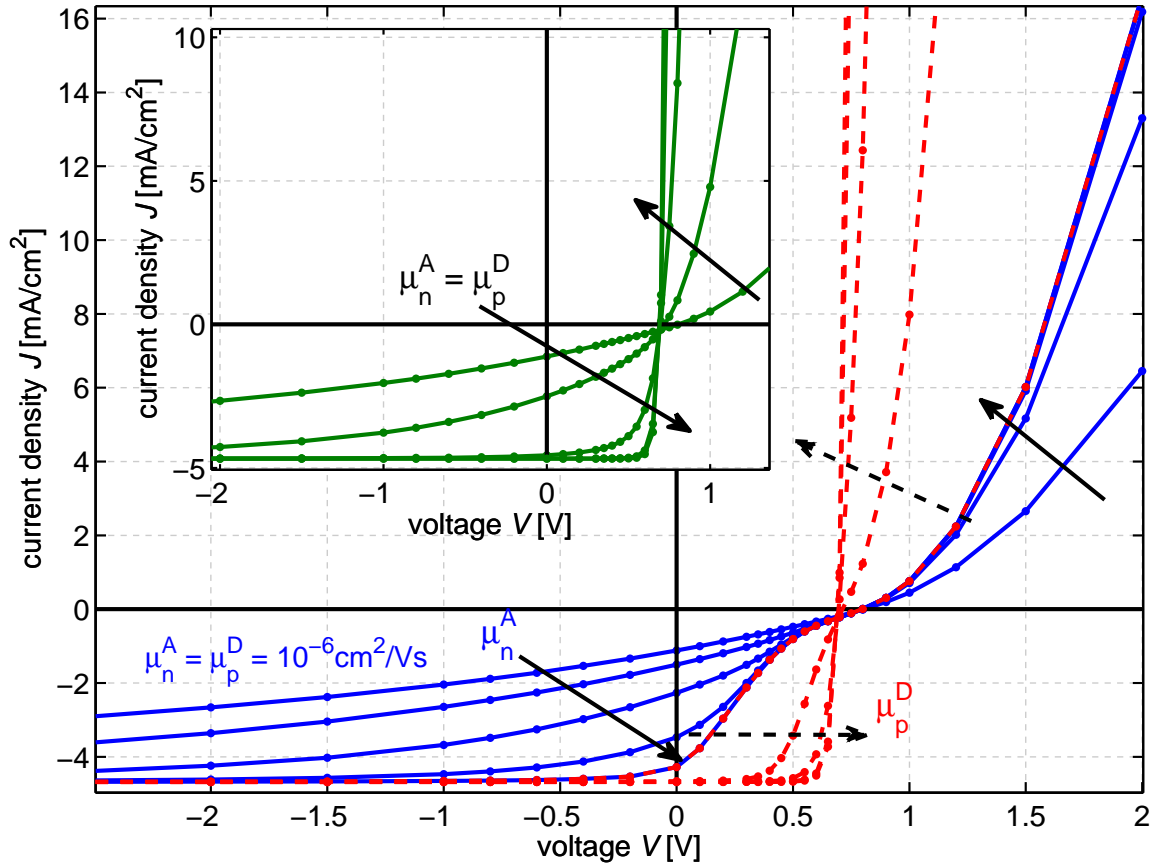
Figure 7.1: Simulation data of a bilayer device with varied mobilities. Solid lines: The hole mobility in the donor μ_p^D is kept constant at $10^{-6} \mathrm{cm}^2/\mathrm{Vs}$, whereas the electron mobility in the acceptor μ_n^A is varied ($10^{-6}, 10^{-5}, 10^{-4}, 10^{-3}, 10^{-2}$ cm^2/Vs). Dashed: μ_n^A is constant at $10^{-2}\mathrm{cm}^2/\mathrm{Vs}$ and μ_p^D is varied $10^{-6} \ldots 10^{-2}$ cm^2/Vs. Inset: Balanced mobilities $\mu_n^A = \mu_p^D = 10^{-6} \ldots 10^{-2}$ cm^2/Vs. A mobility imbalance larger than a factor of 100 leads to S-kinks.

(Eq. 4.46) has a minor effect on the qualitative shape of the *J-V* curve. However, the open-circuit voltage (V_{oc}) significantly changes with recombination probability, which makes a comparable visualization of the strength of the S-kink difficult. This correlation of V_{oc} with mobility in the case of Langevin recombination was discussed in detail in Chapter 5, where it was clearly shown that a change in recombination constants affects V_{oc}.

The simulated *J-V* curves of Fig. 7.1 show that high mobilities lead to high *FF*, whereas low mobilities decrease the *FF* strongly, comparable to the results of a bulk heterojunction (BHJ) in Chapter 5. The lower the mobility, the higher is the required electrical field to extract charge carriers before they recombine at the heterointerface. The novel feature in the case of a flat heterojunction (FHJ) is that an S-kink appears for imbalanced mobilities at a mobility mismatch μ_n^A/μ_p^D (or μ_p^D/μ_n^A, respectively) of $\approx 100 \ldots 1000$. The S-kink

structure		donor	accceptor
thickness	d	30 nm	30 nm
HOMO	E_{ht}	-5.2 eV	-6.4 eV
electrical gap	E_g	2.1 eV	2.3 eV
LUMO density of states	N_C	$2.4 \times 10^{19}\,\mathrm{cm^{-3}}$	$4.2 \times 10^{21}\,\mathrm{cm^{-3}}$
HOMO density of states	N_V	$2.4 \times 10^{19}\,\mathrm{cm^{-3}}$	$7 \times 10^{21}\,\mathrm{cm^{-3}}$
dielectric constant	ϵ_r	3.4	3.4
exciton diffusion length	L_D	7 nm	35 nm

Table 7.1: Default values for bilayer model-solar-cell. The work function of the anode is chosen as 5.2 eV and of the cathode as 4.2 eV. The injection mechanism is thermionic with a backward flowing recombination current (Eq. 4.64). The lifetime of excitons within the layer is much higher than at the D/A interface, recombination of free charges at the D/A interface is assumed to happen within the Coulomb radius, the temperature is 300 K, the discretization is 0.5 nm. A homogeneous exciton generation rate of $1.5 \times 10^{22}\,\mathrm{cm^{-3}s^{-1}}$ is assumed. This assumption does not influence any statement of this chapter, as the exciton generation rate together with the values for L_D determines the saturated photocurrent. This photocurrent is wanted to be constant for a good comparability of the *J-V* curves.

cannot be seen when both mobilities are balanced and low as demonstrated by the inset where data for balanced mobilities are shown. Calculations with other mobility pairs reveal that the relative imbalance factor μ_p/μ_n governs the strength of the S-kink. Furthermore, the strength of the S-kink scales with the thickness ratio of low-mobility to high-mobility layer and is less influenced by the total device thickness. This is visualized by the *J-V* sets of Fig. 7.2, where $\mu_n^A/\mu_p^D = 1000$ is assumed. There, for each ratio between donor and acceptor (different colors) additionally a variation of the total device thickness is done. The S-kink is more pronounced for a thicker low-mobility layer compared to the thickness of the high mobility layer. *J-V* curves with the same ratio of donor to acceptor layer thickness almost coincide in the S-kink region in the fourth quadrant independent of the total device thickness. The effect of the overall device thickness is seen in forward direction where in particular a thicker low-mobility layer decreases the slope due to an increased series resistance effect by this layer.

The comparison of the *J-V* curves of Fig. 7.1 shows that imbalanced high/low mobilities are preferable compared to balanced low mobilities regarding device performance. The power-conversion efficiencies of the S-kink curves is higher due to the higher *FF* compared to the case of low mobilities.

The reason for the S-kink due to imbalanced mobilities can be explained by examining profiles of the electric field and of charge carrier densities within the layers. Figure 7.3 shows data of three mobility pairs at two different applied voltages, 0 V and 0.55 V, which sample the S-kink region. For balanced high mobilities, the electric field (at zero bias
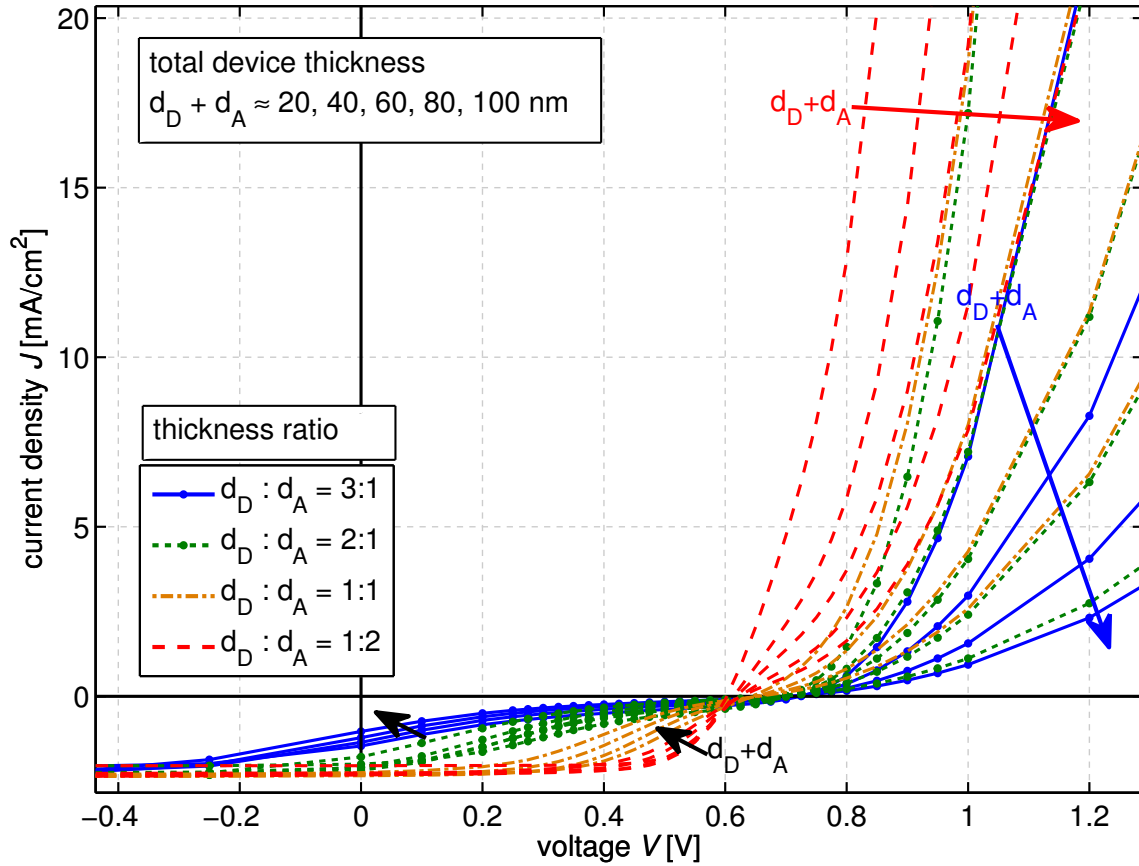
Figure 7.2: Simulation data for a variation of donor and acceptor thicknesses, using $\mu_n^{\mathrm{A}} = 10^{-2}\,\mathrm{cm^2/Vs}$ and $\mu_p^{\mathrm{D}} = 10^{-5}\,\mathrm{cm^2/Vs}$. A variation of the total device thickness and the ratio between donor and acceptor thickness shows that the S-kink is dominated by the ratio.

originating from the built-in voltage) in the device is constant except at the contacts due to the high dark charge carrier density there (cf. Ch. 5.2.6). For both voltages, all charge carriers are extracted due to their high mobilities. The driving force is mainly drift due to the built-in field assisted by diffusion away from the interface. For very low mobilities, a space charge is built up in the complete device, because electrons and holes cannot be extracted sufficiently fast. Their concentration at the D/A interface is increased and hence recombination probability as well, which leads to a lower *FF*.

In the case of imbalanced mobilities, the field distribution is asymmetric, because only the less mobile holes form a space charge. The space charge reduces the drop of the electrical potential in the acceptor and increases the magnitude of the field in the donor. This assures that for every extracted (fast) electron, a hole is extracted in steady state. The rearrangement of the field guarantees the extraction of every photogenerated charge carrier at 0 V. However, with decreasing field, resulting from positive applied bias [Fig. 7.3(b)],
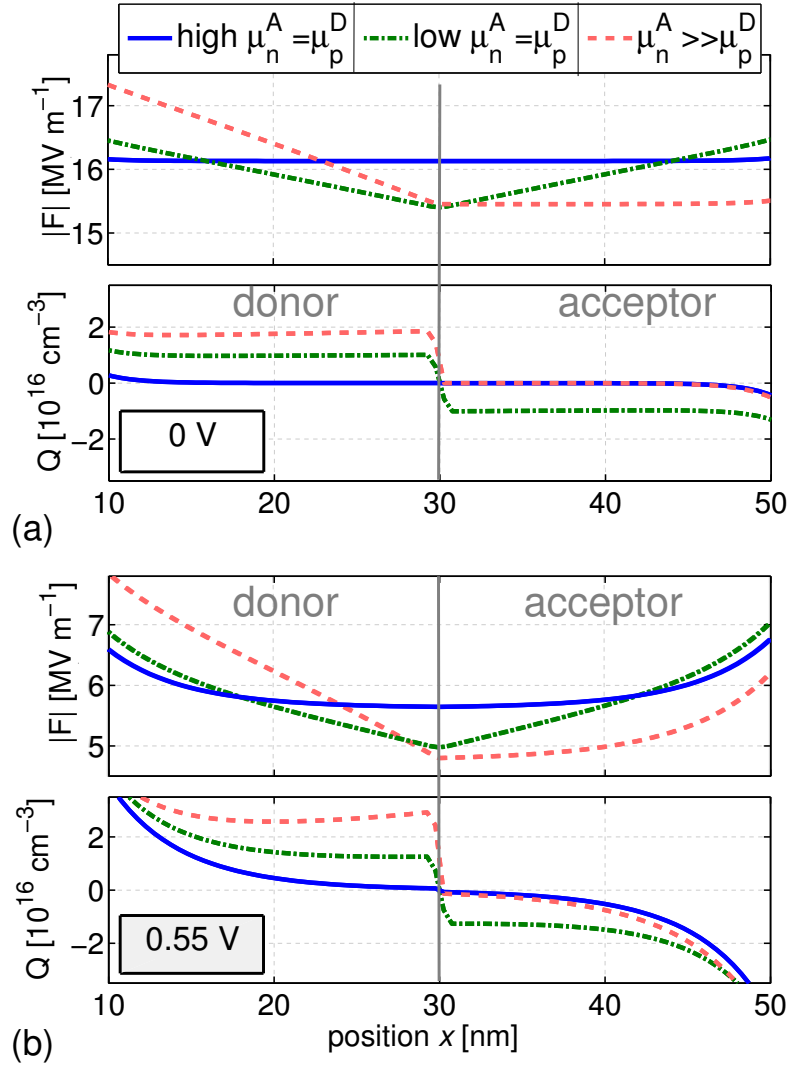
Figure 7.3: Electric field F and charge density Q per elementary charge as a function of distance x from anode. (a) at 0 V, (b) at 0.55 V applied bias in the model device of Fig. 7.1: for high mobilities $\mu_n^A = \mu_p^D = 10^{-2}\,\text{cm}^2/\text{Vs}$ (solid), for low mobilities $\mu_n^A = \mu_p^D = 10^{-5}\,\text{cm}^2/\text{Vs}$ (dash-dotted), and for highly imbalanced mobilities $\mu_n^A = 10^{-2}\,\text{cm}^2/\text{Vs}$, $\mu_p^D = 10^{-5}\,\text{cm}^2/\text{Vs}$ (dashed).

electrons start to pile up at the D/A interface as well. Recombination is increased and hence current is decreased, so that the *J-V* curve approaches the low-mobility curve, resulting in an S-kink. For applied bias voltages larger than V_{oc}, the *J-V* curve follows mainly the curve of the low-mobility case, because current in forward bias in this voltage range is diffusion-driven and hence mainly limited by the charge carrier with the low mobility.

As the S-kink results from the spatial separation of electrons and holes in combination with a redistribution of the electric field, an S-kink is not expected in a bulk heterojunction

213
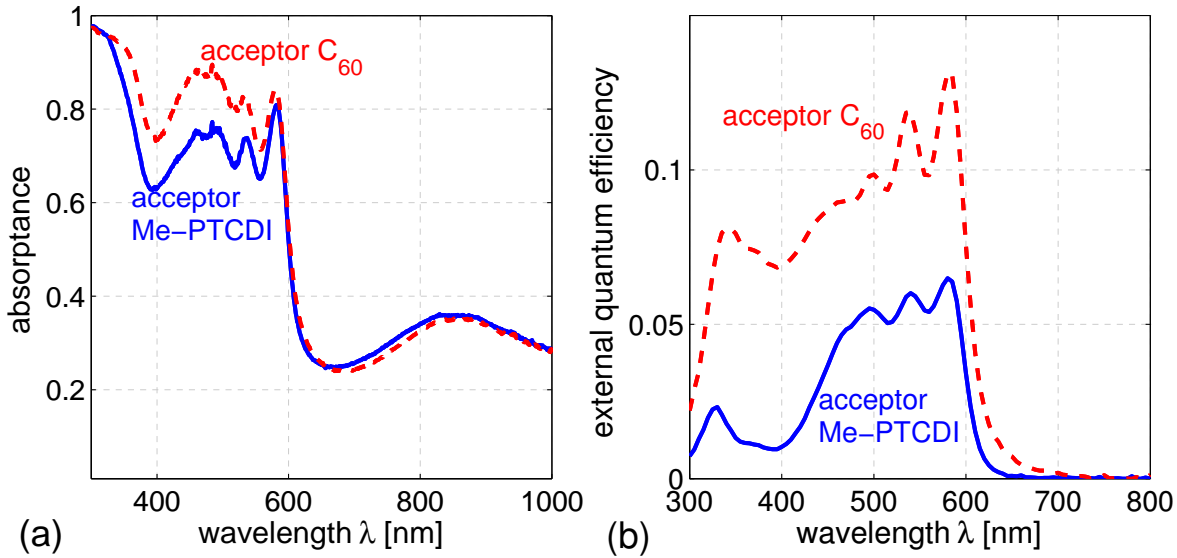
Figure 7.4: (a) Absorptance and (b) external quantum efficiency of a complete solar cell. The stack is ITO/p-doped BPAPF (25 nm)/Ph4-Ph4-DIP (15 nm)/ [C_{60} or Me-PTCDI (20 nm)] /n-doped C_{60} (20 nm)/Al (100 nm).

with imbalanced mobilities. The reason is that in the case of a BHJ, the field-free region (resulting from the μ-imbalance) close to the contact of the more mobile charge carrier, where no photocurrent is collected, decreases continuously with negative applied bias. This leads to a smooth increase of photocurrent, which scales in the extreme case with the square root of the applied bias and with the intensity to the power of $3/4$ [140]. This was discussed with the aid of analytical equations in Ch. 3.3.5 (p. 74).

7.2 Experimental verification

The following items have to be checked for an experimental verification of the simulation results, in particular to discriminate this effect from the barrier case of the previous chapter:

- The *I-V* curve of a FHJ comprising a D/A combination with a high mobility mismatch and with ohmic contacts shows an S-kink.

- The thickness dependence of the S-kink matches the predictions of simulation.

- The S-kink disappears with a decreased imbalance in mobility.

- The S-kink vanishes in a blend without changing V_{oc}.

- Photocurrent transients do not show overshoots.

thickness	V_{oc}	FF	J_{sc}	J_{sat}
10 nm	1.1 V	41 %	2.7 mA/cm^2	2.8 mA/cm^2
20 nm	1.1 V	24 %	2.2 mA/cm^2	2.4 mA/cm^2
40 nm	1.1 V	14 %	0.4 mA/cm^2	1.5 mA/cm^2
60 nm	1.1 V	15 %	0.08 mA/cm^2	1.3 mA/cm^2

Table 7.2: Solar-cell parameters of devices consisting of ITO/p-doped BPAPF(25 nm, 10 weight %)/Ph4-Ph4-DIP(10, 20, 40, 60 nm)/C$_{60}$ (30 nm)/n-C$_{60}$ (10 nm, 3 wt%)/Al. The saturated photocurrent J_{sat} is estimated as the saturation current in reverse bias when correcting the J-V curve by a photoshunt (cf. Chapter 11).

Solar cells of p-i-n type and comprising the donor material Ph4-Ph4-DIP [196] (cf. Fig. 3.26, p. 85) are chosen to prove these points. The stack consists of ITO/p-doped BPAPF(25 nm, 10 wt%)/Ph4-Ph4-DIP(10, 20, 40, 60 nm)/[C$_{60}$ or Me-PTCDI (30 nm)]/n-C$_{60}$ (10 nm, 3 wt%)/Al. NDP9 and NDN1 are used as dopants.

Ph4-Ph4-DIP is synthesized as substitute for the commonly used ZnPc with the aim of shifting the absorption from the red into the green spectral range accompanied by a higher V_{oc}. Thus, additional photons can be harvested which are not accessible by ZnPc/C$_{60}$ solar cells (cf. Fig. 3.27, p. 86). Both goals are realized. However, the photocurrent in a FHJ with C$_{60}$ is low due to a low exciton diffusion length. This can be seen when comparing the absorption data with EQE data shown in Fig. 7.4(a+b). As mobility and exciton diffusion length are expected to follow the same trend (for Dexter transfer, cf. Ch. 3.2.1), a low μ_p can be expected.

Single carrier device data with layer thicknesses between 10 and 60 nm suggest a strong field (F) and also an illumination dependent mobility, probably due to trapping effects. The J-V data shown in Fig. 7.5 are measured under illumination to represent a situation as close as possible to the working conditions of solar cells. Dashed lines show simulation data where a Poole-Frenkel (Eq. 4.42) mobility is assumed. The parameters given in the figure result in a satisfactory reproduction of the experimental data. The values of μ_0 and γ for the four devices with different thicknesses describe a mobility of the same order of magnitude. Thus, the mobility is estimated to be in the range of $\mu_p = 0.5 \ldots 5 \times 10^{-8} \exp(5.5 \ldots 6 \times 10^{-3}(\mathrm{cm/V})^{1/2}F^{1/2})$ cm^2/Vs. This rough estimation describes a very low value and is sufficient for the discussions here. The reason for such a low value could be the phenyl end groups of the molecule (cf. Fig. 3.26, p. 85), which are free to rotate out of plane, hindering close stacking and hence π-electron wave-function overlap between molecules. In contrast, the mobility of the acceptor C$_{60}$ in a thin film is reported to be in the range of 10^{-2} cm^2/Vs [188]. Comparing these mobility data to the predictions of simulation (Fig. 7.1), an S-kink is anticipated for a FHJ consisting of Ph4-Ph4-DIP/C$_{60}$.
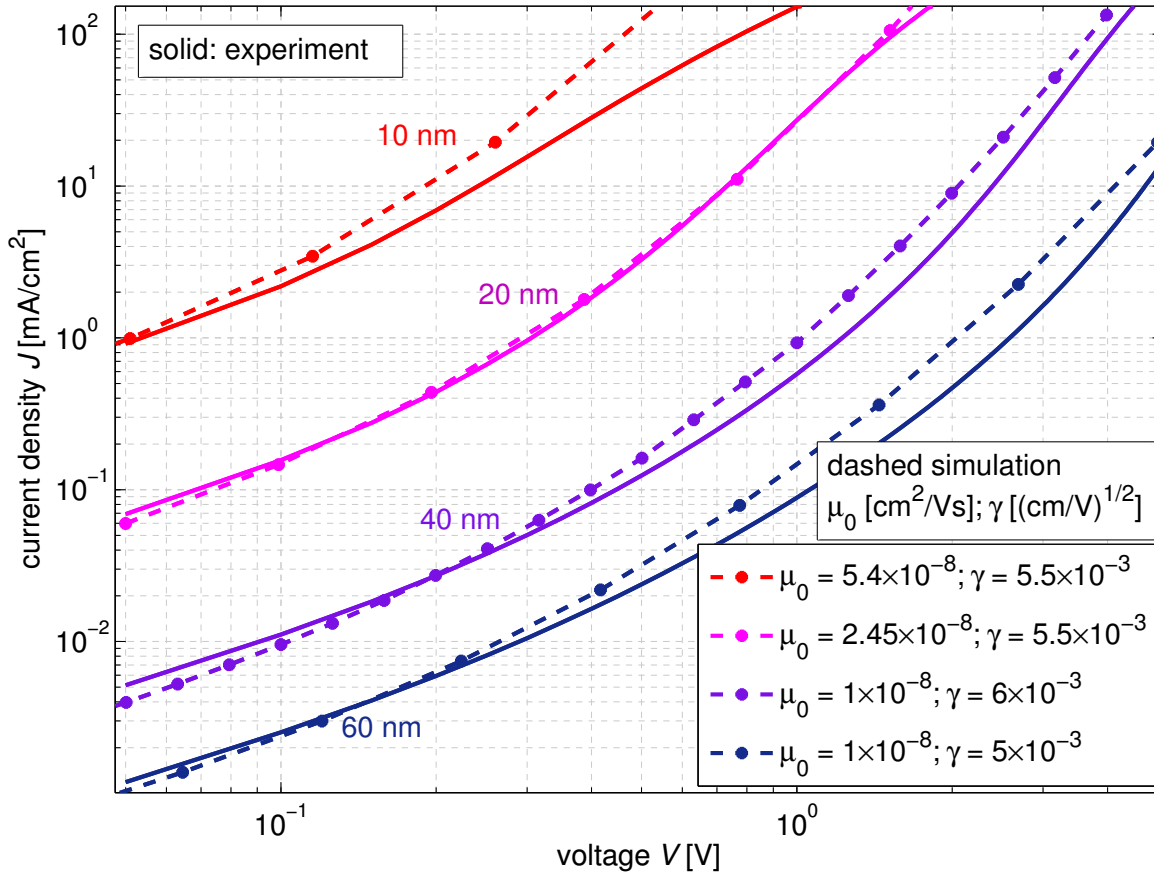
Figure 7.5: Experimental (solid lines) and simulation (dashed) data of single carrier devices with the structure ITO/NDP9(1)/BPAPF:NDP9(25, 10 wt%)/Ph4-Ph4-DIP(10;20;40;60)/BPAPF:NDP9(25, 10 wt%)/NDP9(1)/Au(9)/ Al(100). For high currents the ITO series resistance becomes visible which can be seen at the sample with a 10 nm Ph4-Ph4-DIP layer. The remaining input parameters can be found in Appendix B, p. 326.

7.2.1 Current-voltage characteristics

Figure 7.6 shows J-V curves of Ph4-Ph4-DIP/C_{60} solar cells for different Ph4-Ph4-DIP layer thicknesses measured at a mismatch-corrected intensity of $100\ldots110$ mW/cm^2. The respective solar cell parameters are found in Tab. 7.2. A simulation (dashed lines) of the complete solar cell stack with the mentioned mobilities and without any parameter optimization describes the shape of the S-kink around V_{oc} well, including the strong dependence on donor thickness. This fact and the good alignment of the hole transport levels of BPAPF and Ph4-Ph4-DIP, which is indicated by a similar V_{oc} of $1\ldots1.1$ V in a FHJ with acceptor C_{60} (for BPAPF/C_{60} solar cell, see data of previous chapter, p. 178), exclude large barriers at the contacts as reason for the S-kink.
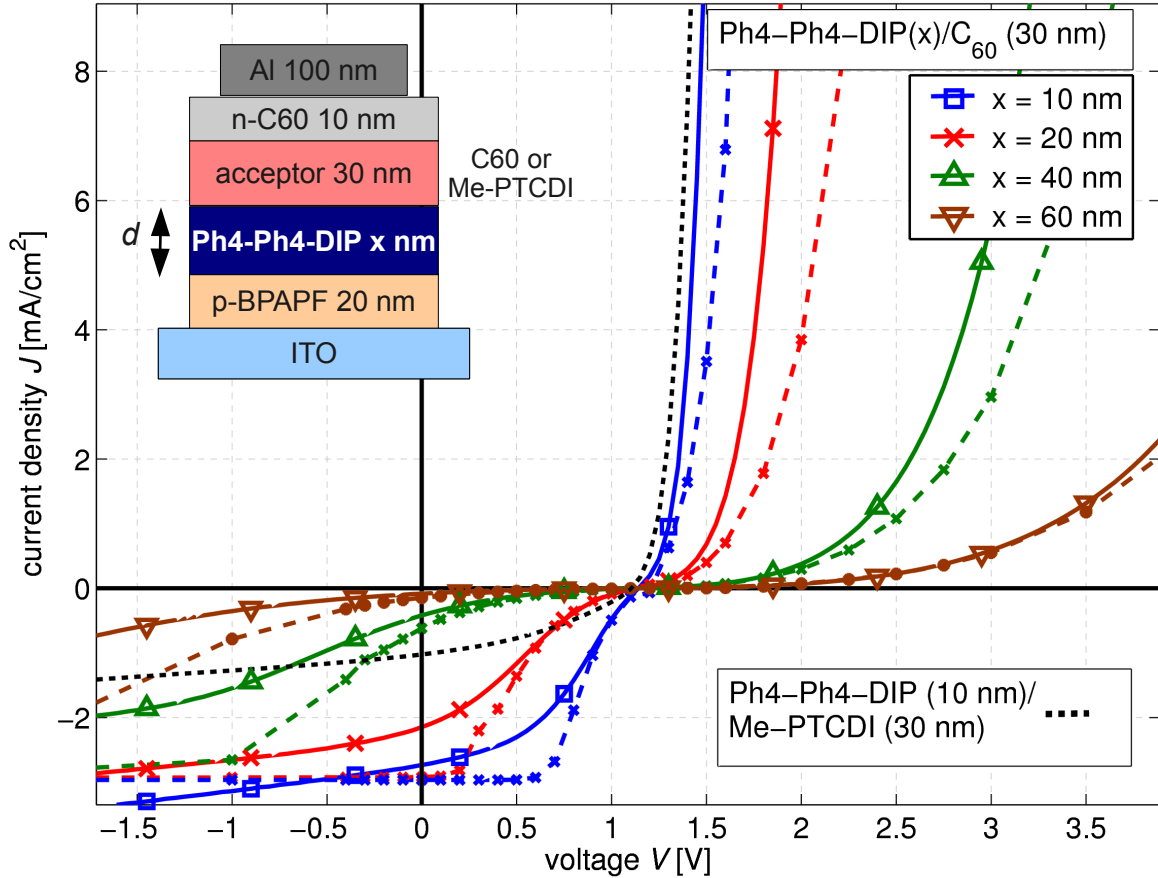
Figure 7.6: Solid lines: Experimental data of devices ITO/p-BPAPF/Ph4-Ph4-DIP/(C$_{60}$ or Me-PTCDI)/n-C$_{60}$/Al. The *FF* is 41 % for 10 nm Ph4-Ph4-DIP/C$_{60}$ and 37 % for 10 nm Ph4-Ph4-DIP/Me-PTCDI. The *I-V* curves are measured under illumination of simulated sunlight with an intensity of 100...110 mW/cm^2 monitored by a calibrated silicon photodiode and roughly corrected for spectral mismatch. Dashed: simulation data. The remaining input parameters can be found in Appendix B, p. 327.

In the following the effect of a decrease in mobility imbalance is investigated: Increasing μ_p^{D} by replacing Ph4-Ph4-DIP with ZnPc leads to well known ZnPc/C$_{60}$ solar cells without S-shapes (cf. previous chapter). Thus, it is more interesting to maintain the donor material Ph4-Ph4-DIP and investigate a decrease of μ_n^{A}. To do so, Me-PTCDI, a material with a comparable electron affinity to C$_{60}$ is used to replace the acceptor C$_{60}$. OFET measurements are used to determine the mobility of the materials and deliver an electron mobility which is significantly lower than in C$_{60}$ (C$_{60}$: 7×10^{-3}, Me-PTCDI: 2×10^{-4},

Ph4-Ph4-DIP: 2×10^{-6} cm^2/Vs)[2]. Although the OFET mobility is determined under different measurement conditions (lateral surface current and high charge carrier densities) than relevant for charge transport in organic solar cells, rough trends can be transferred to layers in solar cell geometry. The dotted *J-V* curve in Fig. 7.6 representing a Ph4-Ph4-DIP (10 nm)/Me-PTCDI device shows indeed no S-kink. This is expected from the simulation data displayed in Fig. 7.1. The *FF* is lower than in the solar cell with C$_{60}$ caused by the lower mobility of Me-PTCDI. The photocurrent is decreased mainly due to a smaller contribution from Me-PTCDI compared to C$_{60}$ and possibly a decreased charge carrier separation efficiency, because the EQE (Fig. 7.4) drops in the whole spectral range. However, the lower photocurrent cannot explain the difference in the shape between C$_{60}$ and Me-PTCDI as acceptor, because a varied illumination intensity does not significantly influence the S-kink. Me-PTCDI solar cells also show an S-kink for thicker Ph4-Ph4-DIP layers, which qualitatively fits to the predicted thickness dependence (data not plotted).

To further confirm the interpretation, inverted cells are made and shown in Fig. 7.7[3]. They show the same trends, which means that the observed features do not depend on the stack order. The open-circuit voltage of the Me-PTCDI samples is reduced which might be due to the inverted stack. Previously for all solar cells, an n-doped C$_{60}$/Al contact was used, whereas here an ITO/C$_{60}$ and ITO/Me-PTCDI contact are used as electron collecting electrode. Furthermore, the material batch was changed. However, the S-kink is significantly present in the FHJ with C$_{60}$, whereas the FHJ with Me-PTCDI shows a reasonable *FF*. So, this is in accordance with the discussions so far. Now the FHJ data is compared to bulk heterojunction (BHJ) data, displayed in Fig. 7.7 as well. The BHJ solar cells (dashed) do not show S-kinks for both acceptors. The *FF* of the C$_{60}$ cell is significantly increased compared to the FHJ. The reason is that charge transport is mainly provided by electrons. This can also be seen in the higher forward currents for the BHJ. Here, the electrons are capable of driving the complete current through the bulk, in contrast to a FHJ where hole current in the pristine donor layer is required as well.

The comparison between FHJ and BHJ reminds us to the previous chapter where we found significant differences dependent on the type of barrier. There, it was shown that in case of extraction barriers, the S-kink remains for FHJ and BHJ, whereas in case of an injection barrier the S-kink of a FHJ vanishes for a BHJ. This is comparable to the observation here. However, in Chapter 6 the removal of the S-kink was accompanied by a reduction of V_{oc}. This is not the case here. V_{oc} is almost independent of the solar cell consisting of a BHJ or FHJ. Thus, an injection barrier as main source of the S-kink is excluded and the S-kink is attributed to the low mobility of Ph4-Ph4-DIP which shows a high imbalance with the electron mobility in C$_{60}$.

---

[2]Measurements done by Moritz Hein, IAPP, at OFETs in bottom-gate geometry with SiO$_2$-dielectrics and Au contacts. The setup is described in Ref. [304]. A later modification of the setup resulted in higher mobilities for C$_{60}$.

[3]Solar cells fabricated by Annette Petrich, IAPP, in vacuum evaporation tool B30.
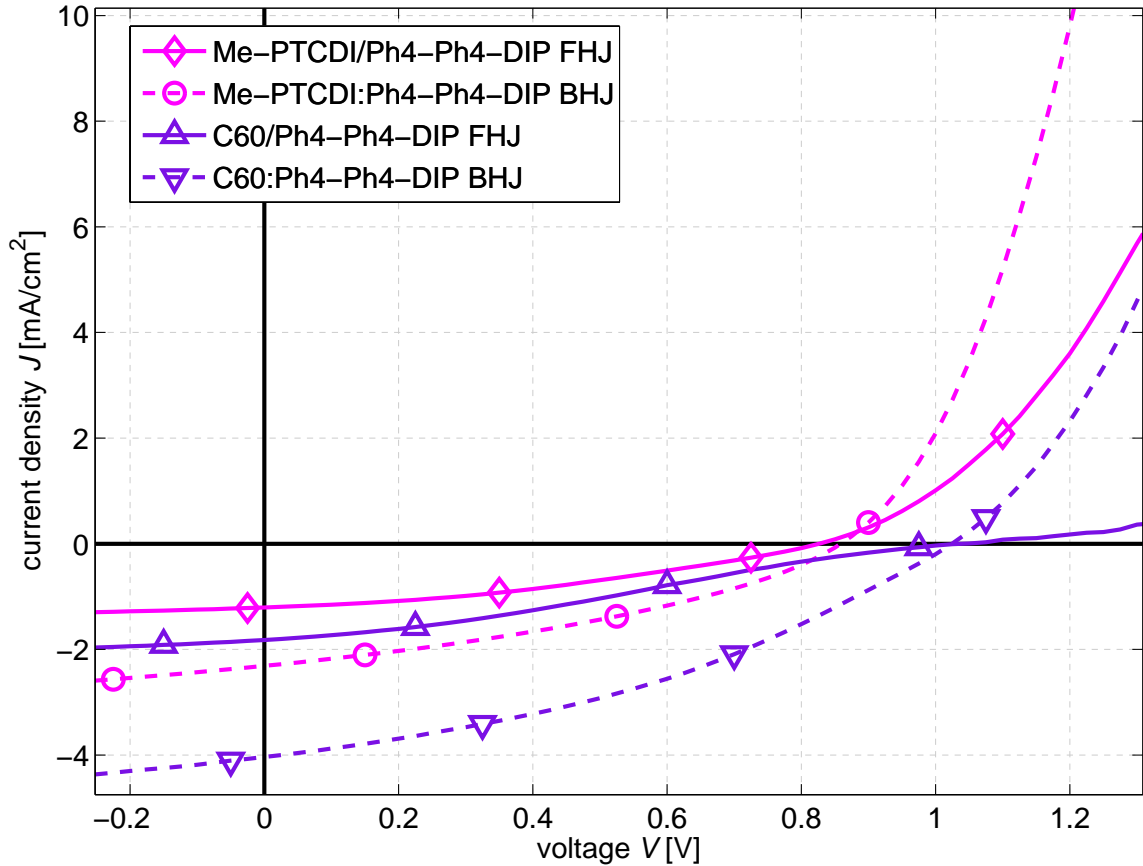
Figure 7.7: Comparison between flat (FHJ) and bulk heterojunction (BHJ) solar cells in inverted architecture: ITO/ETL(20 nm)/ active layer /Ph4-Ph4-DIP(5 nm)/p-BPAPF(40 nm)/p-ZnPc(10 nm)/Au(40 nm) with active layer acceptor(5 nm)/Ph4-Ph4-DIP(25 nm) for FHJ and acceptor:Ph4-Ph4-DIP(25 nm; 3:2) for BHJ. Either C_{60} or Me-PTCDI is used as acceptor and electron transport layer (ETL). The S-kink is only observed for the FHJ with C_{60}.

7.2.2 Transient photocurrents

A further proof of the significance of the low-mobility donor is presented applying photocurrent transient measurement. In the previous chapter (Ch. 6.5.4) this method has already been used to identify the existence of barriers by overshoots in the current signal. There, it was proposed that transient photocurrents are capable of discriminating different reasons for an S-kink. A voltage sweep of transient current data of the device with 20 nm Ph4-Ph4-DIP/C_{60} is shown in Fig. 7.8. Although the shape of the J-V curves of a mobility-mismatch and barrier-induced S-shape look similar (cf. Fig. 7.6 and Fig. 6.4), the transients behave differently. In Fig. 7.8 they are characterized by a very slow response due to the low mobility (time range is milliseconds). There is a small overshoot visible when
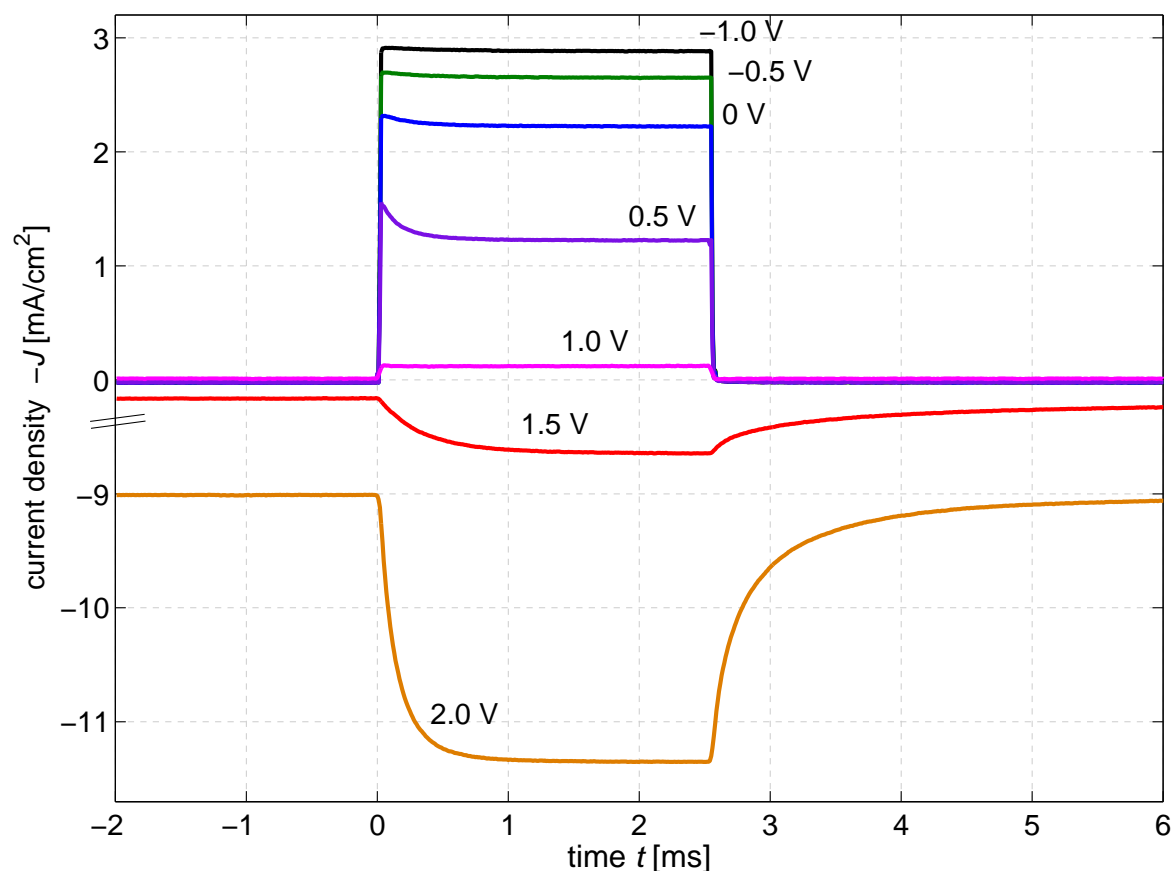
Figure 7.8: Transient current response of the sample containing 20 nm Ph4-Ph4-DIP combined with C_{60}. The response time is in the range of milliseconds. Under forward bias ($> 1.5\,\mathrm{V}$), a photoconductivity effect is seen.

switching on the device, however none when switching off. At V_{oc} there is no transient current measurable at all. This means that there is no redistribution of charges within the device and the hole transport in the donor away from the donor-acceptor interface is the limiting process. The transients at voltages larger than V_{oc} show that illumination results in an increase in forward currents. Possible reasons for this phenomenon were discussed in Ch. 5.3. The absolute value of this current reaches values larger than the photocurrent extracted in reverse direction. This and the increased time constant compared to current extraction clearly indicate that the reason for this increased current is an increase in conductivity of Ph4-Ph4-DIP upon illumination. Thus, this current is no extracted photocurrent, but due to a photoconductivity effect which decreases the series resistance of the device under illumination.

7.3 Field-dependent exciton dissociation as an additional source of S-kinks

The S-kink in the discussed simulations is only caused by transport properties of free charge carriers. Field-dependent exciton dissociation according to Onsager-Braun theory (Ch. 4.4.2) does not significantly modify the effect of the mobility imbalance. However, in the extreme case this process could be an additional source of S-kinks which is mentioned in this context for completeness. Simulations show that this S-kink is more pronounced in the case of a discrete CT state energy compared to a distribution (Eq. 4.52). The simulation
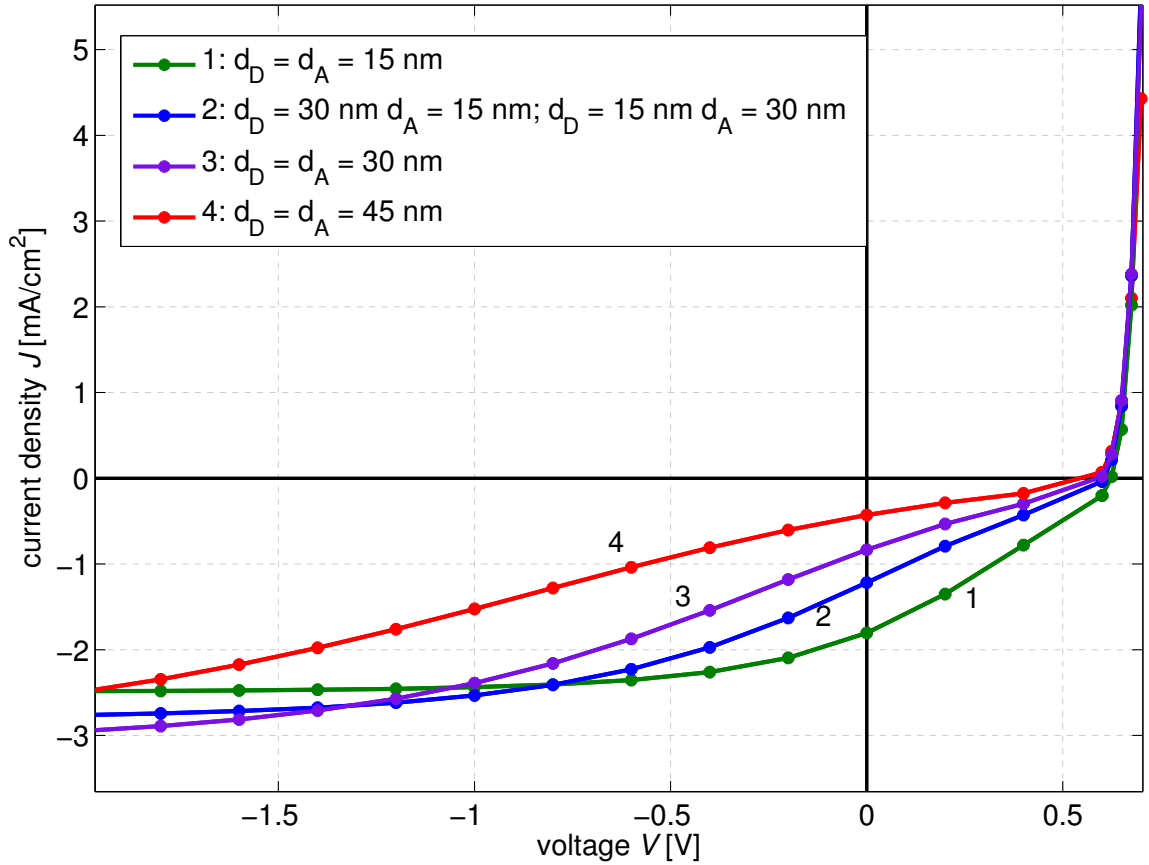
Figure 7.9: S-kink caused by field-dependent exciton dissociation according to Onsager-Braun theory with $a = 1.2\,\mathrm{nm}$ and $k_{\mathrm{relax}} = 5 \times 10^6\,\mathrm{s}^{-1}$. Other parameter pairs, where this process is significant, show a qualitatively similar behavior. In comparison to Fig. 7.1, only the overall device thickness is important for the strength of the S-kink (as long as donor and acceptor show the same dielectric constant and charge transport is not limiting). Forward current is relatively unaffected compared to the data of Fig. 7.1. For details, see Appendix B, p. 327.

data shown in Fig. 7.9 demonstrate that the curvature of such an S-kink is lower than in the case of imbalanced mobilities or barriers. Therefore, the S-kink covers a larger voltage range. The curves for different thicknesses show that the strength of the S-kink scales with the overall device thickness. Characteristic for this kind of S-kink is that forward current is not affected. This allows to discriminate it from the barrier effects discussed in the previous chapter and from the imbalance mobility effect discussed in this chapter. Although reported in literature for polymer [305] and small molecule [306] devices, in this work, no evidence for this effect was found in experimental data of small-molecule solar cells comprising several donor-acceptor combinations.

7.4 Summary

Drift-diffusion simulations of bilayer devices demonstrated that S-kinks in the J-V curve can also be caused by an imbalance in charge carrier mobilities (μ_n^A/μ_p^D) if the imbalance is larger than 100 for comparable layer thicknesses. In this case, instead of the contacts, the charge carrier transport properties of the active material itself are responsible for the S-kink. The simulations showed that the ratio of donor:acceptor thickness mainly dominates the strength of the S-kink.

An experimental verification was done by flat heterojunction solar cells with a low-mobility donor Ph4-Ph4-DIP combined with acceptors C_{60} and Me-PTCDI which show different electron mobilities. Only the flat heterojunctions of Ph4-Ph4-DIP/C_{60} showed significant S-kinks which were strongly dependent on donor layer thickness. Transient photocurrents showed a large response time and no charging effect which excludes barriers as main reason for the S-kink.

Chapter 8

Open-Circuit Voltage and *J-V* Curve Shape of ZnPc:C$_{60}$ Solar Cells with Varied Mixing Ratio and Hole Transport Layer

In this chapter the effect of changes in the active material system and modifications of contact properties are investigated for solar cells consisting of a blend of ZnPc:C$_{60}$. To do so devices with different blend mixing ratios and with a variation of the hole transport layer are prepared. The J-V data is compared to simulation data, where the findings of Chapter 6 are applied to explain the shape of the J-V curves. It is shown that the open-circuit voltage is mainly defined by the mixing ratio, whereas the fill factor is strongly influenced by the choice of the hole transport layer. From Chapter 6 we know that extraction barriers for photogenerated holes lead to S-shaped J-V curves and that the strength of the S-shape scales with the height of the extraction barrier. Therefore, the slope of the J-V curves at open circuit is used to evaluate the effect of the mixing ratio. The data suggest that the observed increase in open-circuit voltage with a higher amount of C$_{60}$ in the blend is due to a down-shift of the highest occupied molecular orbital of ZnPc upon blending with C$_{60}$.[1]

8.1 Experimental approach

Up to now, we mainly discussed contact properties and presented detailed investigations on flat heterojunction solar cells where material variations are easier to analyze. Since the central element of efficient devices is the bulk heterojunction (BHJ), we focus on it in this and the following chapters. We already noted that an optimized BHJ is arranged in a way that a tradeoff between exciton harvesting and charge carrier collection is achieved. The

---

[1]The content of this chapter is published in W. Tress, S. Pfuetzner, K. Leo, and M. Riede, *Open circuit voltage and IV curve shape of ZnPc:C60 solar cells with varied mixing ratio and hole transport layer.* Journal of Photonics for Energy **1**, 011114-1 (2011)
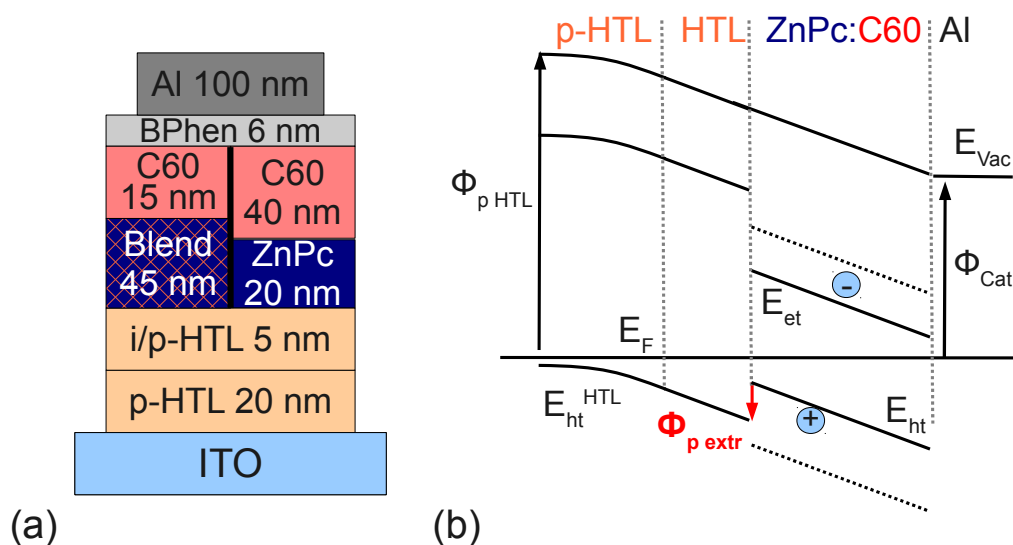
Figure 8.1: (a) Solar-cell stack: ITO / p-doped hole transport layer (HTL) to ensure an Ohmic contact to the ITO / p-doped or intrinsic HTL / the photoactive layers / BPhen-Al contact. The photoactive stack consists in the case of a bulk heterojunction of a blend layer of ZnPc:C$_{60}$ with varied mixing ratio followed by an intrinsic C$_{60}$ layer or in the case of a flat heterojunction of a ZnPc/C$_{60}$ bilayer. (b) Sketch of energy diagram of the stack, neglecting the thin BPhen buffer layer and showing the hole extraction barrier $\phi_{\text{p extr}}$ at the HTL/donor interface.

morphology of the mixed film and especially the grade of demixing can be adjusted by the choice of the appropriate solvents for spin-coated devices [307, 308], by solvent [309] and post annealing [310, 311], or by substrate heating during material deposition [312, 313]. The impact of these treatments can be seen at the current-voltage characteristics (*J-V* curve), changing mainly short-circuit current density J_{sc} and fill factor *FF*.

Another means of influencing the morphology and percolation properties of a BHJ consists of changing the mixing ratio, whose optimization is essential and can result in increased values of J_{sc} and *FF* [314]. Also the open-circuit voltage V_{oc} of several material systems has been observed to depend on mixing ratio [315–317]. However, no clear explanation for this effect has been provided so far.

In this chapter, we separately investigate the effect of different mixing ratios of ZnPc:C$_{60}$ BHJs and the effect of different hole transport layers (HTLs) on V_{oc} and *FF*. The focus is on the impact of hole extraction barriers, emerging when the highest occupied molecular orbital (HOMO) level of the transport material lies below the HOMO level of the donor material (cf. Chapter 6). Furthermore, the role of doping is investigated in the presence

of a barrier by comparing devices with and without an intrinsic HTL interlayer between doped HTL and blend. These experimental variations are accompanied by simulations showing the impact of extraction barriers, doping of the HTL, and changes in the charge carrier mobility on the J-V curve shape.

The device architecture is of p-i-metal type and thus comparable to the ones discussed in previous chapters. A sketch of the device stack can be seen in Fig. 8.1(a). The 45 nm thick active layer of a ZnPc:C_{60} blend with different mixing ratios is embedded between a 25 nm thick HTL and a 15 nm/6 nm C_{60}/BPhen electron transport layer, covered by an Al layer as cathode. For comparison, also flat heterojunction (FHJ) devices are investigated. In this case, the blend layer is replaced by a 20 nm thick ZnPc and 25 nm thick C_{60} layer. The HTL consists of a 20 nm highly doped (1...10 wt%) region at the ITO contact and an optionally (un)doped region of 5 nm thickness. As HTL materials the following already previously employed wide-gap molecules are used: MeO-TPD (HOMO$_{UPS}$ -5.1 eV), Di-NPD (HOMO$_{UPS}$ -5.35 eV), and BF-DPB (HOMO$_{UPS}$ -5.25 eV). Their molecular structures are depicted in Fig. 3.28 (p. 89). As dopants NDP2 (p-dopant) and NDN1 (n-dopant) are employed. A sketch of an energy diagram of the devices is shown in Fig. 8.1(b).

Data of two separate evaporation runs are shown in this chapter. However, additional runs prove the reproducibility of all trends discussed here. I-V measurements are performed under simulated sunlight with a corrected intensity of 100 mA/cm^2 under an assumed spectral mismatch of 0.7. As J_{sc} is not evaluated in detail, an effort for an accurate determination of the mismatch and for an individual correction of the illumination intensity for each sample is not made.

8.2 The open-circuit voltage

In this section the trends in the open-circuit voltage V_{oc} as a function of mixing ratio and HTL material are investigated. To do so, V_{oc} of various samples is depicted versus the volume mixing ratio of the blend ZnPc:C_{60} in Fig. 8.2. A clear and reproducible trend is observed: V_{oc} increases with the amount of C_{60} in the blend layer and is only weakly influenced by the hole transport layer. According to Chapter 6, a V_{oc} which is independent of the HTL is expected. The reason is that the HOMO value of the shown hole transport materials is lower than the HOMO of ZnPc (-5.0 eV...-5.2 eV). Therefore, no injection but possibly extraction barriers for holes are formed at the interface HTL/blend in all cases here. At V_{oc}, where current does not flow, this extraction barrier has no influence on the properties of the device, as we have seen in Chapter 6 as well. Hence, V_{oc} is only governed by the quasi-Fermi level splitting resulting from charge carrier generation and recombination in the photoactive blend layer.

This argument holds without exception for a FHJ, where the HTL is not in contact with photogenerated electrons, but it may be insufficient for blend layers. At the interface HTL/blend, recombination of electrons coming from the blend with holes coming from the HTL can occur. If this recombination is significant compared to the bulk recombination in the blend, it reduces V_{oc} as theoretically discussed in Ch. 2.4 and Ch. 5.2.4. In case of
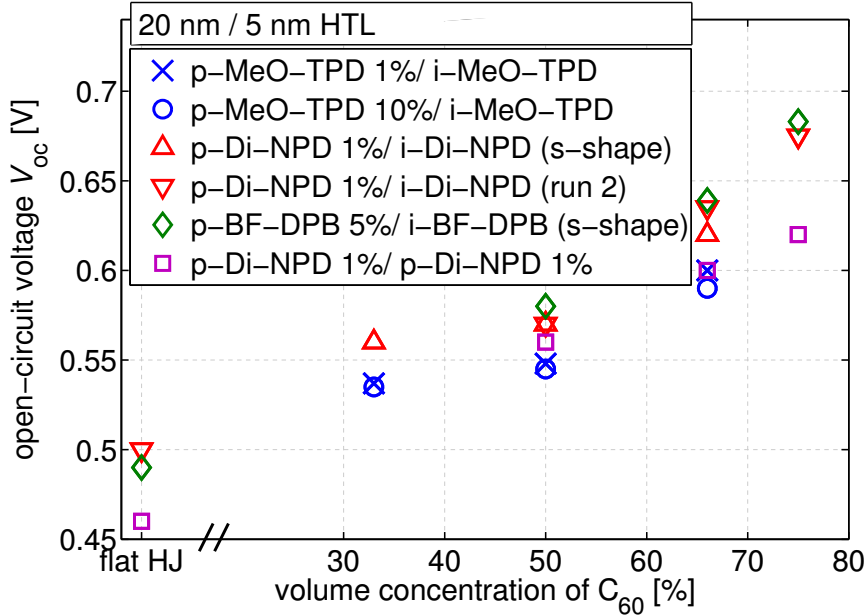
Figure 8.2: V_{oc} as a function of the volume mixing ratio for different HTLs. Trends are reproducible; absolute values, especially for S-shape devices, can differ slightly, as demonstrated by showing some data of another evaporation run.

an extraction barrier, this interface-recombination probability could be modified resulting in a reduced "surface" recombination rate of electrons in the blend with holes in the HTL.

This effect can be explained by the simulated electric field distribution and the charge carrier density profiles in the device shown in Fig. 8.3. Here, we focus on the case of an intrinsic interlayer (solid and dashed lines). The case of a doped interlayer is discussed in the next section. The layer sequence p-HTL/i-HTL constitutes a p-i junction, where holes in the p-doped region face a diffusion gradient towards the intrinsic region. They diffuse into the intrinsic region and leave a space charge behind. The extraction barrier at the HTL/blend interface reduces the probability of holes being located in the intrinsic HTL. Therefore, the hole accumulation region is shifted into the photoactive layer [Fig. 8.3(a)]. There, the hole density is high, whereas it is low in the intrinsic HTL [Fig. 8.3(b)]. This leads to a high field in the intrinsic HTL which behaves like a dielectrics in a capacitor [Fig. 8.3(c)]. Its charge consists of the localized anions (N_A^-) in the p-HTL and the holes in the blend, kept away from the p-HTL/HTL interface by the extraction barrier. The reduced hole concentration at the interface decreases the recombination probability at the interface HTL/blend. This is the explanation for the slight, however systematic, increase of V_{oc} with lower lying HOMO of the HTL in simulation [cf. Fig. 8.4(b)]. It could also play a role in experiment if the recombination at the HTL/blend interface is more probable than recombination in the blend.

When ignoring the data points of the strong S-kink curves, the following maximum
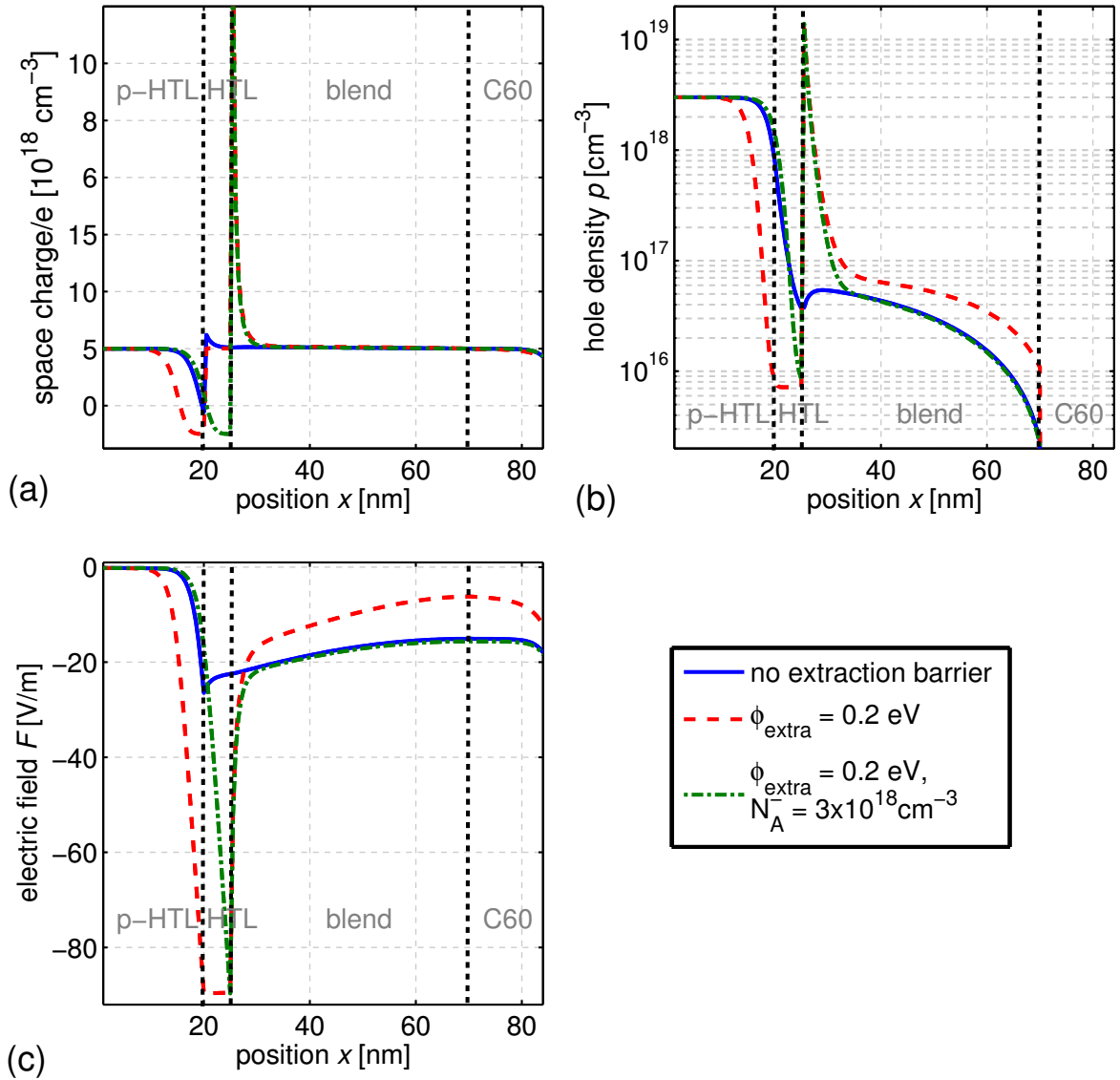
Figure 8.3: Profiles at -0.5 V for selected configurations of Fig. 8.4(b). x denotes distance from anode. (a) Total space charge divided by the elementary charge e, (b) hole density, and (c) electric field F. The extraction barrier causes a pile up of holes in the blend in front of the barrier and a modification of the electric field in the blend. Doping of the 5 nm HTL reduces this effect.

values for V_{oc} can be extracted from Fig. 8.2 (volume mixing ratio ZnPc:C$_{60}$ in brackets): 0.54 V (2:1), 0.56 V (1:1), 0.60 V (1:2), and 0.62 V (1:3). These are supposed to be the intrinsic maxima corresponding to the mixing ratio of this material system under 1 sun illumination at around 300 K. This is supported by additional experiments (*I-V* curves

not shown), considering the electron contact. A replacement of BPhen by n-doped C$_{60}$ as electron transport layer has no influence on V_{oc}. Compared to a FHJ using the same material batch of ZnPc and C$_{60}$, the V_{oc} of all BHJs is significantly larger. Commonly, the opposite effect is observed [301]. The reason might be that V_{oc} of the reported BHJs is limited by contact properties causing an injection barrier, which reduces V_{oc} of a BHJ as elaborated in Chapter 6.

8.3 The role of the hole transport layer and of doping

In Fig. 8.4(a) the *J-V* curves of a 1:1 blend with various HTLs are shown for a detailed investigation of the influence of the HTL. Data of nominally identical samples resulting from two different evaporation runs are also shown to indicate the reproducibility between different runs. We have discussed in Ch. 3.5.3 that the reproducibility within one run is excellent whereas larger deviations between different runs may occur. The *J-V* curves with HTL Di-NPD show that the *J-V* curve shape is maintained. However, the photocurrent originating from the blend is changed by 15…20 %, probably due to a changed material batch. The V_{oc} of all nominally identical samples is almost unchanged as already visualized in Fig. 8.2.

We first study the case where an intrinsic HTL interlayer is inserted between the doped HTL and the donor. For MeO-TPD (HOMO -5.1 eV), whose HOMO is well adjusted to the HOMO of ZnPc (-5.0 …-5.2 eV), the *FF* is highest. In the case of Di-NPD (-5.35 eV) and BF-DPB (-5.25 eV) S-kinks occur in the *I-V* curve. This is attributed to a hole extraction barrier of around 0.2 eV resulting from the HOMO offset between HTL and donor. The scaling of the S-kink with extraction barrier height, as expected from Chapter 6, is demonstrated in simulation data of Fig. 8.4(b) (solid lines). The reason for the S-kink is a pile-up of holes at the HTL/blend interface which is explicitly shown in the charge carrier density profiles of Fig. 8.3(b). When discussing thickness dependencies and photocurrent transients (Ch. 6.5.2 and 6.5.4) we claimed the existence of a high field in the intrinsic HTL. This is displayed by the electric field profiles in Fig. 8.3(c). The high field in the HTL means that a significant part of the built-in potential drops over the intrinsic HTL. Therefore, the field in the blend is reduced, which results in a reduced charge-carrier extraction probability in a certain voltage range. This leads to the S-kink in the *J-V* curve. Di-NPD and BF-DPB fit well into this theory, showing nearly the same strength of S-kinks and having comparable HOMO values. In the simulations shown in Fig. 8.4(c), the current across the interface is calculated using a Boltzmann factor (cf. Ch. 4.6.1), neglecting broadening of the HOMO due to disorder or a field dependent lowering of the barrier (tunneling). This is done for simplicity reasons and due to the fact that the required parameters are not known. However, it is sufficient for demonstrating the qualitative trends of small barriers. A consideration of the mentioned effects leads to a reduction of the strength of the S-kink for a fixed extraction barrier.

Although the interface i-Di-NPD/blend causes a strong S-kink, it can be removed by p-doping the 5 nm Di-NPD layer [−□− Fig. 8.4(a)]. The simulation data in Fig. 8.4(b)
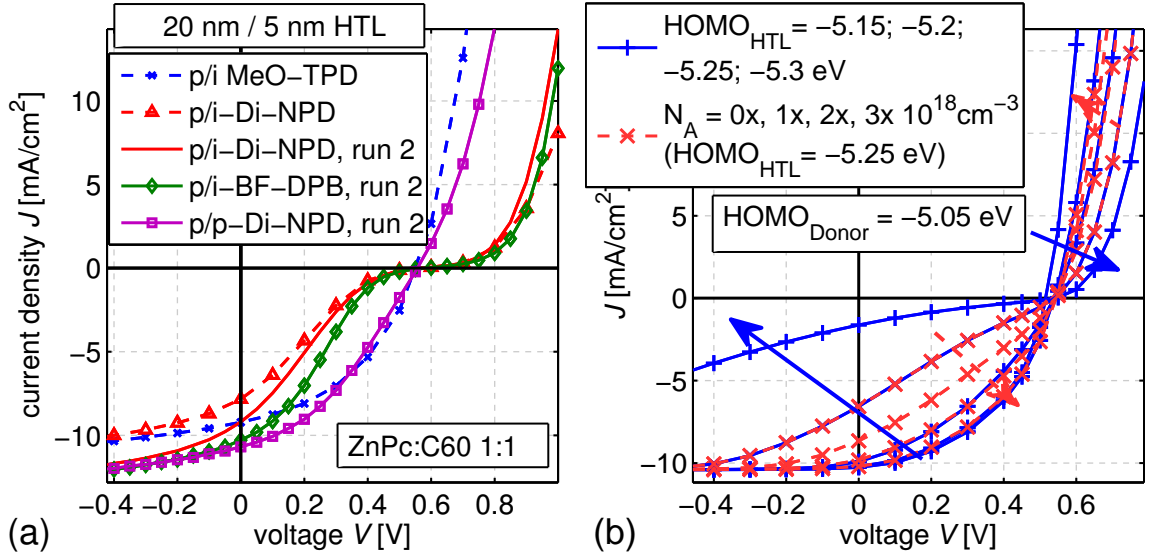
Figure 8.4: (a) **Experimental J-V curves** of 1:1 ZnPc:C_{60} blends with varied HTLs. V_{oc} and the shape of the J-V curves are reproducible between runs, the photocurrent slightly varies between different runs due to variations in layer thicknesses and material purity dependent on the batch used. (b) **Simulation data** with varied HOMO of the HTL, resulting in extraction barriers (HOMO$_{Donor}$ = -5.05 eV) (solid lines) and with varied doping in the 5 nm intrinsic HTL layer for HOMO$_{HTL}$ = -5.2 eV (dashed lines). Further relevant parameters: $\mu_p^{HTL} = 10^{-5}\,cm^2/Vs$, $\mu_p^{blend} = 5 \times 10^{-6}\,cm^2/Vs$, $\mu_n^{blend} = 5 \times 10^{-4}\,cm^2/Vs$, LUMO$_{C_{60}}$ = -4.0 eV, the generation profile is obtained by optical simulations. Details are found in Appendix B, p. 328.

(dashed lines) reproduce this observation. The reason is the following: As the S-kink is due to an insufficient extraction of charge carriers at a low internal field (close to V_{oc}), the field in the blend is expected to be increased by doping the HTL. Exactly this happens [Fig. 8.3(c)], because the drop of the potential over the former intrinsic layer is avoided. In comparison to the previous discussion, the p-i junction is now shifted to the HTL/blend interface. This causes a narrow peak of the electric field at this interface as visible in Fig. 8.3(c). According to Poisson's equation (Eq. 4.16) the high and localized field results in a large gradient in the electrical potential. Therefore, one may assume that also tunneling through a part of the barrier supports photocurrent at the HTL/blend interface. Such a tunneling process is likely, since a hop of a hole from the ZnPc to the Di-NPD molecule covers a finite distance of around 1 nm. For the simulation a concentration of active dopants in the range of $10^{18}\,cm^{-3}$ is assumed, which is a reasonable value for the weight percentage evaporated [156]. It can be seen that the strength of the S-kink is reduced by an increased doping concentration, resulting in comparable values of *FF* of devices with and without extraction barrier.
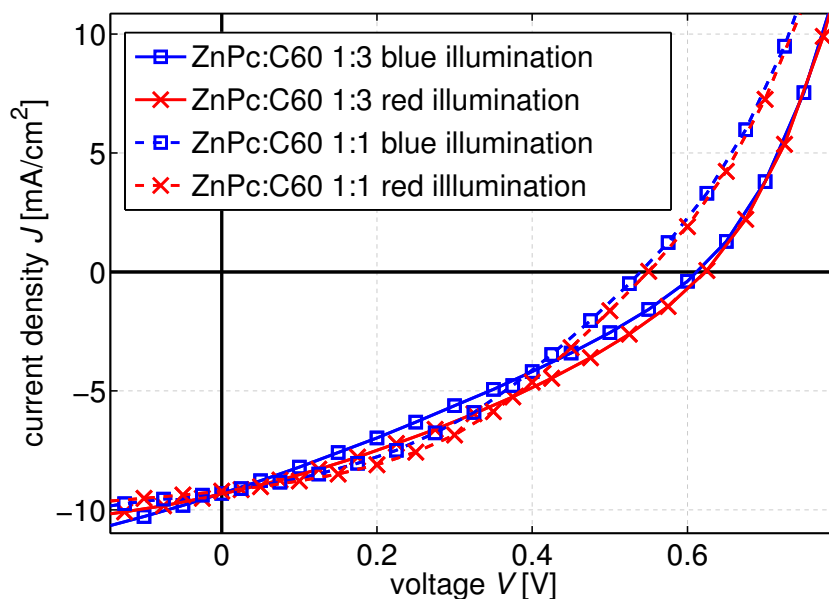
Figure 8.5: *J-V* curves of ZnPc:C$_{60}$ solar cells with different mixing ratio, illuminated with monochromatic LEDs (blue: LUXEON K2 LXK2-PB14-P00, red: LUXEON K2 LXK2-PH12-S00) with an intensity resulting in a photocurrent comparable to AM1.5g illumination. V_{oc} is not affected by the illumination color but by the mixing ratio.

8.4 Explaining the open-circuit voltage as a function of mixing ratio

It was observed that V_{oc} is mainly determined by the mixing ratio of the blend. Furthermore, it was explained why the HTL mainly changes the *FF* by the occurrence of an S-kink in case of extraction barriers. Remaining is the explanation of the behavior of V_{oc}. Therefore, possible reasons for the dependence of V_{oc} on the mixing ratio are suggested and discussed in the following:

1. The HTL/C$_{60}$ interface might act as an additional exciton splitting interface besides ZnPc/C$_{60}$. As the HOMO level of the HTL (especially in the case of Di-NPD) lies lower in energy than the HOMO of ZnPc, the heterojunction HTL/C$_{60}$ is expected to deliver a higher photovoltage for light absorption on C$_{60}$. This junction works in parallel to the ZnPc/C$_{60}$ heterojunction and could be significant, especially if the HTL shows a relatively high surface roughness providing enough interfacial area and an HTL/C$_{60}$ heterojunction that is spatially separated from ZnPc. An increasing C$_{60}$ content should enhance this effect and hence increase its contribution to V_{oc}. This process is examined by separately exciting ZnPc and C$_{60}$. This is done by

illumination with a blue and red high-power light emitting diode while recording *I-V* curves[2]. A comparison of V_{oc} is meaningful, when both light intensities are adjusted to the same J_{sc}. This implies a similar generation rate of charge carriers if the photocurrent around J_{sc} is close to saturation. This is approximately fulfilled for all devices investigated here (for an explanation of the photoshunt, see Chapter 11). If the described effect is dominant, V_{oc} should be higher for blue illumination compared to red illumination, where exciton separation happens only in the blend. However, Fig. 8.5 shows that this is not the case. V_{oc} is mainly independent of the illumination spectrum. This measurement, however, reflects the trend of V_{oc} observed at the *I-V* curves measured under simulated solar illumination, where V_{oc} is significantly higher for a ZnPc:C_{60} ratio of 1:3 compared to a ratio of 1:1.

2. V_{oc} is defined by the equilibrium between recombination and generation at the heterojunction. Due to a change in morphology, the probability of charge-transfer exciton separation [318] or charge carrier recombination might be modified. The experimental results for V_{oc} would fit into a bimolecular recombination model with a modified Langevin expression [255], where the recombination constant β is proportional to the mobility μ of the slower charge carrier ($\beta = e/\epsilon_0\epsilon_r \min(\mu_n, \mu_p)$, e elementary charge, ϵ_0 vacuum permittivity, and ϵ_r dielectric constant, cf. Eq. 4.4.2). This modification was proposed, as the recombination constant in blend layers is often observed to be lower than predicted by conventional Langevin theory, whose overall applicability to organic solar cells is under debate (cf. Ch. 4.4.2). If this hypothesis was correct, the holes being transported on ZnPc would limit recombination, because the hole mobility in ZnPc is lower than the electron mobility in C_{60}. The hole mobility further decreases with increasing C_{60} concentration in ZnPc:C_{60} blends [319] (cf. Chapter 11). This would lead to a decrease in the recombination constant with a higher amount of C_{60} in the blend and hence result in a higher V_{oc}, as discussed in Ch. 5.2.3.

3. V_{oc} scales with the effective gap, which is the difference between the LUMO of the acceptor and the HOMO of the donor (cf. Eq. 3.11 and Ch. 6.2.1). Due to a different local environment, dependent on whether and in which concentration ZnPc is blended with C_{60}, the polarization energy might be changed. This could result in a shift of the HOMO of ZnPc which can then be directly seen in V_{oc}. The V_{oc} data shown in Fig. 8.2 suggest a shift of the HOMO of about 0.1 eV. Therefore, an experimental determination via photoelectron spectroscopy is expected to be difficult. However, Park *et al.* recently showed that the effective gap changes indeed between a FHJ and a BHJ due to dipoles at the heterointerface [320]. The effective gap could also be changed by a shift of the LUMO of C_{60}. However, this is very unlikely, because experiments show that C_{60} attached to a blend layer (ZnPc:C_{60}/C_{60}) does not change V_{oc}, whereas ZnPc attached to a blend layer (ZnPc/ZnPc:C_{60}) significantly decreases V_{oc} (cf. Tab. 9.1 in Chapter 9, p. 240).

---

[2]Measurements performed at the IAPP lifetime setup
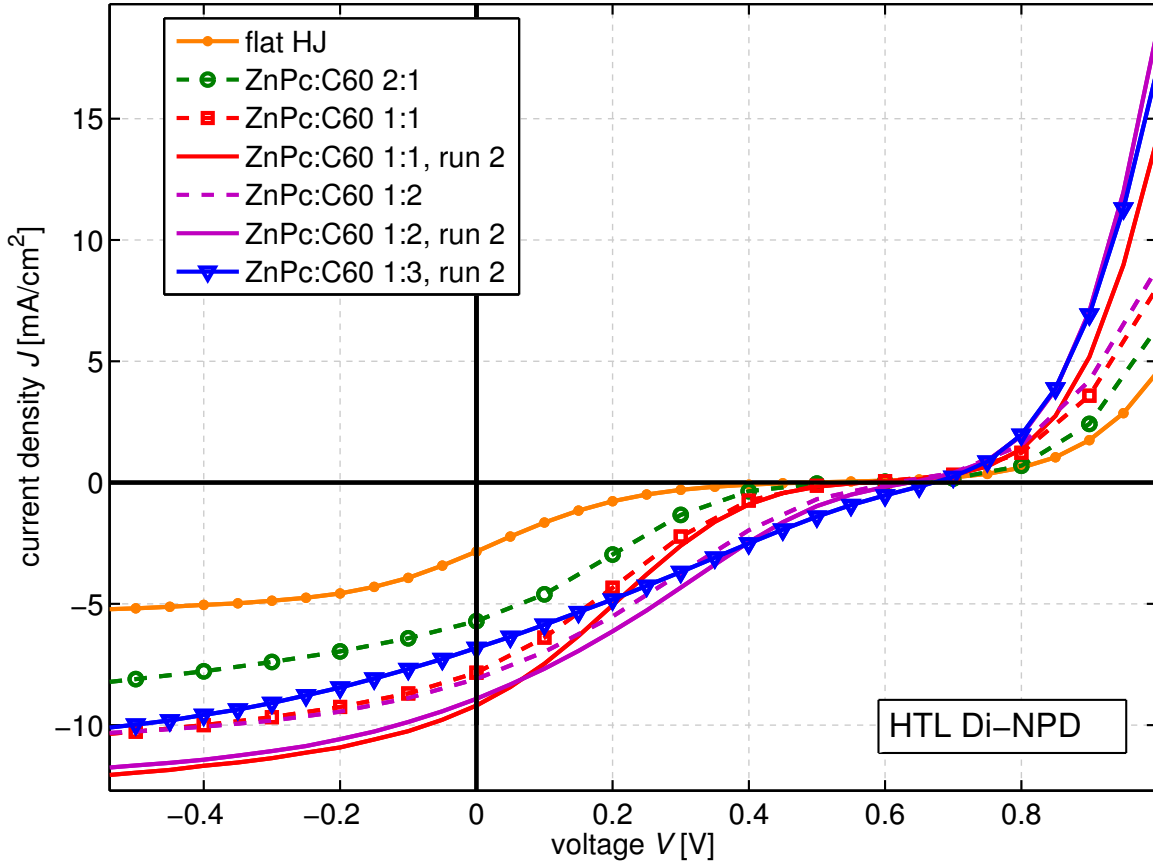
Figure 8.6: (a) **Experimental** *J-V* curves of devices with varied mixing ratio in the blend
    layer and Di-NPD as HTL. The strength of the S-kink is a measure of the
    height of the extraction barrier at the interface HTL/blend.

Now we evaluate the different hypotheses. The first suggestion is already disproved. To distinguish between the latter two possibilities, we qualitatively compare the properties of the experimental S-kink with simulation data. We choose the *I-V* curves of devices with different mixing ratios combined with Di-NPD as HTL, shown in Fig. 8.6. Apart from the slight shift in V_{oc}, there is a more significant difference in the strength of the S-kink. It gets more pronounced for *I-V* curves with lower values of V_{oc}.

As simulations using Onsager-Braun theory [94, 95] do not provide any indication for modified charge-transfer-exciton dissociation, which reproduces the experimental results, we do not follow this effect further. Instead, we investigate the effect of a changed recombination constant caused by a changed mobility. Figure 8.7(a) shows simulation data, where the hole mobility in the blend is modified to cover the experimentally observed range of V_{oc}. The change of hole mobility between 10^{-7} cm^2/Vs and 10^{-4} cm^2/Vs is high, however not unrealistic, as will be shown in Chapter 10. The electron mobility is kept constant.
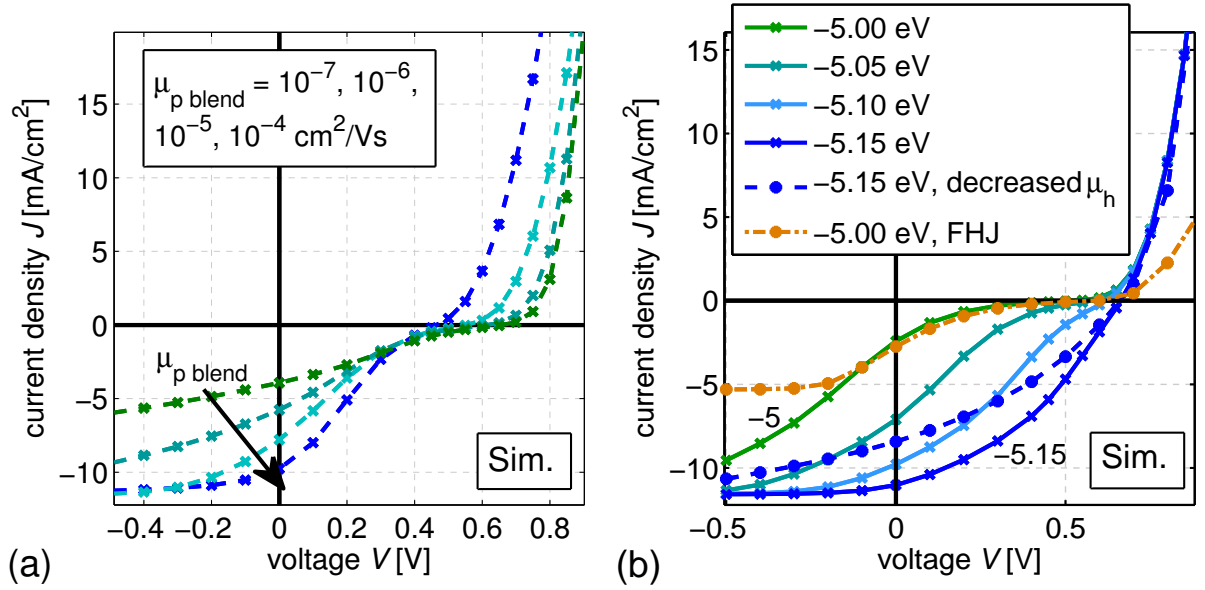
Figure 8.7: **Simulated** *J-V* curves of devices with (a) a varied hole mobility (HOMO$_{blend}$ = -5.05 eV) and (b) a varied HOMO of the blend. The parameter range is chosen to cover the experimental range of V_{oc} (HOMO$_{HTL}$ = -5.35 eV). For a more realistic description, disorder (width of HOMO 50 meV) and barrier lowering (1 nm hop) is included. For the flat heterojunction (FHJ), exciton diffusion lengths of 7 nm (ZnPc) and 15 nm (C$_{60}$) are assumed. The remaining input parameters are found in Appendix B, p. 328.

Its influence on the qualitative trends is negligible due to the assumption of a large value ($\mu_n = 10^{-3}$ cm^2/Vs). The recombination constant is calculated using the discussed modified Langevin expression, which depends on the lower mobility only. Data is shown assuming an extraction barrier (0.3 eV), which is required for an S-kink, because the hole mobility in the blend layer itself cannot be source of an S-shape, as mentioned in the previous chapter. A comparison of the simulation data of Fig. 8.6 with the experimental *J-V* curves does not give good agreement in the trends. Decreasing mobility in simulation increases V_{oc}, however does not reduce the S-shape by a shift as it is seen for the experimental *J-V* data with increased V_{oc} (C$_{60}$ content). The effect of a decreased mobility in simulation results in a larger dependence of photocurrent on voltage. This causes a lower *FF* and leads to a flattening of the S-shape. Hence, the mobility effect is not considered as main reason for the change in V_{oc}.

The investigation of the third effect is done discussing the *J-V* curves shown in Fig. 8.7(b). Here, the HOMO of the donor in the blend is varied from -5 to -5.15 eV and the HOMO of the HTL is kept constant at -5.35 eV. The simulation data show good agreement with the experimental data (Fig. 8.6), as the correlation of V_{oc} with the strength of the S-kink is reproduced. As the extraction barrier gets smaller with a downshift of the HOMO of

the blend, the S-kink becomes less pronounced with a higher V_{oc}. We know this scaling of the S-kink with extraction barrier height from Chapter 6.

To become more realistic and closer to the shape of the experimental J-V curves, a dashed line and a dash-dotted line are added in Fig. 8.7(b). The dashed line is obtained assuming an additional reduction of the hole mobility by a factor of 5 for the 1:3 blend (without changing the recombination constant). A decreased hole mobility is expected at high C$_{60}$ concentrations, because the percolation paths for holes on ZnPc are reduced. This reduction of μ fits well to mobility measurements of Ref. [319] and mobility data presented in Chapter 10. The decreased mobility has less influence on the S-kink, however results in a strong, but smooth, field dependence of photocurrent and hence low *FF*, as seen in experiment. The dash-dotted line is simulation data of a flat heterojunction with a value of -5.0 eV for the HOMO of the donor. This J-V curve fits well to experimental data of a FHJ in Fig. 8.6. These simulations show that most likely a shift in the HOMO of the donor causes the observed changes in V_{oc}. A quantitative data extraction from the simulations is very difficult, as it is not only the barrier which dominates the charge transport between two adjacent molecules.

According to Chapter 6, a more detailed analysis of the strength of the S-kink can be done by examining the slope of the J-V curves at V_{oc}. For doing so the slope of the J-V curve at V_{oc} is plotted as a function of blend ratio for several HTLs in Fig. 8.8. The slope for the S-kink devices (intrinsic Di-NPD and BF-DPB) decreases with increasing ZnPc content, which suggests that the extraction barrier is indeed increased for a larger ZnPc content. For comparison, data of the slope (divided by 10) for devices with MeO-TPD or doped Di-NPD as HTL are shown in the figure as well. These two HTLs provide an efficient hole extraction as discussed previously. This means that the slope at V_{oc} is dominated by the charge extraction properties of the blend rather than by the HTL-blend interface. This is confirmed because the maximum of the slope is found for the 1:1 blend which provides enough percolation paths for electrons and holes. A detailed investigation of the dependence of the mobility on blend mixing ratio will be topic of Chapter 10.

The different values and trends for the devices with efficient charge carrier extraction excludes that the slope in the S-kink case is governed by charge carrier mobilities which depend on mixing ratio. Remaining is only the interface HTL/blend as dominating limitation. The slope at V_{oc} could be influenced by the contact area between HTL and ZnPc, as hole extraction requires a path from ZnPc to the HTL. The contact area is expected to decrease with less amount of ZnPc in the mixture, as long as the sticking coefficients of ZnPc and C$_{60}$ on the HTL are comparable and no reorganization of the blend occurs. There are no indications that these effects play a role for ZnPc:C$_{60}$ deposited at room temperature.

The higher slope for a higher C$_{60}$ content in the blend, however, means that hole extraction works even better, despite the (possibly) decreased contact area between ZnPc phases and the HTL. These considerations lead to the conclusion that the change in extraction barrier induced by a shift of the ZnPc HOMO level in the blend, which is dependent on mixing ratio, is the most likely explanation for the observed behavior. Recent UPS data of Park et al. [320] confirm this interpretation, showing that the ionization potential of
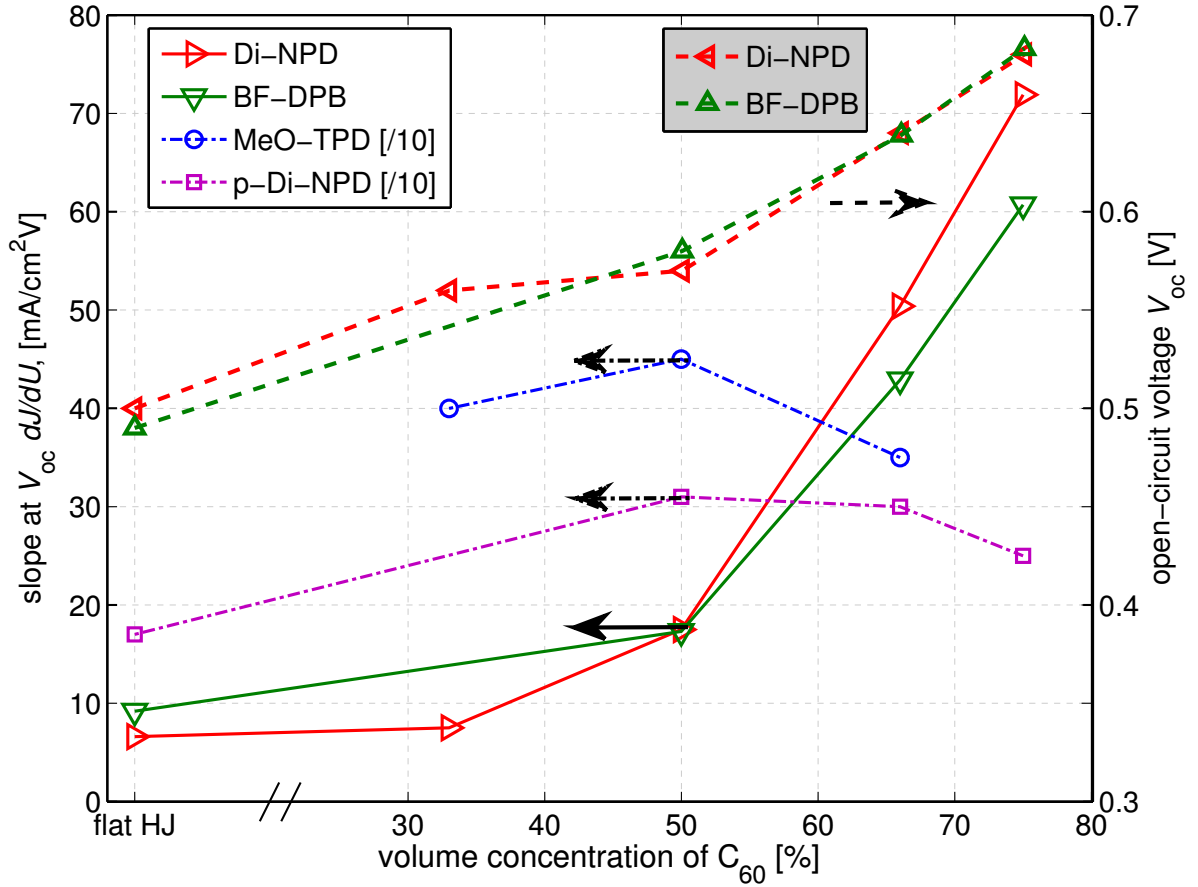
Figure 8.8: Slope dJ/dU at V_{oc} for several HTLs as a function of the mixing ratio. dJ/dU is estimated from $\Delta J/\Delta U$ with $\Delta U = 0.05$ V. Lines are to be seen as guide to the eye. For the S-kink devices, also V_{oc} is shown, which correlates with the dJ/dU.

ZnPc is increased when blended with C_{60}. In the meantime it was possible to perform IP measurements of blend films with different mixing ratios via UPS. As the expected changes in the IP smaller than 0.1 eV are close to the resolution and the threshold of reproducibility of UPS measurements, getting an unambiguous result is difficult. However, choosing the correct substrate (doped HTL), we could acquire reproducible data. These data clearly show a dependence of the IP on mixing ratio, which directly scales with V_{oc} and will be discussed elsewhere [321].

8.5 Summary

The focus of this chapter was on V_{oc} of ZnPc:C$_{60}$ bulk heterojunction solar cells with different mixing ratio. It was shown that V_{oc} depends on the mixing ratio. In the investigated range of mixing ratios (2:1 to 1:3) it increases with increasing C$_{60}$ content independently of the HTL. The HOMO level of the HTL has a minor effect on V_{oc}, however, it reduces the *FF* strongly in the case of extraction barriers for holes at the HTL/blend interface. As known from Chapter 6, this leads to S-kinks in the *J-V* curve. The strength of the S-kink and the slope of the *J-V* curve at V_{oc}, which are supposed to correlate with barrier height, give evidence that the dependency of V_{oc} on mixing ratio is caused by a shift of the ZnPc HOMO level depending on mixing ratio with C$_{60}$. This conclusion predicted by simulation data was confirmed by UPS measurements.

Chapter 9

Effect of Concentration Gradients in ZnPc:C$_{60}$ Bulk Heterojunction Solar Cells

This chapter continues with the description of the electrical properties of ZnPc:C$_{60}$ bulk heterojunctions started in the previous chapter. Now, a concentration gradient in the mixed absorber layer with increasing content of donor (acceptor) towards the hole (electron) collecting contact is discussed. Such an optimization of the morphology is supposed to improve the charge carrier collection in bulk heterojunction solar cells. The gradient is introduced by varying the deposition rate during co-evaporation of a 45 nm thick ZnPc:C$_{60}$ absorber layer in a p-i-metal solar-cell stack. It is shown that the observed increase in performance is mainly caused by a better energy-level alignment and reduced recombination at the p-side. A significant influence on charge carrier transport is not observed. However, regions with a concentration of less than 20 % of one component do not fully contribute to the photocurrent. Voltage dependent external quantum efficiency data are used to identify the photoactive regions.[1]

9.1 Investigated devices

In the previous chapter a variation of the mixing ratio was discussed. Another means of positively influencing the film morphology is to realize a gradient of the donor to acceptor ratio in the active layer. This means a higher concentration of acceptor material close to the cathode and a higher concentration of donor material close to the anode. This graded bulk heterojunction is supposed to assist charge carrier collection as it approaches the ideal morphology introduced in Ch. 3.3.1, Fig. 3.11, p. 59. Here, the major condition for an improvement in charge carrier extraction is the existence of sufficient percolation

---

[1]The content of this chapter is published in W. Tress, K. Leo, and M. Riede, *Effect of concentration gradients in ZnPc:C$_{60}$ bulk heterojunction organic solar cells.* Solar Energy Materials and Solar Cells **95** (Issue 11), 2981-2986 (2011).

paths also on the material with a low concentration in the blend. An increased solar cell performance for a spatially varied blend composition has been observed for polymer [322] and for small-molecule [323–325] solar cells. However, comprehensive physical explanations have not been given and the interpretations are mainly focused on modified charge carrier transport properties due to changes in the film morphology.

In this chapter, solar cells are investigated which comprise a blend of zinc phthalocyanine (ZnPc):fullerene C$_{60}$ with gradients in the volume mixing ratio ranging from 2:1 to 1:2, 3:1 to 1:3, and 4:1 to 1:4. The bulk heterojunction of some devices is sandwiched between neat layers of ZnPc and C$_{60}$ to investigate a potential benefit of a hybrid flat/bulk hetero-junction structure (cf. Ch. 3.5.1). In our discussion optical and electrical considerations as well as the effect of the contacts are included. Absorption measurements, current-voltage characteristics, voltage dependent external quantum efficiency data, and modeling results are used to quantify the properties of the different active-material stacks.

As in the previous chapters a p-i-metal device architecture is chosen. The active layer stack (45 nm ZnPc:C$_{60}$) is embedded between a transparent p-doped hole transport layer (HTL) of MeO-TPD:NDP2 (20/25 nm) and a C$_{60}$ (30/35 nm) /BPhen (6 nm)/Al (100 nm) electrode (inset of Fig. 9.3). MeO-TPD with an ionization potential (IP) of 5.1 eV is chosen as HTL to match the IP of ZnPc (5.0...5.2 eV).

The devices are categorized by their configuration at the p-side (Table 9.1). In devices of type **A** an intrinsic HTL (5 nm) is inserted between the doped HTL (20 nm) and the blend to study the effect of the HTL/blend interface. This intrinsic interlayer is missing in devices of type **C**, where the doped HTL (25 nm) is adjacent to the blend. Hybrid planar/bulk heterojunctions similar to the types **A** and **C** are produced by attaching a neat ZnPc layer to the blend (types **B** and **D**). The gradient is realized stepwise (e.g. 3:1 2:1 1:1 1:2 1:3 in equal distances (9 nm each), **A** and **B**) or gradually (**C** and **D**) by continuously adjusting evaporation rate ratios, e.g., from 0.3:0.1 to 0.1:0.3 Å/s. Devices of types **A** and **B** are produced in one evaporation run; devices of types **C** and **D** in another run using other material batches. Exemplary device stacks can be found in the inset of Fig. 9.3. The exact configurations are shown in Table 9.1. As discussed in Ch. 3.5.3 the total thickness of the blends is estimated under the assumption of a blend density, which is independent of the mixing ratio. The actually determined quantity is the mass of the deposited material, measured via quartz crystal monitors during evaporation. Consequently, the amount of each material, i.e. the number of molecules in the blend, is the same in all symmetrically graded layers.

9.2 Current-voltage results

Three advantages are expected when employing a gradient in a p-i-n geometry with the reflecting contact (Al) at the n-side and C$_{60}$ as acceptor and absorber in the blue spectral range: Additional to the already mentioned better charge carrier collection, the energy-level alignment at the p-side can be improved. As the electron affinity of ZnPc depends on the mixing ratio (cf. Chapter 8 and Refs. [320, 321]), this effect is especially important
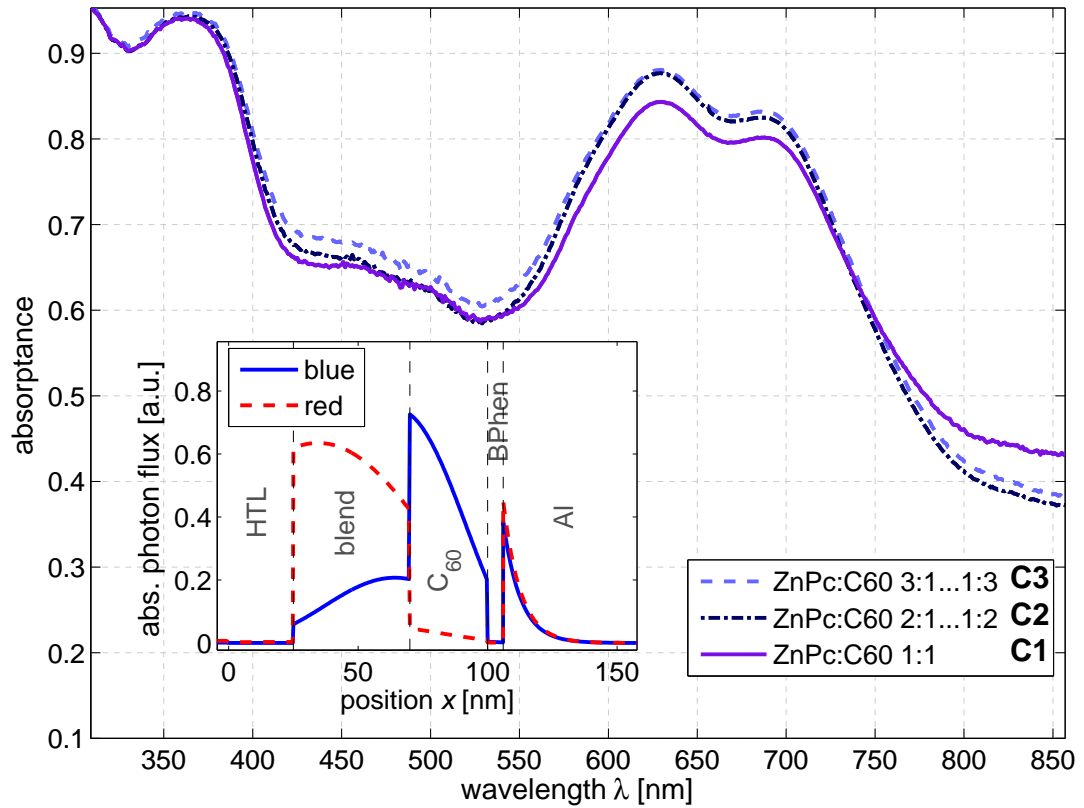
Figure 9.1: Absorptance of devices **C1-C3**. The inset shows the simulated absorbed photon flux per unit volume (physical unit is m⁻³s⁻¹) for monochromatic illuminations of a 1:1 blend. The illumination wavelengths are 630 nm (dashed), which corresponds to the main absorption peak of ZnPc, and 450 nm (solid), where C_{60} absorbs. The incoming photon flux is set equal for both wavelengths. x denotes the distance from the anode. Apart from the profile in the blend, the role of the 30 nm intrinsic C_{60} layer as optical spacer and additional blue absorber is visible.

when employing an adjacent neat ZnPc layer in a hybrid flat/bulk heterojunction. As final point, the absorption should increase for the same device thickness and material amount, because of the favorable positioning of ZnPc as red absorber and C_{60} as blue absorber regarding the optical field distribution, which shows the first interference maximum for short wavelengths closer to the Al cathode compared to longer wavelengths.

type	no	stack	J_{sc}[mA cm^{-2}]	V_{oc} [V]	FF [%]	η^* [%]
A	1	MeO-TPD (5) / ZnPc:C$_{60}$ 1:1 (45) / C$_{60}$ (35)	11.0	0.55	45	2.7
	2	MeO-TPD (5) / ZnPc:C$_{60}$ 2:1 (15) 1:1 (15) 1:2 (15) / C$_{60}$ (35)	11.0	0.56	50	3.1
	3	MeO-TPD (5) / ZnPc:C$_{60}$ 3:1 (9) 2:1 (9) ... 1:2 (9) 1:3 (9) / C$_{60}$ (35)	10.7	0.57	51	3.1
	4	MeO-TPD (5) / ZnPc:C$_{60}$ 4:1 (7) 3:1 (6) ... 1:3 (6) 1:4 (7) / C$_{60}$ (35)	9.62	0.57	51	2.8
B	1	MeO-TPD (5) / **ZnPc (10)** / ZnPc:C$_{60}$ 1:1 (45) / C$_{60}$ (35)	11.1	0.51	37	2.1
	2	MeO-TPD (5) / **ZnPc (10)** / ZnPc:C$_{60}$ 2:1 (15) 1:1 (15) 1:2 (15) / C$_{60}$ (35)	11.9	0.56	44	2.9
	3	MeO-TPD (5) / **ZnPc (10)** / ZnPc:C$_{60}$ 3:1(9) 2:1(9) ... 1:2(9) 1:3(9) / C$_{60}$(35)	11.4	0.57	46	3.0
	4	MeO-TPD (5) / **ZnPc (10)** / ZnPc:C$_{60}$ 4:1(7) 3:1(6) ... 1:3(6) 1:4(7) / C$_{60}$(35)	10.5	0.58	47	2.8
C	1	**p**-MeO-TPD (5) / ZnPc:C$_{60}$ 1:1 (45) / C$_{60}$ (30)	12.6	0.54	52	3.5
	2	**p**-MeO-TPD (5) / ZnPc:C$_{60}$ 2:1...1:2 (45) / C$_{60}$ (30)	13.0	0.55	52	3.7
	3	**p**-MeO-TPD (5) / ZnPc:C$_{60}$ 3:1...1:3 (45) / C$_{60}$ (30)	12.2	0.56	52	3.5
	4	**p**-MeO-TPD (5) / ZnPc:C$_{60}$ 1:1...1:3 (45) / C$_{60}$ (30)	12.1	0.55	50	3.3
D	1	**p**-MeO-TPD (5) / **ZnPc (15)** / ZnPc:C$_{60}$ 1:1 (45) / C$_{60}$ (30)	12.0	0.48	35	2.0
	2	**p**-MeO-TPD (5) / **ZnPc (15)** / ZnPc:C$_{60}$ 2:1...1:2 (45) / C$_{60}$ (30)	12.6	0.54	43	2.9
	3	**p**-MeO-TPD (5) / **ZnPc (15)** / ZnPc:C$_{60}$ 3:1...1:3 (45) / C$_{60}$ (30)	12.3	0.56	45	3.1
	4	**p**-MeO-TPD (5) / **ZnPc (15)** / ZnPc:C$_{60}$ 1:1...1:3 (45) / C$_{60}$ (30)	11.1	0.49	38	2.1

Table 9.1: Solar-cell stacks and parameters measured at the same nominal solar-simulator intensity. The stack shown is embedded between ITO/p-MeO-TPD (20 nm) and BPhen(6 nm)/Al(100 nm). Devices of type **A** and **B** comprise an intrinsic HTL MeO-TPD, which is missing in the devices of type **C** and **D**. In the devices of type **B** and **D** an intrinsic ZnPc donor layer is added. The devices no. 1 of each type employ a homogeneous blend, whereas the active layer of the others is graded. Shown are the values for the volume mixing ratio. Numbers in brackets denote layer thicknesses in nm. The nominal active area is 6.4 mm². All data are average values of four nominally identical samples. *J-V* curves of selected devices are shown in Fig. 9.3.

*As the focus is on a relative comparison, the values for efficiencies η are not corrected for spectral mismatch and are slightly overestimated. For example, device **C2** shows an efficiency of 3.2 % measured in an outdoor test.

The latter effect is taken to prove the presence of the gradient and to exclude a re-arrangement of the film during or after evaporation. Figure 9.1 shows the absorption spectra of devices with a homogeneous blend (**C1**) and with gradient layers (**C2 + C3**). Both, absorption of ZnPc (peaks at 630 and 690 nm) and of C_{60} (≈ 450 nm) (cf. Fig. 3.27), are increased by a graded structure, although the same amount of material is evaporated in all cases. The higher overall absorption indicates an improved positioning of the absorber materials within the optical interference pattern. This is verified by optical simulations. The calculated absorption profiles for a 1:1 blend are plotted in the inset of Fig. 9.1, illustrating that the absorption maximum in the blend with monochromatic blue illumination (450 nm) is located closer to the anode, whereas the profile for red illumination (630 nm) is basically inverted.

Table 9.1 gives an overview of the characteristic electric parameters of all solar cells produced. All measurements are performed with a solar simulator adjusted to the same nominal intensity ((143 ± 2) mW/cm^2) measured by a calibrated silicon reference diode. This means an assumed spectral mismatch factor of 0.7. Devices **C1** and **C2** are also measured in an outdoor setup, where they show an efficiency of 3.2 % (98 mW/cm^2, measured by a silicon reference diode). Thus, the efficiencies given in Table 9.1 are slightly overestimated, because an individual correction for spectral mismatch of each device is not done.

9.2.1 Fill factor

A comparison between devices of type **A** and **C** shows a significant difference in the trend of the fill factor (*FF*). The *FF* increases for devices with a stronger gradient when using an intrinsic MeO-TPD interlayer (**A**, 45...51 %). However, when employing doped MeO-TPD (devices **C**), there is no improvement in efficiency and the *FF* is around 50 %. This leads to the conclusion that the gradient does not improve charge transport in the blend. Percolation paths are already well established in a 45 nm thick homogeneous 1:1 blend and remain even for the 4:1...1:4 graded junctions. Still, the gradient increases the performance in case of an undoped transport layer (**A1-A3**), where a good charge transport over the HTL/blend interface depends on a good energy-level alignment (cf. Ch. 8.3). This effect is even more pronounced for the devices with an intrinsic ZnPc interlayer (**B + D**), where the absolute values of the *FF* are significantly lower (35...47 %). Device **D4** with an asymmetric gradient is an exception which will be separately discussed in the context of V_{oc}.

The observed increase in the *FF* of gradient devices is in accordance with reports from literature [323, 325]. However, the reported conclusions differ from those of this work. In literature the effect is only attributed to better charge transport in the bulk without any investigation of the interface properties to the directly adjacent ITO anode. However, it is demonstrated here that interface effects are not negligible. In the systems of Tab. 9.1 the gradient changes the property of the HTL/blend interface, which causes the observed changes in *FF*. Modifications of charge transport due to a concentration gradient play a minor role.

9.2.2 Short-circuit current

The slight increase in absorption for the gradient devices does not result in a significant change of the short-circuit current density (J_{sc}). A mixing ratio of 4:1 (**A4** + **B4**) is even detrimental: J_{sc} decreases probably due to the formation of isolated molecule clusters, from which charge carriers cannot be extracted. Exciton diffusion is not expected to be the limiting process, as the thickness of the 4:1 layer (6 nm) is in the range of the diffusion length of excitons in ZnPc and C$_{60}$. The 4:1 regions occupy 2/7 of the total blend layer thickness. The decrease of J_{sc} by around 10 % corresponds well to the contribution of the 4:1 and 1:4 regions, if one assumes in a rough estimation that $\lesssim$ 1/2 of the excitons in the 4:1 regions can be harvested. The remaining half is supposed to be lost due to diffusion away from the 3:1 region. The described loss of charge carriers on isolated clusters should be independent of voltage. This is confirmed by an unchanged *FF* and V_{oc} of device **A4** compared to **A3**.

Additional intrinsic ZnPc and C$_{60}$ layers can increase the current, because excitons are created and diffuse to the blend, where they are separated. This effect is observed in some devices with a 10 nm intrinsic ZnPc layer (compare **A2** and **B2**, **A3** and **B3**, . . .), but not in the devices of type **D** with a 15 nm ZnPc interlayer (**C1** and **D1**,...). Two effects can explain this difference: As the exciton diffusion length of ZnPc is in the range of 5-7 nm (our estimation from optical modeling, reported value in Ref. [326] is 10 nm), parasitic absorption in the intrinsic ZnPc layer increases with ZnPc thickness and decreases the absorption in the blend. Second, the exciton lifetime and diffusion length and in turn the contribution of a neat ZnPc layer depend strongly on its purity and hence the material batch, which has been changed between devices **A** and **C**. Comparing devices **C1** with **D1** (**C4** with **D4**) shows even a remarkable decrease of J_{sc} with the additional ZnPc layer. The reason is that the photocurrent saturation is not yet reached for these devices **D** at 0 V applied bias, which is proven by the low values of the *FF* and illustrated in the current-voltage characteristics shown in Fig. 9.3. Summarizing, independent of device type, no improvement of efficiency can be seen in the case of a ZnPc hybrid flat/bulk heterojunction with C$_{60}$.

9.2.3 Open-circuit voltage

The open-circuit voltage (V_{oc}) is not significantly influenced by the gradient in solar cells of type **A** and **C** (0.54. . . 0.57 V). According to Chapter 8, the dependence of V_{oc} of a ZnPc:C$_{60}$ blend on the mixing ratio is 0.54. . . 0.62 V for the mixing ratios employed here. This dependence is most likely canceled by the presence of several mixing ratios in the graded blends. However, in the case of an adjacent ZnPc layer (**B** + **D**), V_{oc} differs significantly between gradient and homogeneous 1:1 blend. For the homogeneous 1:1 blend, V_{oc} is decreased compared to the value of the blend without an additional ZnPc layer (compare **B1**, V_{oc} = 0.51 V with **A1**, 0.55 V or **D1**, 0.48 V with **C1**, 0.54 V). The reason is a lower IP of intrinsic ZnPc ($\approx$ 5.05 eV) compared to ZnPc in a blend with C$_{60}$ ($\approx$ 5.2 eV) [320, 321] (cf. Chapter 8). Assuming that this lower IP causes an injection barrier for holes, the
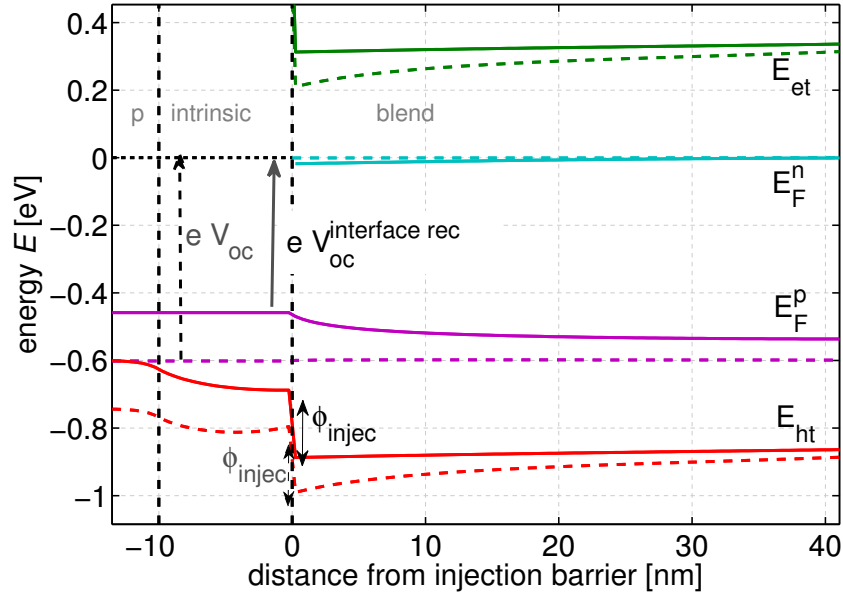
Figure 9.2: Simulated energy-level diagrams at the respective open-circuit voltage of two
model devices with an injection barrier ϕ_{injec}. The solid lines show the case,
where recombination of holes at position 0^- with electrons at 0^+ is allowed with
a rate constant comparable to the one in the blend itself. The dashed lines are
the result of suppressed recombination at the interface. V_{oc} as the difference of
the hole quasi-Fermi level E_{F}^p at the anode $(x < -10)$ and the electron quasi-
Fermi level E_{F}^n at the cathode $(x > 40)$ is governed by the recombination at
$x = 0$ independently of ϕ_{injec} itself, which is kept constant. E_{F}^n at the cathode
is used as common reference for the potential V of both energy-level diagrams.

effect of such a barrier on V_{oc} can be explained by examining energy-level diagrams at
V_{oc} obtained from drift-diffusion simulations (Fig. 9.2). The solid lines show that a lower
IP of the adjacent intrinsic layer reduces V_{oc}, because electrons in the blend recombine
bimolecularly with a relatively high hole density located in the intrinsic layer. This effect
was discussed in detail in Chapter 6. The recombination leads to a gradient in the quasi-
Fermi levels and hence to an energy loss at V_{oc}. Switching off this recombination path
in simulation (dashed lines) re-establishes V_{oc} to the blend value without a barrier. This
is comparable to the case of a flat heterojunction in Chapter 6, where recombination of
electrons at the p-contact is a priori excluded. Thus, it is not the injection barrier itself,
that decreases V_{oc} and hence the maximum electrical energy of the extracted electron-hole
pair. This maximum energy is found in the splitting of the quasi-Fermi levels and not in
the position (and steps) of the IP itself [3, 300]. Therefore, this system provides another
experimental verification of the results from the modeling study presented in Chapter 5.

Employing the gradient in experiment, V_{oc} can indeed be re-established to the originally
achieved blend value (compare **A2/3** with **B2/3** or **C3** with **D3**). This means that
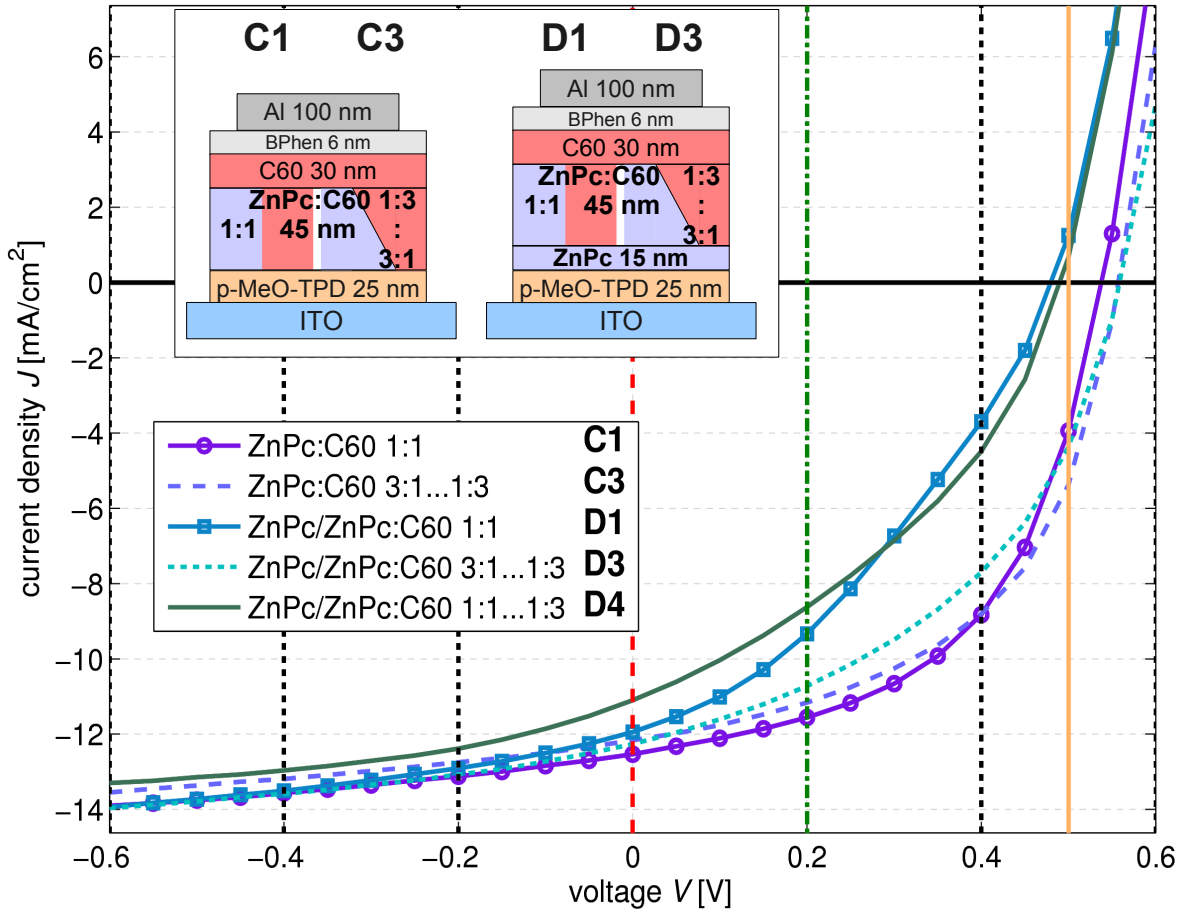
Figure 9.3: *J-V* curves of selected devices of types **C** and **D** with and without an intrinsic interlayer and with different realizations of the blend layer. The illumination is provided by a solar simulator. The colored vertical lines mark the voltages applied during the EQE measurements shown in Fig. 9.4. The inset displays a sketch of the stacks of devices **C1+3** and **D1+3**.

recombination at the ZnPc/blend interface is decreased. Morphological changes of the intrinsic ZnPc layer itself can be excluded, because it is deposited before the different blend layers. One reason for the decreased recombination might be the lower concentration of C$_{60}$ close to the intrinsic ZnPc, reducing the probability of electrons to be located there. Electrically, this could be represented in a reduced density of hopping sites for electrons. Thus, assuming that every molecule constitutes one hopping site and estimating a molecular density of 10^{21} cm^{-3}, a 1:1 blend might have a density of states for electrons and holes of 0.5×10^{21} cm^{-3}, whereas it is changed in a 3:1...1:3 gradient to 0.75×10^{21} cm^{-3} : 0.25×10^{21} cm^{-3} ... 0.25×10^{21} cm^{-3} : 0.75×10^{21} cm^{-3}. This leads to a gradient in the chemical potential, pushing photogenerated holes towards the p-side and electrons towards the n-side. A simulation predicts an increase of V_{oc} by 10 mV for a 2:1...1:2 and by 20 mV

for a 3:1...1:3 gradient compared to the homogeneous blend. These values are independent of the absolute density of states and could correlate with the trend in V_{oc} of devices **A** (0.55 V $\nearrow$ 0.57 V) and **C** (0.54 V $\nearrow$ 0.56 V). A gradient in the chemical potential resulting from the materials' concentration gradients is also proposed by Chen et al. [324] as reason for an improvement of graded devices. However, a change in V_{oc} of 0.02 V is not sufficiently significant for a definite statement, although it is a reproducible effect.

The gradient creates a smooth adjustment of the IP of ZnPc in the blend, which decreases with increased ZnPc content, to the IP of ZnPc. The same, but weaker trend is seen for the electron affinity (EA) of C_{60} [321]. Assuming vacuum level alignment, small steps in the IP and EA create a force for photogenerated holes towards the ZnPc layer and keep the electrons away from it. Whereas the force in the first explanation is due to an inhomogeneity of available states to occupy, it is here due to a gradient in the chemical potentials of the materials (which are IP and EA). Both explanations have to be handled with care for a blend. A blend is supposed to be a partly phase separated two component medium, where the local potential landscape is very difficult to predict. However, this system is another example, which shows that not solely the difference between IP and EA, but the electrochemical potential difference, which is defined by an equilibrium between generation and recombination, governs V_{oc}. This suggestion is confirmed by the comparison of **D1** with **D4**, where a gradient, starting from 1:1, does not increase V_{oc}. Thus, not a gradient itself, but a ZnPc rich phase close to the neat ZnPc layer is of importance.

9.3 Voltage dependent external quantum efficiency data

For a more detailed investigation, we examine voltage dependent external quantum efficiency (EQE) spectra of devices **C1+3** and **D1+3**. The EQEs are measured under constant bias voltages ranging from -1 V to 0.5 V. Figure 9.3 shows the corresponding *J-V* curves of the measured samples, visualizing the behavior of fill factor and open-circuit voltage discussed above. The EQE spectra in Fig. 9.4 are normalized to the ZnPc peak at 630 nm. The spectrum of device **C1** without intrinsic ZnPc decreases homogeneously with higher applied bias, as the normalized EQE does not change its shape [Fig. 9.4(a)]. The relative decrease of the EQE of the gradient sample [**C3**, Fig. 9.4(b)], however, is more strongly pronounced in the blue part of the spectrum (400...500 nm). The reason is that most of the blue light in the gradient is absorbed close to the Al cathode due to the high C_{60} concentration there (compare inset of Fig. 9.1). This means that holes originating from excitons created on C_{60} have to travel through the whole blend layer to the HTL. Since their mobility is lower than the mobility of electrons [188, 327], the probability for a hole to reach the contact is lower compared to the probability of an electron to travel from the region close to the ITO anode through the blend to the cathode. This effect will be discussed in detail in the next chapter.

An intrinsic ZnPc interlayer combined with a homogeneous blend causes a significant difference in the relative spectra (compare **C1** and **D1** [Fig. 9.4(c)]). The contribution from absorption in C_{60} disappears already at 0.4 V, which is the reason for the high decrease of
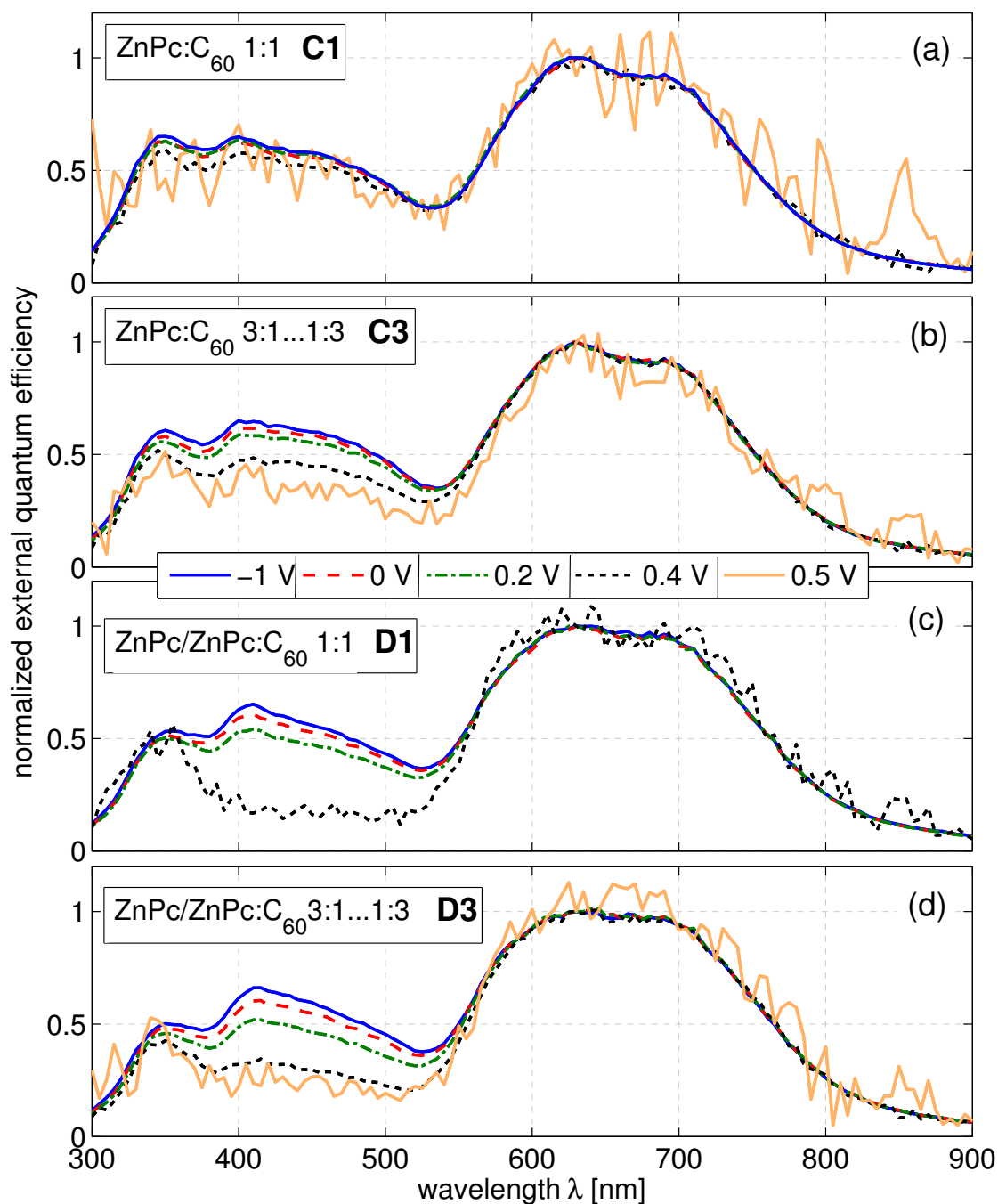
Figure 9.4: Bias-voltage dependent EQE spectra of selected devices of types **C** and **D** with and without an intrinsic ZnPc interlayer and with and without a concentration gradient in the blend. The spectra are normalized to the absorption peak of ZnPc at 630 nm. The decreased signal-to-noise ratio with applied bias is due to the decrease of the absolute signal. The respective *J-V* curves are shown in Fig. 9.3.

photocurrent with voltage in the *J-V* curve (Fig. 9.3). The remaining signal with peaks at 350, 630, and 690 nm follows the absorption spectrum of ZnPc (cf. Fig. 3.27, p. 86). The current at 0.4 V originates probably only from photons absorbed in and close to the intrinsic ZnPc layer, where most of the electric potential drops due to a negative space charge built up by the fast electrons in the blend, so that photocurrent from the blend is close to zero. In the presence of the gradient [**D3**, Fig. 9.4(d)] the EQE is comparable to the case without ZnPc [**C3**, Fig. 9.4(b)], which proves that recombination from charge carriers generated in the blend is reduced compared to device **D1**. In conclusion, the EQE data show additional evidence that a gradient in combination with an intrinsic ZnPc layer increases the probability of charge extraction from the blend.

9.4 Summary

In this chapter a detailed study on concentration gradients in ZnPc:C_{60} solar cells was presented. It has been shown that charge transport within the blend is neither improved nor worsened by the gradient in the system ZnPc:C_{60}. However, V_{oc} and *FF* are enhanced upon grading if the interface HTL/blend limits device performance. In particular, the gradient is beneficial for a hybrid planar/bulk heterojunction structure, decreasing recombination at the ZnPc/blend interface. The open-circuit voltage is governed by the photogenerated quasi-Fermi level splitting in the blend independently of the lower IP of the intrinsic ZnPc layer. A continuously varied donor:acceptor mixing ratio from 0 to 1 should be avoided, as mixing ratios larger than 4:1 result in a decrease of photocurrent, probably due to insufficient percolation paths.

Chapter 10

Role of the Generation Profile and Recombination in ZnPc:C$_{60}$ Solar Cells

The previous experimental chapters mainly addressed the role of the electrodes and the energy levels with focus on V_{oc} and the shape of the J-V curve. This chapter provides an experimental investigation of the most important intrinsic loss mechanism within a bulk heterojunction, which is recombination. Its influence on V_{oc} and fill factor (FF) was already elaborated theoretically in Chapter 5. Here, it is shown that recombination losses and hence the FF depend on the absorption profile which is varied by different spacer layer thicknesses. The influence of the locus of maximum charge carrier generation within the blend becomes more pronounced with a higher imbalance in mobilities, which is adjusted by a variation of donor:acceptor mixing ratios. This approach shows that the FF is limited by recombination due to insufficient charge transport rather than by geminate recombination which is expected to be independent of the absorption profile. An evaluation of J-V data dependent on illumination intensity indicates that the dominant recombination mechanism switches from indirect recombination to direct recombination for higher light intensities. Simulations quantitatively reproduce the measured J-V data.

10.1 Idea and solar-cell design

The dominating recombination mechanism in organic solar cells is highly debated, as presented in Ch. 4.4.2. Since the middle of the last decade the concept of geminate recombination has broadly been applied to P3HT:PCBM and subsequently other polymer solar cells. Simulation approaches included Onsager-Braun theory to model geminate recombination and CT-exciton dissociation (cf. Ch. 4.4.2). The idea of geminate recombination was mainly motivated by a strong dependence of the photocurrent on the applied voltage [96]. Another reason was that the short-circuit current was observed to scale linearly with intensity, although recombination is present. However, it is controversially debated whether a linear scaling of J_{sc} with intensity is a clear sign for geminate recombination [141, 328, 329],
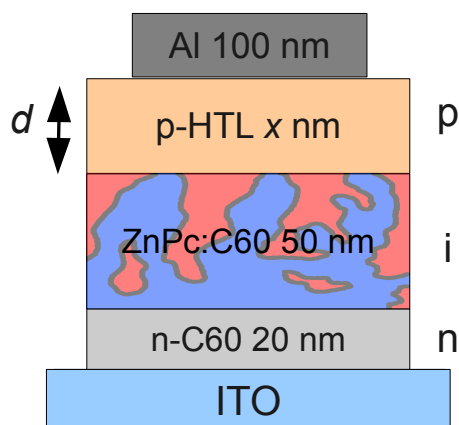
Figure 10.1: Solar-cell stack in n-i-p architecture with varied hole transport layer (HTL) thickness. The HTL acts as a spacer. An NDP9 layer of 2 nm (not shown in the sketch for clarity) is inserted between the HTL and the aluminum electrode: ITO/C$_{60}$:NDN1(20, 3 wt%)/ZnPc:C$_{60}$(50, x : y)/Di-NPD(1)/Di-NPD:NDP9(d, 5 wt%)/NDP9(2)/Al(100). In this stack, Di-NPD is chosen as HTL.

especially in a well-working solar cell where recombination is not significant at J_{sc}. In recent years trap assisted "interface state" recombination became another proposed and debated recombination mechanism [121, 141]. Also direct (bimolecular) recombination between free charge carriers was identified as mechanism describing the photocurrent-voltage relation [127]. All three mechanisms are claimed to dominate the performance of P3HT:PCBM solar cells.

In this chapter a novel approach is presented to determine the mechanism which is limiting the fill factor (FF). Solar cells are designed to achieve highly asymmetric absorption profiles with a distinct position of the maximum within the blend. If the FF of such a solar cell depends on the locus of maximum charge carrier generation, charge transport is limiting the FF instead of geminate recombination. In this case charges with the lower mobility are expected to be predominantly harvested when created close to the collecting electrode. Thus, this effect should be more pronounced with an increased imbalance in electron and hole mobility. The main advantage of this approach compared to, e.g., thickness variations is the fact that the field within the device without illumination is not changed. In cases where the field is changed, both charge carrier extraction and field-dependent exciton dissociation (geminate recombination) are affected. Thus, it is difficult to distinguish between both. To further identify the limiting recombination mechanism, the dependence of V_{oc} on illumination intensity is studied in the second part of this chapter.

For an experimental realization of the outlined idea, the already well-known p-i-n concept is applied. The generation profile is tuned by the thickness of the doped transparent charge transport layer between reflecting contact and blend. Due to the availability of several hole-transporting materials (cf. Chapters 6 and 8), hole transport layers (HTLs) are

used as spacers in a then inverted (n-i-p) stack. The active layer consists of a 50 nm thick ZnPc:C_{60} bulk heterojunction (BHJ) with mixing ratios of 2:1, 1:1, 1:2, and 1:3. In contrast to previous chapters the blend thickness is not estimated by the densities of the single materials, but by reflectance and transmittance data of a thickness series of single-layer samples. The optical data obtained from fitting [264] are used to calculate nominal thicknesses which are 62 nm for ZnPc:C_{60} 2:1, 58 nm (1:1), 56 nm (1:2), and 55 nm (1:3). These corrections are performed because they are essential for a quantitative evaluation of measurement data, which is intended in this study. The BHJ is embedded between an n-doped C_{60} layer deposited on ITO and a p-doped hole transport layer (HTL) consisting of Di-NPD or MeO-TPD and covered by 100 nm Al. Any intrinsic neat layer is avoided to reach ideal charge carrier extraction and injection properties and to omit photocurrent from other sources except the BHJ. The stacks read in detail ITO/C_{60}:NDN1(20, 3 wt%)/ZnPc:C_{60}(50, $x : y$)/Di-NPD(1)/Di-NPD:NDP9(z, 5 wt%)/NDP9(2)/Al(100). In the MeO-TPD samples, Di-NPD is replaced by MeO-TPD, doped with 2 wt% NDP9 (Fig. 10.1).

The thicknesses of the HTLs ($z = 25, 45, 90, 180$ nm) are chosen based on optical simulations to reach extreme cases of the absorption profiles. The mobility imbalance is manipulated by the four different mixing ratios in the blend. Data evaluation is done employing absorption measurements in comparison to optical simulations, monochromatic *J-V* curves to enforce the effect of a narrow generation profile, and EQE data dependent on bias-voltage.

10.1.1 Absorption data

Optical simulation is applied to predict the absorption profile, which is the absorbed photon flux density per unit device thickness in photons $m^{-2}s^{-1}m^{-1}$. As described in Ch. 4.2.4 this profile is assumed to be equal to the charge carrier generation profile. This implies that every absorbed photon (in the UV-vis spectral range) creates an exciton, which is subsequently split and forms an electron/hole pair. Furthermore, the exciton dissociation is assumed to occur close to the locus of its generation which means no significant exciton diffusion. This condition is fulfilled by an intimate intermixing of the bulk heterojunction which is guaranteed by a deposition of the BHJ without substrate heating. Several morphology studies using grazing incidence X-ray diffraction or AFM indeed show very small or no crystalline grains in such ZnPc:C_{60} BHJs [209]. Therefore, it is justified to set the spatial photon absorption profile directly equal to the charge carrier generation profile. Thus, in the following, the expressions absorption, exciton generation, and charge carrier generation profile are used interchangeably.

The simulated absorption profile cannot be directly monitored by a measurement method. However, it can be indirectly verified by a comparison of measured and simulated absorption spectra. The reason is that a particular absorption spectrum is connected to a respective generation profile under a known illumination spectrum.

A comparison of measured (solid) and simulated (dashed) absorption data is shown in Figs. 10.2 and 10.3. The fit of the simulation to the experiment is very good and proves that the nominal thicknesses of the layers are reasonable (nominal HTL thickness
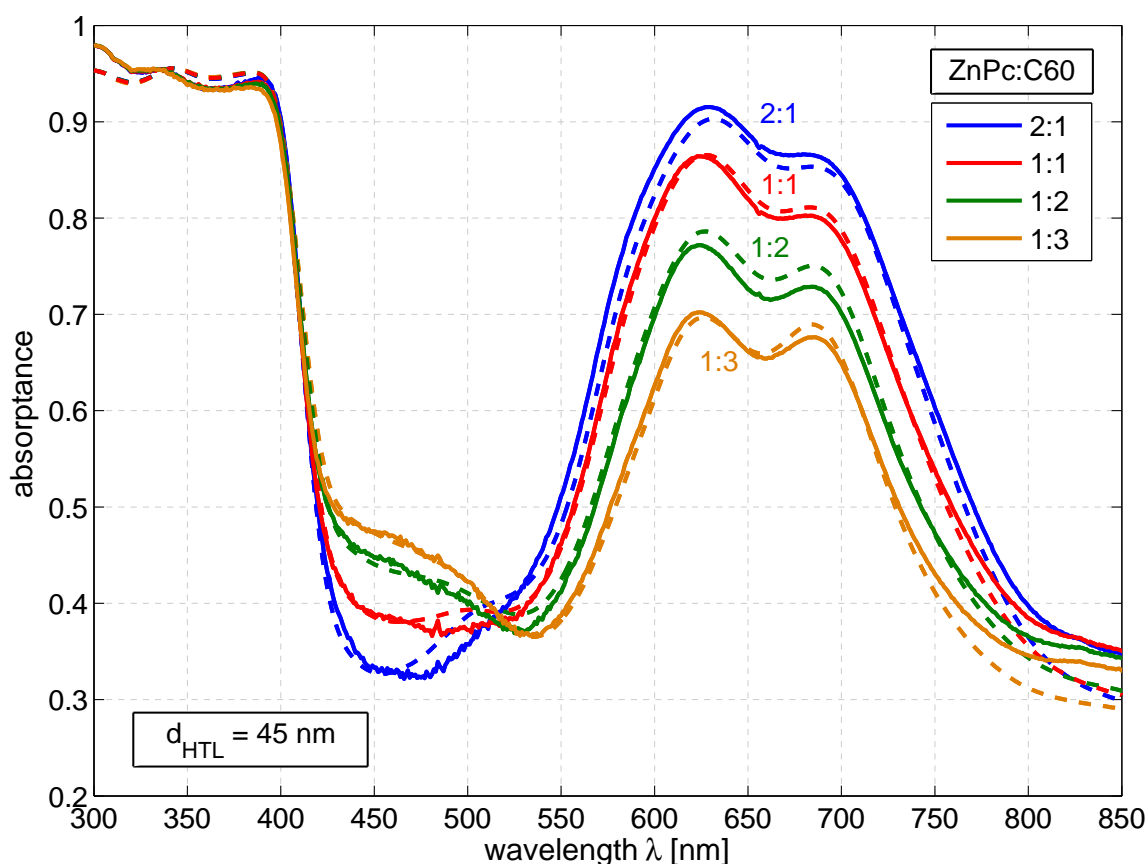
Figure 10.2: Measured (solid lines) and simulated[1](dashed lines) absorption data of solar cells with different blend mixing ratios and an HTL thickness of 45 nm. The absorption increases in the range between 600 and 750 nm and decreases at around 450 nm with increased ZnPc content. This is expected from the absorption spectra of the respective molecules (cf. Fig. 3.27, p. 86). The simulation data fit well.

of 190 nm changed to 180 nm). Figure 10.2 illustrates that the absolute values of the ZnPc (C$_{60}$) absorption peaks (cf. Fig. 3.27, p. 86) change dependent on the amount of ZnPc (C$_{60}$). According to Fig. 10.3 the spacer thickness significantly influences the shape of the absorption spectrum. The reason is the relatively thin absorber layer thickness of 50 nm compared to the distribution of the electro-optical interference maxima of wavelengths between 400 and 800 nm. Here, the sample with 180 nm Di-NPD represents an extreme case where the electro-optical field intensities at 630 and 680 nm differ such significantly that the characteristic double peak of the ZnPc absorption is heavily distorted.

---

[1]Optical constants determined in transmission and reflection measurements of single layers by André Merten, IAPP.
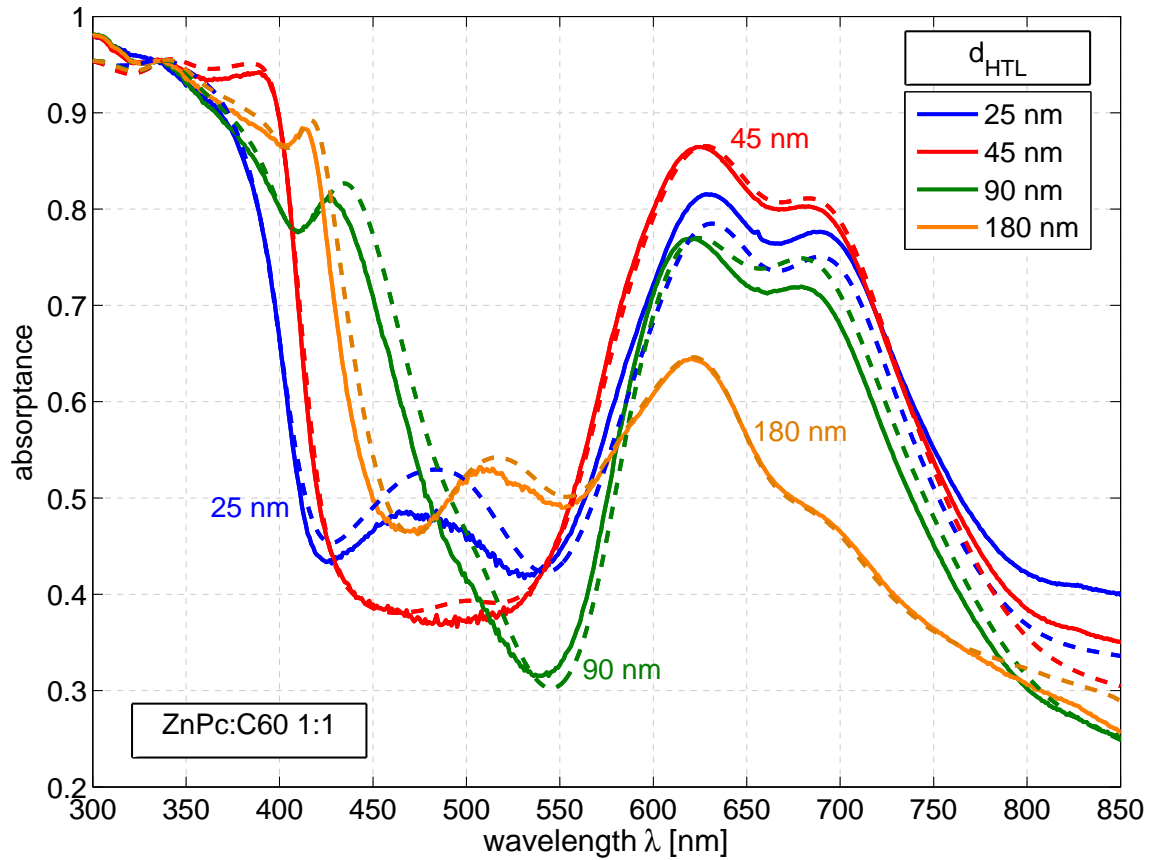
Figure 10.3: Measured (solid lines) and simulated (dashed lines) absorption data of solar cells with blend mixing ratio 1:1 and different HTL layer thicknesses. The samples with a 25 and 180 nm thick HTL show a pronounced absorption in C_{60}.

10.1.2 Simulated generation profiles

The generation profile is obtained from the absorption data as follows. The spectrally resolved simulated absorption has to be known at every position within the device. It can be calculated from the gradient of the Poynting vector. Multiplying this spatially resolved absorbed energy flux with the amount of photons at each specific wavelength (which is the solar simulator spectrum) gives the spectrally resolved absorbed photon flux. As all *J-V* measurements are done under simulated sunlight, the solar simulator spectrum is used here instead of AM 1.5g (for a comparison, see Fig. 3.31, p. 94). An integration of this (spatially resolved) value over the whole spectrum results in the exciton generation rate at each position. A further integration over the absorber layer thickness would give the total amount of generated excitons and thus an upper value of the photocurrent obtainable.

The simulated generation profiles for all samples are shown in Fig. 10.4. Their shapes rationalize the HTL thicknesses which are chosen in a way to create an absorption profile
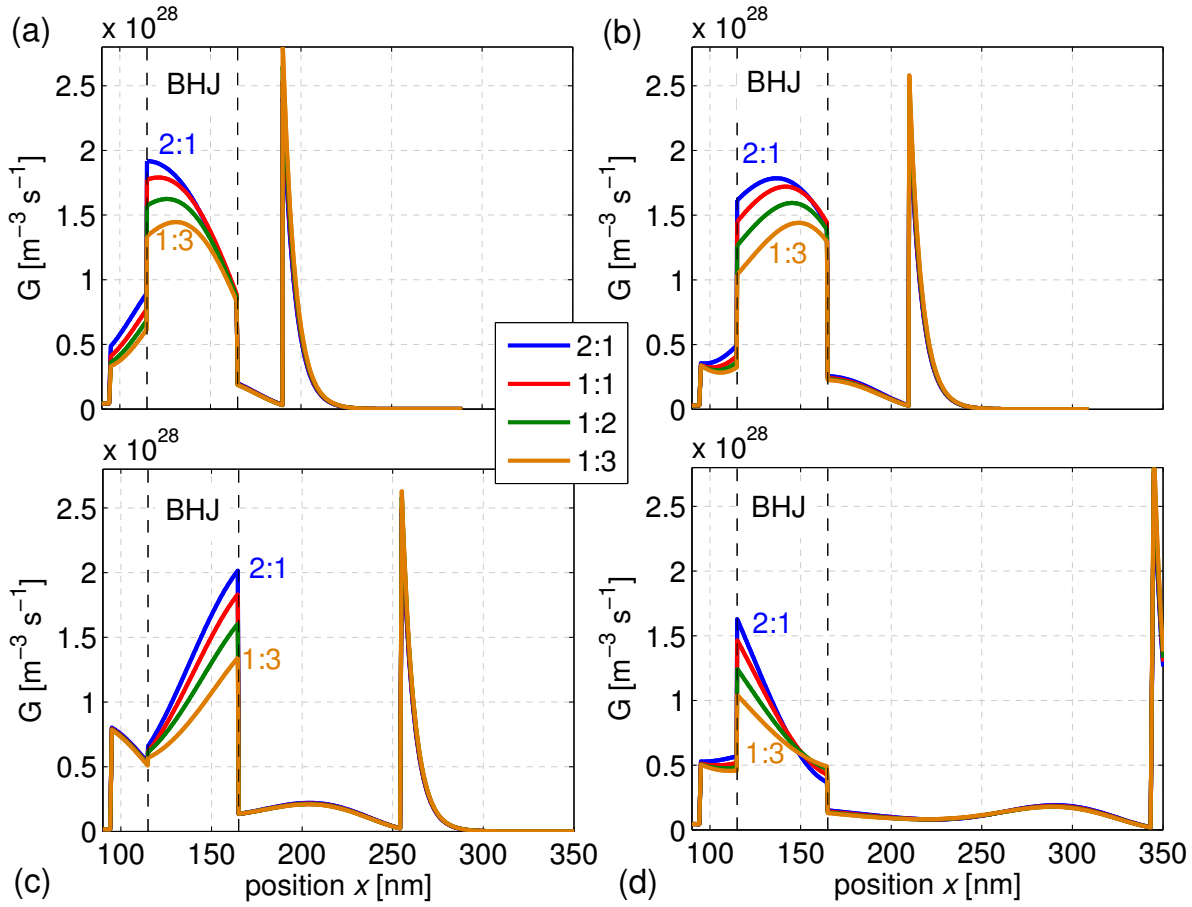
Figure 10.4: Simulated absorption, i.e. exciton-generation profiles G for different ZnPc:C$_{60}$ mixing ratios (colors) and different HTL thicknesses (a) 25 nm, (b) 45 nm, (c) 90 nm, (d) 180 nm. The stack reads: glass(1 μm)/ITO(95 nm)/n-doped C$_{60}$(20)/BHJ(50)/HTL(z)/Al(100). x denotes the distance from the interface glass/ITO. The spectrum of the solar simulator is used as illumination spectrum. The shape of the absorption profile within the BHJ is mainly manipulated by the HTL thickness.

with a maximum close to the HTL (a,d), close to the ETL (c), and a relatively balanced profile (b). Case (a) is a tradeoff between tuning the generation profile and guaranteeing a certain HTL thickness to protect the blend during evaporation of aluminum. The motivation for the two similar shapes of the profiles of cases (a) and (d) is an exclusion of any effect of the HTL thickness itself. In all four cases the qualitative shape of the absorption profile is maintained for all mixing ratios. The overall absorption is highest for the 2:1 blend which can be directly deduced from the absorption spectra (Fig. 10.2) and the spectrum of the sun (Fig. 2.2) or solar simulator (Fig. 3.31) in this case. The absorption maxima for a fixed HTL thickness are shifted to the right with C$_{60}$ content in the blend, because the interference maxima for lower wavelengths where C$_{60}$ absorbs are localized closer to

the reflecting contact. This effect was exploited in the graded heterojunction discussed in Chapter 9 (cf. Fig. 9.1).

10.2 Correlation of the fill factor with generation profile and imbalance in mobilities

10.2.1 Current-voltage data

Table 10.1 summarizes the fingerprints of the solar cells' J-V data for all combinations of HTL thickness and mixing ratio. It shows that V_{oc} is independent of the HTL thickness and defined by the mixing ratio as already explained in Chapter 8. The short-circuit current density is highest for samples with an HTL thickness of 45 nm, as these devices yield the highest integrated generation profile (cf. Fig. 10.4). The short-circuit current is significantly lower for samples with a 180 nm thick HTL due to the operation of the solar cells at the onset of the second interference maximum. When comparing J_{sc} for the different mixing ratios and a fixed HTL, it can be seen that it is highest for the 1:1 blend. It decreases with a higher C_{60} content due to the lower overall absorption in the spectral range where most photons arrive. This was already discussed in the previous section. The decreased J_{sc} of the 2:1 samples cannot be explained by a decreased absorption. One reason for the lower J_{sc} is that the photocurrent is further away from being saturated at J_{sc}. An indication for this is the low FF (43...44 %). The other reason might be an internal quantum efficiency which is decreased independent of applied voltage. This is indicated by J_{sat} in the table, which is lower for the 2:1 blend than for the 1:1 blend. Details are given later on when we discuss simulations of the J-V curves.

Most interesting is the evolution of the FF with HTL thickness in comparison with mobility data, shown in Tab. 10.2. These data are obtained by OFET measurements[2], which are conducted under different conditions compared to the working point of a solar cell. Commonly, measured OFET mobilities of organic semiconductors are one or two orders of magnitude higher than the mobilities observed in a working solar cell [330]. The reason is the dependence of the mobility on charge carrier density which is very high in the channel of an OFET. Nevertheless, the OFET mobility is applicable to show trends. The table shows that the hole mobility of the blend increases with ZnPc content by two orders of magnitude, whereas the electron mobility decreases to a comparable extent. This is expected as holes are transported on ZnPc and electrons on C_{60}. As the electron mobility of C_{60} is much higher than the hole mobility of ZnPc, a 2:1 blend shows almost balanced transport, whereas the imbalance increases with mixing ratios from 1:1 to 1:3.

This change in the mobility (im)balance allows the explanation of the trends in the FF. In the case of balanced mobilities (2:1) the FF does not depend on the HTL thickness and

---

[2]Measurements and data analysis performed by Jens Jankowski and Moritz Hein, both IAPP. The transistor is in bottom-gate geometry with gold electrodes. Data are extracted from the saturation regime. Four gate lengths are investigated, between 2.5 and 20 μm. For details, see Ref. [304].
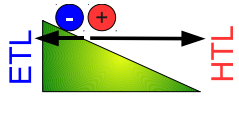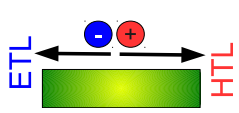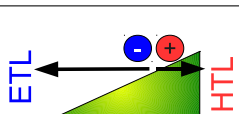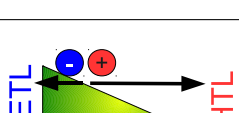
generation profile ↓	d_{HTL} ↓	mixing ratio → μ_n/μ_p →	2:1 2.5	1:1 93	1:2 1300	1:3 > 3000
	25 nm	**FF** [%]	**43.2**	**47.0**	**45.3**	**43.4**
		J_{sc} [mA/cm²]	8.7	9.9	8.8	7.9
		J_{sat} [mA/cm²]	10.8	11.6	10.3	9.2
		V_{oc} [V]	0.54	0.55	0.60	0.63
		η [%]	2.0	2.6	2.4	2.2
	45 nm	**FF** [%]	**43.4**	**47.9**	**46.8**	**45.1**
		J_{sc} [mA/cm²]	9.0	10.5	9.4	8.2
		J_{sat} [mA/cm²]	11.3	12.3	10.8	9.4
		V_{oc} [V]	0.54	0.55	0.60	0.63
		η [%]	2.1	2.8	2.6	2.3
	90 nm	**FF** [%]	**43.9**	**50.1**	**50.0**	**48.6**
		J_{sc} [mA/cm²]	7.5	8.4	7.4	6.4
		J_{sat} [mA/cm²]	9.4	9.6	8.1	7.2
		V_{oc} [V]	0.53	0.55	0.60	0.63
		η [%]	1.7	2.3	2.2	2.0
	180 nm	**FF** [%]	**43.7**	**46.6**	**45.4**	**43.9**
		J_{sc} [mA/cm²]	4.4	4.9	4.2	3.8
		J_{sat} [mA/cm²]	5.4	5.6	5.0	4.4
		V_{oc} [V]	0.51	0.52	0.57	0.60
		η [%]	1.0	1.2	1.1	1.0

Table 10.1: Fingerprints of the solar-cell series fabricated. The first column shows schematic representations of the generation profiles of Fig. 10.4. The saturated photocurrent density J_{sat} is obtained by a correction of the *J-V* curves for a photoshunt as explained in Chapter 11. The ratio between electron and hole mobility μ_n/μ_p is obtained from OFET measurements (Tab. 10.2). The dependence of the *FF* on the generation profile increases with a higher imbalance in mobilities.

mixing ratio	ZnPc	2:1	1:1	1:2	1:3	C₆₀
μ_n[cm²/Vs]	-	1.3×10^{-3}	1.4×10^{-2}	3.9×10^{-2}	9.1×10^{-2}	0.2
μ_p[cm²/Vs]	1.9×10^{-3}	5.2×10^{-4}	1.5×10^{-4}	2.9×10^{-5}	-	-

Table 10.2: Charge carrier mobilities in ZnPc:C₆₀ blends with different mixing ratios obtained from OFET measurements.
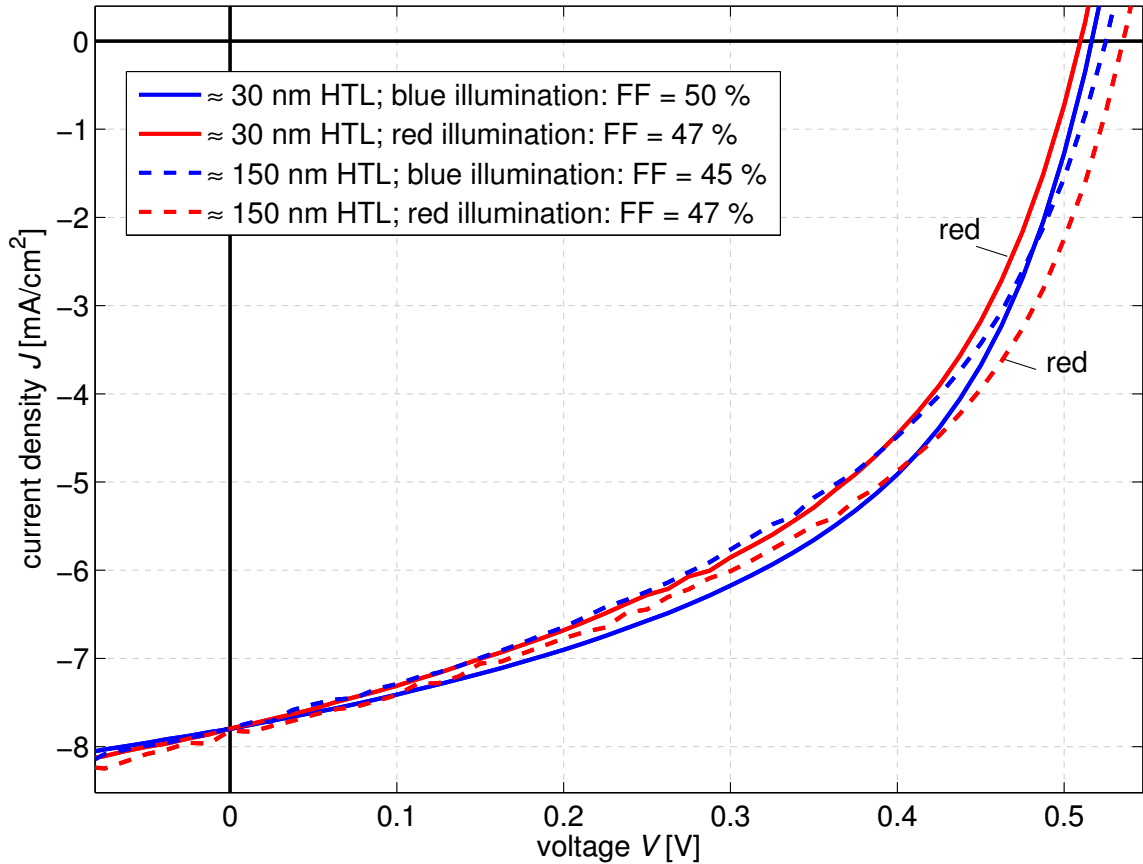
Figure 10.5: "Monochromatic" *J-V* curves of samples with .../ZnPc:C$_{60}$(1:2)/BF-DPB/.... The illumination was provided by high-power LEDs. The intensity is set to obtain the same J_{sc} for all four samples. *FF* and V_{oc} depend on the illumination color due to changed generation profiles.

thus on the generation profile. However, for the samples with another mixing ratio, the *FF* is highest in the case where the absorption maximum is close to the hole-collecting electrode (90 nm HTL). This trend in *FF* becomes more pronounced with increased imbalance ($47\ldots50\,\%(1:1) \rightarrow 43\ldots49\,\%(1:3)$). This means that it is favorable for a high *FF* if the generation is close to the contact collecting the slow holes. The absolute changes in *FF* might look small. However, the relative changes reach $15\,\%$ which is a significant value. All observed trends have been reproduced by further samples containing also other HTL materials like MeO-TPD and BF-DPB. Consequently, the *FF* is limited by charge transport.

Figure 10.6: (a) External quantum efficiency of sample .../ZnPc:C$_{60}$(2:1)/Di-NPD(45 nm)/... for different applied bias voltages. (b) Data normalized to 630 nm. The decrease in forward bias is independent of wavelength.

10.2.2 Monochromatic *J-V* curves

In the previous section the *FF* of samples with the same architecture and the same BHJ thickness have been compared. However, the analysis was based on different samples with varied HTL thickness. This was done to show the importance of the generation profile for devices working under solar illumination. A more strict analysis requires a comparable study based on data which are acquired from one sample itself. This excludes any effect arising from a comparison between different samples. Thus, the approach of this section is to manipulate the generation profile of one sample by an illumination with monochromatic light of different wavelengths. This illumination yields narrower and shifted generation profiles.

J-V measurements are performed under illumination with high-power blue and red LEDs like the data shown in Ch. 8.4 (Fig. 8.2(b), p. 226). Figure 10.5 exemplary shows data of two samples comprising a 1:2 blend and the HTL BF-DPB (30 and 150 nm). The illumination intensity is set to reach the same short-circuit current. This suggests a comparable overall charge carrier generation rate within the blend. It would be more correct to take the reverse saturation current. However, as these samples do not show a clear saturation (cf. Chapter 11), J_{sc} is the best choice. A comparison of the *J-V* curve of one sample under red and blue illumination shows that *FF* and V_{oc} differ significantly. The difference is not caused by the illumination color or the molecule which is excited (donor or acceptor). This is proven by the control experiment with the second sample which shows a reversed trend in V_{oc} and *FF*. The reason is an inverted shape of the monochromatic generation profiles in the second sample compared to the first one. Therefore, the difference between red and
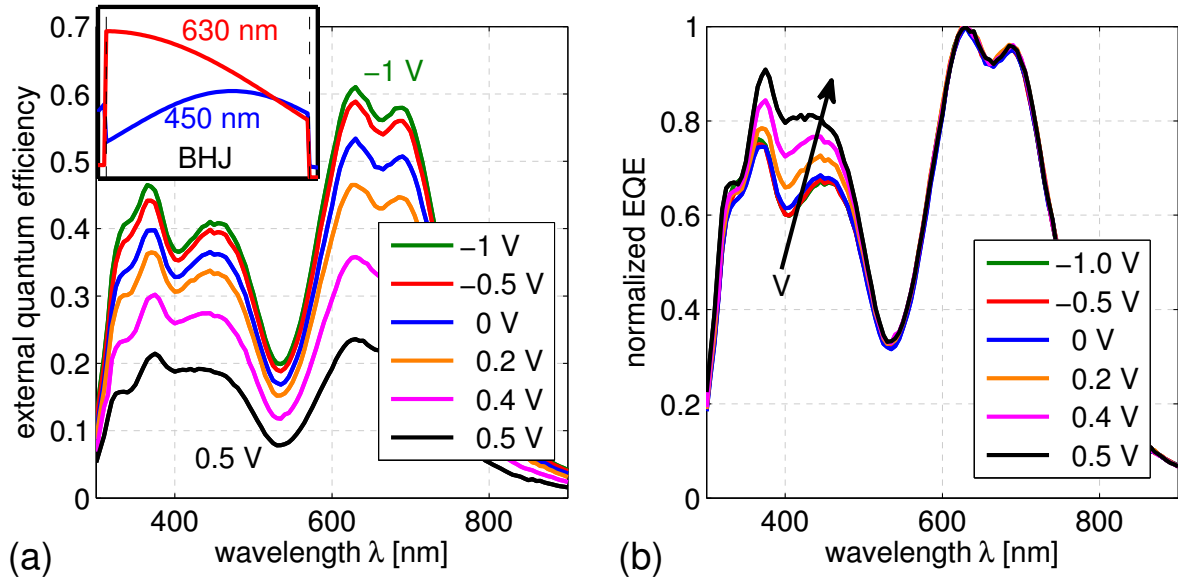
Figure 10.7: (a) External quantum efficiency of sample .../ZnPc:C_{60}(1:2)/Di-NPD(25 nm)/... for different applied bias voltages. The inset shows the shape of the generation profile within the BHJ for monochromatic red and blue illumination. (b) Data normalized to 630 nm. The decrease under forward bias is less pronounced in the shorter wavelength range.

blue illumination of each sample is due to a different generation profile for illumination at different wavelengths.

As the accuracy of the BF-DPB layer thickness in these two samples is in the range of 30 %, a more detailed analysis is avoided and postponed to the subsequent EQE studies of the samples of Tab. 10.1. Nevertheless, the monochromatic *J-V* curves show the influence of the generation profile at one sample. These results also explain the higher *FF* under blue illumination which is commonly observed for p-i-n solar cells comprising C_{60}.

10.2.3 Voltage dependent external quantum efficiency

The subsequent step following quasi-monochromatic excitation is a voltage dependent EQE measurement. This method is also capable of visualizing the effect of the locus of free charge carrier generation directly at measurements on one single sample. Here, the role of tuning the generation profile is passed from the spacer layer thickness in Tab. 10.1 to the wavelength like in the previous case of monochromatic *J-V* curves.

Although all samples of Tab. 10.1 are examined, we restrict ourselves to the discussion of three samples, which consist of a 2:1 blend with a 45 nm thick HTL and a 1:2 blend with HTL thicknesses of 25 nm and 90 nm. Figure 10.6(a) shows the EQE spectra of the first sample for bias voltages between -1 and 0.5 V. The absolute EQE signal decreases with increased applied bias. This behavior is in accordance with a reduced photocurrent
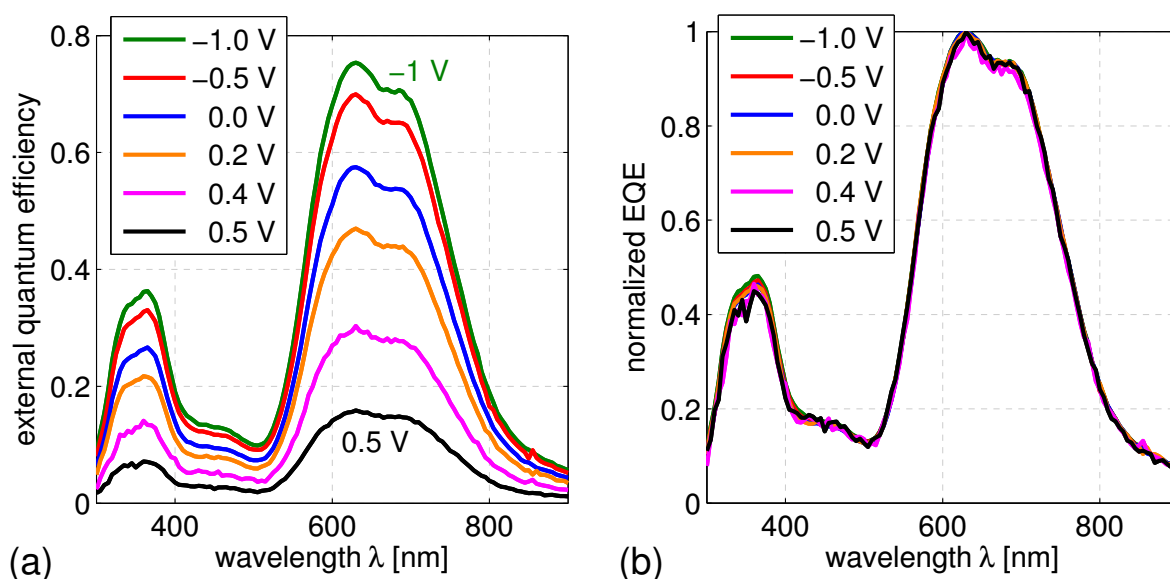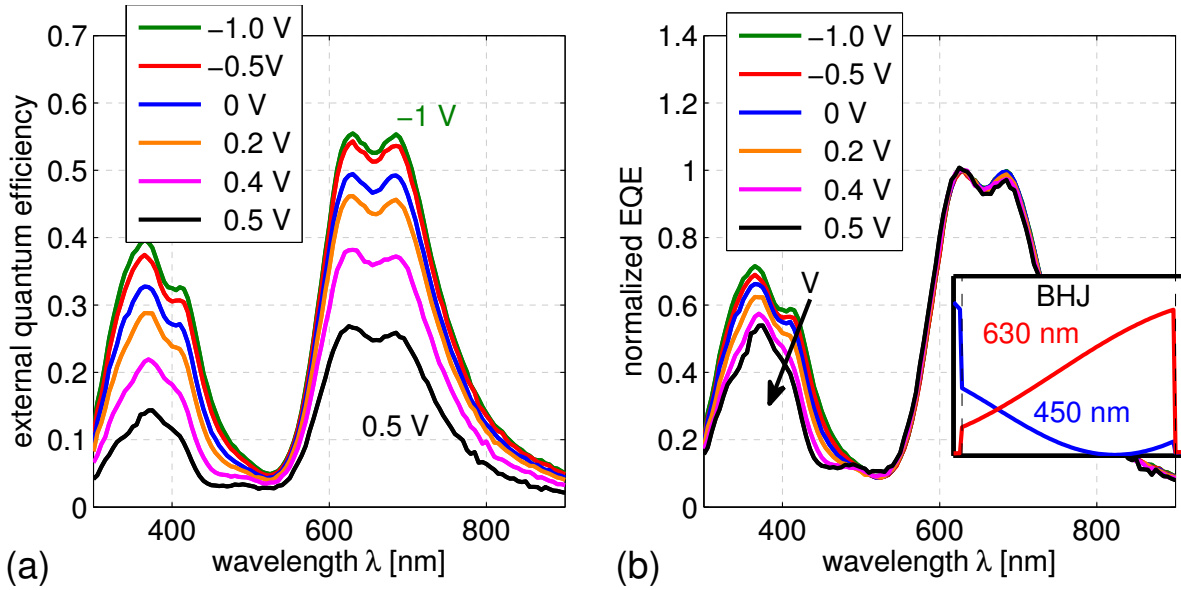
Figure 10.8: (a) External quantum efficiency of sample .../ZnPc:C$_{60}$(1:2)/Di-NPD(90 nm)/... for different applied bias voltages. The inset shows the shape of the generation profile within the BHJ for monochromatic red and blue illumination. (b) Data normalized to 630 nm. The decrease in forward bias is more strongly pronounced in the shorter wavelength range.

with increased bias. In Fig. 10.6(b) the EQE is normalized to the ZnPc peak at 630 nm to visualize the effect of the wavelength on the dependence of charge carrier extraction on voltage. All curves coincide in the whole spectral range. This means that charge carrier collection does not depend on the wavelength and, thus, not on the generation profile, which differs for each wavelength. This holds for the 2:1 samples with other HTL thicknesses as well and is in agreement with the data of Tab. 10.1 which shows no influence of the generation profile on *FF*.

The same analysis is done for the 1:2 samples in Figs. 10.7 and 10.8. The normalized spectra show a different relative dependence of the photocurrent originating from different wavelengths. The sample with a 25 nm HTL [Fig. 10.7(b)] exhibits a weaker decrease of the EQE in the blue compared to the EQE in the red spectral range. The simulated monochromatic generation profiles in the inset prove that this effect is due to different generation profiles. The maximum locus of charge carrier generation in case of the blue illumination is closer to the contact collecting the slower holes. The data of Fig. 10.8 show an inverted generation profile accompanied by a reverse trend in the EQE, where the signal in the blue decreases more strongly than in the red spectral range.

In conclusion, this experiment is a clear proof of the hypothesis of the generation profile dominating the voltage dependence of the photocurrent and consequently the *FF*. Furthermore, it has practical consequences for solar cell characterization under simulated sunlight. It was discussed in Ch. 3.6 that the photocurrent calculated from the EQE(0 V) and the

AM 1.5g spectrum are used to set the solar simulator intensity corrected for the spectral mismatch (MM). If the spectral shape of the EQE depends on the applied voltage, the mismatch factor depends on the applied voltage as well. To correct for this effect, the solar simulator intensity has to be set individually not only for each sample but for each voltage point of the *J-V* curve. Regarding the investigated samples, the MM factor changes from 0.76(-1 V) to 0.75(0.5 V) (from 0.78 to 0.79). This relative deviation of around 1 % is acceptable for a reliable characterization in the existing solar simulator setup, where other more critical effects like the active device area or temperature are less known. However, the voltage dependent MM may not be negligible for other devices and/or very precise efficiency measurements.

10.3 Recombination

Although it was shown that the recombination probability depends on the spatial profile of charge carrier generation and mobilities, we have so far not been able to identify the dominating recombination mechanism. We can only conclude from the previous sections that charge transport limits the *FF*, because the slower charge carriers generated further away from their electrode are predominantly lost. This effect implies that some space charge builds up within the layer (cf. Ch. 3.3.5) which changes the field. Recombination is then dominant in the low-field region close to the contact collecting the faster charge carrier type. However, we cannot distinguish whether this recombination is geminate, direct, or indirect. Therefore, the *J-V* data is further analyzed and measurements under varied illumination intensity are performed.

10.3.1 Exponential region of dark *J-V* curves

The diode ideality factor n_D has been mentioned several times during this work. When introducing the MIM picture (Ch. 3.3.4 and 3.3.5) we stated that such a structure shows an exponential dark *J-V* curve. The current is diffusion driven against the built-in potential V_{bi} and can in principle be described by the Shockley equation. However, in Ch. 6.4 it was demonstrated that the "slope" of the dark curve of a real organic solar cell is influenced by additional layers. Transport layers without aligned charge transport levels decrease the slope in forward, which results in large values of n_D or an n_D which cannot be correctly determined (cf. Fig. 6.8, p. 189). In such a case, an application of the one-diode Shockley equation (Eq. 2.41) is not given. Only if the ideality factor is determined by the active material system itself, it may be capable of giving information about dominating recombination processes.

A brief simulation study shall demonstrate the effect of several material and device parameters on the slope of the exponential region of the dark *J-V* curve. The parameters for the simulation are those of the model device presented in Chapter 5, Tab. 5.1, p. 146. Figure 10.9 shows the *J-V* curve for direct (bimolecular) recombination. The slope is independent of the recombination constant β and charge carrier mobilities. A Shockley fit
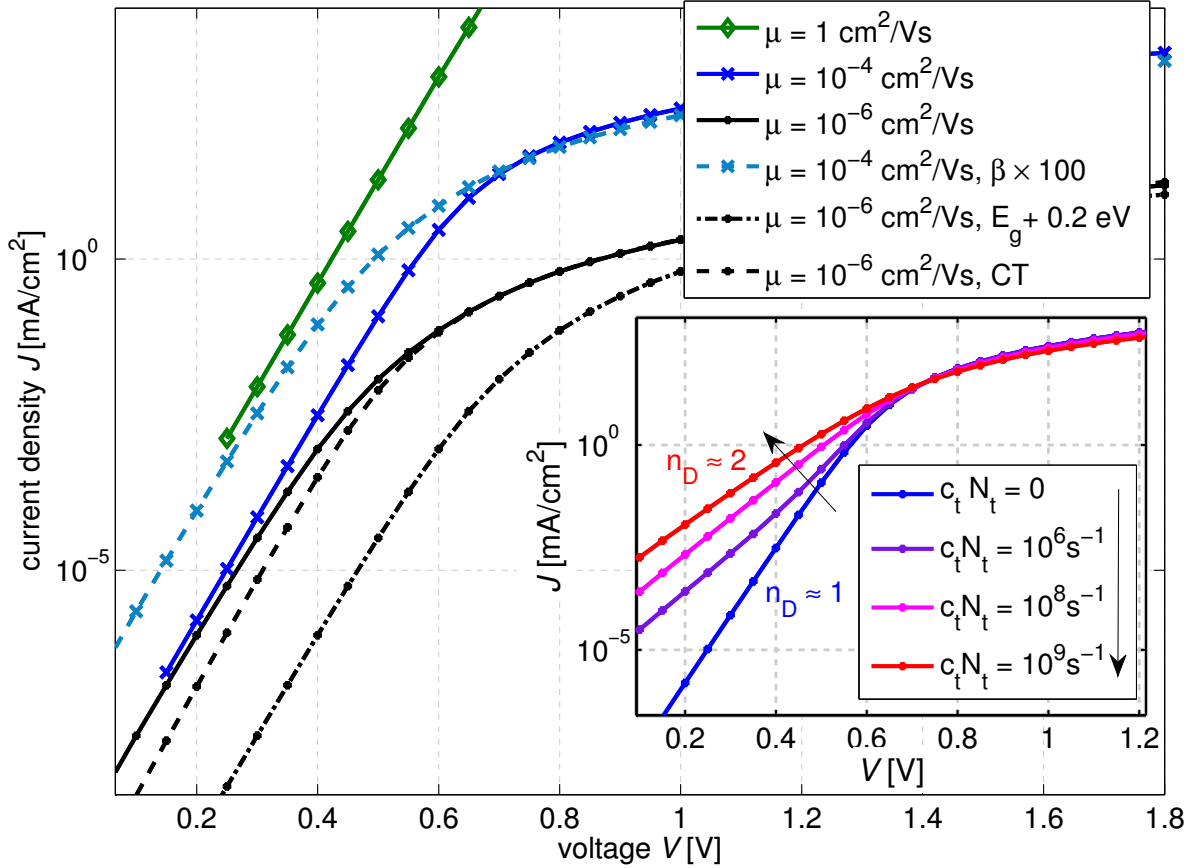
Figure 10.9: Simulation data for different values of μ, β, E_g, and considering recombination via CT states (initial distance $a = 1.2\,\mathrm{nm}$ and $k_{\mathrm{relax}} = 10^6\,\mathrm{s}^{-1}$), which do not influence the slope in the exponential region. The inset shows additional SRH recombination expressed by the effective recombination constant $c_t N_t$. Further input parameters for the simulation are found in Appendix B, p. 329.

yields a value of 1 for n_D. A higher recombination constant or a lower effective gap E_g shifts the onset to lower voltages, which is equivalent to a higher reverse saturation current in the Shockley equation (Eq. 2.41). The high-mobility curve represents a case where charge carriers pass through the device and recombine at the non-selective contacts. This is the case of an ideal diode without recombination in the space charge layer which corresponds to the intrinsic layer in a MIM device. Recombination via a CT state does not change the slope either. It effectively changes E_g and the recombination properties, as elaborated in detail in Ch. 5.2.3 (Eq. 5.14).

The inset of Fig. 10.9 visualizes the effect of a changed recombination mechanism. In case of SRH recombination, n_D approaches 2 as known from inorganics where n_D was introduced to account for recombination in the space charge layer of a p-n junction. In presence of direct and indirect recombination, n_D is found to be between 1 and 2.
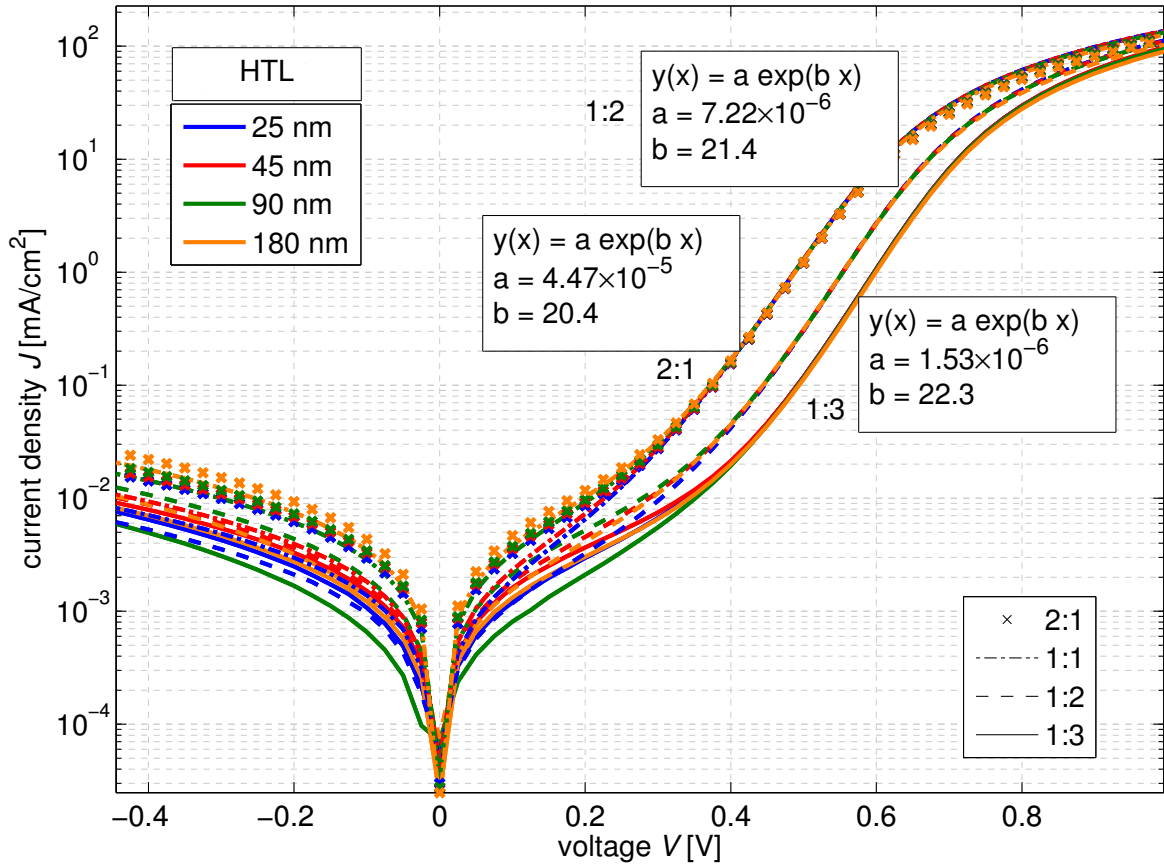
Figure 10.10: Dark *J-V* curves in a logarithmic plot of the current. They are independent of HTL thickness and show a shifted onset due to the changed effective gap. Recombination is hardly changed as the slopes of the curves are comparable for all mixing ratios. They correspond to a diode ideality factor of 1.9, which is a hint for indirect recombination.

Now the *J-V* curves of the devices from Tab. 10.1 are analyzed considering the discussed simulation data. Figure 10.10 shows the dark curves of all devices. Curves for the same mixing ratio and varied HTL thickness coincide as the doped HTL is a highly conductive layer whose thickness does not influence the device performance. All curves show an exponential region between 0.4 and 0.6 V. For higher voltages the ITO series resistance dominates the current and all curves coincide. The shunt resistance causes current for voltages smaller than 0.2 V. The different onsets are due to the dependence of the effective gap on mixing ratio (cf. Ch. 8.4). A fit of the exponential region gives a slope of around $20\,\mathrm{V}^{-1}$ ($n_\mathrm{D} \approx 1.9$), independent of mixing ratio. This result suggests recombination via traps as the mechanism dominating the dark forward current.

The data of Fig. 10.10 are measured at room temperature. According to the Shockley equation and simulations of the MIM device, the slope is expected to decrease with

263
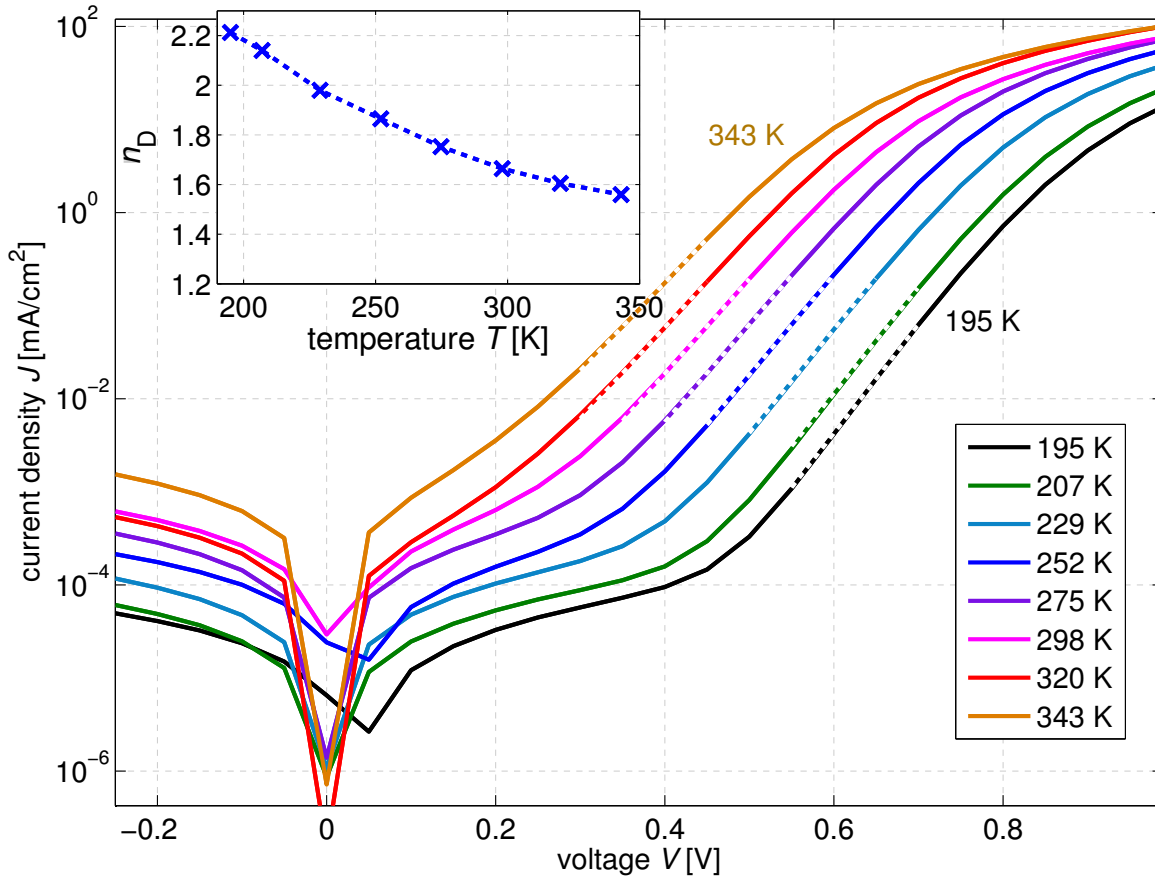
Figure 10.11: Dark *J-V* curves of a p-i-n sample ITO/MeO-TPD:NDP2(20, 10 wt%)/MeO-TPD(5)/ZnPc:C$_{60}$(45, 1:2)/C$_{60}$(15)/BPhen(6)/Al(100) measured at several temperatures. The dashed regions are used for fitting of an exponential function. The slope increases with decreased temperature. However, the decrease is too low to result in a constant diode ideality factor n_{D} (inset).

increased temperature T as long as n_{D} remains constant. Figure 10.11 shows data of a temperature dependent *J-V* measurement[3] on a p-i-n sample ITO/MeO-TPD:NDP2(20, 10 wt%)/MeO-TPD(5)/ ZnPc:C$_{60}$(45, 1:2)/C$_{60}$(15)/BPhen(6)/Al(100). The ideality factor at room temperature is comparable to the one of the devices discussed previously. The slope decreases with T, however not that significantly to result in a constant n_{D}. The ideality factor decreases from values above 2 at 200 K to 1.5 at 350 K. On the one hand, this shows that the ideality factor is a questionable measure. On the other hand, a physical explanation may be provided: $n_{\mathrm{D}} > 2$ for low T might be due to some barrier or strong charge carrier localization effect becoming visible at low temperatures only. The decrease of n_{D} with T may be explained by the dominating mechanism shifting from indirect to direct recombination. A possible reason for this effect is the broad DOS resulting from

---

[3]Measurements performed at a cryostat setup described in Ref. [249].
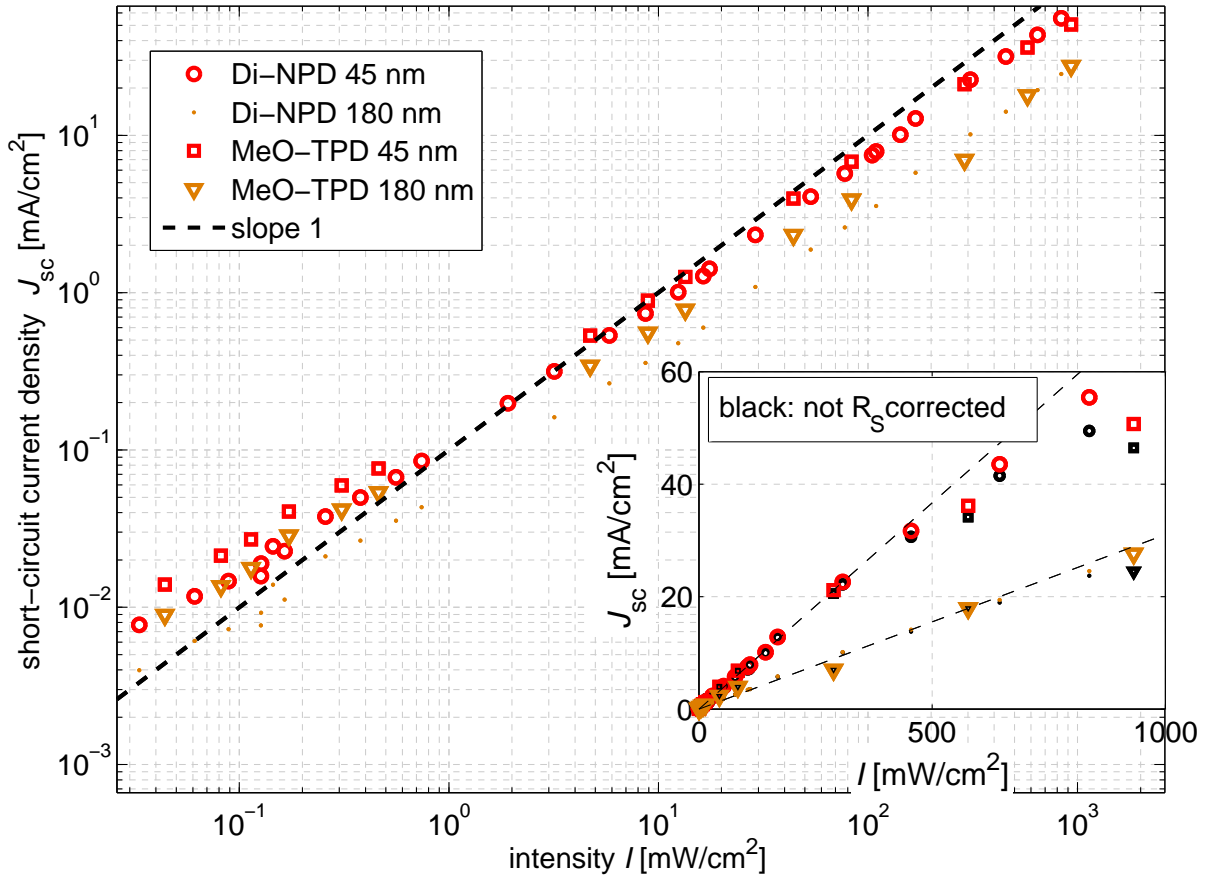
Figure 10.12: J_{sc} as a function of illumination intensity for four different samples comprising a ZnPc:C$_{60}$ 1:3 blend. The light intensity is measured by a silicon reference diode. $128\,\mathrm{mW/cm^2}$ correspond to 1 sun, corrected for spectral mismatch. The data are corrected for a series resistance whose influence can be seen in the inset.

disorder. The fraction of more mobile, quasi-free charge carriers increases with T resulting in more direct recombination. Harada *et. al* [233] explained high values of n_D by the generalized Einstein relation which is also addressed in a recent study on n_D [331, 332].

10.3.2 *J-V* data dependent on illumination intensity

After having discussed the dark carriers, we focus on the photogenerated charge carriers in the second step. For a further comparison also the samples are considered where the HTL Di-NPD is replaced by MeO-TPD. *J-V* data dependent on light intensity are commonly used to distinguish between recombination mechanism. As already discussed, a sublinear dependence of J_{sc} on intensity is attributed to bimolecular recombination, whereas a linear correlation indicates a monomolecular (geminate or trap-assisted) recombination mecha-
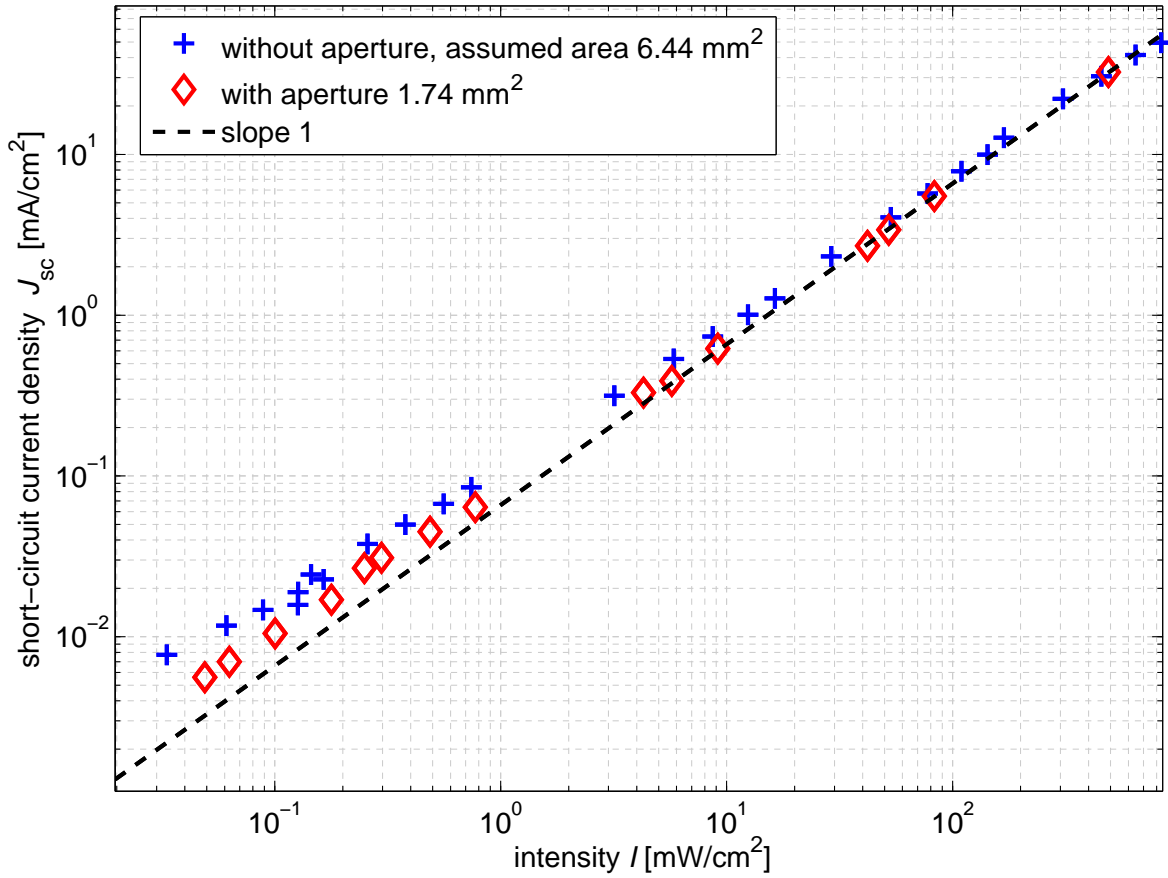
Figure 10.13: J_{sc} as a function of illumination intensity for the sample .../ZnPc:C$_{60}$(2:1)/Di-NPD(90 nm)/..., measured without and with aperture to examine the non-linearity at low intensities. The dashed line represents a linear J_{sc}-intensity relation.

nism. The reason is that charge carrier losses increase superlinearly with light intensity for direct recombination. In case of geminate recombination the losses are proportional to the amount of CT states which scales linearly with light intensity. Trap-assisted recombination losses are only proportional to illumination intensity if the amount of trapped charges is assumed to be mainly independent of the amount of photogenerated charges.

However, investigating J_{sc} has several disadvantages. Especially for high-FF solar cells, there is almost no recombination in the device at this working point (IQE close to 1), because all charges are collected. Therefore, current scales linearly with light intensity independently of the recombination mechanism limiting the FF. Second, recombination via dark carriers at the contacts may lead to a case, where the majority charge carrier density is hardly affected by illumination, so that even in the case of bimolecular recombination, a linear J_{sc} can be observed.

Nevertheless, J_{sc} is shown for four selected samples in Fig. 10.12. Two features can be

observed: First, J_{sc} scales linearly with illumination intensity for intensities in the range of 1 to $200\,\mathrm{mW/cm^2}$. The linear plot in the inset visualizes that J_{sc} increases sublinearly for higher light intensities. Due to the high values of J_{sc} a correction of the J-V data for the parasitic series resistance (R_S) has to be done. The series resistance is obtained for each sample by correcting the logarithmic J-V data to avoid a curvature for high applied bias voltages. R_S is in the range of $2\,\Omega\mathrm{cm^2}$ ($30\,\Omega$), which is basically the ITO series resistance. The coincidence of all J-V curves in Fig. 10.10 indicates that it is indeed the resistance of the ITO which limits the forward current. Thus, the correction is meaningful, although it includes a correction for the resistance of the blend as well. The lateral resistance of the ITO stripes is not exactly known as their dimensions differ from sample to sample probably due to small changes in the alignment of the masks during evaporation. That is why it is preferred to always show the unmodified measurement data together with the data corrected for R_S, which is overestimated. The sublinearity of J_{sc} for higher intensities indicates an increased bimolecular recombination independent of the correction for R_S.

Second, J_{sc} does not scale linearly with light intensity for intensities lower than $1\,\mathrm{mW/cm^2}$, seen in a kink around this value. This transition from sublinear to linear behavior with increased intensity cannot be explained by the expected processes within the device. Consequently, two reasons are remaining: Either the nominal intensity is underestimated or a parasitic effect is observed. Figure 10.13 indicates the latter. A measurement with aperture significantly reduces the overestimated photocurrent for low intensities. Thus, the additional current seems to result from a larger device area compared to the nominal one. It is unclear why this effect becomes more pronounced for very low intensities. One reason might be that the small photocurrent at low intensities results in a small voltage drop over the lateral ITO paths which constitute a series resistance. A lower voltage drop means a higher effective active area which is close to short-circuit conditions and contributes to the photocurrent. Most important is that the data measured with aperture create confidence that the nominal intensity monitored by a silicon reference diode is correct. Therefore, especially the following elaborations on V_{oc} are allowed and a time-consuming repetition of all measurements with aperture can be avoided.

An investigation of V_{oc} is expected to reveal more information on recombination than J_{sc}, as V_{oc} is the point where in the case of selective contacts the optical generation rate equals the recombination rate (cf. Chapter 5). V_{oc} is shown as a function of illumination intensity for 8 different samples in Fig. 10.14. V_{oc} is slightly lower for all samples with a 180 nm thick HTL due to the lower overall generation rate and thus J_{sc} in these samples (cf. Tab 10.1 and Fig. 10.4). Additionally, V_{oc} is lower for the MeO-TPD samples in the case of higher light intensities. Before coming to this phenomenon, the two additional dashed lines are discussed which show theoretical slopes of V_{oc}.

We start with the equation for V_{oc} (Eq. 3.11) which directly results from the quasi-Fermi level splitting:

$$eV_{oc} = E_g^{\mathrm{DA}} - k_B T \ln \frac{N_C N_V}{np}. \tag{10.1}$$

The expression np in Eq. 10.1 can be replaced by following the same approach as in
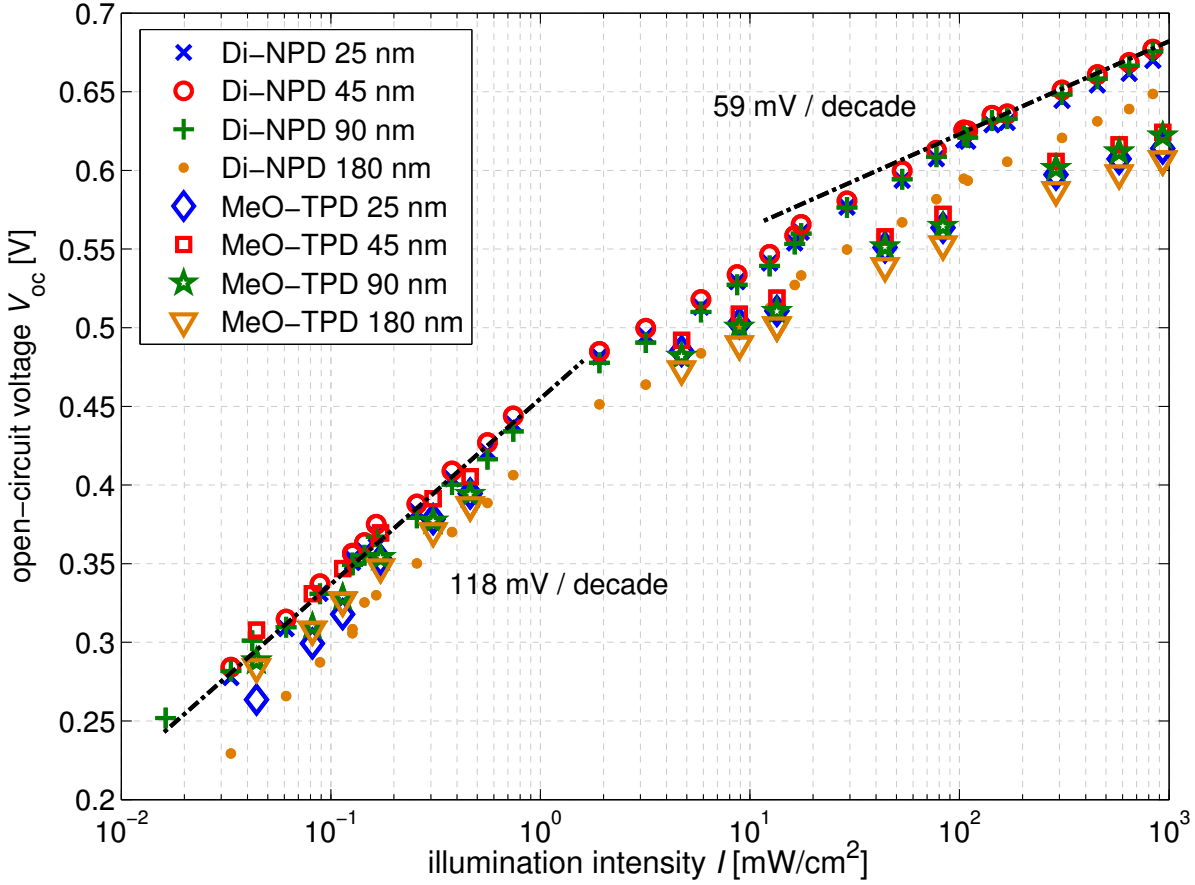
Figure 10.14: V_{oc} of ZnPc:C$_{60}$(1:3) samples with different HTL materials and thicknesses as a function of the light intensity I. Dashed lines visualize the theoretical slope of V_{oc} for SRH recombination at low intensities and for direct recombination at higher intensities.

Ch. 5.2.3. The basic assumption is direct recombination, which equals the generation ($\beta np = G$). This yields Eq. 5.11, which is rewritten here for convenience:

$$eV_{oc} = E_g^{DA} - k_B T \ln \frac{N_C N_V}{G/\beta} = E_g^{DA} - k_B T \ln N_C N_V \beta + k_B T \ln G. \qquad (10.2)$$

This equation shows that V_{oc} scales logarithmically with light intensity because the generation rate G is proportional to the light intensity. The slope in a graph, where the illumination intensity is plotted in the logarithm to the base 10, is $k_B T / \log e^1 \approx 2.3 k_B T \approx 59\,\text{mV/decade}$ ($T = 300\,\text{K}$).

In case of indirect trap assisted recombination it holds $G \approx c_t N_t \frac{np}{n+p}$ (Eqs. 4.47 and 5.7). If the majority of the charge carriers is photogenerated ($n_{ph} = p_{ph}$), this equation results in $G \approx c_t N_t n_{ph}/2 = c_t N_t p_{ph}/2$. Thus, $G \propto n_{ph}$. This proportionality is also valid close to

the contacts, where a high background density (n_d, p_d) of one charge carrier species may exist, e.g. $n_\mathrm{d} \gg n_\mathrm{ph} = p_\mathrm{ph} \gg p_\mathrm{d} \to G \approx c_t N_t p_\mathrm{ph}$.

Replacing np in Eq. 10.1 yields in the SRH case:

$$eV_{oc} = E_\mathrm{g}^\mathrm{DA} - k_\mathrm{B}T \ln \frac{N_\mathrm{C}N_\mathrm{V}}{G^2 C} = E_\mathrm{g}^\mathrm{DA} - k_\mathrm{B}T \ln N_\mathrm{C}N_\mathrm{V}C^{-1} + 2k_\mathrm{B}T \ln G. \qquad (10.3)$$

Here, C is a constant containing c_t and N_t. The slope of V_{oc} is $2k_\mathrm{B}T$ in a logarithmic plot as function of G. This value is double the slope of bimolecular recombination. This difference in the slope was discussed in a similar derivation by Cheyns *et al.* for FHJ solar cells [120].

The two dashed lines in Fig. 10.14 show these two slopes. The experimental data follow the high slope for intensities lower than $1\,\mathrm{mW/cm^2}$ and the lower slope for intensities larger than $10\,\mathrm{mW/cm^2}$. This is a clear indication that the dominating recombination mechanism switches from SRH to bimolecular with increased intensity. Such a behavior is reasonable as the bimolecular recombination grows with the square of intensity. It, therefore, superimposes the trap-assisted recombination at higher intensities. The slope of the experimental data is further decreased for intensities larger than $100\,\mathrm{mW/cm^2}$, especially for MeO-TPD as HTL, as discussed in the following.

To further clarify the dependence of V_{oc} on light intensity, data of samples with different mixing ratios are examined in Fig. 10.15. Several trends are observed: First, the postulated transition from SRH to bimolecular recombination is present for all mixing ratios. Second, the absolute difference between V_oc of samples with different mixing ratios does not change with intensity. This is a clear indication that indeed not recombination, but a changed effective gap causes the different values of V_oc (cf. Ch. 8.4). Third, the difference in V_oc of else identical samples comprising the two different HTLs increases with intensity. On the one hand, this difference remains relatively low for the 2:1 sample, where V_oc is lowest. On the other hand, V_{oc} of the 1:2 and 1:3 samples with HTL MeO-TPD even coincide for high intensities. The reason is that the HTL limits V_oc for voltages larger than around $0.6\,\mathrm{V}$. The HOMO of MeO-TPD lies higher than the HOMO of Di-NPD (-5.1 eV versus -5.35 eV, cf. Chapters 6 and 8). Therefore, samples with MeO-TPD suffer from a lower built-in field and even a slight hole injection barrier into the 1:3 blend, whose HOMO is expected at $\lesssim -5.2\,\mathrm{eV}$ according to the discussions in Ch. 8.4. This limit becomes more relevant for elevated values of V_oc which are present at higher light intensities. Therefore, it is concluded that the dominating recombination mechanism changes form indirect/SRH over direct/bimolecular to contact-limited recombination with increased intensity. In case of direct recombination we cannot say whether this recombination happens via a CT state, because the characteristic behavior of V_oc is the same. According to Ch. 5.2.3, only effective recombination constants are changed and the dependence on illumination intensity remains unmodified.

In Chapter 5 we have studied the influence of recombination on the *FF*. It was found that the *FF* suffers from recombination. Figure 10.16 shows the *FF* as a function of light intensity. Starting from high light intensities the *FF* increases, as charge carrier
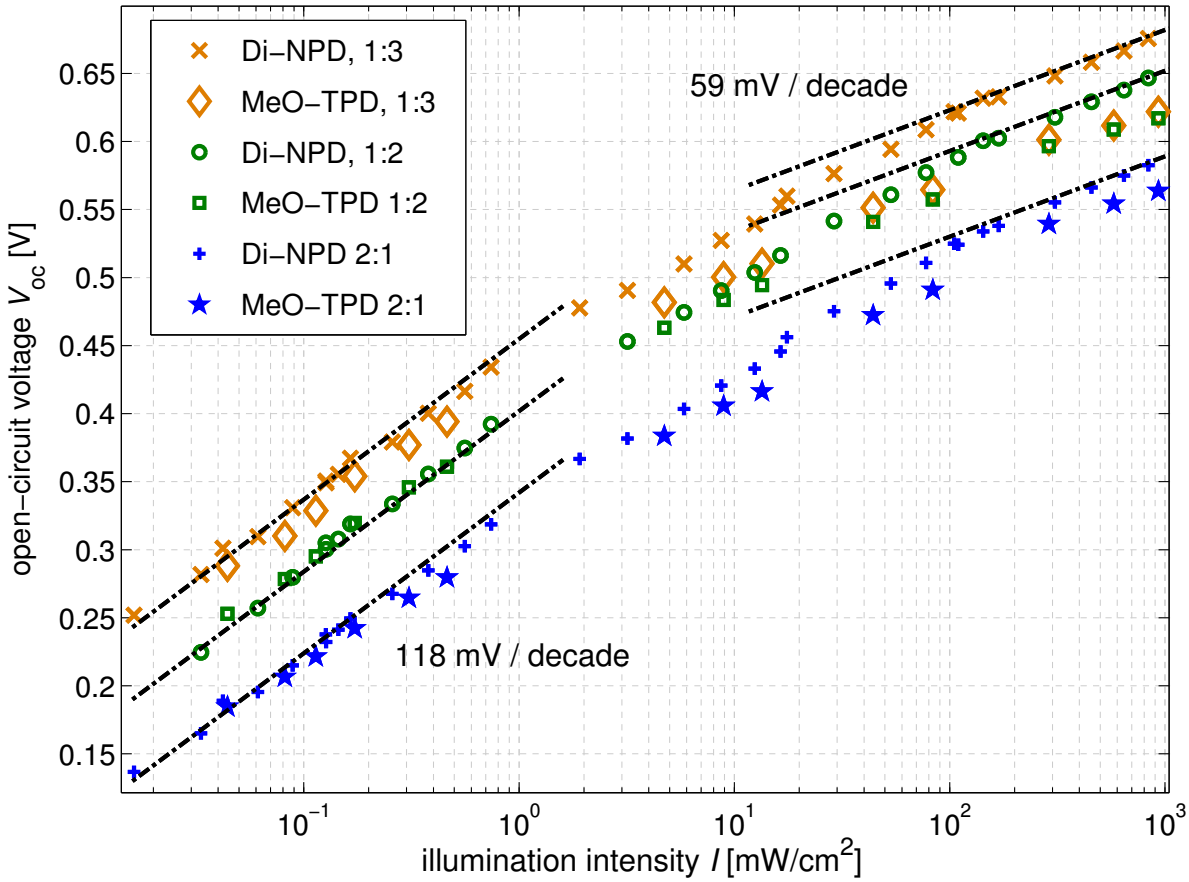
Figure 10.15: V_{oc} as a function of illumination intensity I for devices with an HTL thickness of 90 nm. For higher intensities V_{oc} is limited by the HTL MeO-TPD. The dashed lines show the theoretically expected slope for SRH (118 mV/decade) and direct (59 mV/decade) recombination.

densities and thus recombination probability decrease. However, the *FF* drops at a certain point. This effect does not seem to be related to a change in recombination. Either trapping of charges significantly decreases their mobility, which would then depend on charge carrier density; or the photocurrent becomes such small that the limit by the dark parallel resistance is observed. This holds at least for intensities lower than 1 mW/cm^2.

Also in this plot, measured data and data corrected for R_{S} are shown to visualize the two extrema of the *FF* within the real value is expected. R_{S} becomes significant for intensities larger than 100 mW/cm^2, where the real *FF* is expected to be closer to the corrected data. The decay of the *FF* at higher intensities is most significant for the imbalanced mobility samples (1:3). The reason is that fast electrons pile up close to the ETL and form a space charge region. Recombination equals generation in this almost field-free region. This region increases with electron density and thus light intensity. Consequently, recombination increases significantly.
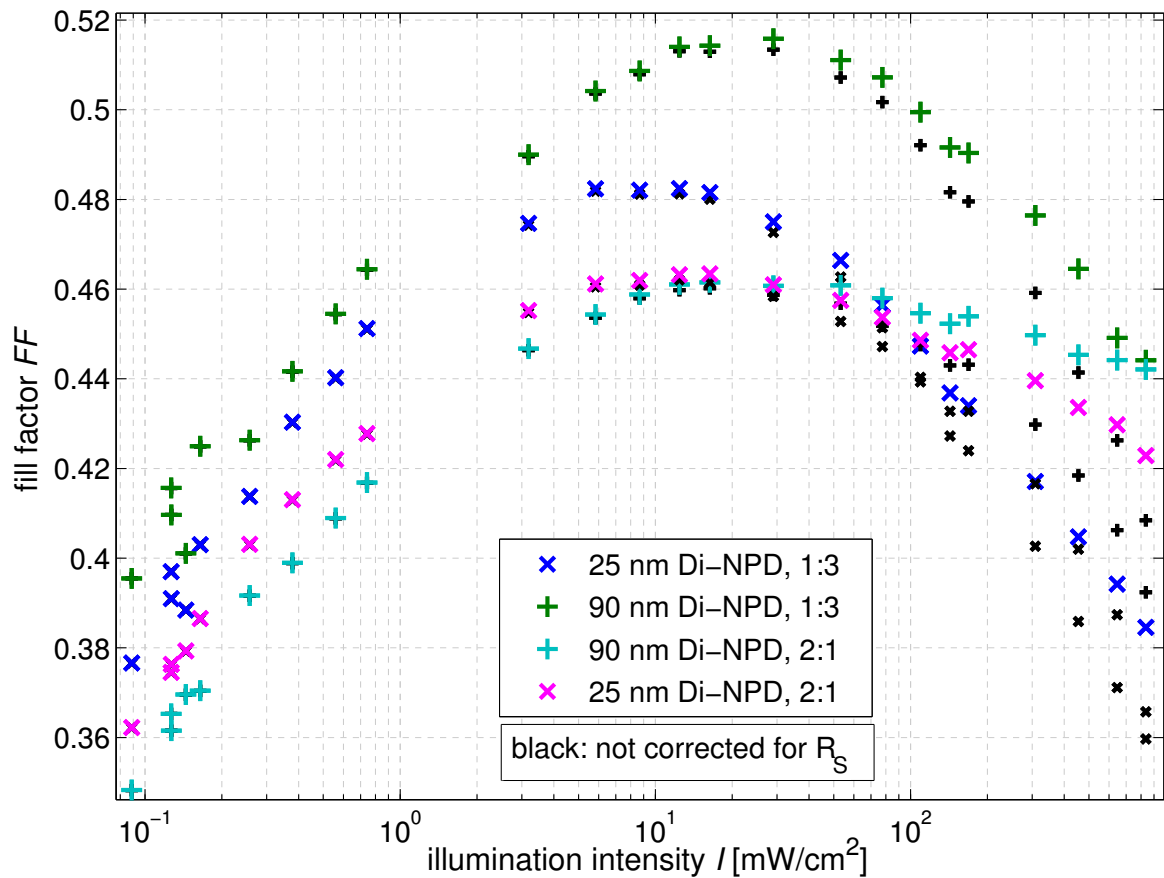
Figure 10.16: Fill factor *FF* as a function of illumination intensity *I* for two HTL thicknesses and two different mixing ratios. Maxima are observed at an intensity of $\approx 10\,\mathrm{mW/cm^2}$.

10.3.3 Lifetime of charge carriers

The dependence of the lifetime of charge carriers on illumination intensity may also give information about the dominating recombination mechanism. A constant lifetime τ indicates recombination of photogenerated charge carriers with a background charge carrier density which is significantly larger than the photogenerated one, as discussed in Ch. 2.2.2. In case of recombination among photogenerated charge carriers, τ is not defined as material property, as it depends on both charge carrier densities and thus on light intensity.

Access to the lifetime is given by transient photovoltage-decay experiments, described in Ch. 3.6. The basic idea is to measure the lifetime of a small density of optically generated excess charge carriers in the presence of a given charge carrier density at open circuit, provided by a constant background illumination. The lifetime is extracted from a fit to the exponential decay of the additional small voltage signal generated by the probe pulse. The results of this measurement are shown in Fig. 10.17, where τ is plotted as a function of
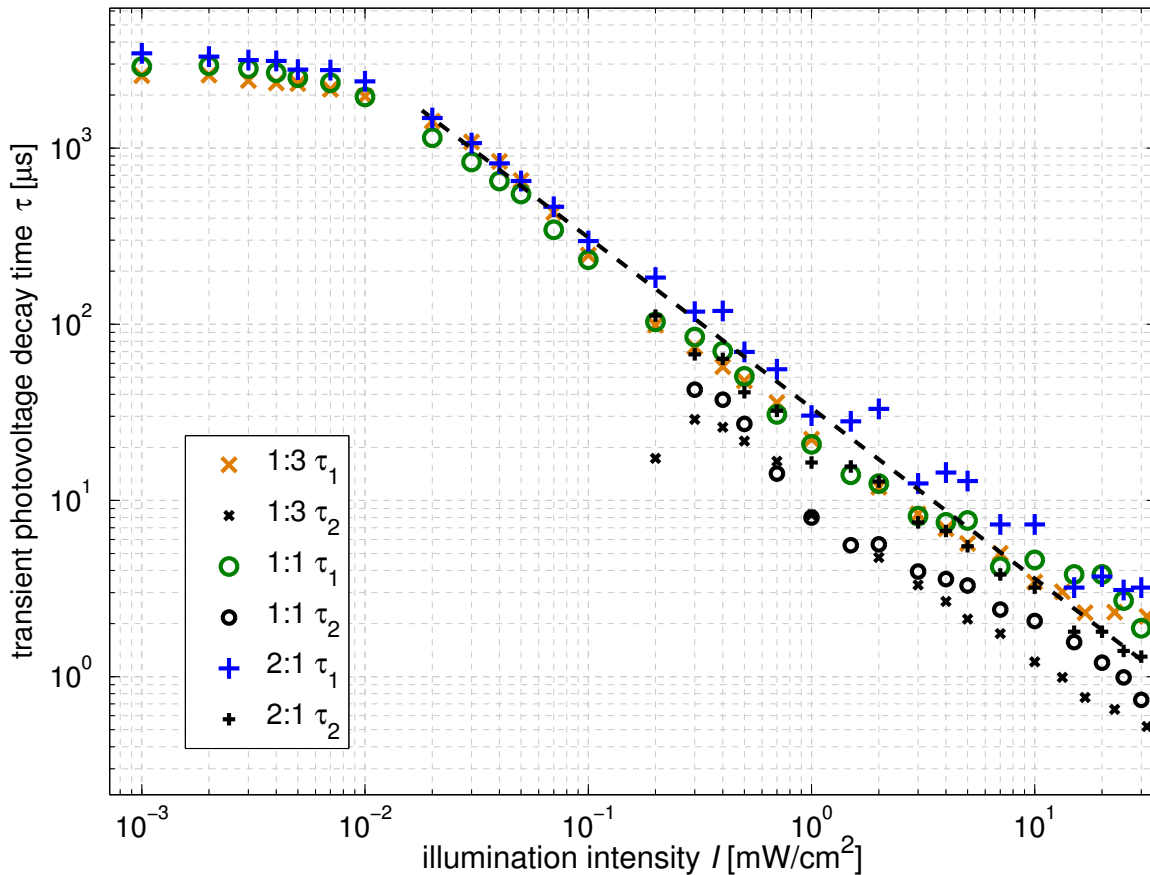
Figure 10.17: Charge carrier lifetimes in ZnPc:C$_{60}$ blends with different mixing ratios. Data are extracted from transient photovoltage measurements at varied illumination intensity provided by a white-light LED. Intensities are measured with a silicon reference diode. Due to a setup-related intensity mismatch $20\ldots 30\,\mathrm{mW/cm^2}$ correspond to 1 sun. The dashed line shows a slope of unity.

light intensity. The samples investigated contain BF-DPB as HTL. For higher intensities two values of τ are shown for each sample, because the voltage decay can be fitted best by a double-exponential function for these intensities. Two lifetimes are an indication for a superposition of two processes, e.g., trap-assisted and direct free-charge carrier recombination. Thus, the slower process could result from some shallow traps, which require to be detrapped before recombining. The reader is referred to the work by S. Corvers regarding further discussions of the double-exponential behavior [216]. The finding most significant for this chapter is that τ decreases almost linearly with intensity (slope -1 in the logarithmic plot). This is a clear indication for recombination between photogenerated charges only, where the density of the "other" charge carrier increases linearly with intensity. At very low intensities, where V_{oc} tends to zero, the lifetime saturates at a value of 2 ms. This is

parameter	2:1	1:1	1:2	1:3
E_{ht} [eV]	-5.08	-5.11	-5.16	-5.2
$E_{\mathrm{g}}^{\mathrm{DA}}$ [eV]	1.05	1.08	1.13	1.18
β [cm^{3}s^{-1}]	2.8×10^{-13}	1.6×10^{-12}	2.0×10^{-12}	3.4×10^{-12}
μ_n [cm^2/Vs]	2.5×10^{-5}	1×10^{-4}	3×10^{-4}	1×10^{-3}
μ_p [cm^2/Vs]	2×10^{-5}	2×10^{-5}	8×10^{-6}	4×10^{-6}
d_{BLEND} [nm]	48	54	50	50
d_{HTL} [nm]	25	45	86	170

Table 10.3: Parameters for the simulation of the ZnPc:C$_{60}$ BHJ. Further input parameters are found in Appendix B, p. 330.

presumably due to the effect that the photogenerated charge carrier density is lower than the background charge density introduced by the contacts. An (*RC*-)limit due to current flowing through the $1\,\mathrm{M\Omega}$ measurement resistor is unlikely as changing this resistor does not result in a changed τ [216].

10.4 Comparison with simulations

So far the discussion focused on a qualitative interpretation of the measurement results. In this section, simulation data are presented which allow for more quantitative statements. However, it is emphasized that the amount of parameters makes an automated fitting difficult. Therefore, the selected parameters represent one possible combination which fits the experimental data relatively well. The strategy applied here to find reasonable parameters for each mixing ratio, which are summarized in Tab. 10.3, is as follows:

1. The lifetime data shown in Fig. 10.17 is used to extract a bimolecular recombination constant β under the condition that generation is equal to recombination at V_{oc} and the charge carrier density is mainly given by photogenerated charge carriers ($G = \beta n_{\mathrm{ph}}^2 = n_{\mathrm{ph}}/\tau$). The scaling of the lifetime with charge carrier density suggests that this approach is legitimate. Thus, it is assumed that bimolecular recombination is dominating at $1\,\mathrm{sun}$ illumination, as deduced from the dependence of V_{oc} on illumination intensity.

2. The effective gap $E_{\mathrm{g}}^{\mathrm{DA}}$ is selected as follows: A constant EA of C$_{60}$ of -4.03 eV is assumed, which is independent of mixing ratio. The hole transport level is taken from the IP measured by UPS for a 1:1 and 1:3 blend. For 1:2 and 2:1 blends, the mean value between adjacent mixing ratios is chosen. This approach leads directly to a very good reproduction of the different values of V_{oc} which are mainly due to the changed effective gap, as the lifetimes do not change much with mixing ratio.

3. Thicknesses are slightly modified to optimize the fit between experimental and optically simulated saturated photocurrent. The experimental saturation current is

obtained by correcting the J-V curves by the photoshunt as discussed in the next chapter.

4. As we have seen from the intensity dependence of V_{oc}, trap-assisted recombination is relevant in particular at low intensities. Therefore, SRH recombination according to Eq. 4.47 is implemented with a recombination constant of $10^6 \, \mathrm{s}^{-1}$. This value is kept fixed and is chosen to reproduce the transition from indirect to direct recombination seen at the dependence of V_{oc} on illumination intensity.

5. Mobilities are determined by a comparison of simulation data to the *FF* data dependent on HTL thickness shown in Tab. 10.1. For simplicity reasons μ is assumed to be independent of the electrical field.

6. For a comparison also dark curves are modeled with the chosen parameters and without changing any parameter or doing any fitting.
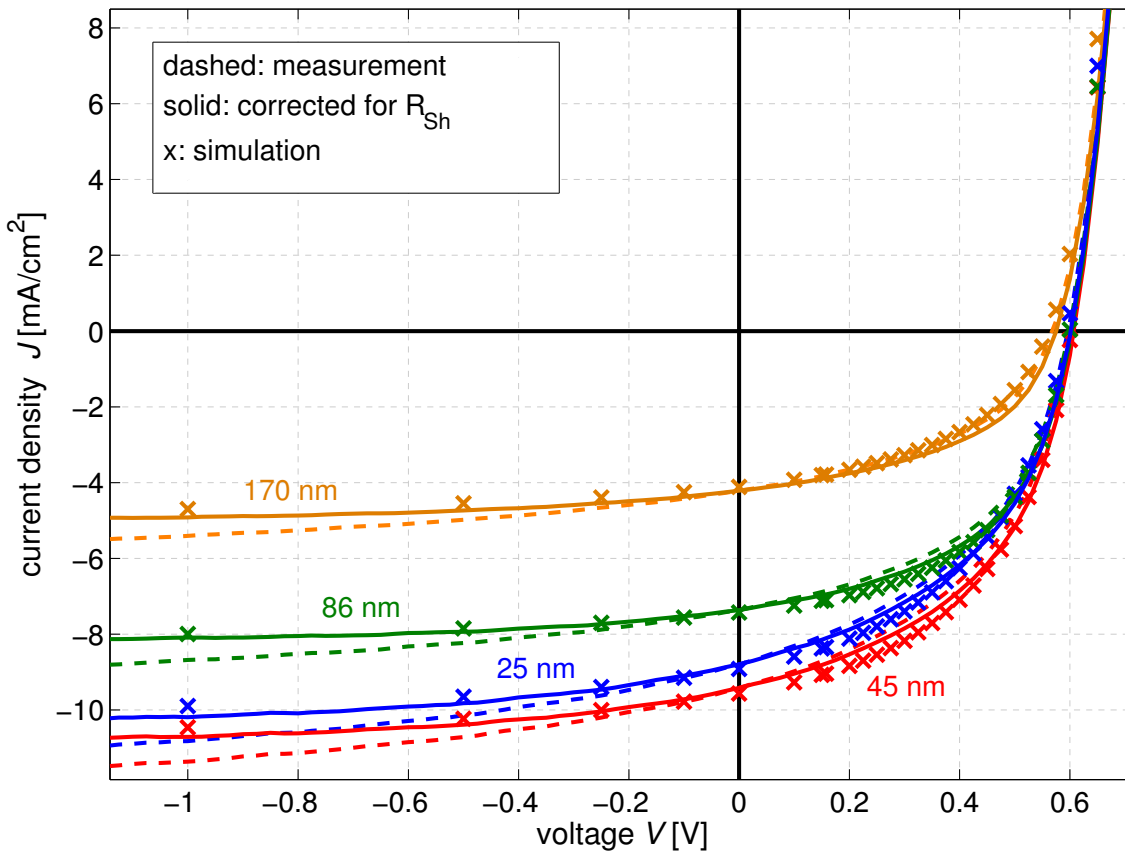
Figure 10.18: *J*-*V* curves of ZnPc:C$_{60}$(1:2) devices for different HTL thicknesses. Dashed lines represent measured data, solid lines are experimental *J*-*V* curves corrected for a photoshunt (cf. Chapter 11), and crosses mark simulation data.
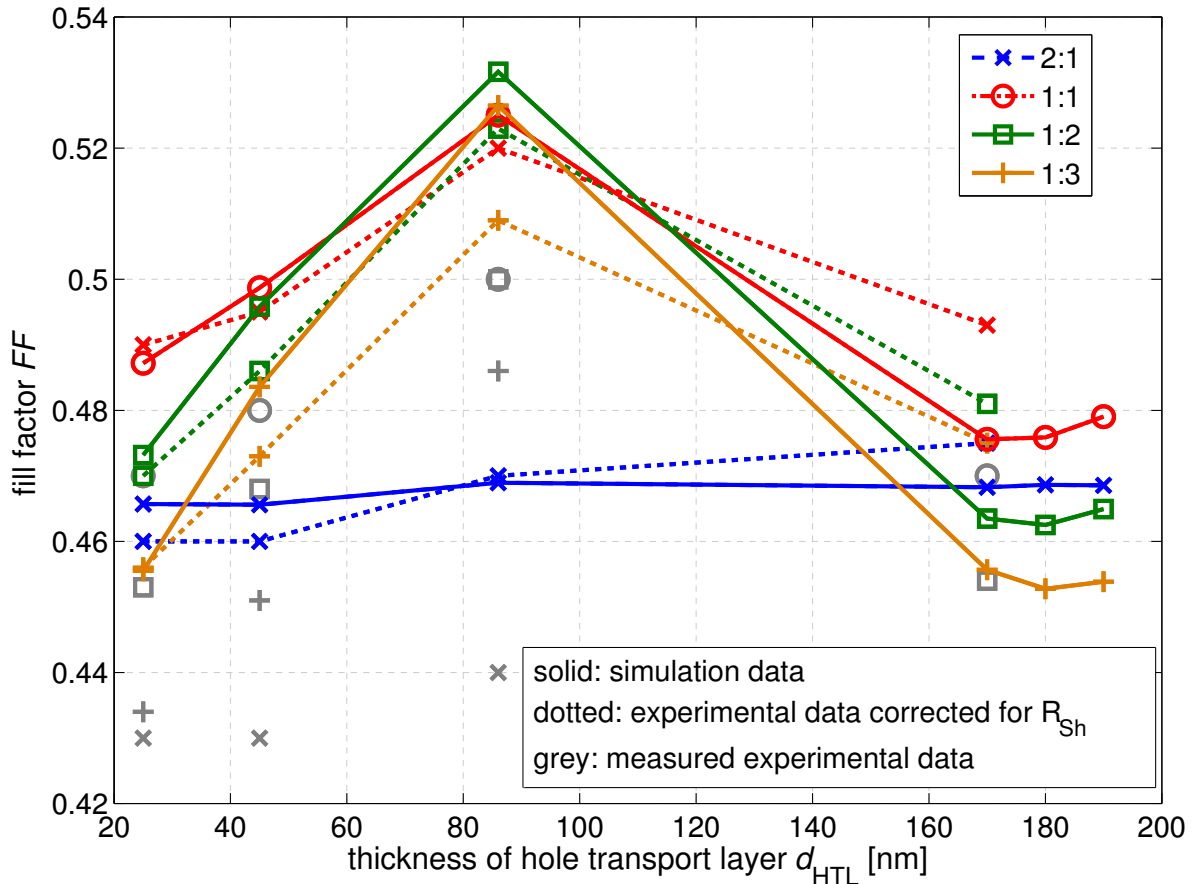
Figure 10.19: Fill factor for all mixing ratios as a function of device thickness. The original measurement data (grey) of Tab. 10.1 are corrected for a photoshunt (colored symbols, dashed lines). Solid lines denote simulation data with the mobilities of Tab. 10.3.

Figure 10.18 shows J-V curves of devices with mixing ratio 1:2 and different HTL thicknesses to visualize the agreement between experiment and simulation. Measured (dashed lines) and J-V curves corrected for the photoshunt (solid lines) are shown. Without correction, the J-V curves do not saturate and reach currents which are larger than the ones predicted by optical simulation. Therefore, the correction is essential and will be discussed in the next chapter (Chapter 11) in detail. The simulated J-V curves follow the experimental ones relatively well. For a better fit, an optimization regarding the saturation current by changing layer thicknesses or introducing a voltage independent maximum IQE value could be done. Also a fine-tuning of mobilities and recombination constants could be done to increase the fitting. However, one should keep in mind that we describe a bulk heterojunction as one effective medium by a very rough model. Thus, even perfect fits will not improve the understanding of the physics of these devices.
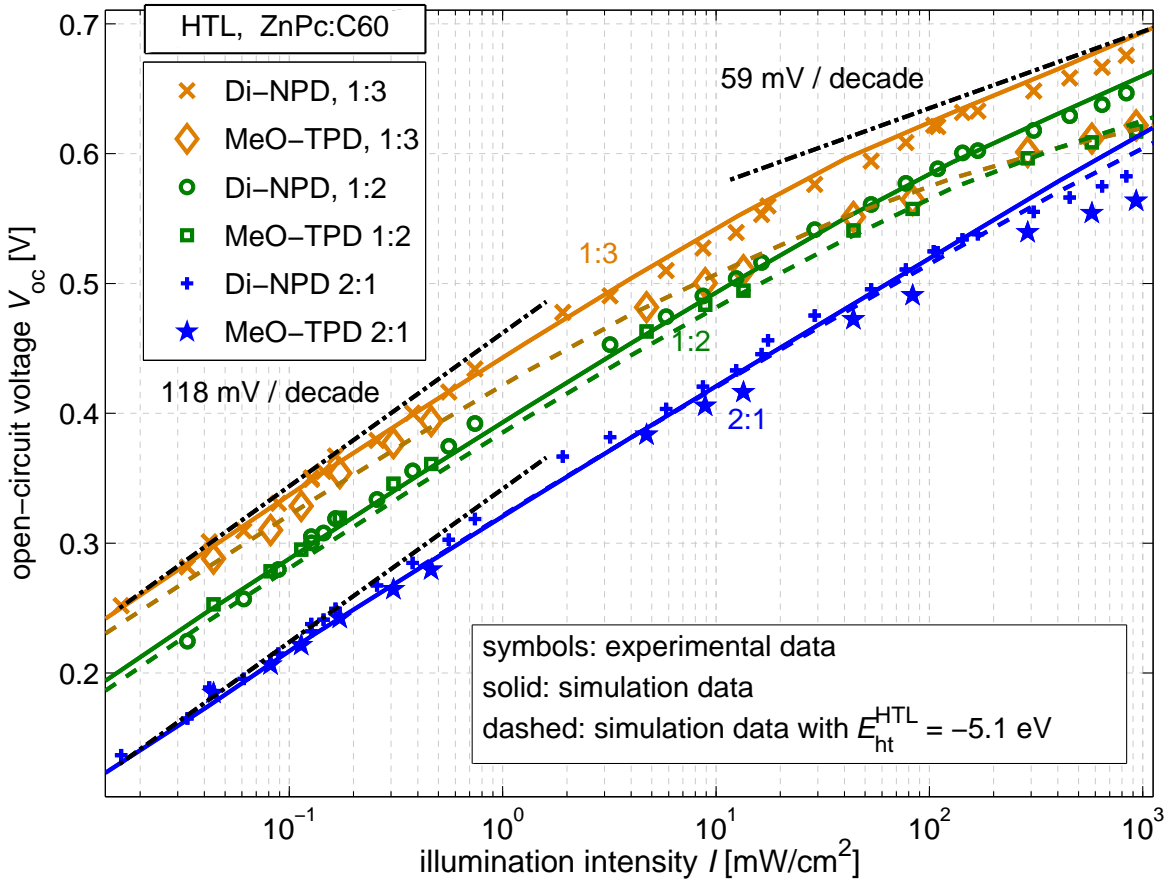
Figure 10.20: The open-circuit voltage dependent on illumination intensity. The simulation data (solid and dashed lines) show good agreement with experiment and show the three limits, which are SRH recombination (low intensities), direct recombination (high intensities), and recombination at the HTL/blend interface (for MeO-TPD at high intensities).

Here, the scope is to show the correlation between generation profile and imbalance in charge carrier mobility. This is demonstrated by a summary of all values of the *FF* dependent on mixing ratio and HTL in Fig. 10.19. The mobilities used in the simulation are lower than those measured by OFET (cf. Tab. 10.2 with Tab. 10.3). This is expected due to the high charge carrier densities in the channel of an OFET. Additionally, the measurement of a blend complicates the application of the simple transistor equations used to extract mobility values, as the geometry of the channel in a blend is not well-defined. The trend in the imbalance, however, follows the OFET measurements. Geminate recombination together with a field-dependent exciton dissociation is not considered here, as the trends can be reproduced well without considering this process, which is highly debated.

Figure 10.20 shows the dependence of V_{oc} on light intensity for different mixing ratios. This graph was already shown in Fig. 10.15. Here, also simulated data are added to the
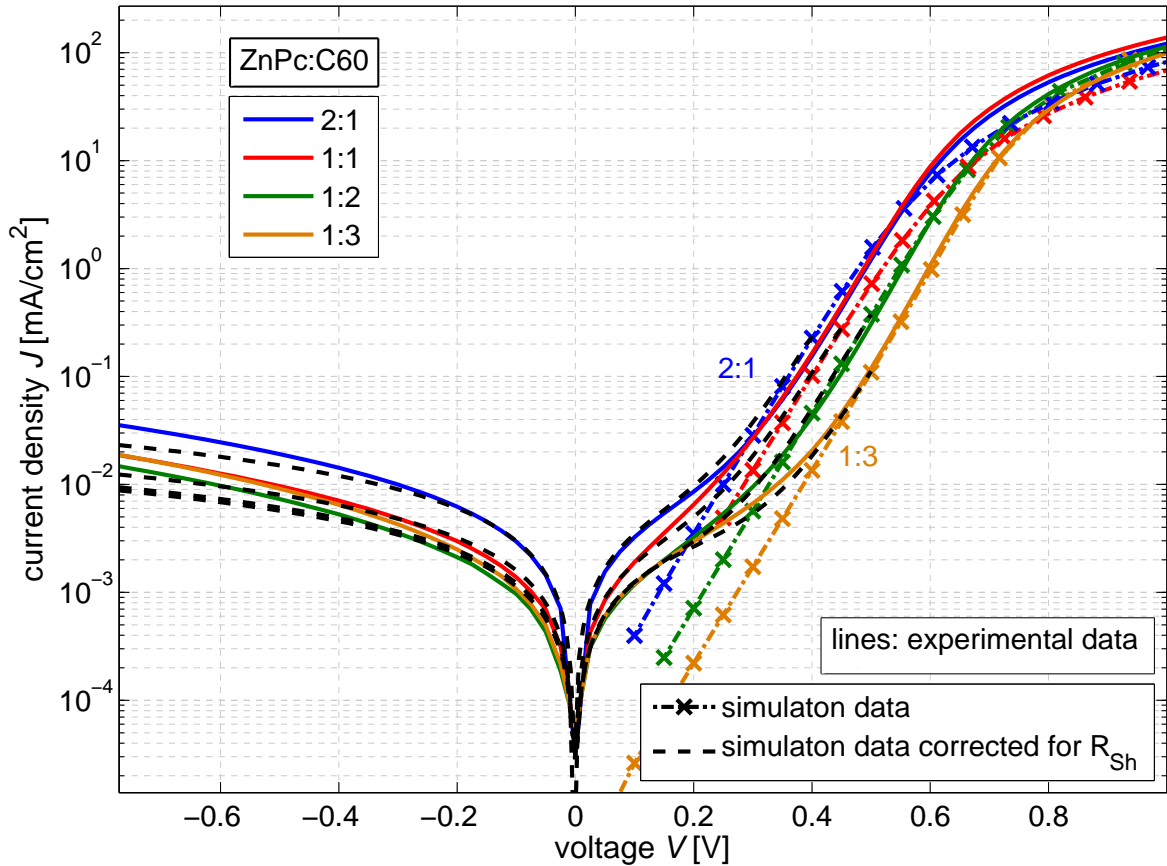
Figure 10.21: Dark J-V curves of devices with different mixing ratios and an HTL thickness of 25 nm. Dash-dotted are simulation data including an ITO series resistance of $1.6\,\Omega\text{cm}^2$. The experimental current close to $0\,\text{V}$ is dominated by a finite shunt resistivity. Adding this contribution to the simulation data results in the black dashed lines which show good agreement with experiment for the overall voltage range.

graph and show excellent agreement with the experimental data over the whole intensity range. The simulation confirms that SRH recombination becomes important for lower light intensities. The fact that the assumption of one SRH constant for each blend and being present at all light intensities shows that this recombination is a very important and definitely present mechanism in ZnPc:C_{60} solar cells. As the SRH recombination constant does not change between different mixing ratios, it seems to be dominated rather by the heterojunction itself than by the morphology of the film. It was mentioned earlier that V_{oc} is limited by the contacts at higher light intensities, especially for the HTL MeO-TPD with a high HOMO of -5.1 eV. If this value is used in the simulation, this limit seen in experiment can be described very well (dashed lines). In experiment this limit is also seen in the 2:1 blend which indicates that there might be a little HOMO offset or an increased

recombination at the interface to the HTL for this mixing ratio as well.

As last point experimental and simulated dark *J-V* curves are compared, where it is found that the region of the onset and the slope (ideality factor) fit very well. This is another indication that the chosen parameters are not completely wrong. It shows in particular that the balance between direct and SRH recombination deduced from V_{oc} is also capable of describing the dark carriers. The simulation data is corrected for the ITO series resistance, which is assumed to be $1.6\,\Omega\text{cm}^2$. The current around $0\,\text{V}$ is due to a dark shunt resistance. Its value is deduced from the slope of the dark *J-V* curve between -0.05 and +0.05 where the curve is indeed linear. Adding this value to the simulated curve gives a good agreement between experiment and simulation over the whole voltage range (dashed lines). Current in negative direction is underestimated. This current results from a reverse tunneling current not included into the simulations here. It will be discussed briefly in Ch. 13.2.

We can conclude that recombination via traps dominates dark current and V_{oc} at low intensities. The dependence of the *FF* on the generation profile provides estimates for values of charge carrier mobilities and leads to good fits without assuming a field-dependent charge carrier generation (exciton dissociation) rate.

10.5 Summary

It was shown that the *FF* in ZnPc:C$_{60}$ solar cells is mainly limited by charge transport. The absorption profile within the blend was found to influence the *FF* in the case of a higher imbalance in charge carrier mobilities. This imbalance increases with a higher amount of C$_{60}$ in the blend. The role of the generation profile was demonstrated by a variation of spacer layer thickness which changes the *FF* of 1:3 devices between 43 and 49 %. Voltage dependent EQE data provided an additional proof for the dependence of the charge extraction probability on the locus of the absorption maximum.

The dependence of V_{oc} on the illumination intensity revealed that trap-assisted recombination dominates V_{oc} at low light intensities. At higher intensities direct electron-hole recombination becomes visible. This mechanism mainly limits the device performance under solar illumination.

Both the dependence of V_{oc} on light intensity and the trends in *FF* were reproduced by numerical simulations.

Chapter 11

Linear Saturation Behavior

All experimental J-V data which were presented in the last chapters showed a linear photo-current-voltage behavior for voltages lower than -3 . . . 0 V. The exact voltage point where this region is reached depends on the actual solar cell stack. As this "shunt" effect is only seen under illumination, it is not caused by a low macroscopic shunt resistance. Nevertheless, this feature can be called "photoshunt" due to the linearity of the J-V curve under illumination. Interestingly, this effect is commonly more pronounced for (ZnPc/C_{60}) FHJs compared to BHJs.

The photoshunt has always been neglected when comparing experimental data with simulation data. This was necessary because simulations with the implemented models did not show the photoshunt. The scope of this chapter is to provide a justification for this approach. The absence of the photoshunt in simulation data indicates that this feature may rather be a parasitic or additional phenomenon. The way to this conclusion is discussed in this chapter. Several indications are found from J-V data dependent on layer thicknesses and from voltage dependent EQE data that the photoshunt results from a photoinduced reverse injection current. This parallel current can be visible in the power-generating regime of the J-V curve as well. It constitutes a loss mechanism since it decreases the FF.

11.1 Definition of the photoshunt

For a clarification of the phenomenon "photoshunt" we refer to experimental *J-V* data. For example, the experimental *J-V* curves in Chapter 6 (Figs. 6.3, p. 180 and 6.4, p. 182) where energy barriers have been discussed, show this effect for voltages lower than the onset of the S-kink regime. The data of hybrid ZnPc/ZnPc:C_{60} cells displayed in Fig. 11.1 show evidence for a linear *J-V* curve starting for voltages lower than -0.5 V. The inverse slope of this linear region is defined as photoshunt. In all cases, the dark curves do not show this shunt. To avid confusion, we clarify that a large shunt resistance means a low slope and good saturation, which is better for solar-cell performance. A low shunt resistance, however, means a high slope and a bad saturation, which is detrimental for the performance (cf. Fig. 3.18). The *J-V* curves of ZnPc/C_{60} FHJ devices (see Fig. 11.8) exhibit the photoshunt effect already around 0 V. This indicates that even the fourth quadrant and thus the *FF*

can be affected by this effect. Therefore, systematic studies on the photoshunt effect are shown in this chapter. We start with modeling results, discussing possible reasons for a low saturation in simulation. Subsequently, a hypothesis is proposed which can explain the photoshunt behavior. This idea suggests that the photoshunt results from an injection current. Finally, experimental investigations are presented which give further details on the nature of the photoshunt effect.

11.2 Quasi-linear photocurrent in simulation

The simulation data presented so far were characterized by the fact that the photocurrent saturates under moderate negative bias voltages (-1. . . -3 V). The reason for this saturation is an extraction of all photogenerated charge carriers at a certain negative bias voltage. The point of saturation can in principle be shifted towards higher negative bias voltages. This may result in a quasi-linear regime of the *J-V* curve for voltages around zero. The following processes or extreme choices of parameters are capable of showing this quasi-linear shape in simulation:

- Geminate recombination in competition with field dependent CT-state dissociation dependent on the electrical field,

- High recombination rates and/or very low mobilities,

- The presence of traps,

- Imbalanced mobilities in a bulk heterojunction,

- Background doping.

At this place, it is omitted to show simulation data of variations of all the involved parameters, which are several for each of the five cases mentioned. The amount of *J-V* curves would be huge without providing a deeper insight into the photoshunt phenomenon. Instead, the overall results of the conducted simulations are summarized in the following.

If high recombination independent of the particular mechanism dominates the linear reverse current, the *FF* of the device is very low (25 . . . 35%). The *J-V* curve is already close to linear in the fourth quadrant. Furthermore, the diode forward current is underestimated in case of low mobilities. In general, high recombination and/or low mobilities result in a low $\mu\tau$ product. Therefore, Eq. 3.18 which describes a linear photocurrent-voltage relation may be applied in a certain voltage range of the *J-V* curve.

Active traps, imbalanced mobilities, or background doping result in a similar effect. These processes have in common that they cause a space charge region close to one electrode. This region is characterized by a low electric field, because the space charge screens the potential applied to the solar cell (cf. Fig. 3.19, p. 73). Charge carriers which are photogenerated in this region predominantly recombine there. The width of this region decreases with a higher reverse bias, following a square root dependence on *V* like the

width of the space charge layer in a p-n junction (cf. Eq. 2.35). This effect was briefly discussed with analytic equations in Ch. 3.3.5 and can result in a *J-V* characteristic under reverse bias which is close to linear. However, this effect only results in a quasi-linear *J-V* relation if the generation rate is constant in space. Optical simulations show that this is not the case as discussed in Chapter 10 in detail. Thus, the photocurrent, which results from a decreased space charge region for higher negative bias, maps the generation profile. This effect may be reduced in pristine films, where exciton diffusion flattens the generation profile.

Usually, all the presented effects result in a low *FF*. Experimental data, however, show the photoshunt despite a relatively high *FF* (Fig. 11.1). Thus, the effective medium BHJ as main source of photocurrent is unlikely to cause the photoshunt. This leads to the idea that an additional low-photocurrent source may be superimposed to the BHJ as main source. This additional source which shows a low saturation would become visible only in the negative bias regime, whereas the fourth quadrant would be dominated by the BHJ providing a high *FF*. This additional source may consist of large domains within a BHJ or of a neat absorber layer if autoionization of excited states is present. Autoionization is a process which directly generates separated charges in a pristine material. In literature this process is discussed as a source of photocurrent which is not negligible in some materials [333–336]. Thus, it may play a role, particularly in FHJs. As the donor (acceptor) is a predominantly p-conducting (n-conducting) material, it shows a high hole (electron) mobility and a low mobility of the other charge carrier species. For example, an intrinsic C_{60} layer can easily deliver photogenerated electrons, whereas the less mobile holes may create a space charge. With increased negative bias voltage, this space charge layer is reduced and more holes can be extracted. Therefore, such a layer may be the source of a low saturation of photocurrent under reverse bias.

In summary, the simulation shows a saturation tendency in all cases which is in contrast to experiments. Although the occurrence of the saturation can be shifted to higher negative bias voltages, a slight curvature remains in the whole voltage range. It is concluded that the simulation is not capable of reproducing the (linear) photoshunt resistance which is experimentally observed. It is further noted that although good *J-V* fits can be achieved for voltages between -0.5 and 0.5 V, these fits are not meaningful as they do not describe the quality of the photoshunt, which is characterized by a non-saturating trend.

11.3 Experimental approach and results

The previous section illustrated that all the processes included in the simulation lead to a visible saturation tendency. However, the experimental data do not show any saturation behavior, but a linear current-voltage relation. Thus, the additional current in reverse is assumed to be an injection current. This would mean that at least one electrode loses its selectivity under high negative bias and illumination. In the case of a FHJ, even one material (either donor or acceptor) becomes (photo-)conductive for the other charge carrier species as well. It is once more stated that this shunt is not present in the dark.

A microscopic reason for this effect could be that the illumination creates free charges or that the excitons are capable of emptying traps so that trap-mediated transport can take place. It is emphasized that the current in reverse is very weak compared to forward current which means a high shunt resistance. If this theory of a photoconductive shunt R_{sh} is true, it should fulfill the following conditions:

- R_{sh} scales with light intensity,

- R_{sh} decreases with layer thickness,

- R_{sh} can lead to gain in photcurrent.

In the following these properties are investigated focusing on ZnPc/C_{60} solar cells.
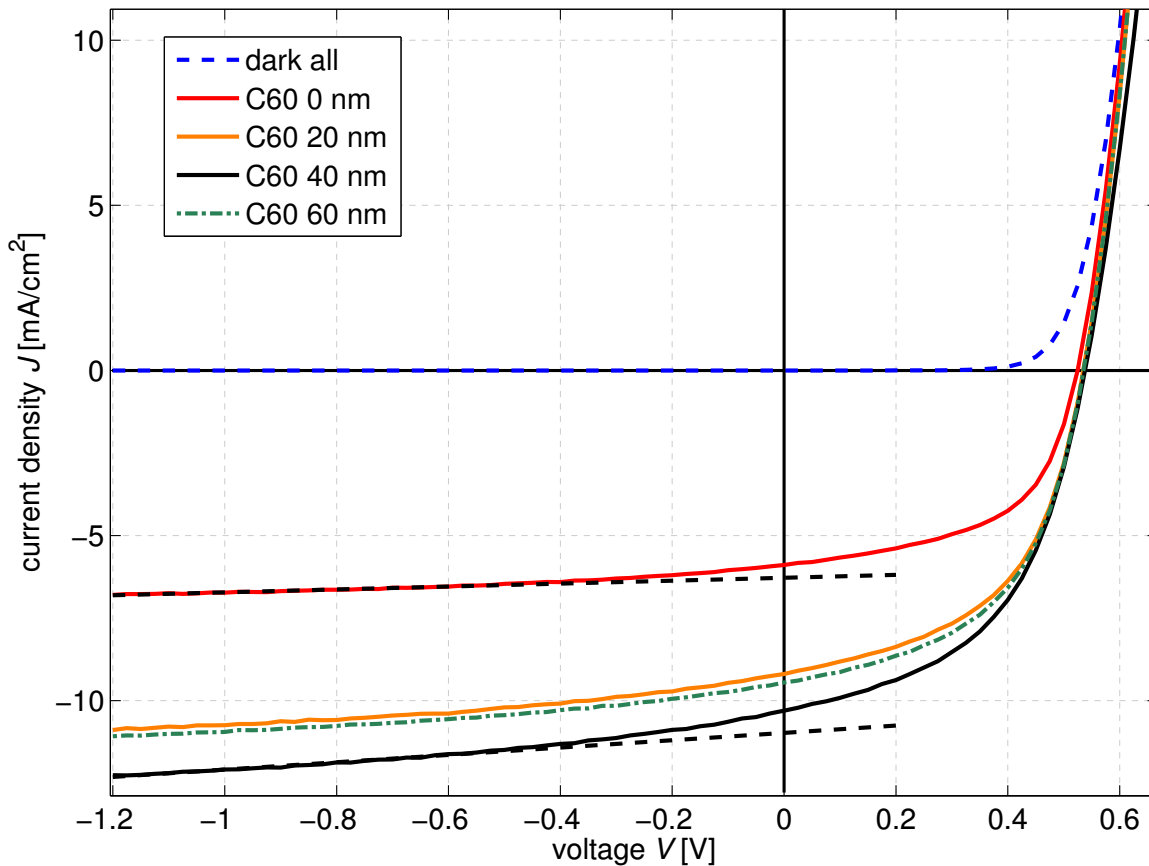
Figure 11.1: *J-V* curves of devices ITO/NDP2(1)/MeO-TPD:NPD2(20, 2 wt%)/ ZnPc: C_{60}(1:1, 45)/C_{60}(x)/BPhen(6)/Al(100) measured under simulated sunlight. A stronger photoshunt behavior is visible for devices with an intrinsic C_{60} layer.
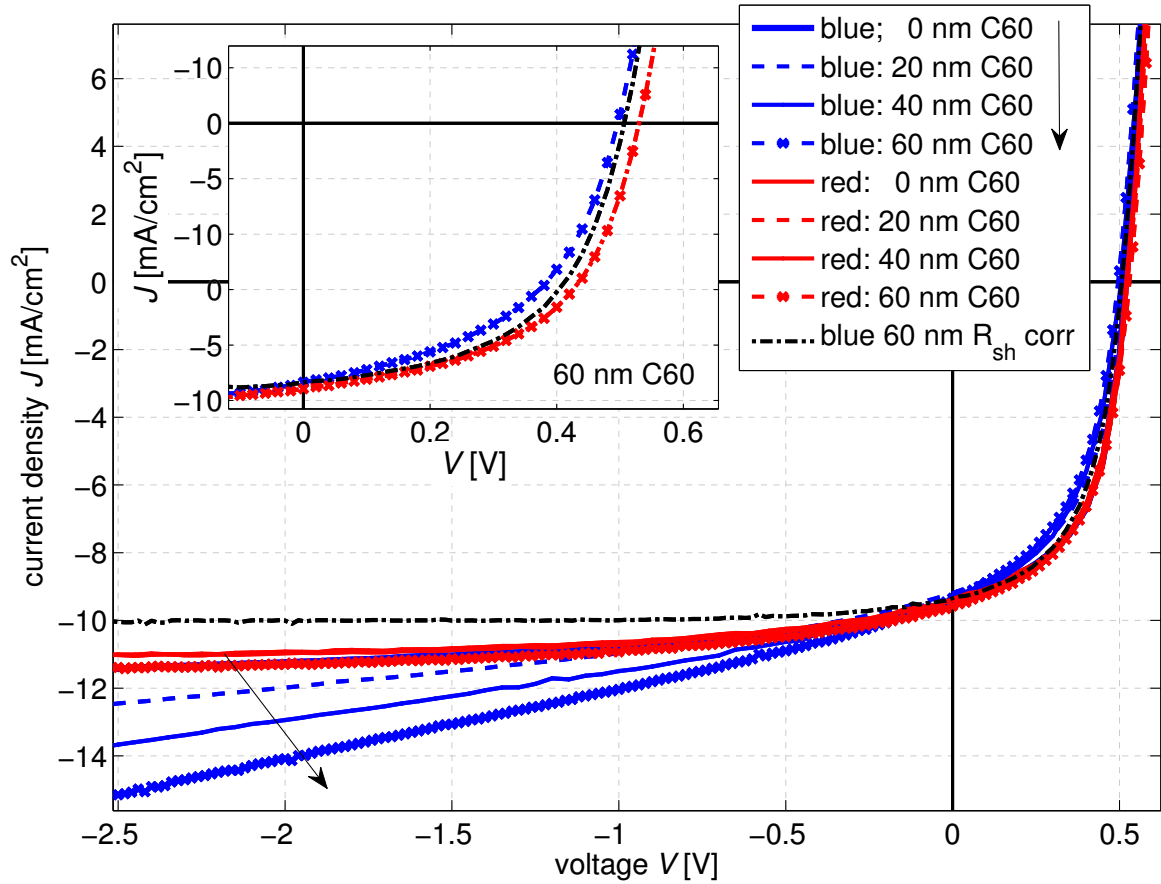
Figure 11.2: *J-V* curves of devices ITO/NDP2(1)/MeO-TPD:NPD2(20, 2 wt%)/ ZnPc: C_{60}(1:1, 45)/C_{60}(x)/BPhen(6)/Al(100) measured under illumination with monochromatic LEDs. The intensity is adjusted to reach the same short-circuit current. The dash-dotted line shows the *J-V* curve of a device with 60 nm intrinsic C_{60} corrected for the shunt.

11.3.1 Identification of the main source of the photoshunt

It was already mentioned that the photoshunt effect is more pronounced for a FHJ than for a BHJ. Now, we investigate p-i-metal BHJ solar cells with and without an intrinsic C_{60} interlayer (BHJ and hybrid BHJ/FHJ). Figure 11.1 demonstrates that devices with a C_{60} interlayer show a weaker saturation in reverse bias and, therefore, a stronger shunt effect (lower shunt resistance). The shown *J-V* curves are measured under simulated sunlight. As the dark *J-V* curves of all devices coincide and do not show any significant reverse current in the investigated voltage region, the influence of the illumination is studied in more detail in the following.

To do so *J-V* measurements are performed under monochromatic blue and red illumination. The *J-V* curves are shown in Fig. 11.2, where the intensity is adjusted to reach the
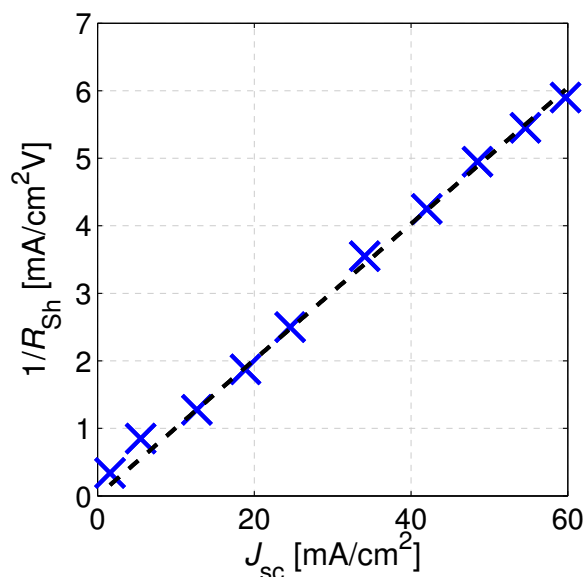
Figure 11.3: The photoshunt of a sample ITO/NDP2(1)/MeO-TPD:NPD2(20, 2 wt%)/ ZnPc: C_{60}(1:1, 45)/C_{60}(20)/BPhen(6)/Al(100) as a function of light intensity monitored by J_{sc}. The dashed line represents a linear fit.

same short-circuit current (J_{sc}) for all solar cells and both illumination colors. A significant photoshunt can be observed for samples containing the intrinsic C_{60} layer, but only if C_{60} is excited by illumination. Under red illumination the photoshunt is less pronounced for all devices. The photoshunt becomes more relevant for large C_{60} layer thicknesses. This is due to the higher intensities required for the samples with larger C_{60} layer thicknesses to reach the same J_{sc}. The reason is the distribution of the optical field. A thicker C_{60} layer shifts the blend out of the optical field maximum and results in a high absorption in the intrinsic C_{60} layer, where not all excitons are collected. In the previous chapter the influence of the illumination color was investigated in detail. By modifying the generation profile, the illumination spectrum lead to changes in the *FF* for a 1:1 blend in the range of 5 %. That effect cannot explain the strong photoshunt seen here.

The *J-V* data of Fig. 11.2 leads to the conclusion that the additional current under reverse bias results from absorption in intrinsic C_{60}, either by additional photogenerated charge carriers being extracted (autoionization) or by the illuminated C_{60} acting as hole injection layer (photoshunt). The device with the worst saturation shows the lowest *FF*. A correction of the *J-V* curve of the sample with 60 nm C_{60} under blue illumination for the photoshunt (dash-dotted line in Fig. 11.2) results in a *J-V* curve which approaches the one under red illumination. This is an indication that the low saturation is indeed caused by an ohmic photoshunt which also acts under forward bias.

Figure 11.3 shows the photoshunt of the sample with 20 nm C_{60} as a function of J_{sc}. The illumination is provided by blue LEDs. A separate measurement proves that J_{sc} scales almost linearly with light intensity in the investigated intensity range. Thus, the

photoconductivity $1/R_{sh}$ scales linearly with light intensity.

In a next step transient photocurrent measurements are performed on the discussed samples to employ the response time as an additional parameter giving information about the reverse photocurrent. We compare the sample without intrinsic C_{60} with the sample with $60\,nm$ C_{60} using the data displayed in Figs. 11.4 and 11.5. These graphs show the current response on a $200\,\mu s$ illumination pulse. The data is normalized to the steady state value of the photocurrent to allow for a visual comparison of the curve shape. This shape is not significantly influenced by the applied bias voltage. However, when zooming into onset and plateau region, changes can be seen. The response time within the first $5\,\mu s$ decreases with reversed bias (inset I, onset). This is expected as the higher negative field enhances charge extraction by an increased drift velocity. This holds for both samples.

Insets II (plateau) show the last $5\,\%$ of the current response over the whole pulse lengths of $200\,\mu s$. These plots in Figs. 11.4 and 11.5 reveal a significant difference between the two samples. Whereas the sample without C_{60} does not show any dependence of the current on voltage in this region, the sample with intrinsic C_{60} shows a clear trend. The response becomes slower for higher applied negative bias voltages. Together with the faster rise for higher negative bias, this results in a crossing of the curves which is found at $\approx 2\,\mu s$. This indicates the existence of a slower current component for the sample with C_{60} under negative bias. In conclusion, the additional reverse current does not have the same origin as the main photocurrent, but results indeed from a separate, slower effect.

The hypothesis, therefore, reads: Illuminated C_{60} becomes hole-conductive, either by the extraction of additional electrons and holes resulting from autoionization or from additionally injected charges. This photoconductivity effect is less pronounced in a blend, because all excitons are instantaneously quenched at the donor. In contrast, they show higher lifetimes in the intrinsic C_{60} where not all excitons reach a quenching interface. The higher lifetime of excitons in pristine films is commonly known and can be experimentally verified by photoluminescence measurements.

If there is really hole injection into C_{60}, the application of a hole blocking layer should stop this effect. Samples comprising a BPhen layer with varied thicknesses, however, did not show a clear trend.

11.3.2 Investigation of the thickness dependence of the saturation

In this section the relationship between saturation and fill factor for high *FF* FHJ solar cells is studied under a variation of the donor layer thickness d to investigate whether the characteristic thickness dependence of a shunt resistance is seen. The donor molecule is the diindeno-perylene derivative P4-Ph4-DIP (2,3,10,11-tetrapropyl-1,4,9,12-tetraphenyl-diindeno[1,2,3-cd:1',2',3'-lm]perylene) which is similar to the Ph4-Ph4-DIP (cf. Fig. 3.26, p. 85). Figure 11.6 shows that only the two phenyl groups at each end of the molecule are replaced by two propyl groups. The complete solar cell stack is of n-i-p type and reads ITO/C_{60}:NDN1(5, 2 wt%)/C_{60}(25)/P4-Ph4-DIP(d)/BPAPF:NDP9(40, 20 wt%)/
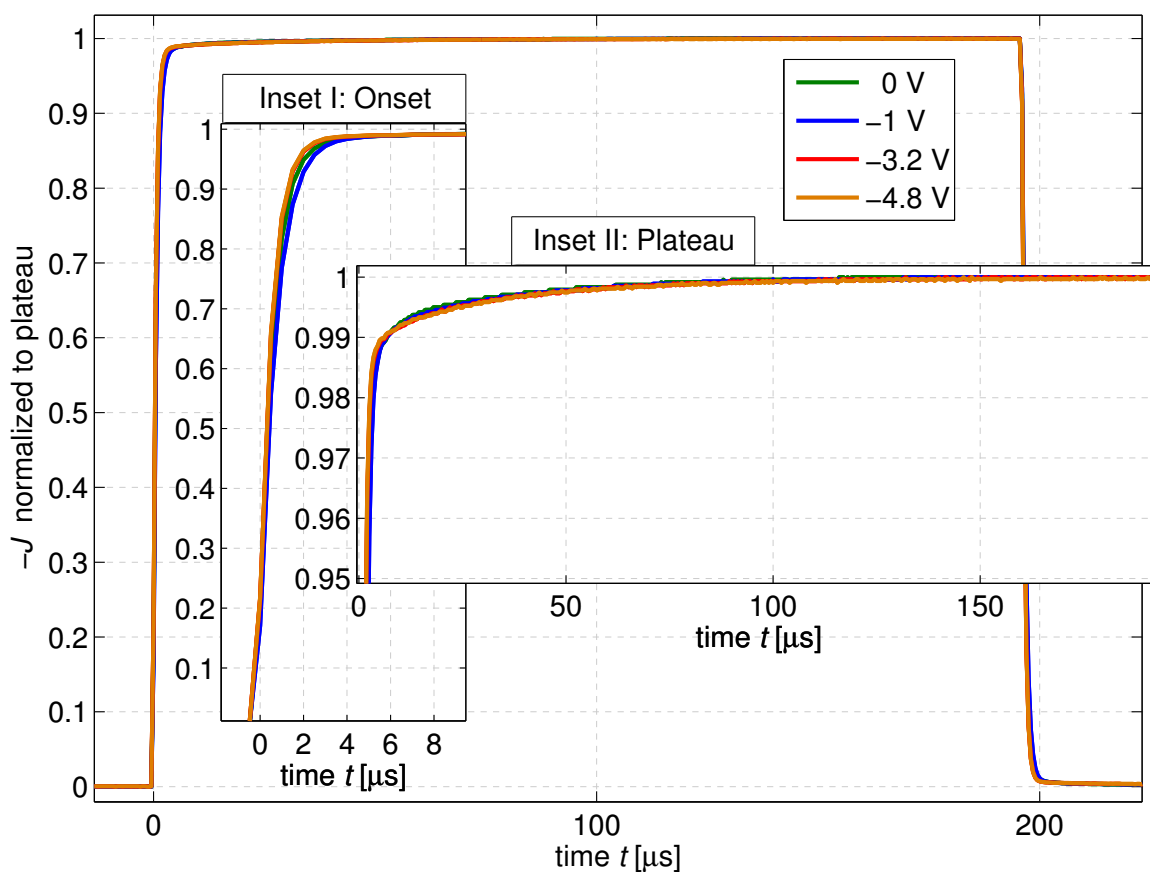
Figure 11.4: Transient photocurrent response of a ZnPc:C_{60} bulk heterojunction sample without additional C_{60} (ITO/NDP2(1)/MeO-TPD:NPD2(20, 2 wt%)/ ZnPc:C_{60}(1:1, 45)/BPhen(6)/Al(100). The length of the illumination pulse is $200\,\mu$s and the intensity of the blue LEDs equivalent to $\approx 1\,$sun. Data under different applied bias voltages are normalized to the steady-state photocurrent. The normalized response is independent of the applied bias. The insets show zooms into two regions: I into the onset (fist $8\,\mu$s) and II into the last $5\,\%$ below the steady-state photocurrent.
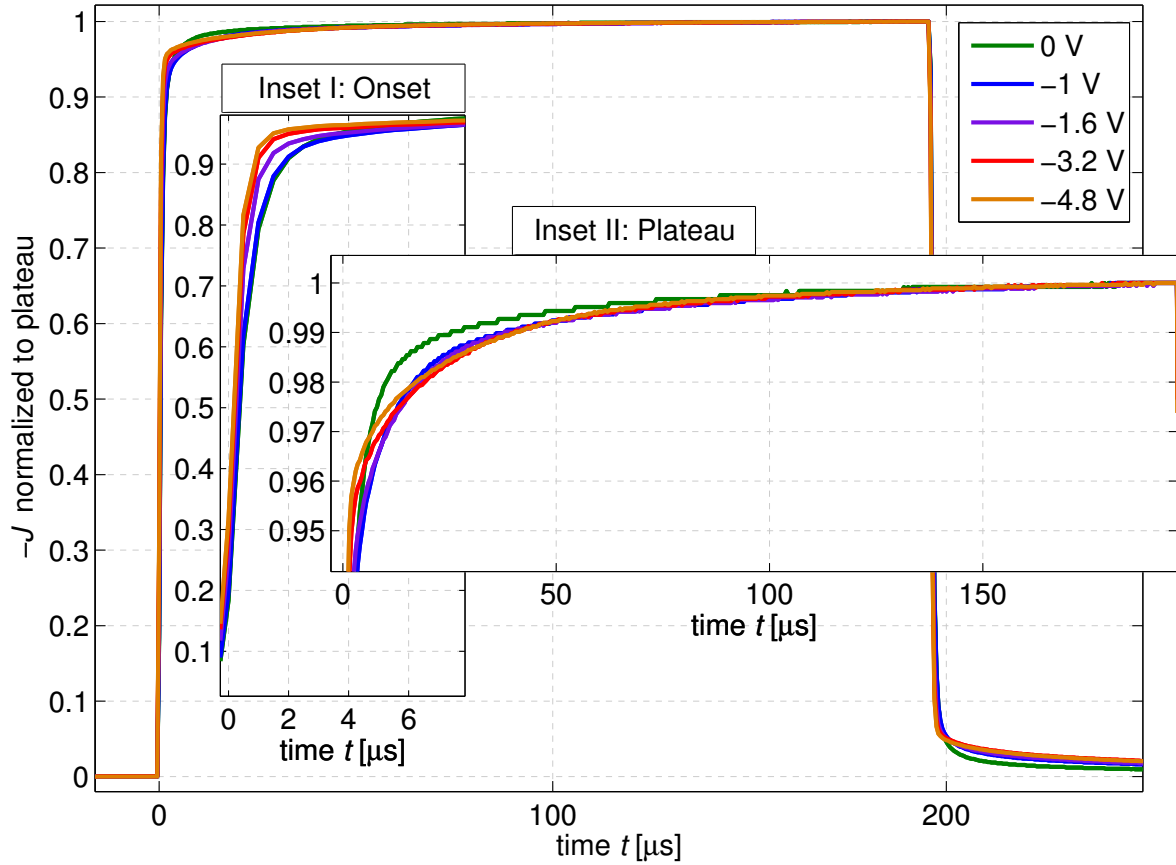
Figure 11.5: Transient photocurrent response of a ZnPc:C_{60} sample with an additional C_{60} layer of 60 nm (ITO/NDP2(1)/MeO-TPD:NPD2(20, 2 wt%)/ ZnPc:C_{60}(1:1, 45)/C_{60}(60)/BPhen(6)/Al(100). The length of the illumination pulse is 200 μs and the intensity of the blue LEDs equivalent to ≈ 1 sun. Data under different applied bias voltages are normalized to the steady-state photocurrent. The insets show zooms into two regions: I into the onset (first 6 μs) and II into the last 5 % below the steady-state photocurrent. The response times in the different regions depend differently on the applied bias indicating an additional contribution of a slow process to current under reverse bias.
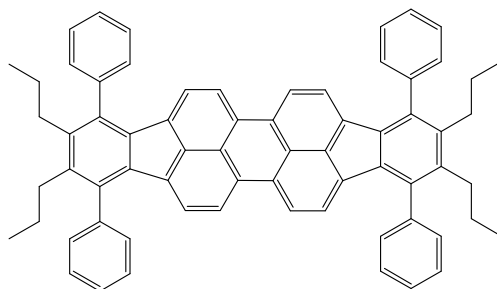
Figure 11.6: Molecular structure of P4-Ph4-DIP which provides a *FF* larger than 75 % in a flat heterojunction with C_{60}.

ZnPc:NDP9(10, 2.5 wt%)/Au(4)/Al(100)[1].

Figure 11.7 shows the evolution of J_{sc}, the *FF*, the ratio between the current at -1 V and J_{sc}, which is called saturation factor, and the photoshunt resistance $R_{sh} \approx {}^{0.5\,V}/_{J(-1\,V)-J(0.5\,V)}$ for donor layer thicknesses between 3 and 69 nm. A saturation factor of 1 means a perfect saturation of the photocurrent whereas higher values indicate a decreased saturation.

In Fig. 11.7 J_{sc} follows basically the generation profile and is limited by the thickness of the donor and its exciton diffusion length [78]. The dashed line shows simulation data. It is calculated by solving the exciton diffusion equation (Eq. 4.22) with the exciton generation profile obtained by an optical simulation of the stack. The derived exciton diffusion lengths are 20 nm for C_{60} and 10 nm for P4-Ph4-DIP.

The *FF* increases to 76 % with thickness before it decreases again to below 60 % at 69 nm. The decrease for higher thicknesses (> 10 nm) is the expected case as the field in the active layers and at the D/A heterointerface decreases with thickness. This results in a lower charge carrier extraction probability at a certain applied bias, because either (CT-) exciton dissociation efficiency or free charge carrier transport properties are reduced. The increase for thicknesses smaller than 9 nm is probably due to a non-closed layer leading to partial shunts.

If the saturation is limited by the same processes as the *FF*, the trend of the saturation factor should follow the trend of the *FF*. This means a lower value of the *FF* should result in a lower saturation of the photocurrent also in the region between -1 and 0 V. Thus, the saturation factor should increase with a lower *FF*. However, it decreases with DIP thickness and saturates at around 24 nm. Therefore, a clear statement cannot be derived from the saturation factor.

Figure 11.7 shows also R_{Sh}, which describes the reverse slope of the *J-V* curve between -0.5 and -1 V. The dash-dotted line indicates that R_{Sh} is growing linearly with the thickness. Such a behavior is expected at the presence of a shunt resistance, given by the active layers of the device. $R_{Sh}(0)$ is then the resistivity of the other layers (C_{60}).

In conclusion, this analysis is an indication that the increase in reverse current is not

---

[1]Designed and characterized by Jan Meiss, IAPP.
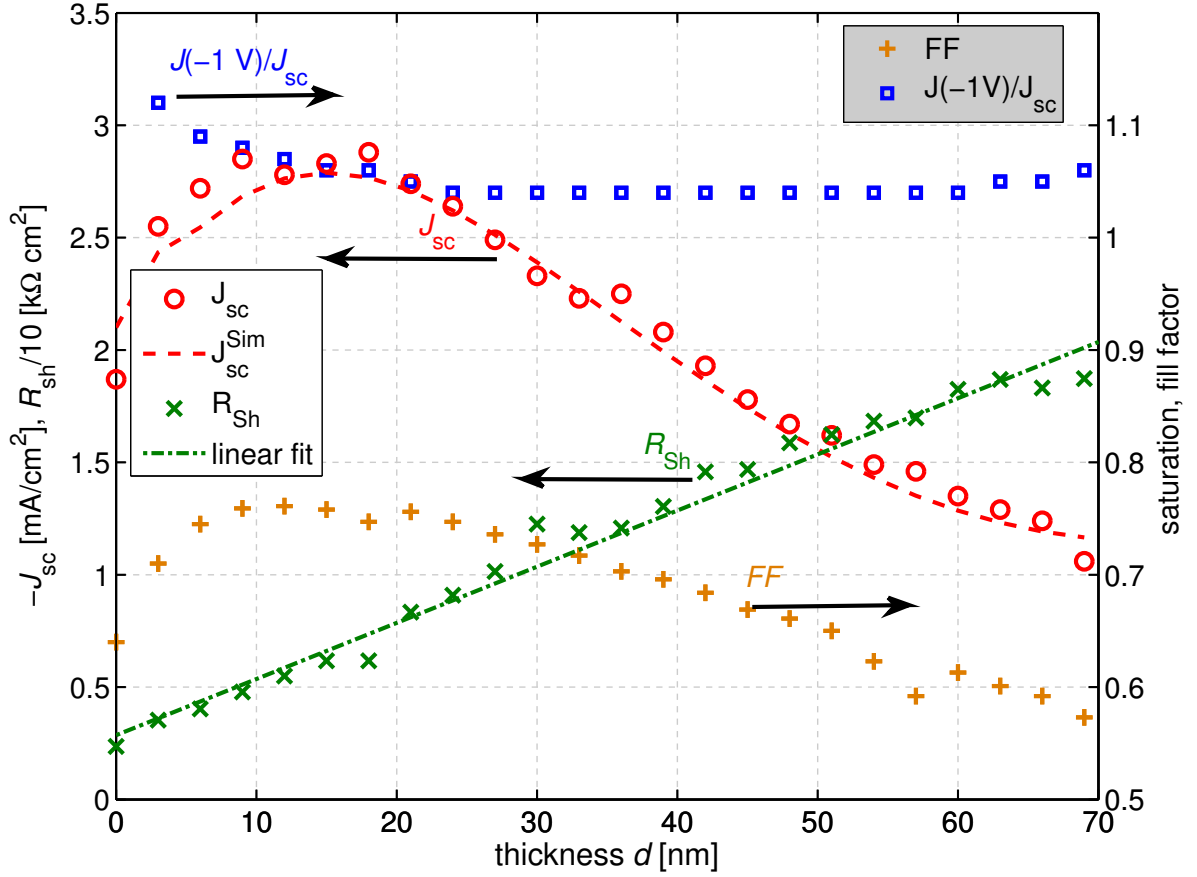
Figure 11.7: Short-circuit current density J_{sc}, FF, $J(-1V)/J_{\mathrm{sc}}$, and the shunt resistance $R_{\mathrm{sh}} \approx {}^{0.5\,\mathrm{V}}/_{J(-1\,\mathrm{V})-J(0.5\,\mathrm{V})}$ for devices ITO/C$_{60}$:NDN1(5, 2 wt%)/ C$_{60}$(25)/P4-Ph4-DIP(d)/BPAPF:NDP9(40, 20 wt%)/ZnPc:NDP9(10, 2.5 wt%)/Au(4)/Al(100). The dashed line is a simulation of J_{sc} under the assumption of a saturated photocurrent at J_{sc} and an exciton diffusion length of 20 nm in C$_{60}$ and 10 nm in P4-Ph4-DIP [78]. The shunt scales linearly with thickness.

caused by a field dependent charge collection but by an additional resistive current.

11.3.3 Photoshunt in flat heterojunction ZnPc/C$_{60}$ solar cells

The unambiguous proof for the photoshunt theory would be an EQE larger than 1 for high negative bias voltages. An EQE larger than the absorptance is also sufficient, because it means an IQE larger than 1. A measurement of this case is challenging, because usually, break-through occurs for larger negative bias voltages. Additionally, parasitic absorption decreases the probability of finding an IQE larger than 1.

Here, ZnPc/C$_{60}$ FHJ solar cells with varied donor and acceptor layer thicknesses are in-
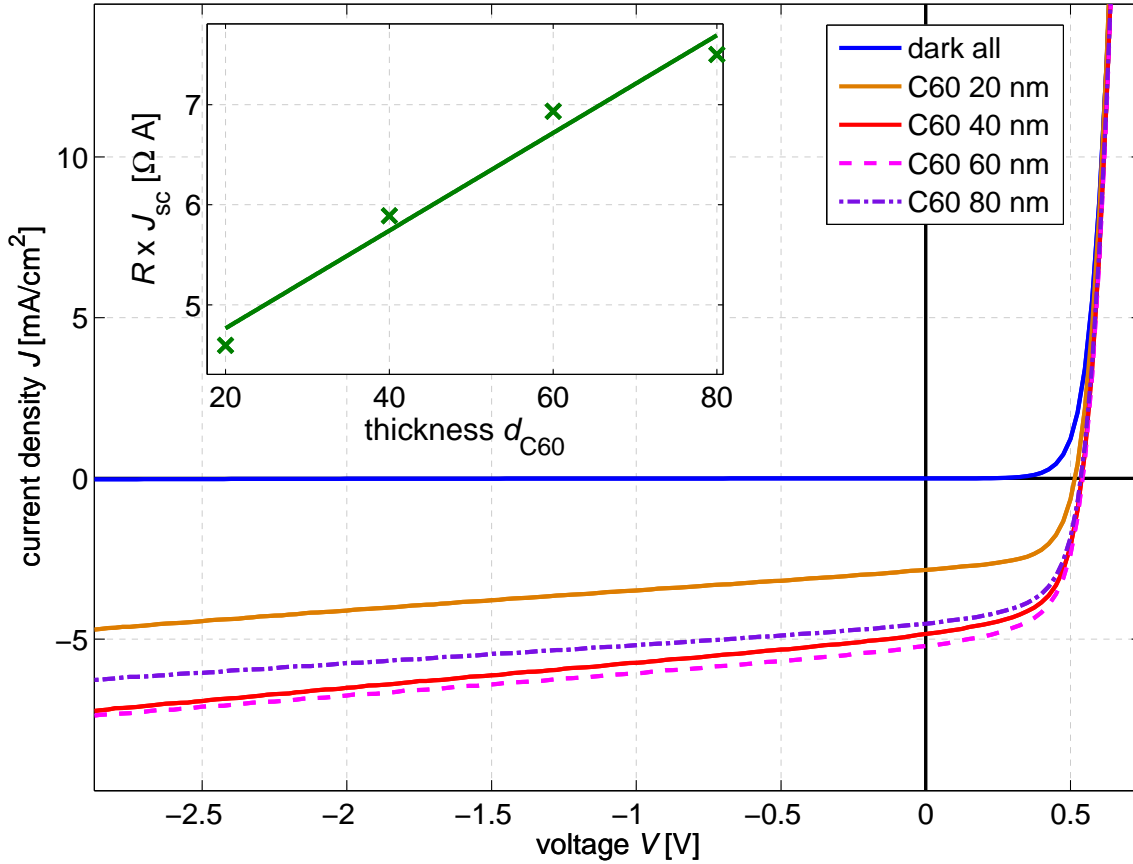
Figure 11.8: *J-V* curves of devices ITO/NDP2(1)/MeO-TPD:NPD2(20, 2 wt%)/ ZnPc(50)/C$_{60}$(*x*)/BPhen(6)/Al(100). A strong photoshunt behavior is visible which reduces the *FF* and becomes weaker with C$_{60}$ thickness. The inset shows the thickness dependence of the shunt resistance multiplied by *J*$_{sc}$. The correction by *J*$_{sc}$ is done as a very rough approximation for the photogenerated charge carriers in the layers.

vestigated. Figure 11.8 shows the *J-V* curves of devices with 50 nm ZnPc. The dark curves coincide and do not show any significant current in reverse direction. The saturation in case of illumination improves with C$_{60}$ layer thickness for samples with 40, 60, and 80 nm thick C$_{60}$ layers where the absorption in C$_{60}$ is comparable. This thickness dependence suggests that photocurrent depends more strongly on the applied voltage for thinner samples. This cannot be explained by photocurrent which is limited by the electric field, as the electric field is larger for thinner layers. However, the linear *J-V* characteristics fit into the photoshunt theory like the results of the previous section. The inset of Fig. 11.8 shows the shunt resistance, which is obtained by fitting the linear region, multiplied with *J*$_{sc}$ plotted as a a function of C$_{60}$ thickness. The correction by *J*$_{sc}$ is done to account for the different absorption dependent on layer thickness. This correction is very rough as it
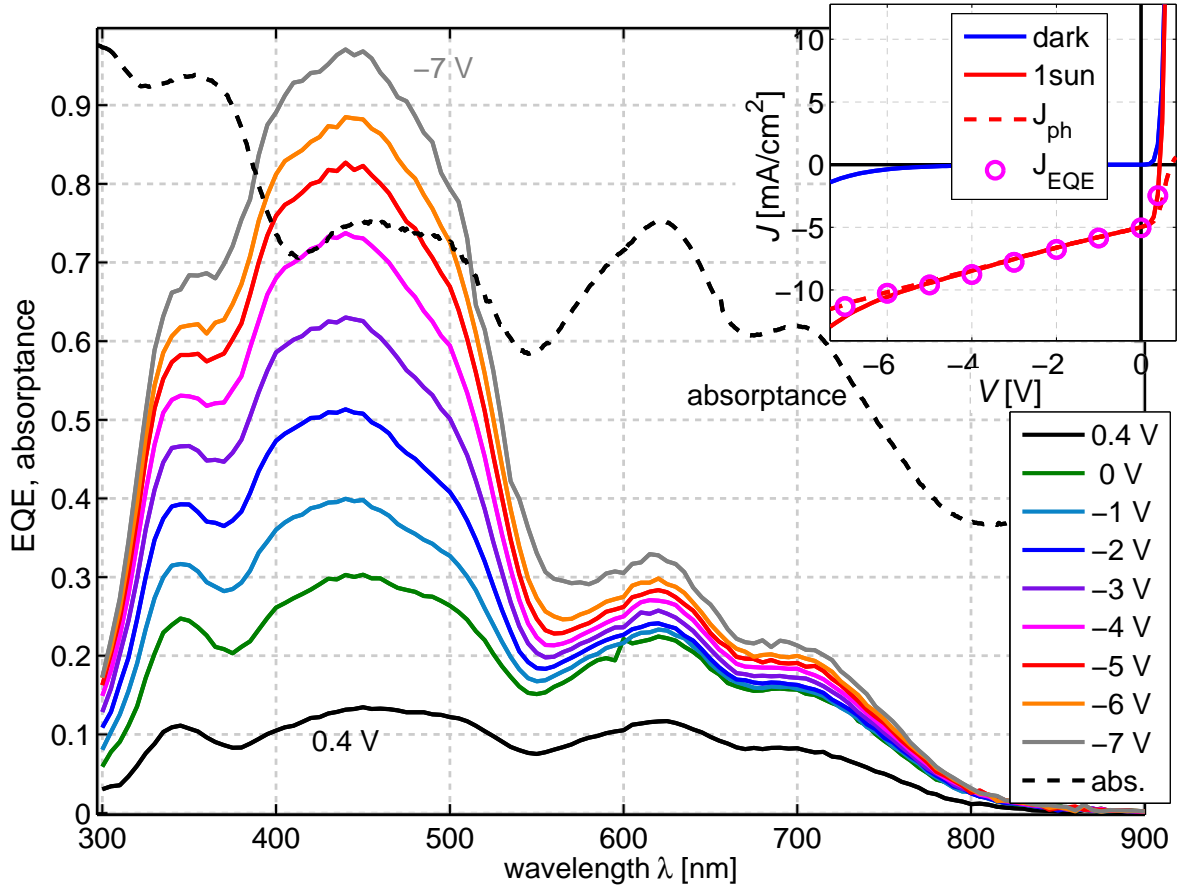
Figure 11.9: Voltage-dependent external quantum efficiency data of the sample …/ZnPc(15)/C$_{60}$(60)/… They exceed the absorption (dashed) for high negative bias voltages ($< -5\,\text{V}$). The inset shows the *J-V* curves, the photocurrent, and the current calculated from the EQE spectrum.

assumes that the photoconductivity caused by the absorption in C$_{60}$ simply scales with J_{sc} ignoring any generation profile. However, the inset and the *J-V* curves unambiguously show that the shunt resistance increases with thickness. Figure 11.8 also shows that the linear *J-V* characteristics are present in the fourth quadrant as well, limiting the *FF* of the solar cells. Therefore, photoconductivity is a relevant loss mechanism, decreasing the efficiency. That is why the term "shunt" is very appropriate for this effect.

The *J-V* curves show that determining the exciton diffusion length of the FHJ cells is not possible from these data alone, because no saturated photocurrent can be measured. Taking J_{sc} is problematic because this might lead to an underestimation of the photocurrent and exciton diffusion length. This is another reason why the discussion of the photoshunt is very important. It allows to find the correct saturation current by correcting the *J-V* curve for the shunt resistance, as done in the previous chapter. In the case of a ZnPc/C$_{60}$ FHJ, the *J-V* curve is, as previously mentioned, already linear around J_{sc}. Thus, the

saturation current is close to J_{sc}. Exciton diffusion lengths obtained from simulations of devices with different ZnPc and C_{60} layer thicknesses are in the range of 7 nm (ZnPc) and 25 nm (C_{60}).

As final point, voltage-dependent EQE data of a sample containing a ZnPc(15)/C_{60}(60) FHJ are displayed in Fig. 11.9. Samples with other layer thicknesses show a similar behavior. It can be seen that the EQE increases with negative bias. The relative change over the total spectrum is in the same range when comparing the EQE at 0.4 and 0 V. However, there is a significant difference for the spectral response at higher negative bias voltages. The photocurrent from ZnPc (500 to 800 nm, cf. Fig. 3.27) tends to saturate, whereas the signal from C_{60} (450 nm) rises continuously. It exceeds the absorption at voltages lower than -5 V. This means an IQE larger than 1 and is an unambiguous proof for charge carrier injection. The EQE confirms the data of Fig. 11.2, where it was demonstrated that the photoshunt effect is mainly present in illuminated intrinsic C_{60}.

Thus, the presented hypothesis that the illumination supports the injection and transport of holes in the pristine C_{60} layer seems to be valid. Although we were not yet able to demonstrate hole injection and conductivity of C_{60} by OFET measurements, work in literature [337, 338] employs C_{60} as hole injection layer. Also the detailed microscopic explanation of photoinduced hole transport in C_{60} is still lacking. One idea might be that the reverse current, which is very low, may be provided by very few filaments which could be, e.g., grain boundaries or inhomogeneities in the C_{60} layer.

11.4 Summary

The puzzle of the linear reverse current in ZnPc/C_{60} solar cells is not yet completely solved. However, there is strong evidence that this effect is really a parasitic phenomenon that does not result from additional field-dependent photocurrent generation. The rigorous linearity indicates that we observe a resistive behavior, which we called photoshunt. As the main source is illuminated C_{60}, a microscopic picture was presented including hole conductivity of an illuminated C_{60} layer. This layer is supposed to provide a flux of holes through the device. The presented thickness dependence and EQE data larger than the absorption are strong indications for the photoshunt effect. In conclusion, it was demonstrated that the most reasonable approach dealing with the photoshunt effect is to correct the *J-V* curve for this shunt resistance before extracting meaningful properties like exciton diffusion lengths.

Part III

Summary and Outlook

Chapter 12

Main Results

This chapter summarizes all the effects discussed separately and for selected specific material (-system)s in the previous chapters. This summary is arranged as a comparison of J-V curves of a fictive device X with its reference device. Therefore, it represents a very compressed guideline on how to interpret J-V curves of organic solar cells from a drift-diffusion point of view. It contains suggestions of simple experimental methods to distinguish several reasons for detrimental device properties like a low V_{oc}, low FFs by S-shapes, and low photocurrents. A further part gives physically motivated design rules for well-working solar cells based on the experience of the author which results from both simulation and experiment, as the basis of this work were several 100,000 of calculated and a few thousands of experimental J-V curves. The applicability of the models discussed in Chapter 4 to properly describe experimental data is summarized in the last part.

12.1 Interpretation of current-voltage curves

Commonly, a discussion of *J-V* data focuses on an analysis of the main parameters short-circuit current density J_{sc}, open-circuit voltage V_{oc}, and fill factor *FF*. We will see in the following that these parameters are not sufficient for a detailed analysis. Especially, J_{sc} and *FF* are relatively arbitrary values, which do not simply reflect a distinct device property. Only if the photocurrent is already saturated at short circuit, a comparable interpretation of J_{sc} of different solar cells is meaningful.

During the following discussions, we imagine a device X, which contains arbitrary modifications compared to a well-working reference device. This is commonly the approach of experimental work, where either one processing condition or material(-combination) is exchanged and the results are compared to a known reference device. Although we stated that the fingerprints alone are not always meaningful, we arrange the subsequent discussion along these values including additional parameters. Furthermore, suggestions are given for further experimental characterizations to complement the *J-V* data.

Changes in J_{sc} and J_{sat}

A change in J_{sc} itself can have several reasons, as long as the photocurrent is not saturated at this point. That is why additionally the saturated photocurrent J_{sat} should be examined. This requires an extended measurement of the *J-V* curve in reverse direction. If no saturation of the current is observed and the curve shows a linear *J-V* curve, the best approximation for J_{sat} is found by a correction of the *J-V* curve for the photoshunt (Chapter 11). If the blocking behavior of the diode is not sufficient, the dark current should be subtracted before doing a correction of the photcurrent by a possibly existent photoshunt.

A change in the saturated photocurrent of device X compared to the reference device results from a changed maximum charge carrier generation rate and can be due to the following reasons:

- A changed absorption (η_{PA}), which can be directly identified by doing absorption measurements of the solar cell. Reasons might be another absorber, changed crystallinity of the absorber, changed layer thicknesses, or a changed stack design, giving a different optical field distribution.

- A changed exciton-diffusion efficiency (η_{ED}), caused by a material or a modified morphology/crystallinity with changed exciton diffusion length, a changed layer thickness, or a changed stack design, giving another optical field distribution (FHJ). In a BHJ a changed phase separation and thus grain size may lead to this effect. This effect can be distinguished from the previous one (η_{PA}) by comparing absorption and EQE measurements at a bias voltage where the photocurrent is saturated. A changed η_{ED} is then seen in a changed IQE. A higher radiative singlet emission of the absorber in a photoluminescence measurement is also an indication for a low η_{ED}.

- Introduction of an (additional) exciton quenching interface or species. This effect can only be distinguished from the previous case by an examination of J_{sat} as a function of layer thickness and a comparison with exciton diffusion modeling data.

All these effects have in common that they do not depend on voltage. Thus, if clearly present, they result in a vertical shift of the *J-V* curve in first approximation.

Changes in V_{oc}

V_{oc} is a very important and meaningful parameter together with J_{sat}. Although it is the point where no current flows, the microscopic conditions within the device at this point are not a priori defined. This was discussed in the context of contact properties (Chapters 5 and 6). The main result is that in the case of selective contacts, all photogenerated charge carriers recombine at V_{oc}, whereas in the case of non-selective contacts, there may be a significant diffusion of (minority) charges to the "wrong" contact. The latter is a potential loss mechanism for V_{oc} (cf. Chapter 9). The most important factors which cause a change in V_{oc} of device X are summarized in the following:

- A changed generation rate due to reasons discussed in the previous section. A higher generation rate leads to a higher charge carrier density in the device and thus a higher V_{oc}. The change in V_{oc} is then accompanied by a change in J_{sat} (J_{sc}). Thus, this effect simply reflects the dependence of V_{oc} on illumination intensity. For changes of J_{sat} by, e.g., a factor of 2, some tens of mV changes in V_{oc} are expected (cf. first and last row of Tab. 10.1, p. 256).

- A changed effective donor-acceptor gap (E_g^{DA}) due to another donor (acceptor) material with another IP (EA). A change in E_g^{DA} can also result from changed polarization energies due to a modified surrounding or crystallinity of a molecular film. Consequently, a change in V_{oc} can originate from different mixing ratios of a donor-acceptor blend (Chapter 8). One approach to identify a changed E_g^{DA} is a characterization of the blend by UPS (IPES). Another option would be the investigation of the energy of the CT state, which, if present, replaces the effective gap (Ch. 5.2.3). This can be done by sensitive absorption, EQE, and electroluminescence measurements.

- Changed recombination dynamics at the heterointerface. A higher recombination decreases the amount of charge carriers for a certain generation rate and thus the quasi-Fermi level splitting and V_{oc} (Ch. 5.2.3). It may result from impurities, acting as recombination centers, or a modified recombination cross section or wave-function overlap between orbitals at a heterojunction. A modified recombination results in a changed lifetime of charge carriers which can be detected, e.g., by transient photo-voltage measurements (Ch. 10.3.3).

- Changed contact properties (η_{CC}). As long as there is no recombination at the interface between active and adjacent transport materials, the work function and thus the built-in potential do not modify V_{oc} (Chapter 5). In this case also the doping concentration and IP/EA of doped charge transport layers are irrelevant for V_{oc}. V_{oc} can only be reduced by additional recombination. This recombination can result from contacts if they are non-selective. In this case, energetically misaligned contacts forming injection barriers reduce V_{oc} of a bulk heterojunction (Chapter 6). The reason is a decreased built-in field, increasing extraction/recombination of charge carriers at the "wrong" electrode.

- Local shunts due to non-closed layers and high surface plane roughness, possibly caused by substrate heating or a highly crystalline material. In this case the blocking behavior of the diode and thus the saturation should be affected as well.

Emergence of a low saturation in reverse

Low saturation means a strong dependence of current on applied negative bias. Here, one has to distinguish between dark and photocurrent. If the dark current is affected as well, the following suggestions are valid:

- Shunting. This gives a linear *J-V* curve and is most likely due to some local shunts originating from processing errors or local inhomogeneities within the layers.

- Break-through. This can be seen at a reverse current showing an exponential dependence on voltage. This effect is observed at high negative bias voltages for all solar cells and accompanied by a shift towards 0 V for thin donor and/or acceptor layers (cf. Ch. 13.2).

- Poor rectification behavior due to a lack of selectivity of the device structure, which can be caused by non-selective contacts and a low built-in potential.

If only the photocurrent of device *X* is affected by a low saturation, other effects may play an important role:

- An increased photoshunt effect. It can be deduced from a linear *J-V* curve in reverse and, in the extreme case, by IQEs larger than unity for negative bias voltages (Chapter 11). It is more pronounced for thinner and intrinsic donor and/or acceptor layers, especially for C_{60}. The microscopic reasons are not yet completely understood.

- The presence of an exciton dissociation process (η_{CD}) which depends on the electric field. Such a process is difficult to identify at the *J-V* curve alone, but should result in a final saturation of photocurrent at reverse bias. It should also show a significant characteristic temperature dependence (Eq. 4.50). Furthermore, the voltage-dependence of the photocurrent should be more pronounced with increased layer thicknesses.

If the trend in saturation follows the trend in *FF*, the content of the following section may be relevant for the saturation as well.

Changes in *FF*

The *FF* reflects the dependence of current under illumination on voltage in the fourth quadrant. Thus, it is related to electrical processes only. A change of *FF* of our device *X* can be caused by the following modifications:

- Changed charge carrier mobilities. Higher charge carrier mobilities increase the probability of charge carrier collection at a certain applied voltage. This results directly in a higher *FF* (cf. Chapter 5). Reasons for a change in mobilities can originate from another blend morphology/crystallinity due to some treatment/annealing/heating during fabrication or when doing post-treatment. Increased mobilities should also affect the forward current as long as the forward current is not limited by a macroscopic (electrode-)series resistance. Consequently, a decrease of forward current and a lower *FF* indicate reduced charge carrier mobilities. In the case of imbalanced mobilities in a BHJ, the forward current can be driven by one charge carrier alone. If the mobility of the slower charge carrier was changed, this would only affect the *FF* and not the forward current.

- Increased recombination. As discussed in Chapter 5, the mobility (i.e. charge extraction) has to be seen in comparison to recombination. An increased recombination probability decreases the *FF*. In contrast to a change in mobility, V_{oc} is also decreased and the rise of forward current is increased if forward current is recombination limited. Thus, the effect of a change in recombination can be distinguished from mobility effects.

- An increased active layer thickness. If the *FF* is limited by charge extraction or field-dependent exciton dissociation, a higher thickness leads to higher recombination losses and therefore a lower *FF*.

- A changed optical generation profile in a bulk heterojunction, especially in case of imbalanced mobilities. Due to an inversion of the solar cell stack or the change of the thickness of the spacer layer(s), the locus of maximum charge carrier generation may be shifted in the blend. This can result in significant changes in *FF* (Tab. 10.1 in Ch. 10.2, p. 256).

- A changed exciton-dissociation probability which was already discussed in the section on low saturation.

- A changed overall absorption. As the *FF* depends also on light intensity (cf. Fig. 10.16, p. 271 in Chapter 10), it is affected by a changed overall absorption which can be identified by changes in J_{sat} (J_{sc}).

- Changes in macroscopic parallel or series resistances seen in the dark curve as well [cf. Fig. 3.18(b), p. 72].

Furthermore, the *FF* can be strongly affected by the presence of an S-kink which is discussed in the following.

Emergence of an S-kink

An S-kink is characterized by two inflection points in the *J-V* curve, the first at negative currents and the second commonly around V_{oc}. Possible reasons for S-kinks are:

- Insufficient charge carrier extraction due to energetic extraction barriers at the contacts or insufficient charge transport in charge transport layers (Ch. 6.3.2). Reasons for the first are misaligned charge transport levels (EA, IP) between active material and charge transport layers/ metal electrodes. Charge transport layers with very low conductivity are responsible for the second effect.

- Diffusion-driven charge carrier extraction against the electric field due to injection barriers decreasing the built-in potential. Selective contacts or a flat heterojunction are essential to establish the required diffusion gradient (Ch. 6.3.1).

- Largely imbalanced mobilities in flat heterojunctions (Chapter 7).

There are several approaches to identify the origin of an S-kink. Each of the three reasons shows another dependence on layer thicknesses and temperature (Ch. 6.5.2, Ch. 6.5.3). Transient photocurrent measurements give a distinct result for each origin (Ch. 6.5.4). Extraction barriers can be identified by overshoots in the transient photocurrent signal showing a pile-up of charge carriers, whereas devices containing a low-mobility material show a slow response. The impact of extraction barriers can be reduced by increasing the doping concentration in the charge transport layer. This results in a high field at the extraction barrier, which increases the charge-carrier-extraction probability (cf. Figs. 8.3 and 8.4, p. 229 in Chapter 8).

12.2 Stack design

The variety of samples prepared and the simulations conducted during this work allow to draw some conclusions concerning an optimum stack design. Especially, the role of intrinsic interlayers between the active layer and the doped charge transport layers is discussed.

Blend layer position and thickness in p-i-n (ZnPc:C$_{60}$) solar cells

All highly efficient organic solar cells comprise a BHJ instead of a FHJ. However, the *FF* of these BHJ is limited by charge extraction. As the current increases with layer thickness due to a higher overall absorption, an optimum layer thickness exists. For ZnPc:C$_{60}$ (1:1 or 1:2), deposited at room temperature, this thickness is in the range of $40\ldots50$ nm. An optimum positioning of the blend concerning the optical field maximum is achieved by a $30\ldots40$ nm intrinsic C$_{60}$ layer in a p-i-n geometry. It is not essential, whether a $6\ldots10$ nm thick n-doped C$_{60}$ or BPhen layer is used as contact layer to the Al electrode. Substrate heating was not studied during this work. However, it increases the efficiency of thicker ZnPc:C$_{60}$ (60 nm) solar cells only slightly (10 %) [209]. A gradient of donor and acceptor does not remarkably increase the efficiency as long as the stack is optimized (Chapter 9). The generation profile within the blend influences the *FF* in the case of imbalanced mobilities (higher C$_{60}$ concentration). Thus, not only an optimization concerning the overall absorption, but also the position of the absorption maximum within the blend can be done. This effect is comparably weak, although it can modify the *FF* by approximately 10 % (Ch. 11.3.1).

Hybrid FHJ/BHJ

In theory, a hybrid FHJ/BHJ is the optimum architecture as long as the nano-morphology of the blend cannot be controlled to create comb-like structures. Absorption in the adjacent intrinsic donor and acceptor layers is supposed to deliver excitons which can be separated at the interface to the blend. This positive effect is observed for an additional C$_{60}$ layer which contributes to photocurrent. However, an additional ZnPc layer does not significantly increase the photocurrent. The reason is not completely understood. The low exciton diffusion length in ZnPc may add to this effect.

In the case of blend layers with a V_{oc} larger than $0.55\,V$, the additional intrinsic ZnPc layer can even be detrimental, because it reduces V_{oc}. Such values of $V_{oc} > 0.55\,V$ are observed for solar cells with ZnPc:C_{60} mixing ratios smaller than 1:1. The proposed reason is that the IP of intrinsic (crystalline) ZnPc is smaller than the one of ZnPc in these blends. Thus, the interface ZnPc/blend exhibits an injection barrier which reduces V_{oc} due to an increased recombination at this interface (Ch. 9.2.3). This means that a change in charge transport levels upon blending has to be considered when fabricating hybrid FHJ/BHJ solar cells.

Intrinsic interlayers of HTL

According to the p-i-n concept the blend is sandwiched between doped charge transport layers. The question arises whether an intrinsic HTL interlayer between doped HTL and blend can change the efficiency. The possible purpose of such a layer is to keep dopants away from the blend, as dopants act as exciton quenching centers. Additionally, dopants diffused into the blend are suspected to decrease the long-term stability of the device and the blocking behavior. However, the volatility of molecular dopants seems to be very low and the observed penetration is in the range of the layer roughnesses. If the dopants act as recombination centers for charge carriers, V_{oc} is affected as well. This additional recombination can explain the lower values of V_{oc} ($\approx 10\,mV$ in Tab. 9.1) and lower photocurrents without intrinsic MeO-TPD as interlayer. The effect seems to be more pronounced for F_4ZnPc devices which can show a difference in V_{oc} of $50\,mV$ between a device with and without an intrinsic Di-NPD interlayer (data not shown).

However, an intrinsic hole transport interlayer can also reduce the efficiency because the amorphous HTL with its low hole mobility causes a significant series resistance which reduces the *FF*. Additionally, the intrinsic layer may cause an S-kink or at least reduce the *FF* in the case of a not completely adjusted hole transport level to the hole transport level of the blend (Ch. 8.3). As a slightly deeper lying HOMO of the HTL guarantees the optimum V_{oc}, an intrinsic HTL may be avoided in most cases.

Best ZnPc:C_{60} stack of this work

During this work, a variety of ZnPc:C_{60} solar cells have been produced, mainly with the focus on showing limiting effects rather than optimizing the efficiency. Nevertheless, some highly efficient ZnPc:C_{60} solar cells were fabricated as well. They do not contain any intrinsic interlayer at the p-side. The best stack on an unheated substrate reads ITO/p-MeO-TPD(25)/ZnPc:C_{60}(1:1, 45)/C_{60}(30)/BPhen(6)/Al(100), where MeO-TPD can be replaced by other doped HTLs like Di-NPD. It gives an efficiency of $3.2\,\%$ measured under an illumination of $1\,sun$ in an outdoor test (Chapter 9).

12.3 Main conclusions on the applicability of the developed drift-diffusion simulation to organic solar cells

This thesis dealt with systematic experimental investigations of small-molecule organic solar cells accompanied by the development and application of a drift-diffusion device model. Based on this approach, it is summarized here to what extent a drift-diffusion simulation is capable of describing organic solar cells. The discussion in the first part of this thesis showed that such an approach to a disordered organic solid characterized by hopping transport is questionable. However, it can be theoretically justified, as long as the device thickness is much smaller than average hopping distances.

The elaborated qualitative comparison to experimental data verified that this kind of simulation is capable of describing several observed effects. It is even concluded that this kind of simulation is currently the most suitable approach to describe complex shapes of J-V curves of multilayer solar cells, as it provides a set of J-V curves within a moderate computational time. The correct quantitative description of the J-V characteristics' dependence on layer thicknesses and illumination intensities is another indication for the applicability of this kind of simulation. The simulation developed during this work is also capable of reproducing transient data. Furthermore, calculated distributions of charge carrier densities and field profiles within devices provided explanations for several observed features.

In detail, the following effects were investigated in simulation and experiment:

- Injection and extraction barriers which can cause S-kinks (Chapters 6 and 8).

- Imbalanced mobilities of a FHJ as an additional source of S-kinks (Chapter 7).

- A gradient of donor and acceptor material in the ZnPc:C$_{60}$ BHJ which reduces surface recombination (Chapter 9).

- The effect of the generation profile within a ZnPc:C$_{60}$ BHJ on FF in combination with (im)balanced mobilities (Chapter 10).

- The influence of trap-assisted and direct recombination in ZnPc:C$_{60}$ BHJ investigated by determining the dependence of V_{oc} on the illumination intensity (Chapter 10).

Considering the validity of the models which have been implemented in simulation (cf. Ch. 4.4), one can summarize:

- Onsager-Braun theory could not be identified as process dominating photocurrent generation in the investigated ZnPc:C$_{60}$ devices, although geminate recombination cannot be excluded completely.

- The Langevin expression for recombination does not seem to be applicable to ZnPc:C$_{60}$ solar cells with different mixing ratios. The recombination constant is mainly independent of the mobility. Therefore, recombination is not diffusion-limited, but by the recombination process itself. A possible reason may be a large lifetime of the charge-transfer state which is formed as an intermediate state during the recombination process.

- Direct and trap-assisted recombination are found to be important. For high light intensities, direct (bimolecular) recombination limits the performance whereas trap-assisted recombination governs V_{oc} at low intensities and the slope of J-V curves in the dark (cf. Chapter 10).

- Sophisticated mobility models including the nature of disorder were not intensively applied as their applicability is not yet proven. Furthermore, they introduce unknown parameters and are less relevant in the working regime of a solar cell (fourth quadrant), which is characterized by low electric fields and moderate charge carrier densities. As long as fundamental issues like recombination are not resolved, charge transport remains the second step of a refinement of solar-cell simulations.

Although the capability of the presented one-dimensional drift-diffusion approach could be demonstrated at a variety of experimental data, there are clear limitations concerning the physical depth of the models. One major limit is the one-dimensionality, which allows a representation of the nano-morphology of mixed layers only in effective parameters like mobilities. This might not be sufficient for a description of the correlation of morphology and the J-V curve. Three dimensional drift-diffusion approaches can better deal with this issue, although charge carrier transport through a nano-morphology might be preferably described by hopping models demanding for Monte-Carlo simulations.

In summary, this work focused on the understanding of fundamental processes and properties of organic solar cells. For this, a reproduction of trends in the electric characteristics and their correct order of magnitude is sufficient. Quantitative descriptions of J-V series are difficult due to the high level of abstraction or due to many unknown parameters of complicated transport and charge carrier generation models. However, it was shown in Ch. 10.4 that the J-V curves of ZnPc:C$_{60}$ solar cells with different mixing ratios and different generation profiles were also quantitatively reproduced. Additionally, the dependence on light intensity and the dark J-V curves could be modeled with the same parameters. The main challenge in modeling organics is to find appropriate models and the required amount of parameters to describe the variety of organic materials well. Predictive simulations will remain very challenging because finding a common parameter set which can be applied to a large amount of different organic molecules is very hard, as electronic processes in a film strongly depend on the configuration and interaction between single adjacent molecules.

In conclusion, drift-diffusion simulations are very valuable to understand physical processes on the device level. This was demonstrated by this work where the interplay between

experiment and simulation lead to both a reproduction of experimental data by the model and a verification of simulation data by tailored experiments.

Chapter 13

Further Analyses and Possible Extensions of the Simulation

In this chapter possible extensions of the simulation are sketched and first results presented which show the feasibility of including additional processes into the simulation. The first section deals with the alternating-current (AC) response of a solar cell, which is simulated in time-domain. The second section presents first results and ideas concerning the electrical modeling of reverse currents and tandem solar cells, where the properties of the recombination contact are highlighted. The chapter concludes with suggestions for further simulation studies and accompanying experiments.

13.1 Frequency response

The transient algorithm developed in this thesis is not only capable of providing steady-state and photocurrent transient solutions but also the AC response of a device. It is noted that small-signal simulations are commonly done in the frequency domain [339], which is less time-consuming than in time domain. Nevertheless, the transient algorithm can calculate the current response on a sinusoidal voltage signal of a certain frequency without any modifications of the algorithm. Thus, for each frequency, the transient current response can be monitored, where the amplitude of the AC signal is set to a hundredth of the DC voltage to guarantee the small signal approximation. The magnitude of the complex impedance Z at each frequency is obtained by dividing the AC voltage amplitude by the simulated AC current amplitude. The phase of Z is extracted from the time difference between current and voltage maxima. A phase of 0 means a purely resistive behavior, as the current instantaneously follows the voltage. A phase of $-\pi/2$ represents purely capacitative behavior and values between 0 and $\pi/2$ commonly indicate inductive behavior. With magnitude and phase it is possible to draw a Bode plot as shown in Fig. 13.1 for a BHJ in dark simulated as MIM device at different applied DC bias voltages.

The phase of $-\pi/2$ and the magnitude following $1/f$ show that the device is purely capacitative at $0.1\,\mathrm{V}$ applied bias. The reason is that this voltage is below the onset of the
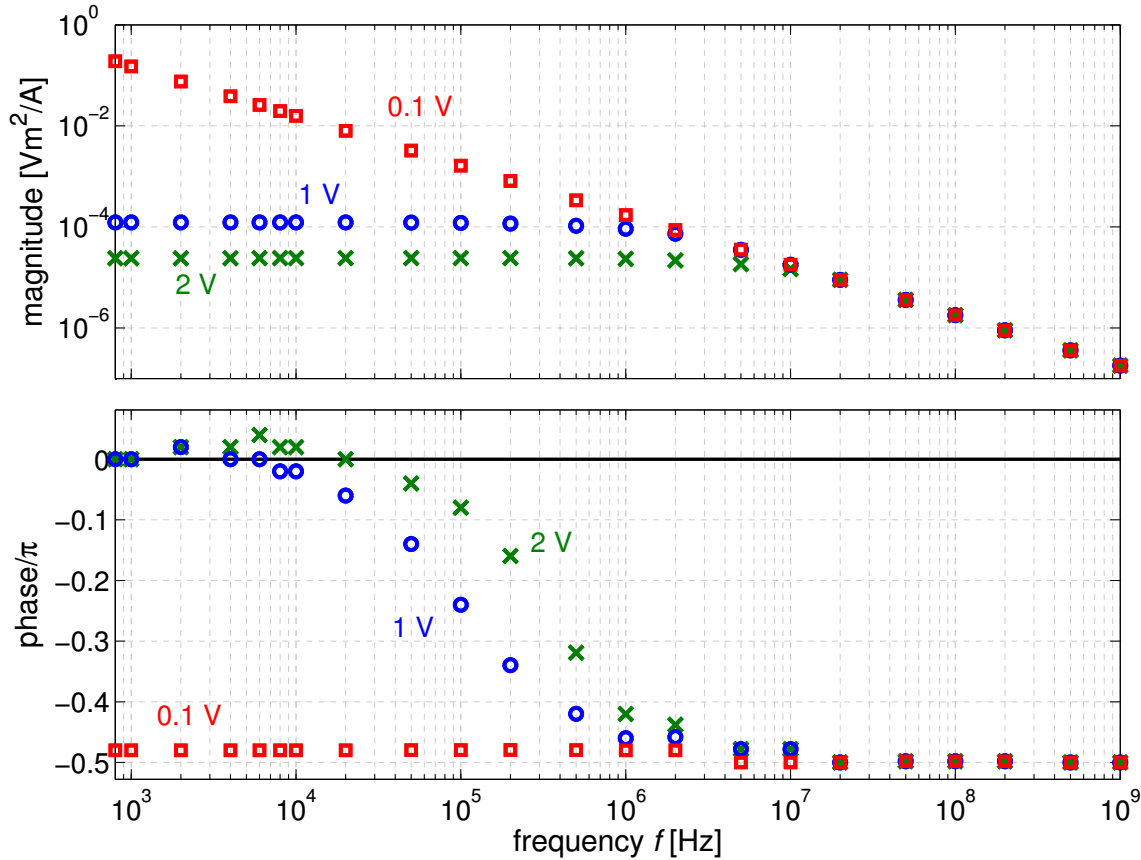
Figure 13.1: Bode plot of magnitude and phase of the impedance of a simulated BHJ as MIM device. The device is purely capacitive for high frequencies. The device shows resistive behavior in forward and for moderate frequencies. At 10^4 Hz a positive phase is seen. Parameters are those of Tab. 5.1 in Chapter 5 and $\mu_n = 10^{-5}\,\mathrm{cm^2/Vs}$, $\mu_p = 10^{-7}\,\mathrm{cm^2/Vs}$, and $\beta = 7.23 \times 10^{-14}\,\mathrm{cm^3/s}$. Details can be found in Appendix B, p. 331.

diode, which means that a charge-carrier current is not possible. In experiment this capacitive behavior will only be observed to a finite frequency from which the series resistance of the electrodes becomes limiting. In forward (1 and 2 V), a resistive behavior can be seen at low frequencies whereas for higher frequencies ($> 10^7$ Hz) the purely capacitive behavior is reached again. The reason is that charge carriers cannot respond to the high frequency due to their low mobility ($10^{-5}\,\mathrm{cm^2/Vs}$). Thus, the geometrical capacitance is observed. In the transition region from resistive to capacitive behavior, the phase shows slightly positive values at 1,000 Hz. These values could be an indication for the negative-capacitance effect, observed in some organic semiconductor devices. This effect is called negative capacitance, because organic semiconductors usually do not show any magnetism and thus no inductance. Several reasons for this effect have been proposed and are under discussion [340, 341].

The simulation data of Fig. 13.1 may be a starting point for describing and explaining this negative capacitance effect in organic diodes with the developed simulation. As preliminary statement, this negative capacitance effect is observed in simulation, if charge carrier recombination, which drives the forward current of the MIM device, is present and located close to one electrode. Furthermore, the charge carrier density of the charge carrier type injected at this electrode has to be sufficiently high to form a space charge and energy-level bending as discussed in Ch. 5.2.6 (Fig. 5.11, p. 163). Such a situation is found in experiment, if both contacts of the MIM device are well-injecting and the mobility is imbalanced, so that the recombination zone is close to the electrode of the less mobile charge carrier. This idea is in agreement with reports in literature [99].

In conclusion, an analysis of the frequency response in simulation allows for a comparison of simulation data with impedance spectroscopy measurement data. Therefore, a comparable investigation, e.g., of trap states on the frequency response and steady-state J-V data of solar cells is possible and can lead to a better understanding of limiting processes in these devices.

13.2 Reverse tunneling currents and tandem cells

Tandem cells are a way of overcoming the Shockley-Queisser limit as described in Ch. 2.7. Furthermore, in the case of organic materials which commonly absorb in a narrow spectral range, not only thermalization losses can be reduced but also the absorbed photon flux can be enhanced. That is why organic tandem cells are attractive and a simulation of such devices is desirable.

The most common layout of a tandem cell is a monolithic stack of the two subcells. Such a configuration shows two major requirements: First, current matching because the same current flows through the two subcells connected in series; Second, an efficient recombination contact between the two subcells to guarantee an iso-energetic recombination of electrons and holes and a high built-in potential for both subcells.

The first issue can be solved by an optical optimization of the stack which can be addressed by optical simulations alone. There, the overall absorbed photon flux of the two subcells is compared and matched by adjusted absorber and spacer thicknesses [342, 343]. Current matching is mostly sufficient for stack optimization. Only subcells which show a low *FF* and thus a high dependence of the photocurrent on voltage close to J_{sc} require further optimization taking into account the whole J-V curve [344, 345].

The second is realized by a thin layer of metal clusters [346] or highly doped charge transport layers forming a p-n tunnel junction [347]. The modeling of such a junction is complicated as it requires a theoretical description of the tunneling mechanism at the recombination contact. This mechanism is essential for modeling forward current of a tandem cell, where the recombination contact operates in reverse direction as charge carrier generation contact.

In the following the idea of modeling the electrics of tandem cells and some preliminary results are presented.
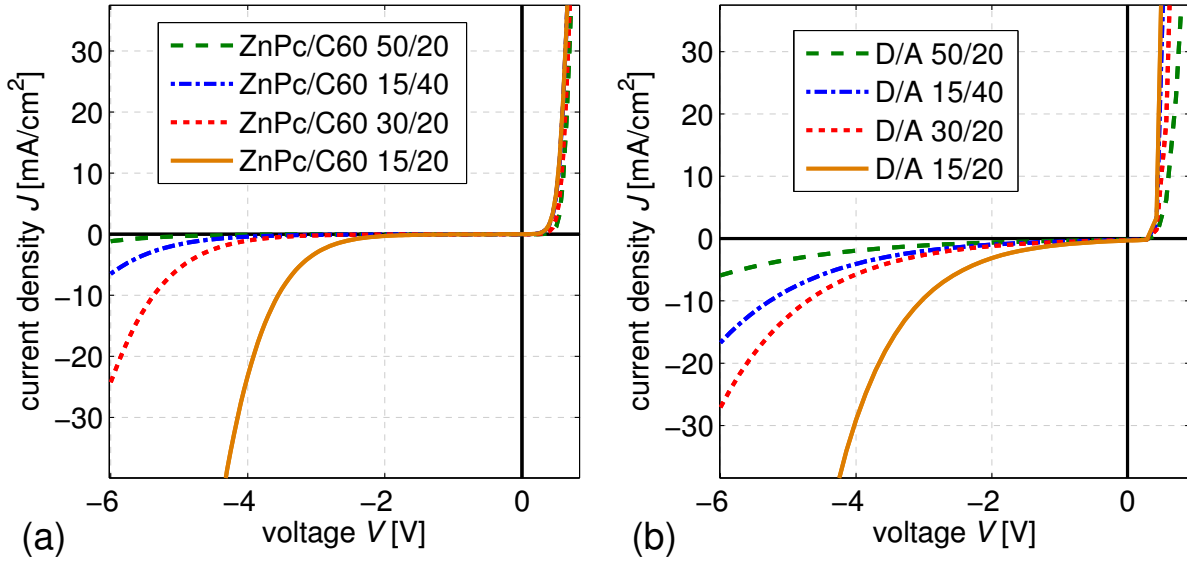
Figure 13.2: The break-through regime of a $ZnPc/C_{60}$ FHJ with different active layer thicknesses in nm. (a) Experimental dark J-V curves and (b) simulations of a bilayer, which show the same trend. Details on the input parameters for the simulation can be found in Appendix B, p. 331.

13.2.1 Reverse current

As proof of principle we do not consider complicated coherent or incoherent tunneling theories, which require effective masses and mostly a description in k-space [42]. We restrict ourselves on a simple description of the "tunneling" process by the introduction of a transition rate of an electron in the HOMO into the LUMO of a neighboring molecule. This approach is oversimplified, however, capable of producing a realistic current at a donor-acceptor interface under high reverse bias. The following equation is applied to describe the transition:

$$\nu_{\text{HOMO–LUMO}} = \nu_0 \exp\left(-\frac{E_{\text{g}}^{\text{DA}} - eFa}{k_{\text{B}}T}\right). \tag{13.1}$$

This equation follows phenomenologically the hopping equation (Eq. 3.2): ν is the hopping rate, ν_0 a pre-factor, F describes the electrical field at the interface and a the average hopping distance, which is set to $1\,\text{nm}$. The overall HOMO-LUMO transition rate is then multiplied by the amount of electrons in the HOMO and the probability of finding a free position in the LUMO.

In the following this approach is applied to the reverse current of a flat heterojunction solar cell (FHJ). The experimental data shown in Fig. 13.2(a) are measured at the devices discussed in Chapter 11. The onset of the break-through of the diodes is mainly defined by the overall thickness of the intrinsic layers. The break-through regime can be

called Zener regime and is exploited in organic Zener diodes [348]. The simulation data in Fig. 13.2(b) reproduces the absolute values of the reverse current and the thickness dependence relatively well. The pre-factor ν_0 in Eq. 13.1 is chosen to $5 \times 10^{19} \, \mathrm{s}^{-1}$. This very large value has to be selected due to the high energy barrier. Allowing for a broadening of the DOS, which reduces the barrier height would lead to a reduction of ν_0. Furthermore, trap-assisted tunneling might play a role, as evidence for trap-assisted recombination was found in Chapter 11. This might be simulated according to the Hurkx model [349, 350]. Although the implementation of Eq. 13.1 does not follow the rigorous principle of detailed balance, the error is acceptable to show an exemplary simulation of a tandem solar cell.

13.2.2 *J-V* curves of tandem cells

Now, we proceed with an exemplary simulation of a tandem solar cell. Figure 13.3 shows simulated *J-V* curves of a p-i-n single-bulk-heterojunction solar cell (BHJ) (10/30/10 nm) and a tandem cell consisting of two identical BHJ with two (doped) layers in between (10/30/10 / 10/30/10). The simulation parameters are chosen according to Tab. 5.1 in Chapter 5 (p. 146). The energy levels of the interlayers are adjusted to block holes from the first BHJ and electrons from the second BHJ to increase the selectivity of the interconnector similar to experimental devices. The energy levels can be deduced from the inset, showing the energy-level diagram of the tandem cell with highly doped interlayers at short circuit.

The simulated *J-V* curves in Fig. 13.3 demonstrate the crucial point of a well-working tandem solar cell, which is a highly efficient recombination contact. Its efficiency is represented in the simulation by the recombination constant β of the interlayers. Also n-doping the first and p-doping the second interlayer helps to shift recombination from the BHJ towards the recombination contact between the two interlayers.

If doping and charge carrier recombination in the interlayers are not sufficient, S-kinks emerge and V_{oc} is reduced. The reason for the S-kink is comparable to an extraction barrier S-kink (cf. Chapter 6), because a non-sufficient recombination at the junction decreases majority charge carrier extraction. The S-kink can also be explained by the injection barrier picture, because no or too low doping of the interlayers does not provide the full built-in potential (V_{bi}) for both subcells. In the case of non-doped transport layers and two identical subcells, V_{bi} over one subcell is half of the one of a single BHJ sandwiched between the doped transport layers.

In addition to the S-kink, V_{oc} is affected by a non-sufficient recombination contact, as it does not show the double value of V_{oc} of the single cell. The reason is a loss in V_{oc} at the recombination contact. If this contact is not efficient, a significant quasi-Fermi level splitting occurs, which reduces V_{oc}. Thus, one can summarize the requirements of the recombination contact by one property: Selective recombination (here electrons from the left side, holes from the right side) which is highly efficient, meaning that additional photogenerated charge carriers do not create a quasi-Fermi level splitting at the junction. Thus, there is no loss of free energy. The distances from E_F to the charge transport levels are irrelevant, which means that it is not necessary to fabricate a degenerate p-n junction. The p-n junction itself is also not urgently required. The best material to
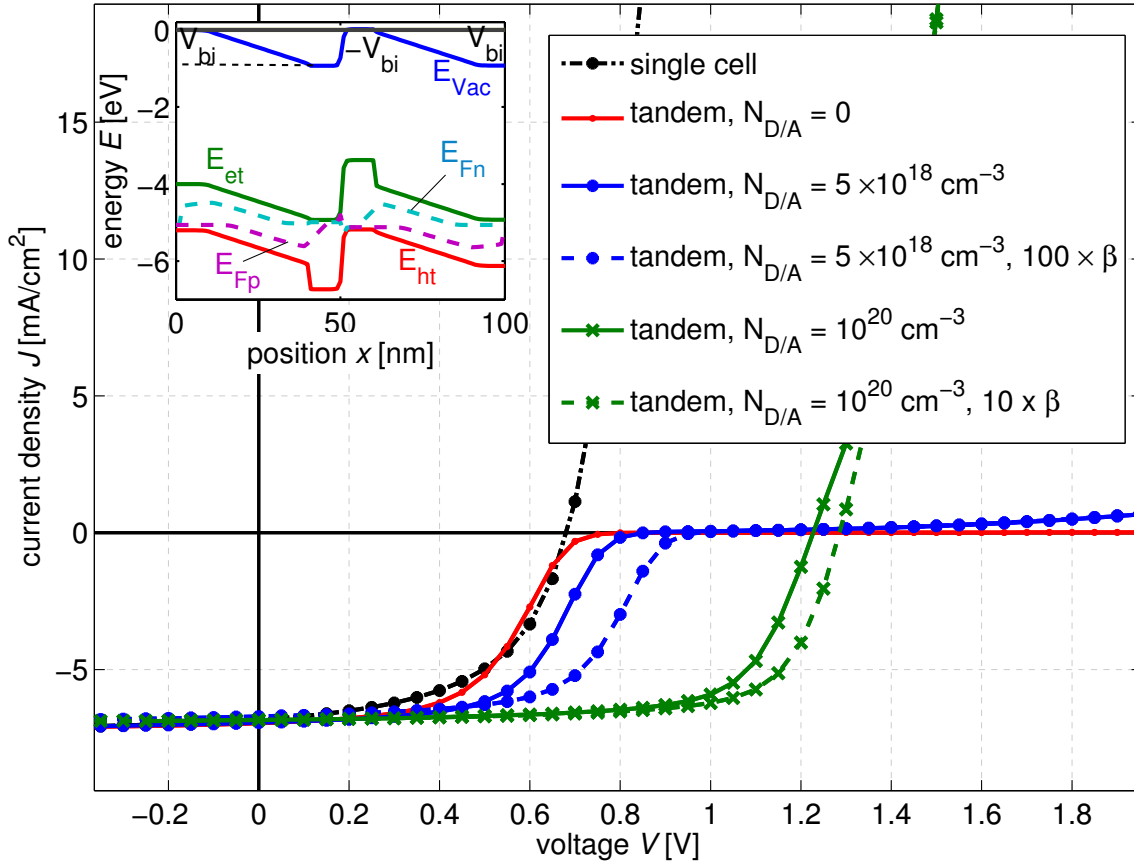
Figure 13.3: Simulated *J-V* curves of a single and a tandem solar cell consisting of two identical subcells. Recombination constant β and doping concentration in the interlayers are varied. The inset shows the energy-level diagram at short circuit in the case of high doping and recombination. All input parameters for the simulation are found in Appendix B, p. 332.

guarantee no Fermi level splitting are metals, which are experimentally embedded into the recombination contact as clusters [346]. In this case, it is crucial to guarantee the selectivity of the recombination contact by incorporating the metal clusters in between a p-type and n-type material.

However, doping the charge transport layers is very helpful for a high *FF*, because it defines the position of E_{F}. Thus, the two subcells each comprise the same V_{bi} as a single cell. As V_{bi} of the tandem cell is fixed by the two doped layers to the same value as in a single junction, the two V_{bi}s of the two subcells are accompanied by a voltage of $-V_{\mathrm{bi}}$ at the p-n junction. This is visible at E_{Vac} in the inset of Fig. 13.3.

In forward bias of the tandem cell, the p-n junction which is then negatively biased works as an electron/hole generation layer due to a transition of electrons from the HOMO of the p-doped material (leaving a hole) to the LUMO of the n-doped material. That is

why forward current flows through the tandem cell which incorporates a p-n junction in reverse.

These preliminary data show that incorporating a physically validated model for the HOMO-LUMO transition probability including energetic disorder and the correct temperature dependence might open the opportunities for simulations of tandem solar cells in comparison to experiment.

13.3 Further points to examine

The investigations presented in this thesis mainly focused on J-V data of ZnPc:C$_{60}$ BHJ solar cells in different geometries and with different HTLs, where mostly J-V curves recorded under room temperature were analyzed. This last section contains a list of suggestions for further investigation in a tight interaction between experiment and simulation:

- An investigation of the relevance of disorder regarding the J-V curve in the fourth quadrant by relating models for the charge carrier mobility to disorder parameters. Additionally, the simulation has the potential to serve as link between ab initio calculations of, e.g., mobilities of specific materials and the respective J-V curves.

- A detailed description of doped layers together with data from UPS and Seebeck measurements. Here, the correlation between conductivity, the position of the Fermi energy, and the role of the Seebeck energy dependent on doping concentration is not yet understood. This is important for solar cells as it influences the built-in potential which is to measure by electro-absorption experiments.

- A quantification of the effect of barriers, where detailed data about barrier heights and the density of states are required. Additionally, an examination of the relevance of further microscopic parameters (overlap integral) governing charge transport over an organic-organic interface might be interesting.

- An estimation of the effect of traps on solar cell performance with, e.g., the aid of impedance spectroscopy data.

- An incorporation of additional states at the donor-acceptor heterointerface and their properties obtained from experiments like triplet or CT-state energies.

- A temperature dependent analysis of J-V curves in experiment and simulation to further describe charge transport, doping, and charge carrier generation and recombination.

- An intensification of experimental approaches giving information about the variables of state of the simulation which are not easily accessible like charge carrier density or electric field distributions.

Part IV

Appendix

Appendix A

Lists

A.1 List of symbols

Symbol	Unit	Description
a	nm	lattice distance
a	nm	initial distance of geminate pair
$a(\hbar\omega)$		absorption
A	cm^2	area
α	cm^{-1}	absorption coefficient
β	cm^{3}s^{-1}	direct/ bimolecular recombination constant
β_r	cm^{3}s^{-1}	radiative recombination constant
β_L	cm^{3}s^{-1}	direct/ bimolecular Langevin recombination constant
d	nm	(device) thickness
D	m^{2}s^{-1}	diffusion coefficient
D_γ	cm^{-3}eV^{-1}	photonic density of states
e_γ	eVcm^{-3}	energy per unit volume
E	eV	energy
E_B	eV	(CT) exciton binding energy
E_C	eV	conduction band edge
E_CT	eV	energy of the CT state
E_et	eV	electron transport level $\approx$ LUMO
E_F	eV	Fermi energy
E_F^n	eV	electron quasi-Fermi level
E_F^p	eV	hole quasi-Fermi level
E_g	eV	energy gap
E_g^DA	eV	effective energy gap between IP$^\mathrm{donor}$ and EA$^\mathrm{acceptor}$
E_ht	eV	hole transport level $\approx$ HOMO
E_T	eV	energy of trap level
E_V	eV	valence band edge
E_Vac	eV	vacuum level

Symbol	Unit	Description
ϵ_{r}		dielectric constant
η		power-conversion efficiency
η_n	eV	electrochemical potential for electrons
η_p	eV	electrochemical potential for holes
η_i		quantum efficiency
$f(E)$		occupation probability
F	$\mathrm{Vm^{-1}}$	electrical field
FF		fill factor
$g(E)$	$\mathrm{cm^{-3}eV^{-1}}$	density of states
G	$\mathrm{s^{-1}}$	optical charge carrier generation rate
G_0	$\mathrm{s^{-1}}$	maximum optical charge carrier generation rate
γ	$\mathrm{(cm/V)^{1/2}}$	Poole-Frenkel factor
I	W	power flux
I	$\mathrm{mWcm^{-2}}$	intensity
I	A	electrical current
I_{S}	$\mathrm{WK^{-1}}$	entropy flux
I_{S}	$\mathrm{mWcm^{-2}}$	diode saturation current
$j_{\gamma,\Omega}$	$\mathrm{W\ m^{-2}\ sr^{-1}}$	radiance
j_E	$\mathrm{W\ m^{-2}}$	energy flux density, intensity
$\partial j_E/\partial\hbar\omega$	$\mathrm{W\ m^{-2}eV^{-1}}$	spectral irradiance
$\partial j_E/\partial\lambda$	$\mathrm{W\ m^{-2}nm^{-1}}$	spectral irradiance
J	$\mathrm{mAcm^{-2}}$	electrical current density
J_{dark}	$\mathrm{mAcm^{-2}}$	current density in the dark
J_{illu}	$\mathrm{mAcm^{-2}}$	current density under illumination
J_{photo}	$\mathrm{mAcm^{-2}}$	photocurrent density
J_{sat}	$\mathrm{mAcm^{-2}}$	saturated photocurrent density (under reverse bias)
J_{sc}	$\mathrm{mAcm^{-2}}$	short-circuit current density
k	$\mathrm{cm^{-3}}$	wave number
k		extinction coefficient
k_{diss}	$\mathrm{s^{-1}}$	dissociation rate of CT states
k_{relax}	$\mathrm{s^{-1}}$	relaxation rate of CT states
l	nm	drift length
L	nm	box length
L_{D}	nm	diffusion length
λ	nm	wavelength
m	kg	mass
m^*	kg	effective mass
m		spectral mismatch factor
Δm	nm	discretization distance
μ	$\mathrm{cm^2V^{-1}s^{-1}}$	charge carrier mobility
N		total number of states
N_{A}^-	$\mathrm{cm^{-3}}$	concentration of ionized acceptor

Symbol	Unit	Description
N_C	cm^{-3}	effective density of states in the conduction band
N_D^+	cm^{-3}	concentration of ionized donors
N_T	cm^{-3}	trap density
N_V	cm^{-3}	effective density of states in the valence band
n	cm^{-3}	electron density/concentration
n		refractive index
n_0	cm^{-3}	equilibrium electron density
n_i	cm^{-3}	intrinsic electron/hole density/concentration
n_t	cm^{-3}	trapped electron density
ν	Hz	frequency
ω	s^{-1}	angular frequency
Ω		solid angle
p	kgms^{-1}	momentum
p	cm^{-3}	hole density/concentration
p_0	cm^{-3}	equilibrium hole density
p_t	cm^{-3}	trapped hole density
P		probability of jump over barrier
P		probability of CT-exciton dissociation
P	eV	polarization energy
ϕ	eV	electrical potential
ϕ	eV	energy barrier
ϕ_{injec}	eV	injection barrier
ϕ_{extra}	eV	extraction barrier
Φ	eV	work function
$\mathbf{r}$	nm	position
R	s^{-1}	charge carrier recombination rate
R_{sep}	s^{-1}	exciton separation rate (at D/A interface)
ρ	Ascm^{-3}	space-charge density
s	ms^{-1}	surface-recombination velocity
s	cm^{-3}	exciton density
σ	cm^2	cross section
σ	Scm^{-1}	specific conductivity
σ	eV	width of a Gaussian density of states
t	s	time
T	K	temperature
τ	s	lifetime
v	ms^{-1}	velocity
V	cm^3	volume
V	V	voltage
V_0	V	compensation voltage, where $J_{photo} = 0$
V_{bi}	V	built-in potential
V_{bias}	V	applied bias voltage

Symbol	Unit	Description
V_{oc}	V	open-circuit voltage
V_{POS}	V	point of optimal symmetry of J_{photo}
x	nm	spatial coordinate
X	cm^{-3}	CT state density
ξ	eV	chemical potential
Z	N	force
Z	VA^{-1}	impedance

A.2 List of abbreviations

abbreviation	full word
AC	alternating current
AM	air mass
BHJ	bulk heterojunction (solar cell)
CT	charge transfer
CV	cyclic voltammetry
DC	direct current
D-A	donor-acceptor
D/A	donor/acceptor (interface)
DOS	density of states
EA	electron affinity
EQE	external quantum efficiency
ETL	electron transport layer
FD	Fermi-Dirac
FHJ	flat/ planar heterojunction (solar cell)
HOMO	highest occupied molecular orbital
HTL	hole transport layer
IP	ionization potential
IQE	internal quantum efficiency: EQE/ absorption efficiency
ITO	tin-doped indium oxide
LUMO	lowest unoccupied molecular orbital
MM	spectral mismatch
OPV	organic photovoltaics
QCM	quartz crystal monitor
SC	semiconductor
SOMO	single occupied molecular orbital
UPS	ultraviolet photoelectron spectroscopy
UV	ultraviolet

A.3 List of constants

Symbol	Value	Description
c	$3 \times 10^8 \, \text{ms}^{-1}$	speed of light
e	$1.602 \times 10^{-19} \, \text{As}$	elementary charge
ϵ_0	$8.854 \times 10^{-12} \, \text{Fm}^{-1}$	vacuum permittivity
h	$6.626 \times 10^{-34} \, \text{m}^2\text{kgs}^{-1}$	Planck's constant
$\hbar$	$1.055 \times 10^{-34} \, \text{m}^2\text{kgs}^{-1}$	Planck's constant divided by 2π
k_{B}	$1.38 \times 10^{-23} \, \text{m}^2\text{kgs}^{-2}\text{K}^{-1}$	Boltzmann constant
σ	$5.67 \times 10^{-8} \, \text{Jm}^{-2}\text{s}^{-1}\text{K}^{-4}$	Stefan-Boltzmann constant

Appendix B

Simulation data

Details on the code and the code itself are not displayed here due to the length of this thesis as well as the length of the code. A documentation of the code will be available as separate document. Here, the input parameters for the simulations are given to complete the parameter lists in the text, which only contain the parameters being most relevant for the respective discussions. The tables in this appendix allow a reproduction of the simulation data although it is once more mentioned that the simulation data in this work was mostly employed to describe trends rather than making quantitative statements.

For each device (series) two tables are shown. The first table contains general and configuration parameters whereas the second table provides the parameters specific for each layer.

Single layer in Chapter 4.8.1

The data of Figs. 4.12 to 4.14 (pp. 131 to 133) are obtained by simulations of a single-layer hole-only device with the following parameters, where metal work functions, doping concentrations, and trap distributions are varied.

parameter	description	configuration value
# of layers	hole-only device	1
G	dark curves	0
left contact	defined by work function/ thermionic	1; 5.1 eV/ 2; 4.3 eV
right contact	defined by work function/ thermionic	1; 5.1 eV/ 2; 4.3 eV
T	temperature	300 K
Δm	discretization distance	0.125…0.5 nm
traps	no / exponential trap distribution	0 / 21

parameter	description	unit	BHJ
d	thickness	nm	100
E_ht	"HOMO"	eV	-5.2
E_g	(effective) gap	eV	2.2
μ_n	electron mobility	cm^2/Vs	10^{-6}
μ_p	hole mobility	cm^2/Vs	10^{-6}
N_C	effective/total density of states n	cm^{-3}	10^{21}
N_V	effective/total density of states p	cm^{-3}	10^{21}
N_D	active n-dopant concentration	cm^{-3}	0
N_A	active p-dopant concentration	cm^{-3}	...
ϵ_r	dielectric constant		5
β	recombination constant	cm^{3}s^{-1}	Langevin
N_pt	hole trap density	cm^{-3}	10^{19}
E_pt	hole trap depth	eV	0.1
blend	direct e/h generation	[0/1]	1

p-n junction in Chapter 4.8.2

Figures 4.15 and 4.16 show simulation data for a silicon p-n junction with the following parameters:

parameter	description	configuration value
# of layers	p-n junction	2
G	dark / constant generation rate	0 / $6.9 \times 10^{20}\,\mathrm{cm^{-3}s^{-1}}$
left contact	doping concentration as BC, selective	200
right contact	doping concentration as BC, selective	100
T	temperature	300 K
Δm	discretization distance	5...10 nm

parameter	description	unit	p-layer	n-layer
d	thickness	nm	2000	2000
E_{ht}	"HOMO"	eV	-5.17	-5.17
E_{g}	(effective) gap	eV	1.12	1.12
μ_{n}	electron mobility	cm^2/Vs	1500	1500
μ_{p}	hole mobility	cm^2/Vs	450	450
N_{C}	effective/total density of states n	cm^{-3}	2.8×10^{19}	2.8×10^{19}
N_{V}	effective/total density of states p	cm^{-3}	1.04×10^{19}	1.04×10^{19}
N_{D}	active n-dopant concentration	cm^{-3}	0	2×10^{16}
N_{A}	active p-dopant concentration	cm^{-3}	1×10^{16}	0
ϵ_{r}	dielectric constant		11.9	11.9
β	recombination constant	cm^{3}s^{-1}	3×10^{-13}	3×10^{-13}
blend	direct e/h generation	[0/1]	1	1

Single-carrier devices in Chapter 5

All relevant parameters are given in Tab. 5.1 and in the text. The discretization distance is set to 0.25 nm. To obtain fingerprints, the applied voltage is corrected for the Fermi level offset at the first monolayer caused by a high charge carrier density and a discretization distance that is not capable of resolving this effect. This is only a numerical issue which can be avoided by smaller discretization distances.

Barrier devices in Chapter 6.3

Here, the input parameters to the simulation data shown in Figs. 6.5 to 6.7 are given. The value for the exciton lifetime is chosen in the μs range such that it is unimportant as the intrinsic relaxation rate is much smaller than the splitting rate at the D/A interface and the quenching rate at the metal contacts ($10^{10}\,\mathrm{s^{-1}}$).

Recombination at a D/A interface is assumed to happen at the Coulomb radius.

Flat heterojunction

parameter	description	configuration value
# of layers	p-i-FHJ	4
G	from OSOLemio	$n\&k$ of BPAPF, ZnPc, C60
left contact	doping concentration as BC	0
right contact	equilibrium with metal or S&M	1/ 13 4.2 eV
T	temperature	310 K
Δm	discretization distance	0.5 / 1 nm
Fermi-Dirac	yes, Gaussian DOS	1
lowering of barrier	yes, hopping distance	1 nm

param.	name	unit	p-HTL	i-HTL	donor	acceptor
d	thickness	nm	20	8	8	40
E_{ht}	"HOMO"	eV	. . .	. . .	. . .	-6.4
E_g	(effective) gap	eV	3	3	2.1/3	2.4/ 2.5
μ_n	electron mobility	cm^2/Vs	10^{-5}	10^{-5}	10^{-5}	$10^{-4}/10^{-2}$
μ_p	hole mobility	cm^2/Vs	10^{-5}	10^{-6}	$10^{-4}/10^{-6}$	10^{-3}
N_C	total DOS n	cm^{-3}	10^{21}	10^{21}	10^{21}	10^{21}
N_V	total DOS p	cm^{-3}	10^{21}	10^{21}	10^{21}	10^{21}
N_D	n-dopant density	cm^{-3}	0	0	0	0
N_A	p-dopant density	cm^{-3}	5×10^{24}	0	0	0
ϵ_r	dielectric constant		3.4	3.4	3.4	3.4
β	recombination const.	cm^{3}s^{-1}		modified Langevin		
σ_{HOMO}	width of DOS	eV	0.1	0.1	0.1	0.1
σ_{LUMO}	width of DOS	eV	0.1	0.1	0.1	0.1
L_D	exciton diff. length	nm	2	2	7	10
blend	direct e/h generation	[0/1]	0	0	0	0

Bulk heterojunction

parameter	description	configuration value
# of layers	p-i-BHJ-ETL	4
G	from OSOLemio	$n\&k$ of BPAPF, C$_{60}$/2 for blend, C$_{60}$
left contact	doping concentration	0
right contact	equilibrium with metal	1 4.2 eV
T	temperature	310 K
Δm	discretization distance	1 nm
Fermi-Dirac	yes, Gaussian DOS	1
lowering of barrier	yes, hopping distance	1 nm

param.	name	unit	p-HTL	i-HTL	BHJ	ETL
d	thickness	nm	20	8	30	18
E_ht	"HOMO"	eV	...	...	-5.6	-6.4
E_g	(effective) gap	eV	3	3	1.7	2.49
μ_n	electron mobility	cm^2/Vs	10^{-5}	10^{-5}	10^{-4}	10^{-3}
μ_p	hole mobility	cm^2/Vs	10^{-5}	10^{-6}	10^{-7}	10^{-4}
N_C	total density of states n	cm^{-3}	10^{21}	10^{21}	10^{21}	10^{21}
N_V	total density of states p	cm^{-3}	10^{21}	10^{21}	10^{21}	10^{21}
N_D	active n-dopant concentration	cm^{-3}	0	0	0	0
N_A	active p-dopant concentration	cm^{-3}	5×10^{24}	0	0	0
ϵ_r	dielectric constant		3.4	3.4	3.4	3.4
β	recombination constant	cm^{3}s^{-1}	modified Langevin			
σ_HOMO	width	eV	0.1	0.1	0.1	0.1
σ_LUMO	width	eV	0.1	0.1	0.1	0.1
L_D	exciton diffusion length	nm	2	2	-	10
blend	direct e/h generation	[0/1]	0	0	1	0

Barrier devices in Chapter 6.5

This appendix displays the input parameters to the simulation data shown in several figures of Ch. 6.5 where injection and extraction barrier devices at varied layer thicknesses and temperatures are investigated. The value for the exciton lifetime is chosen as 10^{-8} s such that it the relaxation is unimportant because it is much smaller than the splitting rate at the D/A interface. At the metal contacts all excitons are assumed to be quenched. Recombination at a D/A interface is assumed to happen at 1 nm distance. The extraction barrier is reduced by an interface dipole, changing the potential by 0.2 eV.

parameter	description	configuration value
# of layers	p-i-FHJ	4
G	from OSOLemio $\times 1.2$	$n\&k$ of p-DiNPD, BPAPF, C$_{60}$
left contact	doping concentration as BC	0
right contact	equilibrium with metal	1; 4.1 eV
T	temperature	300 K / ...
Δm	discretization distance	1 nm
Fermi-Dirac	no Gaussian DOS	0
lowering of barrier	yes, hopping distance	1 nm

param.	name	unit	p-HTL	i-HTL	donor	acceptor
d	thickness	nm	20	...	...	40
E_{ht}	"HOMO"	eV	-5.1/5.6	-5.1/5.6	-5.6/5.1	-6.3
E_{g}	(effective) gap	eV	2.5	2.5	2.5	2.4
μ_{n}	electron mobility	cm^2/Vs	10^{-5}	10^{-5}	10^{-5}	5×10^{-4}
μ_{p}	hole mobility	cm^2/Vs	10^{-5}	10^{-5}	10^{-5}	5×10^{-4}
N_{C}	effective/total DOS n	cm^{-3}	10^{21}	10^{21}	10^{21}	10^{21}
N_{V}	effective/total DOS p	cm^{-3}	10^{21}	10^{21}	10^{21}	10^{21}
N_{D}	n-dopant concentration	cm^{-3}	0	0	0	0
N_{A}	p-dopant concentration	cm^{-3}	5×10^{24}	0	0	0
ϵ_{r}	dielectric constant		5	5	5	5
β	recombination constant	cm^{3}s^{-1}	7.23×10^{-10} / 7.23×10^{-11}			
L_{D}	exciton diffusion length	nm	7	7	7	12
blend	direct e/h generation	[0/1]	0	0	0	0

p-i-p device in Chapter 7.2

The comparison of simulation data to Ph4-Ph4-DIP p-i-p devices shown in Fig. 7.5 is performed using the following parameters:

parameter	description	configuration value
# of layers	p-i-p	3
G	dark	0
left contact	doping concentration as BC	0
right contact	doping concentration as BC	0
T	temperature	300 K
Δm	discretization distance	1 nm
Fermi-Dirac	no Gaussian DOS	0
mobility	Poole-Frenkel	1

param.	name	unit	p	i	p
d	thickness	nm	10	...	10
E_{ht}	"HOMO"	eV	-5.6	-5.6	-5.6
E_{g}	(effective) gap	eV	2	2	2
μ_{n}	electron mobility	cm^2/Vs	5×10^{-8}		
μ_{p}	(zero field) hole mobility	cm^2/Vs	$10^{-8}/10^{-6}$	...	$10^{-8}/10^{-6}$
γ_{p}	Poole-Frenkel factor	(cm/V)$^{0.5}$	0	...	0
N_{C}	eff. density of states n	cm^{-3}	10^{21}	10^{21}	10^{21}
N_{V}	eff. density of states p	cm^{-3}	10^{21}	10^{21}	10^{21}
N_{D}	active n-dopant density	cm^{-3}	0	0	0
N_{A}	active p-dopant density	cm^{-3}	5×10^{18}	$10^{12}/10^{14}$	5×10^{18}
ϵ_{r}	dielectric constant		3.4	3.4	3.4

Ph4-Ph4-DIP solar cells in Chapter 7.2

The *J-V* curves in Fig. 7.6 are calculated with the following values. Exciton harvesting is limited by the diffusion length only.

parameter	description	configuration value
# of layers	p-FHJ-n	4
G	from OSOLemio ×1.1	*n&k* of p-DiNPD, BPAPF, C60
left contact	doping concentration as BC	0
right contact	doping concentration as BC	0
T	temperature	310 K
Δm	discretization distance	1 nm
Fermi-Dirac	no Gaussian DOS	0
mobility	Poole-Frenkel	1

parameter	unit	p-HTL	donor	acceptor	n-ETL
d	nm	25	. . .	30	10
E_{ht}	eV	-5.6	-5.6	-6.4	-6.4
E_{g}	eV	3	2.2	2.4	2.4
μ_{n}	cm^2/Vs	10^{-4}	10^{-4}	10^{-2}	10^{-2}
μ_{p}	cm^2/Vs	10^{-5}	5×10^{-9}	10^{-4}	10^{-4}
γ_{p}	(cm/V)$^{0.5}$	0	0.006	0	0
N_{C}	cm^{-3}	10^{21}	10^{21}	10^{21}	10^{21}
N_{V}	cm^{-3}	10^{21}	10^{21}	10^{21}	10^{21}
N_{D}	cm^{-3}	0	0	0	5×10^{24}
N_{A}	cm^{-3}	5×10^{24}	0	0	0
ϵ_{r}		3.4	3.4	3.4	3.4
β	cm^{3}s^{-1}	modified Langevin			
L_{D}	nm	2	2	20	20
blend	[0/1]	0	0	0	0

CT-exciton dissociation in Chapter 7.3

The parameters for the simulation data shown in Fig. 7.9 are the same as those in Tab. 7.1, only the discretization distance is chosen to 0.5 nm (instead of 1 nm) and L_{D} to 7 nm each. Furthermore, Onsager-Braun theory is activated with the parameters given in the caption of the figure.

Barriers and doping in Chapter 8.3

The data shown in Fig. 8.4 are calculated assuming the following values:

parameter	description	configuration value
# of layers	p-i-BHJ-ETL	4
G	from OSOLemio ×1.11	$n\&k$ of BPAPF, ZnPc:C_{60}, C_{60}
left contact	doping concentration as BC	0
right contact	equilibrium with metal	1 4.2 eV
T	temperature	310 K
Δm	discretization distance	0.5 nm
Fermi-Dirac	no, Gaussian DOS	0
lowering of barrier	no	0

parameter	unit	p-HTL	i-HTL	blend	ETL
d	nm	20	5	45	15
E_{ht}	eV	. . .	. . .	-5.05	-6.4
E_{g}	eV	3	3	1.05	2.4
μ_{n}	cm^2/Vs	5×10^{-5}	5×10^{-5}	5×10^{-4}	5×10^{-4}
μ_{p}	cm^2/Vs	10^{-5}	10^{-5}	5×10^{-6}	10^{-5}
N_{C}	cm^{-3}	10^{21}	10^{21}	10^{21}	10^{21}
N_{V}	cm^{-3}	10^{21}	10^{21}	10^{21}	10^{21}
N_{D}	cm^{-3}	0	0	0	0
N_{A}	cm^{-3}	3×10^{24}	$0/ \ldots$	0	0
ϵ_{r}		3.4	3.4	3.4	3.4
β	cm^{3}s^{-1}	modified Langevin			
blend	[0/1]	0	0	1	0

ZnPc:C_{60} 1:1 in Chapter 8.4

Figure 8.7 shows simulation data with the following input parameters:

parameter	description	configuration value
# of layers	p-i-BHJ-ETL	4
G	from OSOLemio ×1.11	$n\&k$ of BPAPF, ZnPc:C_{60}, C_{60}
left contact	doping concentration as BC	0
right contact	equilibrium with metal	1; 4.2 eV
T	temperature	310 K
Δm	discretization distance	0.5 nm
Fermi-Dirac	yes, Gaussian DOS	1
lowering of barrier	yes	1; 1,5 nm

parameter	unit	p-HTL	i-HTL	blend	ETL
d	nm	20	5	45	15
E_{ht}	eV	-5.35	-5.35	-5.05 / ...	-6.4
E_{g}	eV	3	3	1.15 /...	2.4
μ_{n}	cm^2/Vs	5×10^{-5}	5×10^{-5}	5×10^{-4}	5×10^{-4}
μ_{p}	cm^2/Vs	10^{-5}	10^{-5}	$.../x \times 10^{-6}$	10^{-5}
N_{C}	cm^{-3}	10^{21}	10^{21}	10^{21}	10^{21}
N_{V}	cm^{-3}	10^{21}	10^{21}	10^{21}	10^{21}
N_{D}	cm^{-3}	0	0	0	0
N_{A}	cm^{-3}	3×10^{24}	$0/\ldots$	0	0
ϵ_{r}		3.4	3.4	3.4	3.4
β	cm^{3}s^{-1}		modified Langevin		
σ_{HOMO}	eV	0.05	0.05	0.05	0.05
σ_{LUMO}	eV	0.05	0.05	0.05	0.05
L_{D}	nm	2	2	-	10
blend	[0/1]	0	0	1	0

When changing the mobility in the case of the variation of barriers, the recombination rate is held constant. For the FHJ, d of the 3$^{\mathrm{rd}}$ and 4$^{\mathrm{th}}$ layers are changed to 20, 40 nm, E_{ht} to -5 and -6.3 eV and the gap to 2.1 and 2.4 eV. The recombination constants are taken from the BHJ.

MIM diode in Chapter 10.3.1

The simulation study on the influence of several parameters on the dark J-V curves shown in Fig. 10.9 is done with the following fixed parameters. Different recombination mechanisms are activated with the parameters given in the legend of Fig. 10.9.

parameter	description	configuration value
# of layers	singlelayer	1
G	dark curves	0
left contact	equilibrium with metal	1; 5.1 eV
right contact	equilibrium with metal	1; 4.1 eV
T	temperature	300 K
Δm	discretization distance	0.25 nm

parameter	description	unit	layer
d	thickness	nm	50
E_{ht}	"HOMO"	eV	5.2
E_{g}	(effective) gap	eV	1.2
μ_{n}	electron mobility	cm^2/Vs	. . .
μ_{p}	hole mobility	cm^2/Vs	. . .
N_{C}	effective/total density of states n	cm^{-3}	10^{21}
N_{V}	effective/total density of states p	cm^{-3}	10^{21}
N_{D}	active n-dopant concentration	cm^{-3}	0
N_{A}	active p-dopant concentration	cm^{-3}	0
ϵ_{r}	dielectric constant		5
β	recombination constant	cm^{3}s^{-1}	7.23×10^{-11}

ZnPc:C$_{60}$ mixing ratio and HTL in Chapter 10.4

Most of the crucial parameters of the data shown in Figs. 10.18 to 10.21 are already given in Tab. 10.3. The table here contains the remaining parameters. The SRH recombination rate is set to $10^6\,\mathrm{s}^{-1}$.

parameter	description	configuration value
# of layers	n-i-p	3
G	dark/ OSOLemio	0 / $n\&k$ of p-DiNPD, ZnPc:C$_{60}$, C$_{60}$
left contact	doping concentration as BC	0
right contact	doping concentration as BC	0
T	temperature	300 K
Δm	discretization distance	0.5 nm
Fermi-Dirac	no Gaussian DOS	0

parameter	name	unit	n	i	p
d	thickness	nm	20	. . .	. . .
E_{ht}	"HOMO"	eV	6.4	. . .	5.2
E_{g}	(effective) gap	eV	2.37	. . .	3
μ_{n}	electron mobility	cm^2/Vs	10^{-3}	. . .	8×10^{-5}
μ_{p}	hole mobility	cm^2/Vs	2×10^{-5}	. . .	10^{-4}
N_{C}	effective density of states n	cm^{-3}	10^{21}	10^{21}	10^{21}
N_{V}	effective density of states p	cm^{-3}	10^{21}	10^{21}	10^{21}
N_{D}	active n-dopant concentration	cm^{-3}	5×10^{18}	0	0
N_{A}	active p-dopant concentration	cm^{-3}	0	0	5×10^{18}
ϵ_{r}	dielectric constant		5	4.9	3

Bode diagram in Chapter 13.1

The data of Fig. 13.1 are obtained by applying a sinusoidal voltage and monitoring the time dependence of the current, where the following parameters are used:

parameter	description	configuration value
# of layers	singlelayer	1
G	dark curves	0
left contact	equilibrium with metal, selective	201; 5.1 eV
right contact	equilibrium with metal, selective	101; 4.1 eV
T	temperature	300 K
Δm	discretization distance	0.5 nm

parameter	description	unit	layer
d	thickness	nm	50
E_{ht}	"HOMO"	eV	5.2
E_g	(effective) gap	eV	1.2
μ_n	electron mobility	cm^2/Vs	10^{-5}
μ_p	hole mobility	cm^2/Vs	10^{-7}
N_C	effective/total density of states n	cm^{-3}	10^{21}
N_V	effective/total density of states p	cm^{-3}	10^{21}
N_D	active n-dopant concentration	cm^{-3}	0
N_A	active p-dopant concentration	cm^{-3}	0
ϵ_r	dielectric constant		5
β	recombination constant	cm^{3}s^{-1}	7.23×10^{-14}

Breakthrough in Chapter 13.2

The data of Fig. 13.2 are obtained with the following parameters and with the HOMO-LUMO transition probability described in the text.

parameter	description	configuration value
# of layers	FHJ	2
G	dark	0
left contact	equilibrium with metal	1; 5.1 eV
right contact	equilibrium with metal	1; 4.2 eV
T	temperature	300 K
Δm	discretization distance	0.2 nm
Fermi-Dirac	no Gaussian DOS	0

parameter	name	unit	donor	acceptor
d	thickness	nm	...	...
E_{ht}	"HOMO"	eV	5.2	6.4
E_{g}	(effective) gap	eV	2.1	2.3
μ_{n}	electron mobility	cm^2/Vs	10^{-3}	10^{-3}
μ_{p}	(zero field) hole mobility	cm^2/Vs	10^{-4}	10^{-4}
N_{C}	effective/total density of states n	cm^{-3}	10^{21}	10^{21}
N_{V}	effective/total density of states p	cm^{-3}	10^{21}	10^{21}
N_{D}	active n-dopant concentration	cm^{-3}	0	0
N_{A}	active p-dopant concentration	cm^{-3}	0	0
ϵ_{r}	dielectric constant		3.4	3.4
β	recombination constant	cm^{3}s^{-1}	5×10^{-10}	5×10^{-10}

Tandem solar cell in Chapter 13.2

Figure 13.3 displays simulations with the following parameters and applying the HOMO-LUMO transition probability as mentioned in the previous section.

parameter	description	configuration value
# of layers	tandem p-i-n	6
G	constant in blends, else 0	1.5×10^{22} cm^{-3}s^{-1}
left contact	doping concentration	0
right contact	doping concentration	0
T	temperature	300 K
Δm	discretization distance	1 nm
Fermi-Dirac	no Gaussian DOS	0

parameter	unit	p	blend	n	p	blend	n
d	nm	10	30	10	10	30	10
E_{ht}	eV	-5.2	-5.2	-5.8	-5.2	-5.2	-5.2
E_{g}	eV	1.2	1.2	1.8	1.8	1.2	1.2
μ_{n}	cm^2/Vs			10^{-4}			
μ_{p}	cm^2/Vs			10^{-4}			
N_{C}	cm^{-3}	10^{21}	10^{21}	10^{21}	10^{21}	10^{21}	10^{21}
N_{V}	cm^{-3}	10^{21}	10^{21}	10^{21}	10^{21}	10^{21}	10^{21}
N_{D}	cm^{-3}	0	0	...	0	0	5×10^{18}
N_{A}	cm^{-3}	5×10^{18}	0	0	...	0	0
ϵ_{r}		5	5	5	5	5	5
β	cm^{3}s^{-1}	7.23×10^{-12}		$\cdots \times 7.23 \times 10^{-12}$		7.23×10^{-12}	

Appendix C

Experimental data

Reproducibility and traceability is one major keystone scientific work is based on. This requires a clear organization of data, which might steal time from the even more important keystone of research which is creativity. At the institute where this thesis was done a very helpful tool, which is the OSOL-database, is available. After being installed, the database allowed for an organization of processing and measurement data with justifiable effort. For reasons of clarity, it was avoided to explicitly mention each processing detail (e.g. 1 nm of dopant layer at the ITO, evaporation rates, etc.), which was not relevant for the discussions presented. However, the exact processing sequence and conditions are stored in the database. That is why the labels of the samples produced for this work are given here. As these data is not publicly accessible, all those who are interested in details are asked to directly contact the author of this work.

chapter	run name
Ch. 6.2 and 6.4	OSOL-0203-tress-FlatHJ_HTLs_Barrier
	OSOL-0427-tress-BulkHJ_HTLs_Barrier
Ch. 6.5	OSOL-0408-tress-FlatHJ_Barriers_thickness
	OSOL-0681-tress-FlatHJ_Barriers_thickness_donor
Ch. 7.2	OSOL-0320-tress-MH153_S-Shape
Ch. 8	OSOL-0160-WT-ZnPcC60RatioHTL
	OSOL-0201-WT-ZnPcC60RatioHTL_ExtrBarrier
Ch. 9	OSOL-0161-WT-ZnPcC60Gradient
	OSOL-0202-WT-ZnPcC60KontGradient
Ch. 10	OSOL-0502-tress-GenProfile Repeat
	OSOL-0557-tress-GenProfile DiNPD
	OSOL-0598-tress-GenProfile MeO-TPD
Ch. 11.3.1	OSOL-0263-WT-ZnPcC60 C60 ExcDIff
Ch. 11.3.2	OSOL-0227-meiss-MH200-EDL
	OSOL-0484-tress-PhotoShunt_FHJ

References

Bibliography

[1] Meteonorm. Global irradiance. *http:/meteonorm.com/fileadmin/user_upload/maps/ world_beam_8100.png.*, Accessed 15.08.2011.

[2] IEA. World energy outlook 2010. *http://www.iea.org/weo*, 2010.

[3] P. Würfel. *Physics of Solar Cells: From Basic Principles to Advanced Concepts.* Wiley-VCH, Weinheim, 2009.

[4] M. L. Parry, O. F. Canziani, J. P. Palutikof, P. J. Linden, and C. E. Hanson, editors. *Contribution of Working Group II to the Fourth Assessment Report of the Intergovernmental Panel on Climate Change, 2007.* Cambridge, United Kingdom and New York, NY, USA, 2007.

[5] BP. BP Statistical Review of World Energy 2010. *http://www.bp.com*, 2010.

[6] R. F. Keeling, S. C. Piper, A. F. Bollenbacher, and S. J. Walker. Concentrations of CO2 in the Earth's atmosphere. *http://scrippsco2.ucsd.edu/data/atmospheric_co2.html.*, Accessed 15.08.2011.

[7] Earth Policy Institute from National Aeronautics and Space Administration (NASA) - Goddard Institute for Space Studies (GISS). Global Land-Ocean Temperature Index in 0.01 degrees Celsius. *http://data.giss.nasa.gov/gistemp/tabledata/GLB.Ts+dSST.txt*, 2011.

[8] Bundesverband Windenergie. Installierte Windenergieleistung in Deutschland. *http://www.wind-energie.de/infocenter/statistiken/deutschland/installierte-windenergieleistung-deutschland.*, Accessed 15.08.2011.

[9] Installed photovoltaic capacity. *Solarstrommagazin Photon Ausgabe August*, page 157, 2011.

[10] Bundesnetzagentur. Monitoringbericht 2010. *http://www.bundesnetzagentur.de/ SharedDocs/Pressemitteilungen/DE/2010/101130Monitoringbericht2010.html*, 2010.

[11] IWES. Dynamische Simulation der Stromversorgung in Deutschland nach dem BEE-Szenario: Stromversorgung 2020. *http://www.bee-ev.de.*

[12] BMU. Press release 30.08.2011. *http://erneuerbare-energien.de/inhalt/47718/4590*, (Accessed 14.09.2011), 2011.

Bibliography

[13] Ch. Breyer, A. Gerlach, J. Mueller, H. Behacker, and A. Milner. Grid-parity analysis for EU and US regions and market segments - Dynamics of grid-parity and dependence on solar irradiance, local electricity prices and PV progress ratio. *Proceedings of EU-PVSEC 2009*, 2009.

[14] S. Nowak. Global PV markets and policies. *Proceedings of EU-PVSEC 2011*, 2011.

[15] V. Petrova-Koch. Milestones of Solar Conversion and Photovoltaics. In *High-Efficient Low-Cost Photovoltaics*. Springer Berlin Heidelberg, 2009.

[16] W. Smith. Effect of light on selenium during the passage of an electric current. *Nature*, page 303, 1873.

[17] H. Hertz. Ueber einen Einfluss des ultravioletten Lichtes auf die electrische Entladung. *Annalen der Physik und Chemie*, 267(8):983–1000, 1887.

[18] P. Lenard. Ueber die lichtelektrische Wirkung. *Annalen der Physik*, 313(5):149–198, 1902.

[19] A. Einstein. Über einen die Erzeugung und Verwandlung des Lichtes betreffenden heuristischen Gesichtspunkt. *Annalen der Physik*, 322(6):132–148, 1905.

[20] A. Pochettino. *Rendiconti Academia dei Lincei*, 15:355, 1906.

[21] J. Koenigsberger and K. Schilling. Über Elektrizitätsleitung in festen Elementen und Verbindungen. I. Minima des Widerstandes, Prüfung auf Elektronenleitung, Anwendung der Dissoziationsformeln. *Annalen der Physik*, 337(6):179–230, 1910.

[22] M. Volmer. Die verschiedenen lichtelektrischen Erscheinungen am Anthracen, ihre Beziehungen zueinander, zur Fluoreszenz und Dianthracenbildung. *Annalen der Physik*, 345(4):775–796, 1913.

[23] C. K. Chiang, C. R. Fincher Jr, Y. W. Park, A. J. Heeger, H. Shirakawa, E. J. Louis, S. C. Gau, and A. G. MacDiarmid. Electrical conductivity in doped polyacetylene. *Physical Review Letters*, 39(17):1098–1101, 1977.

[24] C. W. Tang and S. A. VanSlyke. Organic electroluminescent diodes. *Applied Physics Letters*, pages 30–32, 1987.

[25] J. H. Burroughes, D. D. C. Bradley, A. R. Brown, R. N. Marks, K. Mackay, R. H. Friend, P. L. Burns, and A. B. Holmes. Light-emitting diodes based on conjugated polymers. *Nature*, 347(6293):539–541, 1990.

[26] OLED Info. *http://www.oled-info.com.*, Accessed 14.09.2011.

[27] S. Reineke, F. Lindner, G. Schwartz, N. Seidler, K. Walzer, B. Lüssem, and K. Leo. White organic light-emitting diodes with fluorescent tube efficiency. *Nature*, 459(7244):234–238, 2009.

[28] H. Kallmann and M. Pope. Photovoltaic Effect in Organic Crystals. *The Journal of Chemical Physics*, 30(2):585, 1959.

[29] G. A. Chamberlain. Organic solar cells: A review. *Solar Cells*, 8:47 – 83, 1983.

[30] C. W. Tang. Two-layer organic photovoltaic cell. *Applied Physics Letters*, 48(2):183–185, 1986.

[31] M. Hiramoto, H. Fujiwara, and M. Yokoyama. Three-layered organic solar cell with a photoactive interlayer of codeposited pigments. *Applied Physics Letters*, 58(10):1062–1064, 1991.

[32] G. Yu, J. Gao, J. C. Hummelen, F. Wudl, and A. J. Heeger. Polymer photovoltaic cells: enhanced efficiencies via a network of internal donor-acceptor heterojunctions. *Science*, 270(5243):1789, 1995.

[33] H. Spanggaard and F. C. Krebs. A brief history of the development of organic and polymeric photovoltaics. *Solar Energy Materials and Solar Cells*, 83(2-3):125–146, 2004.

[34] M. A. Green, K. Emery, Y. Hishikawa, W. Warta, and E. D. Dunlop. Solar cell efficiency tables (version 39). *Progress in Photovoltaics: Research and Applications*, 20(1):12–20, 2012.

[35] Tandem solar cell by Heliatek with an efficiency of 9.8 % on an area of 1.1 square centimeters, certified at Fraunhofer ISE CalLab (Freiburg, Germany), press release. 2011.

[36] L. Kazmerski. Best research cell efficiencies. *http://upload.wikimedia.org/ wikipedia/commons/1/16/PVeff%28rev110901%29.jpg.*, Accessed 24.10.2011, 2011.

[37] Konarka. Power Plastic Products. *http://www.konarka.com/index.php/power-plastic/ power-plastic-products.*, Accessed 14.09.2011.

[38] J. Hachmann, R. Olivares-Amaya, S. Atahan-Evrenk, C. Amador-Bedolla, R. S. Sanchez-Carrera, A. Gold-Parker, L. Vogt, A. M. Brockway, and A. Aspuru-Guzik. The Harvard Clean Energy Project: Large-Scale Computational Screening and Design of Organic Photovoltaics on the World Community Grid. *The Journal of Physical Chemistry Letters*, 2:2241–2251, 2011.

[39] ASTM Reference Spectra. *http://rredc.nrel.gov/solar/spectra/am1.5/ASTMG173/ ASTMG173.html*, (Accessed 18.09.2011).

[40] DWD. Globalstrahlung in der Bundesrepublik Deutschland. *http://www.dwd.de/bvbw/ appmanager/bvbw/dwdwwwDesktop*, (Accessed 17.08.2011), 2010.

[41] P. Würfel. Thermodynamic limitations to solar energy conversion. *Physica E*, 14:18 – 26, 2002.

[42] S. M. Sze. *Physics of Semiconductor Devices.* John Wiley and Sons, 2nd edition, 1981.

[43] C. Kittel. *Einführung in die Festkörperphysik.* Oldenbourg Wissenschaftsverlag, 2002.

[44] C. Jacoboni. *Theory of Electron Transport in Semiconductors : A Pathway from Elementary Physics to Nonequilibrium Green Functions.* Springer Berlin Heidelberg, 2010.

[45] P. Würfel. The chemical potential of radiation. *Journal of Physics C: Solid State Physics*, 15(18):3967–3985, 1982.

[46] W. Shockley and W. Read. Statistics of the Recombinations of Holes and Electrons. *Physical Review*, 87(5):835–842, 1952.

[47] F. Bloch. Uber die Quantenmechanik der Elekronen in Kristallgittern. *Zeitschrift für Physik A*, pages 555–600, 1929.

[48] K. Leo, P. H. Bolivar, and F. Bruggemann. Observation of Bloch oscillations in a semiconductor superlattice. *Solid State Communications*, 84(10):943–946, 1992.

[49] J. R. Hauser and P. M. Dunbar. Performance limitations of silicon solar cells. *IEEE Transactions on Electron Devices*, 24(4):305–321, 1977.

[50] J. G. Fossum and E. L. Burgess. High-efficiency p+-n-n+ back-surface-field silicon solar cells. *Applied Physics Letters*, 33(3):238–240, 1978.

[51] B. O'regan and M. Grätzel. A low-cost, high-efficiency solar cell based on dye-sensitized colloidal TiO2 films. *Nature*, 353(6346):737–740, 1991.

[52] M. Grätzel. Recent advances in sensitized mesoscopic solar cells. *Accounts of Chemical Research*, 42(11):1788–1798, 2009.

[53] B. Maennig, D. Gebeyehu, P. Simon, F. Kozlowski, A. Werner, F. Li, S. Grundmann, S. Sonntag, M. Koch, K. Leo, M. Pfeiffer, H. Hoppe, D. Meissner, N. S. Sariciftci, I. Riedel, V. Dyakonov, J. Parisi, and J. Drechsel. Organic p-i-n solar cells. *Applied Physics A*, 79(1):1–14, 2004.

[54] W. Shockley and H. J. Queisser. Detailed Balance Limit of Efficiency of p-n Junction Solar Cells. *Journal of Applied Physics*, 32(3):510–519, 1961.

[55] C. H. Henry. Limiting efficiencies of ideal single and multiple energy gap terrestrial solar cells. *Journal of Applied Physics*, 51(8):4494–4500, 1980.

[56] M. A. Green, K. Emery, Y. Hishikawa, W. Warta, and E. D. Dunlop. Solar cell efficiency tables (Version 38). *Progress in Photovoltaics: Research and Applications*, 19(5):565–572, 2011.

[57] M. A. Green. Third generation photovoltaics: Ultra-high conversion efficiency at low cost. *Progress in Photovoltaics: Research and Applications*, 9(2):123–135, 2001.

[58] N. S. Lewis. Toward cost-effective solar energy use. *Science*, 315(5813):798–801, 2007.

[59] R. F. Service. Solar energy. Can the upstarts top silicon? *Science*, 319(5864):718–720, 2008.

[60] A. D. Vos. Detailed balance limit of the efficiency of tandem solar cells. *Journal of Physics D: Applied Physics*, 13:839–846, 1980.

[61] N. V. Sidgwick and H. M. Powell. Bakerian Lecture. Stereochemical Types and Valency Groups. *Proceedings of the Royal Society of London. Series A. Mathematical and Physical Sciences*, 176(965):153, 1940.

[62] P. Atkins and J. de Paula. *Atkins' Physical Chemistry*. Oxford University Press, 2009.

[63] E. Hückel. Quantentheoretische Beiträge zum Benzolproblem. *Zeitschrift für Physik*, 70(3-4):204–286, 1931.

[64] A. Rocke. Hypothesis and experiment in the early development of Kekulé's benzene theory. *Annals of Science*, 42:355–381, 1985.

[65] K. Tamagawa, T. Iijima, and M. Kimura. Molecular structure of benzene. *Journal of Molecular Structure*, 30(2):243–253, 1976.

[66] F. H. Allen, O. Kennard, D. G. Watson, L. Brammer, A. G. Orpen, and R. Taylor. Tables of bond lengths determined by X-ray and neutron diffraction. Part 1. Bond lengths in organic compounds. *Journal of the Chemical Society, Perkin Transactions II*, (12):1–19, 1987.

[67] M. Schwoerer and H. C. Wolf. *Organic molecular solids*. Wiley-VCH, 2007.

[68] H. Kuhn. A quantum-mechanical theory of light absorption of organic dyes and similar compounds. *The Journal of Chemical Physics*, 17(12):1198–1212, 1949.

[69] V. Bulović, M. A. Baldo, and S. R. Forrest. Excitons and energy transfer in molecular materials. In R. Farchioni and G. Gross, editors, *Organic Electronic Materials*, pages 391–404. Springer, 2001.

[70] M. Kasha. Characterization of electronic transitions in complex molecules. *Discussions of the Faraday Society*, 9:14–19, 1950.

[71] T. Koopmans. Über die Zuordnung von Wellenfunktionen und Eigenwerten zu den Einzelnen Elektronen Eines Atoms. *Physica*, 1(1-6):104–113, 1934.

[72] A. Cravino. Origin of the open circuit voltage of donor-acceptor solar cells: Do polaronic energy levels play a role? *Applied Physics Letters*, 91(24):243502, 2007.

[73] Y. Furukawa. Do bipolarons exist in doped or photoirradiated conjugated polymers? - An analysis based on studies of model compounds. In N. S. Sariciftci, editor, *Primary Photoexcitations in Conjugated Polymers: Molecular Exciton Versus Semiconductor Band Model*, pages 496–522. World Scientific, Singapore, 1997.

[74] T. M. Halasinski, D. M. Hudgins, F. Salama, L. J. Allamandola, and T. Bally. Electronic Absorption Spectra of Neutral Pentacene (C22H14) and Its Positive and Negative Ions in Ne, Ar, and Kr Matrices. *The Journal of Physical Chemistry A*, 104(32):7484–7491, 2000.

[75] R. Schueppel, K. Schmidt, C. Uhrich, K. Schulze, D. Wynands, J. Brédas, E. Brier, E. Reinold, H.-B. Bu, P. Baeuerle, B. Maennig, M. Pfeiffer, and K. Leo. Optimizing organic photovoltaics using tailored heterojunctions: A photoinduced absorption study of oligothiophenes with low band gaps. *Physical Review B*, 77(8):085311, 2008.

[76] M. S. Dresselhaus, G. Dresselhaus, R. Saito, and A. Jorio. Exciton photophysics of carbon nanotubes. *Annual Review of Physical Chemistry*, 58:719–747, 2007.

[77] R. R. Lunt, N. C. Giebink, A. A. Belak, J. B. Benziger, and S. R. Forrest. Exciton diffusion lengths of organic semiconductor thin films measured by spectrally resolved photoluminescence quenching. *Journal of Applied Physics*, 105(5):053711, 2009.

[78] J. Meiss, M. Hermenau, W. Tress, C. Schuenemann, F. Selzer, M. Hummert, J. Alex, G. Lackner, K. Leo, and M. Riede. Tetrapropyl-tetraphenyl-diindenoperylene derivative as a green absorber for high-voltage stable organic solar cells. *Physical Review B*, 83(16):165305, 2011.

[79] H. Bässler. Charge Transport in Disordered Organic Photoconductors. *Physica Status Solidi (b)*, 175(15):15–56, 1993.

[80] A. Miller and E. Abrahams. Impurity conduction at low concentrations. *Physical Review*, 257, 1960.

[81] R. A. Marcus. On the Theory of Oxidation-Reduction Reactions Involving Electron Transfer. I. *The Journal of Chemical Physics*, 24(5):966–978, 1956.

[82] J. Frenkel. On pre-breakdown phenomena in insulators and electronic semi-conductors. *Physical Review*, 54(8):647–648, 1938.

[83] L. J. A. Koster. Charge carrier mobility in disordered organic blends for photovoltaics. *Physical Review B*, 81(20):205318, 2010.

[84] A. B. Walker, A. Kambili, and S. J. Martin. Electrical transport modelling in organic electroluminescent devices. *Journal of Physics: Condensed Matter*, 14(42):9825–9876, 2002.

[85] W. F. Pasveer, J. Cottaar, C. Tanase, R. Coehoorn, P. A. Bobbert, P. W. M. Blom, D. M. de Leeuw, and M. A. J. Michels. Unified Description of Charge-Carrier Mobilities in Disordered Semiconducting Polymers. *Physical Review Letters*, 94(20):206601, 2005.

[86] P. Peumans, A. Yakimov, and S. R. Forrest. Small molecular weight organic thin-film photodetectors and solar cells. *Journal of Applied Physics*, 93(7):3693–3723, 2003.

[87] N. S. Sariciftci, L. Smilowitz, A. J. Heeger, and F. Wudl. Photoinduced electron transfer from a conducting polymer to buckminsterfullerene. *Science*, 258(5087):1474, 1992.

[88] C. J. Brabec, G. Zerza, G. Cerullo, and S. De Silvestri. Tracing photoinduced electron transfer process in conjugated polymer/fullerene bulk heterojunctions in real time. *Chemical Physics*, 340(3-4):232–236, 2001.

[89] J. Müller, J. Lupton, J. Feldmann, U. Lemmer, M. Scharber, N. S. Sariciftci, C. Brabec, and U. Scherf. Ultrafast dynamics of charge carrier photogeneration and geminate recombination in conjugated polymer:fullerene solar cells. *Physical Review B*, 72(19):195208, 2005.

[90] A. A. Bakulin, D. S. Martyanov, D. Y. Paraschuk, M. S. Pshenichnikov, and P. H. M. van Loosdrecht. Ultrafast charge photogeneration dynamics in ground-state charge-transfer complexes based on conjugated polymers. *The Journal of Physical Chemistry B*, 112(44):13730–13737, 2008.

[91] S. Cook, R. Katoh, and A. Furube. Ultrafast Studies of Charge Generation in PCBM:P3HT Blend Films following Excitation of the Fullerene PCBM. *The Journal of Physical Chemistry C*, 113(6):2547–2552, 2009.

[92] T. M. Clarke and J. R. Durrant. Charge photogeneration in organic solar cells. *Chemical Reviews*, 110(11):6736–6767, 2010.

[93] P. Würfel. Photovoltaic Principles and Organic Solar Cells. *Chimia*, 61(12):770–774, 2007.

[94] L. Onsager. Initial recombination of ions. *Physical Review*, 54(8):554–557, 1938.

[95] C. L. Braun. Electric field assisted dissociation of charge transfer states as a mechanism of photocarrier production. *The Journal of Chemical Physics*, 80:4157–4161, 1984.

[96] V. D. Mihailetchi, L. J. A. Koster, J. C. Hummelen, and P. W. M. Blom. Photocurrent Generation in Polymer-Fullerene Bulk Heterojunctions. *Physical Review Letters*, 93(21):216601, 2004.

[97] M. Lenes, L. J. A. Koster, V. D. Mihailetchi, and P. W. M. Blom. Thickness dependence of the efficiency of polymer:fullerene bulk heterojunction solar cells. *Applied Physics Letters*, 88(24):243502, 2006.

[98] M. Limpinsel, A. Wagenpfahl, M. Mingebach, and C. Deibel. Photocurrent in bulk heterojunction solar cells. *Physical Review B*, 81(8):085203, 2010.

[99] H. H. P. Gommans, M. Kemerink, J. M. Kramer, and R. A. J. Janssen. Field and temperature dependence of the photocurrent in polymer/fullerene bulk heterojunction solar cells. *Applied Physics Letters*, 87(12):122104, 2005.

[100] C. Deibel. Charge carrier dissociation and recombination in polymer solar cells. *Physica Status Solidi (a)*, 2736(12):2731–2736, 2009.

[101] M. Hilczer and M. Tachiya. Unified Theory of Geminate and Bulk Electron-Hole Recombination in Organic Solar Cells. *The Journal of Physical Chemistry C*, 114(14):6808–6813, 2010.

[102] P. Panda, D. Veldman, J. Sweelssen, J. J. A. M. Bastiaansen, B. M. W. Langeveld-Voss, and S. C. J. Meskers. Charge transfer absorption for pi-conjugated polymers and oligomers mixed with electron acceptors. *The Journal of Physical Chemistry B*, 111(19):5076–5081, 2007.

[103] K. Vandewal, A. Gadisa, W. D. Oosterbaan, S. Bertho, F. Banishoeib, I. Van Severen, L. Lutsen, T. J. Cleij, D. Vanderzande, and J. V. Manca. The Relation Between Open-Circuit Voltage and the Onset of Photocurrent Generation by Charge-Transfer Absorption

in Polymer : Fullerene Bulk Heterojunction Solar Cells. *Advanced Functional Materials*, 18(14):2064–2070, 2008.

[104] M. Hallermann, I. Kriegel, E. Da Como, J. M. Berger, E. Von Hauff, and J. Feldmann. Charge Transfer Excitons in Polymer/Fullerene Blends: The Role of Morphology and Polymer Chain Conformation. *Advanced Functional Materials*, 19(22):3662–3668, 2009.

[105] K. Tvingstedt, K. Vandewal, A. Gadisa, F. Zhang, J. Manca, and O. Inganäs. Electroluminescence from charge transfer states in polymer solar cells. *Journal of the American Chemical Society*, 131(33):11819–24, 2009.

[106] K.. Vandewal, K. Tvingstedt, A. Gadisa, O. Inganäs, and J. V. Manca. On the origin of the open-circuit voltage of polymer-fullerene solar cells. *Nature Materials*, 8(11):904–909, 2009.

[107] K. Vandewal, L. Goris, I. Haeldermans, M. Nesladek, K. Haenen, P. Wagner, and J. V. Manca. Fourier-Transform Photocurrent Spectroscopy for a fast and highly sensitive spectral characterization of organic and hybrid solar cells. *Thin Solid Films*, 516(20):7135–7138, 2008.

[108] Y. Zhou, K. Tvingstedt, F. Zhang, C. Du, W.-X. Ni, M. R. Andersson, and O. Inganäs. Observation of a Charge Transfer State in Low-Bandgap Polymer/Fullerene Blend Systems by Photoluminescence and Electroluminescence Studies. *Advanced Functional Materials*, 19(20):3293–3299, 2009.

[109] D. Veldman, S. C. J. Meskers, and R. A. J. Janssen. The Energy of Charge-Transfer States in Electron Donor-Acceptor Blends: Insight into the Energy Losses in Organic Solar Cells. *Advanced Functional Materials*, 19(12):1939–1948, 2009.

[110] J. Lee, K. Vandewal, S. R. Yost, M. E. Bahlke, L. Goris, M. A. Baldo, J. V. Manca, and T. Van Voorhis. Charge transfer state versus hot exciton dissociation in polymer-fullerene blended solar cells. *Journal of the American Chemical Society*, 132(34):11878–11878, 2010.

[111] H. Ohkita, S. Cook, Y. Astuti, W. Duffy, S. Tierney, W. Zhang, M. Heeney, I. McCulloch, J. Nelson, D. D. C. Bradley, and J. R. Durrant. Charge carrier formation in polythiophene/fullerene blend films studied by transient absorption spectroscopy. *Journal of the American Chemical Society*, 130(10):3030–42, 2008.

[112] X.-Y. Zhu, Q. Yang, and M. Muntwiler. Charge-transfer excitons at organic semiconductor surfaces and interfaces. *Accounts of Chemical Research*, 42(11):1779–1787, 2009.

[113] M. Muntwiler, Q. Yang, W. Tisdale, and X.-Y. Zhu. Coulomb Barrier for Charge Separation at an Organic Semiconductor Interface. *Physical Review Letters*, 101(19):196403, 2008.

[114] R. D. Pensack and J. B. Asbury. Beyond the Adiabatic Limit: Charge Photogeneration in Organic Photovoltaic Materials. *The Journal of Physical Chemistry Letters*, 1(15):2255–2263, 2010.

[115] D. Wynands, M. Levichkova, K. Leo, C. Uhrich, G. Schwartz, D. Hildebrandt, M. Pfeiffer, and M. Riede. Increase in internal quantum efficiency in small molecular oligothiophene: C60 mixed heterojunction solar cells by substrate heating. *Applied Physics Letters*, 97(7):073503, 2010.

[116] C. G. Shuttle, A. Maurano, R. Hamilton, B. O'Regan, J. C. de Mello, and J. R. Durrant. Charge extraction analysis of charge carrier densities in a polythiophene/fullerene solar cell: Analysis of the origin of the device dark current. *Applied Physics Letters*, 93(18):183501, 2008.

[117] M. C. Scharber, D. Mühlbacher, M. Koppe, P. Denk, C. Waldauf, A. J. Heeger, and C. J. Brabec. Design Rules for Donors in Bulk-Heterojunction Solar Cells-Towards 10 % Energy-Conversion Efficiency. *Advanced Materials*, 18(6):789–794, 2006.

[118] G. Garcia-Belmonte. Temperature dependence of open-circuit voltage in organic solar cells from generation-recombination kinetic balance. *Solar Energy Materials and Solar Cells*, 94(12):2166–2169, 2010.

[119] V. D. Mihailetchi, P. W. M. Blom, J. C. Hummelen, and M. T. Rispens. Cathode dependence of the open-circuit voltage of polymer:fullerene bulk heterojunction solar cells. *Journal of Applied Physics*, 94(10):6849–6854, 2003.

[120] D. Cheyns, J. Poortmans, P. Heremans, C. Deibel, S. Verlaak, B. P. Rand, and J. Genoe. Analytical model for the open-circuit voltage and its associated resistance in organic planar heterojunction solar cells. *Physical Review B*, 77(16):165332, 2008.

[121] M. M. Mandoc, F. B. Kooistra, J. C. Hummelen, B. De Boer, and P. W. M. Blom. Effect of traps on the performance of bulk heterojunction organic solar cells. *Applied Physics Letters*, 91(26):263505, 2007.

[122] J. Nelson, S. A. Choulis, and J. R. Durrant. Charge recombination in polymer/fullerene photovoltaic devices. *Thin Solid Films*, 451:508–514, 2004.

[123] T. Kirchartz, B. Pieters, K. Taretto, and U. Rau. Mobility dependent efficiencies of organic bulk heterojunction solar cells: Surface recombination and charge transfer state distribution. *Physical Review B*, 80(3):035334, 2009.

[124] K. Vandewal, K. Tvingstedt, A. Gadisa, O. Inganäs, and J. V. Manca. Relating the open-circuit voltage to interface molecular properties of donor:acceptor bulk heterojunction solar cells. *Physical Review B*, 81(12):125204, 2010.

[125] R. A. Marcus. Relation between charge transfer absorption and fluorescence spectra and the inverted region. *The Journal of Physical Chemistry*, 93(8):3078–3086, 1989.

[126] U. Rau. Reciprocity relation between photovoltaic quantum efficiency and electroluminescent emission of solar cells. *Physical Review B*, 76(8):085303, 2007.

[127] A. Maurano, R. Hamilton, C. G. Shuttle, A. M Ballantyne, J. Nelson, B. O'Regan, W. Zhang, I. McCulloch, H. Azimi, M. Morana, C. J. Brabec, and J. R. Durrant. Recombination Dynamics as a Key Determinant of Open Circuit Voltage in Organic Bulk Heterojunction Solar Cells: A Comparison of Four Different Donor Polymers. *Advanced Materials*, 22(44):4987–92, 2010.

[128] T. Kirchartz, B. Pieters, J. Kirkpatrick, U. Rau, and J. Nelson. Recombination via tail states in polythiophene:fullerene solar cells. *Physical Review B*, 83(11):115209, 2011.

[129] T. Kirchartz, K. Taretto, and U. Rau. Efficiency Limits of Organic Bulk Heterojunction Solar Cells. *The Journal of Physical Chemistry C*, 113(41):17958–17966, 2009.

[130] R. Sokel and R. C. Hughes. Numerical analysis of transient photoconductivity in insulators. *Journal of Applied Physics*, 53(11):7414–7424, 1982.

[131] C. J. Brabec, A. Cravino, G. Zerza, N. S. Sariciftci, R. Kiebooms, D. Vanderzande, and J. C. Hummelen. Photoactive Blends of Poly (para-phenylenevinylene)(PPV) with Methanofullerenes from a Novel Precursor: Photophysics and Device Performance. *The Journal of Physical Chemistry B*, 105(8):1528–1536, 2001.

[132] C. Waldauf, P. Schilinsky, J. Hauch, and C. J. Brabec. Material and device concepts for organic photovoltaics: towards competitive efficiencies. *Thin Solid Films*, 451:503–507, 2004.

[133] C. Waldauf, M. C. Scharber, P. Schilinsky, J. A. Hauch, and C. J. Brabec. Physics of organic bulk heterojunction devices for photovoltaic applications. *Journal of Applied Physics*, 99(10):104503, 2006.

[134] M. S. Roy, P. Balraju, Y. S. Deol, S. K. Sharma, and G. D. Sharma. Charge-transport and photocurrent generation in bulk heterojunction based on Chloro-aluminum phthalocyanine (ClAlPc) and Rose Bengal (RB). *Journal of Materials Science*, 43(16):5551–5563, 2008.

[135] J. Yu, J. Huang, L. Zhang, and Y. Jiang. Energy losing rate and open-circuit voltage analysis of organic solar cells based on detailed photocurrent simulation. *Journal of Applied Physics*, 106(6):063103, 2009.

[136] A. Cheknane, H. Hilal, F. Djeffal, B. Benyoucef, and J. Charles. An equivalent circuit approach to organic solar cell modelling. *Microelectronics Journal*, 39(10):1173–1180, 2008.

[137] P. Schilinsky, C. Waldauf, J. Hauch, and C. J. Brabec. Simulation of light intensity dependent current characteristics of polymer solar cells. *Journal of Applied Physics*, 95(5):2816–2819, 2004.

[138] P. Kumar, S. C. Jain, V. Kumar, S. Chand, and R. P. Tandon. A model for the current-voltage characteristics of organic bulk heterojunction solar cells. *Journal of Physics D: Applied Physics*, 42(5):055102, 2009.

[139] A. M. Goodman and A. Rose. Double extraction of uniformly generated electron-hole pairs form insulators with non-injecting contacts. *Journal of Applied Physics*, 42(7):2823–2830, 1971.

[140] V. D. Mihailetchi, J. Wildeman, and P. W. M. Blom. Space-Charge Limited Photocurrent. *Physical Review Letters*, 94(12):126602, 2005.

[141] R. A. Street and M. Schoendorf. Interface state recombination in organic solar cells. *Physical Review B*, 81(20):205307, 2010.

[142] K. Hecht. Zum Mechanismus des lichtelektrischen Primärstromes in isolierenden Kristallen. *Zeitschrift für Physik A*, 77(3-4):235–245, 1932.

[143] C. Deibel and V. Dyakonov. Polymer-fullerene bulk heterojunction solar cells. *Reports on Progress in Physics*, 73(9):096401, 2010.

[144] T. Strobel, C. Deibel, and V. Dyakonov. Role of Polaron Pair Diffusion and Surface Losses in Organic Semiconductor Devices. *Physical Review Letters*, 105(26):266602, 2010.

[145] W. Schottky. *Zeitschrift für Physik Z*, 41:570, 1940.

[146] N. F. Mott. Note on the contact between a metal and an insulator or semi-conductor. *Mathematical Proceedings of the Cambridge Philosophical Society*, 34(04):568, 1938.

[147] I. G. Hill, D. Milliron, J. Schwartz, and A. Kahn. Organic semiconductor interfaces: electronic structure and transport properties. *Applied Surface Science*, 166(1-4):354–362, 2000.

[148] J. Bardeen. Surface states and rectification at a metal semi-conductor contact. *Physical Review*, 71(10):717–727, 1947.

[149] A. M. Cowley and S. M. Sze. Surface States and Barrier Height of Metal-Semiconductor Systems. *Journal of Applied Physics*, 36(10):3212–3220, 1965.

[150] V. Heine. Theory of surface states. *Physical Review*, 138(6):1689–1696, 1965.

[151] W. Mönch. Metal-semiconductor contacts: electronic properties. *Surface Science*, 299:928–944, 1994.

[152] H. Vazquez, F. Flores, R. Oszwaldowski, J. Ortega, R. Perez, and A. Kahn. Barrier formation at metal-organic interfaces: dipole formation and the charge neutrality level. *Applied Surface Science*, 234(1-4):107–112, 2004.

[153] H. Ishii, K. Sugiyama, E. Ito, and K. Seki. Energy Level Alignment and Interfacial Electronic Structures at Organic/Metal and Organic/Organic Interfaces. *Advanced Materials*, 11(8):605–625, 1999.

[154] J. Hwang, A. Wan, and A. Kahn. Energetics of metal-organic interfaces: New experiments and assessment of the field. *Materials Science and Engineering: R: Reports*, 64(1-2):1–31, 2009.

[155] M. Knupfer and G. Paasch. Origin of the interface dipole at interfaces between undoped organic semiconductors and metals. *Journal of Vacuum Science & Technology A: Vacuum, Surfaces, and Films*, 23(4):1072–1077, 2005.

[156] S. Olthof, W. Tress, R. Meerheim, B. Lüssem, and K. Leo. Photoelectron spectroscopy study of systematically varied doping concentrations in an organic semiconductor layer using a molecular p-dopant. *Journal of Applied Physics*, 106(10):103711, 2009.

[157] A. Crispin, X. Crispin, M. Fahlman, M. Berggren, and W. R. Salaneck. Transition between energy level alignment regimes at a low band gap polymer-electrode interfaces. *Applied Physics Letters*, 89(21):213503, 2006.

[158] M. Fahlman, A. Crispin, X. Crispin, S. K. M. Henze, M. P. de Jong, W. Osikowicz, C. Tengstedt, and W. R. Salaneck. Electronic structure of hybrid interfaces for polymer-based electronics. *Journal of Physics: Condensed Matter*, 19(18):183202, 2007.

[159] C. Tengstedt, W. Osikowicz, W. R. Salaneck, I. D. Parker, C.-H. Hsu, and M. Fahlman. Fermi-level pinning at conjugated polymer interfaces. *Applied Physics Letters*, 88(5):053502, 2006.

[160] P. S. Davids, A. Saxena, and D. L. Smith. Bipolaron lattice formation at metal-polymer interfaces. *Physical Review B*, 53(8):4823–4833, 1996.

[161] J. C. Blakesley and N. C. Greenham. Charge transfer at polymer-electrode interfaces: The effect of energetic disorder and thermal injection on band bending and open-circuit voltage. *Journal of Applied Physics*, 106(3):034507, 2009.

[162] Y. Hirose, A. Kahn, V. Aristov, P. Soukiassian, V. Bulovic, and S. R. Forrest. Chemistry and electronic properties of metal-organic semiconductor interfaces: Al, Ti, In, Sn, Ag, and Au on PTCDA. *Physical Review B*, 54(19):13748–13758, 1996.

[163] Y. Hirose, A. Kahn, V. Aristov, and P. Soukiassian. Chemistry, diffusion, and electronic properties of a metal/organic semiconductor contact: In/perylenetetracarboxylic dianhydride. *Applied Physics Letters*, 68(2):217–219, 1996.

[164] S. T. Lee, Z. Q. Gao, and L. S. Hung. Metal diffusion from electrodes in organic light-emitting diodes. *Applied Physics Letters*, 75(10):1404–1406, 1999.

[165] S. Hagen, Y. Luo, R. Haag, M. Wolf, and P. Tegeder. Electronic structure and electron dynamics at an organic molecule/metal interface: interface states of tetra-tert-butyl-imine/Au(111). *New Journal of Physics*, 12(12):125022, 2010.

[166] P. C. Rusu, G. Giovannetti, C. Weijtens, R. Coehoorn, and G. Brocks. First-principles study of the dipole layer formation at metal-organic interfaces. *Physical Review B*, 81(12):125403, 2010.

[167] M. Lennartz, V. Caciuc, N. Atodiresei, S. Karthäuser, and S. Blügel. Electronic Mapping of Molecular Orbitals at the Molecule-Metal Interface. *Physical Review Letters*, 105(6):066801, 2010.

[168] S. E. Shaheen, R. Radspinner, N. Peyghambarian, and G. E. Jabbour. Fabrication of bulk heterojunction plastic solar cells by screen printing. *Applied Physics Letters*, 79(18):2996–2998, 2001.

[169] F. C. Krebs, M. Jorgensen, K. Norrman, O. Hagemann, J. Alstrup, T. D. Nielsen, J. Fyenbo, K. Larsen, and J. Kristensen. A complete process for production of flexible large area polymer solar cells entirely using screen printing - First public demonstration. *Solar Energy Materials and Solar Cells*, 93(4):422–441, 2009.

[170] F. C. Krebs. Polymer solar cell modules prepared using roll-to-roll methods: Knife-over-edge coating, slot-die coating and screen printing. *Solar Energy Materials and Solar Cells*, 93(4):465–475, 2009.

[171] C. J. Brabec, F. Padinger, J. C. Hummelen, R. A. J. Janssen, and N. S. Sariciftci. Realization of large area flexible fullerene-conjugated polymer photocells: A route to plastic solar cells. *Synthetic Metals*, 102(1-3):861–864, 1999.

[172] F. C. Krebs. Fabrication and processing of polymer solar cells: A review of printing and coating techniques. *Solar Energy Materials and Solar Cells*, 93(4):394–412, 2009.

[173] N. Espinosa, R. García-Valverde, A. Urbina, and F. C. Krebs. A life cycle analysis of polymer solar cell modules prepared using roll-to-roll methods under ambient conditions. *Solar Energy Materials and Solar Cells*, 95(5):1293–1302, 2011.

[174] M. Pfeiffer, A. Beyer, T. Fritz, and K. Leo. Controlled doping of phthalocyanine layers by cosublimation with acceptor molecules: A systematic Seebeck and conductivity study. *Applied Physics Letters*, 73(22):3202–3204, 1998.

[175] M. Pfeiffer. Doped organic semiconductors: Physics and application in light emitting diodes. *Organic Electronics*, 4(2-3):89–103, 2003.

[176] M. Riede, T. Mueller, W. Tress, R. Schueppel, and K. Leo. Small-molecule solar cells - status and perspectives. *Nanotechnology*, 19(42):424001, 2008.

[177] J. Xue, B. P. Rand, S. Uchida, and S. R. Forrest. A Hybrid Planar-Mixed Molecular Heterojunction Photovoltaic Cell. *Advanced Materials*, 17(1):66–71, 2005.

[178] D. Wynands, B. Männig, M. Riede, K. Leo, E. Brier, E. Reinold, and P. Bäuerle. Organic thin film photovoltaic cells based on planar and mixed heterojunctions between fullerene and a low bandgap oligothiophene. *Journal of Applied Physics*, 106(5):054509, 2009.

[179] H. R. Kerp and E. E. Van Faassen. Effects of oxygen on exciton transport in zinc phthalocyanine layers. *Chemical Physics Letters*, 332(1-2):5–12, 2000.

[180] Th. B. Singh, N. S. Sariciftci, H. Yang, L. Yang, B. Plochberger, and H. Sitter. Correlation of crystalline and structural properties of C60 thin films grown at various temperature with charge carrier mobility. *Applied Physics Letters*, 90(21):213512, 2007.

[181] R. R. Lunt, J. B. Benziger, and S. R. Forrest. Relationship between crystalline order and exciton diffusion length in molecular organic semiconductors. *Advanced Materials*, 22(11):1233–1236, 2010.

[182] D. Kurrle and J. Pflaum. Exciton diffusion length in the organic semiconductor diindenoperylene. *Applied Physics Letters*, 92(13):133306, 2008.

[183] S. G. Bratsch. Revised Mulliken electronegativities: II. Applications and limitations. *Journal of Chemical Education*, 65(3):223–227, 1988.

[184] C. Hansch, A. Leo, and R. W. Taft. A survey of Hammett substituent constants and resonance and field parameters. *Chemical Reviews*, 91(2):165–195, 1991.

[185] B. A. Gregg. Bilayer molecular solar cells on spin-coated TiO2 substrates. *Chemical Physics Letters*, 258(3-4):376–380, 1996.

[186] S. Senthilarasu, S. Velumani, R. Sathyamoorthy, G. Canizal, P.. J. Sebastian, J. A. Chavez, R. Perez, A. Subbarayan, and J. A. Ascencio. Characterization of zinc phthalocyanine (ZnPc) for photovoltaic applications. *Applied Physics A*, 77(3-4):383–389, 2003.

[187] M.-S. Liao and S. Scheiner. Electronic structure and bonding in metal phthalocyanines, Metal=Fe, Co, Ni, Cu, Zn, Mg. *The Journal of Chemical Physics*, 114(22):9780–9791, 2001.

[188] B. P. Rand, J. Xue, F. Yang, and S. R. Forrest. Organic solar cells with sensitivity extending into the near infrared. *Applied Physics Letters*, 87(23):233508, 2005.

[189] R. F. Bailey-Salzman, B. P. Rand, and S. R. Forrest. Near-infrared sensitive small molecule organic photovoltaic cells based on chloroaluminum phthalocyanine. *Applied Physics Letters*, 91(1):013508, 2007.

[190] P. N. Day, Z. Wang, and R. Pachter. Calculation of the structure and absorption spectra of phthalocyanines in the gas-phase and in solution. *Journal of Molecular Structure (Theochem)*, 455(1):33–50, 1998.

[191] C. Schünemann, C. Elschner, A. A. Levin, M. Levichkova, K. Leo, and M. Riede. Zinc phthalocyanine - Influence of substrate temperature, film thickness, and kind of substrate on the morphology. *Thin Solid Films*, 519(11):3939–3945, 2011.

[192] J. Meiss, A. Merten, M. Hein, C. Schuenemann, S. Schäfer, M. Tietze, C. Uhrich, M. Pfeiffer, K. Leo, and M. Riede. Fluorinated Zinc Phthalocyanine as Donor for Efficient Vacuum-Deposited Organic Solar Cells. *Advanced Functional Materials*, 2011.

[193] U. Weiler, T. Mayer, W. Jaegermann, C. Kelting, D. Schlettwein, S. Makarov, and D. Wöhrle. Electronic Energy Levels of Organic Dyes on Silicon: A Photoelectron Spectroscopy Study of ZnPc, F 16 ZnPc, and ZnTPP on p-Si(111):H. *The Journal of Physical Chemistry B*, 108(50):19398–19403, 2004.

[194] S. Cho, Y. Yi, M. Noh, M. Cho, K. Yoo, K. Jeong, and C. Whang. Energy level alignment in N,N'-bis(1-naphthyl)-N,N'-diphenyl-1,1'-biphenyl-4,4'-diamine (NPB)/hexadecafluoro copper phthalocyanine (F16CuPc)/Au and NPB/CuPc/Au heterojunction. *Synthetic Metals*, 158(13):539–543, 2008.

[195] W. Chen, H. Huang, S. Chen, Y. L. Huang, X. Y. Gao, and A. T. S. Wee. Molecular orientation-dependent ionization potential of organic thin films. *Chemistry of Materials*, 20(22):7017–7021, 2008.

[196] M. Wehmeier, M. Wagner, and K. Müllen. Novel Perylene Chromophores Obtained by a Facile Oxidative Cyclodehydrogenation Route. *Chemistry - A European Journal*, 7(10):2197–2205, 2001.

[197] A. C. Dürr, F. Schreiber, M. Münch, N. Karl, B. Krause, V. Kruppa, and H. Dosch. High structural order in thin films of the organic semiconductor diindenoperylene. *Applied Physics Letters*, 81(12):2276–2278, 2002.

[198] J. Wagner, M. Gruber, A. Hinderhofer, A. Wilke, B. Bröker, J. Frisch, P. Amsalem, A. Vollmer, A. Opitz, N. Koch, F. Schreiber, and W. Brütting. High Fill Factor and Open Circuit Voltage in Organic Photovoltaic Cells with Diindenoperylene as Donor Material. *Advanced Functional Materials*, 20(24):4295–4303, 2010.

[199] A. J. Ferguson and T. S. Jones. Photophysics of PTCDA and Me-PTCDI thin films: effects of growth temperature. *The Journal of Physical Chemistry B*, 110(13):6891–6898, 2006.

[200] H. W. Kroto, J. R. Heath, S. C. O'Brian, R. F. Curl, and R. E. Smalley. C60: Buckminsterfullerene. *Nature*, 318:162–163, 1985.

[201] W. Krätschmer, L. D. Lamb, K. Fostiropoulos, and D. R. Huffman. Solid C60: a new form of carbon. *Nature*, 347:354–357, 1990.

[202] W. Krätschmer, K. Fostiropoulos, and D. R. Huffman. The infrared and ultraviolet absorption spectra of laboratory-produced carbon dust: evidence for the presence of the C60 molecule. *Chemical Physics Letters*, 170(2-3):167–170, 1990.

[203] K. Hedberg, L. Hedberg, D. S. Bethune, C. A. Brown, H. C. Dorn, R. D. Johnson, and M. De Vries. Bond lengths in free molecules of buckminsterfullerene, C60, from gas-phase electron diffraction. *Science*, 254(5030):410–412, 1991.

[204] S. Liu, Y. J. Lu, M. M. Kappes, and J. A. Ibers. The structure of the C60 molecule: X-ray crystal structure determination of a twin at 110 K. *Science*, 254(5030):408–410, 1991.

[205] M. Wojdyla, B. Derkowska, Z. Lukasiak, and W. Bala. Absorption and photoreflectance spectroscopy of zinc phthalocyanine (ZnPc) thin films grown by thermal evaporation. *Materials Letters*, 60(29-30):3441–3446, 2006.

[206] N. S. Hush and I. S. Woolsey. The electronic absorption spectra of phthalocyanine monomers and dimers. *Molecular Physics*, 21(3):465–474, 1971.

[207] U. Zhokhavets, T. Erb, G. Gobsch, M. Al-Ibrahim, and O. Ambacher. Relation between absorption and crystallinity of poly(3-hexylthiophene)/fullerene films for plastic solar cells. *Chemical Physics Letters*, 418(4-6):347–350, 2006.

[208] I. Bochukov, W. Schindler, B. Johnev, T. Mete, and K. Fostiropoulos. Surface engineering of transparent conductive oxide (TCO) electrode using molecular termination layers. *Chemical Physics Letters*, 511(4-6):363–366, 2011.

[209] C. Schünemann, K. Leo, and M. Riede. *in preparation*.

[210] M. Kröger, S. Hamwi, J. Meyer, T. Riedl, W. Kowalsky, and A. Kahn. P-type doping of organic wide band gap materials by transition metal oxides: A case-study on Molybdenum trioxide. *Organic Electronics*, 10(5):932–938, 2009.

[211] M. Hermenau, M. Riede, K. Leo, S. A. Gevorgyan, F. C. Krebs, and K. Norrman. Water and oxygen induced degradation of small molecule organic solar cells. *Solar Energy Materials and Solar Cells*, 95(5):1268–1277, 2011.

[212] S. Scholz, C. Corten, K. Walzer, D. Kuckling, and K. Leo. Photochemical reactions in organic semiconductor thin films. *Organic Electronics*, 8(6):709–717, 2007.

[213] S. R. Forrest. Ultrathin Organic Films Grown by Organic Molecular Beam Deposition and Related Techniques. *Chemical Reviews*, 97(6):1793–1896, 1997.

[214] J. Drechsel, A. Petrich, M. Koch, S. Pfützner, R. Meerheim, S. Scholz, K. Walzer, M. Pfeiffer, and K. Leo. 53.3: Influence of Material Purification by Vacuum Sublimation on Organic Optoelectronic Device Performance. *SID Symposium Digest of Technical Papers*, 37(1):1692–1695, 2006.

[215] P. Freitag. White Top-Emitting OLEDs on Metal Substrates. *TU Dresden, PhD thesis*, 2010.

[216] S. Corvers. Transients in organic solar cells. *TU Dresden, Master Thesis*, 2012.

[217] Z. Li, F. Gao, N. C. Greenham, and C. R. McNeill. Comparison of the Operation of Polymer/Fullerene, Polymer/Polymer, and Polymer/Nanocrystal Solar Cells: A Transient Photocurrent and Photovoltage Study. *Advanced Functional Materials*, 21(8):1419–1431, 2011.

[218] P. K. Watkins, A. B. Walker, and G. L. B. Verschoor. Dynamical Monte Carlo modelling of organic solar cells: the dependence of internal quantum efficiency on morphology. *Nano Letters*, 5(9):1814–1818, 2005.

[219] J. Nelson, J. J. Kwiatkowski, J. Kirkpatrick, and J. M. Frost. Modeling charge transport in organic photovoltaic materials. *Accounts of Chemical Research*, 42(11):1768–78, 2009.

[220] R. A. Marsh, C. Groves, and N. C. Greenham. A microscopic model for the behavior of nanostructured organic photovoltaic devices. *Journal of Applied Physics*, 101(8):083509, 2007.

[221] F. Yang and S. R. Forrest. Photocurrent generation in nanostructured organic solar cells. *ACS Nano*, 2(5):1022–1032, 2008.

[222] T. Offermans, S. C. J. Meskers, and R. A. J. Janssen. Monte-Carlo simulations of geminate electron-hole pair dissociation in a molecular heterojunction: a two-step dissociation mechanism. *Chemical Physics*, 308(1-2):125–133, 2005.

[223] C. Groves and N. Greenham. Bimolecular recombination in polymer electronic devices. *Physical Review B*, 78(15):155205, 2008.

[224] J. Staudigel, M. Stössel, F. Steuber, and J. Simmerer. A quantitative numerical model of multilayer vapor-deposited organic light emitting diodes. *Journal of Applied Physics*, 86(7):3895–3910, 1999.

[225] P. S. Davids, I. H. Campbell, and D. L. Smith. Device model for single carrier organic diodes. *Journal of Applied Physics*, 82(12):6319, 1997.

[226] L. J. A. Koster, E. C. P. Smits, V. D. Mihailetchi, and P. W. M. Blom. Device model for the operation of polymer/fullerene bulk heterojunction solar cells. *Physical Review B*, 72(8):085205, 2005.

[227] J. Barker, C. Ramsdale, and N. Greenham. Modeling the current-voltage characteristics of bilayer polymer photovoltaic devices. *Physical Review B*, 67(7):075205, 2003.

[228] M. Glatthaar, M. Riede, N. Keegan, K. Sylvester-Hvid, B. Zimmermann, M. Niggemann, A. Hinsch, A. Gombert, and K. Sylvesterhvid. Efficiency limiting factors of organic bulk heterojunction solar cells identified by electrical impedance spectroscopy. *Solar Energy Materials and Solar Cells*, 91(5):390–393, 2007.

[229] S. Lacic and O. Inganäs. Modeling electrical transport in blend heterojunction organic solar cells. *Journal of Applied Physics*, 97(12):124901, 2005.

[230] G. A. Buxton and N. Clarke. Computer simulation of polymer solar cells. *Modelling and Simulation in Materials Science and Engineering*, 15(2):13–26, 2007.

[231] R. Häusermann, E. Knapp, M. Moos, N. A. Reinke, T. Flatz, and B. Ruhstaller. Coupled optoelectronic simulation of organic bulk-heterojunction solar cells: Parameter extraction and sensitivity analysis. *Journal of Applied Physics*, 106(10):104507, 2009.

[232] Y. Roichman and N. Tessler. Generalized Einstein relation for disordered semiconductors - implications for device performance. *Applied Physics Letters*, 80(11):1948–1950, 2002.

[233] K. Harada, A. Werner, M. Pfeiffer, C. Bloom, C. Elliott, and K. Leo. Organic Homojunction Diodes with a High Built-in Potential: Interpretation of the Current-Voltage Characteristics by a Generalized Einstein Relation. *Physical Review Letters*, 94(3):036601, 2005.

[234] Y.-Q. Peng, J.-H. Yang, and F.-P. Lu. Generalization of Einstein relation for doped organic semiconductors. *Applied Physics A*, 83(2):305–311, 2006.

[235] F. Neumann, Y. A. Genenko, and H. Von Seggern. The Einstein relation in systems with trap-controlled transport. *Journal of Applied Physics*, 99(1):013704, 2006.

[236] L. Li, G. Meller, and H. Kosina. Einstein relation in hopping transport of organic semiconductors. *Journal of Applied Physics*, 106(1):013714, 2009.

[237] V. I. Arkhipov, P. Heremans, E. V. Emelianova, and G. J. Adriaenssens. Space-charge-limited currents in materials with Gaussian energy distributions of localized states. *Applied Physics Letters*, 79(25):4154–4156, 2001.

[238] L. A. A. Pettersson, L. S. Roman, and O. Inganäs. Modeling photocurrent action spectra of photovoltaic devices based on organic thin films. *Journal of Applied Physics*, 86(1):487–496, 1999.

[239] E. Centurioni. Generalized matrix method for calculation of internal light energy flux in mixed coherent and incoherent multilayers. *Applied Optics*, 44(35):7532–7539, 2005.

[240] D. L. Scharfetter and H. K. Gummel. Large-signal analysis of a silicon read diode oscillator. *IEEE Transactions on Electron Devices*, 16:64–77, 1969.

[241] H. K. Gummel. A self-consistent iterative scheme for one-dimensional steady state transistor calculations. *IEEE Transactions on Electron Devices*, 11(10):455–465, 1964.

[242] S. Selberherr. *Analysis and Simulation of Semiconductor Devices*. Springer New York Inc., 1984.

[243] Y. A. Omelchenko and H. Karimabadi. Self-adaptive time integration of flux-conservative equations with sources. *Journal of Computational Physics*, 216(1):179–194, 2006.

[244] D. M. Pai. Transient Photoconductivity in Poly (N-vinylcarbazole). *The Journal of Chemical Physics*, 52:2285–2291, 1970.

[245] W. D. Gill. Drift mobilities in amorphous charge-transfer complexes of trinitrofluorenone and poly-n-vinylcarbazole. *Journal of Applied Physics*, 43(12):5033–5040, 1972.

[246] S. E. Debebe, W. Mammo, T. Yohannes, F. Tinti, A. Martelli, and N. Camaioni. Hole-transport properties of a low-band gap alternating polyfluorene. *Journal of Applied Physics*, 108(2):023709, 2010.

[247] D. H. Dunlap, P. E. Parris, and V. M. Kenkre. Charge-Dipole Model for the Universal Field Dependence of Mobilities in Molecularly Doped Polymers. *Physical Review Letters*, 77(3):542–545, 1996.

[248] L. Li, S. Van Winckel, J. Genoe, and P. Heremans. Electric field-dependent charge transport in organic semiconductors. *Applied Physics Letters*, 95(15):153301, 2009.

[249] J. Widmer. Temperature dependent behaviour of organic solar cells. *TU Dresden, Diplomarbeit*, 2009.

[250] W. Tress and S. Schäfer. Simulation of ZnPc devices. *unpublished report*, 2010.

[251] A. Pivrikas, G. Juška, A. J. Mozer, M. Scharber, K. Arlauskas, N. S. Sariciftci, H. Stubb, and R. Österbacka. Bimolecular recombination coefficient as a sensitive testing parameter for low-mobility solar-cell materials. *Physical Review Letters*, 94(17):176806, 2005.

[252] A. Pivrikas, N. S. Sariciftci, G. Juška, and R. Österbacka. A review of charge transport and recombination in polymer/fullerene organic solar cells. *Progress in Photovoltaics: Research and Applications*, 15(8):677–696, 2007.

[253] C. Deibel, A. Baumann, and V. Dyakonov. Polaron recombination in pristine and annealed bulk heterojunction solar cells. *Applied Physics Letters*, 93(16):163303, 2008.

[254] P. Langevin. *Annales des Chimie et des Physique*, VII(28):433, 1903.

[255] L. J. A. Koster, V. D. Mihailetchi, and P. W. M. Blom. Bimolecular recombination in polymer/fullerene bulk heterojunction solar cells. *Applied Physics Letters*, 88(5):052104, 2006.

[256] C. Deibel, A. Wagenpfahl, and V. Dyakonov. Origin of reduced polaron recombination in organic semiconductor devices. *Physical Review B*, 80(7):075203, 2009.

[257] G. J. Adriaenssens and V. I. Arkhipov. Non-Langevin recombination in disordered materials with random potential distributions. *Solid State Communications*, 103(9):541–543, 1997.

[258] L. Tzabari and N. Tessler. Shockley-Read-Hall recombination in P3HT:PCBM solar cells as observed under ultralow light intensities. *Journal of Applied Physics*, 109(6):064501, 2011.

[259] J. C. Scott and G. G. Malliaras. Charge injection and recombination at the metal-organic interface. *Chemical Physics Letters*, 299(2):115–119, 1999.

[260] J. Blochwitz, T. Fritz, M. Pfeiffer, and K. Leo. Interface electronic structure of organic semiconductors with controlled doping levels. *Organic Electronics*, 2(2):97–104, 2001.

[261] S. Olthof, R. Meerheim, M. Schober, and K. Leo. Energy level alignment at the interfaces in a multilayer organic light-emitting diode structure. *Physical Review B*, 79(24):245308, 2009.

[262] N. F. Mott and R. W. Gurney. *Electronic processes in ionic crystals*. Dover Publications Inc., 2nd edition, 1964.

[263] D. A. Cole, J. R. Shallenberger, S. W. Novak, R. L. Moore, M. J. Edgell, S. P. Smith, C. J. Hitzman, J. F. Kirchhoff, E. Principe, W. Nieveen, F. K. Huang, S. Biswas, R. J. Bleiler, and K. Jones. SiO2 thickness determination by x-ray photoelectron spectroscopy, Auger electron spectroscopy, secondary ion mass spectrometry, Rutherford backscattering, transmission electron microscopy, and ellipsometry. *Journal of Vacuum Science & Technology B: Microelectronics and Nanometer Structures*, 18(1):440–444, 2000.

[264] A. B. Djurisic, T. Fritz, and K. Leo. Determination of optical constants of thin absorbing films from normal incidence reflectance and transmittance measurements. *Optics Communications*, 166(1-6):35–42, 1999.

[265] Y. Li, Y. Cao, J. Gao, D. Wang, and G. Yu. Electrochemical properties of luminescent polymers and polymer light-emitting electrochemical cells. *Synthetic Metals*, pages 243–248, 1999.

[266] S. Hüfner. *Photoelectron spectroscopy: principles and applications*. Springer Verlag, 2003.

[267] W. Gao and A. Kahn. Controlled p-doping of zinc phthalocyanine by coevaporation with tetrafluorotetracyanoquinodimethane: A direct and inverse photoemission study. *Applied Physics Letters*, 79(24):4040–4042, 2001.

[268] D. Zahn, G. Gavrila, and M. Gorgoi. The transport gap of organic semiconductors studied using the combination of direct and inverse photoemission. *Chemical Physics*, 325(1):99–112, 2006.

[269] M. Nonnenmacher, M. P. O'Boyle, and H. K. Wickramasinghe. Kelvin probe force microscopy. *Applied Physics Letters*, 58(25):2921–2923, 1991.

[270] A. Kikukawa, S. Hosaka, and R. Imura. Silicon pn junction imaging and characterizations using sensitivity enhanced Kelvin probe force microscopy. *Applied Physics Letters*, 66(25):3510–3512, 1995.

[271] K. P. Puntambekar, P. V. Pesavento, and C. D. Frisbie. Surface potential profiling and contact resistance measurements on operating pentacene thin-film transistors by Kelvin probe force microscopy. *Applied Physics Letters*, 83(26):5539–5541, 2003.

[272] H. Hoppe, T. Glatzel, M. Niggemann, A. Hinsch, M. Ch. Lux-Steiner, and N. S. Sariciftci. Kelvin probe force microscopy study on conjugated polymer/fullerene bulk heterojunction organic solar cells. *Nano Letters*, 5(2):269–274, 2005.

[273] E. Barsoukov and J. R. MacDonald. *Impedance spectroscopy: theory, experiment, and applications.* LibreDigital, 2005.

[274] R. R. Haering and E. N. Adams. Theory and application of thermally stimulated currents in photoconductors. *Physical Review*, 117(2):451–454, 1960.

[275] R. Schmechel and H. Von Seggern. Electronic traps in organic transport layers. *Physica Status Solidi (a)*, 201(6):1215–1235, 2004.

[276] I. H. Campbell, D. L. Smith, C. J. Neef, and J. P. Ferraris. Consistent time-of-flight mobility measurements and polymer light-emitting diode current-voltage characteristics. *Applied Physics Letters*, 74(19):2809–2811, 1999.

[277] S. Berleb and W. Brütting. Dispersive Electron Transport in tris(8-Hydroxyquinoline) Aluminum (Alq3) Probed by Impedance Spectroscopy. *Physical Review Letters*, 89(28):286601, 2002.

[278] S. W. Tsang, S. K. So, and J. B. Xu. Application of admittance spectroscopy to evaluate carrier mobility in organic charge transport materials. *Journal of Applied Physics*, 99(1):013706, 2006.

[279] T. M. Brown, J. S. Kim, R. H. Friend, F. Cacialli, R. Daik, and W. J. Feast. Built-in field electroabsorption spectroscopy of polymer light-emitting diodes incorporating a doped poly (3, 4-ethylene dioxythiophene) hole injection layer. *Applied Physics Letters*, 75(12):1679–1681, 1999.

[280] M. R. McCartney, F. A. Ponce, J. Cai, and D. P. Bour. Mapping electrostatic potential across an AlGaN/InGaN/AlGaN diode by electron holography. *Applied Physics Letters*, 76(21):3055–3057, 2000.

[281] P. Formanek and E. Bugiel. Specimen preparation for electron holography of semiconductor devices. *Ultramicroscopy*, 106(4-5):365–375, 2006.

[282] A. Wagenpfahl, D. Rauh, M. Binder, C. Deibel, and V. Dyakonov. S-shaped current-voltage characteristics of organic solar devices. *Physical Review B*, 82(11):115306, 2010.

[283] M. M. Mandoc, L. J. A. Koster, and P. W. M. Blom. Optimum charge carrier mobility in organic solar cells. *Applied Physics Letters*, 90(13):133504, 2007.

[284] Y.-X. Wang, S.-R. Tseng, H.-F. Meng, K.-C. Lee, C.-H. Liu, and S.-F. Horng. Dark carrier recombination in organic solar cell. *Applied Physics Letters*, 93(13):133501, 2008.

[285] J.-T. Shieh, C.-H. Liu, H.-F. Meng, S.-R. Tseng, Y.-C. Chao, and S.-F. Horng. The effect of carrier mobility in organic solar cells. *Journal of Applied Physics*, 107(8):084503, 2010.

[286] J. D. Kotlarski, D. J. D. Moet, and P. W. M. Blom. Role of balanced charge carrier transport in low band gap polymer:Fullerene bulk heterojunction solar cells. *Journal of Polymer Science Part B: Polymer Physics*, 49(10):708–711, 2011.

[287] A. Wagenpfahl, C. Deibel, and V. Dyakonov. Organic solar cell efficiencies under the aspect of reduced surface recombination velocities. *IEEE Journal of Selected Topics in Quantum Electronics*, 16(6):1759–1763, 2010.

[288] C. J. Brabec, S. E. Shaheen, C. Winder, N. S. Sariciftci, and P. Denk. Effect of LiF/metal electrodes on the performance of plastic solar cells. *Applied Physics Letters*, 80(7):1288–1290, 2002.

[289] V. D. Mihailetchi, P. W. M. Blom, J. C. Hummelen, and M. T. Rispens. Cathode dependence of the open-circuit voltage of polymer:fullerene bulk heterojunction solar cells. *Journal of Applied Physics*, 94(10):6849–6854, 2003.

[290] Z. E. Ooi, R. Jin, J. Huang, Y. F. Loo, A. Sellinger, and J. C. DeMello. On the pseudo-symmetric current-voltage response of bulk heterojunction solar cells. *Journal of Materials Chemistry*, 18(14):1644–1651, 2008.

[291] B. P. Rand, D. P. Burk, and S. R. Forrest. Offset energies at organic semiconductor heterojunctions and their influence on the open-circuit voltage of thin-film solar cells. *Physical Review B*, 75(11):115327, 2007.

[292] C. J. Brabec, A. Cravino, D. Meissner, N. S. Sariciftci, T. Fromherz, M. T. Rispens, L. Sanchez, and J. C. Hummelen. Origin of the Open Circuit Voltage of Plastic Solar Cells. *Advanced Functional Materials*, 11(5):374–380, 2001.

[293] X. Zhou, J. Blochwitz, M. Pfeiffer, A. Nollau, T. Fritz, and K. Leo. Enhanced Hole Injection into Amorphous Hole-Transport Layers of Organic Light-Emitting Diodes Using Controlled p-Type Doping. *Advanced Functional Materials*, 11(4):310–314, 2001.

[294] W. Zhao and A. Kahn. Charge transfer at n-doped organic-organic heterojunctions. *Journal of Applied Physics*, 105(12):123711, 2009.

[295] M. Vogel, S. Doka, Ch. Breyer, M. Ch. Lux-Steiner, and K. Fostiropoulos. On the function of a bathocuproine buffer layer in organic photovoltaic cells. *Applied Physics Letters*, 89(16):163501, 2006.

[296] M. R. Lilliedal, A. J. Medford, M. V. Madsen, K. Norrman, and F. C. Krebs. The effect of post-processing treatments on inflection points in current-voltage curves of roll-to-roll processed polymer photovoltaics. *Solar Energy Materials and Solar Cells*, 94(12):2018–2031, 2010.

[297] K. Schulze, C. Uhrich, R. Schüppel, K. Leo, M. Pfeiffer, E. Brier, E. Reinold, and P. Bäuerle. Efficient Vacuum-Deposited Organic Solar Cells Based on a New Low-Bandgap Oligothiophene and Fullerene C60. *Advanced Materials*, 18(21):2872–2875, 2006.

[298] H. Jin, M. Tuomikoski, J. Hiltunen, P. Kopola, A. Maaninen, and F. Pino. Polymer-Electrode Interfacial Effect on Photovoltaic Performances in Poly(3-hexylthiophene):Phenyl-C61-butyric Acid Methyl Ester Based Solar Cells. *The Journal of Physical Chemistry C*, 113(38):16807–16810, 2009.

[299] C. Uhrich, D. Wynands, S. Olthof, M. Riede, K. Leo, S. Sonntag, B. Maennig, and M. Pfeiffer. Origin of open circuit voltage in planar and bulk heterojunction organic thin-film photovoltaics depending on doped transport layers. *Journal of Applied Physics*, 104(4):43107, 2008.

[300] B. A. Gregg and M. C. Hanna. Comparing organic to inorganic photovoltaic cells: Theory, experiment, and simulation. *Journal of Applied Physics*, 93(6):3605, 2003.

[301] C. Melzer, V. V. Krasnikov, and G. Hadziioannou. Charge transport, injection, and photovoltaic phenomena in oligo (phenylenevinylene) based diodes. *Journal of Polymer Science Part B: Polymer Physics*, 41(21):2665–2673, 2003.

[302] N. S. Christ, S. W. Kettlitz, S. Valouch, S. Züfle, C. Gärtner, M. Punke, and U. Lemmer. Nanosecond response of organic solar cells and photodetectors. *Journal of Applied Physics*, 105(10):104513, 2009.

[303] C. R. McNeill, I. Hwang, and N. C. Greenham. Photocurrent transients in all-polymer solar cells: Trapping and detrapping effects. *Journal of Applied Physics*, 106(2):024507, 2009.

[304] M. Hein. Bestimmung der Ladungsträgerbeweglichkeit in organischen Materialien für organische Solarzellen. *TU Dresden, Diplomarbeit*, pages 52–57, 2010.

[305] M. M. Mandoc, W. Veurman, L. J. A. Koster, B. de Boer, and P. W. M. Blom. Origin of the Reduced Fill Factor and Photocurrent in MDMO-PPV:PCNEPV All-Polymer Solar Cells. *Advanced Functional Materials*, 17(13):2167–2173, 2007.

[306] A. Liu, S. Zhao, S. B. Rim, J. Wu, M. Konemann, P. Erk, and P. Peumans. Control of electric field strength and orientation at the donor-acceptor interface in organic solar cells. *Advanced Materials*, 20(5):1065–1070, 2008.

[307] S. E. Shaheen, C. J. Brabec, N. S. Sariciftci, F. Padinger, T. Fromherz, and J. C. Hummelen. 2.5% efficient organic plastic solar cells. *Applied Physics Letters*, 78(6):841–843, 2001.

[308] M. T. Rispens, A. Meetsma, R. Rittberger, C. J. Brabec, N. S. Sariciftci, and J. C. Hummelen. Influence of the solvent on the crystal structure of PCBM and the efficiency of MDMO-PPV:PCBM 'plastic' solar cells. *Chemical Communications*, (17):2116–2118, 2003.

[309] G. Li, V. Shrotriya, J. Huang, Y. Yao, T. Moriarty, K. Emery, and Y. Yang. High-efficiency solution processable polymer photovoltaic cells by self-organization of polymer blends. *Nature Materials*, 4(11):864–868, 2005.

[310] F. Padinger, R. S. Rittberger, and N. S. Sariciftci. Effects of postproduction treatment on plastic solar cells. *Advanced Functional Materials*, 13(1):85–88, 2003.

[311] L. H. Nguyen, H. Hoppe, T. Erb, S. Günes, G. Gobsch, and N. S. Sariciftci. Effects of Annealing on the Nanomorphology and Performance of Poly(alkylthiophene):Fullerene Bulk-Heterojunction Solar Cells. *Advanced Functional Materials*, 17(7):1071–1078, 2007.

[312] K. Suemori, T. Miyata, M. Hiramoto, and M. Yokoyama. Enhanced Photovoltaic Performance in Fullerene:Phthalocyanine Codeposited Films Deposited on Heated Substrate. *Japanese Journal of Applied Physics*, 43(No. 8A):1014–1016, 2004.

[313] D. Wynands, M. Levichkova, M. Riede, M. Pfeiffer, P. Baeuerle, R. Rentenberger, P. Denner, and K. Leo. Correlation between morphology and performance of low bandgap oligothiophene:C60 mixed heterojunctions in organic solar cells. *Journal of Applied Physics*, 107(1):14517, 2010.

[314] H. Hoppe, M. Niggemann, C. Winder, J. Kraut, R. Hiesgen, A. Hinsch, D. Meissner, and N. S. Sariciftci. Nanoscale Morphology of Conjugated Polymer/Fullerene-Based Bulk-Heterojunction Solar Cells. *Advanced Functional Materials*, 14(10):1005–1011, 2004.

[315] S. Heutz, P. Sullivan, B. M. Sanderson, S. M. Schultes, and T. S. Jones. Influence of molecular architecture and intermixing on the photovoltaic, morphological and spectroscopic properties of CuPc-C60 heterojunctions. *Solar Energy Materials and Solar Cells*, 83(2-3):229–245, 2004.

[316] Y. Kim, S. A. Choulis, J. Nelson, D. D. C. Bradley, S. Cook, and J. R. Durrant. Composition and annealing effects in polythiophene/fullerene solar cells. *Journal of Materials Science*, 40(6):1371–1376, 2005.

[317] J. Sakai, T. Taima, and K. Saito. Efficient oligothiophene:fullerene bulk heterojunction organic photovoltaic cells. *Organic Electronics*, 9(5):582–590, 2008.

[318] C. Yin, M. Schubert, S. Bange, B. Stiller, M. Castellani, D. Neher, M. Kumke, and H.-H. Hörhold. Tuning of the Excited-State Properties and Photovoltaic Performance in PPV-Based Polymer Blends. *The Journal of Physical Chemistry C*, 112(37):14607–14617, 2008.

[319] J. Xue, B. P. Rand, S. Uchida, and S. R. Forrest. Mixed donor-acceptor molecular heterojunctions for photovoltaic applications. II. Device performance. *Journal of Applied Physics*, 98:124903, 2005.

[320] S. H. Park, J. G. Jeong, H.-J. Kim, S.-H. Park, M.-H. Cho, S. W. Cho, Y. Yi, M. Y. Heo, and H. Sohn. The electronic structure of C60/ZnPc interface for organic photovoltaic device with blended layer architecture. *Applied Physics Letters*, 96(1):013302, 2010.

[321] M. Tietze, W. Tress, S. Pfuetzner, S. Olthof, M. Riede, and K. Leo. The correlation of the open-circuit voltage and the ionization potential of ZnPc:C60 solar cells with varied mixing ratio. *in preparation.*

[322] M. Kaur, A. Gopal, R. M. Davis, and J. R. Heflin. Concentration gradient P3OT/PCBM photovoltaic devices fabricated by thermal interdiffusion of separately spin-cast organic layers. *Solar Energy Materials and Solar Cells*, 93(10):1779–1784, 2009.

[323] P. Sullivan, S. Heutz, S. M. Schultes, and T. S. Jones. Influence of codeposition on the performance of CuPc-C60 heterojunction photovoltaic devices. *Applied Physics Letters*, 84(7):1210–1212, 2004.

[324] L. Chen, Y. Tang, X. Fan, C. Zhang, Z. Chu, D. Wang, and D. Zou. Improvement of the efficiency of CuPc/C60-based photovoltaic cells using a multistepped structure. *Organic Electronics*, 10(4):724–728, 2009.

[325] R. Pandey and R. J. Holmes. Graded Donor-Acceptor Heterojunctions for Efficient Organic Photovoltaic Cells. *Advanced Materials*, 22:5301–5305, 2010.

[326] Y. Terao, H. Sasabe, and C. Adachi. Correlation of hole mobility, exciton diffusion length, and solar cell characteristics in phthalocyanine/fullerene organic solar cells. *Applied Physics Letters*, 90(10):103515, 2007.

[327] A. Opitz, J. Wagner, W. Bruetting, A. Hinderhofer, and F. Schreiber. Molecular semiconductor blends: Microstructure, charge carrier transport, and application in photovoltaic cells. *Physica Status Solidi (a)*, 206(12):2683–2694, 2009.

[328] C. Deibel and A. Wagenpfahl. Comment on "Interface state recombination in organic solar cells". *Physical Review B*, 82(20):207301, 2010.

[329] R. Street. Reply to "Comment on 'Interface state recombination in organic solar cells'". *Physical Review B*, 82(20):207302, 2010.

[330] C. Tanase, E. J. Meijer, P. W. M. Blom, and D. M. de Leeuw. Unification of the Hole Transport in Polymeric Field-Effect Transistors and Light-Emitting Diodes. *Physical Review Letters*, 91(21):216601, 2003.

[331] G. A. H. Wetzelaer, M. Kuik, M. Lenes, and P. W. M. Blom. Origin of the dark-current ideality factor in polymer:fullerene bulk heterojunction solar cells. *Applied Physics Letters*, 99(15):153506, 2011.

[332] G. Wetzelaer, L. Koster, and P. Blom. Validity of the Einstein Relation in Disordered Organic Semiconductors. *Physical Review Letters*, 107(6):066605, 2011.

[333] C.-X. Sheng, M. Tong, S. Singh, and Z. Vardeny. Experimental determination of the charge/neutral branching ratio η in the photoexcitation of π-conjugated polymers by broadband ultrafast spectroscopy. *Physical Review B*, 75(8):085206, 2007.

[334] J. Piris, T. E. Dykstra, A. A. Bakulin, P. H. M. Van Loosdrecht, W. Knulst, M. T. Trinh, J. M. Schins, and L. D. A. Siebbeles. Photogeneration and Ultrafast Dynamics of Excitons and Charges in P3HT/PCBM Blends. *The Journal of Physical Chemistry C*, 113(32):14500–14506, 2009.

[335] F. Paquin, G. Latini, M. Sakowicz, P.-L. Karsenti, L. Wang, D. Beljonne, N. Stingelin, and C. Silva. Charge Separation in Semicrystalline Polymeric Semiconductors by Photoexcitation: Is the Mechanism Intrinsic or Extrinsic? *Physical Review Letters*, 106(19):197401, 2011.

[336] D. Ray, M. Furno, E. Siebert-Henze, K. Leo, and M. Riede. Quantitative estimation of electronic quality of zinc phthalocyanine thin films. *Physical Review B*, 84(7):075214, 2011.

[337] I.-H. Hong, M.-W. Lee, Y.-M. Koo, H. Jeong, T.-S. Kim, and O.-K. Song. Effective hole injection of organic light-emitting diodes by introducing buckminsterfullerene on the indium tin oxide anode. *Applied Physics Letters*, 87(6):063502, 2005.

[338] J. Y. Lee. Efficient hole injection in organic light-emitting diodes using C60 as a buffer layer for Al reflective anodes. *Applied Physics Letters*, 88(7):073512, 2006.

[339] E. Knapp and B. Ruhstaller. Numerical impedance analysis for organic semiconductors with exponential distribution of localized states. *Applied Physics Letters*, 99(9):093304, 2011.

[340] B. K. Jones, J. Santana, and M. McPherson. Negative capacitance effects in semiconductor diodes. *Solid State Communications*, 107(2):47–50, 1998.

[341] I. Mora-Seró, J. Bisquert, F. Fabregat-Santiago, G. Garcia-Belmonte, G. Zoppi, K. Durose, Y. Proskuryakov, I. Oja, A. Belaidi, T. Dittrich, R. Tena-Zaera, A. Katty, C. Lévy-Clément, V. Barrioz, and S. J. C. Irvine. Implications of the negative capacitance observed at forward bias in nanocomposite and polycrystalline solar cells. *Nano Letters*, 6(4):640–650, 2006.

[342] G. Dennler, K. Forberich, T. Ameri, C. Waldauf, P. Denk, C. J. Brabec, K. Hingerl, and A. J. Heeger. Design of efficient organic tandem cells: On the interplay between molecular absorption and layer sequence. *Journal of Applied Physics*, 102(12):123109, 2007.

[343] R. Schueppel, R. Timmreck, N. Allinger, T. Mueller, M. Furno, C. Uhrich, K. Leo, and M. Riede. Controlled current matching in small molecule organic tandem solar cells using doped spacer layers. *Journal of Applied Physics*, 107(4):44503, 2010.

[344] J. Gilot, M. M. Wienk, and R. A. J. Janssen. Measuring the External Quantum Efficiency of Two-Terminal Polymer Tandem Solar Cells. *Advanced Functional Materials*, 20(22):3904–3911, 2010.

[345] J. Gilot, M. M. Wienk, and R. A. J. Janssen. Measuring the current density - voltage characteristics of individual subcells in two-terminal polymer tandem solar cells. *Organic Electronics*, 12(4):660–665, 2011.

[346] M. Hiramoto, M. Suezaki, and M. Yokoyama. Effect of thin gold interstitial-layer on the photovoltaic properties of tandem organic solar cell. *Chemistry Letters*, 19(3):327–330, 1990.

[347] R. Timmreck, S. Olthof, K. Leo, and M. Riede. Highly doped layers as efficient electron-hole recombination contacts for tandem organic solar cells. *Journal of Applied Physics*, 108(3):033108, 2010.

[348] H. Kleemann, R. Gutierrez, F. Lindner, S. Avdoshenko, P. D. Manrique, B. Lüssem, G. Cuniberti, and K. Leo. Organic Zener Diodes: Tunneling across the Gap in Organic Semiconductor Materials. *Nano Letters*, pages 4929–4934, 2010.

[349] G. A. M. Hurkx, F. G. O'Hara, and M. P. G. Knuvers. Modelling Forward-Biased Tunneling. *Proceedings of 19th European Solid State Device Research Conference 1989*, pages 793–796, 1989.

[350] G. A. M. Hurkx, D. B. M. Klaassen, and M. P. G. Knuvers. A new recombination model for device simulation including tunneling. *IEEE Transactions on Electron Devices*, 39(2):331–338, 1992.

Acknowledgments

Danksagung

This thesis would not have been possible without the contribution of many people and helping hands. I thank all these individuals mentioning several names in the following and asking for excuse in case of forgetting to mention some names.

Ich möchte allen danken, die mich bei dieser umfangreichen Arbeit unterstützt haben.

Ich bedanke mich bei meinem Doktorvater Professor Dr. Karl Leo für die Möglichkeit, meine Dissertation am Institut für Angewandte Photophysik anzufertigen. Ich habe insbesondere das mir entgegengebrachte Vertrauen und die mir überlassene Freiheit, meine Forschungsschwerpunkte selbst zu setzen, geschätzt, wenngleich dadurch die Arbeit nun einen entsprechenden Umfang angenommen hat. Professor Dr. Uwe Rau sei gedankt für seine Bereitschaft, diese Arbeit zu begutachten.

Besonderer Dank gilt unserem Gruppenleiter und meinem direkten Betreuer Dr. Moritz Riede für die Unterstützung. Trotz seiner vielen Aufgaben fand er die Zeit, sich dieser Arbeit als kritischer Leser anzunehmen. Erwähnt sei insbesondere seine Förderung des Austausches mit anderen Gruppen, die es mir ermöglichte, verschiedene Universitäten und Institute im Ausland zu besuchen und Kontakte in der OPV-Community zu knüpfen.

Ich bedanke mich für das Stipendium der Reiner Lemoine Stiftung einschließlich der interessanten Stipendiatentage. Durch das Stipendium konnte ich mich hauptsächlich auf den wissenschaftlichen Teil meiner Arbeit konzentrieren. Der Heliatek GmbH, Dresden, sei gedankt für die zusätzliche finanzielle Unterstützung, die es mir erlaubte, mehrere internationale Konferenzen zu besuchen.

Den Großteil meiner Arbeitszeit verbrachte ich im Büro Bey95. Ich bin dort immer gerne erschienen und danke meinen (ehemaligen) Bürokollegen Marek Rölke, Toni Müller, Sarah Röttinger, Patricia Freitag, Simone Hofmann, Caroline Weichsel, Tobias Schwab, Franz Selzer, Felix Holzmüller und dem gesamten IAPP, insbesondere der OSOL Gruppe, für die angenehme Arbeitsatmosphäre – sei es am Institut, auf Konferenzen, oder bei weiteren Veranstaltungen wie den Organic Days. Eine besondere Offenheit und Bereitschaft zur wissenschaftlichen Diskussion und gegenseitige Unterstützung zeichnen dieses Institut aus. Dies habe ich sehr geschätzt.

Besonders bedanken möchte ich mich bei folgenden Kollegen und Freunden dafür, dass sie Teile dieser Arbeit und manche Entwürfe meiner Veröffentlichungen Korrektur gelesen haben:

– Johannes Widmer, darüber hinaus für temperaturabhängige Messungen, kritische

Erklärung

Diese Dissertation wurde am Institut für Angewandte Physik/Photophysik der Fakultät Mathematik und Naturwissenschaften an der Technischen Universität Dresden unter wissenschaftlicher Betreuung von Prof. Dr. Karl Leo angefertigt.

Hiermit versichere ich, dass ich die vorliegende Arbeit ohne unzulässige Hilfe Dritter und ohne Benutzung anderer als der angegebenen Hilfsmittel angefertigt habe; die aus fremden Quellen direkt oder indirekt übernommenen Gedanken sind als solche kenntlich gemacht. Die Arbeit wurde bisher weder im Inland noch im Ausland in gleicher oder ähnlicher Form einer anderen Prüfungsbehörde vorgelegt.

Weiterhin versichere ich, dass bisher keine Promotionsverfahren stattgefunden haben.

Ich erkenne die Promotionsordnung der Fakultät Mathematik und Naturwissenschaften an der Technischen Universität Dresden vom 23.02.2011 an.

Dresden, den 21.12.2011

Wolfgang Tress

A book on the device physics of organic solar cells is planned to be published based on this work.

Dissertation

Organic photovoltaics (OPV) is a field of applied research which has been growing rapidly in the last decade leading to a current record value of power-conversion efficiency over ten percent. One major reason for this boom is a potentially low-cost production of solar modules on flexible (polymer) substrate. Furthermore, new applications are expected from flexible or semitransparent organic solar cells.

This dissertation focuses on the electrical processes in organic solar cells developing and employing a one-dimensional drift-diffusion model. The electrical model is combined with an optical model and covers the diffusion of excitons, their separation, and the subsequent transport of charges. In contrast to inorganics, charge-carrier mobilities are low in the investigated materials and charge transport is strongly affected by energy barriers at the electrodes.

The current-voltage characteristics (J-V curve) of a solar cell reflect the electrical processes in the device. Comparing experimental to simulation data, the author discusses the reasons for S-Shaped J-V curves, the role of charge carrier mobilities and energy barriers at interfaces, the dominating recombination mechanisms, the charge carrier generation profile, and other efficiency-limiting processes in small-molecule solar cells.